

AUCKLAND UNIVERSITY OF TECHNOLOGY

DOCTORAL THESIS

COUPLED DYNAMICS RESPONSE ANALYSIS OF A HYBRID FLOATING PLATFORM CONCEPT FOR OFFSHORE WIND TURBINES

Chima CLEMENT
BEng (Hons), MSc (Engineering), MBA (Management)

A thesis submitted in fulfillment of the requirements
for the degree of Doctor of Philosophy

in the

School of Engineering, Computer and Mathematical Sciences
Faculty of Design and Creative Technologies
Department of Mechanical Engineering

January 2021

Declaration of Authorship

I, Chima CLEMENT, declare that this thesis titled, "COUPLED DYNAMICS RESPONSE ANALYSIS OF A HYBRID FLOATING PLATFORM CONCEPT FOR OFFSHORE WIND TURBINES" and the work presented in it are my own. I confirm that:

- This work was done wholly or mainly while in candidature for a research degree at Auckland University of Technology.
- Where any part of this thesis has previously been submitted for a degree or any other qualification at Auckland University of Technology or any other institution, this has been clearly stated.
- Where I have consulted the published work of others, this is always clearly attributed.
- Where I have quoted from the work of others, the source is always given. With the exception of such quotations, this thesis is entirely my own work.
- I have acknowledged all main sources of help.
- Where the thesis is based on work done by myself jointly with others, I have made clear exactly what was done by others and what I have contributed myself.

Signed:

Date: 13th of September 2021

"It is by logic that we prove, but by intuition that we discover. To know how to criticize is good, to know how to create is better.."

Henri Poincare

AUCKLAND UNIVERSITY OF TECHNOLOGY

Abstract

Faculty of Design and Creative Technologies
Department of Mechanical Engineering

Doctor of Philosophy

COUPLED DYNAMICS RESPONSE ANALYSIS OF A HYBRID FLOATING PLATFORM CONCEPT FOR OFFSHORE WIND TURBINES

by Chima CLEMENT

Deepwater Floating platforms for Offshore Wind Turbines (FOWT) are integrated systems that combine Wind Turbine Generators (WTG), floating platforms, and station keeping systems (moorings and/or tethers) responding to wind, wave, and current loadings in a complex way. During the design phase of a FOWT, a coupled dynamics simulation strategy is required to adequately predict the motion responses resulting from the interaction between the environmental loads and the assemblage of the FOWT. Since the introduction of FOWT technology, different coupling methods for numerical dynamic loads simulations have been used to assess and explore the aerodynamic and hydrodynamic response of a FOWT under various environmental conditions. However, an area that needs more attention involves the adequate modelling of coupled dynamics and intricate viscous effect resulting from fluid forces on the FOWT structure under complex environmental loading. This research introduces a streamlined but holistic coupled dynamics simulation strategy known as the SHARPE (**S**treamlined, **H**ydro-**A**ero-**R**igid dynamics, **P**otentials, and viscous **E**ffects) numerical modelling scheme. The SHARPE numerical modelling scheme provides a wholistic assessment of the motion response and loads assessment of a FOWT. In this approach, fluid viscous effects are adequately modelled by performing an unsteady state multi-physics Computational Fluids Dynamics (CFD) simulation. Here, viscous drag force coefficients and viscous damping coefficients are calculated by using a CFD program to solve the Reynolds Averaged Navier Stokes (RANS) equations near the walls of the FOWT assemblage. Thereafter, by introducing a Floating Rigid Body (FRB) model of the FOWT assemblage and a Finite Element (FE) model of the station keeping system, a global performance analysis of the FOWT is performed using an in-house Computer Aided Engineering (CAE) toolset. The FOWT assemblage adopted for this study is the National Renewable Energy Laboratory (NREL) 5-MW baseline wind turbine mounted on a newly developed inhouse hybrid floating platform identified as the TRIgon Hybrid Floater (TRIHF™). The TRIHF™concept for FOWTs is developed based on the design principles that cuts across a Spar-buoy, Tension Leg Platform (TLP), and Semi-Submersible. The SHARPE numerical scheme employed for this study enhances the capability of a potential-based hydrodynamic solver by implementing the viscous damping coefficients obtained from a free decay numerical test and the viscous drag force coefficients due to wind and ocean current loads. The site-specific environmental conditions employed for this research is based on the long-term hindcast data of a pre-assessed OWT Project Development Area (PDA) in New Zealand. Frequency Domain (FD) and Time Domain (TD) analysis are performed to simulate the aerodynamic responses, hydrodynamic responses, structure aerodynamic and hydrodynamic loads, and mooring line tensions...

Acknowledgements

Firstly, a doxology to God almighty for his mercies, grace, favour, and divine strength. I return all the glory to him for all I have achieved and the knowledge he bestowed on me throughout the course of my PhD research.

I am appreciative of the supervisory team Prof. Sascha Kosleck and Prof. Tek Tjing Lie for their unalloyed support and for believing in me. They were always available and very "easy" to work with. Communications with the team throughout my research was excellent. I also want to thank the Auckland University of Technology (AUT) scholarship office for their financial support and for always processing my yearly tuition fees and monthly stipends on time. They made the journey financially smooth and easy for me.

I am immensely grateful for the industry support of Metocean Solutions Limited who provided me with the MetOcean hindcast data that was used in this research. Special credits to Dr. Amy Robertson of the National Renewable Energy Laboratory and Dr. Andrew Goupee of the University Maine for providing me with experimental test data of the DeepCwind-OC5 project that was used in validating the results of my research.

My heartfelt gratitude goes to my amazing parents Elder & Deaconess Chima Clement, thank you for your words of encouragement, prayers, and emotional support. My beloved siblings, Uche, Ebere, Ugo, and Emeka, your words of hope and upliftment will always remain evergreen in my heart. I will not forget the routine phone calls with my best friend and brother from another mother, Obinna Anyanwu. Thank you for always cheering me up with your motivating words.

I am also appreciative of my Church, the Redeemed Christian Church of God (RCCG) Discovery Center. I want to specifically recognise Pastor Ayo & Busola Martins. Thank you for your spiritual guidance and for being a wonderful family and support system to me throughout my PhD research journey. Embarking on this journey without your support is better imagined than experienced.

Contents

Declaration of Authorship **iii**

Abstract **vii**

Acknowledgements **ix**

Contents **xi**

List of Figures **xv**

List of Tables **xxiii**

List of Abbreviations **xxv**

Physical Constants **xxvii**

List of Symbols **xxxv**

1 Introduction **1**
1.1 Background of Study: Wind Energy Trends 1
1.2 Context of Study and Problem Statement 5
1.3 Motivation and Definitions of Research 7
1.4 Goals, Significance, and Scope of Research 10
1.5 Thesis Outline 12

2 Current Research Methodology and Technology Review **15**
2.1 Sources and Mechanism of Aerodynamic Loading 15
2.1.1 Forces and Moments on Wind Turbine Rotors 16
2.1.2 Flow Through Rotor – Axial Momentum Theory 20
2.1.3 Wind Turbine Performance 25
2.2 Aerodynamic Loading Investigation on Offshore Wind Turbines 28
2.2.1 Wind Force Spectrum Modeling 28
2.2.2 Review of Aerodynamic Loading Investigation Methodologies 33
2.3 Sources and Mechanism of Hydrodynamic Loading 40
2.3.1 Wave Theories and Principles 40
2.3.2 Frequency Domain Potential Function Solution for Wave-Structure Interaction 45
2.3.3 Frequency Domain Solution for Wave Pressure, Forces, and Moments . . 51
2.3.4 Time Domain and Frequency Domain Dynamics and Motions 59
2.3.5 Irregular Wave and Wave Spectrum Modelling 62
2.3.6 Ocean Current Forces 63
2.3.7 Wave-Current Interaction 65
2.4 Review of Coupled Dynamics Modelling Methodologies 66

3 Environmental Scoping Assessment and Loads Modelling Strategy 71
3.1 Site Specific Environmental Scoping Assessment . . . 71
3.1.1 Water Depth . . . 74
3.1.2 Proximity to Electrical Substation / Grid Connectivity . . . 74
3.1.3 Inshore Assembly Area . . . 77
3.1.4 Availability and Proximity to Deepwater Navigation Route . . . 78
3.1.5 Socio-Economic Activities . . . 78
Shipping Activity . . . 78
Recreational Sailings and Fishery . . . 79
3.1.6 Military and Civil Radar Considerations/Aviation Activities . . . 80
3.1.7 Marine Protected Areas/Reserves . . . 83
3.1.8 Seabed Conditions . . . 84
3.1.9 Metocean Conditions . . . 85
3.2 Environmental Loads Modelling Strategy . . . 89
3.2.1 Site Specific Metocean Hindcast Data Statistical Analysis . . . 89
3.2.2 Wave Modelling . . . 95
3.2.3 Wind Modelling . . . 98
3.2.4 Ocean Current Modelling . . . 101
3.2.5 Design Load Cases (DLCs) . . . 103

4 The TRIgon Hybrid Floater (TRIHF) FOWT Concept Design 105
4.1 Wind Turbine Baseline . . . 105
4.1.1 Blade Structural and Aerodynamic Properties . . . 106
4.1.2 Rotor-Nacelle Assembly (RNA) Structural Properties . . . 110
4.1.3 Tower Structural Properties . . . 112
4.1.4 Wind Turbine Assemblage Gross Properties . . . 113
4.2 Hybrid Floating Platform Concept Design . . . 114
4.2.1 FOWT Static Stability and Dynamic Stability Resonance . . . 115
4.2.2 TRIgon Hybrid Floater (TRIHF) Concept Rationale and Model Description 126
4.2.3 Theoretical Calculations and Precise Mass Computation . . . 132
4.2.4 Station Keeping Configuration . . . 136

5 SHARPE Numerical Modelling Scheme Development and Validation 141
5.1 SHARPE Numerical Modelling Scheme Description . . . 141
5.2 SHARPE Numerical Modelling Scheme Validation . . . 148
5.2.1 Model Description - The DeepCWind-OC5 Semi-submersible . . . 148
5.2.2 Environmental Conditions and Design Load Case (DLC) . . . 155
5.2.3 Model Validation . . . 156

6 Engineering and Mathematical Analysis 159
6.1 CFD Numerical Simulation Analysis . . . 160
6.1.1 Viscous Damping Numerical Calculation . . . 160
Model Set-up, Boundary Conditions, and Pre-processing Strategies . . . 162
Non-Dimensional Total Damping Coefficient Results and Discussion . . . 169
6.1.2 Viscous Force Numerical Calculation . . . 180
Model Set-up, Boundary Conditions, and Pre-processing Strategies . . . 181
Meshing Strategy and Refinement Study . . . 184
Viscous Force Simulation Results and Discussion . . . 186
6.2 Coupled Dynamics Numerical Simulation . . . 204
6.2.1 Model Set-Up and Analysis Strategy . . . 204

6.2.2 Primal Hydrodynamic Diffraction/Radiation and Stability Analysis in Flat Wave . . . 207
6.2.3 Hydrodynamic Diffraction/Radiation Analysis in Irregular Wave . . . 211
Respond Amplitude Operators (RAOs) . . . 211
Near Field Drift Wave Forces . . . 216
Structure Wave Forces, Panel Pressure and Wave Surface Elevation . . . 218
Hydrostatic Stability Analysis in Irregular Wave . . . 221
6.2.4 Frequency Domain (FD) Hydrodynamic Response Analysis in Irregular Wave . . . 227
6.2.5 Time Domain (TD) Hydrodynamic Response Analysis in Irregular Wave . 240
Structure Position Responses . . . 241
Structure Velocity and Acceleration Responses . . . 248
Structure and Mooring Fairlead Forces . . . 251

7 Conclusion and Outlook **279**

A Matlab Code used for Pre-processing Metocean Hindcast Data **281**
A.1 Current MetOcean Data . . . 282
A.2 Wind MetOcean Data . . . 284
A.3 Wave MetOcean Data . . . 286

B Linearising Element Nodes Definition **289**

C RAO Displacement Results for LC2 **291**

D RAO Displacement Results for LC3 **295**

Bibliography **299**

List of Figures

1.1 Annual Offshore Installations by Country (Left Axis) and Cumulative Capacity (Right Axis)[1]. . . . 2
1.2 Offshore Wind Turbine (OWT) Foundations for Shallow and Mid-Shallow Water Application). . . . 3
1.3 A graphics illustration showing the depth limitation of Fixed Bottom Foundation and Floating Foundation Concepts for Deep and Ultra-deepwater Application | Adopted from [13]. . . . 3
1.4 An illustration showing various fluid-structure interfaces and dynamic loads experienced by a FOWT. . . . 6
1.5 Interfacing Modules in Aero-Hydro-Servo-Elastic Coupled Analysis. Adopted from [25]. . . . 8
1.6 Flow chart showing coupled dynamics strategy comparison between the State-of-the-art approach and New Approach. . . . 14

2.1 An illustration showing various forces and moments acting on a Horizontal Axis Wind Turbine (HAWT) wind components (1) Tower, (2) Nacelle, (3) Hub and (4) Blades. . . . 17
2.2 Geometric Properties and Aerodynamic Forces and Moments Acting on an Aerofoil. . . . 18
2.3 Streamlines around an aerofoil section. . . . 19
2.4 Axial Momentum Flow Model Showing Pressure and Velocity Distribution over a wind turbine rotor acting as a braking disc. . . . 22
2.5 Rotor swept area . . . 24
2.6 Comparison of tangential force (left) and normal force (right) distribution along the blade between numerical predictions and experimental measurements (Adopted from [50]) . . . 34
2.7 Time history of the platform pitch and yaw motion response (Adopted from [51]) 35
2.8 Plot of the normalised equivalent thrust accounting for wind shear and tower shadow (Adopted from [55]) . . . 36
2.9 6 DOF aerodynamic forces Amplitude Spectral Densities (ASDs) for 3 scenarios: a. no platform motion b. platform displacements c. platform displacements + velocities (Adapted from [56]) . . . 36
2.10 Plot showing the fluctuation of power coefficient C_p as a function of pitch angle (left) and thrust coefficient C_T as a function of pitch angle at the optimum tip speed ratio of 8.3 (Adapted from [57]) . . . 37
2.11 NREL 5MW: Vorticity contours (top) and velocity magnitude (bottom) at three stations downstream of the domain (inertial reference frame). Significant vortices emanating from the turbine blade can be observed from the trailing edge. The velocity magnitude is restricted to 10m/s to provide better contrast (Adapted from [58]) . . . 38
2.12 Plot showing normalised mean power against TSR (top left) and reduced frequency (top right), and normalised mean thrust against TSR (bottom left) and reduced frequency (bottom right) (Adapted from [59]) . . . 39

2.13 Plot showing the distribution of the rotor power output (left) and thrust (right) and its association with the platform's surge motion (Adapted from [60]) 39
2.14 Water wave theory selection chart (Adapted from [63]) 41
2.15 Parameters used when defining Airy wave theory 42
2.16 Plot showing changes in flow velocity position with respect to time [71]. 46
2.17 Six Degree of Freedom (6DOF) motion of a floating body under wave action. . . 47
2.18 Hypothetical fluid domain showing boundary conditions for a wave-FOWT structure interaction. 48
2.19 Incident Wave angle, β 49
2.20 Hydrodynamic Gauge pressure on a FOWT (platform only) 52
2.21 Radiation potentials of unit amplitude for 6-DOF on a FOWT 53
2.22 Hydrostatic information on a FOWT. 55
2.23 Regular waves (left) superimposed to produce and irregular wave (right) (Adapted from[75]) 62
2.24 A hypothetical example of an Ocean Wave Spectrum 63
2.25 Interfacing Modules in Aero-Hydro-Servo-Elastic Coupled Analysis [25] 67

3.1 New Zealand's Northland Bathymetric Features | According to Ref [93] 72
3.2 Proposed PDAs for FOWT Project off the coast of New Zealand's North Island. . 73
3.3 New Zealand North Island Electrical Substation Locator Map | Site 1 – Marsden, Whangarei [95]. 75
3.4 New Zealand North Island Electrical Substation Locator Map | Site 2 – Tauranga, Hamilton [95]. 76
3.5 Northport Deepwater Harbour. 77
3.6 New Zealand North Island Marine Traffic Density Map | Site 1 – Whangarei [97]. 78
3.7 New Zealand North Island Marine Traffic Density Map | Site 2 – Hamilton [97]. 79
3.8 New Zealand Recreational Fishing Map | North Island[98]. 80
3.9 New Zealand Commercial Fishing Map | North Island [98]. 80
3.10 New Zealand Airspace Map | North Island [100]. 81
3.11 New Zealand Scheduled Flight Paths Map [100]. 82
3.12 Marine Reserves Map | Site 1 – Whangarei [102]. 83
3.13 Marine Reserves Map | Site 2 – Hamilton [102]. 84
3.14 New Zealand's Ocean Floor [104], [105]. 85
3.15 Metocean Conditions for Mean Significant Wave Height and Mean Wind Speed [106]. 86
3.16 Metocean Conditions for Vector Averaged Current [106]. 87
3.17 Wind rose showing wind speed, direction - blowing from, and frequency for a 10-minute average wind speed for offshore Whangarei at (a) 10 m above sea level (b) 100 m above sea level. 88
3.18 Wind rose showing wind speed, direction - blowing from, and frequency for a 10-minute average wind speed for offshore Tauranga at (a) 10 m above sea level (b) 100 m above sea level. 88
3.19 Process flow chart showing quantitative and qualitative statistical analysis of Metocean hindcast data. 91
3.20 Normal Standard Cumulative Distribution for Wind Resources. 92
3.21 Probability Distribution Curve and Frequency Distribution Histogram for Eastward Wind Resources. 93
3.22 Probability Distribution Curve and Frequency Distribution Histogram for Northward Wind Resources. 94
3.23 Frequency Distribution Histogram for Wind Angle of Attack. 95

3.24 Plot of Wave Period vs JONSWAP Wave Energy Spectra Ordinate for 5 to 1000 Years Return Period. . . . 97
3.25 Site wind Velocity gradient for various return periods for an averaging period of 10 Minutes. . . . 99
3.26 Site wind velocity gradient for various return periods for a reference period of 3 hours. . . . 99
3.27 Plot of Frequency Vs Wind Energy Spectrum for 100 Year Wind Return Period. . . . 100
3.28 Site-specific Current Velocity Depth Profile 102

4.1 Aerofoil used in creating the NREL 5 MW Wind Turbine Rotor Blade. . . . 107
4.2 Full Aerofoil Section for the NREL 5 MW Wind Turbine Rotor Blade. . . . 108
4.3 Side view of blade showing Aerofoil twisted about their Aerodynamic Center. . . . 109
4.4 Completed Loft Surface for Blade Geometry (Label: **Aerofoil Series_Chord Length**).109
4.5 Top and Front view of the Completed Loft Surface for Blade Geometry. . . . 110
4.6 Left: Hub Geometry. Right: Complete Rotor Assemblage with Hub and Blades. . . . 111
4.7 Nacelle CAD model geometry. . . . 111
4.8 Tower CAD model geometry. . . . 112
4.9 The NREL 5 MW wind turbine baseline assemblage CAD model. . . . 113
4.10 An artistic impression of FOWT platform concepts by Joshua Bauer, National Renewable Energy Laboratory (US Department of Energy). Retrieved from [124].Reused with permission. . . . 115
4.11 Inclinations in a floating structure. . . . 116
4.12 Three Centres of a Floating Structure. . . . 116
4.13 Basic Stability Body Force Diagram. . . . 117
4.14 Restoring moment due to heeling inclination on a floating structure. . . . 119
4.15 Radar chart showing platform properties based on boundary conditions and natural periods. . . . 125
4.16 Radar chart showing platform properties based on boundary conditions and natural periods. . . . 126
4.17 An artistic impression of the TRIgon Hybrid Floater (TRIHF) showing its major components and functionality. . . . 129
4.18 TRIHF Platform Components. . . . 130
4.19 Artistic Impression showing the complete FOWT assemblage of TRIHF Platform and NREL 5 MW Wind Turbine Baseline. . . . 131
4.20 Platform precise mass calculation in air (left) and platform hydrostatics precise mass calculation (right). . . . 135
4.21 The TRIHF platform mooring configuration. . . . 136
4.22 Illustration showing mooring connection points on the TRIHF Platform. . . . 137
4.23 Polyester rope and connections used in the taut leg mooring system (adopted from [129]). . . . 138
4.24 Illustration showing mooring line nomenclatures and coordinates. . . . 140

5.1 Abridged version of the SHARPE process flow chart methodology. . . . 142
5.2 Project Schematic for the SHARPE Numerical Modelling Scheme in ANSYS Workbench. . . . 143
5.3 The SHARPE Numerical Modelling Scheme File Structure. . . . 144
5.4 3D model diffracting panels for hydrodynamic diffraction and radiation numerical simulation. . . . 146
5.5 Illustration showing (a) tube elements defined within the diffracting geometry model (b) tube elements. . . . 146

5.6 (a) Image showing the 1/50th scale model of DeepCwind semi-submersible platform used for experimentation in the MARIN offshore basin for the OC4 project. (b) Coordinate system and dimensions of the DeepCwind semi-submersible platform for the OC4 project[29]. . . . 149
5.7 (a) Image showing the 1/50th scale model of DeepCwind semi-submersible platform used for experimentation in the MARIN offshore basin for the OC5 project. (b) The DeepCwind semi-submersible FOWT geometry for the OC5 project [30]. 149
5.8 An artistic impression of the DeepCwind semi-submersible showing (a) front view from the x-direction. (b) top view from the z-direction. (c) isometric view with labelled components. . . . 150
5.9 Artistic impression showing the complete FOWT assemblage of the DeepCwind-OC5 platform and NREL 5 MW wind turbine baseline. . . . 151
5.10 The DeepCwind-OC5 FOWT platform mooring configuration and nomenclature (plan view). . . . 152
5.11 Illustration showing sea domain, mooring line configuration, and coordinates for (a) side view from the y-direction (b) front view from the x-direction used for the validation study. . . . 152
5.12 The DeepCwind FOWT precise mass for each component (left) and assemblage hydrostatics calculation (right). . . . 154
5.13 Illustration showing direction definition for wind and wave. . . . 156
5.14 Free decay test response signal for the DeepCWind-OC5 Floating Platform for heave motion(top) and roll and pitch motion (bottom). . . . 157

6.1 Free decay signals showing peaks with respect to time. . . . 161
6.2 Computation Domain used for Free Decay Size. . . . 163
6.3 Boundary conditions for free decay test simulation. . . . 164
6.4 x-direction section plane with a zoomed view showing meshing scheme for free decay test (4.5 million cells). . . . 165
6.5 Section planes (left) z-direction slice plane and (right) y-direction slice plane showing meshing scheme for free decay test. . . . 166
6.6 Initialised solution of free decay test at 0 s showing Free surface (z-direction slice plane). . . . 167
6.7 Initialised solution of free decay test at 0 s showing structure absolute pressure contour and flow domain vorticity (x-direction slice plane). . . . 168
6.8 Initialised solution of free decay test at 0 s showing structure absolute pressure contour and flow domain vorticity (y-direction slice plane). . . . 168
6.9 Free decay test result for (top) 1DOF heave motion and coupled heave-roll-pitch motion, and (bottom) roll and pitch motion. . . . 170
6.10 Scene demonstrating SWL iso-surface distribution and monitor plots for roll and pitch motion first peak at 6.75 s for the coupled heave-roll-pitch free decay test. . 171
6.11 Scene demonstrating SWL iso-surface distribution and monitor plots for roll and pitch motion second peak at 12.68 s for the coupled heave-roll-pitch free decay test. . . . 172
6.12 Scene demonstrating SWL iso-surface distribution and monitor plots for roll and pitch motion third peak at 18.53 s for the coupled heave-roll-pitch free decay test. 173
6.13 Scene demonstrating vorticity distribution, platform surface absolute pressure distribution, and monitor plots for roll and pitch motion first peak at 6.75 s for the coupled heave-roll-pitch free decay test (x-direction slice plane). . . . 174
6.14 Scene demonstrating vorticity distribution, platform surface absolute pressure distribution, and monitor plots for roll and pitch motion second peak at 12.68 s for the coupled heave-roll-pitch free decay test (x-direction slice plane). . . . 175

6.15 Scene demonstrating vorticity distribution, platform surface absolute pressure distribution, and monitor plots for roll and pitch motion third peak at 18.53 s for the coupled heave-roll-pitch free decay test (x-direction slice plane). 176
6.16 Scene demonstrating vorticity distribution, platform surface absolute pressure distribution, and monitor plots for roll and pitch motion first peak at 6.75 s for the coupled heave-roll-pitch free decay test (y-direction slice plane). 177
6.17 Scene demonstrating vorticity distribution, platform surface absolute pressure distribution, and monitor plots for roll and pitch motion second peak at 12.68 s for the coupled heave-roll-pitch free decay test (y-direction slice plane). 178
6.18 Scene demonstrating vorticity distribution, platform surface absolute pressure distribution, and monitor plots for roll and pitch motion third peak at 18.53 s for the coupled heave-roll-pitch free decay test (y-direction slice plane). 179
6.19 External flow domain used in CFD simulation showing view with respect to (a) z axis (b) y axis (c) x axis and (d) isometric view. 182
6.20 Flow domain boundary conditions for viscous force CFD simulation. 183
6.21 Wind and current velocity profile for inlet boundary condition. 183
6.22 Flow domain mesh distribution for mesh refinement case 3; (a) far field symmetry boundary in y-axis, (b) far field inlet boundary in x-axis, (c) xz-plane, (d) yz-plane, (e) close-up view of blade and tower in yz-plane. 187
6.23 Flow domain mesh distribution for mesh refinement case 3; (a) close-up view of rotor, nacelle, and tower top in yz-plane, (b) close-up view around the FOWT's near field and free surface in xy-plane, (c) close-up view of platform and tower bottom in xz-plane. 188
6.24 A visualisation of the CFD initialised solution at t = 0 s for operating condition design load case showing flow domain wind and current velocity profile direction of 0°, and structure absolute total pressure in (a) xy-plane, (b) xz-plane, (c) xz-plane isometric view, and (d) yz-plane. 190
6.25 Plots showing time history of 3 mesh scenarios for flow direction of 0°; (a) rotor thrust force, (b) rotor thrust coefficient, (c) rotor moment, (d) rotor power, and (e) platform drag force under operating condition load case. 191
6.26 Visualisation showing flow domain velocity magnitude and structure absolute total pressure on the yz-plane with reference to the global coordinate (0,0,0) m, at (a) 3 s, (b) 4 s, (c) 5 s, (d) 6 s, (e) 7 s, and (f) 8 s. 193
6.27 Visualisation showing flow domain velocity magnitude and structure absolute total pressure on the xz-plane with reference to the global coordinate (0,0,0) m, at (a) 3 s, (b) 4 s, (c) 5 s, (d) 6 s, (e) 7 s, and (f) 8 s. 194
6.28 Plot showing the flow domain velocity and pressure profiles in the streamwise direction at the (a) hub height, and (b) MSL under operating condition load case at t = 10 s. 195
6.29 Plots showing time history of 3 mesh refinement cases for flow direction of 0°; (a) parked rotor thrust force under extreme condition load case, (b)parked rotor thrust force under survival condition load case, (c) tower drag force under extreme condition load case, (d) tower drag force under survival condition load case, (e) platform drag force under extreme condition load case, and (f) platform drag force under survival condition load case. 197
6.30 Visualisation showing side by side comparison of flow domain velocity magnitude and structure absolute total pressure on the xz-plane with reference to the global coordinate (0,0,0) m, at (a) 2 s under extreme condition load case (b) 2 s under survival condition load case, (c) 8 s under extreme condition load case, and (d) 8 s under survival condition load case. 199

6.31 Visualisation showing side by side comparison of flow domain velocity magnitude and wall y+ function on the xz-plane with reference to the global coordinate (0,0,0) m, at (a) 2 s under extreme condition load case (b) 2 s under survival condition load case, (c) 8 s under extreme condition load case, and (d) 8 s under survival condition load case. . . . 200
6.32 Visualisation showing side by side comparison of flow domain velocity magnitude and wall y+ function on the xy-plane with reference to the global coordinate (0,0,0) m, at (a) 2 s, (b) 4 s, (c) 6 s, (d) 8 s, and yz-plane with reference to the global coordinate (0,0,0) at (e) 2 s, (f) 4 s, (g) 6 s, (h) 8 s. . . . 201
6.33 An illustration showing the force coefficient definition when the structure is in the position as defined in the geometry (left) and the position during simulation (right). . . . 203
6.34 3D model diffracting panels for HD and HR numerical simulation. . . . 205
6.35 Illustration showing (a) tube elements defined within the diffracting geometry model (b) tube elements. . . . 205
6.36 Illustration showing (a) direction definition for wind, wave and current, and (b) flow domain size. . . . 207
6.37 Plots showing structure (top) added mass and (bottom) radiation damping vs frequency. . . . 209
6.38 FOWT surge motion displacement RAOs for a wave direction of 0° for various scenarios of LC1 . . . 213
6.39 FOWT sway motion displacement RAOs for a wave direction of 0° for various scenarios of LC1 . . . 213
6.40 FOWT heave motion displacement RAOs for a wave direction of 0° for various scenarios of LC1 . . . 214
6.41 FOWT roll motion displacement RAOs for a wave direction of 0° for various scenarios of LC1 . . . 214
6.42 FOWT pitch motion displacement RAOs for a wave direction of 0° for various scenarios of LC1 . . . 215
6.43 FOWT yaw motion displacement RAOs for a wave direction of 0° for various scenarios of LC1 . . . 215
6.44 Near field steady drift force in global (a) X-axis, (b) Y-axis, (c) Z-axis, (d) RX-axis, (e) RY-axis, and (f) RZ-axis for a wave direction of 0° for various scenarios of LC1. 217
6.45 Plot of structure wave force per unit wave amplitude for wave direction of 0°. . . . 218
6.46 Radar chart of structure total wave excitation force including Morison drag per unit wave amplitude (Force vs Direction) for several wave frequencies. . . . 219
6.47 An aerial view (left) and close-up view (right) of wave diffraction/radiation model showing wave surface elevation for a wave amplitude, frequency, and direction of 3.5 m, 0.98 Hz, and 0°, respectively. . . . 222
6.48 An aerial view (left) and close-up view (right) of wave diffraction/radiation model showing structure panel pressure amplitude for a wave amplitude, frequency, and direction of 3.5 m, 0.98 Hz, and 0°, respectively. . . . 223
6.49 An aerial view (left) and close-up view (right) of wave diffraction/radiation model showing amplitudes of wave surface elevation for a wave amplitude, frequency, and direction of 3.5 m, 0.98 Hz, and 0°, respectively. . . . 224
6.50 Modes of motion boundary condition comparison between FOWT concepts and TRIHF. . . . 225
6.51 A comparison of RAOs between TRIHF and DeepCWind-OC5. . . . 227
6.52 Plot of wave spectra density vs platform position/orientation response spectra for (a) surge, (b) sway, (c) heave, (d) roll, (e) pitch, and (f) yaw motion for various scenarios of LC1. . . . 229

6.53 Plot of wave spectra density vs platform position/orientation response spectra for (a) surge, (b) sway, (c) heave, (d) roll, (e) pitch, and (f) yaw motion for various scenarios of LC2. . . . 230
6.54 Plot of wave spectra density vs platform position/orientation response spectra for (a) surge, (b) sway, (c) heave, (d) roll, (e) pitch, and (f) yaw motion for various scenarios of LC3. . . . 231
6.55 Floating marine structure response in random sea state. Adopted from [142]. . . . 232
6.56 Plot of wave spectra density vs platform position/orientation response amplitude for (a) surge, (b) sway, (c) heave, (d) roll, (e) pitch, and (f) yaw motion for various scenarios of LC1. . . . 233
6.57 Plot of wave spectra density vs platform position/orientation response amplitude for (a) surge, (b) sway, (c) heave, (d) roll, (e) pitch, and (f) yaw motion for various scenarios of LC2. . . . 234
6.58 Plot of wave spectra density vs platform position/orientation response amplitude for (a) surge, (b) sway, (c) heave, (d) roll, (e) pitch, and (f) yaw motion for various scenarios of LC3. . . . 235
6.59 Plot of wave spectra density vs platform force/moment spectra for (a) X-axis, (b) Y-axis, (c) Z-axis, (d) RX-axis, (e) RY-axis, and (f) RZ-axis for various scenarios of LC1. . . . 236
6.60 Plot of wave spectra density vs platform force/moment spectra for (a) X-axis, (b) Y-axis, (c) Z-axis, (d) RX-axis, (e) RY-axis, and (f) RZ-axis for various scenarios of LC2. . . . 237
6.61 Plot of wave spectra density vs platform force/moment spectra for (a) X-axis, (b) Y-axis, (c) Z-axis, (d) RX-axis, (e) RY-axis, and (f) RZ-axis for various scenarios of LC3. . . . 238
6.62 Plot of wave spectra density vs platform force/moment response amplitude for global (a) X-axis, (b) Y-axis, (c) Z-axis, (d) RX-axis, (e) RY-axis, and (f) RZ-axis for various scenarios of LC1. . . . 239
6.63 Time series of wave surface elevation for (a) different values of time steps (b) zoomed in plot showing maximum wave height. . . . 242
6.64 Plot of Rayleigh Probability of Exceedance vs. Wave Height according to [143]. . . . 243
6.65 Plots showing time series of structure actual position response for all 6DOF for an irregular wave direction of 0° for various scenarios of LC1. . . . 244
6.66 Plots showing time series of structure low-frequency response for all 6DOFs for an irregular wave direction of 0° for various scenarios of LC1. . . . 245
6.67 Plots showing time series of structure wave frequency response for all 6DOFs for an irregular wave direction of 0° for various scenarios of LC1. . . . 246
6.68 Plots showing time series of structure RAO based response for 6DOFs for an irregular wave direction of 0° for various scenarios of LC1. . . . 247
6.69 Plots showing time series of structure actual velocity response for all 6DOF for an irregular wave direction of 0° for various scenarios of LC1. . . . 249
6.70 Plots showing time series of structure actual acceleration response for all 6DOF for an irregular wave direction of 0° for various scenarios of LC1. . . . 250
6.71 Plots showing time series of (a) mooring cable fairlead tension, (b) hydrodynamic forces, (c) wind loads, and (d) rotor thrust coefficient for an irregular wave direction of 0°, wind direction of 0°, and current direction of 0°. . . . 253

C.1 FOWT surge motion displacement RAOs for a wave direction of 0° for various scenarios of LC2 . . . 291
C.2 FOWT sway motion displacement RAOs for a wave direction of 0° for various scenarios of LC2 . . . 291

C.3 FOWT heave motion displacement RAOs for a wave direction of 0° for various scenarios of LC2 . . . 292
C.4 FOWT roll motion displacement RAOs for a wave direction of 0° for various scenarios of LC2 . . . 292
C.5 FOWT pitch motion displacement RAOs for a wave direction of 0° for various scenarios of LC2 . . . 293
C.6 FOWT yaw motion displacement RAOs for a wave direction of 0° for various scenarios of LC2 . . . 293

D.1 FOWT surge motion displacement RAOs for a wave direction of 0° for various scenarios of LC3 . . . 295
D.2 FOWT sway motion displacement RAOs for a wave direction of 0° for various scenarios of LC3 . . . 295
D.3 FOWT heave motion displacement RAOs for a wave direction of 0° for various scenarios of LC3 . . . 296
D.4 FOWT roll motion displacement RAOs for a wave direction of 0° for various scenarios of LC3 . . . 296
D.5 FOWT pitch motion displacement RAOs for a wave direction of 0° for various scenarios of LC3 . . . 297
D.6 FOWT yaw motion displacement RAOs for a wave direction of 0° for various scenarios of LC3 . . . 297

List of Tables

3.1 Proposed Offshore Project Development Area for Floating Offshore Wind Turbines off the coast of New Zealand's North Island. . . . 73
3.2 Statistical Summary of Wind Data. . . . 92
3.3 Wind Data Return Period using the Frequency Factor Technique as proposed by Chow [109] . . . 93
3.4 Summary of Metocean Data. . . . 95
3.5 Design Load Cases for Various Operating Conditions . . . 103

4.1 NREL 5 MW Baseline Wind Turbine Distributed Blade Aerodynamic Properties. 106
4.2 NREL 5 MW Baseline Wind Turbine Assemblage- Gross Properties [27]. . . . 113
4.3 Qualitative Comparison of Floater Concepts to Hydrodynamic Loads and Susceptibility to Modes of Motion. . . . 123
4.4 Scoring Criteria for Floater Boundary Conditions and Natural Period. . . . 124
4.5 Table showing platform concept boundary conditions for all modes of motion using the scoring criteria. . . . 124
4.6 FOWT Concept Pre-design Selection Rationale. . . . 127
4.6 FOWT Concept Pre-design Selection Rationale (continued). . . . 128
4.7 Main dimensions of TRIHF platform with the NREL 5 Baseline Wind Turbine. . . . 132
4.8 Platform Theoretical Mass Calculations. . . . 133
4.9 Theoretical Buoyancy and Ballast Requirement Calculations. . . . 134
4.10 Mooring Line Stiffness Properties. . . . 140

5.1 A comparison of FOWT parameters between TRIHF and DeepCwind-OC5 project. 151
5.2 The DeepCWind-OC5 Platform Mooring System Properties[30]. . . . 153
5.3 Environmental constants for the validation study. . . . 155
5.4 Design load case for validation studies. . . . 155
5.5 A comparison of simulation and experimental test result for platform natural period. . . . 158
5.6 Platform damping ratio and viscous damping coefficient. . . . 158
5.7 A comparison of time domain statistical summary result between simulation and experimental test.. . . . 158

6.1 Results of non-dimensional total damping coefficients for TRIHF from free decay test. . . . 180
6.2 Mesh metrics used for mesh refinement study. . . . 184
6.3 Calculation summary of first cell height for y+ function. . . . 186
6.4 Comparison of results for different mesh refinement | Operating condition load case. . . . 192
6.5 Comparison of results for different mesh refinement | Extreme condition load case. . . . 198
6.6 Comparison of results for different mesh refinement | Survival condition load case. . . . 198
6.7 Summary of CFD simulation result and calculated viscous force coefficient for operating condition load case. . . . 202

6.8 Summary of CFD simulation result and calculated viscous force coefficient for extreme condition load case. . . . 203
6.9 Summary of CFD simulation result and calculated viscous force coefficient for survival condition load case. . . . 203
6.10 Generated mesh information and parameters. . . . 206
6.11 Mooring stiffness matrix for input into hydrodynamic diffraction/radiation analysis. . . . 208
6.12 Platform hydrostatic results. . . . 208
6.13 Summary of calculation and result for platform added mass, radiation damping, and viscous damping coefficient. . . . 210
6.14 Viscous damping matrix for input into hydrodynamic diffraction/radiation analysis. . . . 210
6.15 Coupled dynamics simulation LCs for Metocean and turbine conditions. . . . 211
6.16 Coupled dynamics simulation LC test matrix. . . . 211
6.17 Natural periods of floater motions for TRIHF platform for various scenarios of LC1. . . . 221
6.18 TRIHF equilibrium position for various scenarios of LC1. . . . 228
6.19 Calculated Wave Parameters for Time Domain Simulation. . . . 241
6.20 Motion Analysis Time History Statistics for LC1A and LC1B. . . . 254
6.20 Motion Analysis Time History Statistics for LC1A and LC1B (contd). . . . 255
6.20 Motion Analysis Time History Statistics for LC1A and LC1B (contd). . . . 256
6.20 Motion Analysis Time History Statistics for LC1A and LC1B (contd). . . . 257
6.21 Motion Analysis Time History Statistics for LC1C and LC1D. . . . 258
6.21 Motion Analysis Time History Statistics for LC1C and LC1D (contd). . . . 259
6.21 Motion Analysis Time History Statistics for LC1C and LC1D (contd). . . . 260
6.21 Motion Analysis Time History Statistics for LC1C and LC1D (contd). . . . 261
6.22 Motion Analysis Time History Statistics for LC2A and LC2B. . . . 262
6.22 Motion Analysis Time History Statistics for LC2A and LC2B (contd). . . . 263
6.22 Motion Analysis Time History Statistics for LC2A and LC2B (contd). . . . 264
6.22 Motion Analysis Time History Statistics for LC2A and LC2B (contd). . . . 265
6.23 Motion Analysis Time History Statistics for LC2C and LC2D. . . . 266
6.23 Motion Analysis Time History Statistics for LC2C and LC2D (contd). . . . 267
6.23 Motion Analysis Time History Statistics for LC2C and LC2D (contd). . . . 268
6.23 Motion Analysis Time History Statistics for LC2C and LC2D (contd). . . . 269
6.24 Motion Analysis Time History Statistics for LC3A and LC3B. . . . 270
6.24 Motion Analysis Time History Statistics for LC3A and LC3B (contd). . . . 271
6.24 Motion Analysis Time History Statistics for LC3A and LC3B (contd). . . . 272
6.24 Motion Analysis Time History Statistics for LC3A and LC3B (contd). . . . 273
6.25 Motion Analysis Time History Statistics for LC3C and LC3D. . . . 274
6.25 Motion Analysis Time History Statistics for LC3C and LC3D (contd). . . . 275
6.25 Motion Analysis Time History Statistics for LC3C and LC3D (contd). . . . 276
6.25 Motion Analysis Time History Statistics for LC3C and LC3D (contd). . . . 277

B.1 Linearising Element Nodes Definition . . . 289

List of Abbreviations

6DOF	**S**ix **D**egrees **O**f **F**reedom
AAF	**A**erodynamic **A**dmittance **F**unction
ADAMS	**A**utomatic **D**ynamic **A**nalysis of **M**echanical **S**ystems
AOA	**A**ngle **O**f **A**ttack
AOO	**A**ngle **O**f **O**rientation
AUT	**A**uckland **U**niversity of **T**echnology
BEM	**B**lade **E**lement **M**omentum
CAA	**C**ivil **A**viation **A**uthority
CAE	**C**omputer **A**ided **E**ngineering
CAGR	**C**ompound **A**nnual **G**rowth **R**ate
CB	**C**enter of **B**uoyancy
CFD	**C**omputational **F**luid **D**ynamics
CG	**C**enter of **G**ravity
CM	**C**enter of **M**ass
DFBI	**D**ynamic **F**luid **B**ody **I**nteraction
DLC	**D**esign **L**oad **C**ase
DNS	**D**irect **N**umerical **S**imulation
DOWEC	**D**utch **O**ffshore **W**ind **E**nergy **C**onverter
EEZ	**E**xclusive **E**conomic **Z**one
EWEA	**E**uropean **W**ind **E**nergy **A**ssociation
FAST	**F**atigue, **A**erodynamics, **S**tructures, and **T**urbulence
FD	**F**requency **D**omain
FE	**F**inite **E**lement
FOWT	**F**loating **O**ffshore **W**ind **T**urbine
FRA	**F**ixed **R**eference **A**xis
FRB	**F**loating **R**igid **B**ody
FRBD	**F**loating **R**igid **B**ody **D**ynamics
FSI	**F**luid **S**tructure **I**nterface
GWEC	**G**lobal **W**ind **E**nergy **C**ouncil
HAWT	**H**orizontal **A**xis **W**ind **T**urbine
HD	**H**ydrodynamic **D**iffraction
HF	**H**igh **F**requency
HMB	**H**elicopter **M**ulti **B**lock
HR	**H**ydrodynamic **R**esponse
IEA	**I**nternational **E**nergy **A**gency
LBL	**L**aminar **B**oundary **L**ayer
LC	**L**oad **C**ase
LF	**L**ow **F**requency
LFTF	**L**inear **F**orce **T**ransfer **F**unction
LFZ	**L**ow **F**lying **Z**one
LHS	**L**eft **H**and **S**ide
LMTF	**L**inear **M**otion **T**ransfer **F**unction
LVL	**L**aminated **V**eneer **L**umber
LWT	**L**inear **W**ave **T**heory

MARIN	**MA**ritime **R**esearch **I**nstitute **N**etherland
MBL	**M**inimum **B**reaking **L**oad
MRF	**M**ultiple **R**eference **F**rame
MSL	**M**ean **S**ea **L**evel
NACA	**N**ational **A**dvisory **C**ommittee for **A**eronoautics
NetCDF	**Net**work **C**ommon **D**ata **F**orm
NIWA	**N**ational **I**nstitute of **W**ater and **A**tmospheric Research
NREL	**N**ational **R**enewable **E**nergy **L**aboratory
OC4	**O**ffshore **C**ode **C**ollaboration **C**ontinuation
OC5	**O**ffshore **C**ode **C**ollaboration, **C**ontinued, with **C**orrelation
OWTs	**O**ffshore **W**ind **T**urbines
PDAs	**P**roject **D**evelopment **A**reas
PDEs	**P**artial **D**ifferential **E**quations
PSD	**P**ower **S**pectral **D**ensity
RANSE	**R**eynolds **A**veraged **N**avier **S**tokes **E**quation
RAOs	**R**espond **A**mplitude **O**perators
RHS	**R**ight **H**and **S**ide
RMS	**R**oot **M**eans **S**quare
ROMS	**R**egional **O**cean **M**odelling **S**ystem
RPM	**R**evolutions **P**er **M**inute
SHARPE	**S**treamlined **H**ydro- **A**ero- **R**igid body dynamics, **P**otentials, and viscous **E**ffect
SLC	**S**urvival **L**oad **C**ase
SMI	**S**liding **M**esh **I**nterface
SPH	**S**moothed **P**article **H**ydrodynamics
SST	**S**hear **S**tress **T**ransport
STI	**S**hip **T**racking **I**ntelligence
SWAN	**S**imulating **WA**ves **N**earshore
SWL	**S**till **W**ater **L**evel
TBL	**T**urbulent **B**oundary **L**ayer
TD	**T**ime **D**omain
TLP	**T**ension **L**eg **P**latform
TRIHF™	**TRI**gon **H**ybrid **F**loater
TSR	**T**ip **S**peed **R**atio
TSR	**T**ip **S**peed **R**atio
UNF	**U**ndamped **N**atural **F**requency
VIM	**V**ortex **I**nduced **M**otion
VIV	**V**ortex **I**nduced **V**ibration
VOF	**V**olume **O**f **F**luid
WF	**W**ave **F**requency
WRF	**W**eather **R**esearch and **F**orecasting
WTG	**W**ind **T**urbine **G**enerator

Physical Constants

Acceleration due to gravity	$g = 9.81\,\mathrm{m/s^2}$
Betz Limit	$C_{P,opt} = 59.3\,\%$
Density of Air	$\rho_{air} = 1.225\,\mathrm{kg/m^3}$
Density of Seawater	$\rho_{sw} = 1025\,\mathrm{kg/m^3}$
Dynamic Viscosity of Air	$\mu_{air} = 1.868 \times 10^{-5}\,\mathrm{Pa \cdot s}$
Dynamic Viscosity of Sea Water	$\mu_{sw} = 8.89 \times 10^{-4}\,\mathrm{Pa \cdot s}$
Density of Steel	$\rho_{steel} = 7850\,\mathrm{kg/m^3}$
Speed of Sound in Air	$c = 344\,\mathrm{m\,s^{-1}}$

List of Symbols

$\bar{x}$	Sample Mean	
β	Incident Wave Angle	$^\circ$
$\ddot{u}$	Horizontal Water Particle Acceleration	$\mathrm{m/s^2}$
$\ddot{v}$	Vertical Water Particle Acceleration	$\mathrm{m/s^2}$
$\ddot{x}$	Acceleration of the Slender Member	$\mathrm{m/s^2}$
Δa_{mom}	Rate of Axial Momentum Change	$\mathrm{kg \cdot m^2/s}$
ΔL_{cbl}	Cable Extension	m
Δp_{rotor}	Rate of Pressure Change	$\mathrm{N/m^2}$
ΔU_{sys}	Whole System Velocity Change	$\mathrm{m\,s^{-1}}$
δ	Surface Drag Coefficient (Offshore Location)	
$\dot{u}$	Horizontal Water Particle Velocity	$\mathrm{m\,s^{-1}}$
$\dot{v}$	Vertical Water Particle Velocity	$\mathrm{m\,s^{-1}}$
$\dot{x}$	Velocity of the Slender Member	$\mathrm{m\,s^{-1}}$
ϵ	Spectral Width Parameter	
η	Wave Surface Elevation	m
$\forall$	Volume of Fluid Displaced by the Floating Structure	$\mathrm{m^3}$
γ	Peak Enhancement Factor	
λ	Wave Length	m
λ_{TSR}	Tip Speed Ratio	
μ_{air}	Dynamic Viscosity of Air	$\mathrm{Pa \cdot s}$
μ_{sw}	Dynamic Viscosity of Sea Water	$\mathrm{Pa \cdot s}$
$\nabla\Phi$	Time Dependent Velocity Potential	$\mathrm{m^2/s}$
ω	Angular Velocity	$\mathrm{rad\,s^{-1}}$
ω_p	Peak Frequency	$\mathrm{rad\,s^{-1}}$
$\overline{BM_x}$	Transverse Metacentric Radius	m
$\overline{BM_y}$	Longitudinal Metacentric Radius	m
$\overline{BM}$	Metacentric Radius	m

$\overline{GM}$	Metacentric Height	m
$\overline{GZ}$	Righting Arm	m
$\overline{KB}$	Distance between Keel and Center of Buoyancy	m
$\overline{KG}$	Distance between Keel and Center of Gravity	m
Φ	Velocity Potential	m^2/s
ρ_{air}	Density of Air	kg/m^3
ρ_{sw}	Density of Sea Water	kg/m^3
σ	Sample Standard Deviation	
θ	Aerodynamic Angle of Attack	$^\circ$
φ	Velocity Potential Function	m^2/s
φ_D	Diffracted Wave Velocity Potential	m^2/s
φ_o	Incident Wave Velocity Potential	m^2/s
φ_R	Radiated Wave Velocity Potential	m^2/s
ς_{ij}	Non Dimensional Total Damping Coefficient where $i, j = 1,\ 2,\ .....6$	
ϑ_n	Peak Response Signals from the Free Decay Test for Translational/Rotational Motionm or $^\circ$	
ϑ_o	Forced Translational/Angular Displacement	m or $^\circ$
$\vec{M}$	Pure Moment	$N \cdot m$
$\vec{V}$	Velocity Vector of Structure Motion	$m\,s^{-1}$
$\widetilde{f}$	Non-dimensional Frequency	
ξ_1	Radiation Potential for Surge Motion	m^2/s
ξ_2	Radiation Potential for Sway Motion	m^2/s
ξ_3	Radiation Potential for Heave Motion	m^2/s
ξ_4	Radiation Potential for Row Motion	m^2/s
ξ_5	Radiation Potential for Pitch Motion	m^2/s
ξ_6	Radiation Potential for Yaw Motion	m^2/s
a	Axial Induction Factor	
a	Generalised Philip's Constant	
a_n	Water Particle Acceleration Normal to the Axis of the Slender Member	m/s^2
A_∞	Free Stream Reference Area	m^2
A_{cbl}	Cable Cross Sectional Area	Pa
a_{ij}	Added Mass due to Wave Radiation $i, j = 1, 2...6$	kg or $kg \cdot m$

A_{rotor}	Rotor Swept Area	m^2
A_{wake}	Wake Region Reference Area	m^2
b_{33}	Total Damping Coefficient for Heave Motion	$\mathrm{N}/(\mathrm{m}/\mathrm{s})$
b_{33}^{ψ}	Viscous Damping Coefficient for Heave Motion	$\mathrm{N}/(\mathrm{m}/\mathrm{s})$
$b_{33}^{r}\left(\omega_{0,33}\right)$	Radiation Damping Coefficient at UNF for Heave Motion	$\mathrm{N}/(\mathrm{m}/\mathrm{s})$
b_{44}	Total Damping Coefficient for Roll Motion	$\mathrm{N}\cdot\mathrm{m}/(^{\circ}/\mathrm{s})$
b_{44}^{ψ}	Viscous Damping Coefficient for Roll Motion	$\mathrm{N}\cdot\mathrm{m}/(^{\circ}/\mathrm{s})$
$b_{44}^{r}\left(\omega_{0,44}\right)$	Radiation Damping Coefficient at UNF for Roll Motion	$\mathrm{N}\cdot\mathrm{m}/(^{\circ}/\mathrm{s})$
b_{55}	Total Damping Coefficient for Pitch Motion	$\mathrm{N}\cdot\mathrm{m}/(^{\circ}/\mathrm{s})$
b_{55}^{ψ}	Viscous Damping Coefficient for Pitch Motion	$\mathrm{N}\cdot\mathrm{m}/(^{\circ}/\mathrm{s})$
$b_{55}^{r}\left(\omega_{0,55}\right)$	Radiation Damping Coefficient at UNF for Pitch Motion	$\mathrm{N}\cdot\mathrm{m}/(^{\circ}/\mathrm{s})$
b_{ij}	Radiation Damping due to Wave Radiation $i, j = 1, 2...6$	kg/s or $\mathrm{kg}\cdot\mathrm{m}/\mathrm{s}$
C	Chord Length of the Aerofoil	m
c	Speed of Sound in Air	$\mathrm{m\,s^{-1}}$
$C1$	Fairly Compliant	
$C2$	Compliant	
$C3$	Well Compliant	
$C4$	Strongly Compliant	
C_a	Hydrodynamic Added Mass Coefficient	
C_D	Drag Force Coefficient	
C_d	Hydrodynamic Drag Coefficient	
C_L	Lift Force Coefficient	
C_m	Hydrodynamic Inertia Coefficient	
C_T	Thrust Coefficient	
C_w	Wind Pressure Coefficient	N
$C_{\tau_{c/4}}$	Pitching Moment Coefficient	
$C_{P,opt}$	Rotor Optimum Power Efficiency	
C_P	Power Coefficient	
C_{tor}	Torque Coefficient	
d	Water Depth	m
d_0	Wind Generated Current Reference Depth (50 m)	m

dA	Exposed Cross-sectional Area of the Slender Member	m^2
dV	Displaced Volume of Water per Unit Length of the Slender Member	m^3/m
E_{cbl}	Cable Young Modulus	Pa
f	Wave Frequency	Hz
F_D	Drag Force	N
F_g	Gust Factor	
F_h	Hydrodynamic Force	N
F_i	Forces for each Transnational Motion mode where $i = 1, 2, 3$	N
F_i^0	Total Incident Wave (Froude Krylov) Force	N
F_i^D	Total Diffraction Wave Force	N
F_i^R	Total Radiation Wave Force	N
F_i^S	Hydrostatic Forces (Moments) for all 6-DOF where $i = 1, 2...6$	N or $N \cdot m$
F_i^{ex}	Total Wave Excitation Force	N
F_L	Lift Force	N
f_p	Spectral Peak Frequency	Hz
F_T	Thrust Force	N
F_w	Wind Load Force	N
$F_w(t)$	Dynamic Wind Force	N
F_{cbl}	Cable Force	N
f_{ij}	Complex Force Coefficient $i, j = 1, 2...6$	
H	Wave Height	m
$H^{(1)}\omega$	Linear Force Transfer Function	m/N or °/N
H_s	Significant Wave Height	m
H_{max}	Maximum Wave height in a random sea	m
I_{ij}	Moment of Inertia of Structure $i, j = 1, 2...6$	$kg \cdot m^2$
J	Number of waves in a random sea	
k	Wave Number	m^{-1}
K_T	Frequency Factor	
k_{cbl}	Cable Stiffness	$N \cdot m$
$K_{ij}(t)$	Fourier Transform of the Radiation Damping Coefficient	
KE_{rotor}	Kinetic Energy Generated by the Rotor	J

$L\ (\omega)$	Linear Structural Operator	$\mathrm{N/m}$ or $\mathrm{N \cdot m/^\circ}$
L_u	Integral Length Scale	m
L_{0cbl}	Cable Unstretched Length	Pa
m	Mass of Structure	kg
M_i	Moments for each Rotational Motion mode where $i = 4, 5, 6$	$\mathrm{N \cdot m}$
m_r	Normal Distribution Sample Rank Position	
m_{air}	Air Mass Flow Rate at the Upstream Rotor Region	$\mathrm{kg\,s^{-1}}$
Ma	Mach Number	
N	Neutral	
n	Normal Distribution Sample Size	
N_{rotor}	Rotor Speed	revolutions/min
p_{atm}	Atmospheric Pressure	$\mathrm{N/m^2}$
P_i	Estimate of Exceedance Probability	
P_{max}	Maximum Theoretical Available Power	W
P_{rotor}	Power Generated by the Rotor	W
p^D_{rotor}	Pressure at the Downstream Region of the Rotor	$\mathrm{N/m^2}$
p^U_{rotor}	Pressure at the Upstream Region of the Rotor	$\mathrm{N/m^2}$
q_{CU}	Current Drag Force	N
q_{ext}	External Force	N
q_{W1}	Wind Drag Force	N
$q^{(1)}_{WA}$	First Order Wave Excitation Force	N
$q^{(2)}_{WA}$	Second Order Wave Excitation Force	N
r	Radial Location Along the Surface of the Rotor Blade	m
$R1$	Fairly Restrained	
$R2$	Restrained	
$R3$	Well Restrained	
$R4$	Strongly Restrained	
R_{rotor}	Rotor Radius	m
Re	Reynolds Number	
$S_\eta\ (\omega)$	Wave Spectrum	$\mathrm{m^2/Hz}$
S_b	Surface Body Boundary Condition	$\mathrm{m^2}$

S_c	Control Surface Boundary Condition	m^2
S_f	Free Surface Boundary Condition	m^2
$S_F^+(\omega)$	Power Spectral Density (PSD) of the Wind Process	$W\,Hz^{-1}$
$S_R(\omega)$	Structure Response Spectrum	m^2/Hz or $^{\circ 2}/Hz$
$S_U^+(\omega)$	Wind Spectrum	m^2/s
S_z	Sea Bed Boundary Condition	m^2
T	Wave Period	s
t	Instantaneous Time	s
T_0	Natural Period	s
T_p	Peak Wave Period	s
T_R	Return Period	years
T_z	Zero Crossing Period	s
T_{max}	Maximum Theoretical Torque Generated by the Rotor	$N \cdot m$
U_∞	Free Stream Wind Velocity	$m\,s^{-1}$
$U_c(z)$	Total Current Velocity at Level z	$m\,s^{-1}$
U_g	Gust Component of Wind Speed	$m\,s^{-1}$
U_R	Maximum Resultant Velocity	$m\,s^{-1}$
U_s	Sustained Wind Speed	$m\,s^{-1}$
U_w	Wind Velocity	$m\,s^{-1}$
$U_w(t)$	Time Varying Wind Speed due to Turbulence or Gusts	$m\,s^{-1}$
U_z	Wind Speed at z m Elevation above MSL	$m\,s^{-1}$
U_{10}	Wind Speed at 10 m Elevation above MSL	$m\,s^{-1}$
U_{rotor}	Wind Axial Velocity Around the Rotor Plane	$m\,s^{-1}$
U_{tide0}	Tidal Current Velocity at MSL	$m\,s^{-1}$
U_{wake}	Wake Region Wind Velocity	$m\,s^{-1}$
U_{wind0}	Wind Generated Current Velocity at MSL	$m\,s^{-1}$
v_n	Water Particle Velocity Normal to the Axis of the Slender Member	$m\,s^{-1}$
x	Direction of Wave Advancement	
x_g	Structure Centre of Gravity w.r.t x axis	m
x_T	Estimated Event Magnitude at a Return Period T_R	
y^+	y plus Function	

y_g	Structure Centre of Gravity w.r.t y axis	m
z	Reference Height Above MSL	m
z_g	Structure Centre of Gravity w.r.t z axis	m
z_s	Surface Layer Thickness	m
z_{dist}	Standard Normal Distribution	
$\bar{F}_w$	Static Wind Force	N
$\bar{U}_p$	Peak Velocity	$\mathrm{m\,s^{-1}}$
$\bar{U}_w$	Wind Mean Velocity	$\mathrm{m\,s^{-1}}$
${\delta_u}^2$	Variance of $U_w(t)$ at a Reference Height of 10 m	$\mathrm{m^2/s^2}$
${\delta_z}^2$	Variance of $U_w(t)$	$\mathrm{m^2/s^2}$
$\overline{GM}_L$	Initial Metacentric Height	m
$\overline{GM}_T$	Transverse Initial Metacentric Height	m
$\vec{F}_h$	Hydrodynamic Forces on the Floating Structure	N
$\vec{M}_h$	Hydrodynamic Moments on the Floating Structure	$\mathrm{N \cdot m}$
I_x	Transverse Second Moment of Water Plane Area	m
I_y	Longitudinal Second Moment of Water Plane Area	m
KE_{max}	Maximum Theoretical Available Kinetic Energy	J
${x_{WA}}^{(1)}(\omega)$	Linear Motion Transfer Function (RAO)	m/m or °/m

Dedicated to God, the Author and Finisher of my Faith…

Chapter 1

Introduction

This chapter outlines the background (section 1.1) and problem statement (section 1.2) of the research. Section 1.3 provides its motivation and definitions of terms used. Section 1.4 describes the goals, significance, and scope of this research. Finally, section 1.5 includes an outline of the remaining chapters of the thesis.

1.1 Background of Study: Wind Energy Trends

Our world is changing rapidly, and we rely profoundly on access to energy to power our way of life. It is obvious that the conventional forms of energy are compromising our climate and conscious effort must be made to pave the way for a wholly green energy (decarbonised) world for future generations. These efforts have already begun and there has been a rapid increase in the harnessing of wind energy as an alternative and clean source of energy. According to the European Wind Energy Association (EWEA), 502 new offshore wind turbines were fully grid-connected across 10 projects in 2019, totalling 3,623 MW [1]. Fig. 1.1 highlights the statistics of wind energy trend across Europe. The total installation and grid-connection of 5,047 turbines represent a cumulative 22,072 MW.

Also, the Global Wind Statistics (2019) report published by the Global Wind Energy Council (GWEC) stipulated that a total of 51.3 GW of new wind power capacity was installed in 2018 which was a 4% increase of the total wind power capacity installed at the end of 2017 [2].Transparency Market Research latest report disclosed that the global installed capacity in the offshore wind industry is poised to grow from 7,045.4 MW in 2013 to 52,120.9 MW in 2022 at a vigorous Compound Annual Growth Rate (CAGR) of 25% during the forecast period of 2014 – 2022 [3]. Indeed, these statistical trends suggest that the global offshore energy market is projected to demonstrate healthy growth in the coming few years.

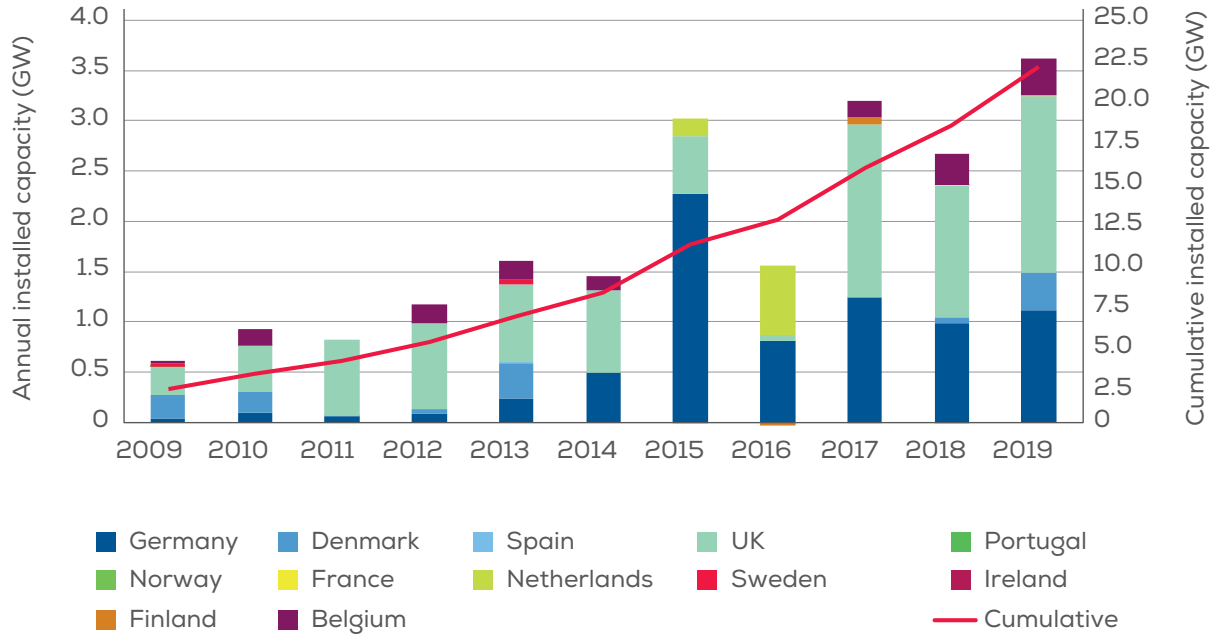

FIGURE 1.1: Annual Offshore Installations by Country (Left Axis) and Cumulative Capacity (Right Axis)[1].

Across Europe, there is an increasing number of wind turbines installed in offshore areas near the coastlines on fixed bottom foundations. A clear majority of these Offshore Wind Turbines (OWTs) are placed on monopile foundations in water depths of up to 40 m. For mid-shallow waters, 40 – 60 m, the tripod and jacket foundations have proven to be successful in providing support for OWTs (see Fig. 1.2).

Current fixed-bottom technology has seen limited deployment to water depth exceeding 60 m. By drawing from the experience of the oil and gas industry that has developed various offshore floating oil-drilling platforms that drill in waters deeper than 2 km, the offshore renewable energy industry has made some recent advancements in the deployment of floating platforms for wind turbines [4]–[12]. See Fig. 1.3 illustrating an artist impression of some floating concepts in comparison to some fixed bottom foundation concepts. In general, all three concepts make use of catenary or taut mooring. Any concept must provide enough buoyancy to support the weight of the turbine in addition to keeping motions in Six Degrees of Freedom (6DOF) within the acceptable limits.

Observing from a cost perspective, the investment in marinized fixed bottom foundation Wind Turbine Generator (WTG) in shallow water is not significantly higher

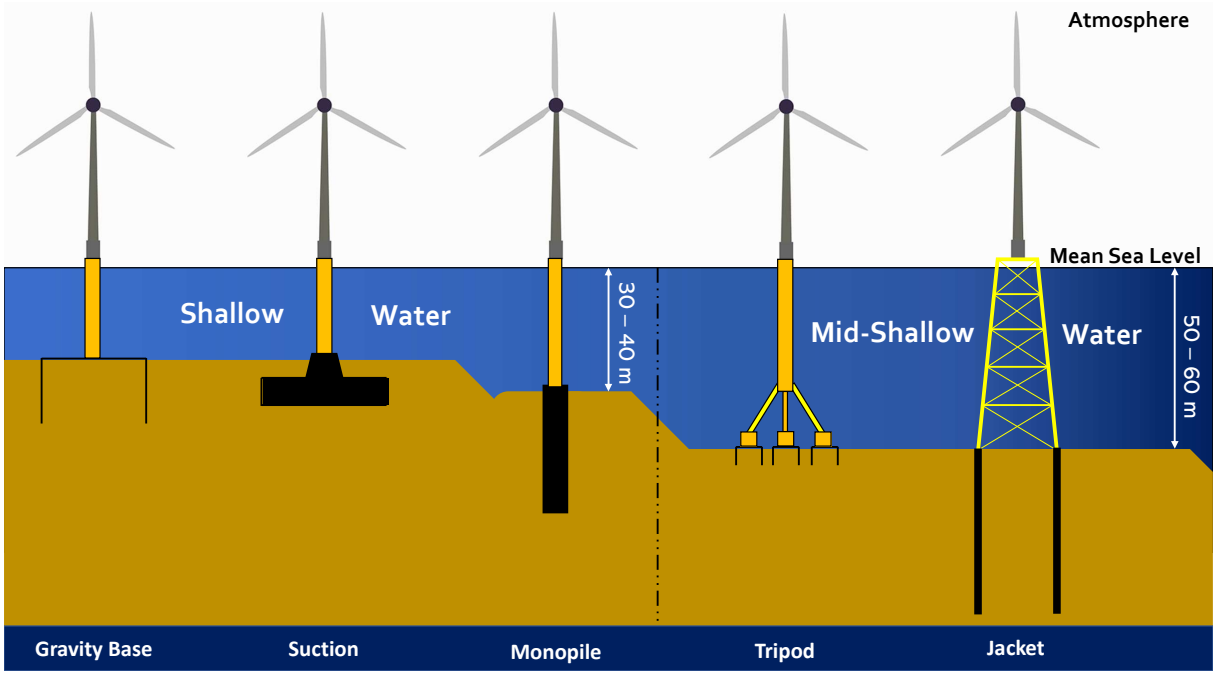

FIGURE 1.2: Offshore Wind Turbine (OWT) Foundations for Shallow and Mid-Shallow Water Application.

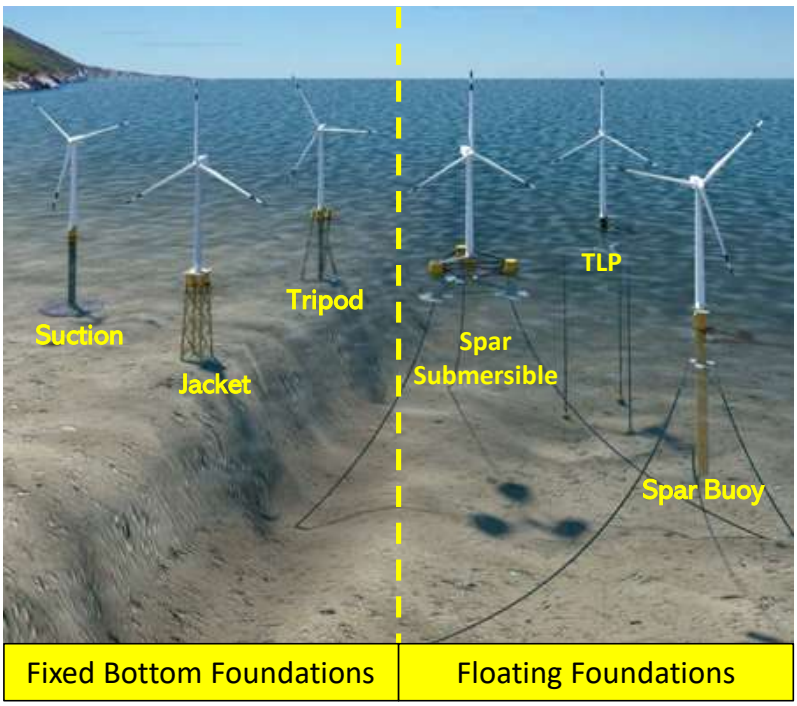

FIGURE 1.3: A graphics illustration showing the depth limitation of Fixed Bottom Foundation and Floating Foundation Concepts for Deep and Ultra-deepwater Application | Adopted from [13].

than that for an onshore WTG. Consequently, the economics of a deepwater Floating Offshore Wind Turbine (FOWT) will be primarily determined by the additional costs of the floating platform, the mooring system, and power distribution. These economic encounters impart technological challenges which in turn can be ultimately addressed through conceptual design and performing the right turnkey engineering analysis.Some projects across the world where FOWT have shown to be a proven technology are;

- The Statoil Hywind commercial project situated 25 km off the coast of Peterhead, Scotland with an installed capacity of 30 MW installed in a water depth of 120 m [4],
- Wind Float 1 (pilot/prototype project) and Wind Float 2 (commercial demonstration project) which are 5 and 15 km off the coast of Aguçadoura, Portugal with an installed capacity of 2 MW and 8 MW in water depths of 50 m and 100 m respectively [5],
- 2 MW floating spar wind turbine deployed of the coast of Goto Islands, Nagazaki, Japan [6],
- Fukushima Forward 1 and 2 demonstration projects off the coast of Japan with an installed capacity of 7 and 5 MW respectively [7], and
- The French pre-commercial farms (EOLMED and Floatgen) each of 24 MW capacity [7].

Other FOWT projects currently undergoing conceptual design assessment are;

- The Tetra Spar concept by Stiesdal Offshore Technology A/S [9], [10],
- GICON SOF floating foundation [11], and
- Saitec Floating Wind [12].

These recent projects and conceptual studies have shown that floating platform technology has made it possible to extend the positioning of wind turbines in deeper waters where superior wind characteristic exists for electric power production.

Floating foundation technology for OWTs is the future of deepwater wind energy production. In addition to exposing the prospects for installing WTGs further from

the shore in deeper waters where untapped wind resources can be accessed, it also minimises visual impact. In comparison to an onshore location, an offshore location offers more superior wind resources due to the presence of dense "heavy" air near the sea level which drives the turbine rotors more effectively [14].

Furthermore, a floating foundation provides more merits in that their construction is predominantly yard based which ultimately reduces offshore construction activity. Besides, it reduces the impact of offshore construction on the marine ecosystem. The subsea structure is constructed, and the turbine installed in a dry dock or inshore assembly area. Extensive piling operations are not required which makes it more beneficial over fixed bottom platforms in terms of reduced construction and installation cost. In addition to reduced seabed footprints, the impact of potential noise on sea mammals during installation is significantly minimised.

1.2 Context of Study and Problem Statement

Deepwater FOWTs are integrated systems that combine WTG, floating platforms, and mooring systems (moorings and/or tethers) responding to wind, wave, and current loadings in a complex way (Fig. 1.4). During the design phase of a FOWT, a coupled dynamics simulation strategy is required to adequately predict the motion responses resulting from the interaction between environmental loads and the assemblage of the FOWT. FOWTs will experience further stability limitations because of its floatation. Fig. 1.4 is an illustration of the various interfaces (fluid-structure and fluid-fluid) and dynamic loads encountered by a FOWT structure under marine environmental conditions. The assemblage of the wind turbine structure above the MSL will experience aerodynamic loads while the rest of the structure below the MSL will experience hydrodynamic (wave and current) loads, where both loads are expected to be transient or unsteady.

Predicting these responses is complicated because of the complex load interaction between the FOWT assemblage and the marine environment. Especially for extreme environmental conditions of wind, wave, and current, examining the dynamic forces and motion responses of the FOWT structure can be very challenging.

Hitherto, a common strategy has been to evaluate these dynamic forces by using the Morison equation to estimate the loading on individual members of the FOWT

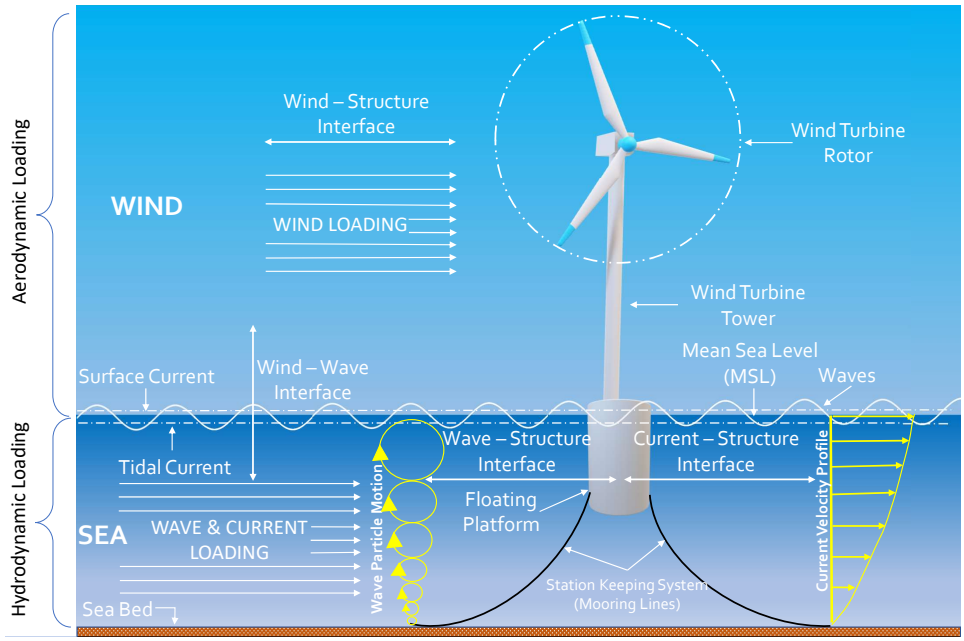

FIGURE 1.4: An illustration showing various fluid-structure interfaces and dynamic loads experienced by a FOWT.

assembly and integrate to get the total dynamic loading. Although this approach is guided by practical experience from similar test data, it requires many assumptions regarding force coefficients and the flow interactions. These assumptions include flow acceleration being uniform at the fluid-structure interface and that the diameter of the cylindrical members being much smaller than the wavelength. This method can lead to over or under-estimation of the dynamic loading and imprecise prediction of motion responses for the FOWT.

An underestimation of the dynamic loads leads to under designing the structure. This makes it vulnerable to devastation under extreme conditions while an overestimation of the loading results in impractically large requirements for structural stability. Consequently, a possible approach is to implement an additional near-wall numerical modelling process that uses Computational Fluid Dynamics (CFD) to determine the fluid force coefficients of the various components in the FOWT assemblage. Present standard approaches for coupled dynamics modelling can be further enhanced to yield more precise results by adequately accounting for intricate viscous effects arising from extreme dynamic loads and provide more insight into dynamic loads and motion responses by simultaneously delivering results in both the Frequency Domain (FD) and Time Domain (TD).

1.3 Motivation and Definitions of Research

Several studies [15]–[24] on coupled dynamic load simulations have been performed to assess and explore the aerodynamic and hydrodynamic response of a FOWT under various environmental conditions. A state-of-the-art coupled dynamics simulation approach that is commonly used in the offshore wind industry today and referenced by offshore standards for the design of FOWTs is the aero-hydro-servo-elastic coupled analysis as proposed by [25]–[28] and exemplified in Fig. 1.5.

This approach developed by Jonkman et al. employs five different subroutine packages WAMIT, TurbSim, AeroDyn, HydroDyn, and FAST/ADAMS (originally designed for predicting coupled dynamics responses and extreme loads for land-based wind turbines). These programs run independently and are interfaced by using additional programming codes. WAMIT is a frequency domain module used to perform a diffraction analysis while the other subroutine packages are time domain modules. Consequently, the aero-hydro-servo-elastic approach delivers only time domain results from the hydrodynamic load analysis onwards (Fig. 1.5).

A time domain representation delivers good results but is limited by the time frame simulated. For a more comprehensive analysis that involves assessing the global performance of a FOWT under extreme environmental condition in long term period, it is crucial to know the frequency content of the results (forces and motions). In other words, a frequency domain representation will provide more insight and intuitive understanding of the dynamic behaviour of the FOWT when it is subjected to severe environmental loading by providing how much of these loads are present in each frequency range.

In addition to only providing time domain results from the hydrodynamic analysis onwards, the aero-hydro-servo elastic approach does not account for viscous damping effects during a coupled dynamics simulation. Viscous damping effects due to wave impact on the floating structure are not negligible especially when it comes to rotary motions like roll for structures with large metacentric heights. Another limitation that needs to be addressed is the adequate modelling of intricate viscous effect resulting from the simultaneous occurrence of fluid forces on the structure, above and below the free water surface.

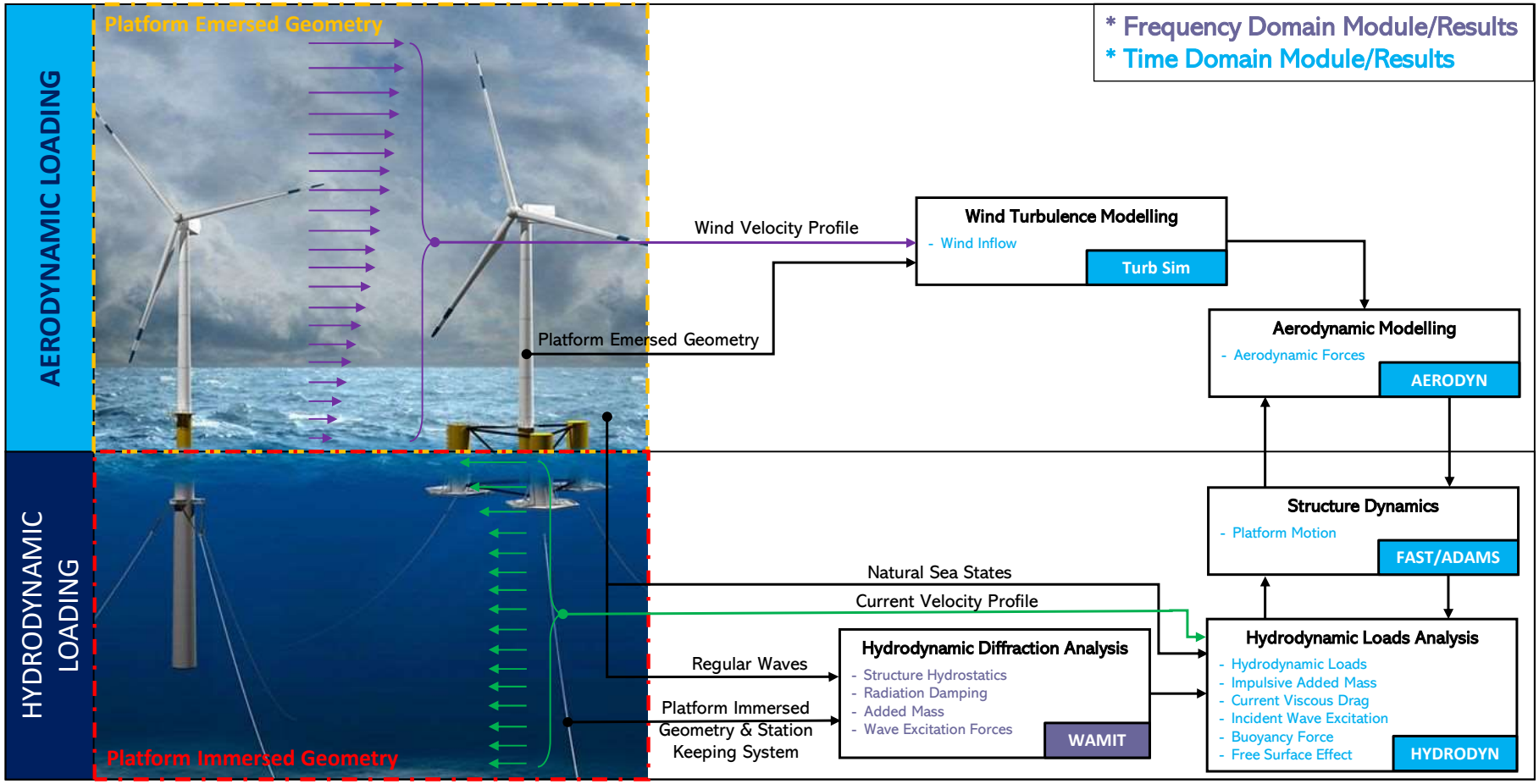

FIGURE 1.5: Interfacing Modules in Aero-Hydro-Servo-Elastic Coupled Analysis. Adopted from [25].

The motivation for this research is to introduce a streamlined, holistic coupled dynamics simulation strategy known as SHARPE (**S**treamlined **H**ydrodynamics, **A**erodynamics, **R**igid body, **P**otentials, and viscous **E**ffects) numerical scheme for FOWTs under various environmental loads. The SHARPE numerical scheme employs the effective use of only one Computer Aided Engineering (CAE) tool kit within the ANSYS software workbench. In the SHARPE numerical scheme, fluid viscous effects are adequately modelled by performing an unsteady state multi-physics and Volume of Fluid (VoF) simulation wherein fluid force coefficients and viscous damping effects are calculated using a CFD toolkit (STAR-CCM+) to solve the Reynolds Averaged Navier Stokes (RANS) equations near the walls of the FOWT assemblage. Thereafter, by introducing a Floating Rigid Body (FRB) load model of the FOWT assemblage and a Finite Element (FE) model of the station keeping system, a global performance analysis; Hydrodynamic Diffraction (HD) and Hydrodynamic Response (HR) analysis of the FOWT may be performed by using the ANSYS AQWA CAE toolkit. Some of the key highlights of the SHARPE numerical scheme (Fig. 1.6) in comparison to the aero-hydro-servo-elastic approach are:

- Utilising the full FOWT geometry for the HD analysis rather than only the platform immersed geometry.
- Accounting for second-order effects of drift forces and sum-frequency excitation.
- Computing all viscous effects concurrently and implementing the same into the HR analysis onwards.
- Application of stability analysis to establish equilibrium positions and FOWT natural modes for all six degrees of freedom.
- Provision of aerodynamic and hydrodynamic loads and motions results in both frequency domain and time domain.

1.4 Goals, Significance, and Scope of Research

This research aims to address some of the limitations present in the current approach being utilised for coupled dynamic analysis of FOWTs by implementing a numerical process that uses CFD to adequately account for fluid viscous effects and developing a coupled dynamic simulation strategy that sufficiently determines the behaviour of a FOWT assembly under environmental loading. The following objectives have been identified of importance in helping to achieve the research aim;

- Identify the dominant forces driving hydrodynamic and aerodynamic loading on offshore deepwater wind turbine structures under operating and extreme environmental conditions.
- Address the current limitations in coupled dynamics simulation by developing a streamlined and holistic coupled dynamic modelling approach (SHARPE) for investigating the global dynamic performance of a FOWT.
- Perform multi-physics CFD simulation and coupled dynamics analysis of a FOWT structure under various scenarios of environmental loading.
- Conceptualise an in-house hybrid floating platform for FOWTs identified as the TRIgon Hybrid Floater (TRIHF).
- Validate results of the approach developed using standards, scaled model test experiments from similar projects, theoretical hand calculations, and other published test data.

A sound understanding of a floating platform's behaviour will provide more insight towards design optimisation for FOWTs. More importantly, gaining insight in the dynamic behaviour of the floating platform will offer cost and time reductions for performing preliminary engineering analysis which will ultimately yield a more profitable wind energy value chain for FOWTs. The scope of this research will address near to long-term needs for the offshore wind power industry in terms of a hybrid floating foundation concept and wind turbine installation for deep and ultra-deepwater location under various environmental conditions.

The investigation carried out in this research will involve the adequate modelling of fluid viscous effects due to the impact of wind and ocean current on the FOWT assembly, and viscous damping modelling on the floating platform from a free decay test. This is achieved by performing an unsteady state VoF multi-physics CFD simulation.

Next, the hydrodynamic radiation/diffraction model of the floating foundation will be solved for various wave spectra (related to operational, extreme and survivability conditions) to generate motion Response Amplitude Operators (RAOs) for all translational and rotational motions. By implementing the prior knowledge of force coefficients and viscous damping coefficients from the CFD simulation, the hydrostatic loads and loads effects on the global stability of the FOWT will be calculated to gain an understanding of the floater's equilibrium state. Results from the hydrodynamic radiation/diffraction model will serve as an input for the coupled dynamics simulation. Here, the stability of the platform, as well as motion responses in frequency and time domain are studied. In addition to investigating mooring line fairlead tensions, the coupled dynamics modelling will involve performing numerical simulations to examine coupling effects arising from hydrostatic loads, current loads, and wave loads on three different motion time scales;

- Wave Frequency (WF) motions created by;
  - first-order wave excitation forces,
  - Froude Krylov forces (incident wave forces) &,
  - Diffracting forces
- Low Frequency (LF) motions created by;
  - the wind drag force,
  - current drag force and,
  - second-order wave excitation forces (slowly varying wave drift forces)
- High Frequency (HF) motions created by the sum-frequency second-order wave excitation force.

To validate and measure the performance of the SHARPE numerical scheme, results will be compared to theoretical hand calculations, model tests results, and common standards in a bid to demonstrate the importance of viscous effects. The FOWT assemblage adopted for this study is the NREL 5 MW baseline wind turbine mounted on a

newly developed inhouse hybrid floating platform concept identified as the TRIgon Hybrid Floater (TRIHF). The site-specific environmental conditions employed for this research are based on hindcast data of potential offshore wind turbine Project Development Areas (PDAs) in New Zealand.

1.5 Thesis Outline

In Chapter 2 the basic concept surrounding aerodynamic and hydrodynamic loading is introduced. Also, the main challenges surrounding the accurate investigation of aerodynamic and hydrodynamic loading for FOWTs are discussed. More importantly, a review of current methodologies and technologies as it relates to coupled dynamics global performance investigation of FOWTs under environmental loading is debated.

Chapter 3 presents an environmental scoping assessment performed for two potential Project Development Areas (PDAs) for FOWTs in New Zealand's northland. In this Chapter, quantitative and qualitative statistical analysis were performed for the site-specific long-term Metocean hindcast data (wind, wave, and ocean current) obtained for the PDAs. The results of the statistical analysis are further investigated to develop site-specific wind, wave, and ocean current models for various operating conditions and return periods. Deriving these site-specific models is a preamble to performing the CFD numerical simulations and coupled dynamics simulation described in Chapter 5 and Chapter 6.

In Chapter 4, the wind turbine baseline and the newly developed hybrid floating platform concept known as the TRIgon Hybrid Floater (TRIHF) are discussed. The wind turbine baseline adopted for this research is the National Renewable Energy Laboratory five megawatts (NREL - 5 MW) WTG system. Interesting details of the TRIHF concept design which is inspired by the hybridisation of the generic floating platform concepts (TLP, Spar, Semi-submersible) are provided.

To give the audience a better understanding of the analysis and discussions done in Chapter 6, Chapter 5 describes the modus-operandi of SHARPE numerical scheme, the newly developed coupled dynamics simulation strategy employed for this research. Here, the most relevant schemes behind the SHARPE coupled dynamics modelling approach and the basis for developing a more streamlined yet wholistic coupled dynamics modelling strategy are discussed. The SHARPE numerical modelling scheme

developed for this research consists of two main components. The first being the use of CFD for wind and ocean current viscous force coefficient calculations, and viscous damping coefficient investigation. The CAE toolkit employed for the CFD simulation is the STAR-CCM+. The results from the CFD numerical simulation is subsequently implemented as part of the second component of the modelling scheme which involves the use of a potential based Floating Rigid Body Dynamics (FRBD) finite element solver (ANSYS AQWA). With results from the CFD numerical simulation and wave model as input, ANSYS AQWA is utilised to further investigate the dynamic response of the FOWT under operating, extreme, and survival aerodynamic and hydrodynamic loads. More importantly, Chapter 5 also present the validation of the SHARPE numerical modelling scheme. This was achieved by comparing the simulation results of the SHARPE numerical scheme with the published test data of a scaled model experiment performed for the DeepCwind-OC5 project [29], [30].

In Chapter 6, engineering and mathematical analysis are performed to obtain time domain and frequency domain results for motion responses and forces for the TRIHF platform. Results from the CFD numerical simulation and coupled dynamics numerical modelling are discussed and compared with the results from published test and/or experimental data in works of literature. This is done to gain an understanding of the rationality of the predicted global performance of the TRIHF's aerodynamic and hydrodynamic response to environmental loads. Chapter 7 will present the conclusion, outlook, and key learnings from the research, and recommendations for further works.

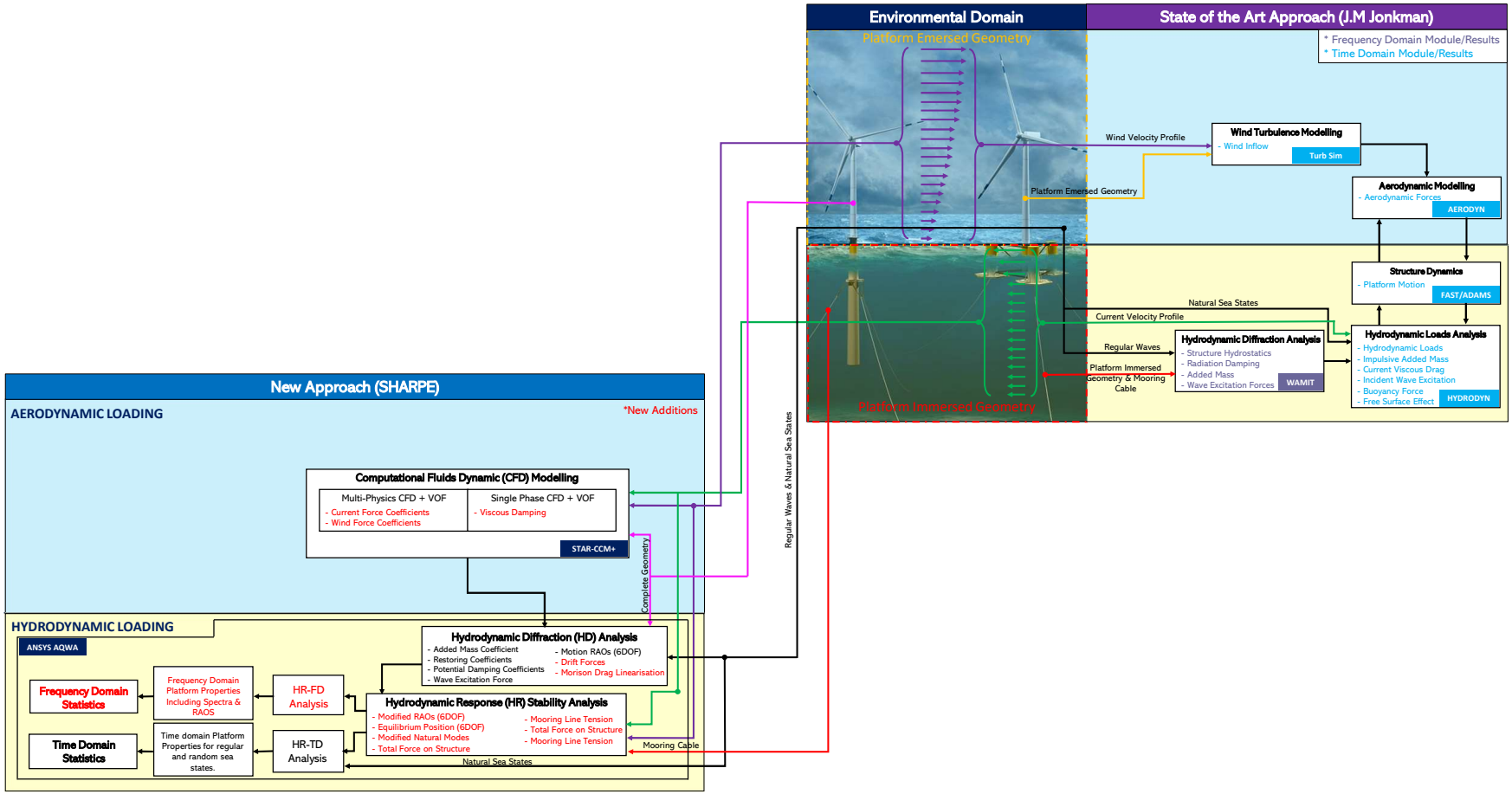

FIGURE 1.6: Flow chart showing coupled dynamics strategy comparison between the State-of-the-art approach and New Approach

.

Chapter 2

Current Research Methodology and Technology Review

This literature review will present some basic theories, principles, concepts, and key parameters relating to the aerodynamic and hydrodynamic loads experienced by a structure in general and more specifically, a Floating Offshore Wind Turbine (FOWT). The challenges surrounding the investigation of aerodynamic and hydrodynamic loads on FOWT assemblies with complex geometry are discussed. Current models/methodologies for coupled dynamics analysis used for exploring the global performance of a FOWT assemblage will be debated and their limitations highlighted. At the end of this chapter, it is anticipated that an understanding of the key challenges associated with investigating aerodynamic and hydrodynamic loads on a FOWT is demonstrated, that the reader will be better informed in these areas, and that there will emerge a clear focus and justification for undertaking this research.

2.1 Sources and Mechanism of Aerodynamic Loading

Aerodynamic loads arise from the force exerted on a FOWT whenever there is a relative velocity between the topside assemblage of the FOWT and the oncoming free air-stream. The two main sources of aerodynamic loads emanate from; the pressure distribution (form drag) and the frictional shear stress distribution (friction drag). These forces are exerted by the free air-stream on the topside of the FOWT assemblage. The pressure exerted by the free air-stream at a point on the surface of the FOWT acts perpendicular to the surface at that point. In the same vein, the shear stress which is due to the frictional action of the free stream air rubbing against the FOWT surface acts tangentially to the surface at that point. The distribution of frictional shear stress and

pressure represents a distributed load over the surface of the FOWT because they simultaneously act on each point on the body. Thus, the net aerodynamic force exerted on a FOWT's surface arises from the net imbalance between the distributed loads as they are integrated over the entire surface of the FOWT. This section will elucidate the mechanism around the aerodynamic forces and moments experienced by FOWTs. Information on how wind-generated pressure distribution and tangential stresses distribution drive wind turbine rotors will be elaborated. Also, the basic principles around the aerodynamic performance of the horizontal axis wind turbine adopted for this research are presented by explaining the concept of axial momentum and the theory behind the evaluation of a wind turbine's rotor performance. The discussion of these aforementioned concepts is the basis for the engineering calculations performed in section 6.1.2 where the viscous drag forces due to wind and ocean current acting on the surfaces of the FOWT were determined under various environmental conditions.

2.1.1 Forces and Moments on Wind Turbine Rotors

A widely used approach for investigating aerodynamic loads on a wind turbine rotor involves performing Computational Fluid Dynamics (CFD) numerical simulation. The goal of a CFD study is to investigate the flow interaction around the wind turbine rotor and the resulting aerodynamic loading. The primary focus of such study is to determine any or a combination of the following;

- calculate the thrust force resulting from drag due to the rotor's swept area,
- analyse the lift force ensuing from the impact of the wind on the rotor,
- explore the aerodynamic performance of the aerofoil sections of the rotor blades, and
- estimate the torque and moments resulting from the rotor's rotation.

As depicted in Fig. 2.1 below, a wind turbine rotor consists of the blades (4) and hub (3). The impact of the upstream wind on the rotor results in a pressure differential between the upstream and downstream wind across the face of the blades which yields a net lift force (F_L) resulting in the rotation of the rotor.

The impact of the upstream wind on the rotor also results in a net thrust force (F_T) normal to the swept area of the rotor, (A_{rotor}). The rotor's revolution results in a torque

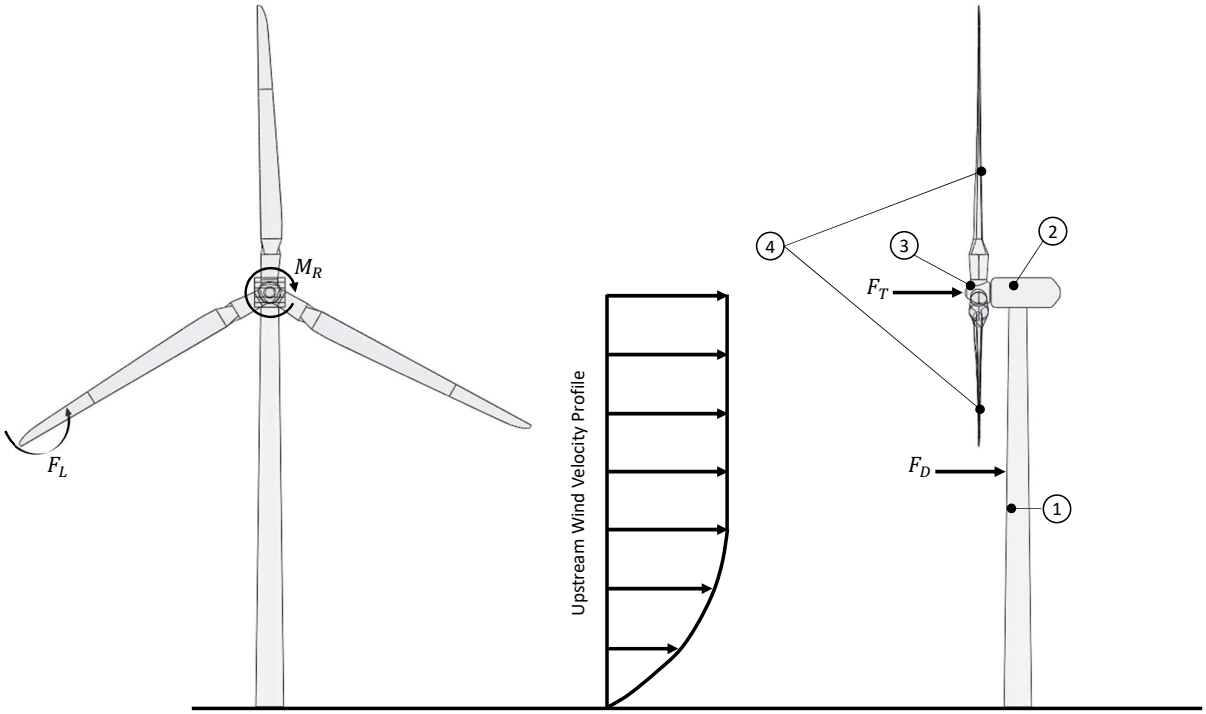

FIGURE 2.1: An illustration showing various forces and moments acting on a Horizontal Axis Wind Turbine (HAWT) wind components (1) Tower, (2) Nacelle, (3) Hub and (4) Blades.

force or moment (M_R) which drives a generator housed in the nacelle (2). The generated electric power from the generator housed in the nacelle is transported through a cable contained in the tower (1) to a power storage facility.

Furthermore, the illustration in Fig. 2.1 further elucidates the principle on how HAWTs blades extract kinetic energy from the wind using aerodynamic forces developed on the rotor's blade. The extracted kinetic energy is transformed into mechanical energy in a shaft and subsequently into electrical energy in a generator. The efficiency of the rotor extracting kinetic energy from the wind is a function of the aerodynamic characteristics of the aerofoil sections used in the design of the rotor's blade.

An aerofoil is technically a curved surface or body designed to produce an aerodynamic force (lift) perpendicular to its direction of motion, for a slight resistance force (drag) in that plane. The aerodynamic characteristics of a wind turbine rotor are largely affected by the shape of the aerofoils that make up various sections of the blades. The aerofoil sections implemented for the wind turbine baseline utilised for this research is presented in section 4.1.1. Fig. 2.2 represents an aerofoil and its characteristic geometrical quantities. The shape of an aerofoil is characterised by coordinates of the lower

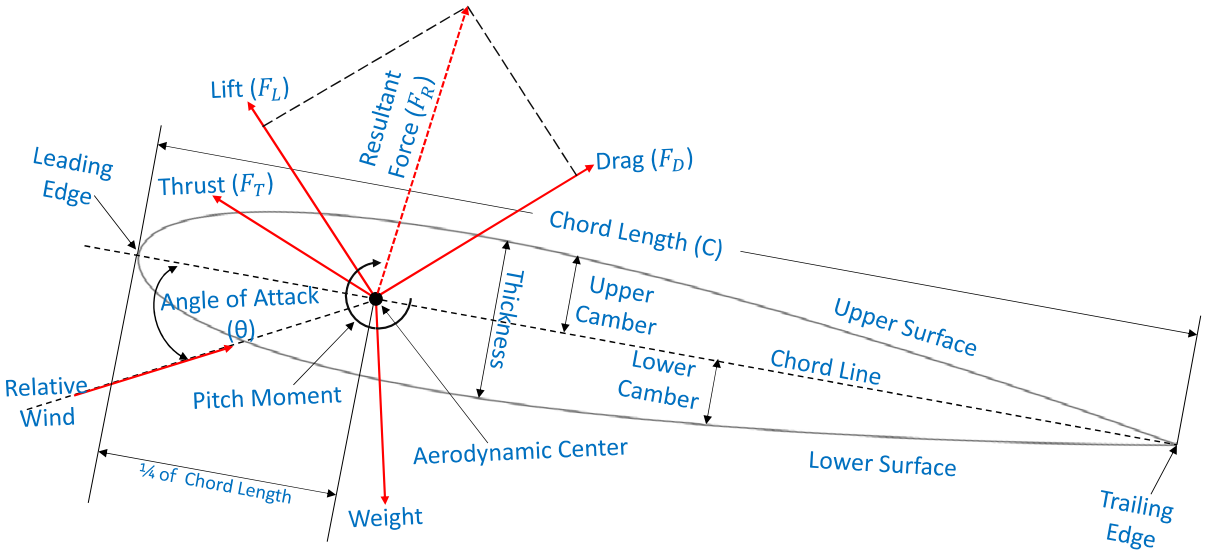

FIGURE 2.2: Geometric Properties and Aerodynamic Forces and Moments Acting on an Aerofoil.

surface and upper surface also known as the lower camber and upper camber, respectively. As Fig. 2.2 indicates, the thick section of the aerofoil is known as the leading edge while the small tapering end is known as the trailing edge.

The chord line of an aerofoil is a straight line linking the leading edge with the trailing edge while its chord length is the distance between its leading edge and trailing edge when measured along the chord line. The camber is the maximum distance between the aerofoil's surface and its chord line while the thickness of a section is the distance between the upper and lower surfaces of the section measured perpendicularly to the chord line. Given the parameters of the coordinates for the upper camber, lower camber, maximum thickness, and position of maximum thickness, an aerofoil can be generated.

The aerodynamic angle of attack is the pitch angle at which the incident flow encounters the aerofoil's surface while the pitch moment acts at one-quarter of the aerofoil's chord length (also known as the aerodynamic centre) and does not change with the angle of attack. The concept of aerofoils was first developed by Eastman Jacobs in the early 1930s where he created a family of aerofoils known as the NACA (National Advisory Committee for Aeronautics) sections [31], [32].

Fig. 2.3 illustrates a hypothetical flow behaviour around an aerofoil where streamlines have been represented. As the wind arrives at the leading edge of the aerofoil horizontally, the aerofoil changes the direction of the upstream wind by deflecting it

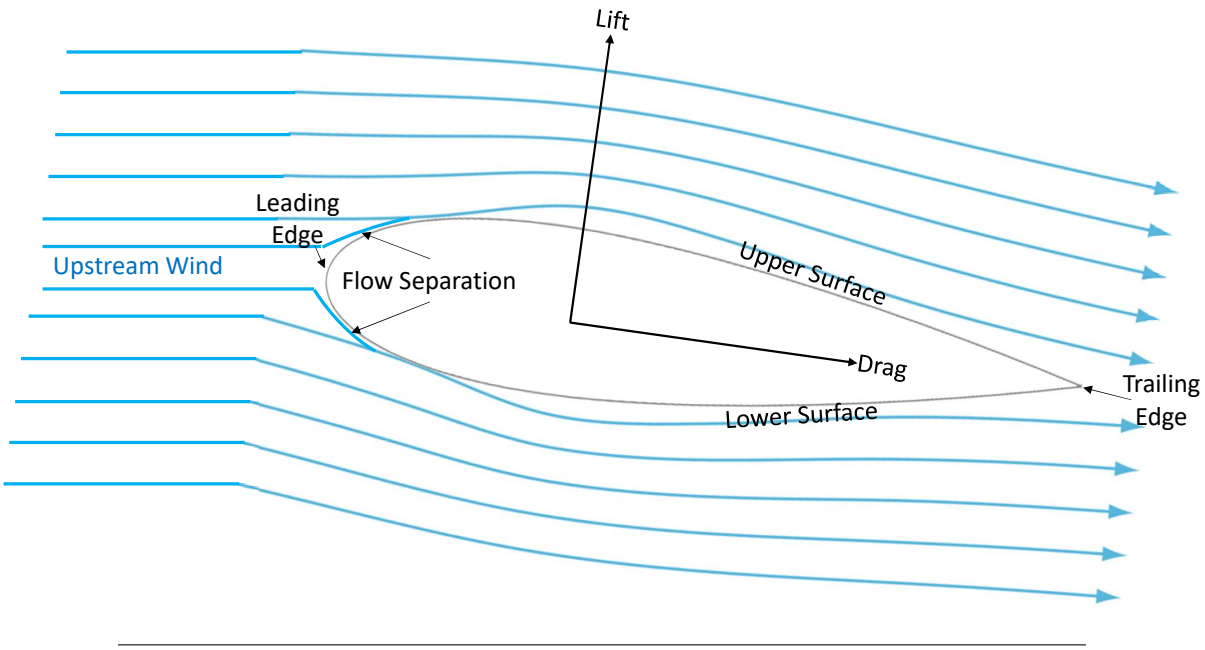

FIGURE 2.3: Streamlines around an aerofoil section.

downwards. According to Newton's third law of motion, since the surface of aerofoil causes the air to be deflected downwards, an equivalent force in the opposite direction causes the aerofoils to rotate in the opposite direction (upwards). The angle of attack of the wind against the aerofoil's surface greatly affects how much of these aerodynamic reactive forces come into play.

A second explanation which is common in literature revolves around a theory labelled "Longer Path" theory, or the "Equal Transit Time" theory. This theory is based on an observation that the distance from the leading edge to the trailing edge along the upper surface of an aerofoil is greater than the distance along the lower surface. It can be presumed that the two neighbouring fluid particles which split at the leading edge will meet at the trailing edge. Thus, this will require that the average velocity of the air-stream along the upper surface is greater than that on the lower surface. From Bernoulli's equation which implies that larger velocities imply lower pressures and vice-versa, then a net upward pressure force will be generated because the force will be lower along the aerofoil's upper surface than for the lower surface. While this may be true, the aerofoil of Fig. 2.3 does not exhibit a greater distance between the leading and trailing edge along the upper and lower surface. Thus, the Longer Path Theory may not be a necessary condition for lift production [31]–[33]. Symmetric aerofoil generates lift despite its upper surface being the same length as the lower surface.

The relationship between the lift coefficient, (C_L) and lift force, (F_L) per unit span of an aerofoil due to aerodynamic interaction around the surfaces of the aerofoil is expressed as;

$$C_L = \frac{F_L}{\frac{1}{2}\rho_{air} U_w^2 C} \tag{2.1}$$

where ρ_{air}, U_w, and C are the air mass density ($1.225 kg/m^3$), wind velocity and chord length of the aerofoil, respectively. The lift coefficient (C_L) of an aerofoil section is a function of the aerodynamic angle of attack, θ, Reynolds number, Re, and Mach number, Ma;

$$C_L = f\left(\theta,\ Re, Ma\right) \tag{2.2}$$

where;

$$Re = \frac{\rho_{air}\ U_w C}{\mu_{air}} \tag{2.3}$$

and

$$M_a = \frac{U_w}{c} \tag{2.4}$$

where μ_{air} is the dynamic viscosity of air ($1.85508 \times 10^{-5}\ Pa.s$), and c is defined as the speed of sound in the surrounding medium of the flow boundary (air in this case, $c = 344\ m/s$). Similarly, the drag coefficient, C_D and pitching moment coefficient, $C_{\tau_{c/4}}$ about the quarter-chord location per unit span of the aerofoil is given by;

$$C_D = \frac{F_D}{\frac{1}{2}\rho_{air} U_w^2 C} = f\left(\theta,\ Re, Ma\right) \tag{2.5}$$

and

$$C_{\tau_{c/4}} = \frac{\tau}{\frac{1}{2}\rho_{air} U_w^2 C^2} = f\left(\theta,\ Re, Ma\right) \tag{2.6}$$

2.1.2 Flow Through Rotor – Axial Momentum Theory

In the axial momentum theory, the wind turbine rotor is mimicked to behave like an actuator or braking disc with zero thickness. In other words, the disc is considered ideal, frictionless and with no rotational velocity in the wake region [34]. Fig. 2.4 depicts the pressure and velocity distribution over a wind turbine rotor acting as a braking disc. Four key regions (free-stream region, upstream rotor region, downstream rotor region, and far-wake region) have been identified of importance in understanding the

flow phenomena around wind turbine rotors. As can be understood from the illustration in Fig. 2.4, when the wind in the free stream region flow at a velocity U_∞ through the swept region of the wind turbine rotor, it loses velocity between the upstream and downstream region of the rotor (U_{rotor}) because the wind perceives the rotor as a braking disc (see black dashed line). Once the wind in the free stream region makes an impact with the blades, it causes the rotor to rotate at an angular velocity (ω) which in turn generates torque on the blades and a further reduction in velocity towards the far wake region (U_{wake}). The torque on the blade forces the air particles around the downstream rotor region and far wake region to rotate in the opposite direction at the angular velocity of the rotor.

From Fig. 2.4 and according to the law of conservation of mass, the mass flow rate will be equal in every identified region. Hence;

$$\rho_{air} A_\infty U_\infty = \rho_{air} A_{rotor} U_{rotor} = \rho_{air} A_{wake} U_{wake} \tag{2.7}$$

where A_{rotor} is the total swept area of the rotor as illustrated in Fig. 2.5 below. The degree of decay in the axial velocity component of the wind as the free stream velocity, U_∞, is reduced to the axial velocity around the rotor plane, U_{rotor}, is given by a property known as the axial induction factor, a, which is expressed as;

$$a = \frac{U_\infty - U_{rotor}}{U_\infty} \tag{2.8}$$

In addition, the overall change in velocity in the whole system, ΔU_{sys} can be said to be the difference in velocity between the free stream region and the far-wake region;

$$\Delta U_{sys} = U_\infty - U_{wake} \tag{2.9}$$

Thus, the rate of axial momentum change, Δa_{mom} around the rotor region can be expressed;

$$\Delta a_{mom} = \Delta U_{sys} \rho_{air} A_{rotor} U_{rotor} \tag{2.10}$$

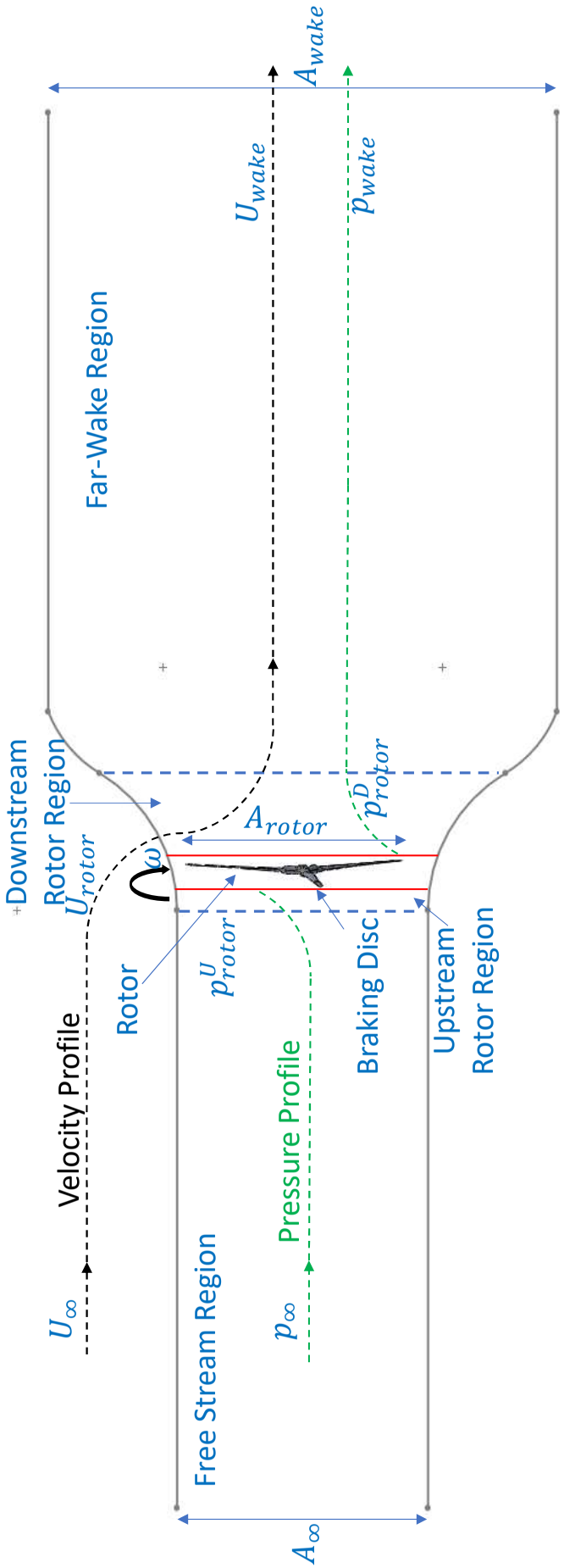

FIGURE 2.4: Axial Momentum Flow Model Showing Pressure and Velocity Distribution over a wind turbine rotor acting as a braking disc.

As indicated in Fig. 2.4, the rotor region is likened to a braking disc causing an interruption of the wind flow. There is a rotational wake reaction generated behind the rotor because of the torque applied to the rotor by the wind. Accordingly, there is energy loss which ultimately reduces the optimum power efficiency, $C_{P,opt}$ also known as tip losses. Rotor tip losses occur due to the pressure at the downstream region of the rotor (p^{D}_{rotor}) being lower than the pressure on the upstream region on the rotor (p^{U}_{rotor}). Thus, wind tends to flow around the tip from the lower to the upper surface of the blade, thereby reducing the lift and power produced near the blade tip [35]. Consequently, the axial momentum changes between the free stream region and far wake region are because of the pressure difference between the upstream rotor region and downstream rotor region (i.e., across the disc area). Hence, the force causing the change in momentum can be stated as;

$$\left(p^{U}_{rotor} - p^{D}_{rotor}\right) A_{rotor} = \Delta U_{sys} \rho_{air} A_{rotor} U_{rotor} \tag{2.11}$$

By considering an assumption that the static pressure at the free stream region and far wake region is equal to the atmospheric pressure, p_{atm} and applying the Bernoulli's equation at these regions then;

$$p_{atm} + \frac{\rho_{air} U^{2}_{\infty}}{2} = p^{U}_{rotor} + \frac{\rho_{air} U^{2}_{rotor}}{2} \tag{2.12}$$

and

$$p_{atm} + \frac{\rho_{air} U^{2}_{wake}}{2} = p^{D}_{rotor} + \frac{\rho_{air} U^{2}_{rotor}}{2} \tag{2.13}$$

By applying the continuity and momentum theories to equations 2.12 and 2.13, and as referenced in [34], [36] the rate of pressure change Δp_{rotor}, between the upstream and downstream region of the rotor surface at the disc section can be defined as;

$$\Delta p_{rotor} = \left(p^{U}_{rotor} - p^{D}_{rotor}\right) = 0.5 \rho_{air} \left(U^{2}_{\infty} - U^{2}_{wake}\right) \tag{2.14}$$

The thrust force (F_T) experienced by the rotor is due to the difference in momentum between the free stream region and far wake region which is given by;

$$F_T = \rho_{air} (A_{\infty} U^{2}_{\infty} - A_{wake} U^{2}_{wake}) \tag{2.15}$$

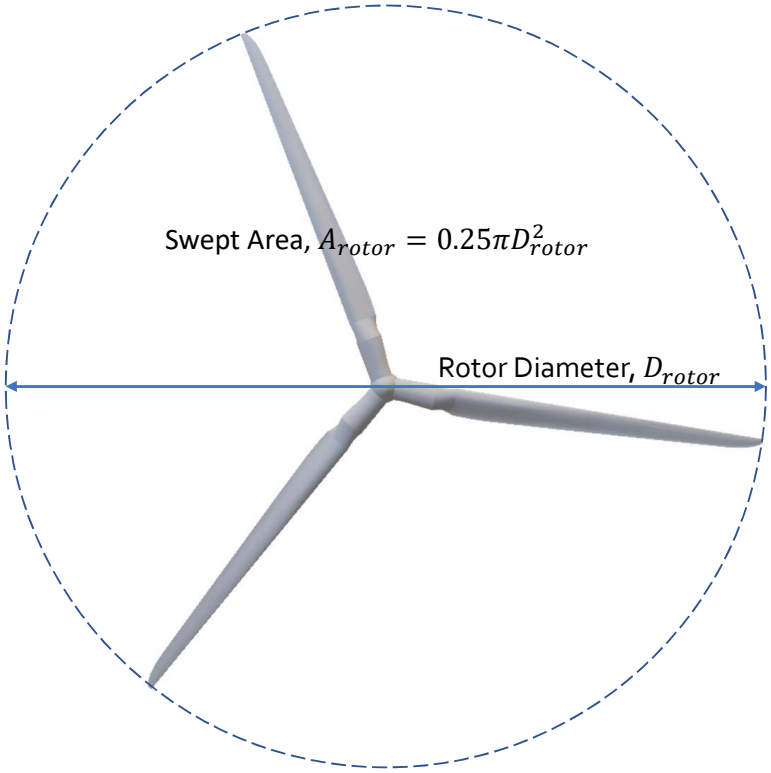

FIGURE 2.5: Rotor swept area

From equation 2.7, $A_\infty U_\infty = A_{rotor} U_{rotor} = A_{wake} U_{wake}$. By introducing an additional term due to drag (C_T) known as the thrust coefficient, the thrust force due to rotor-filtered wind loads can be expressed as;

$$F_T = C_T \rho_{air} A_{rotor} U_{rotor} \left(U_\infty - U_{wake}\right) \tag{2.16}$$

Furthermore, the thrust force can also be expressed as the pressure difference between the upstream and downstream sides of the rotor. Hence;

$$F_T = C_T \left(p_{rotor}^U - p_{rotor}^D\right) A_{rotor} \tag{2.17}$$

Substituting equation 2.14 into 2.17 the thrust force due to rotor-filtered wind loads can be expressed as;

$$F_T = 0.5 C_T \rho_{air} A_{rotor} \left(U_\infty^2 - U_{wake}^2\right) \tag{2.18}$$

Comparing equations 2.16 and 2.18 gives;

$$U_{rotor} = 0.5 \left(U_\infty - U_{wake}\right) \tag{2.19}$$

As can be seen from equation 2.19, the velocity of the wind stream at the rotor region is the average of the velocities at its far stream and far wake regions. The axial induction factor (a) which indicates the degree with which the wind velocity in the far stream region is slowed down by the rotor was expressed in equation 2.8. Combining equations 2.8 and 2.19 yields;

$$U_{rotor} = U_{\infty}(1 - a) \tag{2.20}$$

and

$$U_{wake} = U_{\infty}(1 - 2a) \tag{2.21}$$

The maximum theoretical torque generated by the rotor blades (T_{max}), can be represented as;

$$T_{max} = 0.5\rho_{air} A_{rotor} U_{\infty}^2 R_{rotor} \tag{2.22}$$

where R_{rotor} is the radius of the rotor. However, the rotor shaft can develop only a fraction of the maximum theoretical torque. The torque coefficient (C_{tor}) is used to define the ratio between the actual torque developed by the rotor and the theoretical torque. Thus, the rotor torque coefficient can be expressed as;

$$C_{tor} = \frac{2T_{rotor}}{\rho_{air} A_{rotor} U_{\infty}^2 R_{rotor}} \tag{2.23}$$

where T_{rotor} is the actual torque generated by the rotor.

During the CFD numerical simulation (see section 6.1), an expression language in star CCM+ was used to compute the the rotor torque resulting from the rotor's rotation and subsequently the power of the rotor was calculated from the computed torque using a predefined expression language. The power generated by the rotor as a function of the rotor torque can be defined as[37];

$$P_{rotor} = \frac{\pi}{30} T_{rotor} N_{Rotor} \tag{2.24}$$

Where N_{rotor} is the rotor speed in revolutions per minute.

2.1.3 Wind Turbine Performance

On a wind turbine rotor, the velocity of the blade elements at any section along the blade is a function of the wind speed (U_{∞}) and the rotational velocity of the rotor

per radial location (ωr), where (r) is a radial location along the surface of the rotor blade. The resultant velocity along the radial location of the rotor blade increases as $r \rightarrow R_{rotor}$. What this means is that the maximum speed along the radial location of the rotor blade occurs at the blade tip. Thus, the maximum resultant velocity (U_R) at the rotor blade tip is the vector sum of the wind speed and blade rotational velocity. The vector sum of these two velocity components can be expressed as;

$$U_R = \sqrt{U_\infty^2 + (\omega R_{rotor})^2} \tag{2.25}$$

where ω is expressed in rad/s. The rotor power at a certain speed is a function of the wind velocity and the rotor blade tip speed. If the rotor revolves at a very low speed and the free stream wind is approaching at a very high velocity, a portion of the wind stream approaching the rotor may flow through without it interacting with the blades and thus no kinetic energy transfer which ultimately results to a loss in energy. In the same vein, if the rotor is rotating fast and the free stream wind approaches with a low velocity, the wind stream may be deflected from the rotor which again ultimately results to a loss in energy due to vortex shedding and turbulence. The tip speed ratio (λ_{TSR}) is used to envisage the phenomena between wind speed and the rotor tip speed. The Tip Speed Ratio (TSR) is simply the ratio between the rotor blade tip and wind speed. Thus;

$$\lambda_{TSR} = \frac{\omega R_{rotor}}{U_\infty} = \frac{2\pi N_{rotor} R_{rotor}}{U_\infty} \tag{2.26}$$

The rotor's power coefficient and torque coefficient vary with its TSR. Hence, there is an optimum TSR for a given rotor at which the kinetic energy transfer from the wind unto the rotor surface is most resourceful and thus the power coefficient is optimum ($C_{P,opt}$).

As has been discussed earlier in section 2.1.1, the power generated by the wind turbine rotor is due to the transfer of kinetic energy from the wind to the rotor. From the equation of mass conservation expressed in equation 2.7, the mass flow at the upstream stream rotor region over a unit time can be expressed as;

$$m_{air} = \rho_{air} A_{rotor} U_\infty \tag{2.27}$$

while the mass flow at the rotor region due to the flow of wind through the rotor over a unit time is;

$$m_{air} = \rho_{air} A_{rotor} U_{rotor} \tag{2.28}$$

From the fundamental kinetic energy equation, the maximum theoretically available energy, KE_{max} that can be extracted from the wind can be expressed as;

$$KE_{max} = \frac{1}{2} m_{air} U_{\infty}^2 \tag{2.29}$$

While the energy generated by the rotor due to the transfer of kinetic energy from the wind onto the blade's surface is;

$$KE_{rotor} = \frac{1}{2} m_{air} U_{rotor}^2 \tag{2.30}$$

Substituting equation 2.27 into equation 2.29, and equation 2.28 into equation 2.30 gives;

$$KE_{max} = \frac{1}{2} \rho_{air} A_{rotor} U_{\infty}^3 \tag{2.31}$$

and

$$KE_{rotor} = \frac{1}{2} \rho_{air} A_{rotor} U_{rotor}^3 \tag{2.32}$$

As can be fathomed from equation 2.31 and 2.32, the magnitude of the wind velocity available at a potential wind turbine site is crucial in determining maximum available power available for extraction because the power increases with the cube of the wind speed and only linearly with the density of the wind and swept area of the rotor. Thus, prior information on data for the available wind at a given site over a period is needed before a wind energy project can be initiated.

In principle, not all the energy in the wind can be extracted by the wind turbine rotor because some volume of wind will flow past the rotor without making any contact with the aerofoil surface of the rotor. Consequently, the power coefficient, C_P is used to define the actual power produced by the rotor which is a ratio of the power extracted from the wind by the rotor (P_{rotor}) to the maximum power (P_{max}) available for extraction. From this definition, C_P can be stated as;

$$C_P = \frac{P_{rotor}}{P_{max}} \tag{2.33}$$

Consequently;

$$P_{rotor} = P_{max} C_P = \frac{1}{2} C_P \rho_{air} A_{rotor} U_\infty^3 \tag{2.34}$$

The theoretical optimum power efficiency is known as the Betz Limit $C_{P,opt}$ and have been established to be equal to 0.593. A $C_{P,opt}$ value of 0.593 indicates that a wind turbine rotor can only account for a maximum of 59.3% of the incoming flow and does not take into consideration the energy required to drive the rotor behind the turbine [34], [36].

2.2 Aerodynamic Loading Investigation on Offshore Wind Turbines

Oftentimes, our expectations of what will happen in a fluid dynamics situation might be wrong. This has suggested to researchers that many phenomena in fluid mechanics are very complicated indeed and caution needs to be taken to guard against the attainment of overly simple conclusions. Quite a few types of research have investigated aerodynamic loading on FOWTs. However, more attention needs to be given to studying the complexities of the wind dynamics in an offshore environment with extreme weather conditions, and how it impacts the amount of wind thrust being experienced by a FOWT. Amongst others, the absence of prior study(ies) investigating aerodynamic loads for a site-specific data in one of New Zealand's potential offshore location for an OWT is part of the motivation for undertaking this research. The author's previous dissertation which can be found in [38] contains more information on the theories and concepts of viscous drag force modelling for marine structures.

In section 6.1.2, the meshing strategy and refinement study performed for the viscous force numerical calculations implemented the y^+ function to address the occurrence of high solution gradients that may occur near the solid boundary of the FOWT structure. The y^+ function (see equation 6.8) is useful in determining the mesh's first cell height that is deemed suitable to adequately resolve the high solution gradient arising from the turbulent flow conditions around the solid boundaries of the structure.

2.2.1 Wind Force Spectrum Modeling

In addition to creating wind-induced waves, wind creates significant loads on a FOWT because the portion of its structure above the MSL is significant. The natural wind has

two components accountable for this phenomenon; a static component and a dynamic component. Thus, the magnitude of the wind velocity responsible for aerodynamic load stems from three important parameters [39], [40];

- a mean velocity (static component) which is the average wind speed over a given period of time (generally 1 hour) at a standard height above the water surface (typically 10 m), $\bar{U}_w$,
- a mean speed profile described as the velocity of the mean wind variation with elevation above the water surface, and
- turbulence or gusts (dynamic component) depicted as the time-varying wind speed about the mean speed, $U_w(t)$.

For simplification, it is assumed that there is no vertical component of the wind velocity in the Fixed Reference Axes (FRA), i.e., the wind speed is always in the horizontal plane of the FRA. As a result, the wind spectrum above the water surface is modelled using the $1/7^{th}$ power-law decay which is given by [41];

$$U_z = U_{10}\left[\frac{z}{10}\right]^{\frac{1}{7}} \tag{2.35}$$

where U_z is the wind speed at zm elevation above MSL, U_{10} is the wind speed at $10m$ above MSL, and $10m$ is called the reference height. The power-law model is simply empirical and conventional and has been tested and proven with actual field measurements. Equation 2.35 provides the mean wind velocity component. The gust factor, F_g, which ranges from 1.35 - 1.45 is used to obtain the gust component, U_g, using equation 2.36;

$$U_g = F_g \times U_s \tag{2.36}$$

where U_s is the sustained wind speed[1]. For offshore locations, the mean wind speed is significantly higher than the gust component which means that the use of static analysis for wind loading investigation will suffice. However, since wind introduces low-frequency excitation, its fluctuating component is modelled probabilistically. Most international codes such as the DNV proffer the use of quasi-static analysis for examining wind loads on marine structures.

[1]The sustained wind speed is the one-minute average wind speed.

A parameter known as the Aerodynamic Admittance Function (AAF) provides an intelligent way to define cross-spectrum in the analysis of wind loads. The AAF helps circumvent a rigorous random analysis, in addition to providing the possibility of accurate measurement through wind tunnel experiments. In this fashion, the altitudinal variations of wind velocity are calculated judiciously in wind load analysis. The wind load force, F_w , can be calculated using the equation below;

$$\begin{aligned} F_w = \frac{1}{2}\rho_{air} C_w {U_w}^2 A_{ref} & \\ = \frac{1}{2}\rho_{air} C_w A_{ref} \left[\bar{U}_w + U_w(t)\right]^2 & \\ = \frac{1}{2}\rho_{air} C_w A_{ref} \left[\bar{U}_w^2 + \left(U_w(t)\right)^2 + 2\bar{U}_w U_w(t)\right] & \end{aligned} \tag{2.37}$$

neglecting gust component with high power yields,

$$F_w \cong \bar{F}_w + \rho_{air} C_w A_{ref} \bar{U}_w U_w(t) = \bar{F}_w + F_w(t) \tag{2.38}$$

where C_w is the wind pressure coefficient determined during wind tunnel experiment under controlled stationary wind flow conditions. $\bar{F}_w$ and $F_w(t)$ are the static and dynamic wind force, respectively. As can be seen from equation 2.38, the total wind force is expressed as the sum of the mean component and gust component. It is logical to consider wind as an ergodic[2] process. Hence, a nexus between the Power Spectral Density (PSD) of the wind process and the wind spectrum can be defined as;

$$S_F^+(\omega) = \left[\rho_{air} C_w A_{ref} \bar{U}_w\right]^2 S_U^+(\omega) \tag{2.39}$$

The total wind-induced force is given by;

$$F_w = p_w A_{ref} = \frac{1}{2}\rho_{air} C_w U_w A_{ref} \tag{2.40}$$

where p_w is the net wind pressure. Substituting equation 2.40 into equation 2.39 and rearranging the terms gives;

$$S_F^+(\omega) = \frac{4\left[\bar{F}_w\right]^2}{\left[\bar{U}_w\right]^2}\left[\chi\left\{\frac{\omega\sqrt{A_{ref}}}{2\pi\bar{U}_w}\right\}\right]^2 S_U^+(\omega) \tag{2.41}$$

[2]Its statistical properties can be deduced from a single, sufficiently long, random sample of process.

In equation 2.41, the AAF creates the relationship between response spectra and force, and varies as shown in equation 2.42 below;

$$\begin{aligned} for \quad & \frac{\omega\sqrt{A_{ref}}}{2\pi\bar{U}_w} \Longrightarrow 0, \;\; \chi\left\{\frac{\omega\sqrt{A_{ref}}}{2\pi\bar{U}_w}\right\} \Longrightarrow 1 \\ for \quad & \frac{\omega\sqrt{A_{ref}}}{2\pi\bar{U}_w} \Longrightarrow \infty, \;\; \chi\left\{\frac{\omega\sqrt{A_{ref}}}{2\pi\bar{U}_w}\right\} \Longrightarrow 0 \end{aligned} \tag{2.42}$$

Davenport (1961) proposed an empirical relationship for the aerodynamic admittance function using the equation below [42];

$$\chi(x) = \frac{1}{\left[1 + (2x)^{4/3}\right]} \tag{2.43}$$

For a reference height of $z = 10\ m$ above MSL, wind spectra are modelled on offshore marine structures in terms of circular frequency which is expressed as;

$$S_u^+(\omega) = fG_u^+(f) \tag{2.44}$$

where;

1. Davenport Spectrum

$$\frac{\omega S_u^+(\omega)}{\delta\bar{U}_p^2} = \frac{4\theta^2}{(1+\theta^2)^{4/3}} \tag{2.45}$$

2. Harris Spectrum

$$\frac{\omega S_u^+(\omega)}{\delta\bar{U}_p^2} = \frac{4\theta}{(2+\theta^2)^{5/6}} \tag{2.46}$$

3. Kaimal Spectrum

$$\frac{\omega S_u^+(\omega)}{\delta_u^2} = \frac{6.8\theta}{(1+10.2\theta)^{5/3}} \tag{2.47}$$

4. API (2000) spectrum

$$\frac{\omega S_u^+(\omega)}{\delta_u(z)^2} = \frac{(\omega/\omega_p)}{\left[1 + 1.5\,(\omega/\omega_p)\right]^{5/3}} \tag{2.48}$$

θ is a derived variable that is expressed as;

$$\frac{\omega L_u}{2\pi \bar{U}_{10}} = \frac{\delta L_u}{\bar{U}_{10}}, \quad 0 < \theta < \infty \tag{2.49}$$

where L_u is the integral length scale and is equal to $1,200\ m$ and $1,800\ m$ for Davenport and Harris spectrum, respectively. δ is the surface drag coefficient which is equal to 0.001 for offshore locations. ${\delta_u}^2$ is the variance of $U_w(t)$ at reference height of $10\ m$. $\bar{U}_p$ is the peak velocity and ω_p is the peak frequency. ${\delta_z}^2$ is the variance of $U_w(t)$ and is valid when the non-dimensional frequency, $\widetilde{f}$ is;

$$0.01 \leq \frac{\omega S_u^+(\omega)}{\delta_u^2} \leq 0.1 \tag{2.50}$$

alternatively;

$$0.01 \leq \frac{\omega_p z}{\bar{U}(z)} \leq 0.1 \tag{2.51}$$

A non-dimensional frequency value of 0.025 is usually obtained from equation 2.50 and 2.51 above. However, the standard deviation and speed are given by;

$$\delta_u(z) = \left\{ \begin{array}{l} 0.15\bar{U}(z)\left(\frac{z_s}{z}\right)^{0.125} : z \leq z_s \\ \\ 0.15\bar{U}(z)\left(\frac{z_s}{z}\right)^{0.275} : z \leq z_s \end{array} \right\} \tag{2.52}$$

z_s is the surface layer thickness which is taken as $20\ m$. It is noteworthy that the Davenport [42], Harris [43], Kaimal [44], and API (2000) [45] spectra are based on wind speeds recorded for onshore locations. They are energy spectra models designed to represent wind over land. Consequently, their application for offshore location is questionable because they cannot adequately resolve low-frequency loads for a marine floating structure. For this research, the wind spectrum ordinate suitable for offshore locations will be calculated from the publication by M.K. Ochi and Y.S. Shin [46].

The Ochi & Shin spectrum provide an adequate representation of wind power spectral density in the low-frequency range and gust events. It has more energy content in the low-frequency range ($f < 0.01\ Hz$) than other land-based wind spectrum and is developed from measured spectra over seaway (DNV-RP-C205)[47]. The Ochi and Shin

Wind Spectral energy is given by;

$$\frac{\omega S_u^+(\omega)}{\delta_u^2} = \left\{ \begin{array}{ll} 583\widetilde{f} & for\ 0 \leq \widetilde{f} \leq 0.003 \\ \frac{420\widetilde{f}^{0.7}}{\left(1+\widetilde{f}^{0.35}\right)^{11.5}} & for\ 0.003 < \widetilde{f} \leq 0.1 \\ \frac{838\widetilde{f}}{\left(1+\widetilde{f}^{0.35}\right)} & for\ 0.1 \leq \widetilde{f} \end{array} \right\} \tag{2.53}$$

Section 3.2.3 presents a comparison between these spectra to show for a fact that the Ochi & Shin spectra have more energy content in the low-frequency range than other land-based wind spectra models. The comparison will be performed using live Metocean hindcast data obtained from an offshore location in New Zealand.

2.2.2 Review of Aerodynamic Loading Investigation Methodologies

The FOWT rotor is the primary contributor of aerodynamic loads when compared to other parts of its assemblage above the MSL. Consequently, this section will be focused on reviewing aerodynamic loads on the wind turbine rotor. A preliminary assessment for estimating aerodynamic thrust coefficients for rotor diameters between 100 m − 120 m have been presented by Det Norske Veritas (DNV) in an offshore standard for the design of floating wind turbine structures (DNV-OS-J103) where a plot of rotor thrust coefficients versus 10 minutes mean wind speed have been established [48]. Also, DNV-OS-C301 provides a simplified manner for calculating wind loads for offshore structures by providing shape and height dependent coefficients [49]. These standards serve as a quick look approach in estimating aerodynamic forces on offshore structures before performing a proper CFD study. Though, using this approach may severely over or underestimate the thrust force experienced by an offshore wind turbine rotor because the wind turbine rotor blades have complex geometries that do not adequately fit into any of the shape parameters described in DNV-OS-C301[49]. More so, every offshore environment offers its unique climate in terms of wind speed and flow angle of attack. Hence, performing a CFD study with site-specific wind data is crucial in executing a successful investigation of aerodynamic loading on FOWTs.

Studies by Ye Zhang et al. [50] attempted to explain the overprediction of aerodynamic loads by CFD when compared to model experimentation in a bid to improve

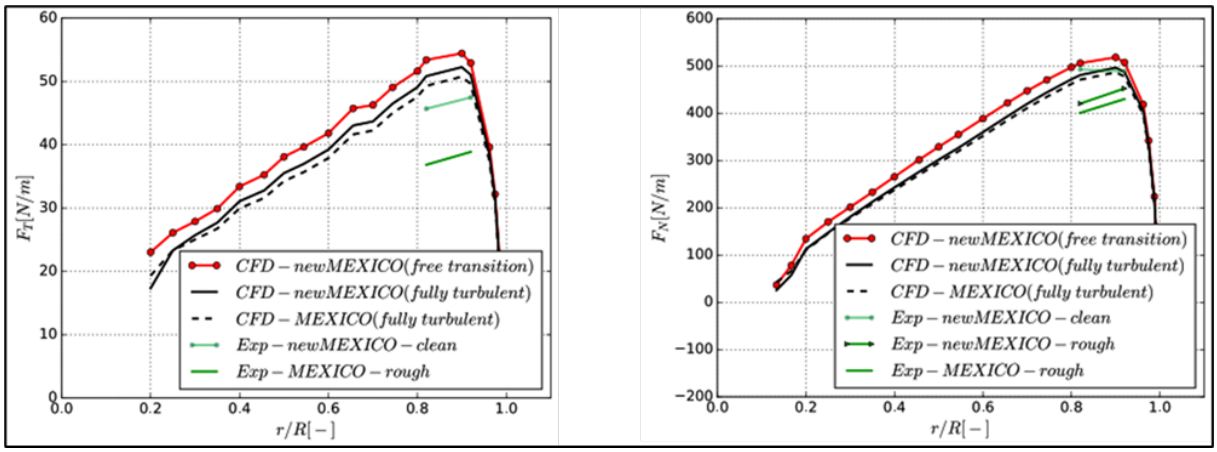

FIGURE 2.6: Comparison of tangential force (left) and normal force (right) distribution along the blade between numerical predictions and experimental measurements (Adopted from [50])

the CFD predictions by considering laminar-turbulent transition modelling . Their approach involved performing Model EXperiment in Controlled Condition (MEXICO) where a single non-rotating blade is analysed for boundary layer transition and zig-zag tape effect. Considerable deviations between CFD results and experimental study were observed in terms of normal and tangential forces at the blade tip (Fig. 2.6). The effects of viscous contribution are excluded in the tangential force for CFD and experimental studies. Only pressure contribution was considered for the tangential force simulation along the sections of the blade.

Wind turbine rotors can be subjected to a parked condition because of several reasons ranging from a failed pitch control system, maintenance shutdown, or emergency shutdown arising from extreme weather conditions. Zhiyu et al. [51] investigated the dynamic response of an onshore and a spar type floating offshore wind turbine under parked condition due to pitch system fault, grid loss, and shutdown events. In their study, a hydraulic pitch system was considered and the faults under study were because of the wind turbine rotor running out of control or seized. Their analysis was performed based on a time-domain simulation. Results from their study for the FOWT revealed that significant dynamic effects are triggered during an emergency shutdown. Negative pitch motion is generated after the introduction of a shutdown event as shown in Fig. 2.7 (left). Although the yaw motion of the platform does not change significantly after the initiation of an emergency shutdown as can be observed in Fig. 2.7 (right), it became excessive due to uneven aerodynamic excitations on the rotor. Similar studies on the dynamic load response for an offshore wind turbine in

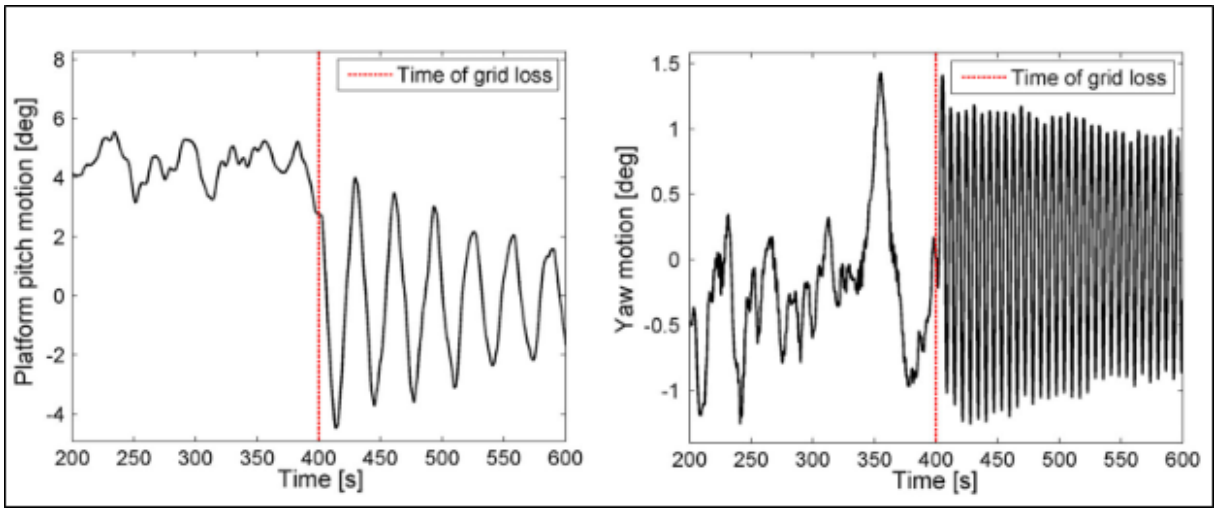

FIGURE 2.7: Time history of the platform pitch and yaw motion response (Adopted from [51])

parked conditions were performed by Politis et al. [52], Rasoul et al. [53], and Mahmoud et al. [54]. These studies all point to one direction that flow conditions are subjected to considerable uncertainties when dealing with substantial flow separation from aerodynamic loads.

Aerodynamic thrust induces vibrations on the FOWT assemblage above the MSL and consequently causes increased fatigue. Emil et al. [55] performed computational simulations to model for thrust variations on a wind turbine. Their approach accounted for wind shear, tower shadow, turbulence, and rotational sampling. From their studies, wind shear was found to have a depleting effect on the mean rotor thrust although the effect of wind shear was less significant when compared to the effect of tower shadow (Fig. 2.8).

Using a coupled dynamics model, M. Borg et al. [56] investigated the frequency domain characteristics of aerodynamic loads of a vertical axis wind turbine. Their study examined the impact of platform induced motion on aerodynamic loads. Key findings from their research paper showed that there is an increase in aerodynamic loads of several orders of magnitude over the range of wave frequencies with high energy content. It can be seen in Fig. 2.9 that the increased aerodynamic forces in the range of 0.2 to 1 rad/s are still approximately two orders of magnitude lower than the peak aerodynamic force around 1.1 rad/s.

The flexibility in soft mooring systems for FOWTs makes them susceptible to large oscillations due to aerodynamic and hydrodynamic loading. Qing'an Li et al. [57]

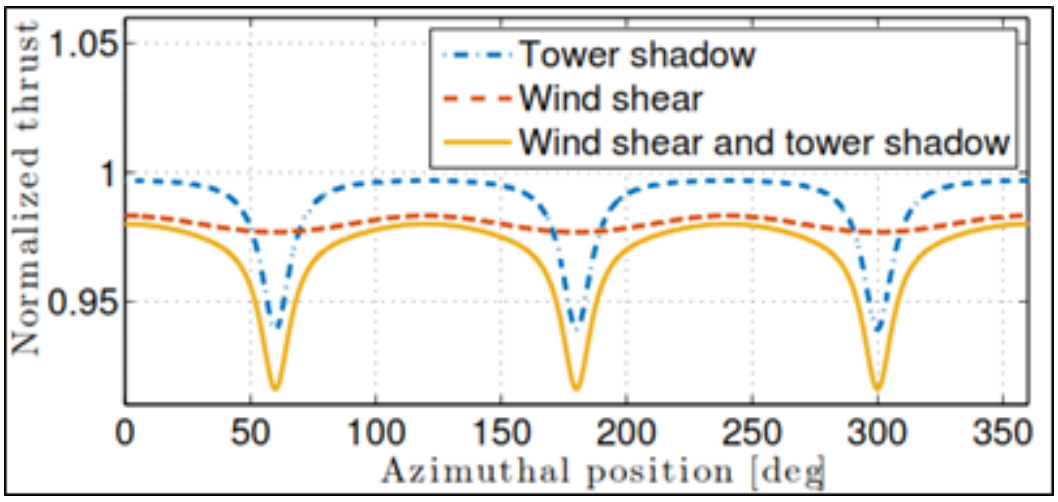

FIGURE 2.8: Plot of the normalised equivalent thrust accounting for wind shear and tower shadow (Adopted from [55])

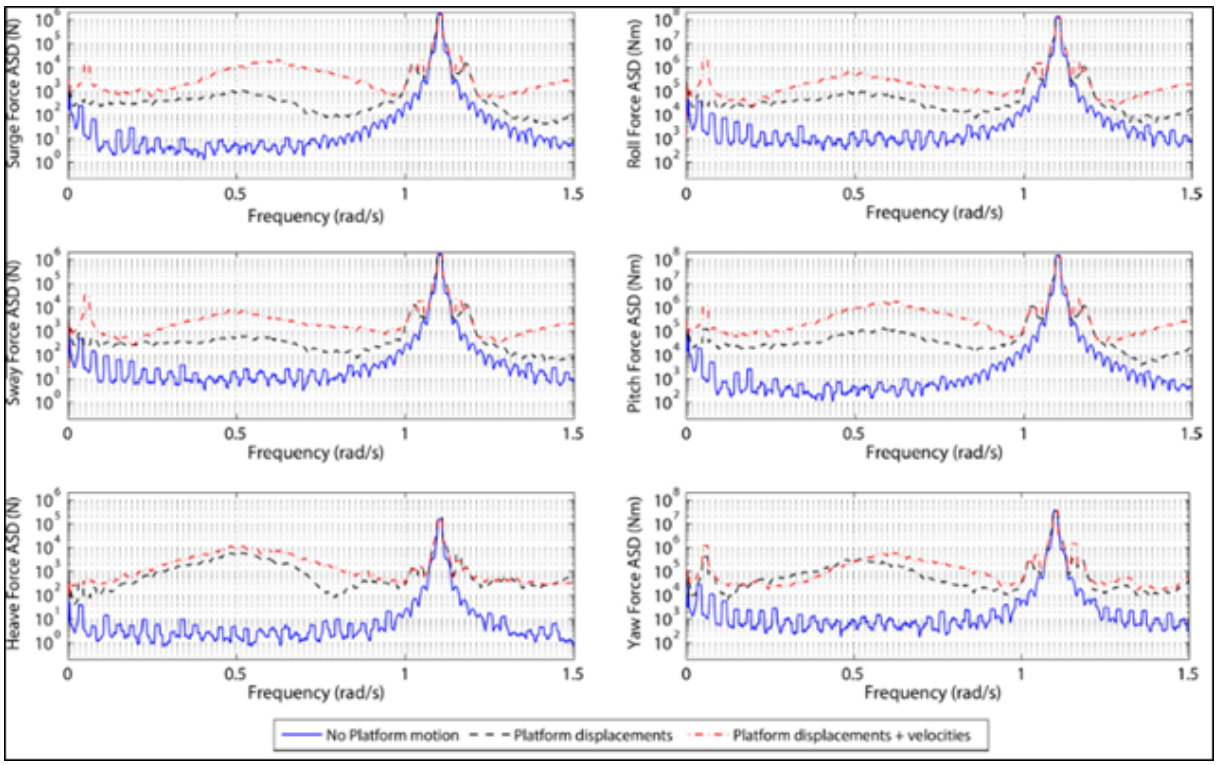

FIGURE 2.9: 6 DOF aerodynamic forces Amplitude Spectral Densities (ASDs) for 3 scenarios: a. no platform motion b. platform displacements c. platform displacements + velocities (Adapted from [56])

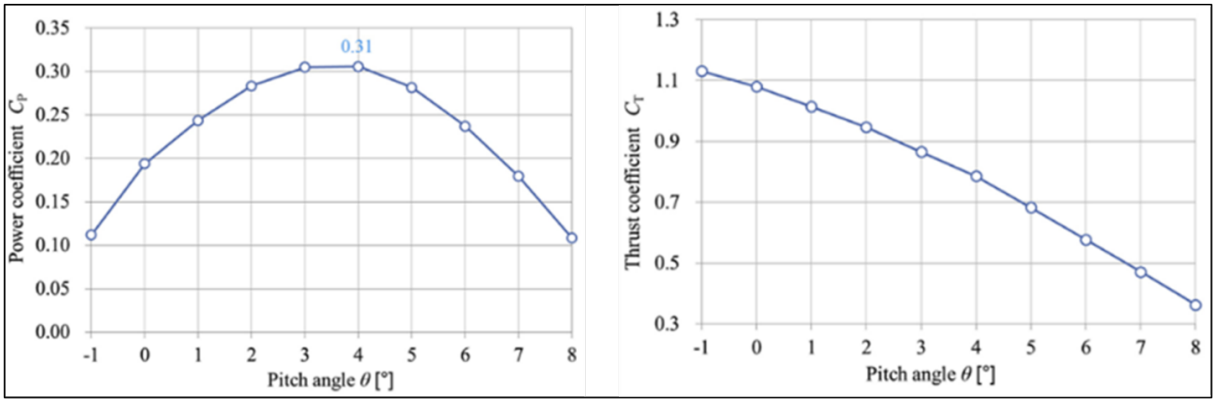

FIGURE 2.10: Plot showing the fluctuation of power coefficient C_p as a function of pitch angle (left) and thrust coefficient C_T as a function of pitch angle at the optimum tip speed ratio of 8.3 (Adapted from [57])

carried out a fundamental study on the aerodynamic force for FOWTs with cyclic pitch mechanism. Their study evaluated aerodynamic forces where undesired platform motions were suppressed with the use of rotor thrust control conditioned by pitch changes. Their wind tunnel experimental results revealed that the pitch angle has a significant effect on the aerodynamic performance of the rotor while the thrust coefficient decreased with almost linear function when pitch angle is increased (Fig. 2.10).

Salman et al. [58] performed quasi-static & dynamic numerical modelling of full-scale NREL 5 MW wind turbine using the Multiple Reference Frame (MRF) and dynamic Sliding Mesh Interface (SMI) methodologies where the predictive capabilities of both methodologies were employed. The results from their studies were verified against the Blade Element Momentum (BEM) and literature. The wake and torque characteristics showed close agreement by those established on existing literature (Fig. 2.11).

FOWTs are subjected to surge motion due to the impact of waves and currents on the floating support platform. Thus, the power and thrust characteristics of a FOWT does not only depend on the rotor's Tip Speed Ratio (TSR) and blade pitch angle but also the platform motion characteristics. Binrong et al. [59] in their paper investigated the influences of surge motion on the power and thrust characteristics of a spar-type FOWT using the Free Vortex Method. In their study, power and thrust curves were derived as a function of the rotor's TSR and reduced surge with the blade pitch angle constant at zero. Results from their study showed that variations in power and thrust

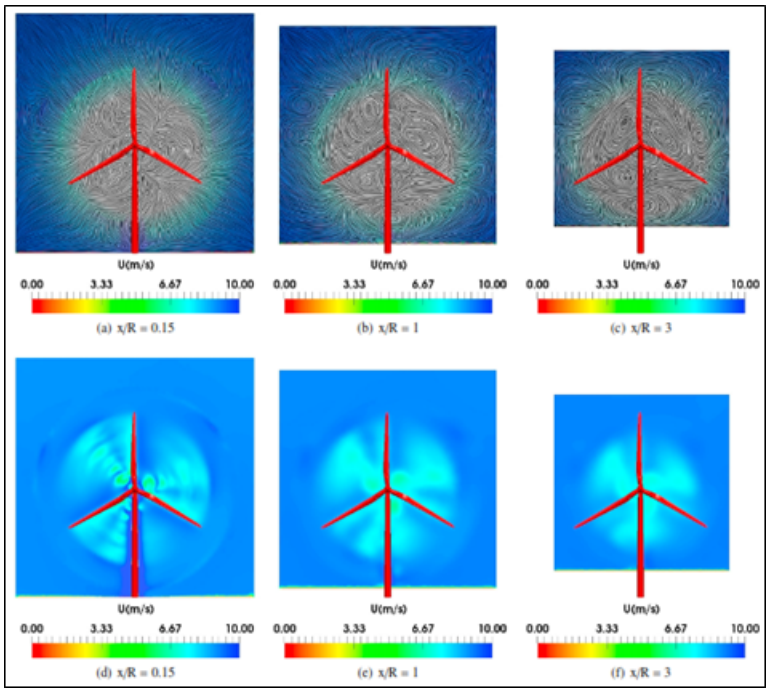

FIGURE 2.11: NREL 5MW: Vorticity contours (top) and velocity magnitude (bottom) at three stations downstream of the domain (inertial reference frame). Significant vortices emanating from the turbine blade can be observed from the trailing edge. The velocity magnitude is restricted to 10m/s to provide better contrast (Adapted from [58])

increases as TSR or reduced frequency increases while power and thrust coefficient declined with an increasing reduced frequency (Fig. 2.12).

More recent studies were done by Xin et al. [60] and Dose et al. [61] where unsteady aerodynamics for FOWT and fluid-structure coupled computation employing CFD were investigated respectively. Xin et al. [60] modelled an unsteady lifting surface with a free wake where the rotor's unsteady performance under floating motion due to surge was examined. Their study suggested that the rotor may gain more aerodynamic power output under certain surge motion than under steady-state condition (Fig. 2.13). Dose et al. [61] developed a coupled solver framework for exploring the effect of blade deformations on the rotor's key aerodynamic parameters such as power, thrust and sectional forces. Results from two methodologies; rigid geometry CFD simulation and Fluid-Structure Interaction (FSI) coupled framework were compared. Conclusions from their study revealed that structural deformations have a significant influence on the aerodynamic performance of the rotor.

So far, all these studies took different methodologies towards achieving one goal, which is to investigate the aerodynamic loading on FOWT. This has provided some

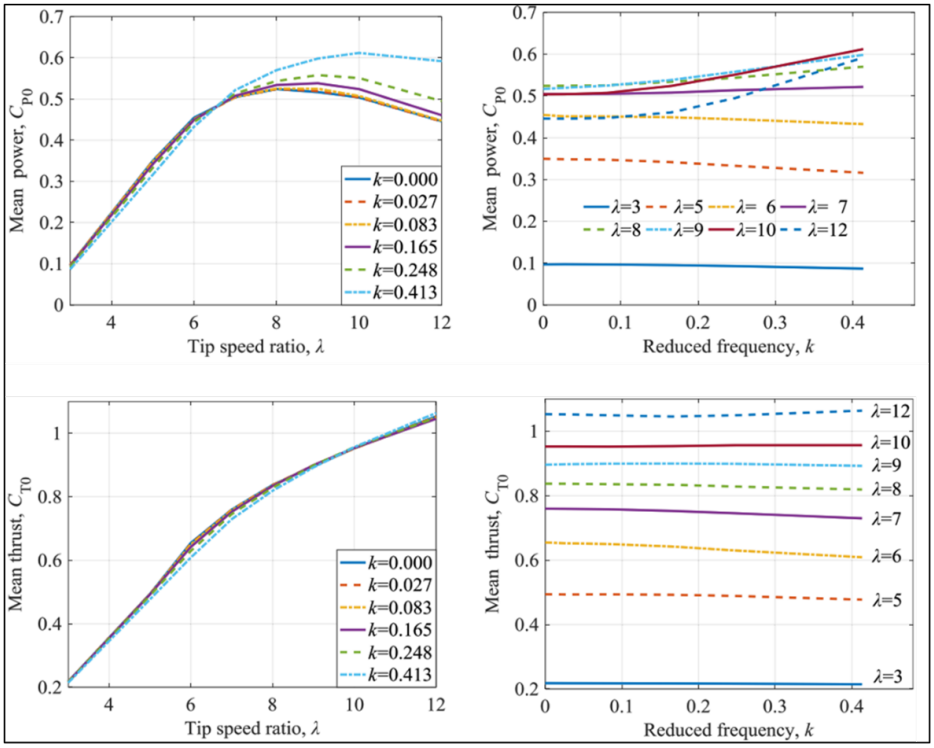

FIGURE 2.12: Plot showing normalised mean power against TSR (top left) and reduced frequency (top right), and normalised mean thrust against TSR (bottom left) and reduced frequency (bottom right) (Adapted from [59])

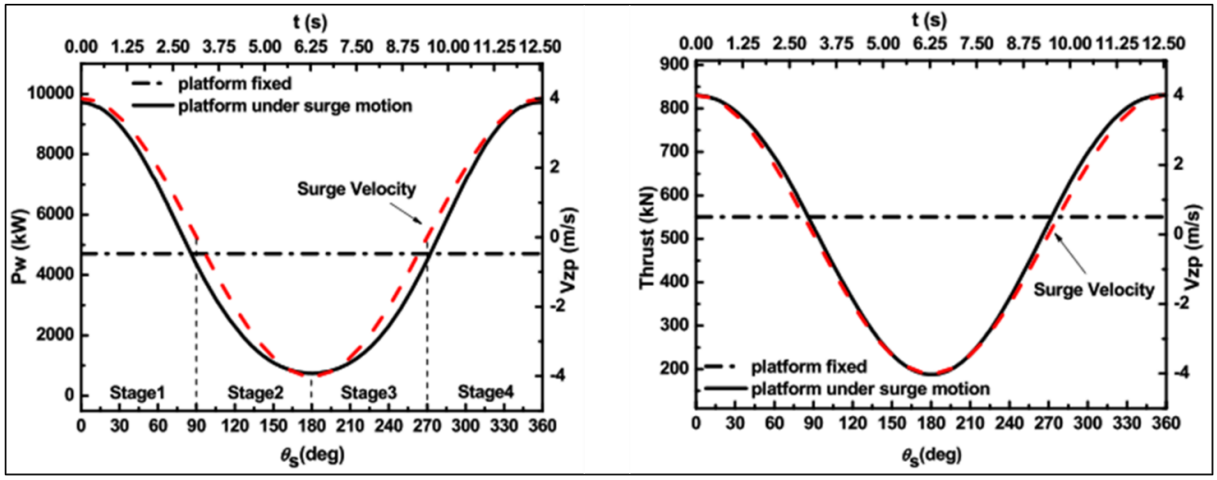

FIGURE 2.13: Plot showing the distribution of the rotor power output (left) and thrust (right) and its association with the platform's surge motion (Adapted from [60])

reliable insight and enlightenment as to how important the subject of aerodynamic loading is to offshore wind engineering. During extreme weather conditions where the prevailing wind speed is above the rated wind speed of the wind turbine generator, the rotor goes into a parked condition to prevent the WTG from self-destructing due to mechanical overloading. So far, not much has been researched on the global stability performance and coupled dynamics response of a wind turbine in its parked condition using frequency domain analysis. Therefore, the researcher strongly believes more study needs to be done in terms of investigating aerodynamic loads under extreme environmental conditions and this thesis is poised to provide new information in this regard.

2.3 Sources and Mechanism of Hydrodynamic Loading

Water particle velocity and acceleration are the main sources of hydrodynamic (wave and current) forces. These forces can be fluctuating (caused by waves) or constant (caused by steady ocean currents) and result in a dynamic load pattern on the floating platform of an offshore wind turbine. Drag, inertia, and lift forces are of interest when analysing the behaviour of a FOWT subjected to ocean wave and current loading. An over-estimation of the hydrodynamic loading can result in impractically large floating platform requirements for structural stability while an underestimation can also facilitate performance penalties during the life-of-field service for a FOWT. This section is devoted to discussing the mechanism around hydrodynamic forces and moments experienced by floating platforms for offshore wind turbines. The theories and principles surrounding ocean wave and current forces will be elucidated. These theories are the backbones of the CFD/FEA models and simulation tool kits being utilised for this research.

2.3.1 Wave Theories and Principles

A combination of a series of regular waves is generated by wind. These regular waves are of different magnitude and wavelengths, come from different directions and combine to represent the sea surface elevation. As highlighted in Fig. 2.14, various wave theories are used to describe the water particle kinematics of regular waves that is represented by sea surface elevation [62]. Airy's wave theory is commonly used amongst

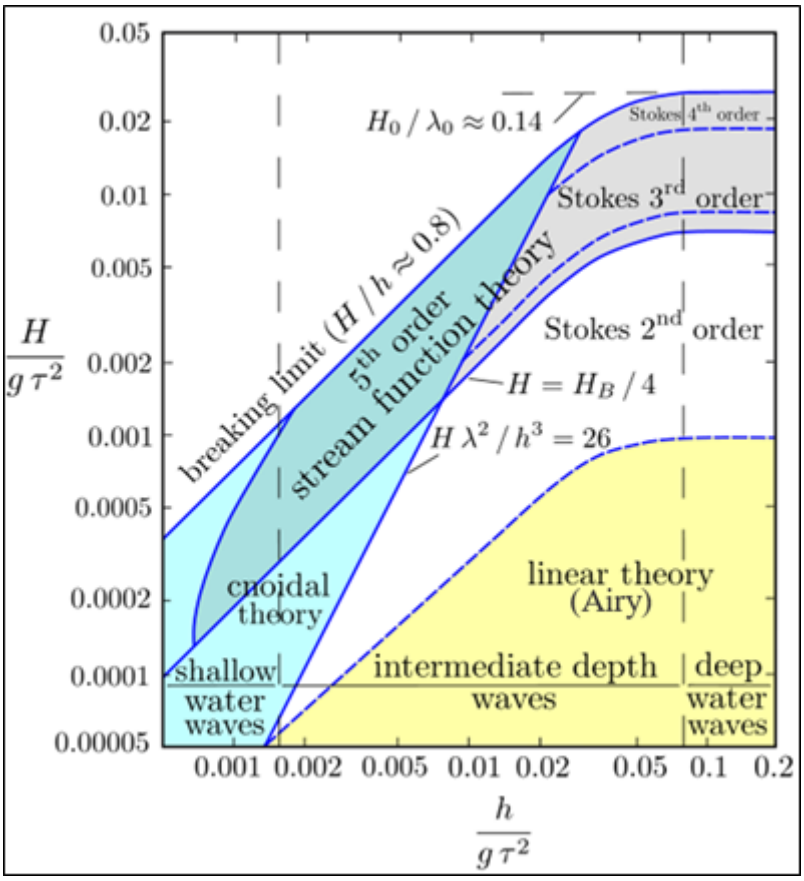

FIGURE 2.14: Water wave theory selection chart (Adapted from [63])

all other theories because it assumes linearity between the wave height and kinematic quantities, thus making it over-simplistic for the complex flow created under extreme weather conditions. Airy's wave theory (see Fig. 2.15) also known as the Linear Wave Theory (LWT) assumes a sinusoidal waveform of wave height (H), which is small in comparison with the wavelength (λ), and water depth (d) using the expression below;

$$\eta\left(x,t\right) = \frac{H}{2}\cos\left(kx - \omega t\right) \tag{2.54}$$

From equation 2.54, the wave surface elevation, η, is a function of x which is the direction of wave advancement, and t is the instantaneous time. k is known as the wave number and is expressed as;

$$k = \frac{2\pi}{\lambda} \tag{2.55}$$

and ω denotes the wave circular frequency which is expressed as;

$$\omega = \frac{2\pi}{T} \tag{2.56}$$

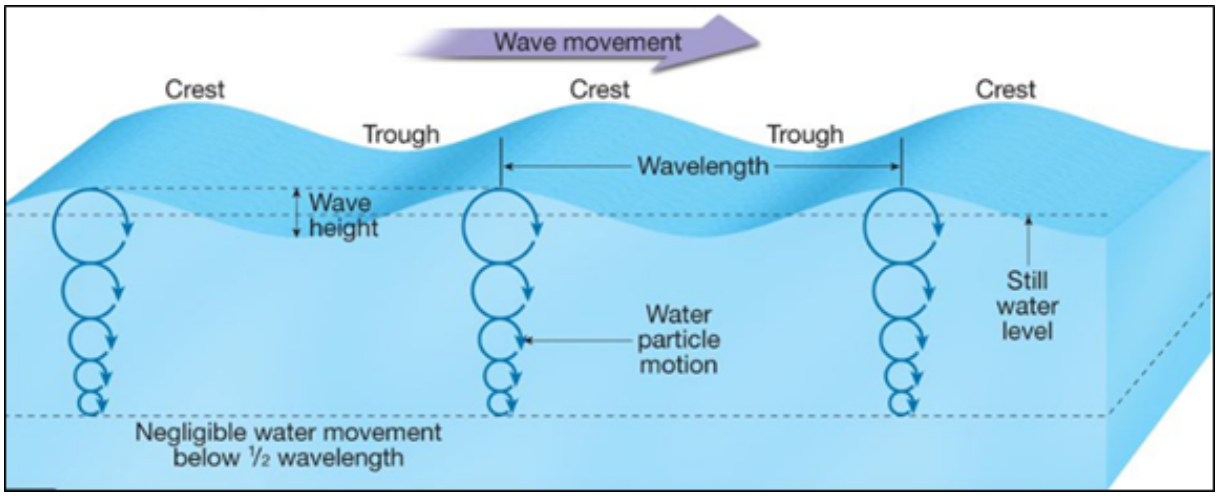

FIGURE 2.15: Parameters used when defining Airy wave theory.

where T is the wave period. The horizontal and vertical water particle velocities and accelerations are expressed as;

$$\begin{aligned}
\dot{u} &= \frac{\omega H}{2}\frac{\cosh(ky)}{\sinh(kd)}\cos(kx-\omega t)\\
\dot{v} &= \frac{\omega H}{2}\frac{\sinh(ky)}{\sinh(kd)}\sin(kx-\omega t)\\
\ddot{u} &= \frac{\omega^2 H}{2}\frac{\cosh(ky)}{\sinh(kd)}\sin(kx-\omega t)\\
\ddot{v} &= \frac{\omega^2 H}{2}\frac{\sinh(ky)}{\sinh(kd)}\cos(kx-\omega t)
\end{aligned} \tag{2.57}$$

where $\dot{u}$, $\dot{v}$, $\ddot{u}$, and $\ddot{v}$ represent the horizontal water particle velocity, vertical water particle velocity, horizontal water particle acceleration, and vertical water particle acceleration, respectively. In principle, the LWT applies to only small waves and is valid up to the Still Water Level (SWL) only because it does not predict kinematics for points above the SWL. Bearing in mind that the platform of a FOWT will have a continuously changing submerged length, the linear wave theory will not adequately capture the wave loads on the alternating submerging and emerging members of the floating platform. In addition, the variable submergence effect of the floating platform will attract

additional forces at any given time. Therefore, to satisfactorily compute water particle kinematics up to the actual level of submergence, the LWT needs to be stretched to cover points above the SWL. Wheeler [64] and Chakrabarti [65] provided some stretching modifications that account for the limitations identified in using LWT.

- Wheeler [64] suggested the inclusion of the actual level of submergence of the floating platform's member in the horizontal water particle velocity and acceleration equations;

$$\dot{u} = \frac{\omega H}{2} \frac{\cosh\left(ky\left[\frac{d}{d+\eta}\right]\right)}{\sinh\left(kd\right)} \cos\left(kx - \omega t\right)$$
$$\ddot{u} = \frac{\omega^2 H}{2} \frac{\cosh\left(ky\left[\frac{d}{d+\eta}\right]\right)}{\sinh\left(kd\right)} \sin\left(kx - \omega t\right) \tag{2.58}$$

- Chakrabarti [65] in a similar fashion suggested the following modification;

$$\dot{u} = \frac{\omega H}{2} \frac{\cosh\left(ky\right)}{\sinh\left(k\left(d+\eta\right)\right)} \cos\left(kx - \omega t\right)$$
$$\ddot{u} = \frac{\omega^2 H}{2} \frac{\cosh\left(ky\right)}{\sinh\left(k\left(d+\eta\right)\right)} \sin\left(kx - \omega t\right) \tag{2.59}$$

Other stretching techniques such as delta stretching and vertical stretching as proposed by Rodenbusch et al. [66] and Marshall et al. [67], respectively are other empirical techniques commonly used in the industry.

Wave theories provide the means of calculating water particle velocities, accelerations, and dynamic pressures as a function of the waves surface elevation. Several comprehensive studies have been performed to identify the most compatible wave theory for representing the near-surface kinematics due to the non-linearities created by moderate to severe wave action. Non-linearities are important when studying the impact of wave kinematics on the stability performance of a FOWT. Consequently, the use of advanced wave theories is inevitable in addressing the complex flow behaviour around a floating platform during severe wave condition [68], [69]. As highlighted in Fig. 2.14, the application of second-order Stokes wave theory for severe wave conditions provide a means for estimating the non-linear load known as the Froude-Krylov

force over the wetted surface of a floating platform. The Stokes second-order waves theory is defined by;

$$\eta\left(x,t\right)=\frac{H}{2}\cos\left(kx-\omega t\right)+\frac{1}{2}k\left(\frac{H}{2}\right)^{2}\cos^{2}\left(kx-\omega t\right) \tag{2.60}$$

Froude-Krylov force is one of the main force components initiated by wave loads. It is created by pressure effects from undisturbed incident waves. Other components of wave loads on a floating marine structure are;

- diffraction force triggered by pressure effects due to the structure's influence around the vicinity of the fluid-flow domain,
- radiation force initiated by pressure effects due to the structure's oscillation, which causes waves to radiate away from it. The radiated wave forces are zero for a fixed structure,
- the hydrodynamic added mass and potential damping forces produced by pressure effects due to the structure's six Degree of Freedom (6-DOF) in the fluid-flow domain, and
- viscous drag force generated by pressure effects due to the relative velocity between the water particle and the structural components of the floating platform.

For a slender cylindrical element ($^{d}/_{\lambda} < 0.2$), the hydrodynamic force (F_h) acting normal on the surface of is calculated using Morison equation which is expressed as;

$$F_h=C_m\rho_{sw}dV\cdot a_n-\left(C_m-1\right)\rho_w dV\ddot{x}_n+\frac{1}{2}\rho_{sw}C_d dA\left(v_n-\dot{x}_n\right)\left|v_n-\dot{x}_n\right| \tag{2.61}$$

where ρ_{sw} is the density of seawater (1025 kg/m^3). C_m and C_d are drag and inertia coefficients, respectively. The recommended value for C_m is 1.2 to 2.0, while for C_d is 0.6 to 1.2, as seen in API RP 2A [70]. The Froude Krylov and wave inertia terms are sometimes combined and written in terms of the added mass coefficient, C_a. Where;

$$C_a=\ C_m-1 \tag{2.62}$$

v_n and a_n are the velocity and acceleration of the water particle normal to the axis of the slender member. $\dot{x}$ and $\ddot{x}$ are the velocity and acceleration of structure, while

dA and dV are the exposed cross-sectional area and displaced volume of water per unit length of the slender member, respectively. For this research, the engineering toolkit that will be used to investigate the global performance of the floating platform being studied has a capability that allows its users to linearise the members of the platform using Morison elements such as tubes and discs. The use of Morison elements to linearise the members of a floating platform makes it possible to satisfy the initial condition ($^d/_\lambda < 0.2$) that permits the use of equation 2.61 in calculating the total wave forces on the structure. The next sub-sections will discuss the boundary condition of floating marine structure and wave-structure interaction from the perspective of the Boundary Element Method (BEM). More importantly, the frequency domain and time domain potential functions, and the nexus between both domains' potential functions are discussed. The construction of Green's theorem for wave structure interaction and the use of the Green function to satisfy free surface around a floating structure will be presented.

2.3.2 Frequency Domain Potential Function Solution for Wave-Structure Interaction

For the coupled dynamics simulation employed in this research, the boundary integral equation was used to establish a numerical scheme for the wave-structure interaction at a water depth of 300 m. Thus, the wave velocity potential function for deepwater is expressed as;

$$\varphi_o = \frac{igA}{\omega} e^{kz+ikx} e^{i\omega t} \tag{2.63}$$

with the flow particle velocity component expressed as;

$$\begin{aligned} u &= \frac{\partial \varphi_o}{\partial x} = Ae^{kz+ikx} e^{i\omega t} \\ w &= \frac{\partial \varphi_o}{\partial z} = iAe^{kz+ikx} e^{i\omega t} \end{aligned} \tag{2.64}$$

where A is the wave amplitude which is equal to half of the wavelength. In Fig. 2.16, it can be observed that the flow velocity is changing spatially (x, y, z) with position and time. Consequently, the floating structure will move freely under the wave action in six Degrees of Freedom (6-DOF) motion (Fig. 2.17). The flow for wave-structure interaction can be regarded as an irrotational and incompressible flow as the linear/linearised

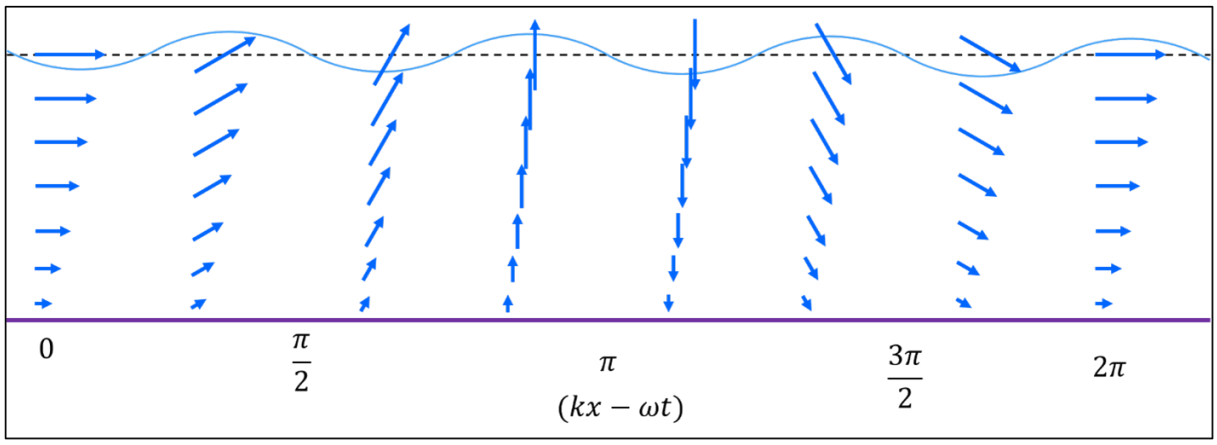

FIGURE 2.16: Plot showing changes in flow velocity position with respect to time [71].

systems, thus the velocity potential $\Phi(x, y, z, t)$ can be a function of both space and time, given as;

$$\Phi(x, y, z, t) = Re\left[\varphi(x, y, z)\, e^{i\omega t}\right] \tag{2.65}$$

Or simply;

$$\Phi(x, y, z, t) = \varphi(x, y, z)\, e^{i\omega t} \tag{2.66}$$

where φ is the complex amplitude of the potential Φ, and they both satisfy the Laplace equation;

$$\nabla^2\Phi = 0 \nabla^2\varphi = 0 \tag{2.67}$$

The goal of using the boundary element method is to solve the Frequency Domain (FD) potential function φ. First, the total potential φ can be considered as the sum of three-wave components (incident wave, diffracted wave, and radiated wave), and all three potentials satisfy the Laplace. For simplifying the potential function problem for the floating structure, and a better physical understanding, we can separate the potential into three parts that represent each of the wave components so that;

$$\begin{gathered} \varphi = \varphi_0 + \varphi_D + \varphi_R \\ \text{and} \\ \nabla^2\varphi_0 = \nabla^2\varphi_D = \nabla^2\varphi_R = 0 \end{gathered} \tag{2.68}$$

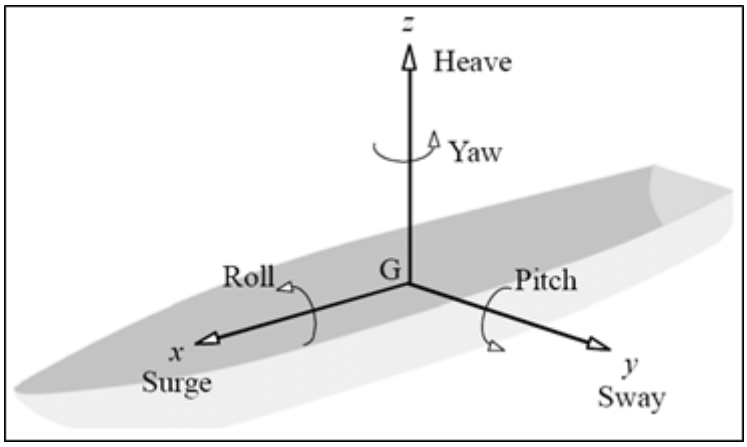

FIGURE 2.17: Six Degree of Freedom (6DOF) motion of a floating body under wave action.

where φ_0, φ_D, and φ_R represents the potential for the incident wave, diffracted wave, and radiated wave, respectively. The linear super-imposition of these three potentials can form a perfect dynamic system for the wave-structure interaction. For the wave structures interaction problems, the fluid domain of interest is enclosed by the body surface, S_b, the free surface, S_f, the seabed, S_z, and the control surface, S_c as seen in Fig. 2.18. For all three potential functions, the linearised free surface boundary condition, S_f is given as;

$$z = 0 \begin{cases} \frac{\partial \varphi_o}{\partial z} = K\varphi_0 \\ \frac{\partial \varphi_D}{\partial z} = K\varphi_D \\ \frac{\partial \varphi_R}{\partial z} = K\varphi_R \end{cases} \tag{2.69}$$

In equation 2.69 above, the free surface boundary conditions are given in the frequency domain where $K = \omega^2/g$ is the wave number in deepwater. The free surface boundary condition can be derived from the linearised free surface equation given by;

$$\frac{\partial^2 \varphi}{\partial t^2} + g\frac{\partial \varphi}{\partial z} = 0 \tag{2.70}$$

Such that by substituting equation 2.69 into 2.70;

$$\frac{\partial^2 \varphi}{\partial t^2} = -\omega^2 \varphi \tag{2.71}$$

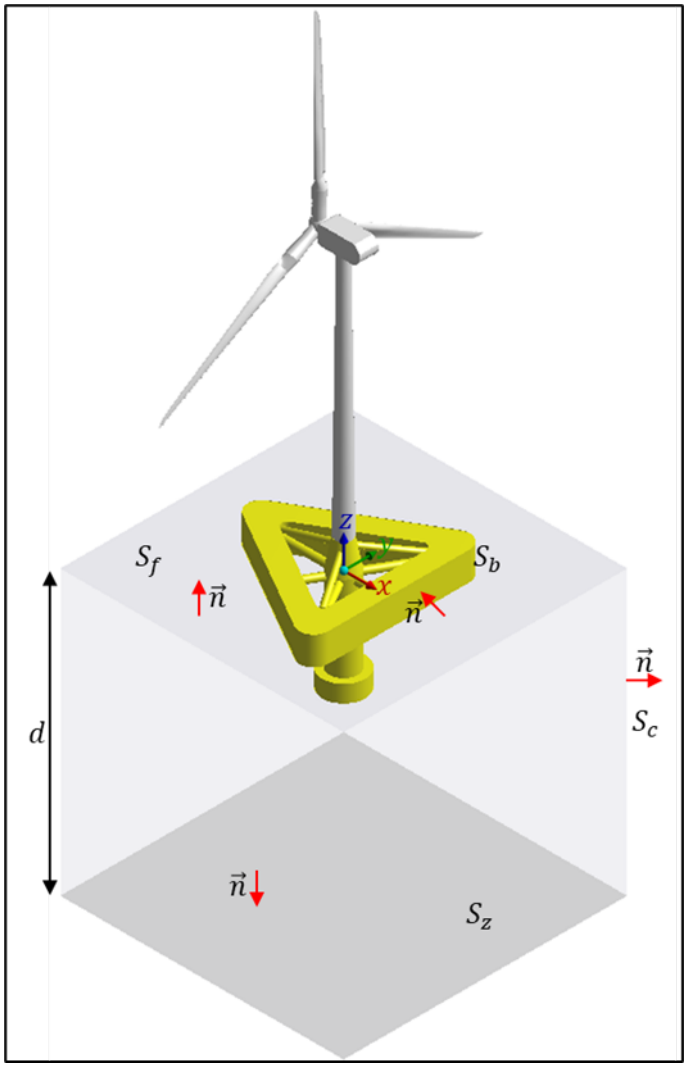

FIGURE 2.18: Hypothetical fluid domain showing boundary conditions for a wave-FOWT structure interaction.

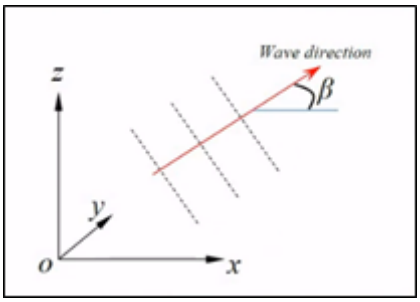

FIGURE 2.19: Incident Wave angle, β.

Similarly, for all three potential functions, the linearised seabed boundary condition, S_z is given as;

$$at \;\; z = -d \begin{cases} \frac{\partial \varphi_o}{\partial z} = 0 \\ \frac{\partial \varphi_D}{\partial z} = 0 \\ \frac{\partial \varphi_R}{\partial z} = 0 \end{cases} \tag{2.72}$$

Equation 2.72 assumes the no-penetration boundary condition. Based on the free surface and seabed conditions, and by studying the Laplace equation, the velocity potential function for the incident wave can be obtained. In deep water wave where $d \geq \lambda/2$, the potential function for the incident wave is given by;

$$\varphi_o = \frac{igA}{\omega} e^{Kz - iKx\cos\beta - iKy\sin\beta} \tag{2.73}$$

where β is the incident wave angle defined with respect to the x axis as illustrated in Fig. 2.19. In a finite water depth, d, the potential function of the incident wave is given by;

$$\varphi_o = \frac{igA}{\omega} \frac{\cosh\left[k\left(z+d\right)\right]}{\cosh kd} e^{-ikx\cos\beta - iky\sin\beta} \tag{2.74}$$

k in this instance is the wave number and can be solved from the dispersion duration given by;

$$k = \frac{\omega^2}{g\tanh kh} \tag{2.75}$$

The diffracted and radiated wave potentials are subject to the body condition and far-field condition of the structure. For the body (wetted) surface, S_b, the boundary condition for the diffracted wave is given by;

$$\begin{aligned} \frac{\partial \varphi_D}{\partial n} &= -\frac{\partial \varphi_0}{\partial n} \\ &or \\ \frac{\partial (\varphi_D + \varphi_0)}{\partial n} &= 0 \end{aligned} \tag{2.76}$$

Equation 2.76 means that there is no-penetration condition for the diffracted wave and incident wave. For the radiated wave, the body boundary condition is given by;

$$\frac{\partial \varphi_R}{\partial n} = \vec{V} \cdot \vec{n} \tag{2.77}$$

where $\vec{V}$ is the velocity vector of the structure motion, with the no-penetration condition. The body boundary condition given in equation 2.77 means that due to the motion of the structure, the fluid have the same normal velocity as on the body surface. The far-field conditions are given for the potential of diffracted and radiated wave, both of which are disturbance potentials for the incoming wave. The far-field boundary condition is given by;

$$\begin{cases} \lim\limits_{R\to\infty} \left[\sqrt{R} \left(i \dfrac{\partial \varphi_D}{\partial R} + K \varphi_D \right) \right] = 0 \\ \\ \lim\limits_{R\to\infty} \left[\sqrt{R} \left(i \dfrac{\partial \varphi_R}{\partial R} + K \varphi_R \right) \right] = 0 \end{cases} \tag{2.78}$$

when $R = \left(x^2 + y^2\right)^{1/2} \to \infty$. The boundary condition expressed in equation 2.93 means that the disturbance potentials to the incoming waves (φ_D and φ_R), and the water particle velocities vanish in distance due to the conservation of mass and energy. Within the fluid domain of interest, we suppose there are two velocity potential functions which satisfy the Laplace equation;

- the target potential function, φ;
- a known potential function, φ_o. For instance, the potential for the Green function or the Rankine source [72].

Both potential functions satisfy the Laplace equation given in equation 2.68. Using the Gauss divergence theorem [73], [74], we have;

$$\oint \oint_{S_c+S_b+S_f+S_z} \left(\varphi \frac{\partial \phi_o}{\partial n} - \phi_o \frac{\partial \varphi}{\partial n}\right) dS = \iiint_V \nabla \cdot (\varphi \nabla \phi_o - \phi_o \nabla \varphi) dV \tag{2.79}$$

As can be seen from equation 2.79, the volume, V on the right hand side of the equation is enclosed by the body surface, S_b, the free surface, S_f, the seabed, S_z, and the control surface, S_c as illustrated in Fig. 2.18. With some mathematical manipulations, as well as the application of the Laplace equation, we can obtain the Green's theorem as;

$$\oint \oint_{S_c+S_b+S_f+S_z} \left(\varphi \frac{\partial \phi_o}{\partial n} - \phi_o \frac{\partial \varphi}{\partial n}\right) dS = 0 \tag{2.80}$$

The Green's theorem expressed in equation 2.80 is a very important and fundamental equation for the boundary element method in wave-structure interaction based on the potential flow theory. However, the theorem is only valid for a three-dimensional domain and not a two-dimensional domain.

2.3.3 Frequency Domain Solution for Wave Pressure, Forces, and Moments

This section focuses on how the hydrostatic and hydrodynamic forces and moments can be calculated once the relevant potential functions have been solved. This will include the hydrostatic force, waves excitation force, as well as radiation force in terms of added mass and radiation damping coefficient. The fluid pressure (see Fig. 2.20), or more specifically the gauge pressure (p_g) in fluid can be simply obtained from the Bernoulli's equation which is given as;

$$p_g = -\rho_{sw} \frac{\partial \Phi}{\partial t} - \frac{1}{2} \rho_{sw} \nabla \Phi \cdot \nabla \Phi - \rho_{sw} g z \tag{2.81}$$

Here, $\nabla \Phi$ is the time-dependent velocity potential. For many practical applications in wave-structure interactions, the higher-order term in pressure is normally omitted in the analysis for the first-order forces and motions as a result of the linearisation of the problem, thus;

$$p_g = -\rho_{sw} \frac{\partial \Phi}{\partial t} - \rho_{sw} g z \tag{2.82}$$

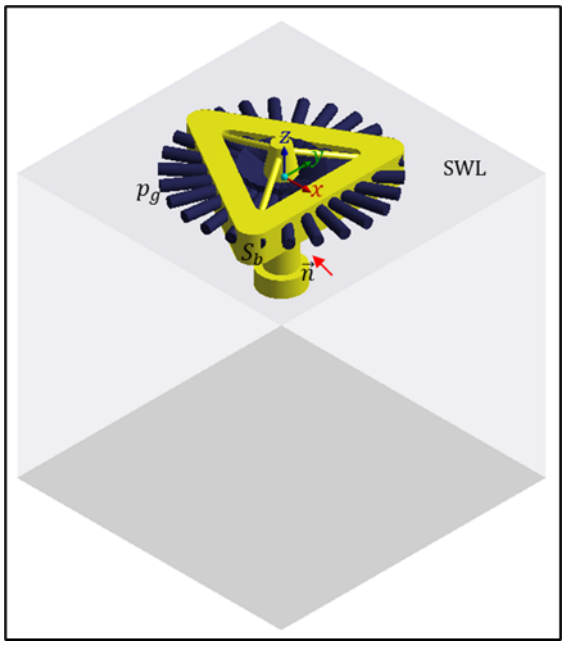

FIGURE 2.20: Hydrodynamic Gauge pressure on a FOWT (platform only).

In the frequency domain, the pressure can be expressed as;

$$p_g = -i\omega\rho_{sw}\varphi - \rho_{sw}gz \tag{2.83}$$

Here, the potential φ is the complex amplitude of the potential function. By substituting the diffraction and radiation potentials into the linearised pressure equation yields;

$$p_g = -i\omega\rho_{sw}\left(\varphi_D + i\omega\sum_{j=1}^{6}\xi_j\varphi_j\right) - \rho_{sw}gz \tag{2.84}$$

From equation 2.84, we can see that the radiation potential is the sum of the radiation potentials of unit amplitudes for 6-DOF motion (ξ_j) for translational motion ($j = 1$: surge; $j = 2$: sway; $j = 3$: heave) and rotational motion ($j = 4$: row; $j = 5$: pitch; $j = 6$: yaw) as illustrated in Fig. 2.21.

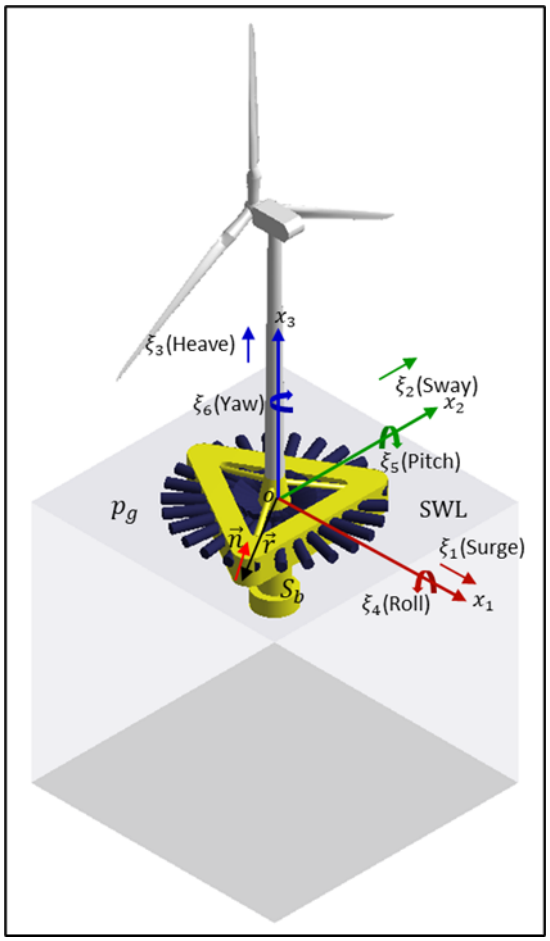

FIGURE 2.21: Radiation potentials of unit amplitude for 6-DOF on a FOWT.

The hydrodynamic forces, $\vec{F}_h$, and the moments, $\vec{M}_h$, acting on the marine structure by the fluid are calculated as;

$$\begin{gathered} \vec{F}_h = \iint_{S_b} p_g \vec{n} dS \\ and \\ \vec{M}_h = \iint_{S_b} p_g \left(\vec{r} \times \vec{n}\right) dS \end{gathered} \tag{2.85}$$

The vector $\vec{n}$ and $\vec{r}\,(x, y, z)$ can be seen in equation 2.85 and Fig. 2.21 as the normal vector acting on the body surface and vector around the origin of the coordinate to the body surface. For convenience, we can define the following vector components; $(n_1, n_2, n_3) = \vec{n}$ for the translational motion and $(n_4, n_5, n_6) = \vec{r} \times \vec{n}$ with $\vec{r} = (x, y, z)$ for the rotational motion. These vector components are the same as those we have used for defining the body boundary condition for the radiation potentials. As such, the forces

and moments can be written in a simpler form for each motion mode, i , as;

$$F_i = \iint_{S_b} p_g n_i dS \tag{2.86}$$

Here, the subscript i equals one through six corresponding to the 6-DOF such that for translational motion (i=1: surge; i=2: sway; i=3: heave) and for rotational motion (i=4: row; i=5: pitch; i=6: yaw) as illustrated in Fig. 2.21. Substituting the fluid pressure expressed in equation 2.84 into the integral for force components, we derive F_i as;

$$F_i = \iint_{S_b} \left[-i\omega\rho_w \left(\varphi_D + i\omega \sum_{j=1}^{6} \xi_j \varphi_j \right) - \rho_w g z \right] n_i dS \tag{2.87}$$

A further separation of the total force will yield the expression for the hydrodynamic and hydrostatic forces;

$$F_i = -i\omega\rho_w \iint_{S_b} \varphi_D n_i dS + \omega^2 \rho_w \iint_{S_b} \sum_{j=1}^{6} \xi_j \varphi_j n_i dS - \rho_w g \iint_{S_b} z n_i dS \tag{2.88}$$

From equation 2.88, the terms in magenta font colour is the wave excitation force, the terms in red font colour is the radiation added mass and radiation damping force, while the terms in blue font colour is the hydrostatic force. For formulating the hydrodynamic and hydrostatic forces due to the structure's motion, the parameters for hydrostatics is first defined. The volume of fluid displaced by the floating structure (see Fig. 2.22), $\forall$, in all three directions (x, y, z) is given by;

$$\forall = -\iint_{S_b} x n_1 dS = -\iint_{S_b} y n_2 dS = -\iint_{S_b} z n_3 dS \tag{2.89}$$

All three volumes displaced should be the same if the calculation is accurate enough. When performing hydrostatic analysis using an engineering tool-kit such as ANSYS-AQWA, obtaining the hydrostatic result is important because the information it provides can be very useful in wave-structure interaction analysis where we need to check whether all generated panels of the 3D model are oriented correctly. If all panels are oriented correctly, these three volumes should be very close if they are not identical.

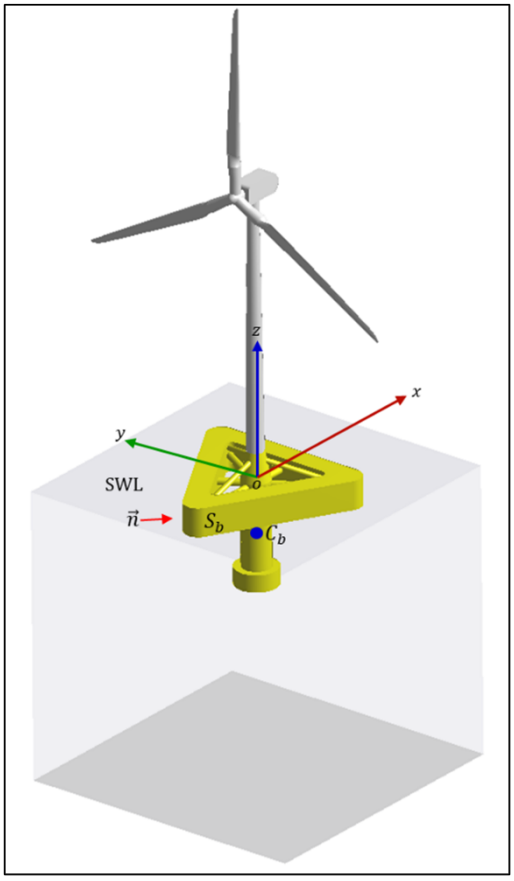

FIGURE 2.22: Hydrostatic information on a FOWT.

The coordinates of the buoyancy centre are calculated for all three directions as expressed in equation 2.90 below. The coordinates of the buoyancy centre are needed when we calculate the hydrostatic restoring coefficients for the floating structure.

$$\begin{cases} x_b = -\frac{1}{2\forall} \iint_{S_b} x^2 n_1 dS \\ y_b = -\frac{1}{2\forall} \iint_{S_b} y^2 n_2 dS \\ z_b = -\frac{1}{2\forall} \iint_{S_b} z^2 n_3 dS \end{cases} \tag{2.90}$$

The hydrostatic forces for all 6-DOF can be calculated using this expression;

$$F_i^S = -\rho_w g \iint_{S_b} z n_i dS \tag{2.91}$$

In principle, these hydrostatic forces (and moments) are the so-called zero-order forces and will be largest for wave-structure interaction. However, a large portion of it will be fully balanced out with the structure's mass in an equilibrium state, and due to

the motion of the structure. Thus, the net hydrostatic forces (and moments) can be expressed as;

$$F_i^S = -\sum_{j=1}^{6} c_{ij}\xi_j \tag{2.92}$$

Equation 2.92 can be regarded as the restoring forces. Where the values of non-zero c_{ij} is given as;

$$\begin{aligned}
C_{33} &= \rho_w g \iint_{S_b} n_3 dS & C_{45} &= -\rho_w g \iint_{S_b} xyn_3 dS \\
C_{34} &= \rho_w g \iint_{S_b} yn_3 dS & C_{46} &= -\rho_w g \forall x_b + mgz_g \\
C_{35} &= -\rho_w g \iint_{S_b} xn_3 dS & C_{55} &= \rho_w g \iint_{S_b} x^2 n_3 dS + \rho_w g \forall z_b - mgz_g \\
C_{44} &= \rho_w g \iint_{S_b} y^2 n_3 dS + \rho_w g \forall z_b - mgz_g & C_{56} &= -\rho_w g \forall y_b + mgy_g
\end{aligned} \tag{2.93}$$

For other values of (i, j), $c_{ik} = 0$. Some of the terms in equation 2.93 above may vanish depending on the symmetry of the structure. For the radiation forces, if we exchange the order of the summation and integral, we have;

$$F_i^R = \omega^2 \rho_w \sum_{j=1}^{6} \xi_j \iint_{S_b} \varphi_j n_i dS \tag{2.94}$$

substituting the radiation boundary condition into equation 2.94 yields the expression;

$$F_i^R = \omega^2 \sum_{j=1}^{6} \xi_j \rho_w \iint_{S_b} \varphi_j \frac{\partial \varphi_i}{\partial n} dS \tag{2.95}$$

By introducing a coefficient, f_{ij}, which is understood as the complex force in the direction, i, due to a motion of unit amplitude in the direction j, gives the expression for the total radiation force as;

$$F_i^R = \omega^2 \sum_{j=1}^{6} \xi_j f_{ij} \tag{2.96}$$

If we enclose the fluid domain using the various boundary surfaces illustrated in Fig. 2.18, we can formulate an equation for the added mass and radiation damping using the Green's theorem for the radiation potentials. For radiation damping, the integral for a very large control surface, S_c, a free surface, S_f, and the sea bed, S_z is equal to

zero. Thus, the radiation integral potential for the body surface, S_b, will be given as;

$$\iint_{S_b} \left(\varphi_j \frac{\partial \varphi_i}{\partial n} - \varphi_i \frac{\partial \varphi_j}{\partial n} \right) dS = 0 \tag{2.97}$$

Equation 2.97 shows that the coefficient $f_{ij} = f_{ji}$, i.e it is symmetric. In the wave structure problem, the coefficient f_{ij} can be expressed based on its real and imaginary parts as;

$$f_{ij} = \rho_w \iint_{S_b} \varphi_j \frac{\partial \varphi_i}{\partial n} dS = a_{ij} - \frac{i}{\omega} b_{ij} \tag{2.98}$$

where a_{ij} and b_{ij} are the added mass and radiation damping due to wave radiation, respectively. By substituting equation 2.96 into 2.98, the total radiation force can be written as;

$$F_i^R = \omega^2 \sum_{j=1}^{6} \xi_j f_{ij} = \sum_{j=1}^{6} \left(\omega^2 a_{ij} - i\omega b_{ij} \right) \xi_j = \sum_{j=1}^{6} \left(a_{ij} \dot{V}_j + b_{ij} V_j \right) \tag{2.99}$$

As defined earlier in section 2.3.1, the Froude-Krylov force is one of the main force components initiated by wave loads that are created by pressure effects from undisturbed incident (incoming) waves. However, the total wave excitation force (F_i^{ex}), is due to the incoming wave and the diffracted wave which is given as;

$$F_i^{ex} = -i\omega\rho_w \iint_{S_b} (\varphi_O + \varphi_D)\, n_i dS = -i\omega\rho_w \iint_{S_b} (\varphi_O + \varphi_D) \frac{\partial \varphi_i}{\partial n} dS \tag{2.100}$$

Equation 2.100 is the direct integration for the wave excitation force if the diffracted potentials, φ_D, and radiation potentials, φ_R, are both solved. The incoming wave potential, φ_O is a known function if the wave amplitude, wave frequency, and water depth are given. Based on Green's theorem, we can construct the equation for the diffraction and radiation potentials when we enclose the surface boundaries as illustrated in Fig. 2.18. For similar reasons leading to the formulation of equation 2.97, the integral on the surface body due to diffraction and radiation potentials is given as;

$$\iint_{S_b} \left(\varphi_s \frac{\partial \varphi_i}{\partial n} - \varphi_i \frac{\partial \varphi_s}{\partial n} \right) dS = 0 \tag{2.101}$$

Therefore, the wave excitation forces can be expressed as;

$$F_i^{ex} = -i\omega\rho_w \iint_{S_b} (\varphi_O + \varphi_D) \frac{\partial \varphi_i}{\partial n} dS = -i\omega\rho_w \iint_{S_b} \left(\varphi_o \frac{\partial \varphi_i}{\partial n} + \varphi_i \frac{\partial \varphi_s}{\partial n} \right) dS \tag{2.102}$$

Applying the surface body boundary condition for the diffraction potential gives the new expression for the wave excitation force as;

$$F_i^{ex} = -i\omega\rho_w \iint_{S_b} \left(\varphi_o \frac{\partial \varphi_i}{\partial n} - \varphi_i \frac{\partial \varphi_o}{\partial n} \right) dS \tag{2.103}$$

Equation 2.103 is known as Haskind relation which means that the exciting force is in a form independent of the diffraction potential. As such, the diffracted problem may not be necessary to be solved for the whole problem. Thus, the radiation potential can be used to calculate the wave excitation forces even when the diffraction potential is not solved. Once the forces and moments are calculated, we can establish the dynamic equation for the structure's motion based on Newton's second law of motion; for translational motion and rotational motion which is expressed as;

$$\begin{aligned} m\dot{\vec{V}} &= \vec{F}(translationalmotion) \\ m\dot{\vec{\omega}} &= \vec{M}(rotationalmotion) \end{aligned} \tag{2.104}$$

Or in a more compact form, the dynamic equation can be written as;

$$\sum_{j=1}^{6} M_{ij}\dot{V}_j = F_i \, (i = 1, 2, \ldots, 6) \tag{2.105}$$

In equation 2.105, F_i is the total hydrostatic and hydrodynamic forces, and it is generally expressed as the sum of hydrostatic forces, F_i^S, radiation forces, F_i^R, and exciting forces, F_i^{ex}, which is mathematically expressed as;

$$F_i = F_i^S + F_i^R + F_i^{ex} \tag{2.106}$$

The mass matrix of the structure, M_{ij} is given as;

$$M_{ij} = \begin{bmatrix} m & 0 & 0 & 0 & mz_g & -my_g \\ 0 & m & 0 & -mz_g & 0 & mx_g \\ 0 & 0 & m & my_g & -mx_g & 0 \\ 0 & -mz_g & my_g & I_{11} & I_{12} & I_{13} \\ mz_g & 0 & -mx_g & I_{21} & I_{22} & I_{23} \\ -my_g & mx_g & 0 & I_{31} & I_{32} & I_{33} \end{bmatrix} \tag{2.107}$$

Where x_g, y_g, and z_g are the coordinates of the centre of gravity. m and I_{ij} are the mass of the structure, and moment of inertia of the structure, respectively.

2.3.4 Time Domain and Frequency Domain Dynamics and Motions

The focus of this section is to establish the dynamic equations for a floating marine structure's motion in waves. This is done to provide the readers with some enlightenment as to what is involved in the analysis that will be performed in subsequent chapters of this thesis. In the frequency domain, for a motion of a complex amplitude, ξ_j, the corresponding velocity and acceleration is given as;

$$\begin{aligned} V_j &= i\omega\xi_j \\ a_j &= -\omega^2\xi_j \end{aligned} \tag{2.108}$$

From these expressions, it can be understood that the velocity has a phase difference of 90° with regards to the motion. However, the acceleration has a 180° phase difference with regards to the motion. Thus, the hydrodynamic equation of the 6-DOF motions of the structure under the wave action in the frequency domain is given as;

$$\sum_{j=1}^{6} \left[-\omega^2 \left(M_{ij} + a_{ij} \right) + i\omega b_{ij} + c_{ij} \right] \xi_j = F_i \tag{2.109}$$

As can be observed, equation 2.109 is the frequency domain solution of a dynamic system and it is expressed in the mass-spring-damper model with the action of sinusoidal forces. The terms in the red, blue, and green font are the mass term, damping term, and restoring term, respectively. F_i is the forcing term. Equation 2.109 can be re-written in

a simpler form;

$$\sum_{j=1}^{6} C_{ij}\xi_j = F_i \tag{2.110}$$

where $C_{ij} = -\omega^2\left(M_{ij} + a_{ij}\right) + i\omega b_{ij} + c_{ij}$ Using the boundary element method, the important terms (F_i, a_{ij}, b_{ij}) can be calculated. For this research, the ANSYS AQWA code is used to solve the radiation and diffraction potential. Once these potentials are solved, the hydrodynamic forces are calculated, and the motion amplitude, ξ_j is solved using equation 2.110. A Response Amplitude Operator (RAO) is used to represent the result better which is given as;

$$Z_j\left(\omega, \beta\right) \equiv \frac{\xi_j}{A} \tag{2.111}$$

The RAO is a complex response which depends on the wave frequency, ω and the wave incident angle, β. In the real world, the physical parameters are time-dependent, i.e., the hydrodynamic equation in the frequency domain is actually derived from the hydrodynamic equation in the time domain. In a linear dynamic system under a sinusoidal action, the motion response of the system would be sinusoidal and having the same frequency. This linearity can be represented mathematically as;

$$f_t\left(t\right) \equiv F_i e^{i\omega t} \Rightarrow x_j\left(t\right) \equiv \xi_j e^{i\omega t} \tag{2.112}$$

Then, the corresponding motion velocity and acceleration of the structure are calculated as;

$$\begin{aligned} \dot{x}_j\left(t\right) &= i\omega\xi_j e^{i\omega t} \\ \ddot{x}_j\left(t\right) &= -\omega^2\xi_j e^{i\omega t} \end{aligned} \tag{2.113}$$

Based on Newton's second law of motion, the dynamic system for the structure's motion after applying hydrostatic and hydrodynamic forces can be given as;

$$\sum_{j=1}^{6}(M_{ij} + a_{ij})\ddot{x}_j(t) + \sum_{j=1}^{6} b_{ij}\dot{x}_j(t) + \sum_{j=1}^{6} c_{ij}x_j = f_i(t) \tag{2.114}$$

Similar to equation 2.109, equation 2.114 is the time-domain solution of a dynamic system and it is expressed in the mass-spring-damper model with the action of sinusoidal forces. The terms in the red, cyan, and magenta font are the mass term, damping term, and restoring term, respectively. $f_i(t)$ is the forcing term from wave excitation. Here, the added mass from the radiation forces has been taken as part of the total mass. The damping term is the radiation damping, while the restoring force is from the net hydrostatic forces. By substituting the sinusoidal force motion velocity and acceleration into equation 2.114 yields;

$$\sum_{j=1}^{6}\left[-\omega^2(M_{ij}+a_{ij})\right]\xi_j e^{i\omega t}+\sum_{j=1}^{6} i\omega b_{ij}\xi_j e^{i\omega t}+\sum_{j=1}^{6} c_{ij}\xi_j e^{i\omega t}=F_i e^{i\omega t} \tag{2.115}$$

Cancelling out the time factor in equation 2.115 will give the frequency domain solution previously expressed in equation 2.109. It has been shown that the frequency domain equation to a dynamic system is derived from the time domain equation. However, when the frequency domain equation is transformed to the time domain equation, care must be taken in doing so since in the frequency domain equation for a floating structure the hydrodynamic parameters a_{ij}, b_{ij}, and F_i are all frequency dependent.

It is noteworthy that the time-domain equation is only correct when the forcing term $f_i(t)$ is sinusoidal for which the frequency of the linear dynamic system of the forces and motions is well defined, and that the whole dynamic system has a single frequency. For a specific frequency, the hydrodynamic parameters a_{ij}, b_{ij}, and F_i can be correctly obtained. However, for a dynamic system having multi-frequencies, the hydrodynamic parameters are uncertain and would become meaningless if the forcing term is not sinusoidal, or without a uniquely defined frequency. Consequently, the complete time-domain equation transformed from the frequency-domain equation is given as;

$$\sum_{j=1}^{6}\left[M_{ij}+a_{ij}(\infty)\right]\ddot{x}_j(t)+\sum_{j=1}^{6}\int_0^t K_{ij}(t-\tau)\dot{x}_j(\tau)d\tau+\sum_{j=1}^{6} c_{ij}x_j(t)=f_i(t) \tag{2.116}$$

In equation 2.116, a_{ij}, is the added mass at infinite frequency, while the impulse function, $K_{ij}(t)$, is a Fourier transform of the radiation damping coefficient which is given

as;

$$K_{ij}(t) = \frac{2}{\pi}\int_0^\infty b_{ij}(\omega)\, cos\omega t d\omega \tag{2.117}$$

In the time domain solution expressed in equation 2.117, the forcing term $f_i(t)$ can be any type of forcing, i.e., the time domain equation can be easily changed to accommodate non-linear forces.

2.3.5 Irregular Wave and Wave Spectrum Modelling

By definition, an irregular wave is the superposition of regular waves with random periods and wave heights (see Fig. 2.23). Realistic ocean waves do not look like a simple sine curve, rather they are completely random in nature. Thus, an irregular wave is employed to adequately represent the realistic environmental loads on a floating structure. When a signal is random, it can be analysed statistically to characterise its unpredictability. The statistical analysis applied is based on a wave scatter diagram and site-specific.

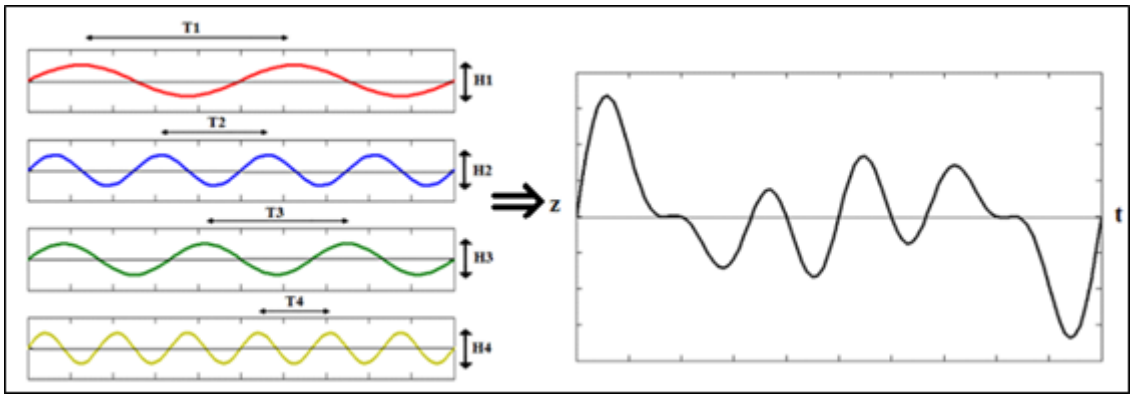

FIGURE 2.23: Regular waves (left) superimposed to produce and irregular wave (right) (Adapted from[75]).

The spectrum of ocean waves changes in different weather conditions, from calms to storms. As the wind speed increases, the intensity of the large surge waves increases dramatically while short ripples increase much less. Fig. 2.24 is a hypothetical example of wave spectra of ocean waves at different conditions. At low wind speeds, the sea is relatively calm. Not only are the wave heights small, but they also have a broad spectrum across frequencies. As the seas get higher and choppier, a peak is developed

at low frequencies and low frequencies indicate long wavelength. As the wind speed increases, the peak of the spectrum increases accordingly.

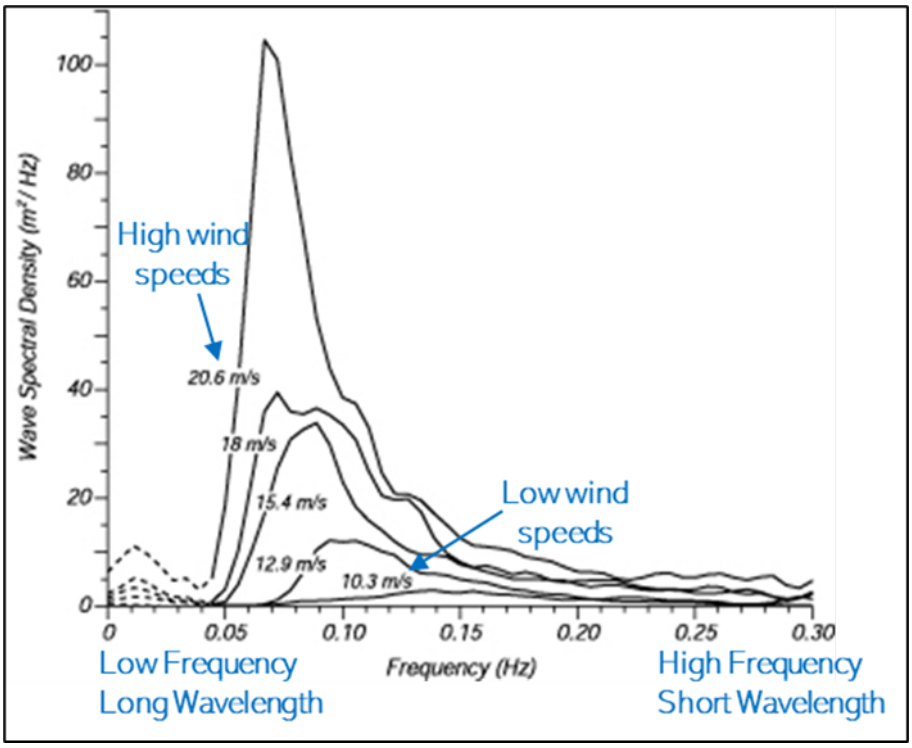

FIGURE 2.24: A hypothetical example of an Ocean Wave Spectrum.

There are several pre-configured wave spectra (JONSWAP and Pierson-Moskowitz) that only require knowledge of a couple of statistical parameters to fully define the sea state. Here, the sea state is typically assumed to be a zero-mean, ergodic Gaussian process for a short term, usually 3 hours. However, the wave spectral density are often calculated by a series of static, non-zero-mean Gaussian process, that is specified by the significant wave height (H_s), and peak wave period (T_p). In the coupled dynamics simulation toolkit used for this research (ANSYS AQWA and STAR CCM+), these spectra are available as an input option. In the next chapter, the philosophy behind the choice of a wave spectra density used in providing the solution of a site-specific wave energy spectra density will be presented.

2.3.6 Ocean Current Forces

The concept and theories surrounding the current drag force are synonymous to the aerodynamic drag force experienced by the assemblage of the wind turbine above the

MSL. Current moves in a horizontal direction and its velocity decreases slowly with increase in water depth. However, a slight increase in the magnitude of current velocity can yield a significant increase in current drag force. The presence of current around a floating structure causes it to generate waves from the diffraction of water particles created by the structure, which in turn creates diffraction forces. However, current diffraction forces are negligible for the realistic value of current acting on the main assemblage of the floating structure. It is common knowledge that the current can create significant loads on marine structures. Depending on the type of current, the magnitude of the load varies. There are different types of currents such as;

- surface current, which is driven by surface wind circulation,
- thermohaline current which is a deepwater current that moves around the ocean basins by density-driven forces and gravity,
- tidal current which occurs because of the rise and fall of the tide[3], and
- currents due to the internal waves at the boundary between two different densities of water layers.

Hydrodynamic current load created from surface current and tidal current are important in determining the overall hydrodynamic drag force experienced by a floating structure as referenced in [76]. The change in tidal current with water depth follows the $1/7th$ power-law decay model. However, a logarithmic profile may be observed in the vicinity of the surface layer for current initiated by storm surge [68]. As revealed by Barltrop [68], the total current may be significant even though tides and storm surge currents become less important at larger water depths.

The current velocity profile with depth modelling approach provides a more accurate representation of the anticipated current load on a floating platform when compared to using a uniform current velocity from the seabed to the water surface. The use of a uniform velocity will yield an overestimation of the current load, whereas the current velocity profile with a depth approach will deliver a more realistic current force calculation.

Considering the water depth defined with respect to the FRA whose origin is at the MSL, the total current velocity $\vec{U}_c(z)$ at a specified position z below the water surface,

[3]The vertical motion of near-shore tides initiates the horizontal movement of water, creating currents.

having a flow direction angle, θ_z, can be defined spatially in terms of the uniform current velocity, U_o, and profiled current velocity, U_z, as;

$$\vec{U}_c(z) = (U_o cos\theta_0, U_o sin\theta_0, 0) + (U_z cos\theta_z, U_o sin\theta_z, 0) \tag{2.118}$$

More details on the ocean current load modelling approach adopted for this research is discussed in section 3.2.4 of the next chapter of this thesis.

2.3.7 Wave-Current Interaction

The relevance of wave-current interaction in coupled dynamics simulation of a FOWT cannot be overemphasised. Fluid drag force on the smaller diameter components (e.g. mooring cables) of the assemblage of a FOWT can be increased by the combined fluid particle velocity of currents and waves. Also, wave diffraction and radiation forces experienced by the floating platform are affected by the currents to some considerable extent. Wave-current interaction causes a shift in wave phase or a Doppler shift to the wave period. As described by Barltrop [68], the conventional wave theory can be used to model a regular wave travelling on the current under the assumptions of constant water depth and constant steady current with depth. The wave period is shifted relative to a stationary observer using the expression;

$$\frac{\lambda}{T_e} = \frac{\lambda}{T} + U_c cos\theta' \tag{2.119}$$

where T_e is the wave period relative to a stationary observer. T is wave period relative to current as predicted by the zero-current theory. U_c and θ' are the current speed amplitude and the angle between wave and current, respectively. Equation 2.119 can be expressed in an alternate form as;

$$\omega_e = \omega + U_c k cos\theta' \tag{2.120}$$

where ω_e is the wave frequency relative to a stationary observer.

2.4 Review of Coupled Dynamics Modelling Methodologies

The offshore wind energy industry relies heavily on Computer Aided Engineering (CAE) toolkits for FOWT dynamic loads and stability analyses. Modelling and predicting the complex nature of the offshore environment requires a full understanding of the interactions between Metocean elements (wind, wave and current) which can also be a herculean task when it relates to forecasting the dynamic response of a FOWT due to its presence in a thrilling marine environment. Consequently, the limitations and resulting inaccuracies in the toolkits utilised in the modelling and prediction of dynamic loads and responses of a floating platform slows down the advancement of floating foundation technology for next-generation capacity ($\geq 10MW$) wind turbines. Thus, the need for precision modelling tools and/or coupled dynamics methodology geared towards a more ground-breaking, optimised, reliable and cost-effective FOWT technology cannot be overemphasised. By overcoming current modelling limitations, inaccuracies, and oversimplification in the tools and techniques currently being used for the stability, loads and wind power performance analyses of a FOWT, the offshore wind energy industry will be better positioned to scale towards a larger capacity WTG unit on floating platforms.

Since the introduction of FOWT technology, quite a few experimental and numerical studies have been performed to explore the aerodynamic and hydrodynamic response of a FOWT under various environmental conditions. As the need for computationally inexpensive numerical simulation increases, several coupled simulation tools have been developed to assess the dynamic behaviour of a FOWT for preliminary design assessment. Different coupling methods for load dynamics numerical simulations have been extensively studied in the past two decades. A common methodology that is being utilised in the assessment of dynamic loading on a FOWT is the aero-hydro-servo elastic coupling approach as proposed by Jonkman [28]. The aero-hydro-servo-elastic coupled simulation approach infers the numerical investigation of the coupling between aerodynamic loads on the member structures of a FOWT above the MSL and their responses (tower and rotor, nacelle assembly (RNA)), coupling between hydrodynamic loads and responses of the FOWT assemblage below the MSL (submerged platform and station keeping system), and the WTG control system and the deformation response of the structure due to elasticity. Fig. 2.25 shows the interfacing software

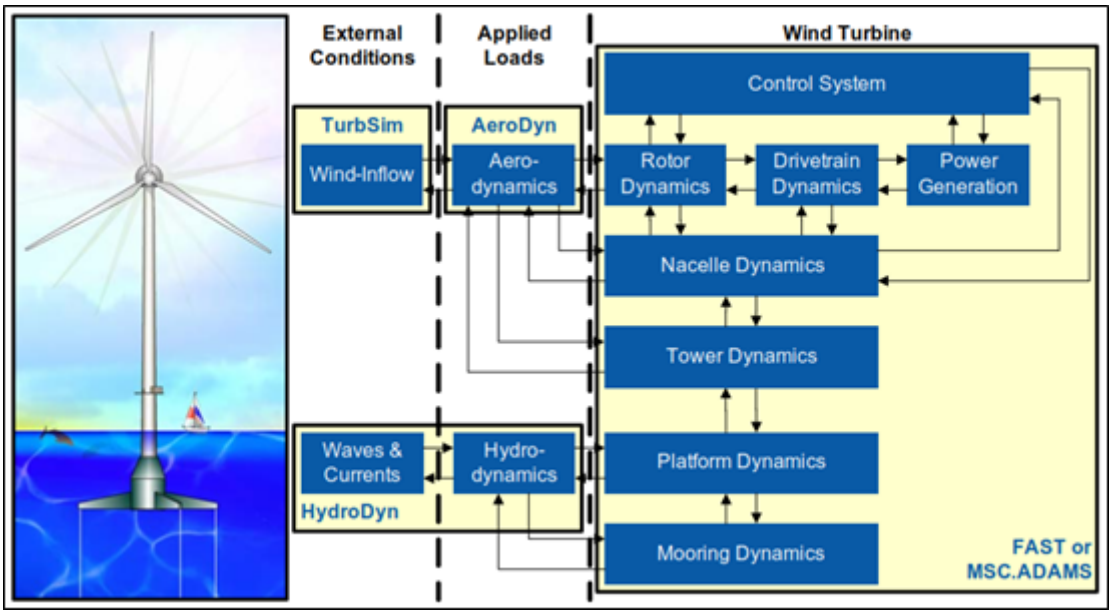

FIGURE 2.25: Interfacing Modules in Aero-Hydro-Servo-Elastic Coupled Analysis [25].

toolkits applied to achieve an aero-hydro-servo elastic coupled analysis.

The Fatigue, Aerodynamics, Structures, and Turbulence (FAST) and Automatic Dynamic Analysis of Mechanical Systems (ADAMS) toolkits are a time-domain simulator that employs a combined modal and multibody structural dynamics formulation. These famous programs can be run independently and were originally developed for predicting coupled dynamic response and extreme loads for land-based horizontal axis wind turbines. With the use of additional codes, the FAST and ADAMS programs were interfaced with AeroDyn (an aerodynamic subroutine package for calculating rotor aerodynamic forces using blade element momentum theory) to facilitate a fully coupled aero-servo elastic modelling in the time domain. The FAST model is known to have a limited number of structural DOFs and may not be able to adequately model unconventional FOWT configurations. Furthermore, the rotor and tower were characterised using linear modal representation. The ADAMS program on the other hand is a mechanical system that models six-DOF for rigid bodies and thus not a toolkit specific to wind turbines. In the development of their model, several assumptions were invoked such that three-small angle rotational displacements were assigned to the floating foundation kinematics and kinetics. The implication of this assumption can be critical as it may not correctly predict the floating platform's motion under extreme environmental excitation. The hydrodynamic module (HydroDyn) model is based on

the fundamental assumption of a linearized hydrodynamics problem. Linearized hydrodynamics here implies a situation where the wavelengths are much larger than the wave amplitudes thus permitting the use of the simplest incident wave kinematics theory known as the Airy wave theory. This assumption is not a good fit for sea states that are in the realm of higher-order wave kinematics theories such as the Stokes 2nd, 3rd, and 4th order theories. Also noteworthy is the simplification of diffraction analysis by their approach where incident wave directional spreading was not considered but assumed to be long-crested. Second-order mean-drift forces on the floating platform were also ignored which is crucial for investigating loads on the mooring system due to the displacements experienced by the floating platform. Loads and loads effects from Vortex Induced Vibrations (VIV) due to the impact of sea currents on the platform was not investigated. The VIV assessment can become critical for the stability of some FOWT designs because, for VIV frequencies above the typical wave frequencies or close to high-frequency band relating to fast-varying responses, a resonance phenomenon resulting to ringing and springing responses can occur.

Several studies have been conducted on the hydrodynamic loading and response of a FOWT. As have been discussed earlier, wave and current loading are the main sources of hydrodynamic loads on a FOWT structure. These hydrodynamic loads and structure interaction have been studied from different activities by several academic researchers. Articles by Marino et al.[77], Ma et al.[78], Ullah et al.[79], and Ye and Ji [80] are some of the papers that have performed studies around the dynamic response of FOWT under hydrodynamic loading, and potential theory as a coupled hydrodynamic response technique of a spar-type FOWT in regular and irregular waves. These studies adopted a similar methodology proposed by Jonkman [28]. A more recent study by Zhenju et al. [81] investigated the influence of second-order wave excitation loads on the coupled response of an offshore wind turbine using the OC4 DeepCWind as a case study. Their emphasis was to investigate how the wave mean drift force and slow -drift wave excitation load influence the platform's motions, mooring line tension, and tower base bending moments. Antonio et al. presented and validated a linear-frequency domain model known as Quick Load Analysis of Floating wind turbine (QuLAF)[82]. Hydrodynamic and aerodynamic loads were pre-computed using WAMIT and FAST, respectively. MoorDyn was used to linearise the mooring system dynamics for wind speeds being investigated.

Furthermore, several studies have performed concept design verification of a floating foundation for OWTs using coupled dynamics. For hydrodynamic loading calculations, some of these studies assumed a constant current over the draft of the floater and a collinear flow direction for wind, waves and currents [20], [24]. This oversimplification in the interaction between Metocean elements can often lead to under-designing or over-designing a FOWT system which in turn can ultimately lead to some performance penalty for an under-designed system or avoidable cost implications for an over-designed system. Thanh et al. [83] in their study investigated hydrodynamic loading on the OC4 DeepCWind spar submersible OWT floating platform using the panel method modelling where the structure was created using surface panels with a predetermined element size. Their study omitted the acceleration terms (added mass and fluid inertia) in Morison's equation thereby reducing the equation to a drag-only formulation. Matthew et al. [84] also performed a similar study on the OC4 DeepCWind platform where validation of a lumped-mass mooring line model was examined using the FAST program. However, inconsistencies and impracticable hydrodynamic data (negative added mass and damping values) when using the panel method in the time domain analysis have been observed for certain studies [19], [85].

Leble and his co-author conducted a coupled dynamics numerical computation study for a 10-MW rated power FOWT using a mesh-free method [86]. In their approach, the aerodynamic forces were computed using the Helicopter Multiblock (HMB3) flow solver[18] while the hydrodynamic loads on the floating platform were calculated using Smoothed Particle Hydrodynamics (SPH) [87], [88] wherein both methods, the fluids and structures have been represented by a set of particles and the FOWT characterised by a lump mass model. Results from their study show a reasonable agreement in translational and rotational displacements for a conventional FOWT unit. However, the sea current effect was neglected, and some uncertainties were surrounding the representative scenario of the waveform used to investigate the platform's motion responses. Although, multibody dynamics modelling of a spar buoy FOWT based on OC3-Hywind concept[27] by Mohammed et al. [89] and other similar studies by Antoni et al. [17], Bea and Kim[90], [91], Madjid et al. [15], Alexander et al. [16], and Yanqinq et al. [22] provided some good understanding of coupled fluid dynamics analysis for wave-wind induced motion but wave-current interaction modelling and its effects on the floating platform were ignored.

The coupled dynamics studies reviewed so far took different approaches to achieve one goal, which is predicting an OWT floating platform's motion responses due to the influence of the coupled interaction of the environmental elements (wind, wave, and currents) and the likelihood of such responses on the wind turbine power generation system. However, there are other limitations that must be addressed to pave the way for larger capacity WTG unit. Setting up scaled model experiments or developing a scaled pilot project for an intending FOWT farm project can be prohibitively expensive and time-consuming. Consequently, a sound understanding of a floating platform's behaviour will provide insight towards design optimisation and cut down the cost and time for performing preliminary engineering analysis for floating platform technology which will ultimately yield a more profitable offshore wind turbine power generating asset. The author hopes that the studies reviewed so far have provided some dependable understanding and clarification as to how vital the subject of coupled dynamics for the investigation of aerodynamic and hydrodynamic loading is to the offshore wind energy industry.

Chapter 3

Environmental Scoping Assessment and Loads Modelling Strategy

This chapter will present an environmental scoping assessment for two potential FOWT Project Development Areas (PDAs) in New Zealand's northland. The methodology for the qualitative and quantitative statistical analysis that were performed on the long term MetOcean hindcast data obtained for the PDAs are demonstrated. The environmental loads modelling strategy for wind, wave and current are discussed, and the choice of the energy spectra models used in modelling wind and wave loads are highlighted. These energy spectra models formed the basis for the Design Load Cases (DLC) that were established and implemented for the coupled dynamics modelling of the TRIHF. The DLCs were developed based on the industry standards for the design of FOWTs (DNV-OS-J101 [92], DNV-OS-J103 [48], DNV-OS-C301 [49] and DNV-ST-0437 [76]). By the end of this chapter, the author anticipates that the audience will be more informed on the goals and objectives of this research and that there will be a clearer understanding about floating platforms for offshore wind turbines and how having a sound understanding of the environmental loads is crucial in providing an accurate analysis.

3.1 Site Specific Environmental Scoping Assessment

As New Zealand and the world at large increasingly focus on the pressing challenge of limiting greenhouse gas emissions, there is growing feasibility of harvesting offshore wind energy to meet these growing energy demands. The use of a floating platform for the installation of wind turbines has many benefits. For instance, in New

Zealand, and as can also be observed in other parts of the world, there are vast deep-water sites suitable for the installation of FOWTs while sites for installing fixed-bottom foundation in shallow waters are scarce. As can be understood from Fig. 3.1 demonstrating New Zealand's bathymetric undersea feature names, the average water depth of New Zealand's North Island coastlines is about 250 m, making it very unsuitable for fixed bottom foundations [93]. Also, consenting onshore wind farms can become prohibitively difficult due to local objections. Therefore, the use of floating platform technology to provide support for OWTs may be necessary due to the abundance of deepwater sites off the coast of New Zealand.

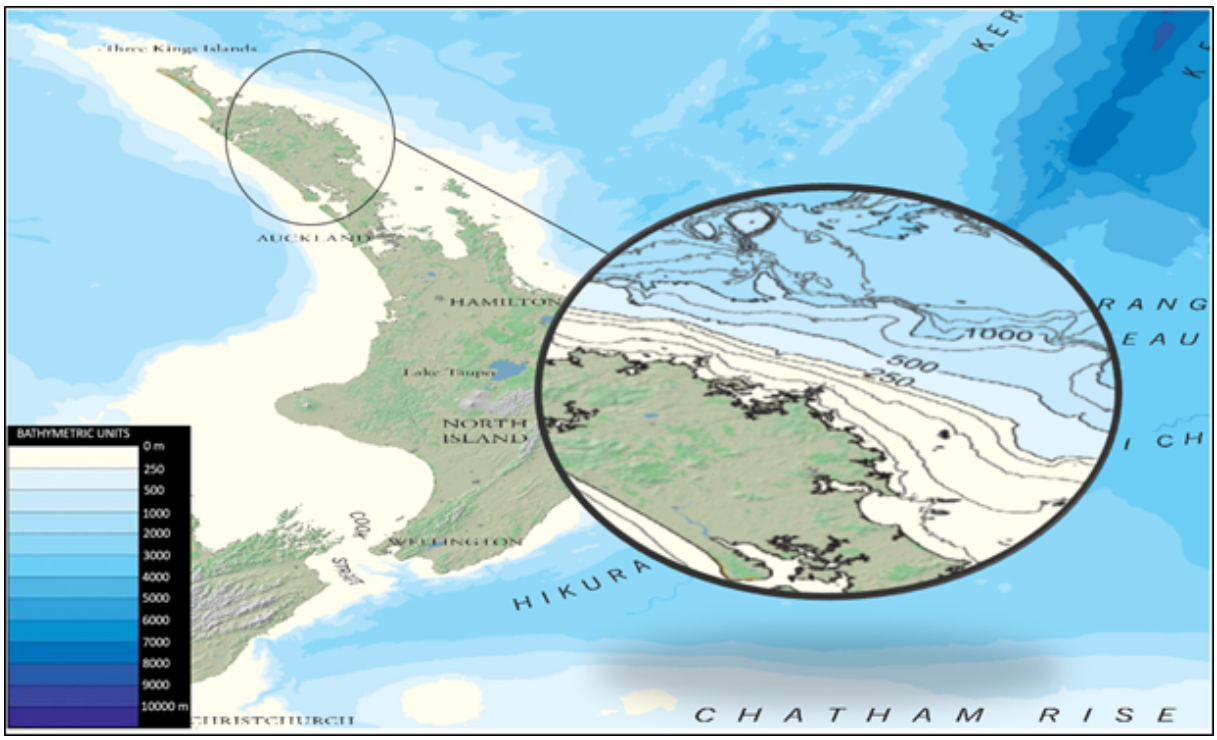

FIGURE 3.1: New Zealand's Northland Bathymetric Features | According to Ref [93]

Performing engineering design studies for FOWTs requires the obtainment of loads and site conditions for the offshore project location where the wind turbine farm is intended. By considering some key factors, two locations have been identified in New Zealand's North Island seaway that presents a promising future for OWT projects. Table 3.1 below shows the coordinates and seamarks for the proposed offshore wind farm Project Development Area (PDA)[1]. Fig. 3.2 contains a map of these locations.

[1]Presently, this research will be focused on the possible PDAs in New Zealand's North Island seaways due to time constraint and the availability of information required to perform this research.

TABLE 3.1: Proposed Offshore Project Development Area for Floating Offshore Wind Turbines off the coast of New Zealand's North Island.

Locations	Coordinates		Distance from Shoreline	Seamarks
	Latitude	Longitude		
Site 1 - Whangarei	S35° 51'30.41	E174° 31'20.20	20.6 km off the Coast of Marsden Point, Auckland.	3.12 km off Alice Island, and 3.82 km off Whatupuke Island
Site 2 - Tauranga	S37° 33'47.10	E176° 21'48.11	16.8 km off the coast of Tauranga, Hamilton.	30 km off Mayor Island, and 7.47 km of Motiti Island

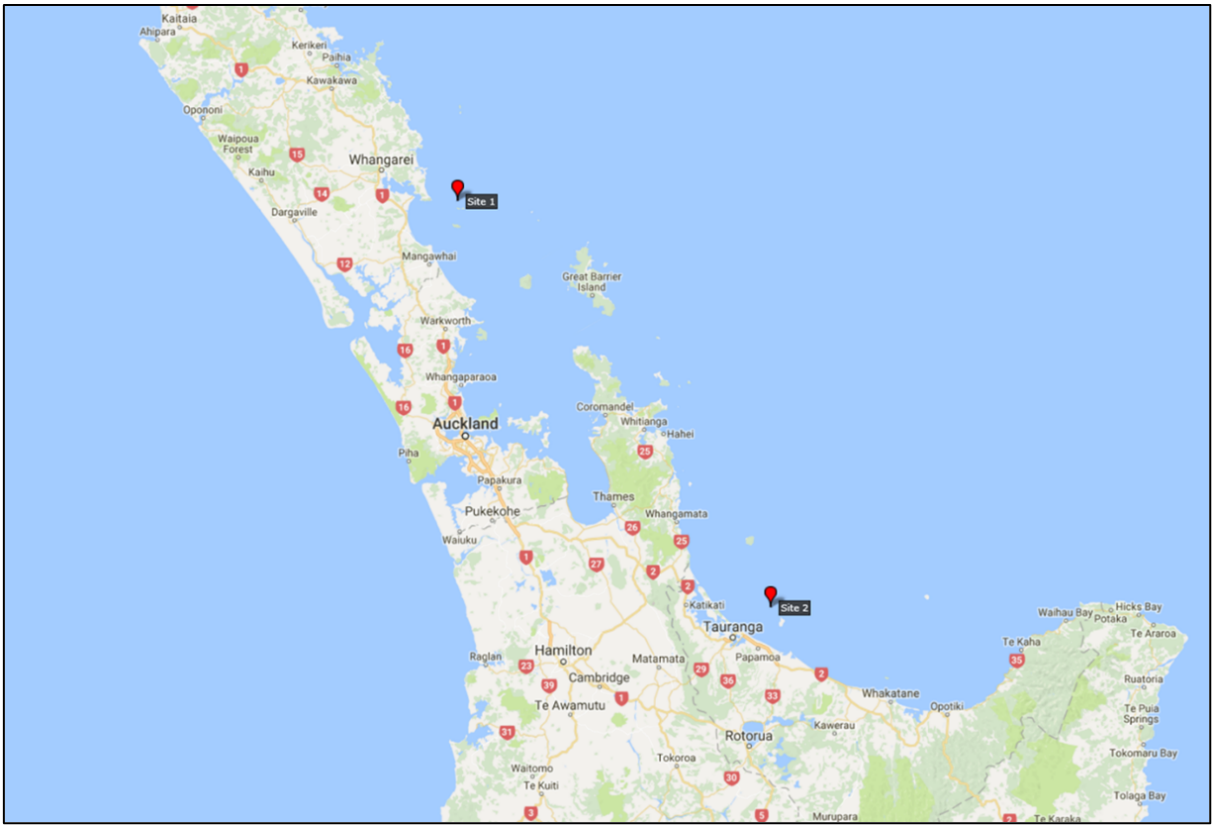

FIGURE 3.2: Proposed PDAs for FOWT Project off the coast of New Zealand's North Island.

Some of the key factors considered for the proposed offshore development area for OWT projects were;

3.1.1 Water Depth

Across Europe and North America, monopiles are the widely installed type of OWT foundation in water depths around 30 m. For water depths beyond the depths suitable for monopiles, jacket foundations are installed. It is generally acceptable in the OWT industry that the limiting water depths for commercially viable jacket foundation is 50-60 m. Consequently, the choice of FOWT over fixed bottom foundation OWTs is the depth limitation presented by the jacket foundations ($\leq$ 60 m). Thus, the floating foundation for OWTs requires a water depth of more than 60 m to justify its application [94]. As presented earlier in Fig. 3.1 containing New Zealand's bathymetric undersea features with contours, the FOWT PDAs under consideration have water depths ranging between 250 to 500 m which are beyond the technical scope of current fixed bottom foundation technologies, therefore justifying the applicability of floating technology for OWT installation.

3.1.2 Proximity to Electrical Substation / Grid Connectivity

Potential development sites for FOWTs need to be close enough to the coast to facilitate cost-effectiveness in exporting the generated power from the WTG unit to an electric distribution grid without the use of offshore sub-station and transformation. According to ref [95], Fig. 3.3 and Fig. 3.4 illustrates New Zealand North Island's grid zones and electrical substations network. As can be observed from this substation locator map, grid connectivity options are numerous with electrical substations available in the vicinity of the proposed PDAs. The closest (Marsden, Bream Bay, and Kensington substations) are potential candidates for grid connecting a FOWT located at approximately 20 km from site 1. For site 2, Tauranga, Kaitimako, Te Matai, and Mt. Maunganui are substations for potential grid connection points which are approximately 16.8 km away. All these substations are single to double-circuit towers running from 110 to 220 kV.

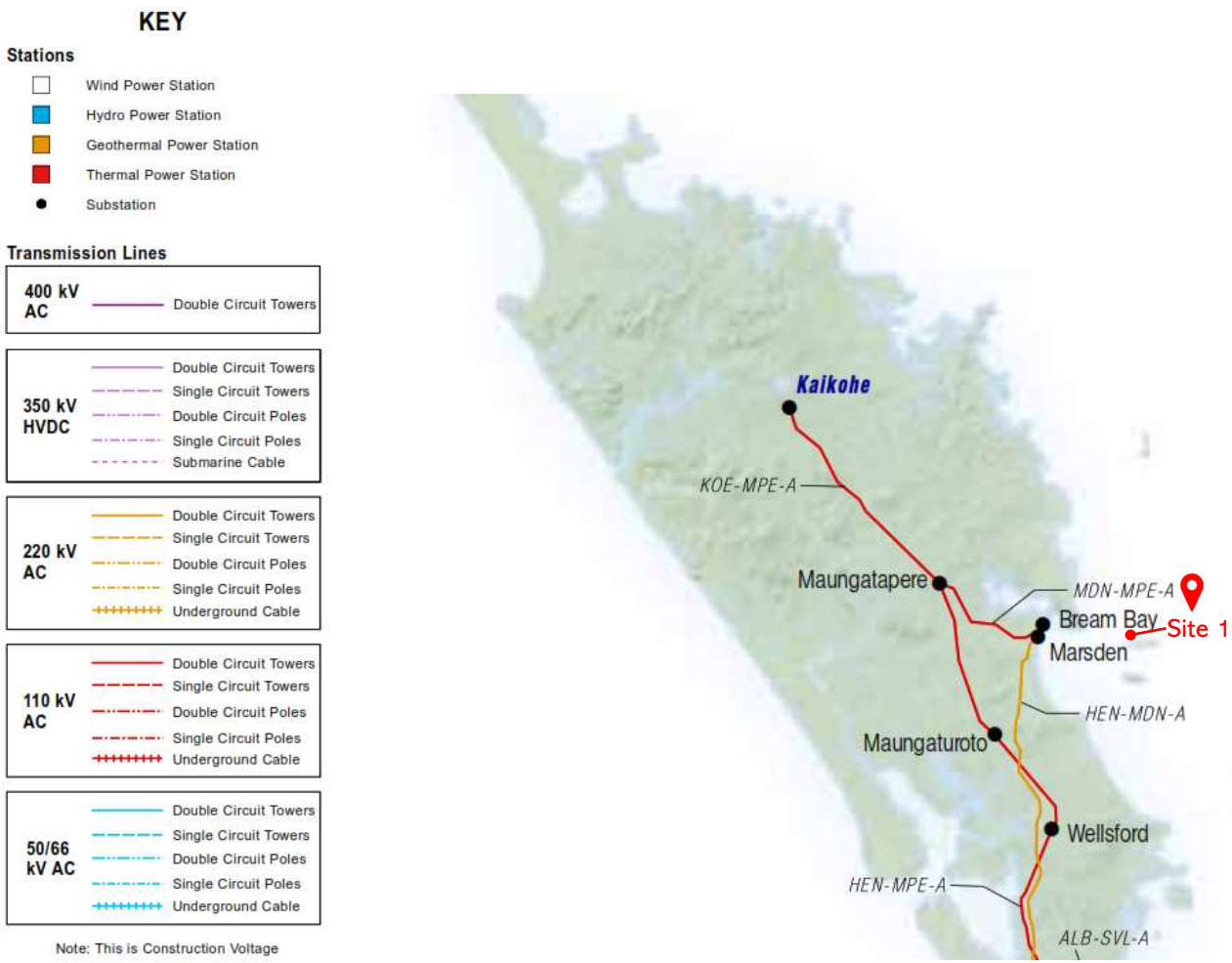

FIGURE 3.3: New Zealand North Island Electrical Substation Locator Map | Site 1 – Marsden, Whangarei [95]

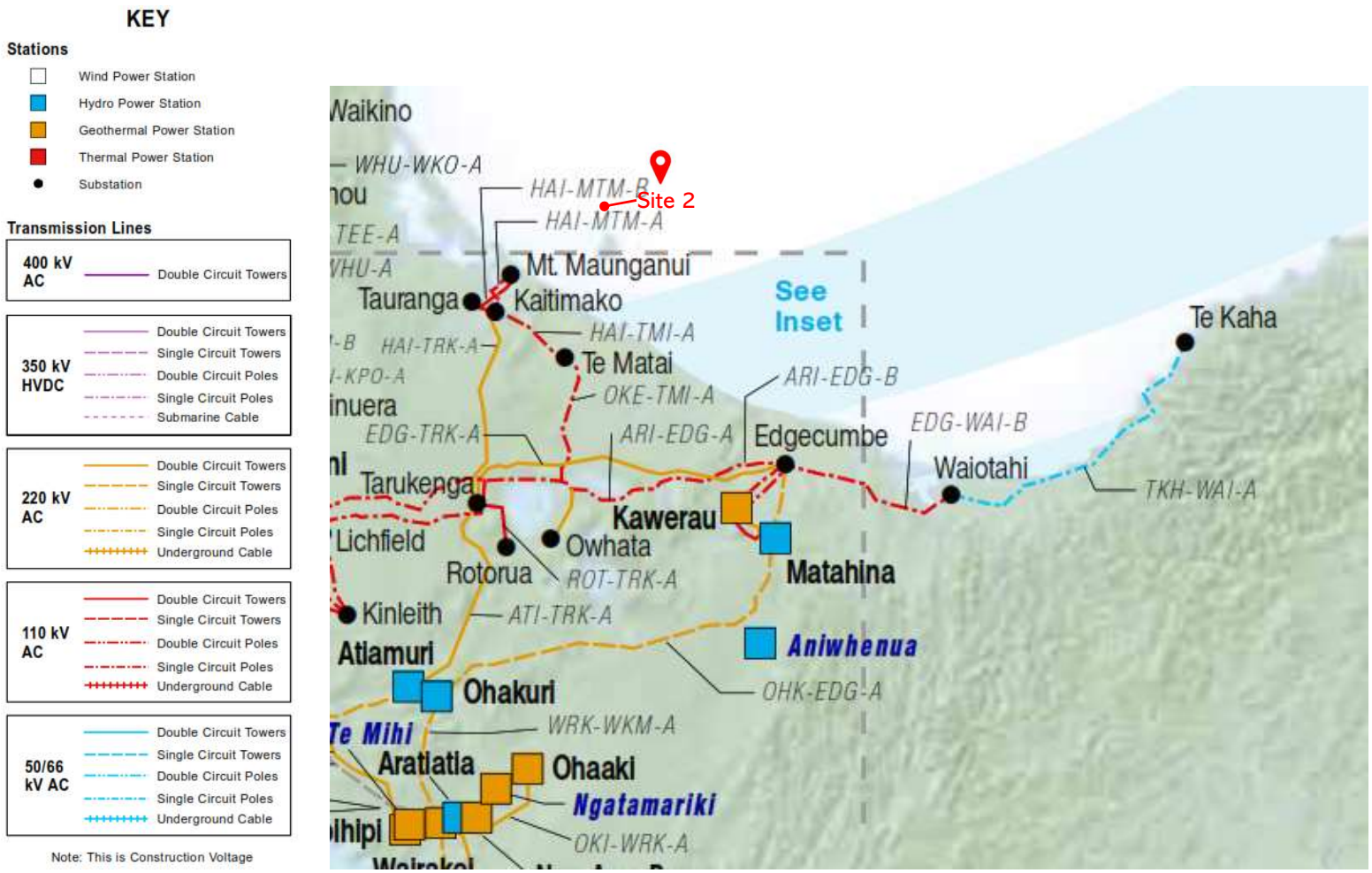

FIGURE 3.4: New Zealand North Island Electrical Substation Locator Map | Site 2 – Tauranga, Hamilton [95].

3.1.3 Inshore Assembly Area

The availability of inshore assembly area for the WTG unit is crucial to the success of a FOWT project. This is a vital aspect of a FOWT project which allows the WTG units to be assembled in a sheltered inshore environment rather than performing assemblage activities in an offshore location which can have huge cost implications. The Northport[2] situated at Marsden point offers natural deep-water access to facilitate the successful inshore assembly for a FOWT. In addition to having 180 hectares of immediately available 'greenfield' commercially-zoned land adjacent to the port boundary, the Northport has a lot to offer in terms of providing the necessary basic amenities needed for the fabrication, installation, and assembly of a FOWT unit [96]. Fig. 3.5 shows the terrain map for the prospective inshore deepwater harbour area that can be utilised for the fabrication, installation, and assembly of a FOWT unit.



FIGURE 3.5: Northport Deepwater Harbour.

[2]Northport offers deep-water access to the world – www.northport.co.nz

3.1.4 Availability and Proximity to Deepwater Navigation Route

The assembled FOWT unit need to be towed to the desired offshore location from the inshore assembly area. The navigation route must have enough draft for the FOWT to be towed safely. Consequently, the availability and proximity of an inshore assembly area to a deepwater navigation route is key to ensuring the safe sailing of the WTG to the desired project site. The bathymetric map in Fig. 3.1 suggests that the navigation route from the potential inshore assembly area (Northport) to the project site offers enough draft of more than 200 m to ensure safe sailing from the inshore assembly area to the PDA.

3.1.5 Socio-Economic Activities

Shipping Activity

Marine traffic is also a key factor to be considered when proposing a project location for FOWTs. As can be seen from Fig. 3.6 and Fig. 3.7, the nearest seaports to the proposed PDAs are Marsden Point/Northport and Tauranga for sites 1 and 2 respectively. Marsden Point is home to New Zealand's only oil refinery (Refining NZ), Northport (Deepwater Port), and Carter Holts Laminated Veneer Lumber (LVL) plant. These ports handle tankers for oil and gas products (Refining NZ), and general cargo ships most especially for loading logs, LVLs, and wood chips, and discharging cargo containers (Northport).

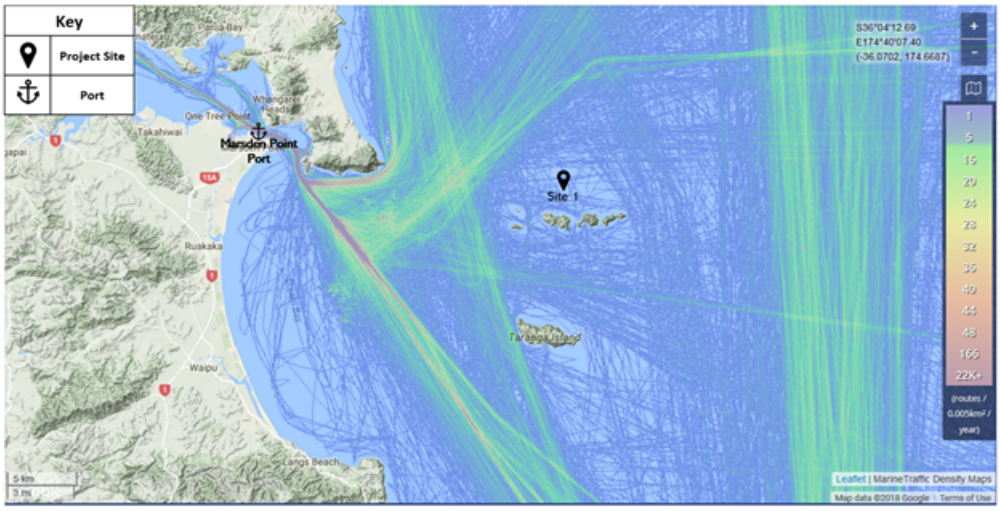

FIGURE 3.6: New Zealand North Island Marine Traffic Density Map | Site 1 – Whangarei [97].

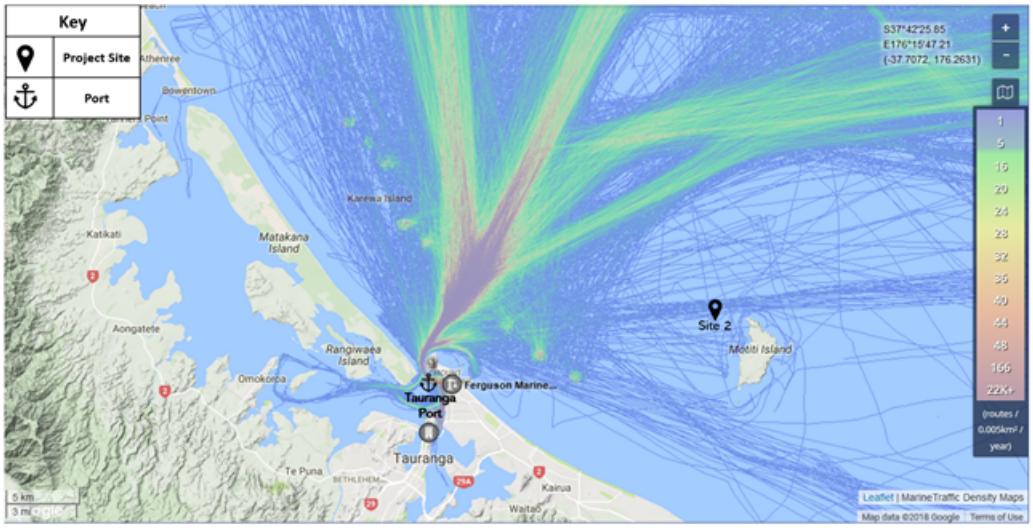

FIGURE 3.7: New Zealand North Island Marine Traffic Density Map | Site 2 – Hamilton [97].

By utilising the freemium Ship Tracking Intelligence (STI) service offered by marinetraffic.com, the marine traffic density map for site 1 and 2 is presented in Fig. 3.6 and Fig. 3.7, respectively. As can be observed, the proposed PDAs have low vessel traffic levels which range from 1 to 5 routes per 0.005 km^2 per year for both sites 1 and 2 [97]. High levels of traffic to the west of sites 1 and 2 are because of traffic bound to and from the busy ports in Marsden point (Northport) and Tauranga port, respectively. The presence of low levels of marine traffic around these proposed project locations for the deployment of a FOWT is a very favourable condition for NZ's marine industry from an operational safety perspective during the life of field service for the WTG.

Recreational Sailings and Fishery

Fig. 3.8 illustrates a map containing the distribution of recreational fishing measured in number of vessels per km^2. This data represents the combination of aerial flights and boat ramp surveys from 2005 to 2012, and statutory catch and activity returns from charter vessels from 2011 to 2014. Fishing areas are indicative estimates only [98]. A keen observation from the map reveals that the recreational sailings and fishery around the proposed PDA for FOWT exhibit low to medium levels of recreational fishing activities which is mutually beneficial for a FOWT project and New Zealand's recreational sailings/fishing industry. A similar trend can also be observed in Fig. 3.9 which illustrates commercial fishing map measured in catch per km^2.

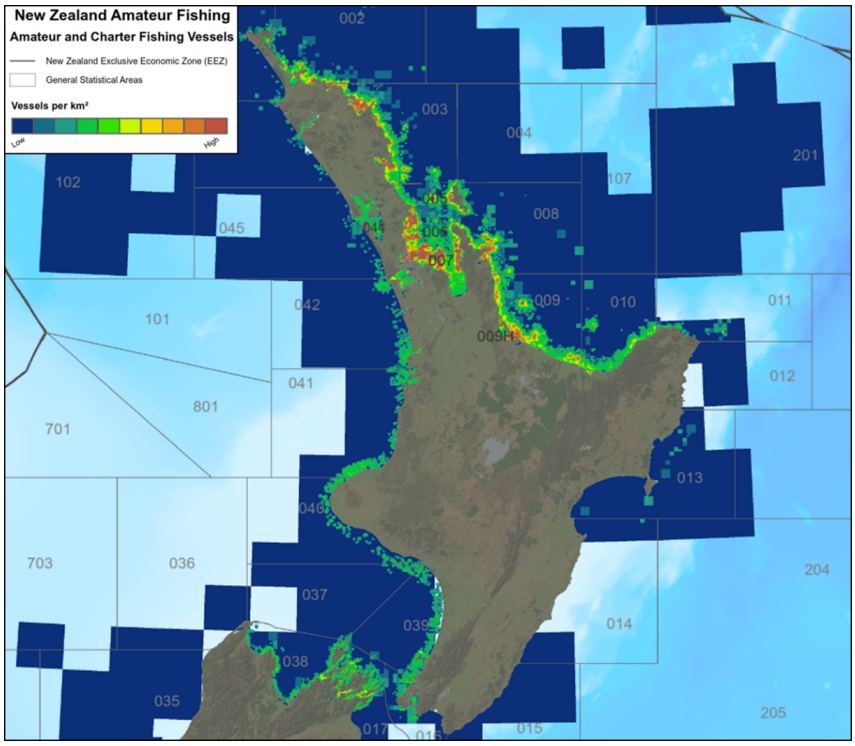

FIGURE 3.8: New Zealand Recreational Fishing Map | North Island[98]

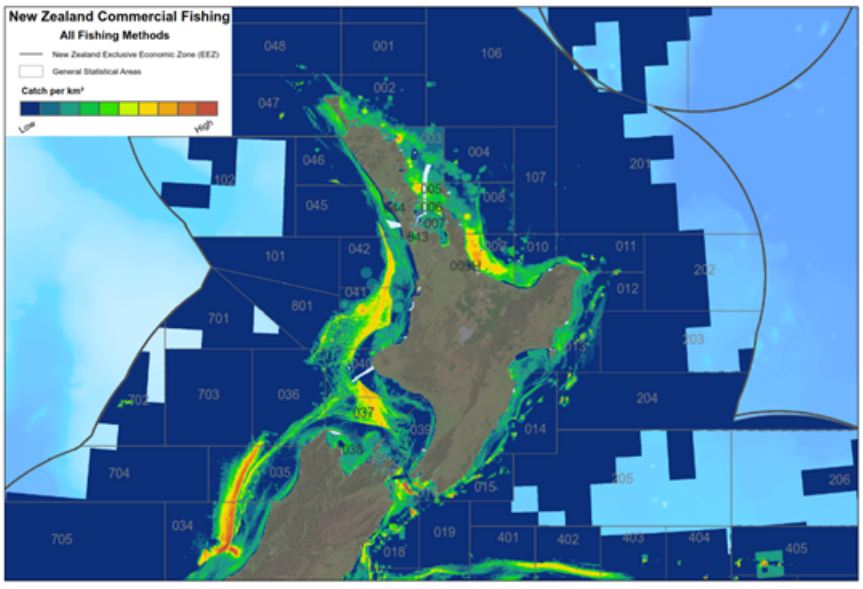

FIGURE 3.9: New Zealand Commercial Fishing Map | North Island [98]

3.1.6 Military and Civil Radar Considerations/Aviation Activities

The impact of a FOWT scheme on civil aviation radar operations is another key factor that needs to be examined. Investigating this impact will include the identification of

potentially sensitive receptors to the FOWT farm, including all known military and civil aviation facilities such as airfields, airports, and radar installations both shipping and airborne. A typical 5 MW WTG unit having a swept area of about 12,500 m^2 can reach a total height up to 170 m (560 ft) when measured from the blade tip to the mean sea level. These large geometrical features can pose as an obstacle to civil and military radar when an offshore wind turbine PDA falls within civil or military aerodrome buffer zones. According to Civil Aviation Authority (CAA) of New Zealand, any activity in the vicinity of aerodromes must be conducted within 4 km off an aerodrome or heliport boundary if it is at or below 120 m (400 ft) in height or must be 8 km of an aerodrome/heliport boundary if it may exceed 120 m (400 ft) in height [99]. Fig. 3.10 contains New Zealand's Airspace map (North Island) showing aerodromes, aerodrome control zones, Low Flying Zones (LFZ), military operating areas and restricted areas [100].

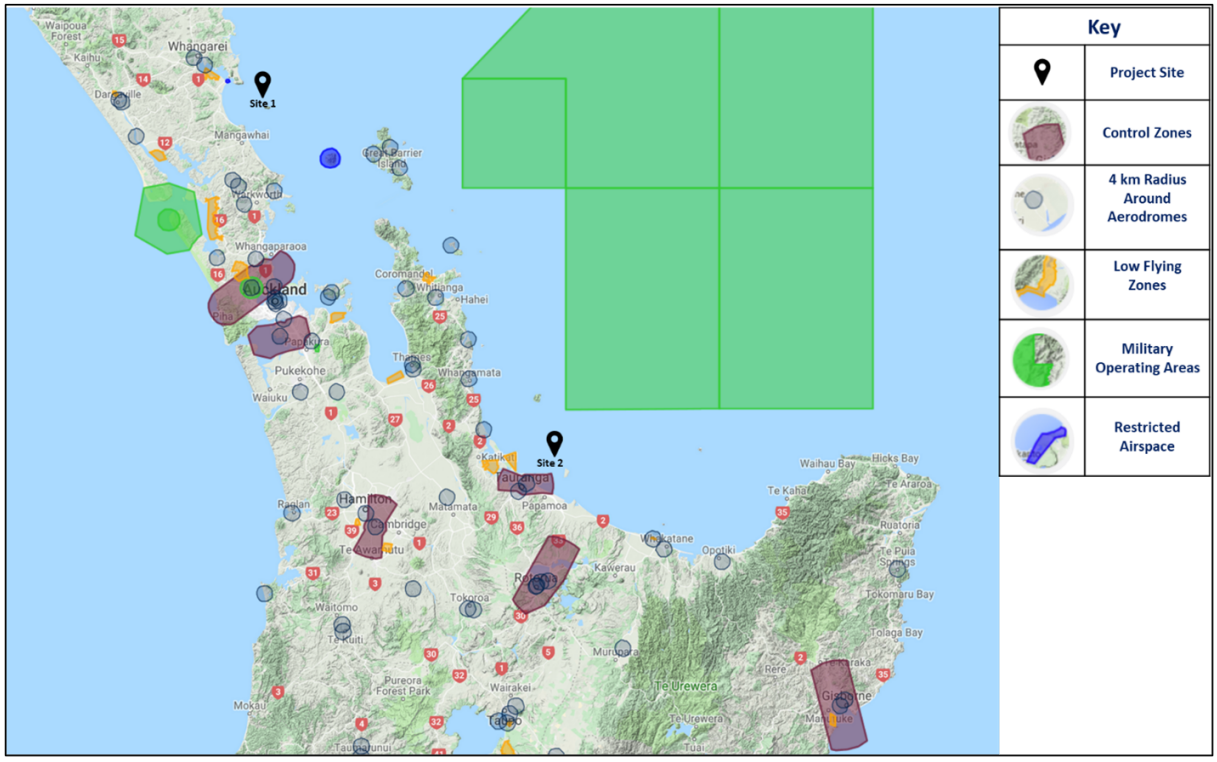

FIGURE 3.10: New Zealand Airspace Map | North Island [100].

The control zones are managed by air traffic control and extend down to ground level. As can be seen from the map, the closest aerodrome (Whangarei and Tauranga) is located onshore and are some 20 km away from the locality of the proposed PDA

for the offshore wind farm. Most importantly, the PDA does not overlap any military zones and control zones. From a safety perspective, caution needs to be taken to ensure that the total vertical height of the wind turbine does not exceed the LFZ height within the vicinity where the wind farm is situated to prevent air flight disasters and airspace hazards from aeroplanes and helicopters flying over the offshore wind farm site. The simplified flight route map on Fig. 3.11 illustrates instances of the major instrument flight rule routes frequently flown by military and civil aircraft in New Zealand [101].

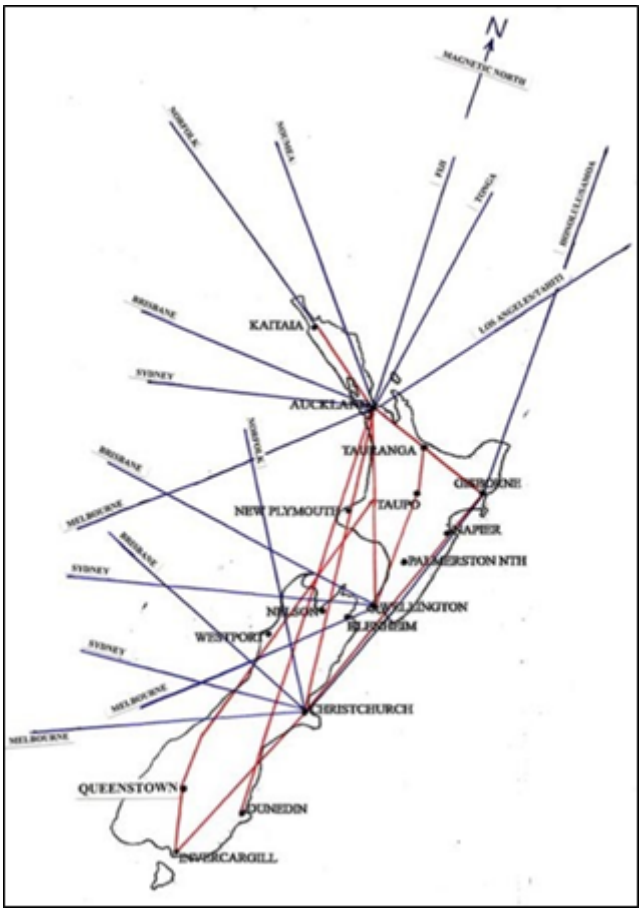

FIGURE 3.11: New Zealand Scheduled Flight Paths Map [100].

Aircraft approaching to land or departing from the associated airports comply with these tracks. The two international airports closest to the PDAs being investigated are the Auckland Airport and Hamilton Airport for site 1 and 2, respectively. As can be observed from the map, the proposed PDAs is located outwit any domestic, international, or military aircraft routes. Even though the presumed total vertical height of the wind turbine (560 ft) is greater than the upper limit of the LFZ (500 ft above ground

level) around the cities and harbours in New Zealand[3], the PDA is located offshore and is not foreseen to overlap any LFZ or any area of economic, civil, or military interest as clearly shown in Fig. 3.11.

3.1.7 Marine Protected Areas/Reserves

Marine reserve maps obtained from the Department of Conservation (*Te Papa Atawhai*) New Zealand for the PDAs being investigated is contained in Fig. 3.12 and Fig. 3.13 [102]. As can be realised from the marine reserve maps, the PDAs does not fall within or overlap any current designated marine protected areas. However, the seaway surrounding the PDAs and the adjacent coastlines are important for wildlife and their supporting habitats. There are several designated protected reserve sites at the coast. Consequently, an appropriate assessment for sensitive species found within the proximity of the PDAs need to be performed.

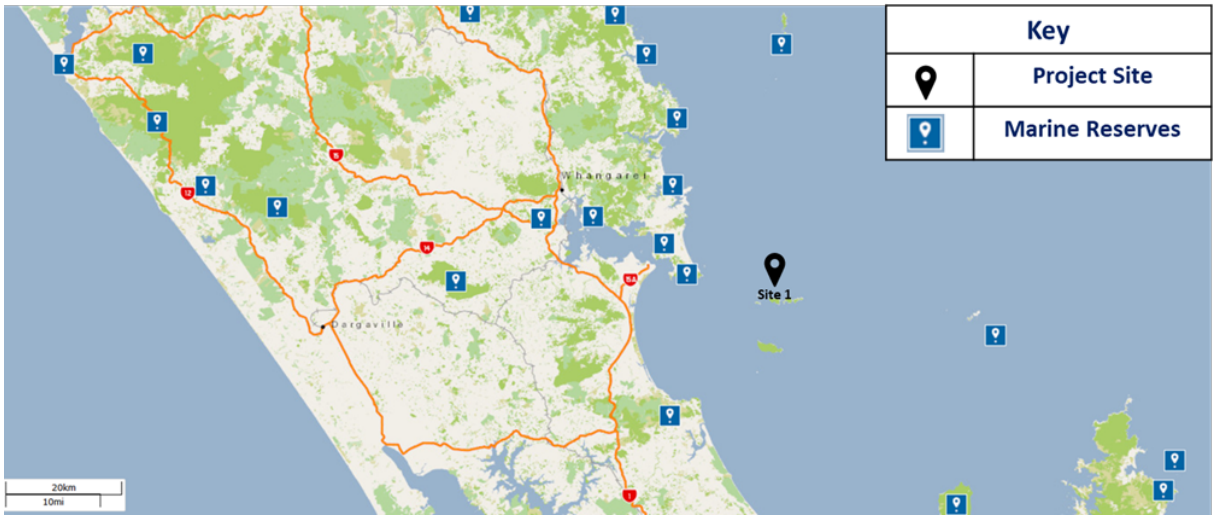

FIGURE 3.12: Marine Reserves Map | Site 1 – Whangarei [102].

[3]According to Civil Aviation Authority (CAA) of New Zealand, the Low Flying Zone (LFZ) upper limit around the cities and harbours in New Zealand is 500 ft

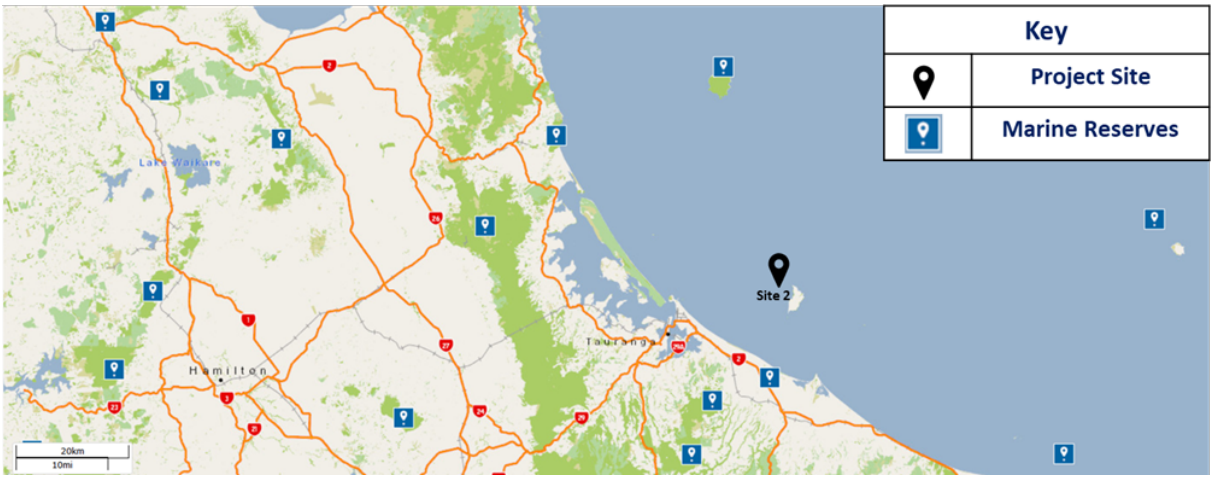

FIGURE 3.13: Marine Reserves Map | Site 2 – Hamilton [102].

3.1.8 Seabed Conditions

To gain insight into the shape of the ocean floor around the proposed PDAs, the publicly available 250-metre-resolution digital terrain map of New Zealand's Exclusive Economic Zone (EEZ) were obtained from the National Institute of Water and Atmospheric Research (NIWA) [103]. Examination of the available seabed data revealed a largely submerged continental landmass consisting of a series of plateaux, seamounts, trenches and elongated ridges (Fig. 3.14)[104], [105]. The New Zealand ocean floor spans over 4 million km^2 and comprises a narrow continental shelf with extensive underwater plateaus, continental steep slopes, deep seafloor, and deep ocean trenches [105]. These features of the seabed further buttress the use of a floating foundation technology for the offshore wind farm as the use of fixed bottom foundation may not be technically feasible with seafloor having obtrusive features such as steep slopes and plateaus. More observable, the seafloor of the undersea realm is subject to earthquakes and volcanic eruptions, as well as vigorous weather systems. The seabed formation across the PDA indicates that the seabed is predominantly muddy sand and muddy. Information on the nature of the seabed soil conditions is vital because it aids with the geotechnical design of the anchoring scheme that transfer loads between the station keeping system and the seabed soils. A geotechnical study provides all necessary soil data for detailed design and forms the basis for anchor type selection [91].

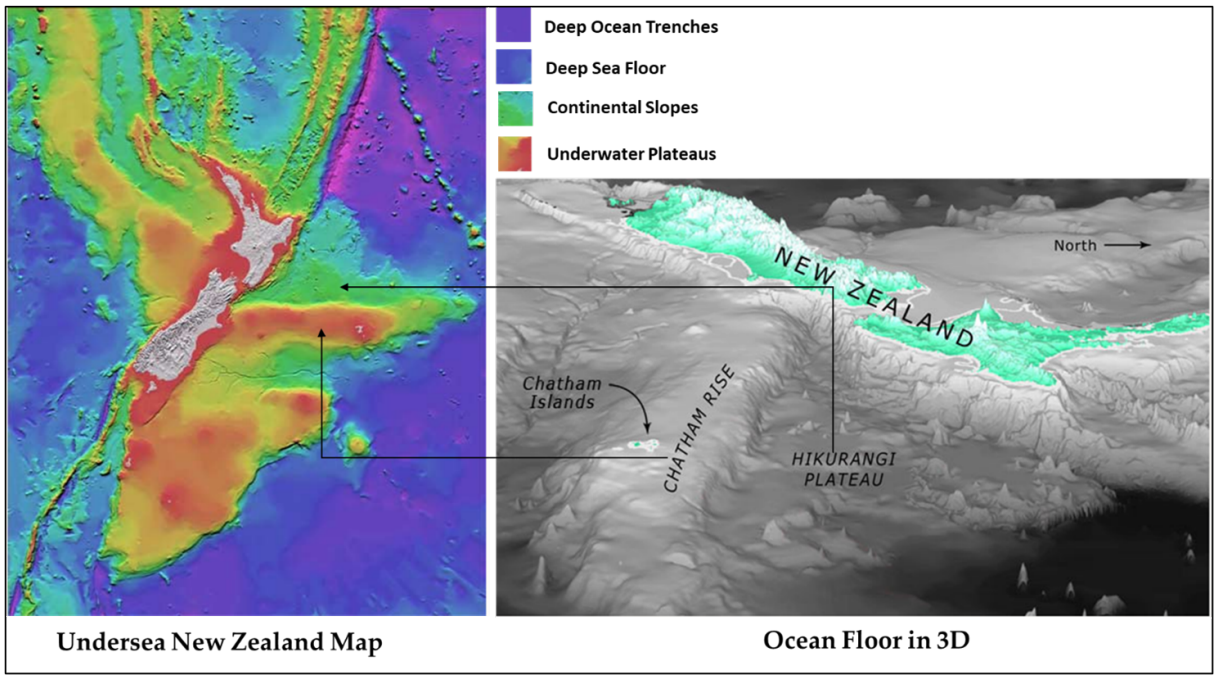

FIGURE 3.14: New Zealand's Ocean Floor [104], [105].

3.1.9 Metocean Conditions

Publicly available hindcast data concerning the meteorological and oceanographic (Metocean) characteristics around the vicinity of the proposed PDAs were observed at MetoOcean-View [106]. As presented in Fig. 3.15, the wave significant height was modelled using the Simulating WAves Nearshore (SWAN) wave model and was observed to have a mean annual height of 1.5 m around the vicinity of the planned PDAs. Also, the mean annual wind speed was modelled using Weather Research & Forecasting (WRF) atmospheric model and is detected to have a mean annual speed of 11 knots (5.7 ms^{-1}). The vector averaged current around the environs of the PDA as shown in Fig. 3.16 was assessed to be 0.6 knots (0.3 ms^{-1}) based on the Regional Ocean Modelling System (ROMS) current model. On a general note, the Metocean conditions of the east coast are observed to be more benign than the west coast, thus making the east coast a choicer location over the west coast for the proposed PDAs from an environmental loading and load effects standpoint.

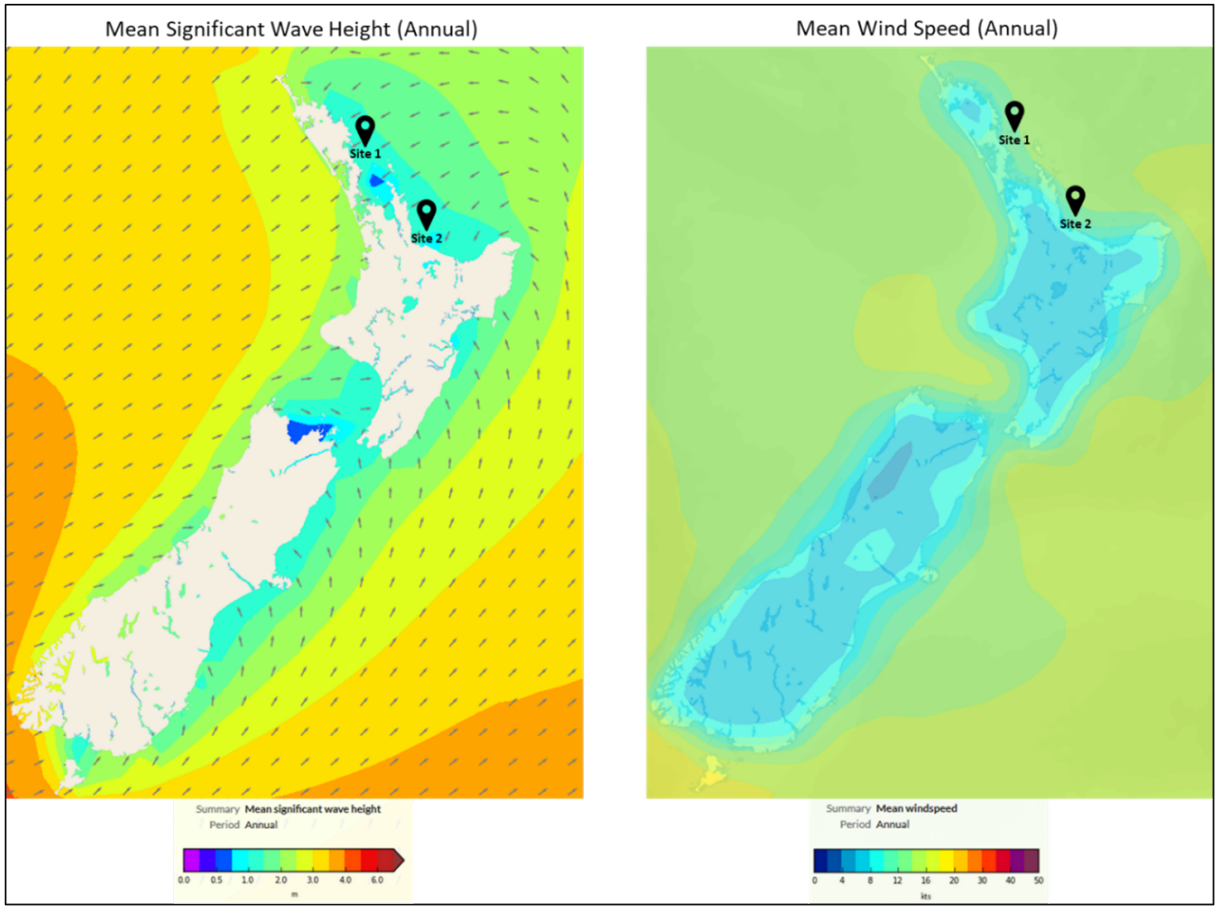

FIGURE 3.15: Metocean Conditions for Mean Significant Wave Height and Mean Wind Speed [106].

As will be discussed later in sections 3.2.1 and 3.2.3, the site specific hindcast data were obtained for the PDAs of interest. Fig. 3.17 and Fig. 3.18 contains the wind rose plot for a 10-minute average wind speed at (a) 10 m above sea level and (b) at a hub height of 100 m for PDAs 1 and 2, respectively. The wind rose plot was created after post-processing the NetCDF file of the hindcast data using the Matlab code presented in Appendix A. As can be observed from the wind rose plots, dominant northeast wind patterns prevails for both PDAs 1 and 2. At 10 m above sea level, the wind very frequently blows at 4 to 8 ms^{-1} for PDA 1 and 8 to 12 ms^{-1} for PDA 2. At a height of 100 m above sea level, the wind frequently blows at 8 to 12 ms^{-1} and rarely at 16 to 20 ms^{-1} for PDA1, while for PDA 2 the wind frequently blows at 8 to 16 ms^{-1} and rarely at 16 to 20 ms^{-1}. Also noteworthy are the wind scattering from north-northwest to south-southwest for both offshore locations. Although the frequency of these winds may not be as dominant as their counterparts from the north-northeast to the south-southeast, it shows the huge potential for the amount of wind renewable energy that

can be harnessed from offshore locations. For offshore locations where a considerable amount of wind blows from all directions, a vertical axis wind turbine will provide to some extent more efficiency in harnessing the wind energy because all its blades will contribute to energy production.

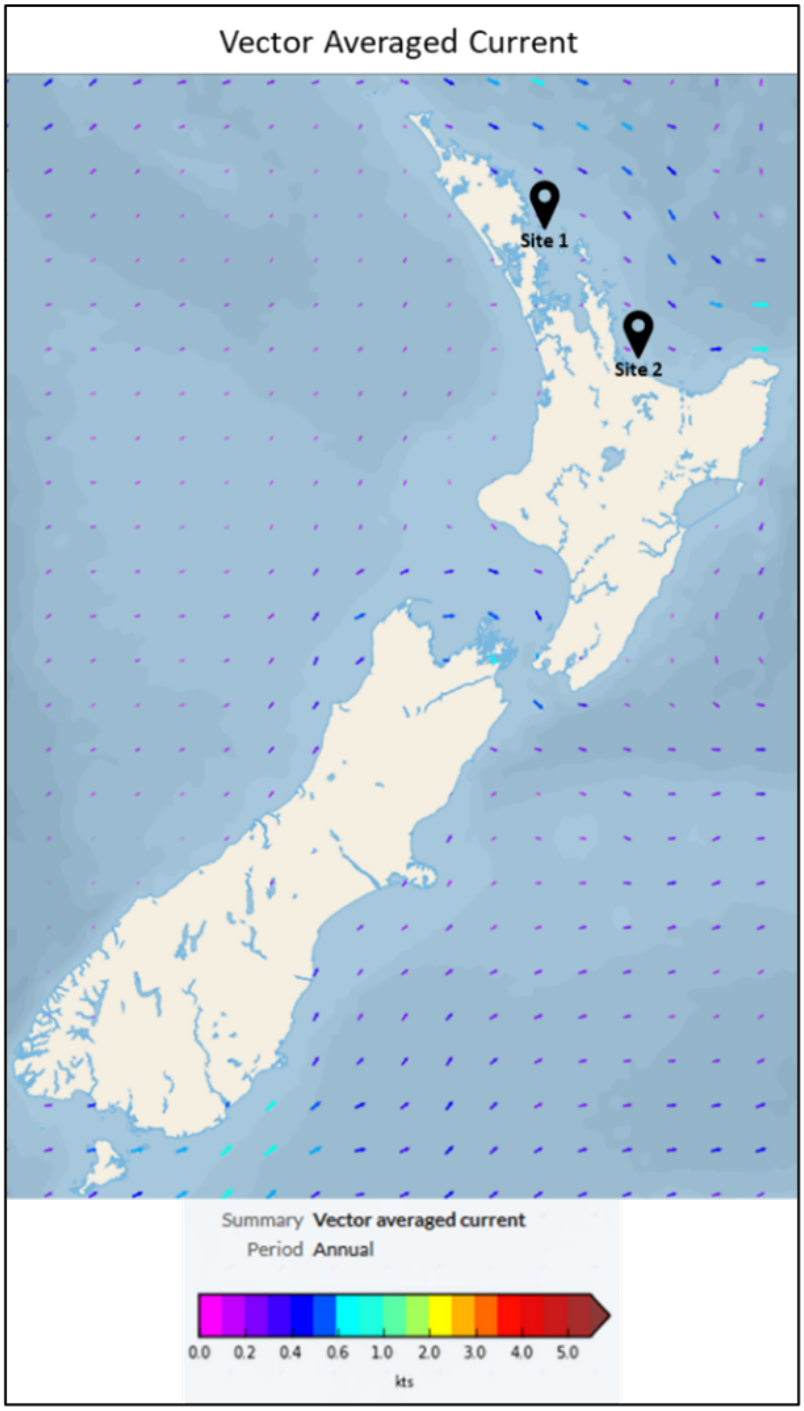

FIGURE 3.16: Metocean Conditions for Vector Averaged Current [106].

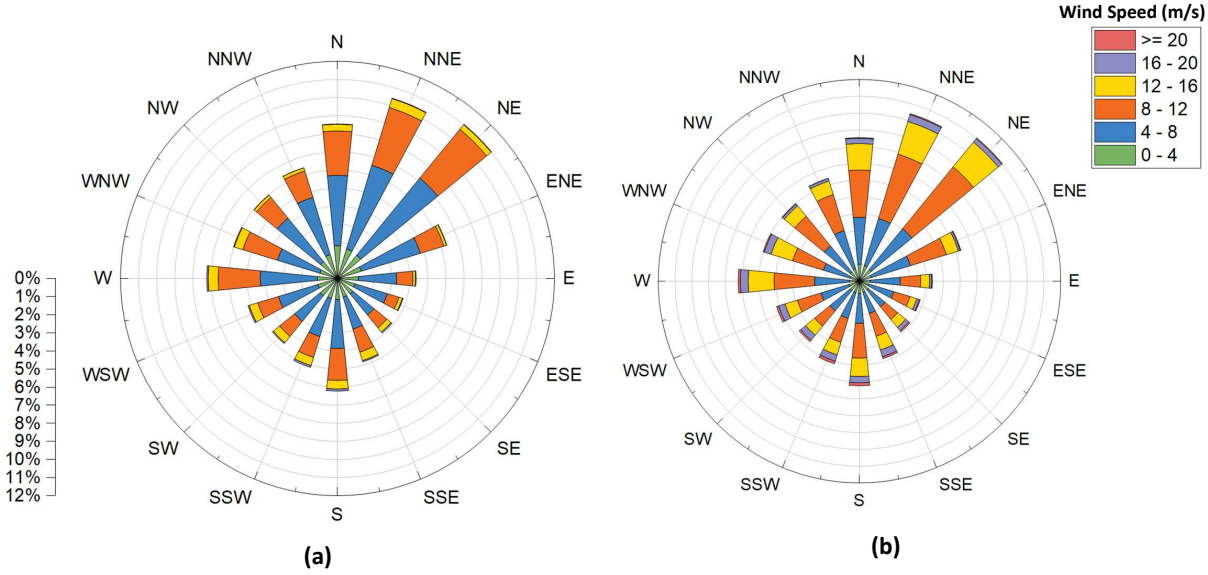

FIGURE 3.17: Wind rose showing wind speed, direction - blowing from, and frequency for a 10-minute average wind speed for offshore Whangarei at (a) 10 m above sea level (b) 100 m above sea level.

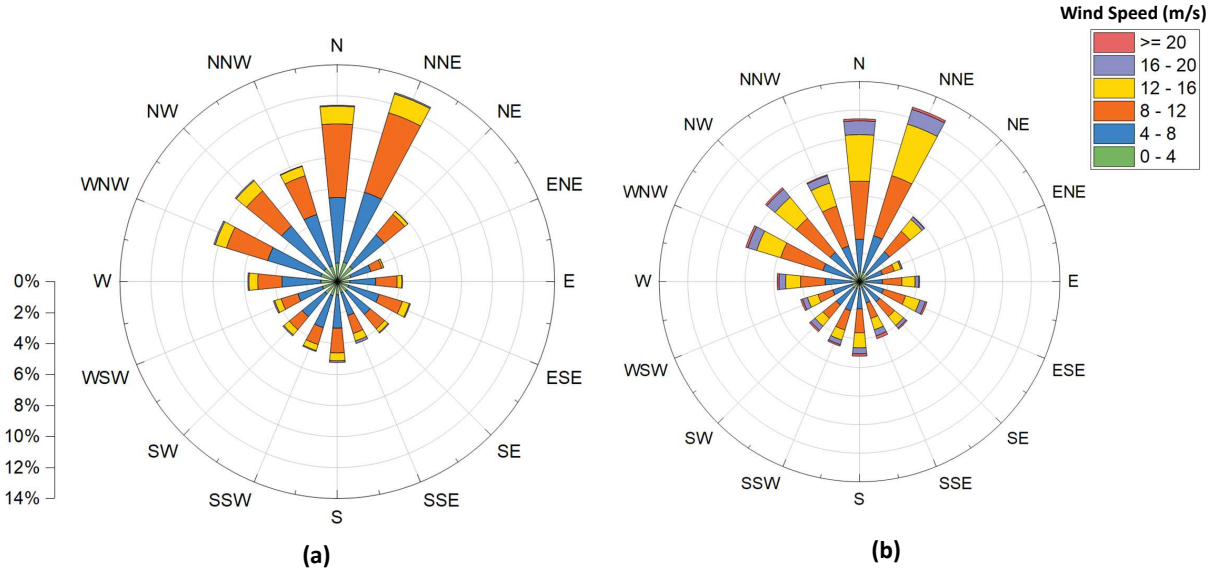

FIGURE 3.18: Wind rose showing wind speed, direction - blowing from, and frequency for a 10-minute average wind speed for offshore Tauranga at (a) 10 m above sea level (b) 100 m above sea level.

3.2 Environmental Loads Modelling Strategy

For this thesis, site-specific meteorological data for the proposed offshore wind energy PDAs discussed in Section 3.1 were acquired. These long term hindcast data include; wind (northward and eastward velocities), wave (peak periods and significant wave heights), and current (wind-generated and tidal current). These data were provided by Metocean Solutions Limited [106] in Network Common Data Form (NetCDF) file format. The NetCDF is a file format for storing multi-dimensional scientific data. In this form, the data is raw and unusable thus requiring the use of Matlab codes to read, squeeze, transpose, and write the data into excel before performing a quantitative and qualitative statistical analysis to extract the desired information needed for environmental loads modelling.

3.2.1 Site Specific Metocean Hindcast Data Statistical Analysis

Fig. 3.19 contains a flowchart illustrating the methodology adopted for performing the quantitative and qualitative statistical analysis. The focus of this thesis will be on-site one only (see Table 3.1) due to resource and time constraint, in addition to site one being the most favourable location due to its proximity to an inshore deepwater harbour area at Marsden point.

The wind meteorological data obtained consists of 10 minutes daily mean wind speed hindcast data measured 10 m above mean sea level for 324,336 days. For wave, the hindcast data consist of significant wave height of the sea component ($< 8s$) and peak wave period of the sea component ($< 8s$) for a duration of 108,555 days. Also, the hindcast data for ocean current provided consists of eastwards and northwards non-tidal sea level and current velocities for a duration of 109,769 days. Quantitative and qualitative statistical analysis was performed using Microsoft excel to develop the desired environmental loads information needed to perform the CFD numerical simulation and coupled dynamic simulation. Probability plot was used as a graphical tool to assess whether the data fits a particular distribution. The data are fitted with a theoretical distribution in such a way that the points should form approximately a straight line (distribution function linearization). Any departures from a straight line indicate a departure from the theoretical distribution. Firstly, the daily mean speed data was sorted into years by splitting the data sample size into 365 data points per column to

mimic yearly hindcast. Next, the annual maximum for each column was obtained and then sorted from lowest maximum to highest maximum. The wind speeds were then assigned a plotting position, and estimates of exceedance probability from the lowest to the highest were calculated using the expression [107], [108];

$$P_i = \frac{m_r - 0.375}{n + 0.15} \tag{3.1}$$

where m_r is the rank position and n is the sample size which is the number of years in this case. On assigning the plotting position of exceedance probability, the standard normal variable z corresponding to the plotting position was computed using the NORMSINV function in Excel and then plotted against the wind speeds. Thus;

$$z_{dist} = NORMSINV\,(P_i) \tag{3.2}$$

Fig. 3.20 below shows a plot of the normal cumulative distribution against the wind speed. As can be observed, the plot falls on a straight line showing that it comes from a normal distribution. However, there are considerable deviations from the normal distribution at low and high wind speeds in the northerly direction. The reason for this deviation is unknown and should not be of any concern since the overall R square (R^2) value for each curve is higher than 0.9 which shows a strong correlation to the normal distribution curve. For a normal distribution data, the frequency factor technique as proposed by Chow [107], [109] was used to estimate the magnitude of wind speed over a given return period using a frequency factor which is expressed as;

$$x_T = \bar{x} + K_T\sigma \tag{3.3}$$

where x_T is the estimated event magnitude at a return period T_R, $\bar{x}$ is the sample mean, σ is the sample standard deviation and K_T is the frequency factor which is expressed as;

$$K_T = z_T = -NORMSINV\left(\frac{1}{T_R}\right) \tag{3.4}$$

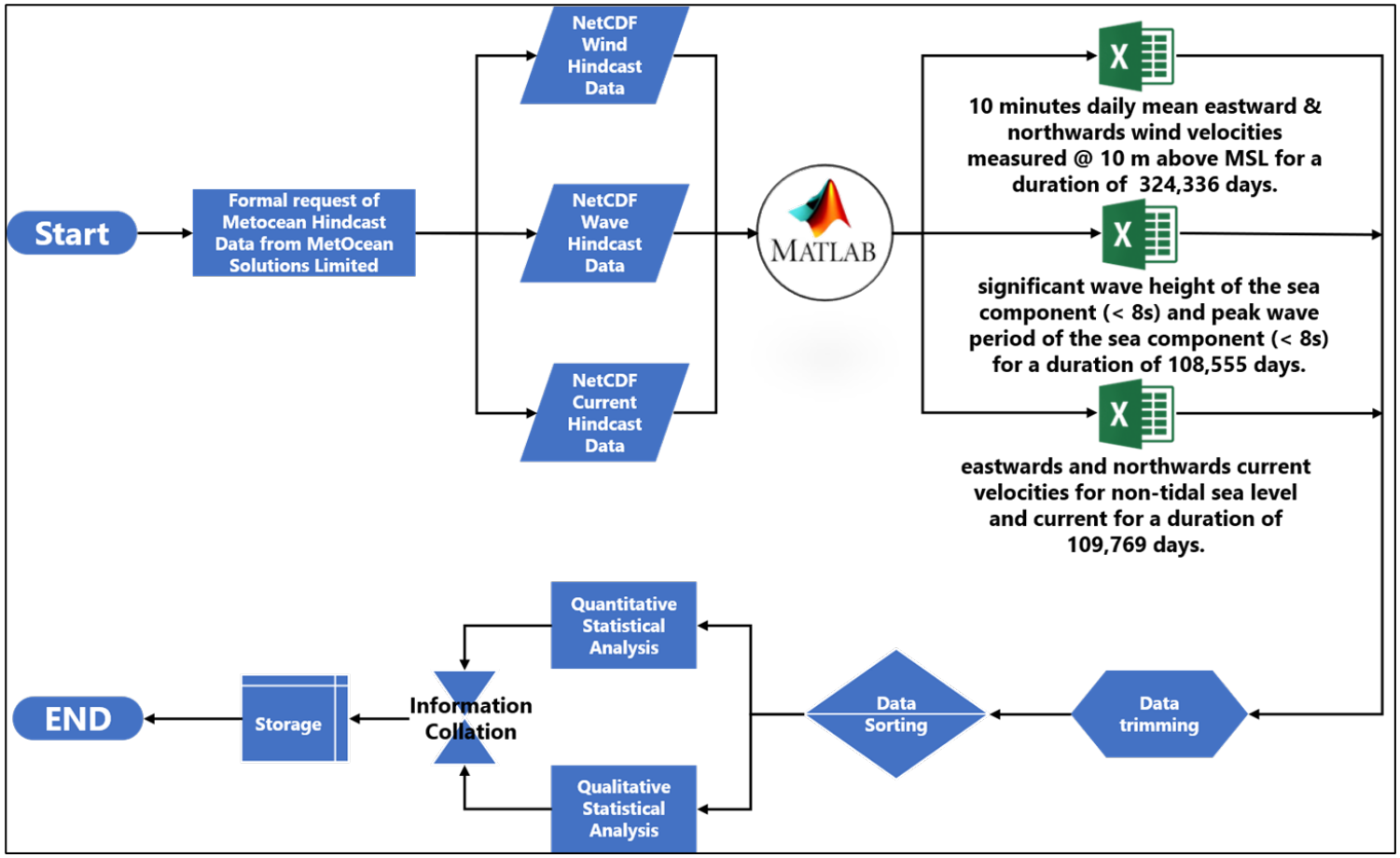

FIGURE 3.19: Process flow chart showing quantitative and qualitative statistical analysis of Metocean hindcast data.

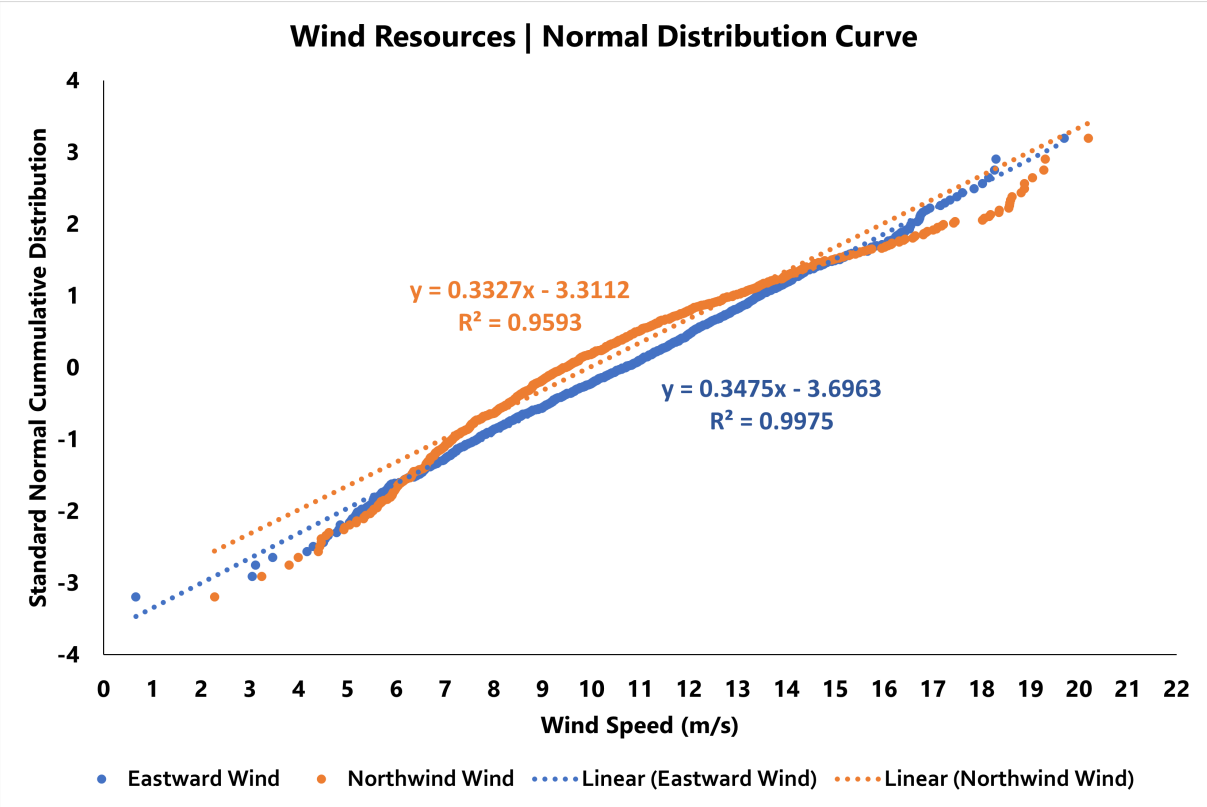

FIGURE 3.20: Normal Standard Cumulative Distribution for Wind Resources.

Table 3.2 below highlights the statistical summary for the hindcast data for northward and eastward wind velocities for the period under study. The turbulence intensity is defined as the ratio of standard deviation and mean of the sample wind data under investigation and is a measure of the level of velocity fluctuations.

TABLE 3.2: Statistical Summary of Wind Data.

	Eastward Wind (m/s)	Northward Wind (m/s)
Maximum	19.70	20.19
Minimum	0.66	2.28
Mean ($\bar{x}$)	10.64	9.95
Standard Deviation (σ)	2.87	2.94
Turbulence Intensity	0.27	0.30

Table 3.3 presents the wind data return periods using the frequency factor technique as discussed and presented in equations 3.1 to 3.4. The wind direction as presented is the arctan of the ratio of the northward wind to the eastward wind.

TABLE 3.3: Wind Data Return Period using the Frequency Factor Technique as proposed by Chow [109]

Return Periods (years)	K_T	Wind Speed (x_T)		Wind Direction (θ)
		Eastward Wind (m/s)	Northward Wind (m/s)	
5	0.8416	13.05	12.42	43.59°
10	1.2816	14.31	13.72	43.78°
20	1.6449	15.36	14.78	43.91°
50	2.0537	16.53	15.99	44.04°
100	2.3263	17.31	16.79	44.12°
500	2.8782	18.89	18.41	43.25°
1000	3.0902	19.50	19.03	44.30°

Fig. 3.21 and Fig. 3.22 depicts the frequency distribution histogram and probability distribution curve for the eastward and northward winds, respectively. As can be understood from these charts, wind speeds of 10 ms^{-1} to 13 ms^{-1} were discovered to be the most prevalent conditions at a probability of occurrence of approximately 51% for the eastward wind. Whereas, for the northward winds, wind speeds of 8 ms^{-1} to 11 ms^{-1} appeared to be the most prevalent with speed at a total probability of occurrence of approximately 56%.

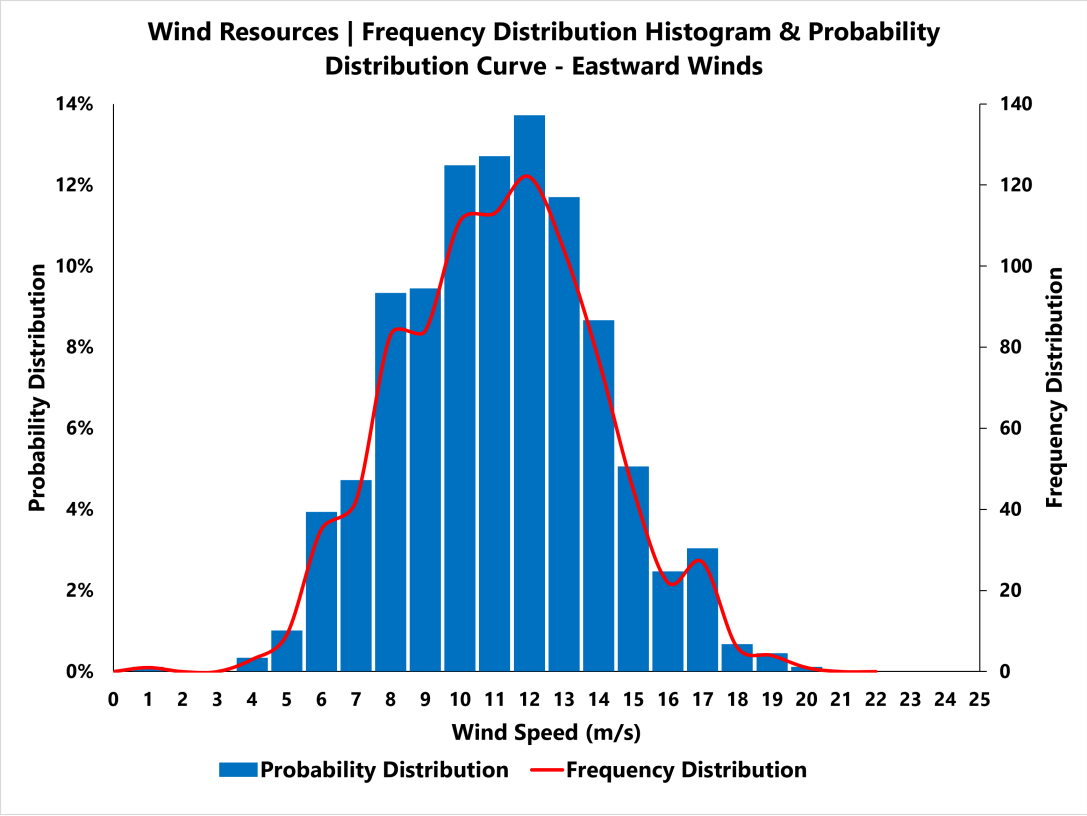

FIGURE 3.21: Probability Distribution Curve and Frequency Distribution Histogram for Eastward Wind Resources.

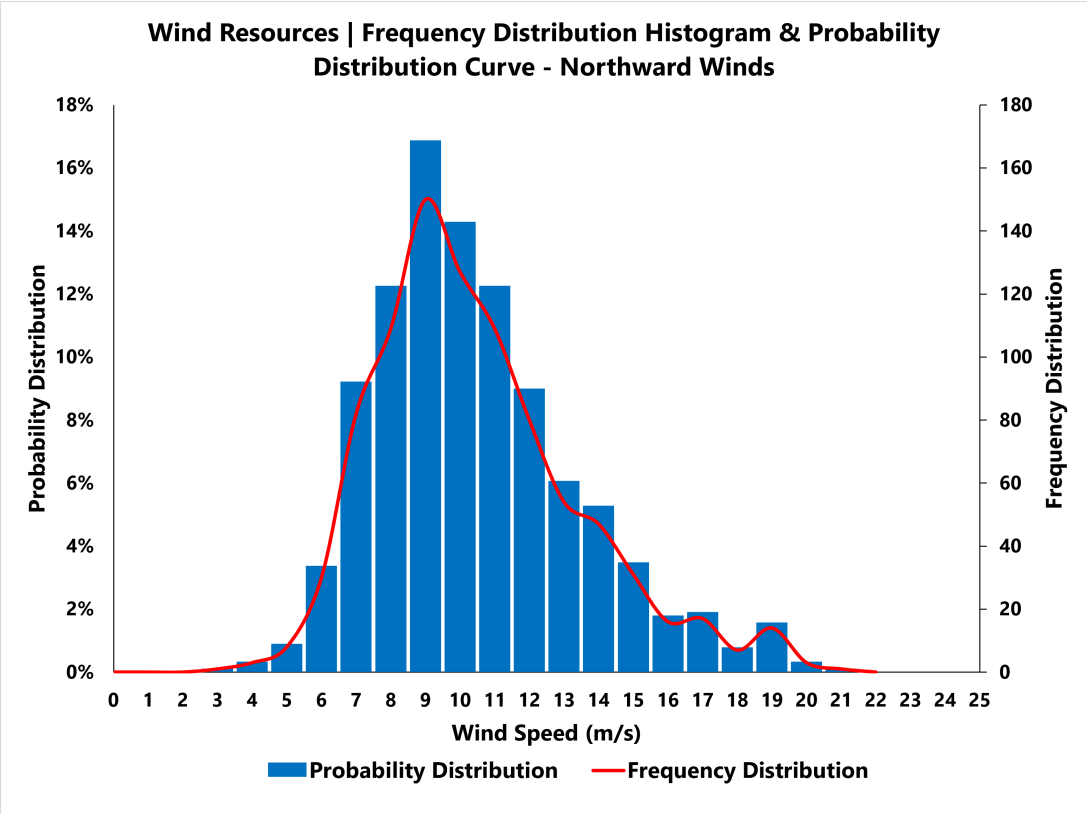

FIGURE 3.22: Probability Distribution Curve and Frequency Distribution Histogram for Northward Wind Resources.

Fig. 3.23 is a frequency distribution histogram for the wind's angle of attack which was calculated as arctan of the ratio of the northward wind to the eastward wind. As can be observed from the chat, the prevalent wind direction is estimated to be between 42° and 43°. Outliers with frequencies less than 2 and probabilities less than 0.5% were ignored.

The quantitative and qualitative statistical analyses that was performed for the wind hindcast data was also performed for the hindcast data obtained for wave and current to produce the desired information needed to complete the numerical simulation. Table 3.4 introduces a summary of the Metocean parameters. Appendix A contains the Matlab code used in pre-processing the MetOcean hindcast data before completing the qualitative and quantitative statistical calculations in excel.

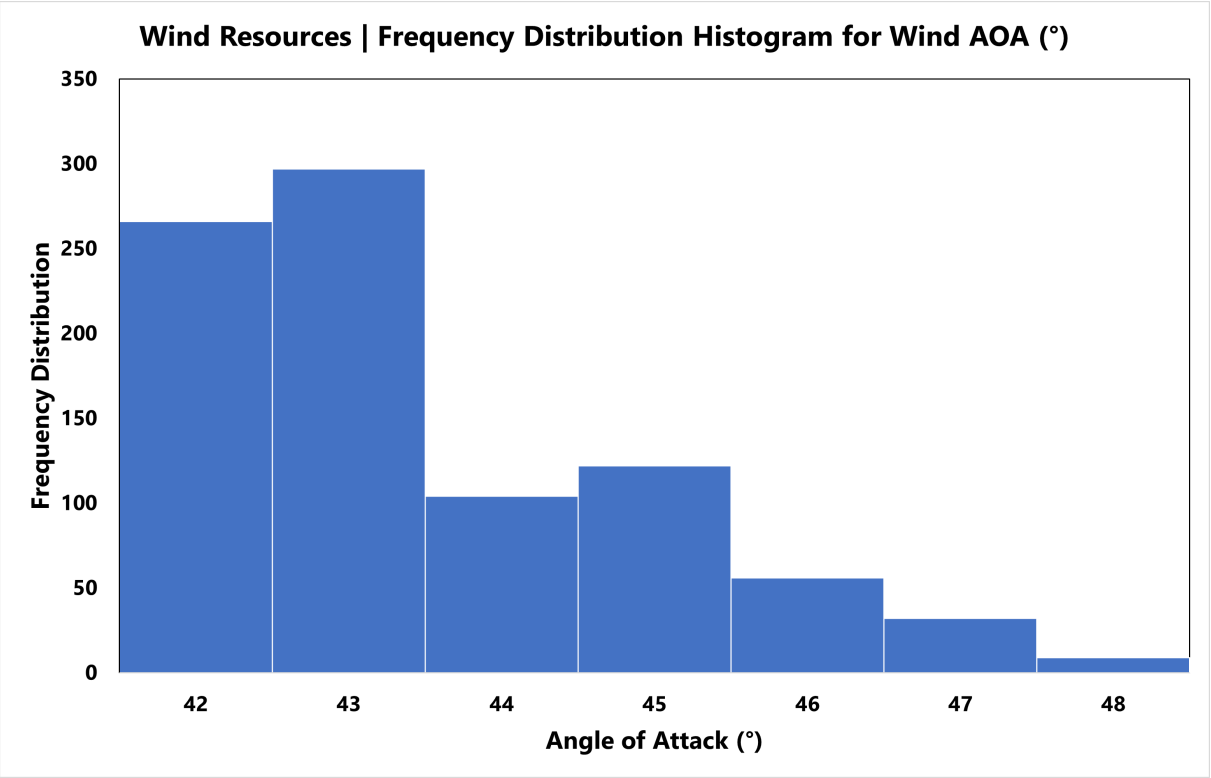

FIGURE 3.23: Frequency Distribution Histogram for Wind Angle of Attack.

TABLE 3.4: Summary of Metocean Data.

Return Period (Yrs.)	WIND		WAVE		CURRENT			
					Maximum Wind Generated Current		Maximum Total Current [Tidal + Wind Generated Current]	
	Wind Speeds @10 m Above MSL (m/s)	Direction	Significant Wave Height (m)	Peak Period (s)	Velocity (m/s)	Direction	Velocity (m/s)	Direction
5	17.52	43°	4.85	17.52	1.40	26°	1.52	23°
10	19.92	43°	5.53	18.99	1.40	26°	1.52	23°
20	22.2	43°	6.18	20.40	1.40	26°	1.52	23°
50	25.21	43°	7.02	22.22	1.40	26°	1.52	23°
100	27.44	43°	7.65	23.59	1.40	26°	1.52	23°
500	32.61	43°	9.11	26.74	1.40	26°	1.52	23°
1000	34.83	43°	9.74	28.10	1.40	26°	1.52	23°

3.2.2 Wave Modelling

Site-specific sea surface elevation spectral densities were computed from acquired wave hindcast data. Since the sea elevation process from hindcast data did not possess any significant swell component, it was found appropriate to represent the spectral density of the sea elevation by the Joint North Sea Wave Observation Project (JONSWAP)

spectrum which is given by [92].

$$S(f) = \frac{ag^2}{(2\pi)^4} f^{-5} e^{\left(-\frac{5}{4}\left(\frac{f}{f_p}\right)^{-4}\right)} \gamma^{e^{\left(-0.5\left(\frac{f-f_p}{\epsilon f_p}\right)^2\right)}} \tag{3.5}$$

where f is the wave frequency and equal to $1/T$. T is defined as the wave period and f_p the spectral peak frequency and equal to $1/T_p$. T_p and g is the peak period and acceleration due to gravity, respectively. a is the generalised Philip's constant which is given by;

$$a = 5 \cdot \left(H_s{}^2 f_p{}^4 / g^2\right) \cdot (1 - 0.287 ln\gamma) \cdot \pi^4 \tag{3.6}$$

H_s is the significant wave height. ϵ is defined as the spectral width parameter which is equal to 0.07 for $f < f_p$ and 0.09 for $f > f_p$. γ is known as the peak enhancement factor which is a function of H_s and T_p and is defined as;

$$\begin{cases} 5 & for\ \frac{T_p}{\sqrt{H_s}} \leq 3.6 \\ e^{\left(5.75 - 1.15\frac{T_p}{\sqrt{H_s}}\right)} & for\ 3.6 < \frac{T_p}{\sqrt{H_s}} \leq 5 \\ 1 & for\ 5 < \frac{T_p}{\sqrt{H_s}} \end{cases} \tag{3.7}$$

The JONSWAP spectrum is based on the notion that a wave spectrum is never fully developed and that it continues to develop through non-linear, wave-wave interactions for over a long period of time and long distances. The peak enhancement factor as presented in equation 3.7 is an artificial factor added to the Pierson-Moskowitz spectrum to improve the fit for a partially developed wave spectrum. Thus, the JONSWAP spectrum is a Pierson-Moskowitz spectrum multiplied by the peak enhancement factor γ. When $\gamma = 1$, the JONSWAP spectrum reduces to the Pierson-Moskowitz spectrum. Observing the Metocean wave data presented in Table 3.4 and computing the peak enhancement factor conditions defined in equation 3.6, it can be noted that the waves for the site under investigation are fully developed because $5 < \frac{T_p}{\sqrt{H_s}}$ which results to a peak enhancement factor equal to 1 and ultimately reducing the JONSWAP spectrum to the Pierson-Moskowitz spectrum. However, for the design of FOWTs, it is a recommended practice to assume a none-fully developed wave spectrum to make a conservative design. A peak enhancement factor of 3.3 is usually adopted to represent a typically developed wind sea [110]. Thus, a peak enhancement factor of 3.3 is used in

calculating the wave energy spectrum for the sea state under study. The zero-crossing period T_z depends on the peak period T_p through the following relationship;

$$T_z = T_p \sqrt{\frac{5+\gamma}{11+\gamma}} \tag{3.8}$$

Fig. 3.24 shows a plot of the wave energy spectral density using the JONSWAP spectrum and a peak enhancement factor of 3.3 for various return periods.

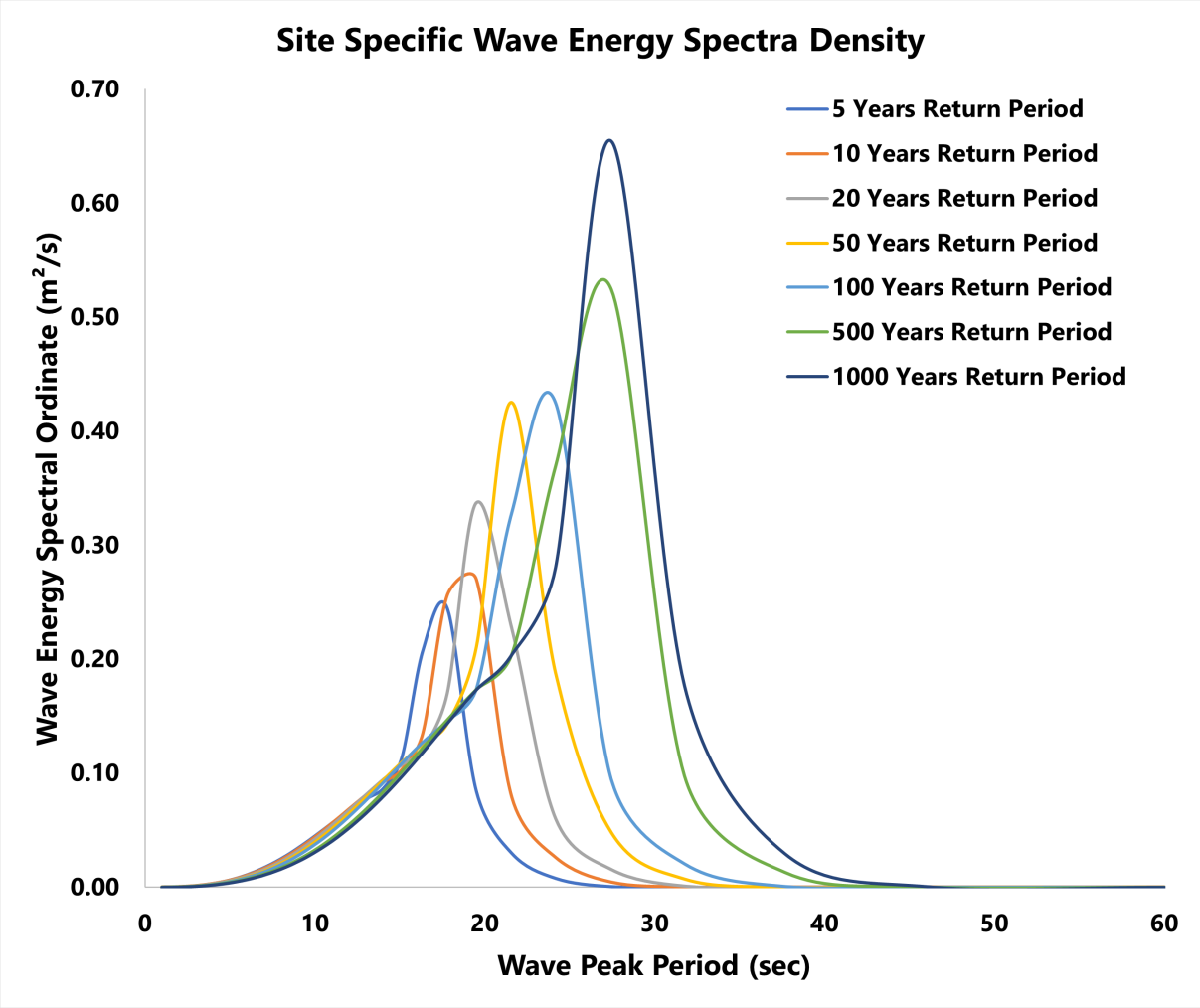

FIGURE 3.24: Plot of Wave Period vs JONSWAP Wave Energy Spectra Ordinate for 5 to 1000 Years Return Period.

3.2.3 Wind Modelling

Wind loading is a vital component in the prediction of global motion response of FOWTs. Consequently, accurate modelling of wind loads, and load effects is essential because wind loads can sometimes be the dominating excitation force for some floating platform concepts. Steady wind force $\bar{q}_{wind}$, on the assemblage of the wind turbine above the MSL can be calculated using this expression;

$$\bar{q}_{wind} = \rho_{air} c_w(\alpha) L^2 U_w^2 \tag{3.9}$$

where ρ_{air}, U_w, L, and α have their usual meaning. As several studies have shown, aerodynamics dominates the power performance of a FOWT rotor. However, the loads on a FOWT are driven by the floating platform displacement [23], [26]. For FOWTs, the wind speed increases with increase in elevation above the mean sea level. Thus, the aerodynamic analysis for the investigation of thrust force is with reference to the 10-minute mean speed at the hub height of the wind turbine rotor. The relationship between the hub height and the wind speed as referenced in DNV-OS-J101 (Design of Offshore Wind Turbine Structures) is governed by this equation [92];

$$v(T,z) = v_{10}\left(1 + 0.137 ln\frac{z}{h} - 0.047 ln\frac{t}{t_{10}}\right) \tag{3.10}$$

where $h = 10\ m$, $t_{10} = 10\ minutes$, t is the averaging period and z is the height above sea level. The expression in equation 3.10 converts mean wind speeds between different averaging periods for a specified reference height. In operating mode, the hub height of the wind turbine under investigation is 100.85 m. Thus, a reference height of 100.85 m was used to obtain the wind speed at the hub height for the investigation of aerodynamic forces on the rotor. As discussed in section 3.2.2, the wave climate is represented by H_s and T_p. Stationary wave conditions with constant H_s and T_p are assumed to prevail over a 3-hour or 6-hour period [48], [92]. Since the current study is combining wind data and wave data in the time domain coupled dynamics simulation, the 10-minutes mean wind speed has to be converted to the same reference period of the wave data. Consequently, by computing the mathematical model in equation 3.10, the site wind velocity gradient for various return periods for an averaging period of 10 minutes and reference duration of 3 hours are presented in Fig. 3.25 and Fig. 3.26,

respectively.

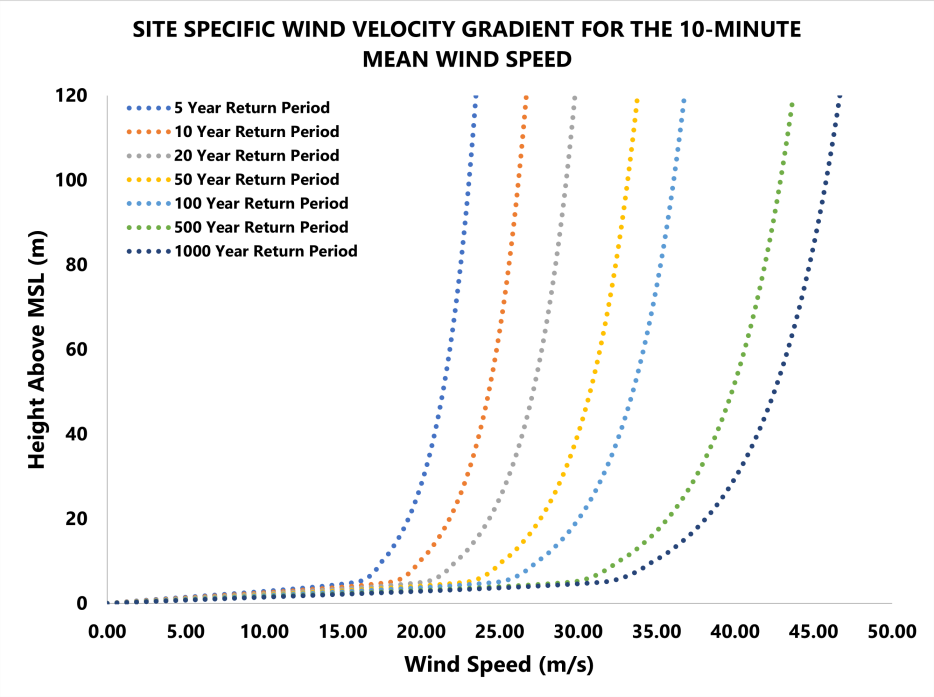

FIGURE 3.25: Site wind Velocity gradient for various return periods for an averaging period of 10 Minutes.

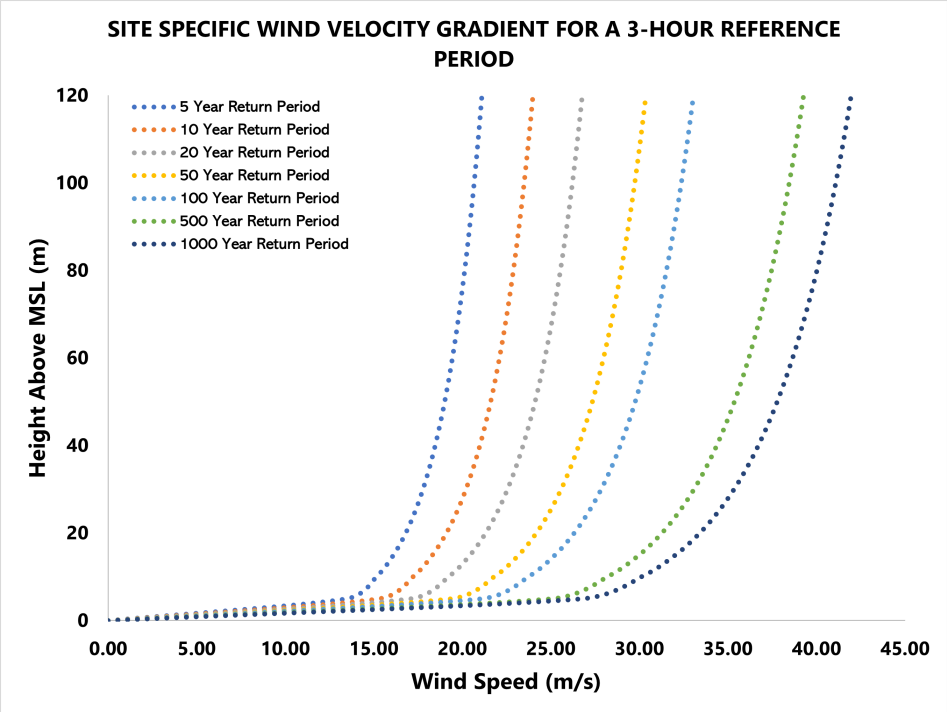

FIGURE 3.26: Site wind velocity gradient for various return periods for a reference period of 3 hours.

Furthermore, the wind spectrum models previously highlighted in equations 2.45 to 2.53 were used to describe the short-term wind conditions for the site under study, i.e., the power spectral density curves of the wind speed. The selection of an appropriate wind power spectral density model for the design of a FOWT is key to ensuring that the model is valid for wind over water in addition to providing a good representation in the high and low-frequency range. More importantly, when a substantial amount of wind energy exists in a frequency range close to the FOWT's natural response frequency, the dynamic effect of turbulent winds on the FOWT's aerodynamic response can become a challenging operational problem. The wind spectrum ordinate for the intended offshore site was calculated from the publication by M.K. Ochi & Y.S. Shin [46]. The Ochi & Shin spectrum provide an adequate representation of wind power spectral density in the low-frequency range and gust events. It has more energy content in the low-frequency range ($f < 0.01\ Hz$) than the Davenport [42], Kaimal[44], and Harris[43] spectra which are models designed to represent wind over land while the Ochi & Shin Spectrum is developed from measured spectra over seaway (DNV-RP-C205)[47]. Fig. 3.27 shows a plot comparison of frequency against wind spectral energy density (100-year return period) for the intended site for Ochi & Shin, Kaimal, Davenport, and Harris winds spectral model.

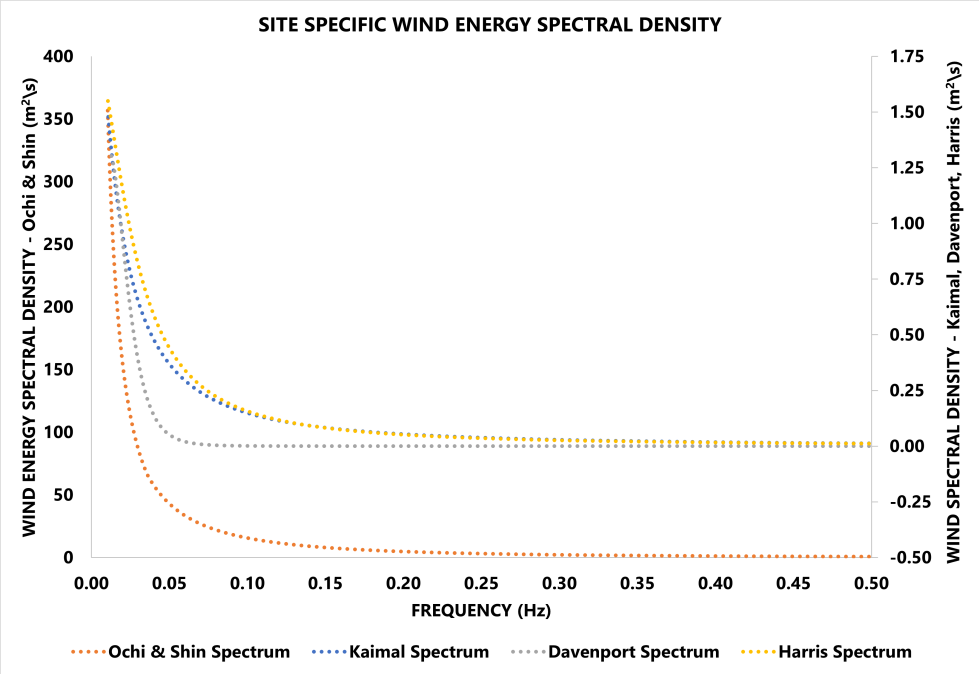

FIGURE 3.27: Plot of Frequency Vs Wind Energy Spectrum for 100 Year Wind Return Period.

As can be seen from the plot, there is more energy content in the low frequency for the Ochi & Shin model when compared with other wind energy spectral models.

3.2.4 Ocean Current Modelling

The current load calculation is challenging due to its strong dependence on local topographic conditions and unpredictability in magnitude and direction with depth. Currents may induce Vortex Induced Motion (VIM) and/or Vortex Induced Vibration (VIV) on slender members of a floating platform. Steady current yields steady force in the horizontal plane and rotational moment in the vertical plane. Floating platforms having many slender structures can also experience current loading as a dominating contributor to the total steady force. The strip theory approximation can be used to calculate viscous current forces on floating platforms that are made up of slender structural parts (mooring, braces, columns).

Current velocity is decomposed into two components, one in the crossflow direction and another in the longitudinal direction. Current velocities in the longitudinal direction cause shear forces while the current in the crossflow direction is responsible for flow separation arising from high flow Reynolds number and the source of inline drag force. Current shear forces are negligible. Hindcast data for sea surface current velocities (wind-generated and tidal) were available for the project site. However, a variation of current velocity with depth was not available and thus computed using the following equation as referenced in [76];

$$U_c\left(z\right) = U_{tide}\left(z\right) + U_{wind}\left(z\right) \tag{3.11}$$

where

$$U_{tide}\left(z\right) = U_{tide0}\left(\frac{d+z}{d}\right)^{1/7} \tag{3.12}$$

for $z \leq 0$

and

$$U_{wind}\left(z\right) = U_{wind0}\left(\frac{d_0+z}{d_0}\right) \tag{3.13}$$

where $U_c\left(z\right)$ is defined as the total current velocity at level z, while z is the vertical

coordinate from MSL, positive upwards. U_{tide0} and U_{wind0} are tidal current and wind-generated current at MSL, respectively. d and d_0 are water depth from MSL taken as positive and reference depth for wind-generated current, respectively. For wind-generated currents, $d_0 = 50\ m$ as per [76]. Fig. 3.28 shows a graphical representation of the current depth velocity profile for the project site. As can be observed from the plot, the wind-generated current decays with increasing water depth whereas tidal generated current advances with increasing water depth although the wind-generated current is the dominating condition.

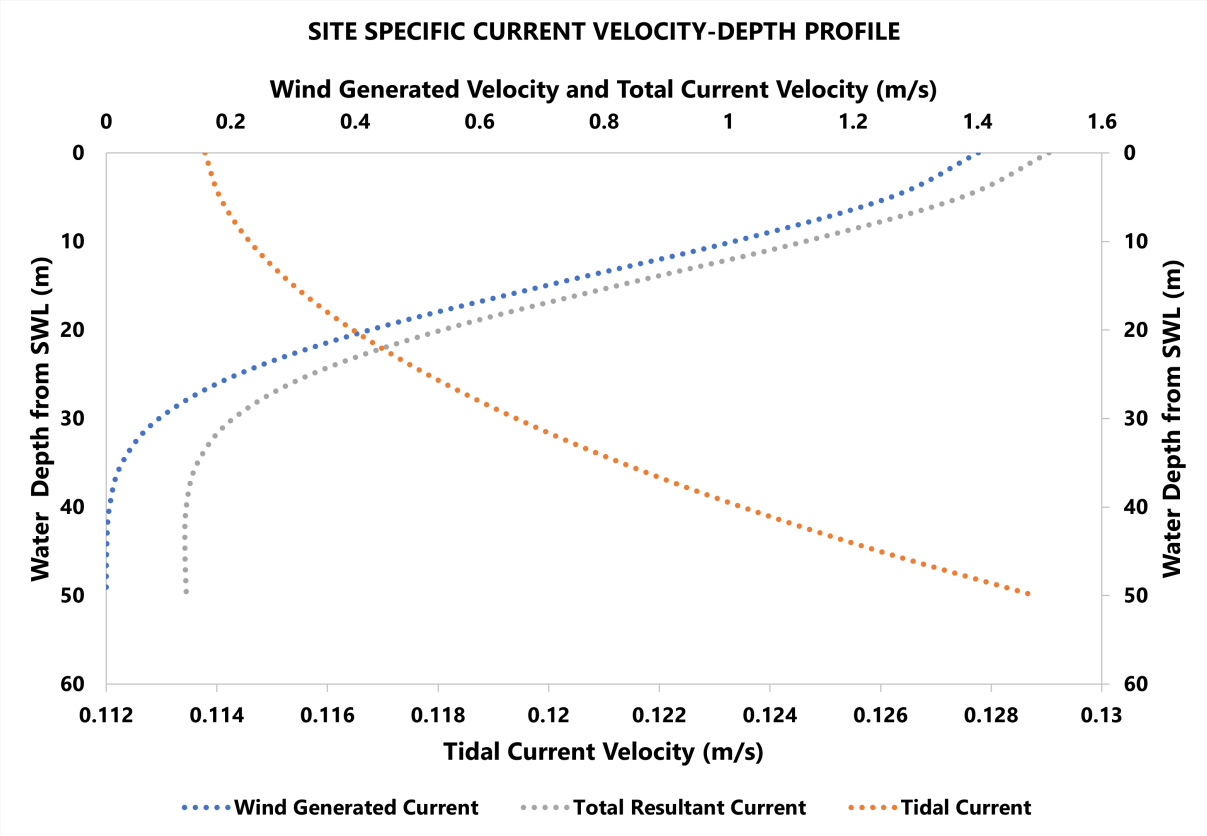

FIGURE 3.28: Site-specific Current Velocity Depth Profile.

3.2.5 Design Load Cases (DLCs)

By fusing the various environmental conditions and load components, the load combinations to be considered in the overall coupled dynamic motion analyses of the FOWT are specified. The environmental design conditions in terms of values for the; significant wave height, wave peak period, 10 minutes mean wind speed at hub height, 3 hours reference period wind speed at hub height, and ocean current velocity for various platform conditions and sea states are defined based on the statistical analyses performed for the site-specific long term hindcast data. Table 3.5 shows the Design Load Cases (DLCs) based on the DNV offshore standard (DNV-OS-J101) [76], [92]. The water depth considered is 300 m.

TABLE 3.5: Design Load Cases for Various Operating Conditions

FOWT Design Situation	Turbine Condition	DNV DLC	Wind Condition @ Hub		Wave Condition		Wave-Wind Directionality	Sea Current
			10 Min	180 Min	H_s	T_p		
Operating	Power Production	1.3	11.40 m/s	11.40 m/s	4.85 m	17.52 s	COD, UNI	1.52 m/s
		1.6	23.04 m/s	20.66 m/s	4.85 m	17.52 s		1.52 m/s
Extreme	Parked	6.1a	33.16 m/s	29.73 m/s	7.02 m	22.22 s	MIS, MUL	1.52 m/s
Survival		SLC	36.10 m/s	32.37 m/s	7.65 m	23.59 s		1.52 m/s

With regard to Table 3.5 above;

- DLC 1.3 relates to the rated turbine wind speed of 11.4 m/s and the corresponding oceanographic conditions for a 5-year return period.
- DLC 1.6 relates to the prevailing Metocean conditions for a 5-year return period.
- COD, UNI means that wave–wind directionality is co-directional in one Direction (Unidirectional).
- MIS, MUL means that wave–wind directionality is misaligned in multiple direction.
- DLC 6.1a is for the extreme environmental condition which relates to a 50-year return period.
- The Survival Load Case (SLC) DLC relates to a 100-year return period.

Chapter 4

The TRIgon Hybrid Floater (TRIHF) FOWT Concept Design

In this Chapter, the newly developed floating platform model (TRIHF) which is inspired by the hybridisation of the generic floating platform concepts (TLP, Spar, Semi-submersible) is introduced. Also, the detailed three-dimensional (3D) Computer-Aided Design (CAD) model of the National Renewable Energy Laboratory five mega-watts (NREL - 5MW) wind turbine baseline adopted for the coupled dynamics modelling is defined. The precise mass calculations of the FOWT assembly (TRIHF + NREL 5 MW) and station keeping configuration are discussed. More interestingly, a novel approach for graphically characterising the floater boundary conditions for FOWTs is established.

4.1 Wind Turbine Baseline

The provision of floating support for offshore wind turbines is capital intensive. Consequently, for a deep-water wind turbine project to be economically viable, the proposed wind turbine unit needs to have a considerable rated capacity that will justify the goal of the investment. A 5 MW wind turbine has good precedence regarding performing feasibility studies and executing pilot projects for offshore wind farms in addition to being a typical utility-scale for onshore and offshore wind turbine projects[111], [112].

To support one of the goals of this research which is aimed at assessing the global performance of a FOWT technology, a representative utility-scale multimegawatt turbine known as the 'NREL offshore 5-MW baseline wind turbine' is implemented. The theoretical National Renewable Energy Laboratory (NREL) offshore 5 MW baseline wind turbine rotor which is employed for this research is a conventional three-bladed

upwind turbine established to support conceptual studies for the offshore wind energy industry and is based on the specifications of the commercially available information on the Multibird 5000 and REPower 5M prototype wind turbine generator (WTG) systems [113], [114].

4.1.1 Blade Structural and Aerodynamic Properties

The blade aerodynamic properties of the wind turbine rotor are based on the publicly available information on the Dutch Offshore Wind Energy Converter (DOWEC) project [113]. The aerodynamic blade properties are composed of 5 Delft University (DU) aerofoil and 1 National Advisory Committee for Aeronautics (NACA) aerofoil. To adequately represent the large structural gradients at the blade's root and large aerodynamic gradients at the blade's tip, 3 inboard elements (cylinders) and 3 outboard elements (aerofoils) were geometricized to occupy two-thirds the size of the 11 equally spaced midspan elements. Table 4.1 highlights the aerofoil distribution and aerodynamic properties at the blade nodes which are situated at the centre of the blade elements[27].

TABLE 4.1: NREL 5 MW Baseline Wind Turbine Distributed Blade Aerodynamic Properties.

Distributed Blade Properties					
Node No	Blade Node Location (m)	Aerofoil Twist (°)	Element Length (m)	Aerofoil Chord Length (m)	Profile Type
1	2.8667	13.308	2.7333	3.542	Cylinder 1 (Root)
2	5.6000	13.308	2.7333	3.854	Cylinder 2
3	8.3333	13.308	2.7333	4.167	Cylinder 3
4	11.7500	13.308	4.1000	4.557	DU40
5	15.8500	11.480	4.1000	4.652	DU35
6	19.9500	10.162	4.1000	4.458	DU35
7	24.0500	9.011	4.1000	4.249	DU30
8	28.1500	7.795	4.1000	4.007	DU25
9	32.2500	6.544	4.1000	3.748	DU25
10	36.3500	5.361	4.1000	3.502	DU21
11	40.4500	4.188	4.1000	3.256	DU21
12	44.5500	3.125	4.1000	3.010	NACA64
13	48.6500	2.319	4.1000	2.764	NACA64
14	52.7500	1.526	4.1000	2.518	NACA64
15	56.1667	0.863	2.7333	2.313	NACA64
16	58.900	0.370	2.7333	2.086	NACA64
17	61.6333	0.106	2.7333	1.419	NACA64

The blade node locations are directed along the blade-pitch axis (one-quarter of the chord length for each aerofoil sections of the blade) from the rotor centre to the blade cross-sections. As can be observed from Table 4.1, perfect cylinders of different

diameters are used to define the geometry for the first 3 portions of the blade (up to 8.33 m in length) and then smoothly blended into the equally spanned DU aerofoil series (up to 40.45 m). At 44.55 m away from the rotor root, the NACA series is used to fully define the shape of the blade up to its tip, resulting in a total blade length of 61.63 m. The non-dimensional chord length and shape of the aerofoil types used in creating the geometry are presented in Fig. 4.1.

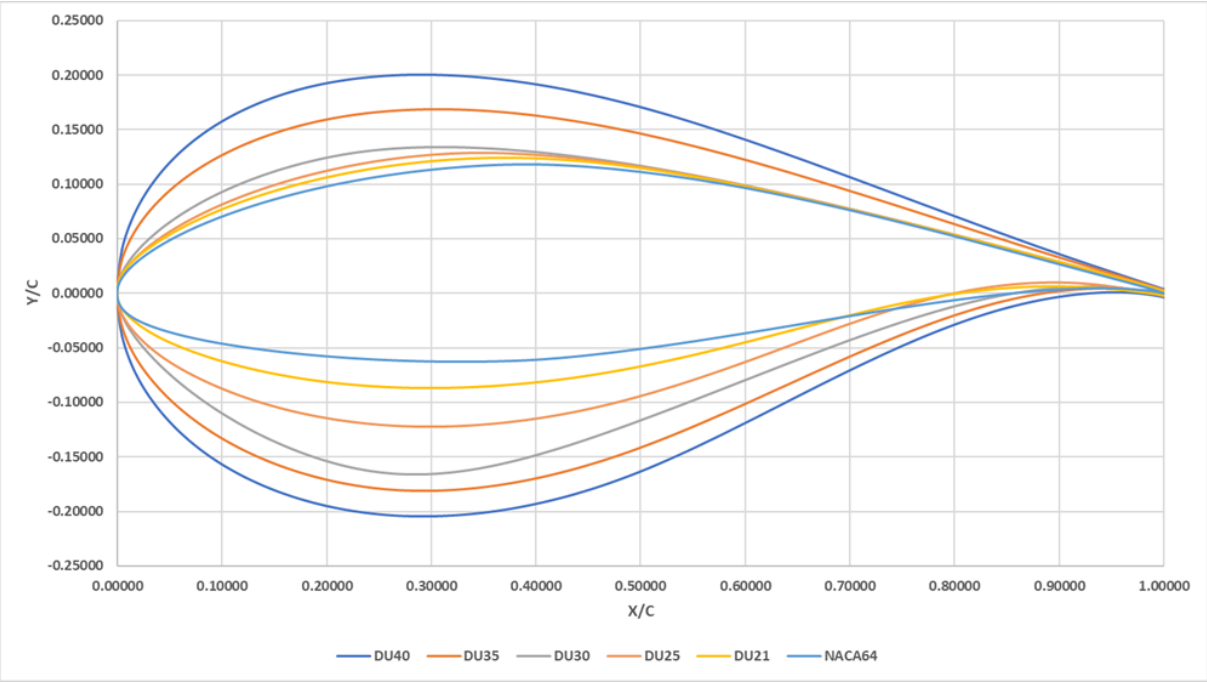

FIGURE 4.1: Aerofoil used in creating the NREL 5 MW Wind Turbine Rotor Blade.

First, the non-dimensional aerofoil chord length data for each of the blade's section were obtained from an online aerofoil database [114], [115]. As can be observed from Fig. 4.1, the non-dimensional data for x and y coordinate of the aerofoil is usually expressed as a ratio of the chord length. Each aerofoil coordinates were converted to the desired chord length by multiplying x/c and y/c with its corresponding chord lengths for each aerofoil section as shown on the fifth column of Table 4.1 and then exported as splines to the CAD software for processing.

Creation of 3D geometry for the wind turbine blade was performed using Solidworks CAD package due to author's knowledge with the program, in addition to being the most efficient way of managing the creation of the blade geometry before exporting to the CFD simulation toolkit. To facilitate optimum flexibility and computational efficiency during numerical simulation, the blade geometry was created as a

lofted surface which has the same likeness in building shell elements. Essentially, each of the blade section was generated by pasting each aerofoil element on a plane placed at the appropriate distance from the rotor root (blade node location shown in column 2 of Table 4.1). Fig. 4.2 illustrates the aerofoils that make up the blade sections where each plane has been labelled using the convention **Aerofoil Series_Chord Length**.

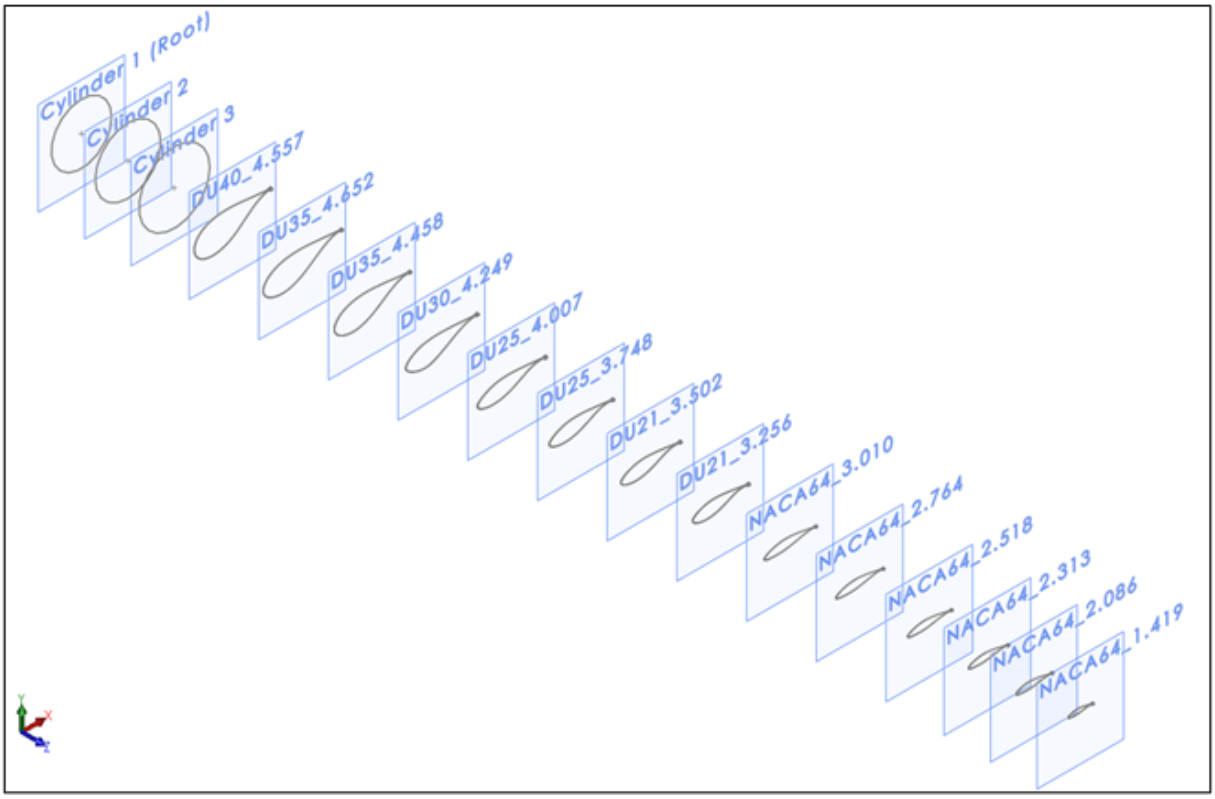

FIGURE 4.2: Full Aerofoil Section for the NREL 5 MW Wind Turbine Rotor Blade.

The aerodynamic properties of the rotor presented in column 3 of Table 4.1 show that the root of the blade is generally more twisted than the tip of the blade. To capture this twist, the aerofoil on each section of the blade was rotated about the aerodynamic centre (pitch-moment) by the desired angle after creating each aerofoil on their respective planes. Fig. 4.3 indicates the side view of the blade section with the aerofoils twisted about its aerodynamic centre.

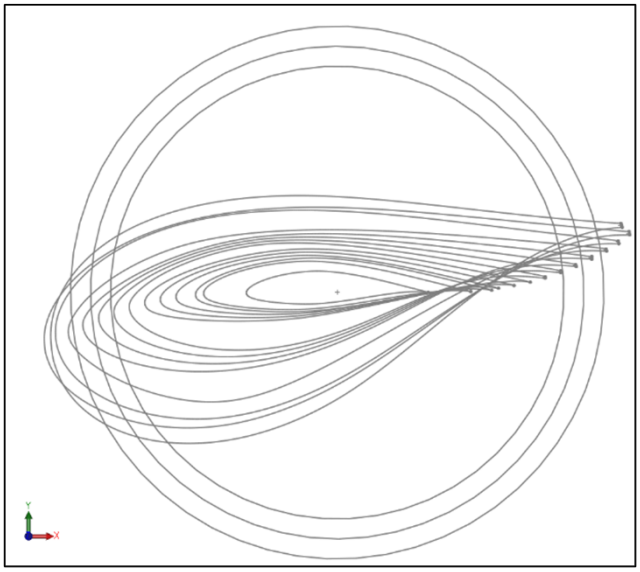

FIGURE 4.3: Side view of blade showing Aerofoil twisted about their Aerodynamic Center.

On completion of creating the aerofoil according to the desired specifications presented in Table 4.1, a surface loft command was performed to generate the entire blade surface. Fig. 4.4 and Fig. 4.5 below shows the finalised blade geometry.

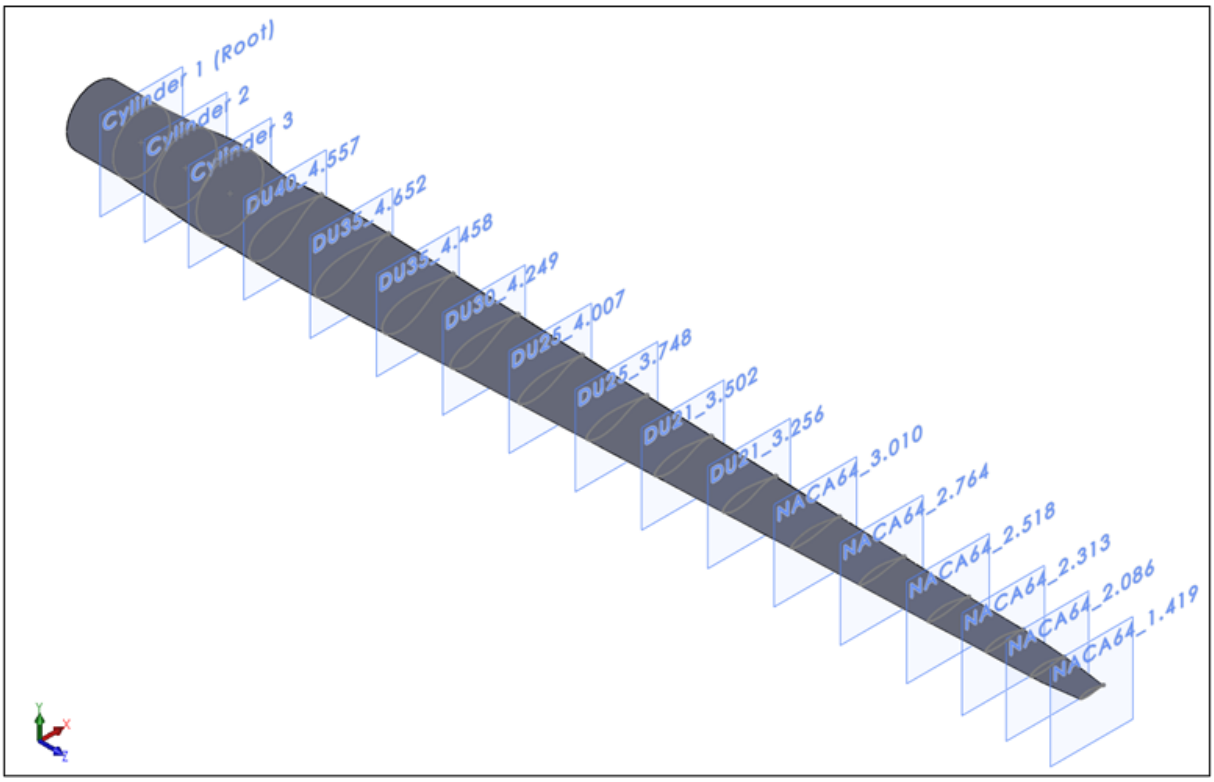

FIGURE 4.4: Completed Loft Surface for Blade Geometry (Label: **Aerofoil Series_Chord Length**).

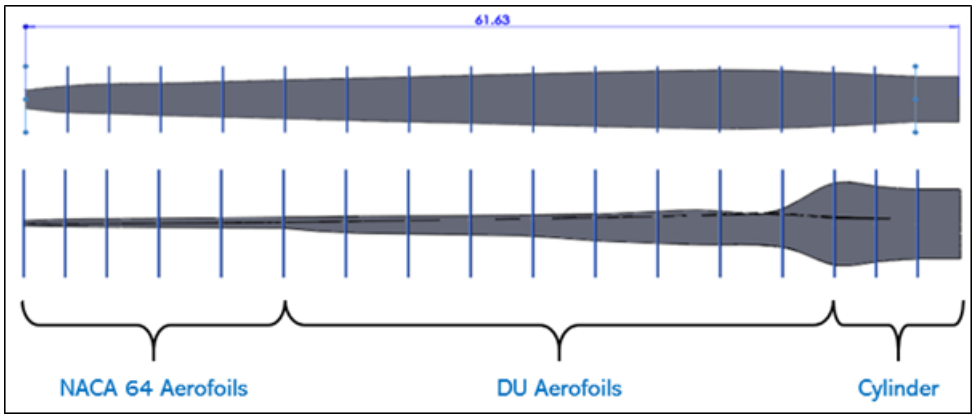

FIGURE 4.5: Top and Front view of the Completed Loft Surface for Blade Geometry.

The overall integrated mass of the blade is 17,740 kg. For each blade, the nominal radial Center of Mass (CM) location, nominal first mass moment of inertia, and the nominal second mass moment of inertia is 20.475 m, 363,231 $kg.m$, and 11,776,047 $kg.m^2$ with respect to the blade of the root, respectively [27].

4.1.2 Rotor-Nacelle Assembly (RNA) Structural Properties

There is no adequate information available in prior literature regarding the exact geometry of the rotor hub for the NREL 5 MW wind turbine. Thus, a typical hub geometry was developed to facilitate a complete rotor assemblage. The hub shape and dimension have a negligible influence on the aerodynamic properties of the rotor due to its relatively small area (around 125 m^2) when compared to the whole projection and total swept area of the rotor assembly (approximately 12,500 m^2). Fig. 4.6 shows the created hub geometry and complete assemblage of the wind turbine rotor. The hub of the rotor is located 5 m upwind of the tower centre line and at an elevation of 9m above the base of the tower when the wind turbine assemblage is undeflected. The mass of the hub is specified to be 56,780 kg [27] with its CM located at the centre of its geometry. Consequently, the total mass of the rotor (i.e. the mass of 3 blades and the hub) is 110,000 kg. Just like the hub, there is also no adequate information available in prior literature regarding the exact geometry of the nacelle for the NREL 5 MW wind turbine. Hence, new geometry for the nacelle was developed based on the author's investigation of recent WTG models available in the industry. Fig. 4.7 illustrates the nacelle CAD model geometry established for this research [27]. The drive train properties of the NREL 5

MW baseline wind turbine will not be discussed because it is beyond the scope and of no significance to the goals of this research. However, it is worth mentioning that the rated generator speed and gearbox ratio were specified as 1173.7 RPM and 97:1, respectively [27].

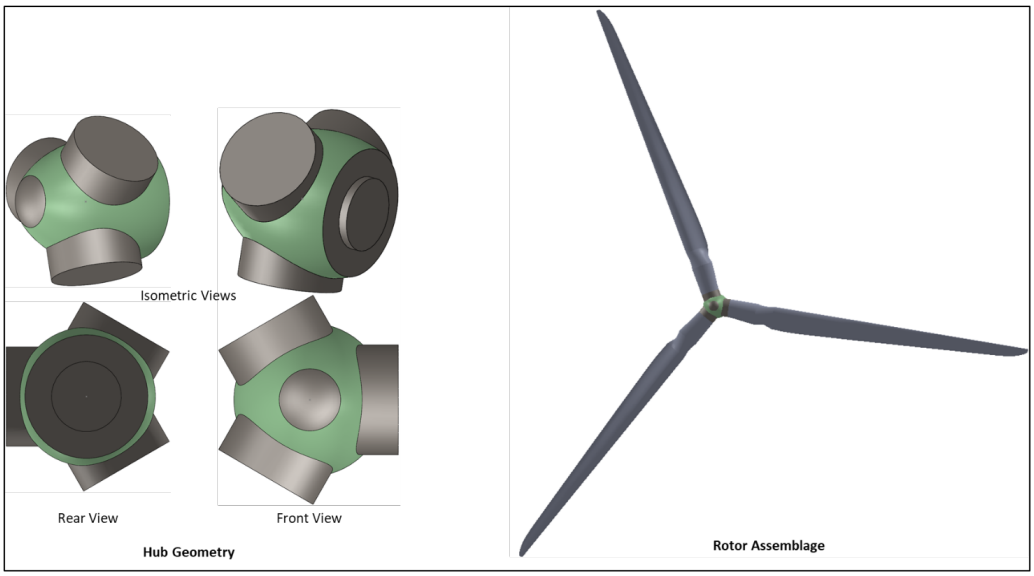

FIGURE 4.6: Left: Hub Geometry. Right: Complete Rotor Assemblage with Hub and Blades.

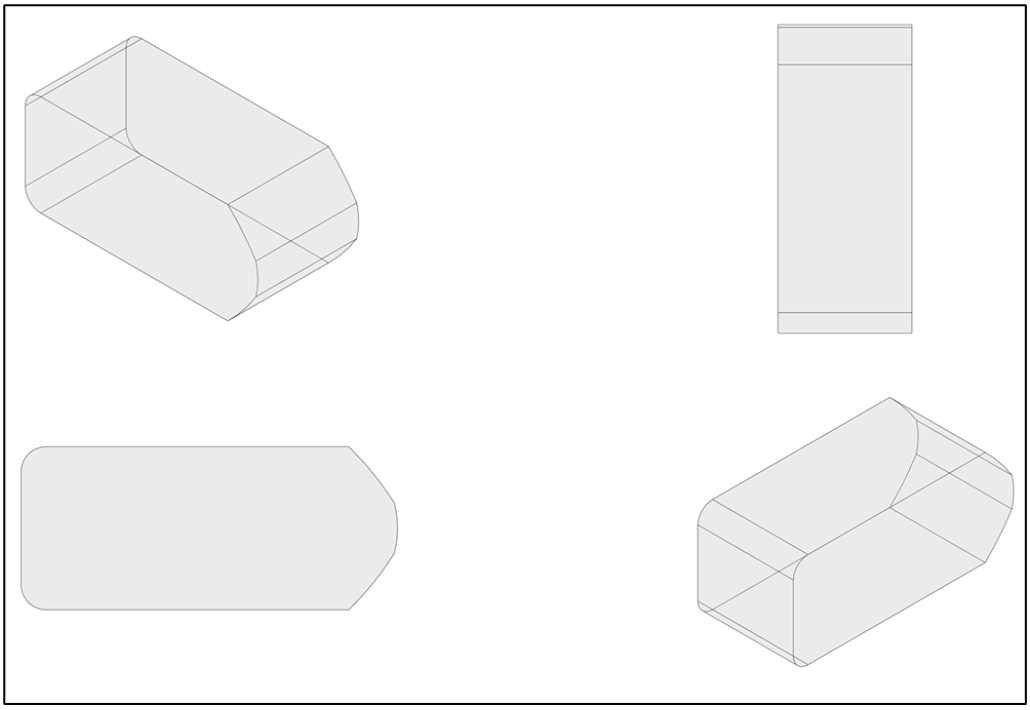

FIGURE 4.7: Nacelle CAD model geometry.

4.1.3 Tower Structural Properties

The properties of the tower for a wind turbine assembly depend principally on the type of offshore foundation structure used to provide support for the RNA. In the same vein, the type of offshore support structure is determined by the installation location whose properties vary significantly through differences in Metocean conditions of the offshore location. This section documents the structural properties for the equivalent offshore-based version of the NREL 5-MW baseline wind turbine.

The distributed properties of the offshore-based tower for the NREL 5-MW baseline wind turbine is built on a base diameter of 6 m and thickness of 0.027 m, and top diameter of 3.87 m and thickness of 0.019 m. The radius and thickness of the tower are linearly tapered from the tower base to tower top. The tower is assumed to be made of steel and its effective mechanical properties were taken to be $210GPa$ and $80.8GPa$ for its Young's modulus and shear modulus, respectively. The effective density of steel was taken to be $8,500kg/m^3$ which is above the typical value of $7,850\ kg/m^3$ to account for welds, flanges, bolts, and marine corrosion resistance paint that are not accounted for in the tower thickness profile. The overall tower height is 87.6 m, resulting in an integrated total mass of $347,460\ kg$ [27]. Fig. 4.8 shows the geometry representation of the tower.

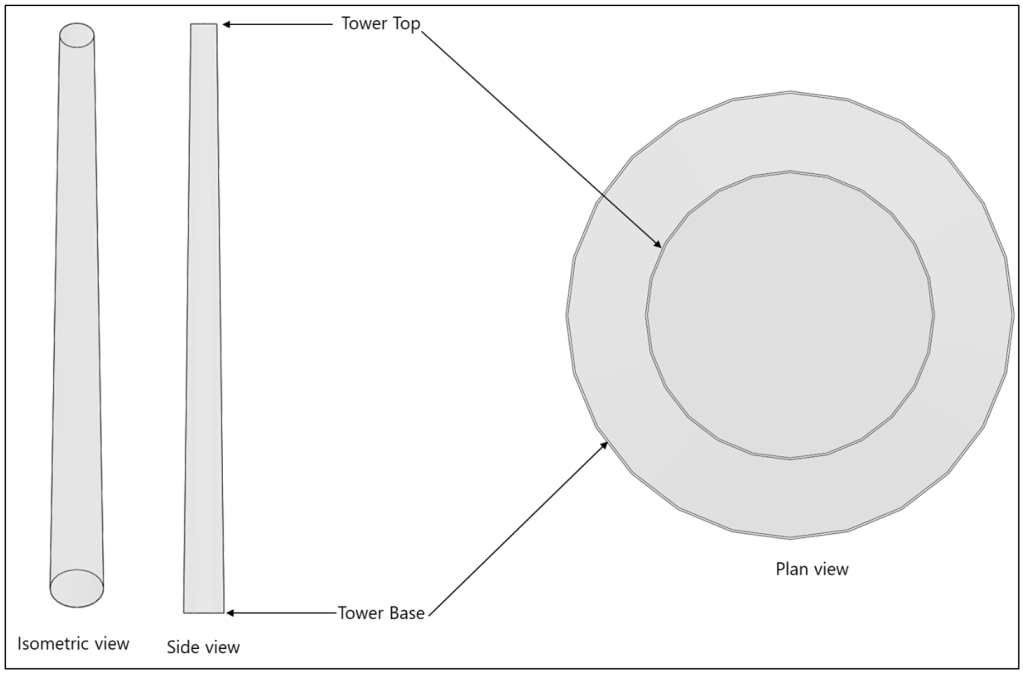

FIGURE 4.8: Tower CAD model geometry.

4.1.4 Wind Turbine Assemblage Gross Properties

To support the goal of this research which is aimed at assessing the global performance of a FOWT under extreme aerodynamic and hydrodynamic loading, this section presents the gross properties of the wind turbine assemblage. The gross properties and geometry of the NREL 5 MW baseline wind turbine assemblage are shown in Table 4.2 and Fig. 4.9, respectively.

TABLE 4.2: NREL 5 MW Baseline Wind Turbine Assemblage- Gross Properties [27].

NREL 5 MW Baseline Wind Turbine Assemblage Gross Properties	
Power Rating	5 MW
Rotor Diameter (D_{Rotor})	126 m
Cut-in Wind Speed	3 m/s
Rated Wind Speed	11.4 m/s
Cut-out Wind Speed	25 m/s
Cut-in Rotor Speed	6.9 rpm
Rated Rotor Speed	12.1 rpm
Rated Tip Speed	80 m/s
Tip Speed Ratio (TSR) @ Peak Power	7.55
Hub Height (H_{Hub})	90 m
Rotor Orientation, Configuration	Upwind, 3 Blades
Drive Train	High Speed, multiple-stage Gear Box
Hub Diameter (D_{Hub})	3 m
Tower Height (H_{Tower})	87.6 m
Rotor Mass	110,000 kg
Nacelle Mass	240,000 kg
Tower Mass	347,460 kg

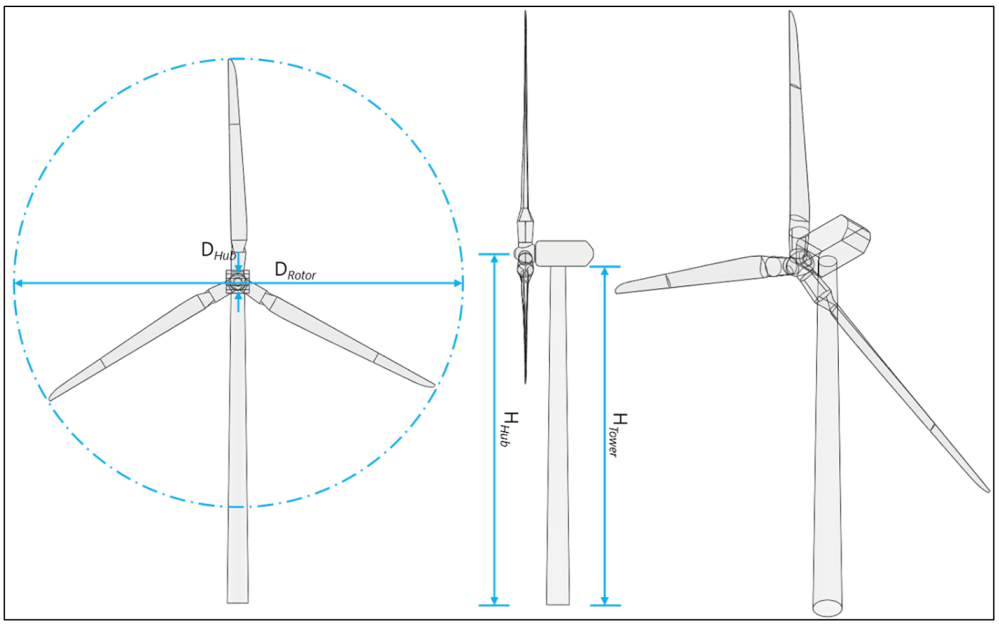

FIGURE 4.9: The NREL 5 MW wind turbine baseline assemblage CAD model.

In the next section, the focus will be on the introduction of the concepts and relevant factors that determine how the stability of a floating marine structure can be increased or adjusted. Also, some key theories will be discussed to illustrate the important aspects of stability as it relates to FOWTs.

4.2 Hybrid Floating Platform Concept Design

There has been a significant increase in the rate at which literature relating to offshore wind energy generation is delivered due to the diversion of research efforts to emerging areas of clean energy. Several papers [116]–[123] have presented specific areas of research around floating offshore structure design for wind energy. In addition to the environmental scoping assessment discussed in section 3.1, some of the key engineering challenges identified in these studies for FOWTs are associated with site surveys (geophysical and geotechnical) in offshore deepwater locations with severe environmental conditions, mooring and anchor system complexity/cost, mooring system footprint, platform compatibility with a broad range of water depths, ballast system and buoyancy tank complexity/cost, inshore assembling and onsite installation ease, in-service maintainability and decommissioning, and sensitivity to hydrodynamic load. These investigations have broadly grouped these floating offshore structures into three main categories based on their source of stability (Fig. 4.10);

- Spar-buoy: ballast stabilised resulting in a low centre of gravity.
- Tension Leg Platform (TLP): mooring line stabilised.
- Semi-submersible: buoyancy and/or water plane stabilised.

Advancements in wind renewable energy technology have followed the logical and conventional route, i.e. land-based foundation to offshore fixed-bottom support to floating platform support. As discussed in Chapter 1, current fixed-bottom technology has seen limited deployment to water depth exceeding 60 m. Consequently, it is generally acceptable to deploy floating platform technology for water depths exceeding 60 m. Although economics is the key element for the choice of a floating platform concept, other aspects such as seabed conditions can play an equally important role. Nevertheless, a remarkable consideration is that floating platforms enhance the flexibility

for site selection and lessen the cost dependence on the water depth of the installation site.

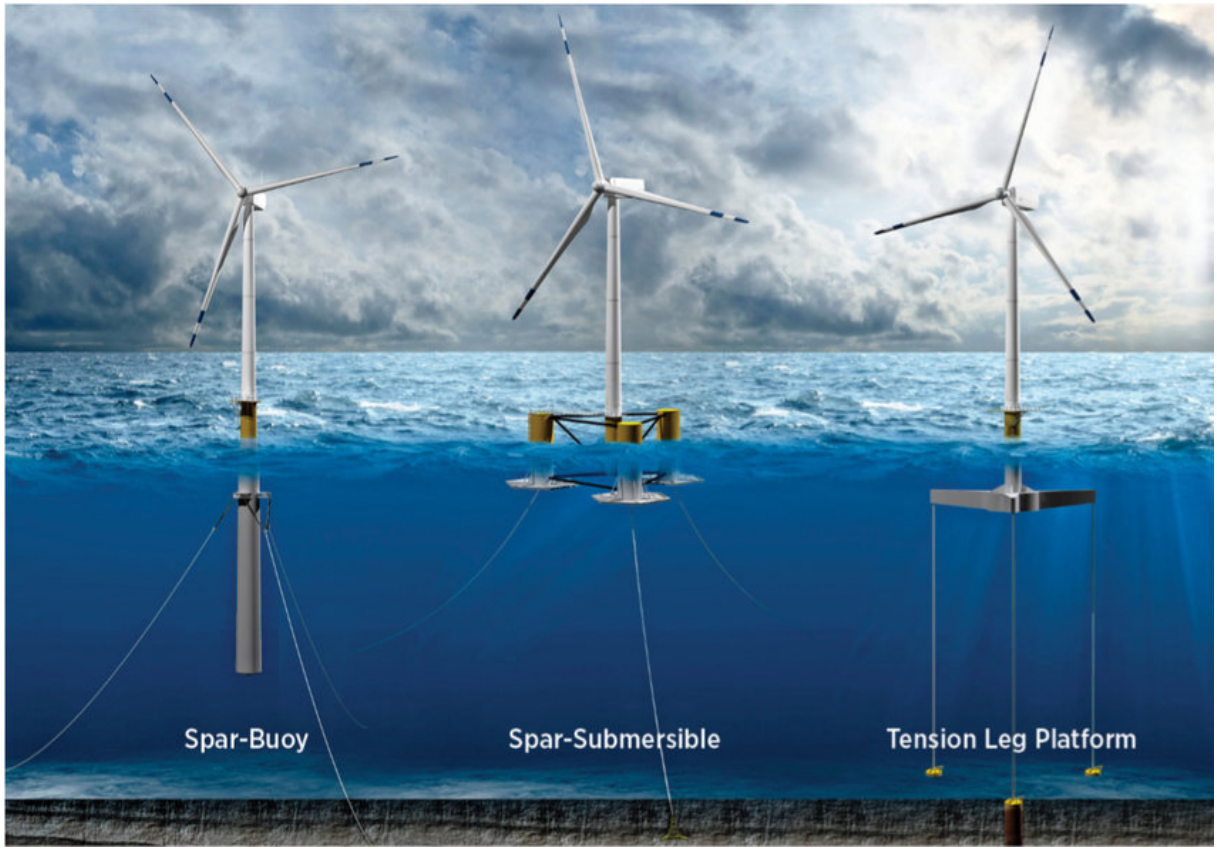

FIGURE 4.10: An artistic impression of FOWT platform concepts by Joshua Bauer, National Renewable Energy Laboratory (US Department of Energy). Retrieved from [124].Reused with permission.

4.2.1 FOWT Static Stability and Dynamic Stability Resonance

Speaking of a structure floating on water, the Archimedes principle implies that the buoyancy of the structure must be equal to the weight of the structure for it to stay afloat. The buoyancy here implies the weight of the displaced volume from the submerged part of the structure. For structures subjected to different types of dynamic load (wave and wind), enough stability (statically and dynamically) is essential. Sinking happens when buoyancy is not enough, while capsizing happens when stability is not enough. However, for a moored floating structure such as the TLP, its buoyancy might be larger than the mass of the structure.

From a stability perspective, two types of inclinations are considered for floating structures; heeling and trimming. Heeling is the inclination around the longitudinal horizontal axis and is responsible for transverse stability while trimming is difference

between forward and aft draft of the floating structure and is responsible for longitudinal stability (see Fig. 4.11).

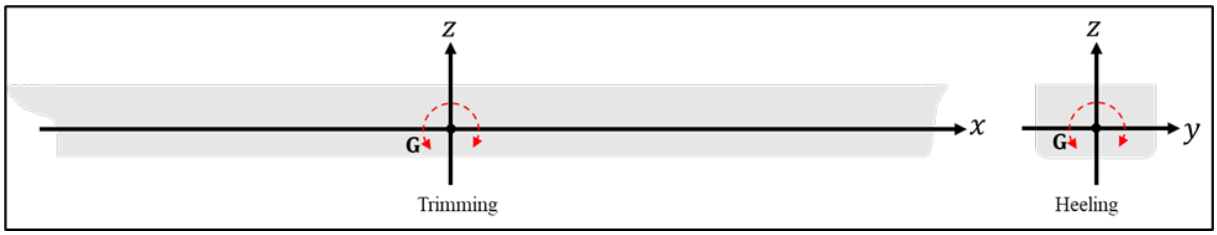

FIGURE 4.11: Inclinations in a floating structure.

To understand the stability of a floating structure, three points of interest must first be understood (Fig. 4.12). The first is the Center of Gravity (CG) represented by G, which is a fixed point for a given loading of the floating structure regardless of how the structure floats on water. For instance, in an upright floating (or with an inclination), the CG is fixed. The second centre is the Centre of Buoyancy (CB) represented by B. CB is the geometrical centre of the water displaced by the floating structure, it is very related to the structure's floating status, and movable due to inclinations. The third is the Metacentre (M). The metacentre is fixed for small heeling/trimming angles. Unlike the other two real centres, the metacentre is not a physical centre, but a very important concept for the stability of a floating structure.



FIGURE 4.12: Three Centres of a Floating Structure.

The stability of a floating structure is determined by the relative position of its CB and CG. The ability for a floating platform to restore its equilibrium positions is

weighted against external overturning forces due to environmental loads. In the upright floating position, these three centres would be on the same vertical line as seen in the plot illustrated in Fig. 4.12 (left). When the structure inclines, the buoyancy centre would change to a different position, B'. It can be seen from the illustration in Fig. 4.12 (right) that the crossing point of the vertical line through the buoyancy centre and structure central line is the metacentre. In the inclination, the gravitational force and the buoyancy force make the force couple, thus a pure moment, $\vec{M}$ would be produced as demonstrated. Obviously, this moment would make the floating structure return to the upright floating position (stable equilibrium). Thus, the metacentre must be above the centre of gravity and the metacentric height, $GM > 0$ to achieve a stable equilibrium. Fig. 4.13 below further illustrates the forces and moments experienced by a floating body.

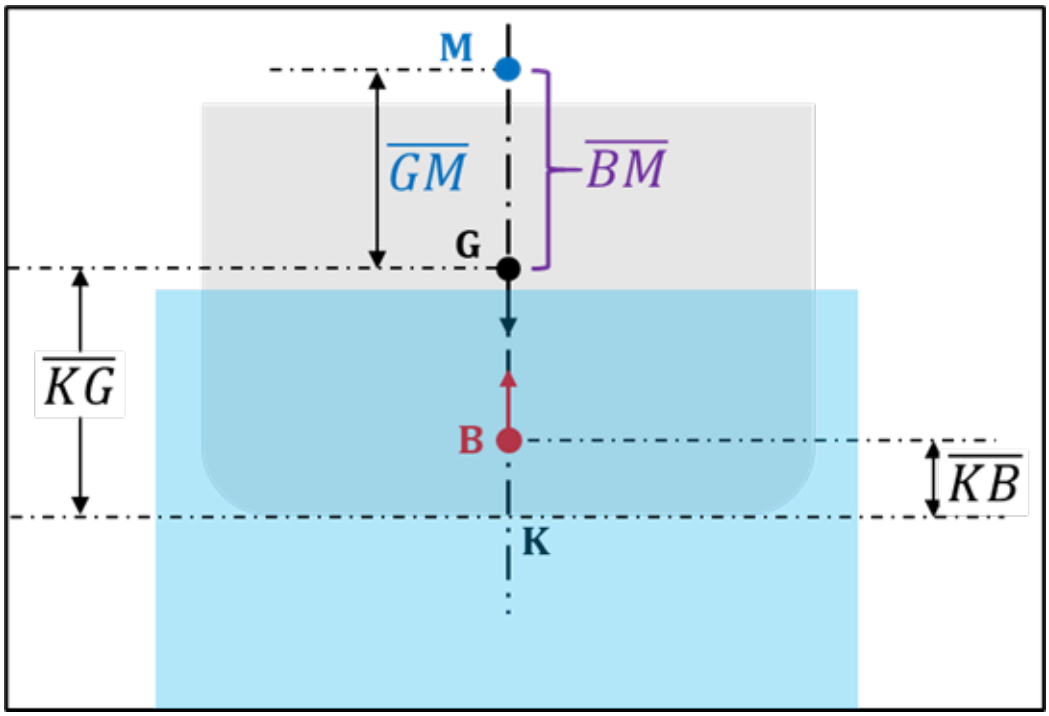

FIGURE 4.13: Basic Stability Body Force Diagram.

From Fig. 4.13 above, the metacentric height can be evaluated as;

$$\overline{GM} = \overline{KB} + \overline{BM} - \overline{KG} \tag{4.1}$$

where K is the keel point, G the centre of gravity, and B the centre of Buoyancy. The metacentric height, $\overline{GM}$ is the distance between G and M. $\overline{KB}$ and $\overline{KG}$ are the distance from the Keel of the floating structure to $\overline{CB}$ and $\overline{CG}$, respectively. $\overline{BM}$ is the metacentric radius. To obtain $\overline{BM}$, the second moment of the waterplane area (I_x and I_y) need to be calculated using the integral;

$$I_x = \int_{Y_1}^{Y_2} y^2 x dy \tag{4.2}$$

similarly;

$$I_y = \int_{X_1}^{X_2} x^2 y dx \tag{4.3}$$

Thus, the metacentric radii $\overline{BM}_x$ (transverse metacentric radius) and $\overline{BM}_y$ (longitudinal metacentric radius) are calculated as;

$$\overline{BM}_x = \frac{I_x}{\forall} \tag{4.4}$$

and

$$\overline{BM}_y = \frac{I_y}{\forall} \tag{4.5}$$

respectively. $\forall$ is the volume of fluid displaced by the floating structure. The above expressions suggest that the stability of a floating structure can be increased in several ways. For instance, the waterplane area can be increased to achieve a high second moment of the waterplane area. Similarly, the centre of gravity can be lowered to decrease $\overline{KG}$. The restoring moments, $\vec{M}$, and the related righting arm, $\overline{GZ}$ are important parameters associated with the stability of a floating structure. It aids in investigating if the FOWT can self-restore to the upright floating position in the occurrence of extreme weather conditions. Fig. 4.14 illustrates the body force diagram for a floating structure undergoing a heeling inclination, ϕ.

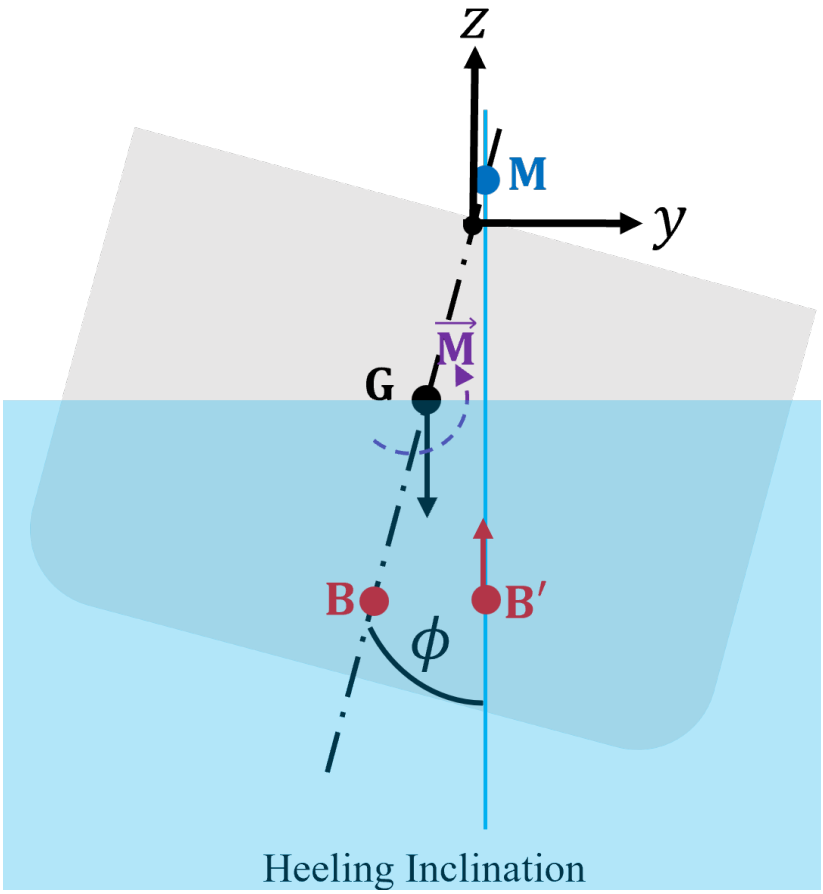

FIGURE 4.14: Restoring moment due to heeling inclination on a floating structure.

Supposing the FOWT has a heel angle, ϕ, the coordinate transformation will be given by x', y', and z' which are expressed as;

$$\begin{cases} x' = x \\ y' = y\cos\phi - z\sin\phi \\ z' = y\sin\phi + z\cos\phi \end{cases} \tag{4.6}$$

As can be seen from equation 4.6, x' is unchanged. Similarly, around the y-axis (trim angle, θ), the coordinates transformation will be given by;

$$\begin{cases} x' = xcos\theta + zsin\theta \\ y' = y \\ z' = -xsin\theta + zcos\theta \end{cases} \tag{4.7}$$

The use of these coordinate transform solution expressed in equations 4.6 and 4.7 are in the calculation of the new centre of gravity and buoyancy when the FOWT undergoes a heeling or trimming inclination. Thus, the new centres of gravity due to heeling and trimming are defined as;

$$\begin{cases} x'_g = x_g \\ y'_g = y_g \cos\phi - z_g \sin\phi \\ z'_g = y_g \sin\phi + z_g \cos\phi \end{cases} \tag{4.8}$$

and

$$\begin{cases} x'_g = x_g cos\theta + z_g sin\theta \\ y'_g = y_g \\ z'_g = -x_g sin\theta + z_g cos\theta \end{cases} \tag{4.9}$$

for heeling and trimming inclination angle, respectively. Under extreme environmental loads, the FOWT is anticipated to undergo large inclination. To calculate the restoring moment in large inclination, a numerical method is introduced which uses the same panel method as those employed in ANSYS AQWA. After the coordinate transform, the displacement can be calculated as;

$$\begin{aligned} \forall_x &= -\iint_{S_b} x' n_x dS \\ \forall_y &= -\iint_{S_b} y' n_y dS \\ \forall_z &= -\iint_{S_b} z' n_z dS \end{aligned} \tag{4.10}$$

If the panels are accurate enough, $\forall_x = \forall_y = \forall_z$. Similarly, the buoyancy centre will be calculated using these expressions;

$$\begin{aligned} x'_b &= -\frac{1}{2\forall} \iint_{S_b} x'^2 n_x dS \\ y'_b &= -\frac{1}{2\forall} \iint_{S_b} y'^2 n_y dS \\ z'_b &= -\frac{1}{2\forall} \iint_{S_b} z'^2 n_z dS \end{aligned} \tag{4.11}$$

By examining Fig. 4.14, it can be observed that in an inclination of a floating structure, two forces are acting on the structure; gravitational force and buoyancy. Principally, they are equal in magnitude but opposite directions. Also, in an inclination, these two forces are not on the same line, hence they could form a force couple. The distance between these two forces is the righting arm, $\overline{GZ}$. Thus, the restoring moment is calculated as;

$$\vec{M}(\phi) = mg\overline{GZ} \tag{4.12}$$

Also, it is clear from Fig. 4.14 that the righting arm $\overline{GZ}$ can be calculated as;

$$\overline{GZ}(\phi) = y_b - y_g \tag{4.13}$$

When the heel angle is small ($\leq 5°$), the righting arm curve, $\overline{GZ}$ is determined as;

$$\overline{GZ} = \overline{GM}\sin\phi \tag{4.14}$$

Therefore, $\overline{GM}$ can be calculated with regards to the inclination angle using a differential equation defined as;

$$\overline{GM} = \frac{d\overline{GZ}}{d\phi}|_{\phi=0} \tag{4.15}$$

From a viewpoint of stability, the larger the initial metacentric height, the better the dynamic stability performance of the floating structure. However, in reality, a large $\overline{GM}$ might cause large motion for the floating structure or unpleasant motion. For rotational motion (i.e. roll and pitch), their natural period is calculated as;

$$T_0 = 2\pi\sqrt{\frac{I + I_a}{\rho_w g \forall \cdot \overline{GM}}} \tag{4.16}$$

Here, I is the moment of inertia while I_a is the added moment of inertia. Hence, it can be observed that the rotational natural period is directly proportional to the square root of the initial metacentric height, $\overline{GM}$. In details for roll motion, the natural period

T_4 is given as;

$$T_4 = 2\pi\sqrt{\frac{I_{44} + I_{a44}}{\rho_w g \forall \cdot \overline{GM}_T}} \tag{4.17}$$

Here, I_{44} is the transverse moment of inertia, while I_{a44} is the corresponding added moment of inertia. $\overline{GM}_T$ is the transverse initial metacentric height. Similarly, for pitch motion, the natural period is calculated as;

$$T_5 = 2\pi\sqrt{\frac{I_{55} + I_{a55}}{\rho_w g \forall \cdot \overline{GM}_L}} \tag{4.18}$$

$\overline{GM}_L$ is the initial metacentric height. In reality, to avoid large motions in many cases, the corresponding natural periods are normally designed to be much larger or much smaller than the wave periods. Thus, $\overline{GM}$ maybe requested to be very small to have a high natural period or very large to have small natural periods.

Understanding the key characteristics of the three main floating concepts (TLP, spar-buoy, semi-submersible) for offshore wind turbines is crucial when developing an entirely new concept that cuts across the design principles of either two or all these concepts. As discussed earlier, one prominent feature of all the floaters is that they employ buoyancy to support deck payload arising from the weight of the WTG assembly in addition to providing tensions for slender structures such as moorings. Also, the natural periods of motions are key parameters and, in many ways, reflects the design philosophy for a floating platform. Typical motion natural periods and hydrodynamic load effects of different FOWT platform are presented in Table 4.3 according to ref [48], [125].

As can be observed from the data presented in Table 4.3b, a common characteristic of all floater types is that they are compliant (C) or "soft" in the horizontal plane with the surge, sway and yaw periods generally $> 100\ s$. The essential differences among the floaters are related to their modes of motions in the vertical plane (heave, roll, and pitch) which are decisive for the choice of a station-keeping system. However, Tension Leg Platforms (TLPs) differ fundamentally from other floater concepts because the stiffness in the vertical plane is governed by tendons rather than water plane. Hence, TLPs are compliant to surge, sway, and yaw motions but restrained (R)

in heave, roll and pitch motion.

TABLE 4.3: Qualitative Comparison of Floater Concepts to Hydrodynamic Loads and Susceptibility to Modes of Motion.

a. Hydrodynamic Load and Load Effects on OWT Floater Concepts			
Loads	**TLPs**	**Spar-Submersible**	**Spar Buoy**
Wave Frequency Loads	•	•	•
Low Frequency Loads	•	•	•
High-Frequency Loads	•		•
Mathieu Instability			•
Hull Vortex Shedding			•
Wave in Deck Loads	•	•	•
Slamming Loads	•	•	

b. Floater Boundary Conditions (BC) and Natural Periods						
Modes of Motion	**TLPs**		**Spar-Submersible**		**Spar Buoy**	
	BC	**Period**	**BC**	**Period**	**BC**	**Period**
Surge	C	> 100 s	C	> 100 s	C	> 100 s
Sway	C	> 100 s	C	> 100 s	C	> 100 s
Heave	R	< 5 s	C	20 – 50 s	C	20 – 35 s
Roll	R	< 5 s	C	30 – 60 s	C	50 – 90 s
Pitch	R	< 5 s	C	30 – 60 s	C	50 – 90 s
Yaw	C	> 100 s	C	> 100 s	C	> 100 s

As presented in Table 4.3a, TLPs generally experience wave frequency motions (induced by first order wave loads in the frequency range of the incoming wave) in the horizontal plane that are of the same order of magnitude as those of a spar-submersible of comparable size but behave more like a fixed structure in the vertical plane and practically experience no wave motion response because wave motion force are directly counteracted by the tendon stiffness force. Spar buoys are characterised by small heave motions with natural periods less than 5 s. Due to the deep draft for a spar buoy floater, a large area of the submerged platform is exposed to ocean current force which are usually the dominant environmental load.

For a spar-submersible, the main source of stability are the columns of the floater which also provide small waterplane area and giving natural periods slightly > 20 s in the vertical modes of motion. A hybrid mooring system can be fitted in a spar-submersible floater concept. Additionally, spar-submersible are very sensitive to weight change and experience large ocean current force due to the bluff shape of its submerged columns and pontoons. As shown in Table 4.3b, a spar-submersible is characterised by being compliant with all modes of motion having natural periods above the range of the natural wave period. However, wave frequency loads can become significantly important in extreme environmental loads.

To graphically characterise the information on the three platform concept using a radar chart, the author has developed a methodology for assigning scores based on

the boundary conditions highlighted in Table 4.3b. Table 4.4 shows the scoring criteria that were developed for this purpose, while Table 4.5 shows the scores based on the information in Table 4.3b.

TABLE 4.4: Scoring Criteria for Floater Boundary Conditions and Natural Period.

Boundary Condition	Scoring Criteria	Period	Definition
C4	-1.00	100 s < T < 120 s	Strongly Compliant
C3	-0.75	80 s < T< 100 s	Well Compliant
C2	-0.50	40 s < T < 80 s	Compliant
C1	-0.25	20 s < T < 40 s	Fairy Compliant
N	0.00	15 s < T < 20 s	Neutral
R1	0.25	10 s < T < 15 s	Fairly Restrained
R2	0.50	5 s < T < 10 s	Restrained
R3	0.75	1 s < T < 5 s	Well Restrained
R4	1.00	T < 1s	Strongly Restrained

TABLE 4.5: Table showing platform concept boundary conditions for all modes of motion using the scoring criteria.

Floater Concepts	Six DOF Modes of Motion					
	Surge	Sway	Heave	Roll	Pitch	Yaw
Semi-submersible	C4	C4	C2	C2	C2	C4
Spar Buoy	C4	C4	C1	C3	C3	C4
TLP	C4	C4	R3	R3	R3	C4

Fig. 4.15 contains the radar chart showing the graphical representation of the floater boundary condition for modes of motion. From the radar chart, it can be observed that the TLP has more flexibility and attractive stability properties due to its retrained motion for heave, roll and pitch modes of motion. These modes of motion are the most important parameters as regards to the static and dynamic stability of a FOWT. Having characterised the boundary conditions of the three floating platform concepts for FOWT for the six modes of motion using a radar chart, the key question becomes; what should the "ideal floating platform" boundary conditions for all six modes of motion look like? Fig. 4.16 shows the radar chart of a "perfect" floating platform for an offshore wind turbine in comparison to all other floating concepts.

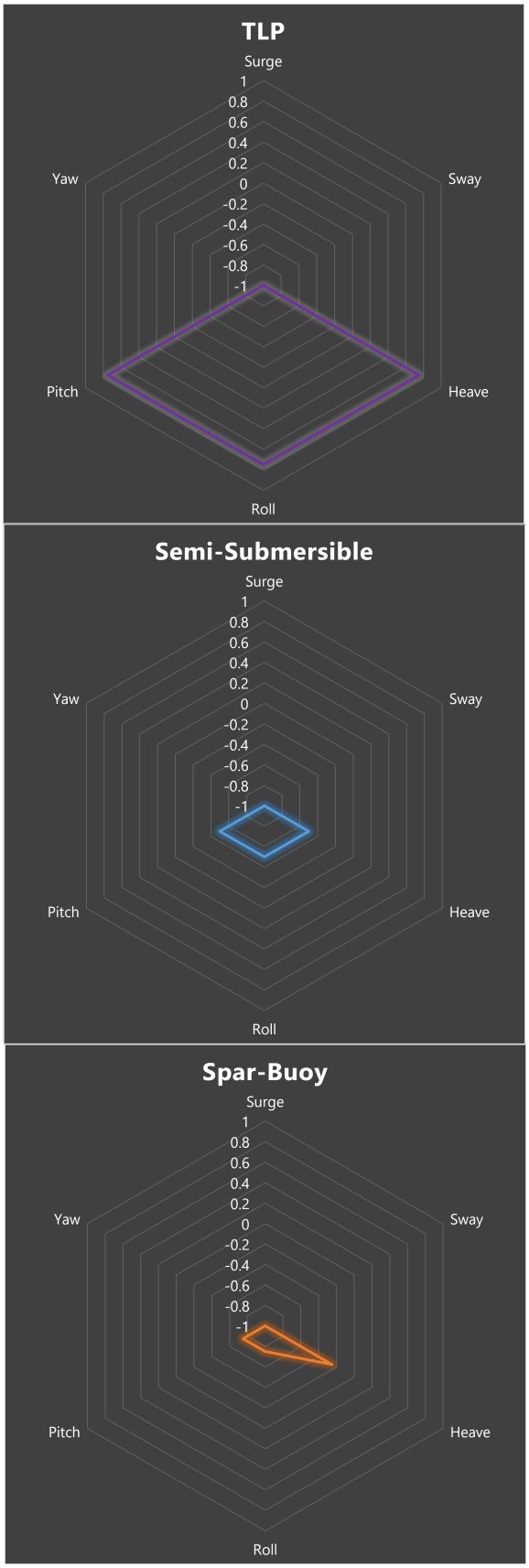

FIGURE 4.15: Radar chart showing platform properties based on boundary conditions and natural periods.

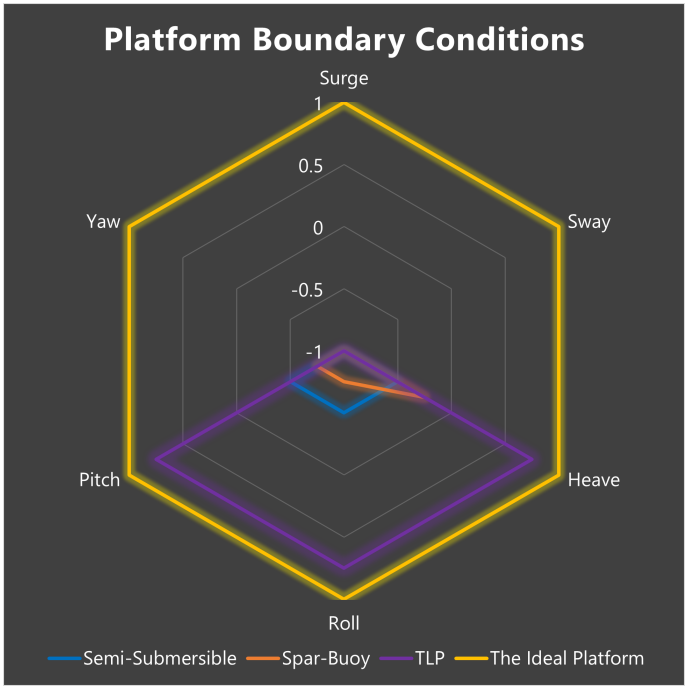

FIGURE 4.16: Radar chart showing platform properties based on boundary conditions and natural periods.

4.2.2 TRIgon Hybrid Floater (TRIHF) Concept Rationale and Model Description

As highlighted earlier in Section 1.4, one of the goals of this research is to conceptualise an in-house hybrid floating platform for FOWTs identified as TRIHF. Table 4.6 contains the FOWT concept pre-design selection rationale. By combining the benefits from the three floater concepts and considering various design aspects from engineering, construction, fabrication, installation, and maintenance, the TRIHF concept design is developed. Fig. 4.17 shows an artistic impression of the TRIHF concept. The TRIHF platform consists of a trigon hull (three-sided polygon) made from steel (Fig. 4.18). The trigon shaped hull is designed for optimal motion response in wind and wave and provide the main source of buoyancy. The radial braces, diagonal braces, and centre column provide structural support for the trigon hull and WTG system. The trigon hull serves three main purposes which are to provide buoyancy support, water plane stability, and ballasting for draft control. Also, the hull provides a connection for the mooring assembly on the floater.

TABLE 4.6: FOWT Concept Pre-design Selection Rationale.

Characteristics			Semi-Submersible	Spar-Buoy	Tension Leg Platform
MOTION	Translational	Surge	• No restoring force unless restrained by mooring system.	• No restoring force unless restrained by mooring system.	• Complies to surge motion due to wave loading with natural surge periods well above significant wave period.
		Sway	• No restoring force unless restrained by mooring system.	• No restoring force unless restrained by mooring system.	• Complies to sway motion due wave loading with natural sway periods well above significant wave period.
		Heave	• Complies to heave motion from wave loading. • Restoring heave force is determined by number of columns, column diameter, and distance between the columns.	• Very small heave motion from wave loading due to deep draft.	• Non-complaint to heave motion from wave loading. • Platform heave motions are restrained/virtually eliminated using structural elastic stiffness via high tensioned vertical tethers moored to the seabed which shortens natural heave period below energetic wave periods.
	Rotational	Roll	• Complies to roll motion from wave loading. • Restoring Roll force is determined by number of columns, column diameter, and distance between the columns.	• Negligible compliance to roll motion from wave loading.	• Non-complaint to Roll motion from wave loading. • Platform Roll motions are restrained/virtually eliminated using structural elastic stiffness via high tensioned vertical tethers moored to the seabed which shortens natural roll period below energetic wave periods.
		Pitch	• Complies to pitch motion from wave loading. • Pitch stiffness can be increased by either increasing the water plane area or increasing the distance between the columns.	• Negligible compliance to pitch motion from wave loading.	• Non-complaint to pitch motion from wave loading. • Platform pitch motions are restrained/virtually eliminated using structural elastic stiffness via high tensioned vertical tethers moored to the seabed which shortens natural pitch period below energetic wave periods.
		Yaw	• No restoring force unless restrained by mooring system	• No restoring force unless restrained by mooring system	• Complies to yaw motion due wave loading with natural yaw periods well above significant wave period.

TABLE 4.6: FOWT Concept Pre-design Selection Rationale (continued).

Characteristics	Semi-Submersible	Spar-Buoy	Tension Leg Platform
Pros	• Turbine can be installed at harbour and then towed to offshore location. • Suitable for shallow water due to shallow draft and wide range of water depths. • Simple mooring system. • Transportable.	• Inherently gravity stable due to distance between the mass center and the buoyancy center. • Moderate wave load due to deep draft that limits vertical wave forces (heave) making vertical motions of the spar buoy negligible and small water plane that limits horizontal motion from wave loading. • Relatively simple and cheap to build.	• Turbine can be installed at harbour and then towed to offshore location. • Advantageous in operations where vertical motions are critical. • Light weight and moderate wave loads. • Passively dynamic.
Cons	• Overall structure is heavy and unit cost is higher than for a Spar or Monohull because of increased structural complexities. • Subject to large wave loads and actively dynamic. • Stability is crucial and can be impaired if hull is damaged and water ingress occurs in empty hull compartments. • May require ballasting or increased dimensions of main structural members to compensate for buoyancy and stability to minimise tilting.	• Requires deep draft of minimum between 80 m to 100 m. • Too heavy. • Difficult to transport in upright position in shallow water. • Turbine cannot be installed at harbour.	• Tethers require careful design and maintenance due to high stresses and installation is usually complex and costly. • Tethers need to be pretensioned enough from been slacked and require seabed foundation capable of withstanding large upward forces as a result of deep wave trough from large waves. • Depth range limitations unless supplemented by mooring.

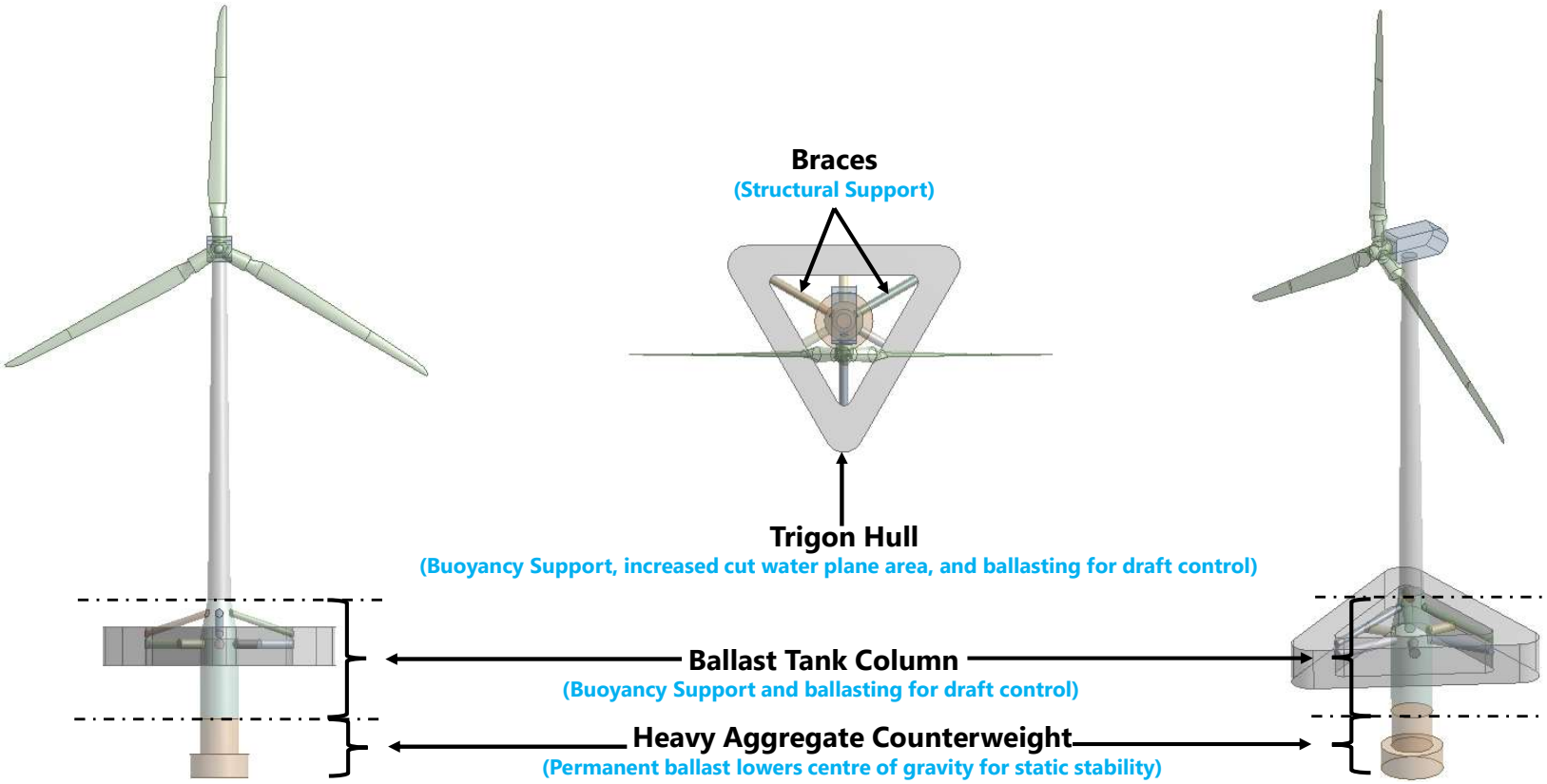

FIGURE 4.17: An artistic impression of the TRIgon Hybrid Floater (TRIHF) showing its major components and functionality.

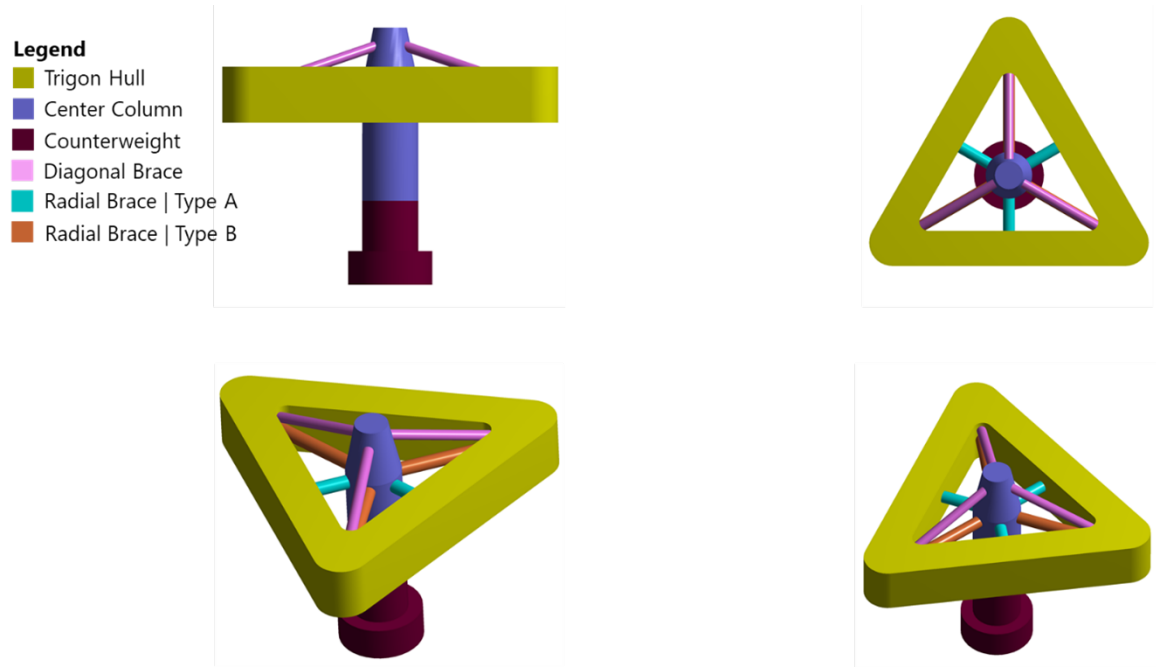

FIGURE 4.18: TRIHF Platform Components.

Fig. 4.19 contains an artistic impression showing the complete FOWT assemblage of TRIHF platform and the NREL 5 MW Wind Turbine Baseline. When in transit, the floating stability of the TRIHF platform is mainly obtained from the cut waterplane area of the trigon hull and correspondingly a high restoring stiffness especially in the vertical plane (heave, pitch, and row). Consequently, the fully assembled FOWT system can be towed out on its keel using conventional tugboats and with its full cut waterline area exposed to the waves. At the desired offshore wind farm project site, the centre column tank is partially ballasted to partly submerge the trigon hull below the sea surface, thus lowering the FOWT's centre of gravity. The circumference and height of the trigon hull also provide more inertia which reduces the platform's motion and improves stability. The heavy counterweight at the bottom of the centre column is a permanent ballast component made from high-density material ($5000 kg/m^3$). Some heavy aggregate manufactured from the mineral Magnetite reaches densities up to $5200 kg/m^3$ [126]. One of the key benefits of using a high-density aggregate as a counterweight is due to its high density to volume ratio, thus saving space by reducing the bulk volume of the floating platform. The geometric dimensions of the TRIHF platform are presented in Table 4.7.

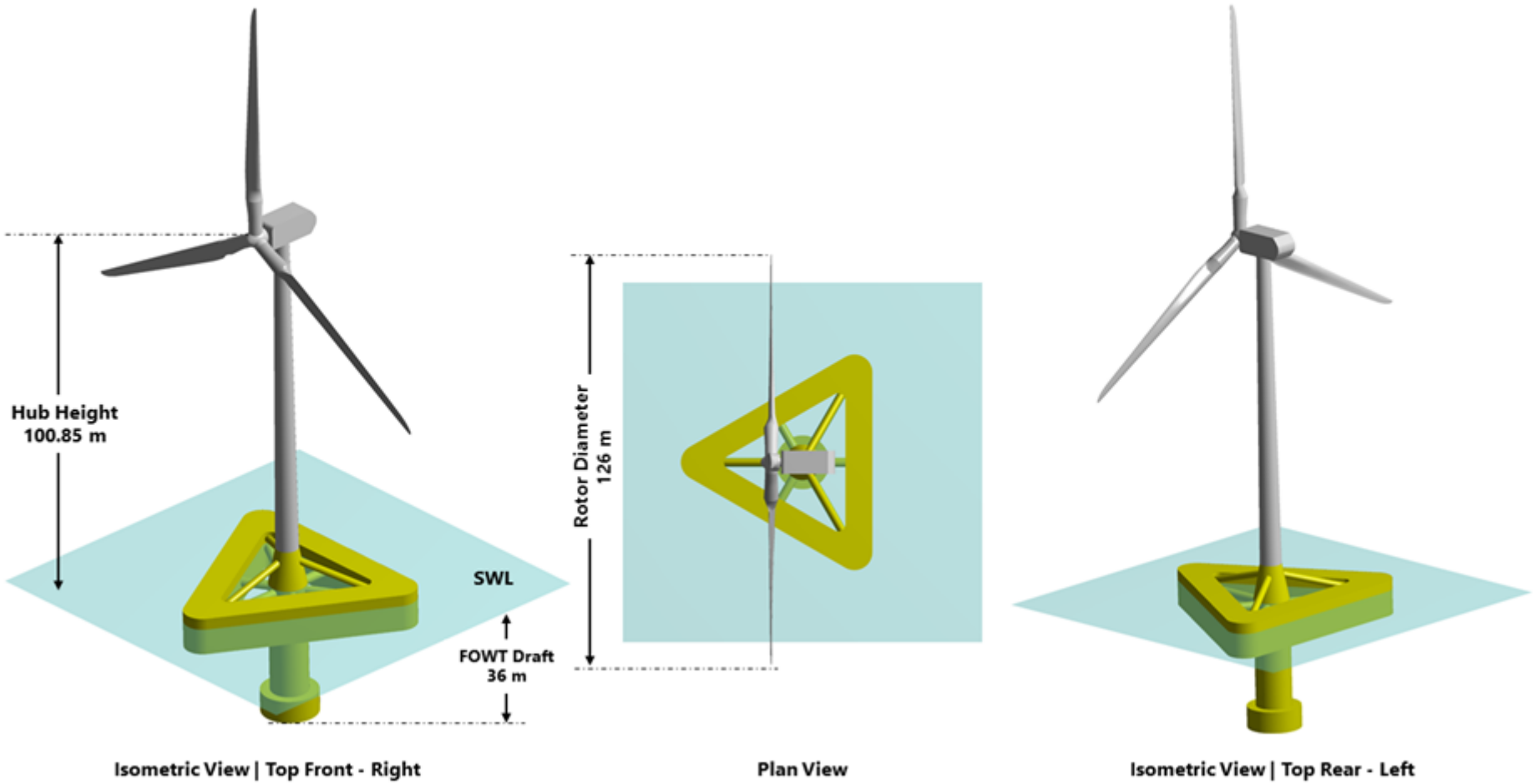

FIGURE 4.19: Artistic Impression showing the complete FOWT assemblage of TRIHF Platform and NREL 5 MW Wind Turbine Baseline.

TABLE 4.7: Main dimensions of TRIHF platform with the NREL 5 Baseline Wind Turbine.

TRIHF Platform Properties	
Hub Height Above MSL	100.85 m
Center Column Diameter	10 m
Radial and Diagonal Brace Diameter	2.5 m
Trigon Hull Radius, Height	30 m, 10 m
Design Draft, Actual Volumetric Displacement	36 m, 12,007 m^3

More importantly, the WTG assemblage is positioned at the centre of the TRIHF platform to facilitate the needless use of additional ballasting to counteract the weight of the turbine. The result of this is a reduced draft of the platform to enable easy navigation into a port, dry dock, or sheltered area. A key merit of a shallow draft FOWT platform is that it allows performing operations related to the fabrication, construction, assembling, and pre-commissioning of the floater at an inshore rather than offshore location. It is noteworthy that one of the key disadvantages of the TRIHF platform is its lack of hydrodynamic transparency because the hull will be subjected to high incident wave forces. However, this disadvantage is compensated by the platform's high water plane area which aids in water plane stability and pitch stiffness.

4.2.3 Theoretical Calculations and Precise Mass Computation

The theoretical mass calculation notes for the individual components of the TRIHF platform and ballast requirements are presented in Table 4.8 and Table 4.9, respectively. Passive water ballast of approximately $1,418$ *tons* is required to reach the design draft of 36 m. Thus, the TRIHF achieves pitch restoring from a combination of passive ballasting and buoyancy. The use of an active ballast system for TRIHF is unnecessary which reduces the number of active components in the system and ultimately the associated risk of component failures. One of the main drivers for the design of the trigon hull is the ease of fabrication and robustness of the structure. The structural design of the trigon hull is based on stiffened steel plates like the material specification used in the offshore oil and gas industry. The theoretical mass calculation also takes into the account the additional weight due to fabrication. The fabrication weight is the additional weight gained by the structure due to welding, marine resistance corrosion control coating, and other fabrication parts such as bolts and flanges [127], [128]. Fig. 4.20 illustrates the precise mass calculations performed for the TRIHF platform using ANSYS static structural (left) and AQWA (right).

TABLE 4.8: Platform Theoretical Mass Calculations.

FOWT Segment	Surface Area A_{suf} (m^2)	Material				Mass $A_{suf} \times t_{mat} \times \rho_{mat} \times (1 + W_{fab})$ (kg)	Mass (N)	Mass (tons)
		Type	Thickness $[t_{mat}]$ (m)	Density $[\rho_{mat}]$ (Kg/m^3)	Fabrication Weight $[W_{fab}]$			
Trigon Hull	5330.7	Steel	0.02	7850	20%	1,004,303.88	9,852,221.06	1,004.30
Center Column	1021.4	Steel	0.02	7850	20%	192,431.76	1,887,755.57	192.43
Diagonal Brace 1	119.42	Steel	0.015	7850	20%	16,874.05	165,534.39	16.87
Diagonal Brace 2	119.42	Steel	0.015	7850	20%	16,874.05	165,534.39	16.87
Diagonal Brace 3	119.42	Steel	0.015	7850	20%	16,874.05	165,534.39	16.87
Radial Brace Type B 1	141.53	Steel	0.015	7850	20%	19,998.19	196,182.23	20.00
Radial Brace Type B 2	141.53	Steel	0.015	7850	20%	19,998.19	196,182.23	20.00
Radial Brace Type B 3	141.53	Steel	0.015	7850	20%	19,998.19	196,182.23	20.00
Radial Brace Type A 1	64.913	Steel	0.015	7850	20%	9,172.21	89,979.35	9.17
Radial Brace Type A 2	64.913	Steel	0.015	7850	20%	9,172.21	89,979.35	9.17
Radial Brace Type A 3	64.913	Steel	0.015	7850	20%	9,172.21	89,979.35	9.17
		Material		Volume V_{agg} (m^3)	Density ρ_{agg} (Kg/m^3)	Mass $V_{agg} \times \rho_{agg}$ (kg)	Mass (N)	Mass (tons)
Counterweight		Heavy Aggregate		1767.16	5000	86,679,198.00	86,679,198.00	8,835.80
Rotor		NREL 5 MW WTG System				110,000.00	1,079,100.00	110.00
Nacelle						240,000.00	2,354,400.00	240.00
Tower						347,460.00	3,408,583.60	347.46
					Total	**10,868,128.97**	**106,616,345.15**	**10,868.13**

TABLE 4.9: Theoretical Buoyancy and Ballast Requirement Calculations.

Theoretical Buoyancy and Ballast Requirement Calculation		
Parameter	**Value**	**Unit**
Submerged Volume	12,021.60	m^3
Buoyancy Force from Submerged Volume	120,880,163.23	N
Total Mass of FOWT Assemblage	106,616,345.15	N
Buoyancy Reserve	14,263,818.08	N
Water Ballast Volume	1,418.54	m^3
Radius of Ballast Column	5.00	m
Height of Water in Ballast Column	18.06	m

In Fig. 4.20 (left), the centre of mass and principal moment of inertia for each component of the FOWT were set-up discretely and then solved to provide a combined solution for centre of mass and principal moment of inertia. The combined solution yielded a new position for the centre of mass at $[0.00,\ 0.00,\ -19.25]\ m$ and a principal moment of inertia about the centre of mass $[8.79E+09,\ 8.78E+09,\ 7.44E+08]\ kg.m^2$. Concerning the result for the hydrostatics centre of mass and principal moment of inertia, as shown in Fig. 4.20 (right), it can be observed that the centre of mass moved slightly upwards toward the MSL by 0.25 m. A logical explanation for this transformation can be attributed to the inclusion of the internal ballast tank in the model.

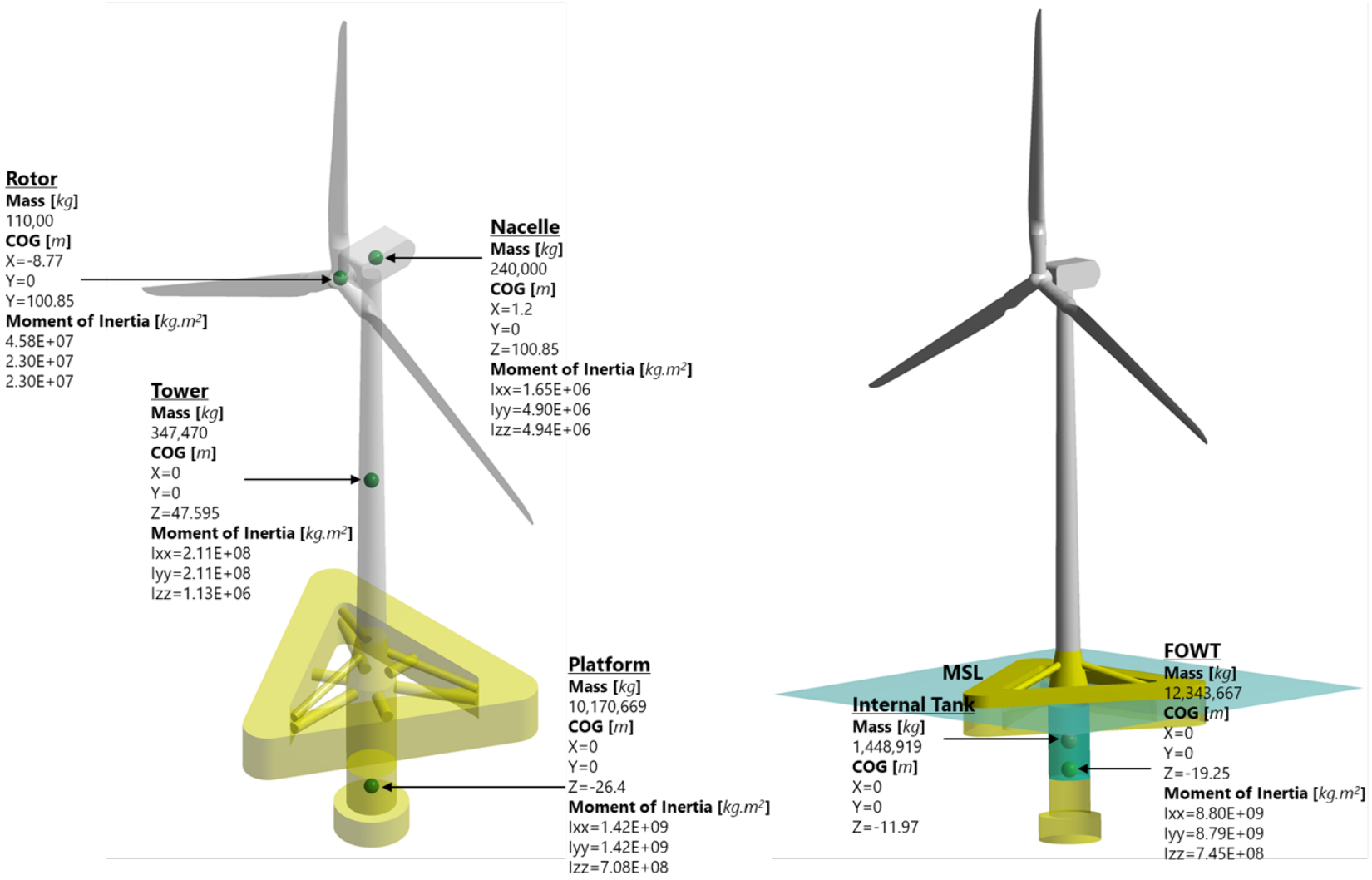

FIGURE 4.20: Platform precise mass calculation in air (left) and platform hydrostatics precise mass calculation (right).

4.2.4 Station Keeping Configuration

A four-line taut leg mooring configuration is the principal choice for the TRIHF platform. The taut leg mooring configuration is desired in other to reap the benefits of the restoring forces generated by the elasticity of the mooring line. Fig. 4.21 presents an illustration of the mooring configuration.

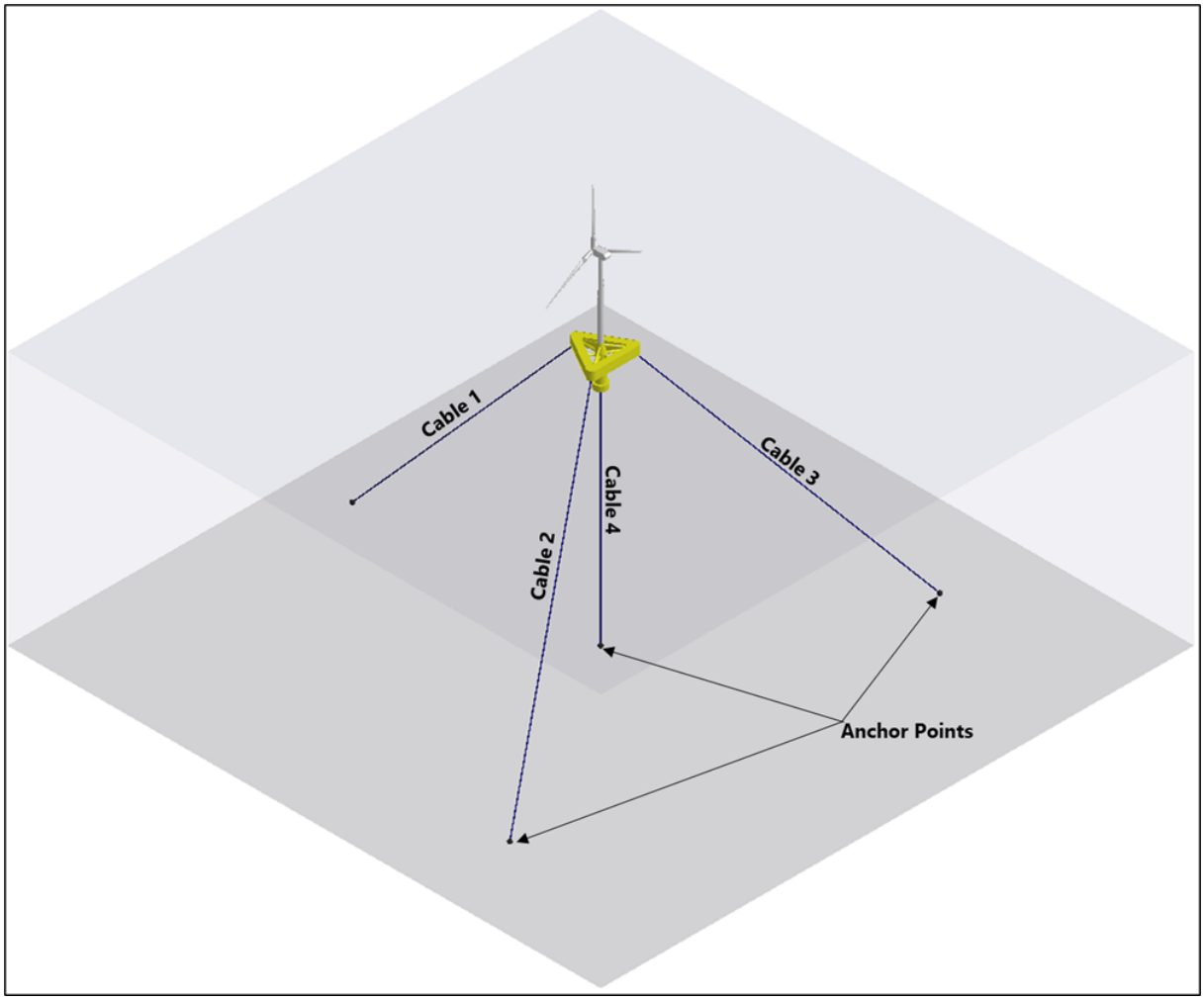

FIGURE 4.21: The TRIHF platform mooring configuration.

As can be observed from Fig. 4.21, a symmetrical arrangement for the mooring line orientation is adopted. The mooring connection points for cables 1, 2, and 3 on the floater are located at the base of the hull while cable 4 is connected to the base of the counterweight (see Fig. 4.22). This mooring arrangement precludes any need for balancing cable tensions. The platform coordinate system definition used in performing the numerical analysis are consistent with recommended standards and practices [48],

[76], [92] where z-direction corresponds with height and positive from points above the MSL and negative for points below the MSL. The global coordinate centre (0,0,0) m is located at the centre of the hull on the MSL. Wind and current direction are positive toward the x-direction and angle of attack is measured in a clockwise direction.

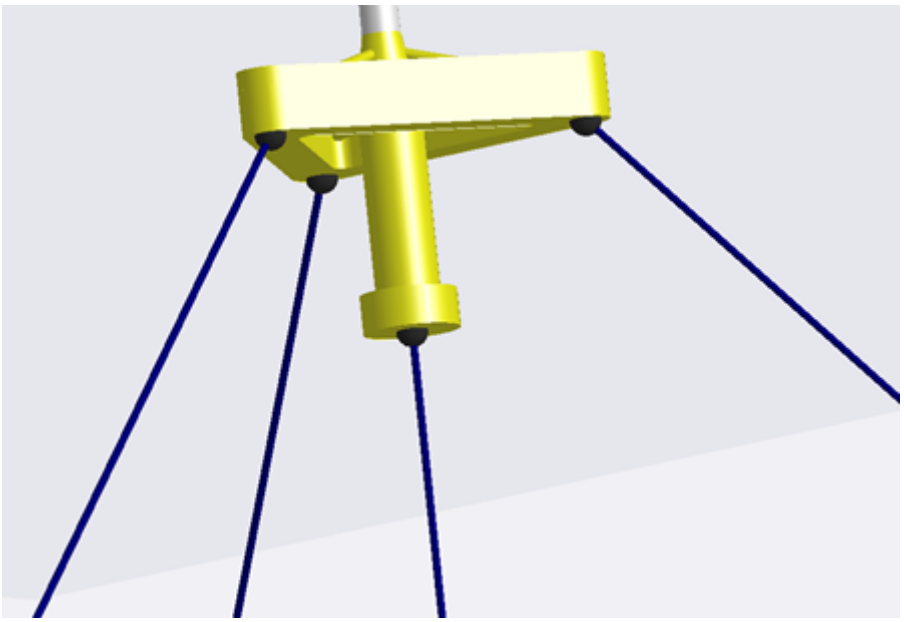

FIGURE 4.22: Illustration showing mooring connection points on the TRIHF Platform.

The taut leg mooring configuration is characterised by the pre-tensioning of the mooring lines until they are taut. The mooring line terminates at an angle of 30° to 45° on the seabed. As a result, the anchor point of the taut leg is loaded by perpendicular and parallel forces. For the taut leg system, elastic stretching rather than geometry changes are the main source of the restoring force. The key advantage of the taut leg system over the catenary system is due to its higher magnitude of line's stiffness. Thus, the offset under mean load arising from the FOWT's motion response to dynamic loads is better controlled which ultimately make the total mooring line tensions smaller. Furthermore, a supplementary advantage of the taut leg system is the enhanced load sharing amongst adjacent mooring lines. However, a key disadvantage is that the mooring line must have sufficient elasticity to absorb the FOWT's wave motion responses without overloading.

A commonly used material for the mooring line used in a taut leg system is the polyester rope (see Fig. 4.23) because it has the required stiffness characteristics for a taut leg mooring configuration as well as being a cost-effective solution for deepwater

installations. From experimental testing and findings, the fatigue life of the polyester rope is quoted to be around 80 decades superior to steel wire rope [129].

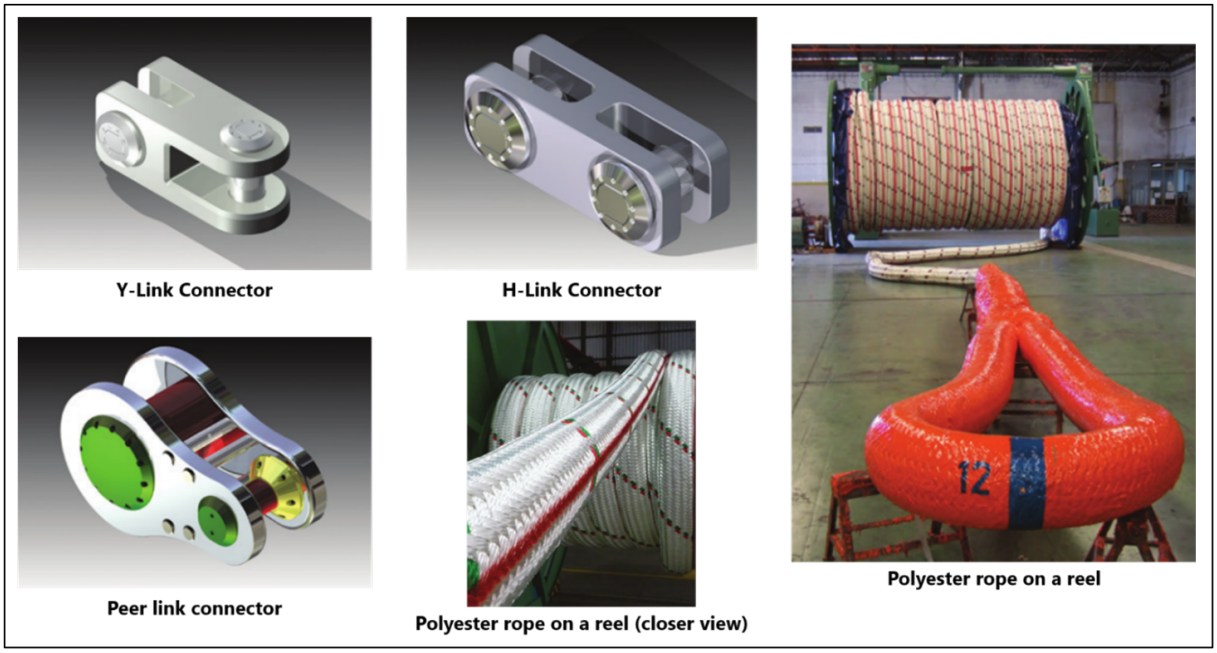

FIGURE 4.23: Polyester rope and connections used in the taut leg mooring system (adopted from [129].

The choice of connector solution (see Fig. 4.23) depends largely on the handling, deployment, and installation methodology. The connector design may also be impacted by the pre-tensioning methodology. In terms of performance characteristics, polyesters ropes exhibit a combination of permanent and visco-elastic extension when loaded. The visco-elastics extension behaviour determines the stiffness performance of the rope which is an important consideration of the mooring system [130]. For this thesis, the ANSYS AQWA toolkit used in performing the hydrodynamic response analysis requires the linear stiffness parameter of the mooring line.

ANSYS AQWA models the linear stiffness as tension only spring where the tension is directly proportional to the extension. During the analysis, the extension of the polyester rope may vary because the floating platform to which the rope is attached will experience a force of varying magnitude and direction. Assuming the polyester rope is 100% torque-free, the magnitude of the varying force which it will experience which is equal to the cable tension is given by;

$$F_{cbl} = k_{cbl} \times \Delta L_{cbl} \tag{4.19}$$

where F_{cbl}, k_{cbl} and ΔL_{cbl} are the cable force (N), cable stiffness (N/m) and cable extension (m), respectively. Al-Solihat and Nahon [131] investigated the mooring and hydrostatic restoring stiffness of three FOWT platform concepts. In their study, they presented a new analytical form of mooring stiffness matrix for a taut-leg configuration. The analytical calculation was subsequently used to formulate the mooring stiffness for a TLP. When the mooring line is extremely taut and no sag exists, the polyester rope deflection will be as a result of structural deformation. Consequently, the stiffness of the polyester rope along its chord can be assumed equal to its optimum stiffness which is given by;

$$k_{cab} = \frac{E_{cbl} A_{cbl}}{L_{0cbl}} = \frac{Minimum\ Breaking\ Load\ (MBL)}{L_{0cbl}} \tag{4.20}$$

where E_{cbl}, A_{cbl}, and L_{0cbl} are the young modulus, cable cross-sectional area, and cable unstretched length, respectively. The unstretched length for the mooring cables as illustrated in Fig. 4.23 are presented in Table 4.10. According to two leading fibre rope solution providers [129], [130], the stiffness for a 258 mm diameter polyester rope for load ranges cycling between 40% to 50% of MBL is $10.4 \times 10^8\ N$. Thus, by substituting the values for MBL and unstretched length into equation 4.20, the spring constant stiffness for the mooring cables were calculated as per the results presented in Table 4.10.

As have been discussed in this section, the TRIHF platform consists of the major elements that qualify it as a Spar-buoy due to the presence of a passive ballast system and a permanent counterweight ballast using heavy aggregate; as a semi-submersible due to its buoyancy and large waterplane area, and a TLP due to its taut leg mooring configuration that is pre-tensioned under the excess buoyancy offered by the platform. The author desires that the rationale behind the hybrid platform concept has been sufficiently explained and that the audience have a clearer understanding of how the new concept portrays the characteristics of the three main floating platform concepts for offshore wind turbines.

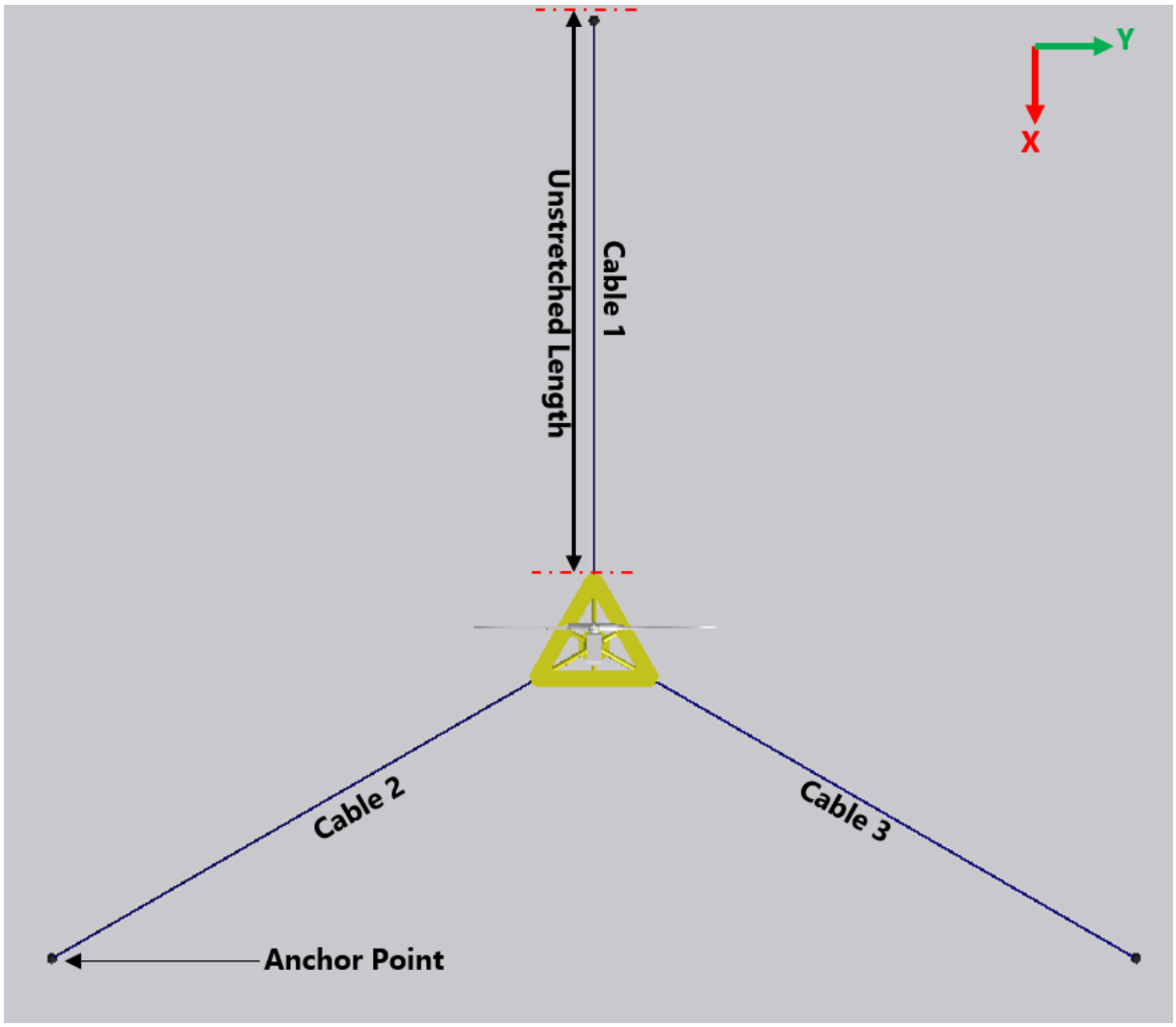

FIGURE 4.24: Illustration showing mooring line nomenclatures and coordinates.

TABLE 4.10: Mooring Line Stiffness Properties.

Cables	Unstretched Length (m)	Diameter (mm)	MBL (MN)	Stiffness (MN/m)
1	393.72	258	1039.9	2.64
2	393.72	258	1039.9	2.64
3	393.72	258	1039.9	2.64
4	264.00	258	1039.9	3.94

Chapter 5

SHARPE Numerical Modelling Scheme Development and Validation

To give the audience a superior understanding of the engineering and mathematical analysis offered in Chapter 6, this chapter attempts to discuss and validate the Streamlined Hydro-Aero-Rigid dynamics, and viscous Effect (SHARPE) numerical modelling scheme created for this study. To validate the SHARPE numerical modelling scheme, results from the numerical simulation is compared with the scaled model test results performed by Robertson et al. [30] for the DeepCWind-OC5[1] project which was executed under the auspices of the International Energy Agency (IEA) research for wind energy.

5.1 SHARPE Numerical Modelling Scheme Description

A comprehensive process flow chart of the SHARPE numerical modelling scheme was presented earlier in Fig. 1.6. However, for the sake of re-emphasising the methodology process flow chart, the abridged version is presented in Fig. 5.1. Fig. 5.2 and Fig. 5.3 contains the ANSYS workbench project schematic and model file structure, respectively for the SHARPE numerical modelling scheme. The key attribute of the SHARPE numerical scheme is the streamlined and top-down structured approach employed for the coupled dynamics simulation.

The SHARPE numerical modelling approach involves a mixed Floating Rigid Body (FRB) model (i.e., physical geometry + linearisation elements) of the FOWT and a Finite Element (FE) model of the mooring system. The FRB load model accounts for mass, volume, inertia, hydrostatic stiffness, added mass, damping, and excitations from wind, waves, and current on the floating platform. The term "linearisation" as

[1] Offshore Code Comparison Collaboration, Continued, with Correlation (OC5)

used in the context of this thesis means that the velocity potential is directly proportional to the wave amplitude and that the average wetted area of the floating platform up to the MSL is considered. The inclusion of linearisation in the diffraction/radiation analyses provides key information on first order excitation forces, first-order motions in rigid body DOF, second order mean drift forces/moments, hydrostatics, potential wave damping, and added mass. Also, the mean wave drift forces are dependent on only first-order quantities which can only be calculated in linear modelling.

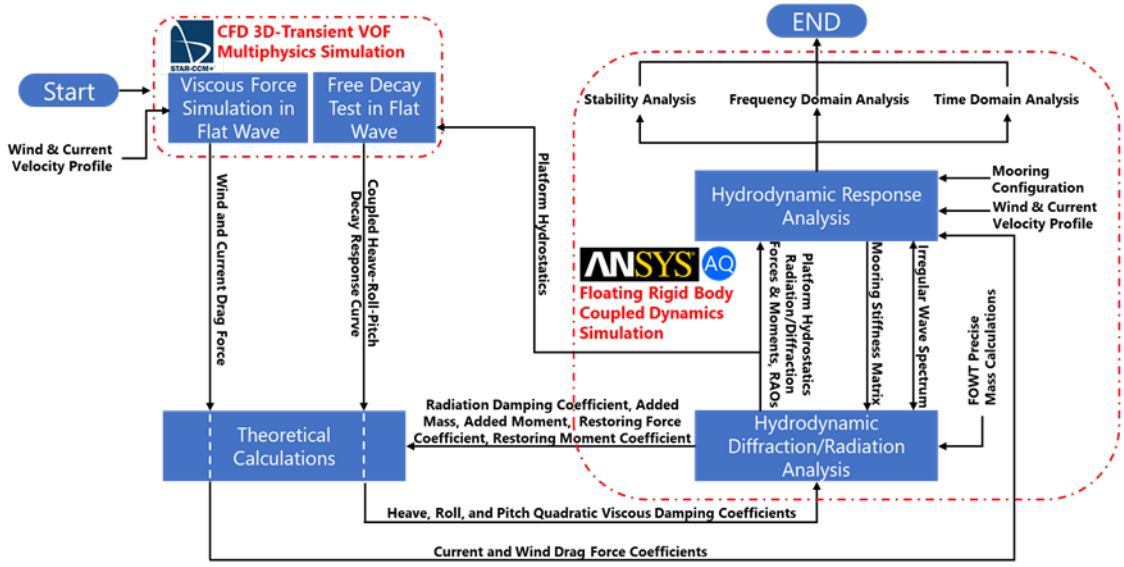

FIGURE 5.1: Abridged version of the SHARPE process flow chart methodology.

The kinematics of water particles in waves, motions of the structure, and FSIs between waves and the structure are the main sources of hydrodynamic loading on a floating marine structure. Wave exciting load, drag load, and inertia load are the three categories of hydrodynamic loading that are of central concern in a hydrodynamic diffraction/radiation analysis. Wave excitation loads are induced by first order and second order wave loads. First order wave loads are loads that emanate from Froude-Krylov wave forces and diffraction forces. Second order wave loads are loads induced by high frequency loads (loads from the sum of first-order wave frequencies) and low frequency loads (loads from the difference of first order wave frequencies). The analysis of both first order and second-order wave forces are essential are essential in the coupled dynamics simulation of a FOWT.

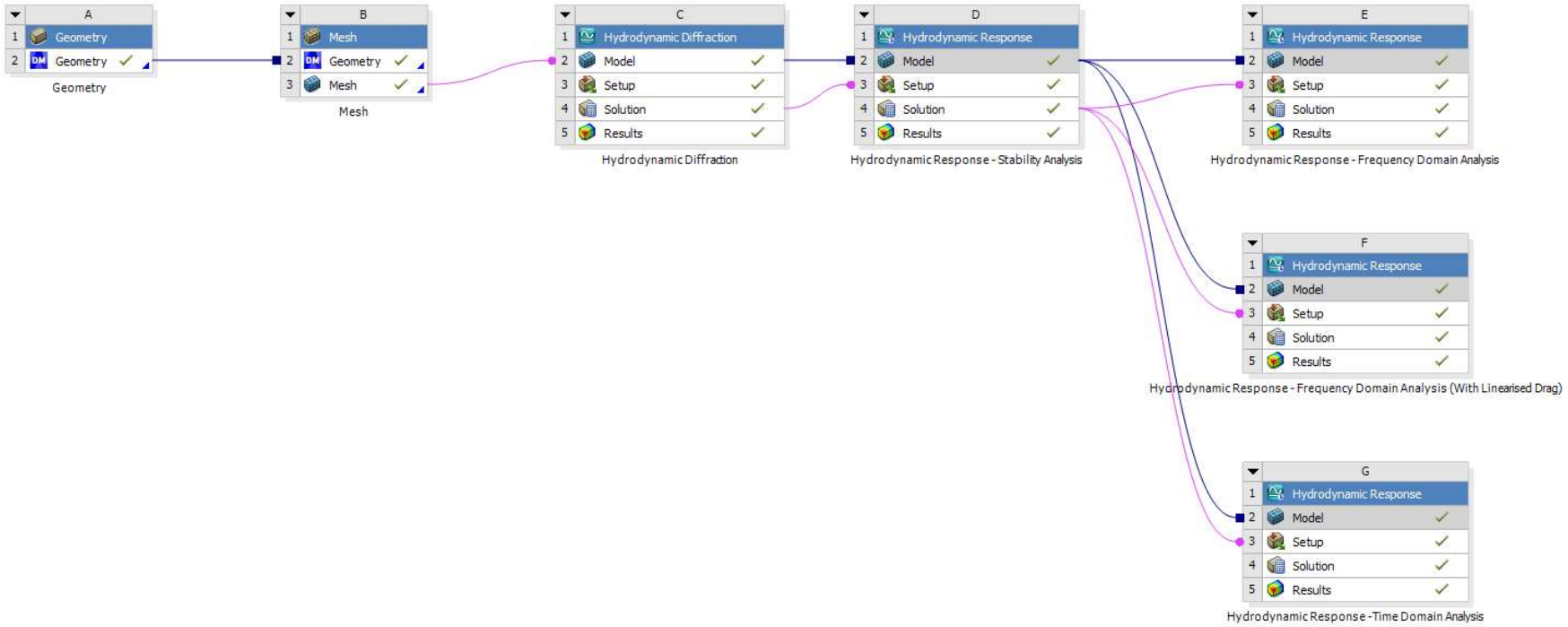

FIGURE 5.2: Project Schematic for the SHARPE Numerical Modelling Scheme in ANSYS Workbench.

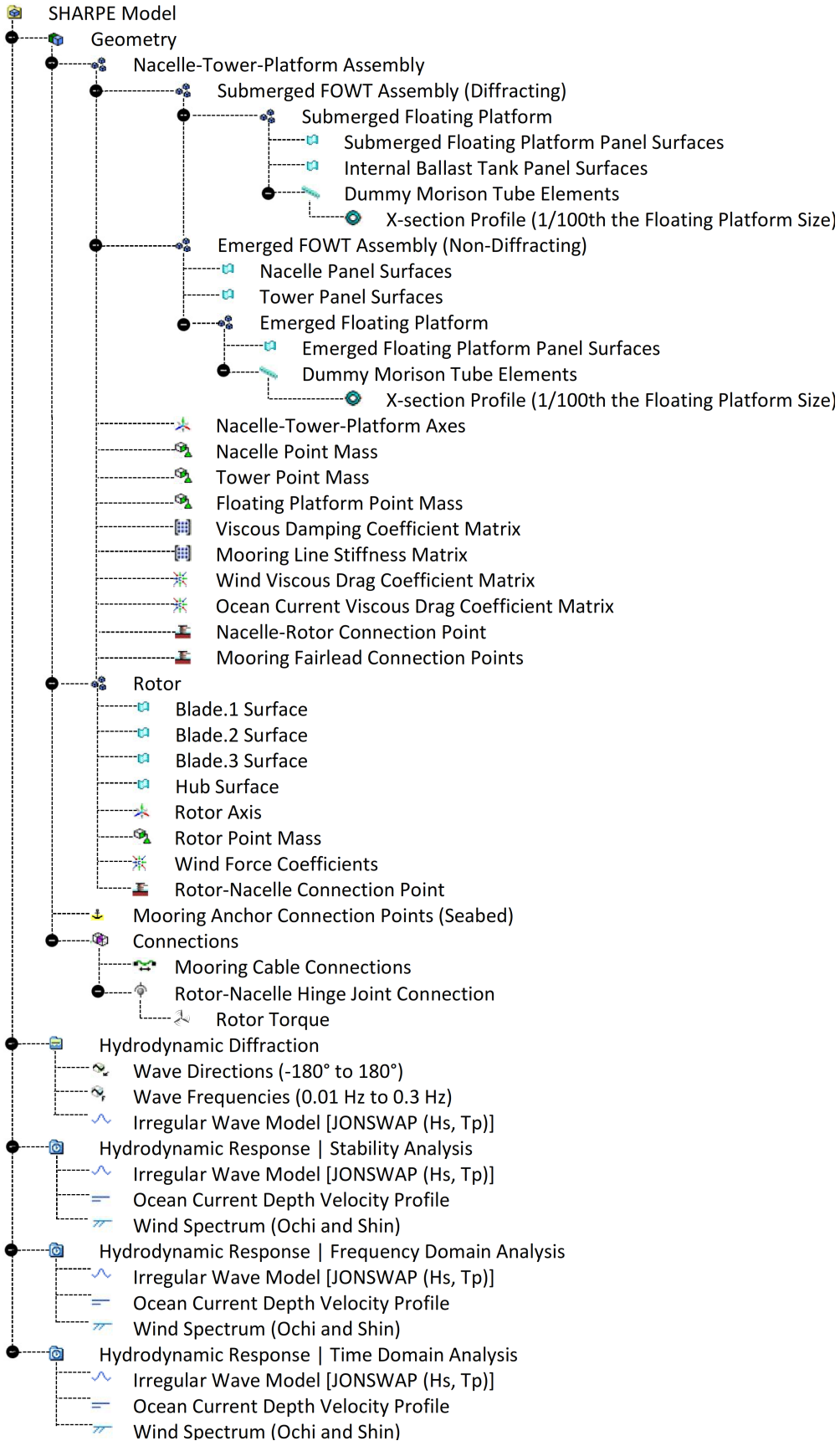

FIGURE 5.3: The SHARPE Numerical Modelling Scheme File Structure.

Drag loads are produced by viscosity and are directly proportional to the square of the relative velocity between the water particles and structure surface. However, the investigation of drag load is more crucial when the wave amplitude is large, and the structural members of the floating structure are slender. Wave inertia (radiation) load is initiated by the disturbed waves created by the motions of the floating body.

The Hydrodynamic Diffraction (HD) and Hydrodynamic Response (HR) numerical tools utilised in the SHARPE numerical modelling scheme employs three-dimensional panel methods to analyse the hydrodynamic behaviour of the structure in waves (see Fig. 5.4. As illustrated in Fig. 5.5 A mixed model comprising of diffracting panels and slender body components were created to investigate the effects of drag linearisation on the radiation/diffraction behaviour of the floater and to further compare frequency and time domain solutions when including viscous drag. Dummy Morison tube elements were included within the DeepCwind-OC5 and TRIHF structure to investigate the linearised solution for wave-structure interaction.

The HD and HR numerical tools are based on fluid potential theory and the representation of the structure surface using a series of diffracting panels (mesh) as presented in Fig. 5.4 and Fig. 6.34 for the DeepCWind-OC5 and the TRIHF platform, respectively. Fig. 5.5 and Fig. 6.35 contains an illustration of the dummy Morison drag modelling elements for the DeepCWind-OC5 and the TRIHF platform, respectively. The tube elements have a small diameter that is $1/100th$ to the size of real diameter of the floating platform parts. This is done so that the added mass effect is not doubled up since this is computed by AQWA from the diffraction model. Consequently, to include the viscous effect, the standard drag coefficient is multiplied by 100.

For the coupled dynamics simulation strategy, Linear Force Transfer Functions (LFTF) were computed as the main output of the frequency domain analysis for the platform motion per unit wave amplitude. The LFTF is a first-order term denoted by $H^{(1)}\omega$. The Response Amplitude Operator (RAO) also known as the Linear Motion Transfer Function (LMTF), ${x_{WA}}^{(1)}(\omega)$ gives the response per unit amplitude of wave excitation. The RAO can be expressed as a function of the wave frequency by;

$$ {x_{WA}}^{(1)}(\omega) = H^{(1)}\omega L^{-1}(\omega) \tag{5.1} $$

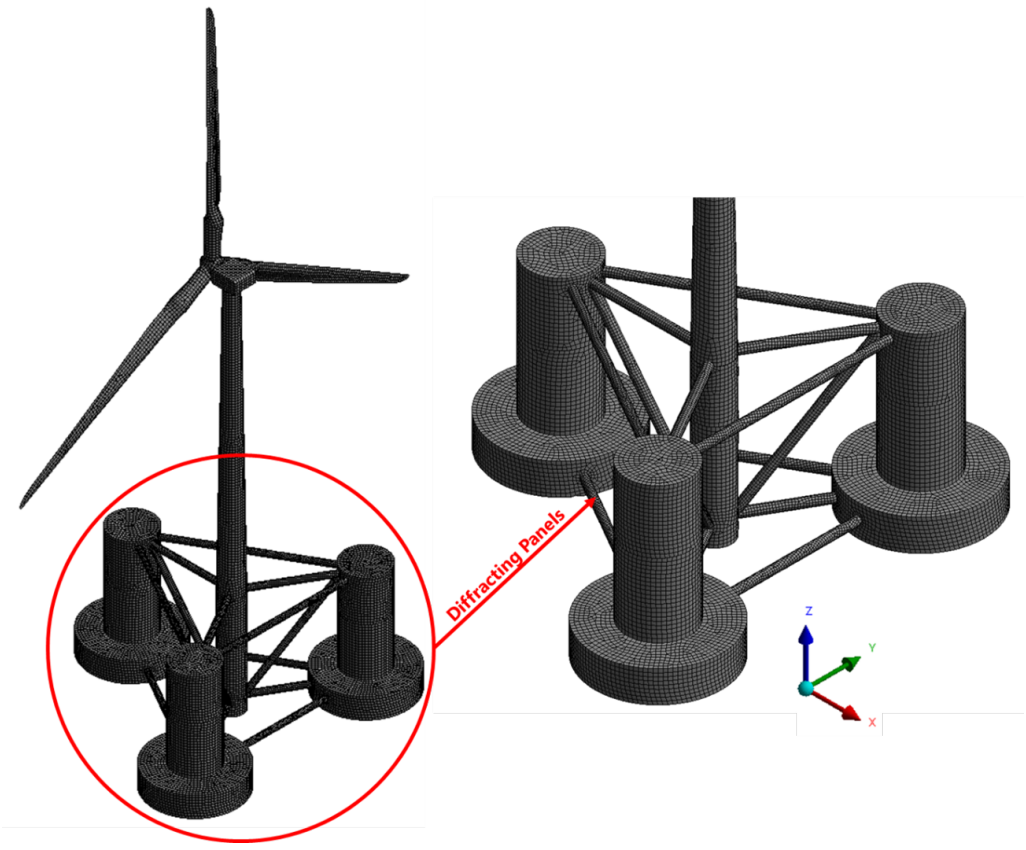

FIGURE 5.4: 3D model diffracting panels for hydrodynamic diffraction and radiation numerical simulation.

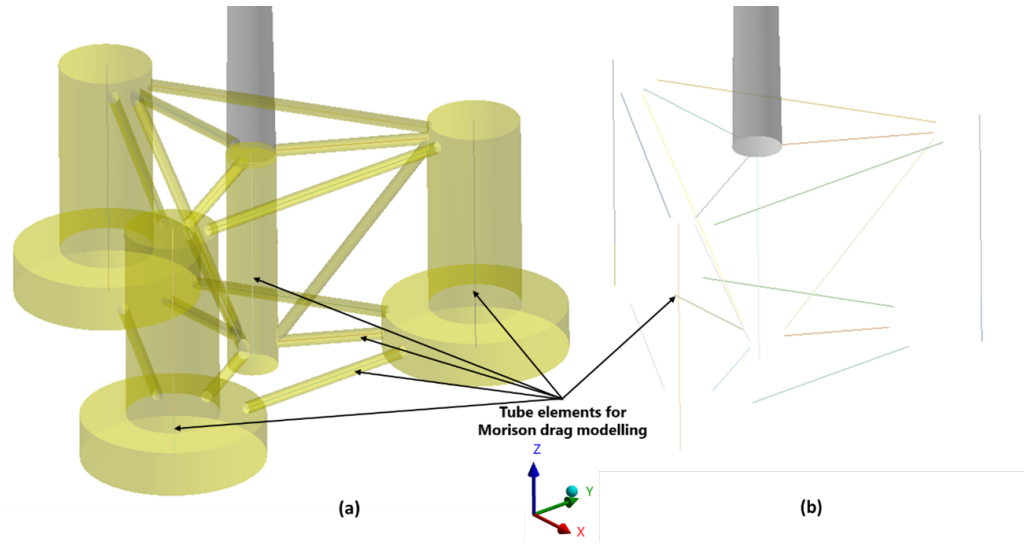

FIGURE 5.5: Illustration showing (a) tube elements defined within the diffracting geometry model (b) tube elements.

where $L\ (\omega)$ is an equation of motion characterised by the linear structural operator and can be expressed as;

$$L\left(\omega\right) = -\omega^2\left[M + A\left(\omega\right)\right] + i\omega B\left(\omega\right) + C \tag{5.2}$$

where M is the mass of the platform, A is the added mass, B the wave damping and C is hydrostatic and structural stiffness. Since the sea environment being modelled for the FOWT platform is an irregular wave spectrum, the frequency domain is very appropriate for floating structures exposed to random environments. The short-term response statistics of a floating structure can be estimated based on a response spectrum, $S_R\left(\omega\right)$, using the LMTF, ${x_{WA}}^{(1)}\left(\omega\right)$ and wave spectrum, $S_\eta\left(\omega\right)$ by the following relationship;

$$S_R\left(\omega\right) = \left|{x_{WA}}^{(1)}\left(\omega\right)\right|^2 S_\eta\left(\omega\right) \tag{5.3}$$

where $\omega = 2\pi/T$ is the angular frequency.

The time-domain solution for the coupled dynamics model was achieved using a non-linear integration scheme to facilitate consistency in the coupling effects between the WTG, floating platform, and the mooring system. The equation of motion modelled for the freely floating FOWT structure is given by;

$$M\ddot{x} + B\dot{x} + D_1\dot{x} + D_2 f\left(\dot{x}\right) + Kx = q\left(t, x, \dot{x}\right) \tag{5.4}$$

where M is the mass matrix, $m + A\left(\omega\right)$, including added mass and m is the structural mass. D_1 and D_2 are the linear damping matrix (including wave drift damping) and quadratic damping matrix, respectively. B is the potential damping matrix such that $B = B\left(\omega\right)$. f is the vector function and each element are given by $x_i\left|x_i\right|$. The position hydrostatic stiffness is represented by K and x is the position vector. The excitation forces, q on the right-hand side of equation 5.4 is given by;

$$q\left(t, x, \dot{x}\right) = q_{WA}^{(1)} + q_{WA}^{(2)} + q_{CU} + q_{W1} + q_{ext} \tag{5.5}$$

$q_{WA}^{(1)}$ and $q_{WA}^{(2)}$ are first order and second-order wave excitation force, respectively. Wave Frequency (WF) motions are created by the first-order wave excitation force while Low Frequency (LF) motions are excited by the wind drag force q_{W1}, current drag force q_{CU}, and slow varying second-order wave excitation as well as viscous drift. Sum frequency

second-order wave excitation force is the major source of High Frequency (HF) motions. The variable q_{ext} are any other forces such as the force from additional stiffness provided by the mooring system, user-defined forces and moments, and force coupling effects. For the rotor torque, a user-defined moment[2] of 3.95 MN.m was initiated about the x axis of the rotor's centre of mass to produce a synchronous rotor speed of 12.1 rpm for every time step of the simulation. The complete system of equations accounting for the FOWT rigid body model as well as the slender structure model of the mooring cables are solved simultaneously using a non-linear time-domain approach.

5.2 SHARPE Numerical Modelling Scheme Validation

5.2.1 Model Description - The DeepCWind-OC5 Semi-submersible

Coulling et al.'s OC4[3] [29] (see Fig. 5.6) project was a model experimentation performed in the Maritime Research Institute Netherlands (MARIN) wave basin, while Robertson et al.'s OC5 [30] (see Fig. 5.7) project was a revision of the OC4 project two years later. Both projects utilized the NREL 5-MW wind turbine system for the case study. Thus, the floating platform model for the current validation study is the DeepCwind-OC5 semi-submersible as illustrated in Fig. 5.8. The DeepCwind is a buoyancy stabilised floating platform that consists of three offset columns. The offset columns are made up of an upper column (Ø12 m) and a larger diameter base column (Ø24 m). The offset columns induce large buoyancy forces from the volumes of water displaced. The 6.5 m diameter centre column provides support for the wind turbine unit.

Three sets of 1.6 m diameter pontoons connect the offset columns to each other at the top and bottom. Similarly, another three sets of the pontoons connect the offset columns to the centre column at the top and bottom. Additionally, three cross braces connect the top of the offset columns to the base of the centre column. Fig. 5.9 contains an artistic impression showing the complete FOWT assemblage of the DeepCwind platform and the NREL 5 MW wind turbine baseline. A comparison of the FOWT geometric properties between the DeepCWind-OC5 and TRIHF are presented in Table 5.1.

[2] Rotor Torque $(N.m) = \frac{30 \times Rotor\ Power\ (Watts)}{\pi \times Rotor\ Rotation\ (rpm)}$

[3] Offshore Code Comparison Collaboration Continuation (OC4)

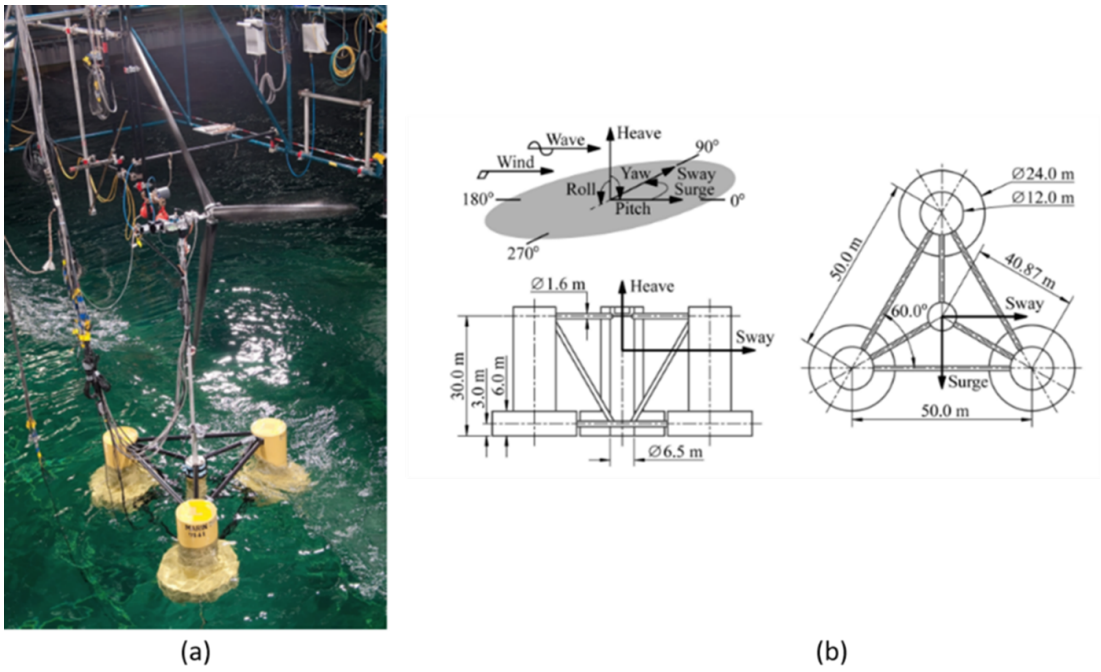

FIGURE 5.6: (a) Image showing the 1/50th scale model of DeepCwind semi-submersible platform used for experimentation in the MARIN offshore basin for the OC4 project. (b) Coordinate system and dimensions of the DeepCwind semi-submersible platform for the OC4 project[29].

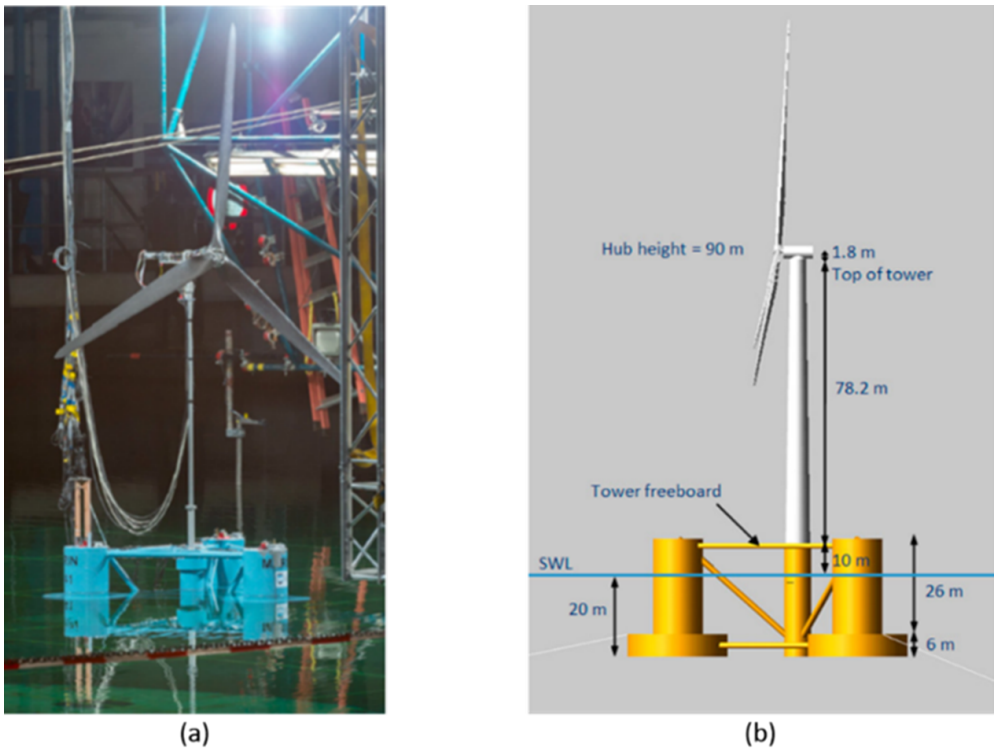

FIGURE 5.7: (a) Image showing the 1/50th scale model of DeepCwind semi-submersible platform used for experimentation in the MARIN offshore basin for the OC5 project. (b) The DeepCwind semi-submersible FOWT geometry for the OC5 project [30].

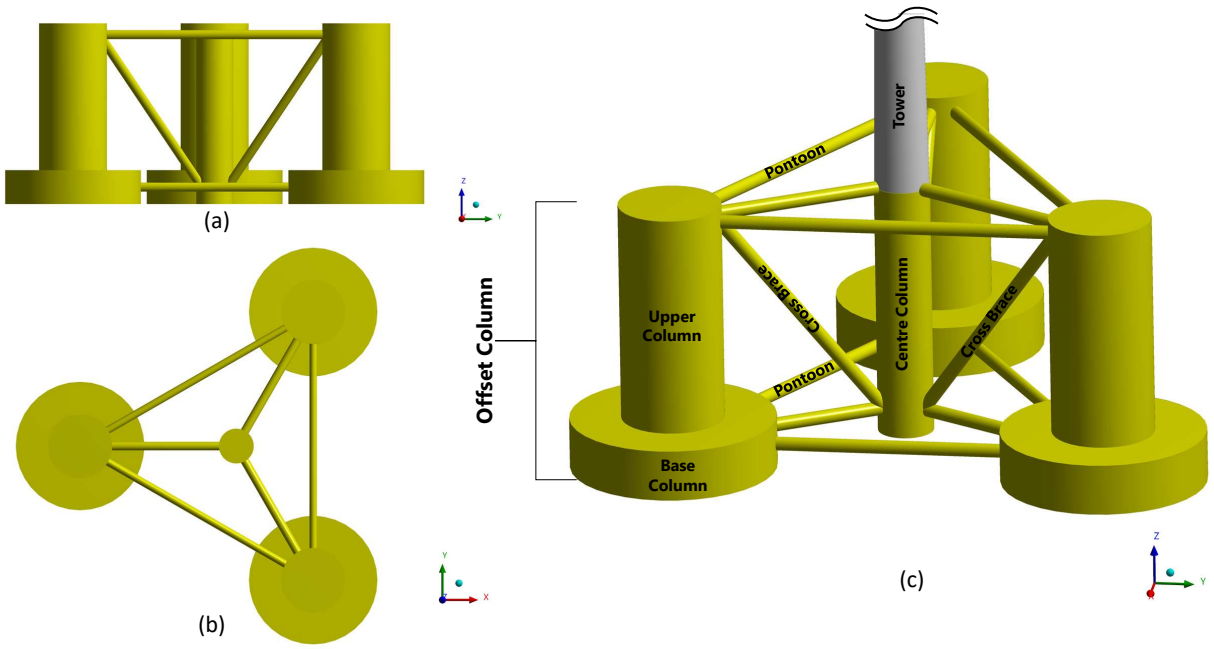

FIGURE 5.8: An artistic impression of the DeepCwind semi-submersible showing (a) front view from the x-direction. (b) top view from the z-direction. (c) isometric view with labelled components.

A three-line catenary mooring configuration symmetrically arranged about the z-axis of is the principal choice for the DeepCwind platform which yields an angle of 120° between adjacent lines. The depth of the fairleads below SWL is 14 m. Each of the mooring line has an unstrectched length of 835.5 m. Fig. 5.10 presents an illustration of the mooring configuration and nomenclature while Fig. 5.11 shows the mooring line arrangements with respect to the sea domain. Table 5.2 contains the mooring system properties.

As can be observed from Fig. 4.17 and Fig. 5.6 to Fig. 5.9, the TRIHF and the DeepCwind floating structure are a bit similar in geometry. However, an obvious difference can be noted in the drafts of both structures, installed water depth, mooring configuration, and overall mass. The static equilibrium parameters highlighted in Table 5.1 stresses some key differences in the floating platform's structural properties. It is noteworthy that the hydrostatic stiffness for TRIHF considers the additional stiffness offered by the taut leg mooring line. In addition, the DeepCwind is a buoyancy stabilised floating platform, unlike TRIHF which uses a combination stability (buoyancy, mooring line stiffness, and ballast) concept.

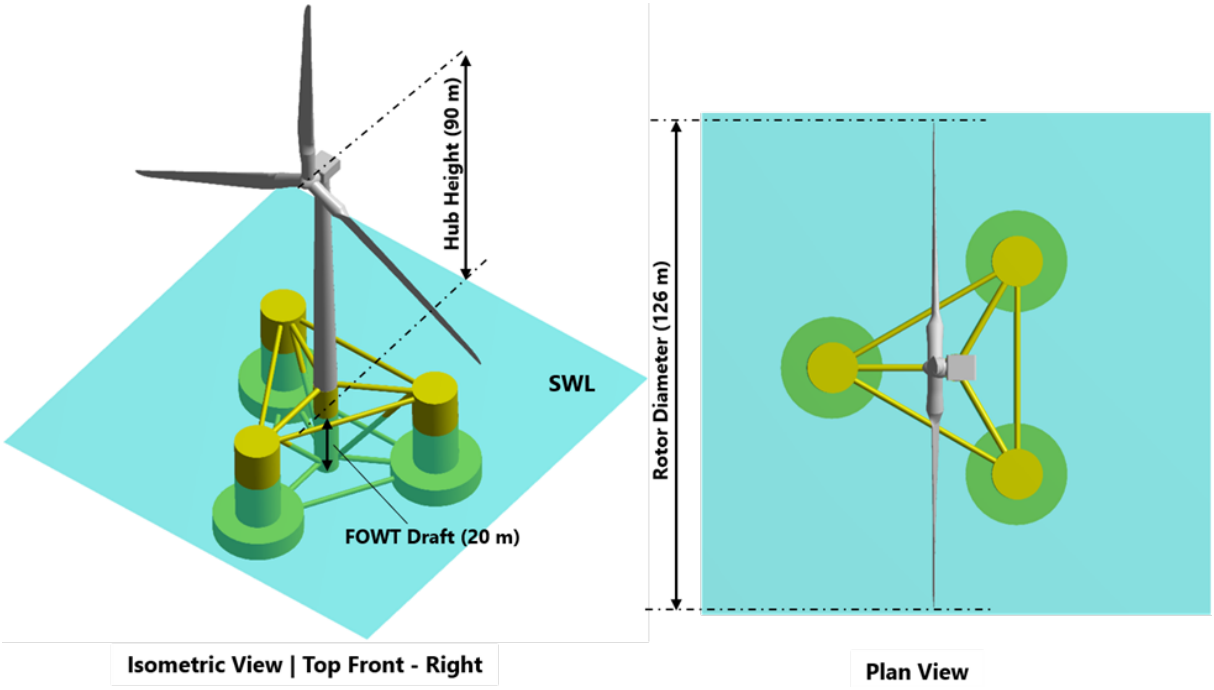

FIGURE 5.9: Artistic impression showing the complete FOWT assemblage of the DeepCwind-OC5 platform and NREL 5 MW wind turbine baseline.

TABLE 5.1: A comparison of FOWT parameters between TRIHF and DeepCwind-OC5 project.

Parameters	FOWT	
	DeepCwind-OC5	TRIHF
Rotor Diameter (m)	126	126
Hub Height above SWL (m)	90	100.85
Design Draft (m)	20	36
Volumetric Displacement (m^3)	13,917	12,022
Total Mass of FOWT (kg)	13,958,000	10,868,129
Mass of Platform only, including Ballast (kg)	12,919,000	10,170,669
Centre of Mass (CM) below SWL (m)	14.09	19.94
Centre of Buoyancy (CB) below SWL (m)	13.15	8.29
Installed Water Depth (m)	200	300
Cut Water Plan Area (m^2)	1,390	1,258
Static Buoyancy Force (N)	1.40E+08	1.21E+08
Hydrostatic Restoring in heave (N/m)	3.84E+06	1.26E+07
Hydrostatic Restoring in roll (N-m/rad)	3.78E+08	4.30E+09
Hydrostatic Restoring in pitch (N-m/rad)	3.78E+08	4.30E+09
Roll Inertia about CM (kg-m^2)	1.39E+10	8.79E+09
Pitch Inertia about CM (kg-m^2)	1.56E+10	8.78E+09
Yaw Inertia about CM (kg-m^2)	1.37E+10	7.45E+08

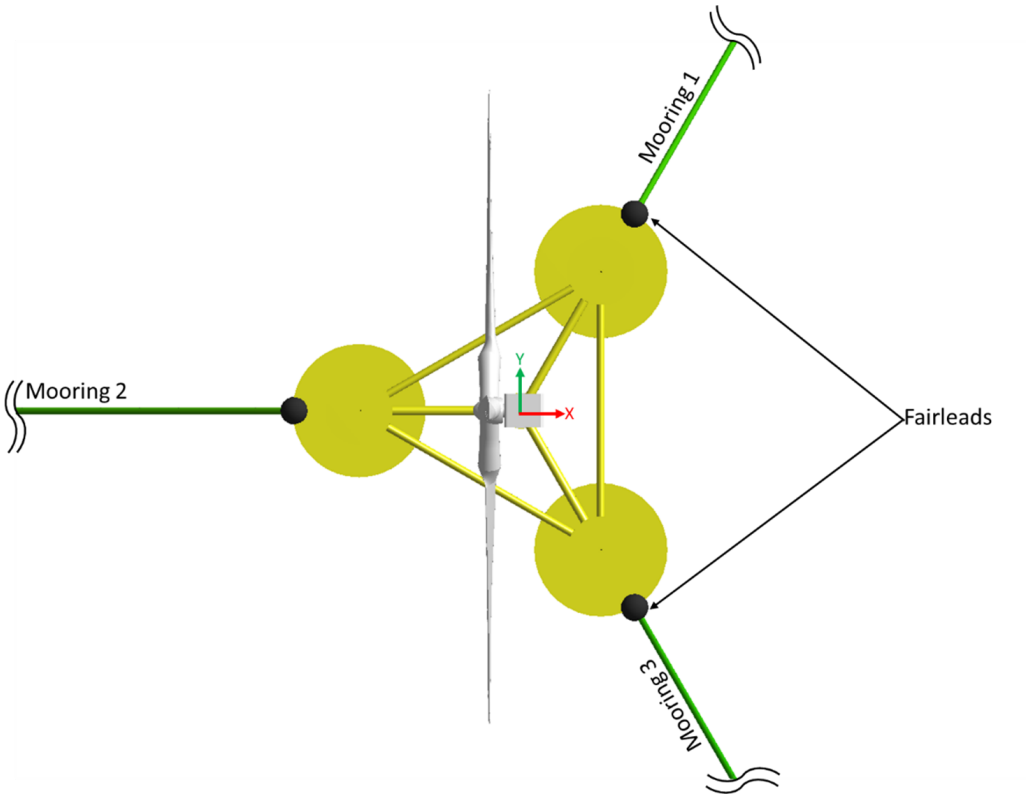

FIGURE 5.10: The DeepCwind-OC5 FOWT platform mooring configuration and nomenclature (plan view).

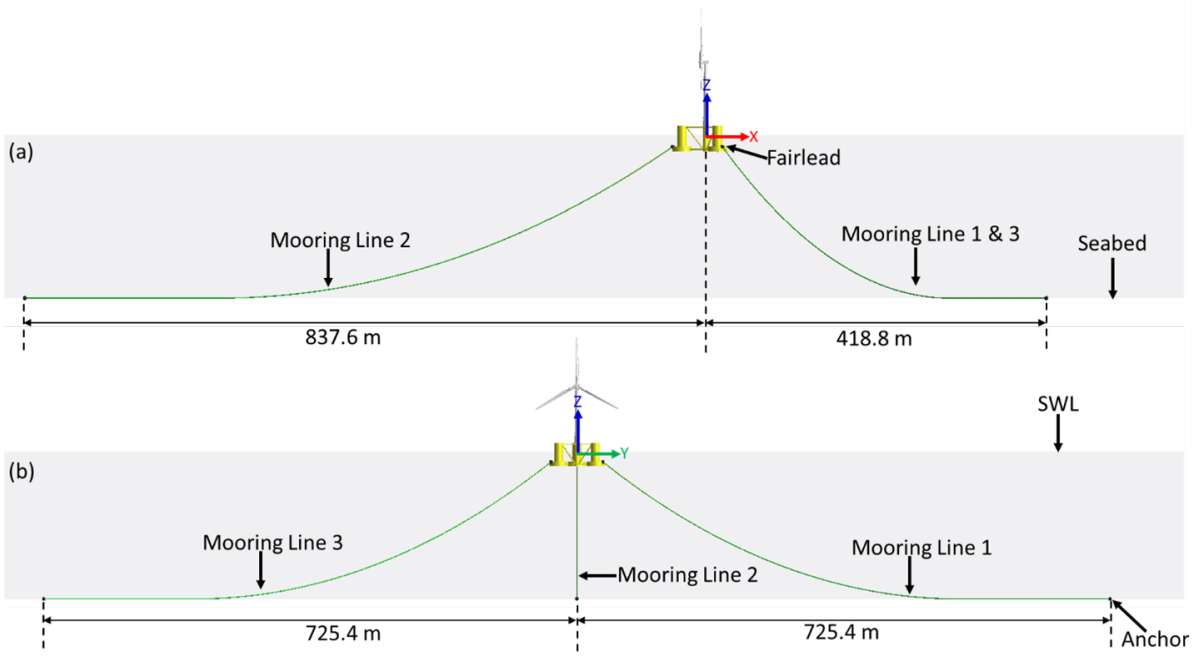

FIGURE 5.11: Illustration showing sea domain, mooring line configuration, and coordinates for (a) side view from the y-direction (b) front view from the x-direction used for the validation study.

TABLE 5.2: The DeepCWind-OC5 Platform Mooring System Properties[30].

Parameters	Value
Number of mooring lines	3
Angle between adjacent mooring lines	120°
Anchor depth	200 m
Fairlead depth	14 m
Anchor radius from FOWT centerline	837.6 m
Fairlead radius from FOWT centerline	40.868 m
Mooring line unstretched length	835.5 m
Mooring line diameter (Line 1)	0.1369 m
Mooring line diameter (Line 2)	0.1398 m
Mooring line diameter (Line 3)	0.1393 m
Mooring line mass density (Line 1)	125.6 kg/m
Mooring line mass density (Line 2)	125.8 kg/m
Mooring line mass density (Line 3)	125.4 kg/m
Mooring line submerged weight (Line 1)	9.051×10^5 N
Mooring line submerged weight (Line 2)	9.017×10^5 N
Mooring line submerged weight (Line 3)	8.997×10^5 N
Mooring line stiffness (Line 1)	7.52×10^8 N
Mooring line stiffness (Line 2)	7.46×10^8 N
Mooring line stiffness (Line 3)	7.47×10^8 N
Mooring line pre-tension (Line 1)	1.107×10^6 N
Mooring line pre-tension (Line 2)	1.112×10^6 N
Mooring line pre-tension (Line 3)	1.148×10^6 N

The platform coordinate system definition used in performing the hydrodynamic diffraction/radiation and hydrodynamic response analysis are consistent with recommended standards and practices [48], [76], [92] where z-direction corresponds with height and positive from points above the MSL and negative for points below the MSL. The global coordinate centre (0,0,0) m is located at the centre of the platform on the SWL. Wind and wave direction are positive toward the x-direction and angle of attack is measured in a clockwise direction. Fig. 5.12 (left) contains the precise mass for each of the DeepCWind-OC5's platform component while Fig. 5.12 (right) shows the total hydrostatic precise mass for the assemblage. In Fig. 5.12 (left), the centre of mass and principal moment of inertia for each component of the FOWT were set-up discretely and then solved to provide a combined solution for centre of mass and principal moment of inertia shown in Fig. 5.12 (right).

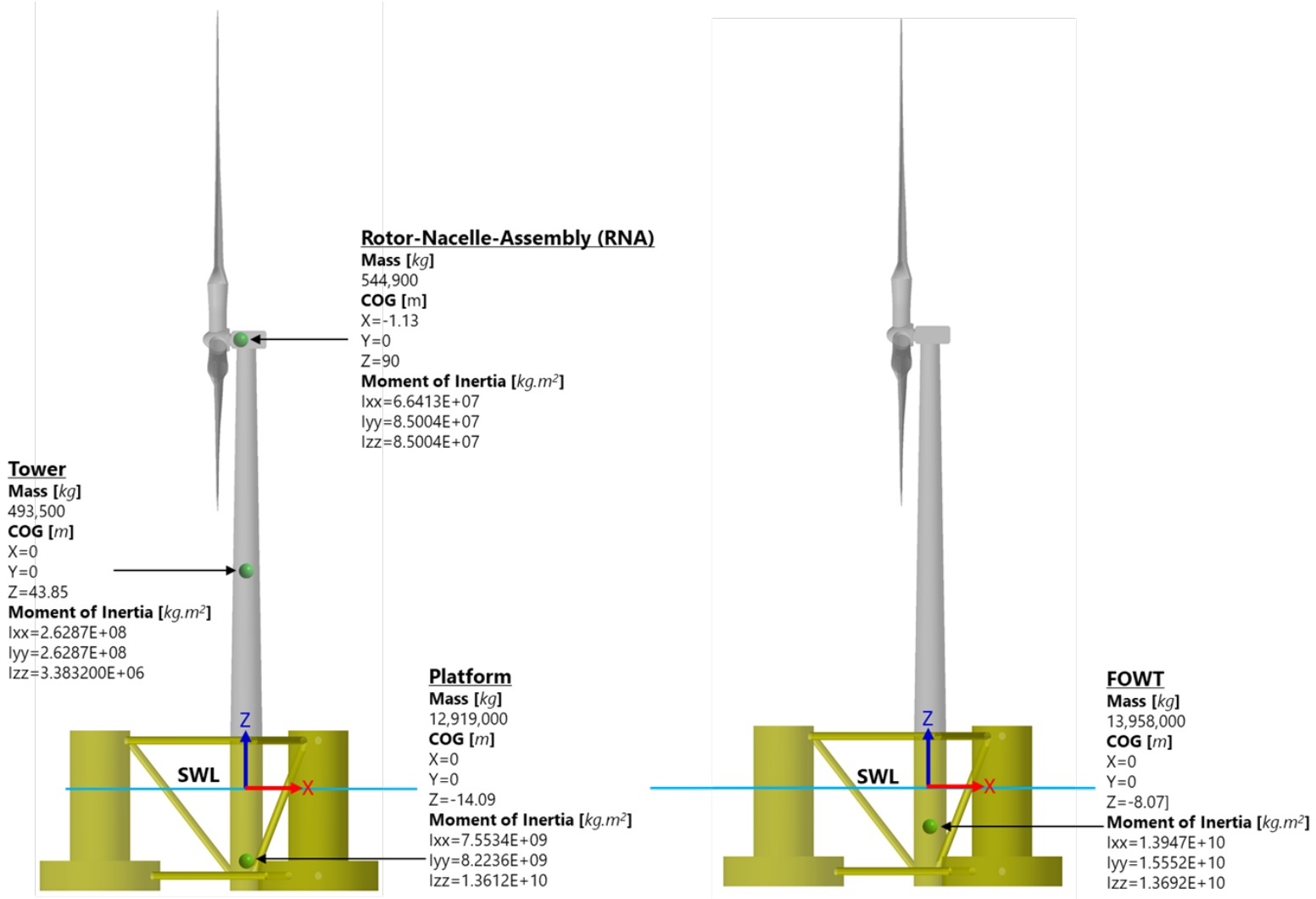

FIGURE 5.12: The DeepCwind FOWT precise mass for each component (left) and assemblage hydrostatics calculation (right).

5.2.2 Environmental Conditions and Design Load Case (DLC)

The environmental constants employed for the validation study are highlighted in Table 5.3 while Table 5.4 contains the Load Case (LC) used in performing the coupled dynamics simulation. The LC is performed under the operational wave with the inclusion of steady wind. The irregular Airy wave model with a JONSWAP spectrum having a gamma factor of 2.2 was modelled in the flow domain. The LC presented in Table 5.3 is consistent with LC 4.1 (MARIN Test No 906007) in the scaled model experimental test performed by Robertson et.al where they studied and validated the global loads of the DeepCwind-OC5 floating semi-submersible Wind Turbine [30]. The time domain simulation was performed for 180 min using a time step of 0.1 s. Fig. 5.13 contains an illustration showing the direction definition for wind and wave loads. Since there was no mention of ocean current load in the experimental study by Robertson et al. [30], it was not considered in the validation study for the SHARPE numerical scheme.

TABLE 5.3: Environmental constants for the validation study.

Environmental Constants	Value
Water Depth	200 m
Water Density	1025 kg/m^3
Water Size X	1000 m
Water Size Y	1000 m
Gravity	9.80665 m/s^2
Seabed Type	No composite cable seabed

TABLE 5.4: Design load case for validation studies.

Load Case	Turbine Condition	MARIN Test No	Wind Condition @ Hub	Irregular Wave Condition		Time Domain Simulation Length
				H_s	T_p	
4.1	12.1 RPM	906007	12.91 m/s	7.1 m	12.1 s	180 min

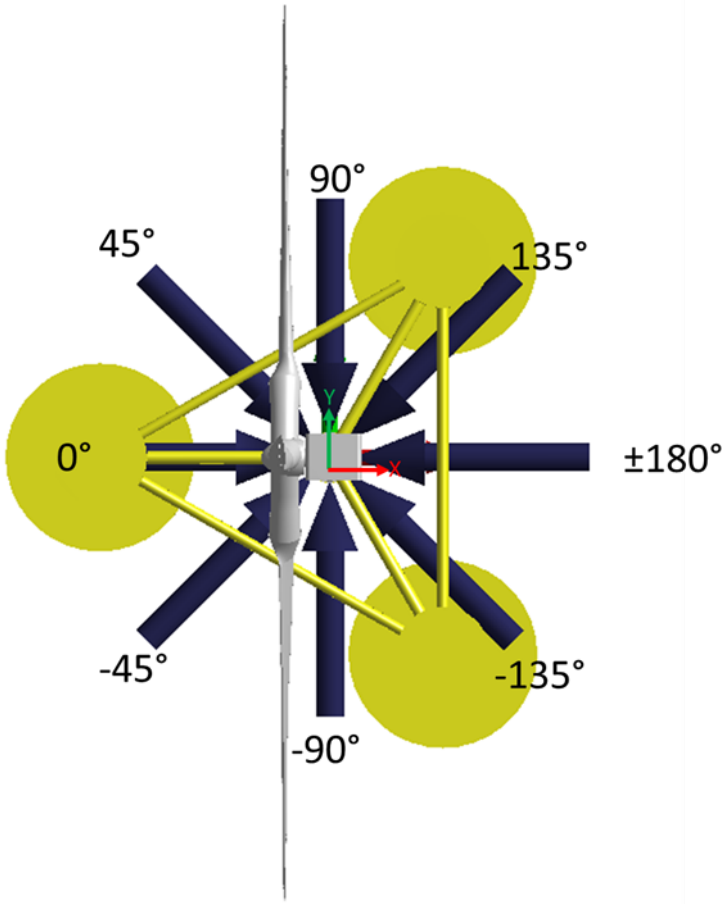

FIGURE 5.13: Illustration showing direction definition for wind and wave.

5.2.3 Model Validation

A free decay test was performed To evaluate the natural period and damping properties of the DeepCWind-OC5 platform with respect to motion in the vertical plane (heave, roll, and pitch). As shown in Fig. 5.14, the platform's centre of gravity was shifted by a distance (-2.5 m for heave) and tilted by an angle (-4°for roll and pitch) from its equilibrium position in still water at time t = 0 s. A time history of the freely decaying response was then calculated in the TD analysis.

A comparison of the natural period results between the numerical simulation and the experimental test are presented in Table 5.5 while Table 5.6 contains a summary of the platform's total damping and viscous damping properties. The results presented in Table 5.6 are based on the calculation procedures discussed in Section 6.1.1. As can be observed from the results presented in Table 5.5, the calculated natural periods for

heave, roll, and pitch motion for the numerical simulation are in good agreement with the experimental test results.

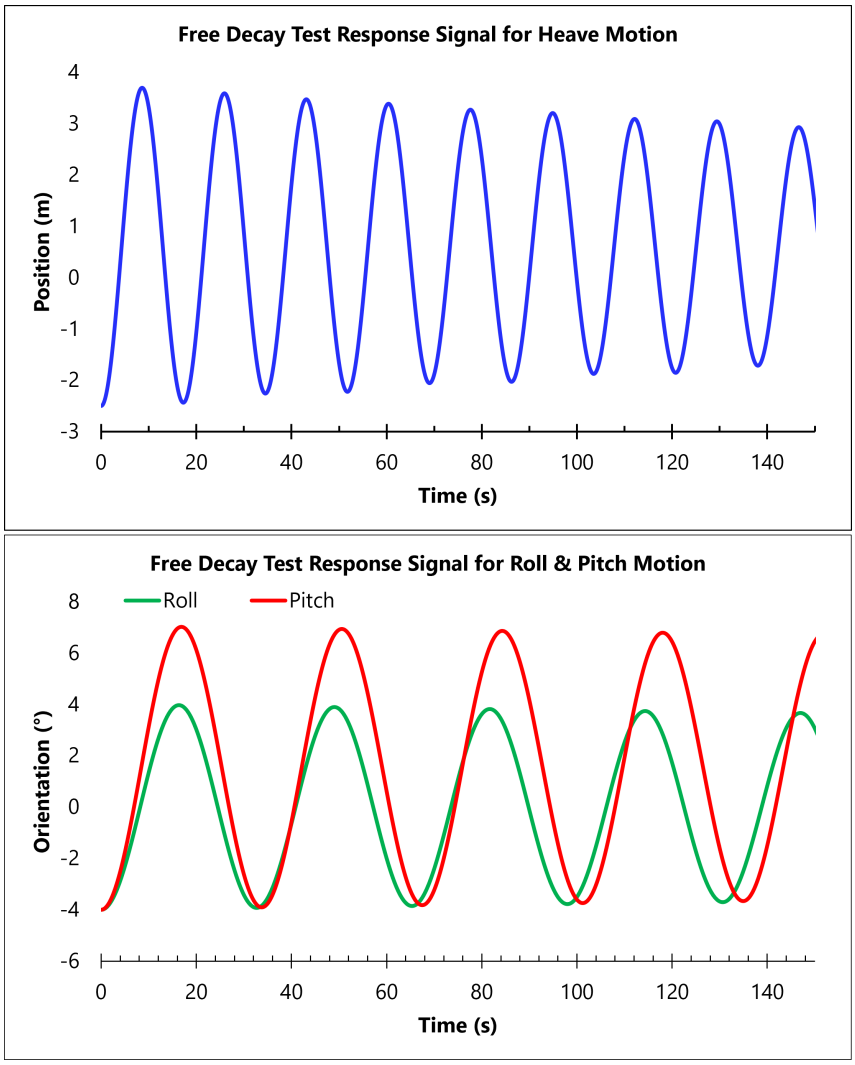

FIGURE 5.14: Free decay test response signal for the DeepCWind-OC5 Floating Platform for heave motion(top) and roll and pitch motion (bottom).

An important observation can be made from the calculated damping properties of the DeepCWind-OC5 platform as shown in Table 5.6. Here, it is clear that viscous damping constitutes 98% of the total damping for heave motion and 100% of the total damping for roll and pitch motion. Consequently, it is imperative to account for viscous damping when performing a coupled dynamics simulation for FOWTs.

TABLE 5.5: A comparison of simulation and experimental test result for platform natural period.

Degree of Freedom	Natural Period (s)	
	Simulation	Experiment
Heave	17.3	17.5
Roll	32.7	32.8
Pitch	33.7	32.5

TABLE 5.6: Platform damping ratio and viscous damping coefficient.

Degree of Freedom	Total Damping Ratio	Total Damping Coefficient	Viscous Damping Coefficient	Ratio of Viscous Damping to Total Damping
Heave	0.0045	9.39E+04 N/(m/s)	7.34 E+04 N/(m/s)	98%
Roll	0.0030	4.07E+05 N.m/(°/s)	4.07 E+05 N.m/(°/s)	100%
Pitch	0.0026	3.70E+05 N.m/(°/s)	3.70 E+05 N.m/(°/s)	100%

A comparison of the time series statistics results between the experimental test data and simulation are provided in Table 5.7. The SHARPE numerical modelling scheme for the current study provides a satisfactory agreement with the test data for most of the parameters investigated. The statistics for surge motion, heave motion, and pitch motion are in very good agreement with the test data. Also, the fairlead tensions statistics for the simulation compares fairly with the test data although the standard deviations are in very good agreement.

TABLE 5.7: A comparison of time domain statistical summary result between simulation and experimental test..

Parameter	Unit	Average		Max		Min		Std.Dev	
		Sim	Exp	Sim	Exp	Sim	Exp	Sim	Exp
Wave Surface Elevation	[m]	-0.001	-0.01	6.06	7.94	-6.32	-6.80	1.78	1.75
Surge	[m]	12.45	10.38	18.04	16.71	8.11	6.43	1.42	1.36
Sway	[m]	-0.08	-1.08	0.27	-0.23	-0.38	-1.66	-0.08	0.16
Heave	[m]	0.22	-0.05	5.20	2.33	-4.83	-2.14	2.00	0.48
Roll	[°]	-0.05	-0.20	0.97	0.34	-1.10	-0.65	0.25	0.12
Pitch	[°]	-0.36	4.74	1.53	7.78	-2.27	1.80	0.52	0.78
Yaw	[°]	0.09	0.19	074	1.11	-0.53	-0.83	0.17	0.28
Fairlead Tension (Line 1)	[kN]	485.66	891.51	685.28	1092.82	338.57	648.96	38.82	44.08
Fairlead Tension (Line 2)	[kN]	1505.65	1778.97	3386.64	4085.82	36.52	308.68	502.69	302.71
Fairlead Tension (Line 3)	[kN]	355.12	906.34	681.96	1102.51	355.12	656.77	39.62	41.49
Rotor Thrust Coefficient		0.69	0.74	1.19	1.28	0.30	0.16	0.12	0.14

Chapter 6

Engineering and Mathematical Analysis

This chapter will present all the most relevant schemes surrounding the engineering and mathematical simulations performed for the TRIHF-OWT concept. The modus-operandi and significant concepts behind the coupled dynamics modelling are deliberated and the basis for developing a more streamlined yet wholistic (time domain and frequency domain) coupled dynamics simulation strategy is discussed. The numerical scheme for the current research incorporates potential based rigid body motion analysis where viscous damping coefficients from free decay tests of the floating platform and force coefficients from wind and ocean current loads of the FOWT assemblage were obtained using CFD. Here, the CFD numerical simulation is executed to determine the viscous force from wind and ocean current loads, and viscous damping coefficients for heave, roll, and pitch motions. The boundary conditions, pre-processing strategies, solver strategies, and the mesh refinement studies implemented for the CFD numerical simulation will be argued in detail. The results from the CFD numerical simulation is then applied as part of the solver strategy of the Floating Rigid Body Dynamics (FRBD) potential based solver employed for this research (ANSYS AQWA). The implementation of the CFD results in the FRBD solver enhances its capability by creating a wholistic finite element model that provides a true representation of the dynamic loads in a marine offshore environment. The static stability solution derived from the Hydrodynamic Diffraction (HD) calculations and the dynamic stability primal solution derived from the Hydrodynamic Response (HR) calculations for the TRIHF design concept are also explored. A published journal article by the author for the viscous damping investigation study is available here [132].

6.1 CFD Numerical Simulation Analysis

Viscous flow around a FOWT in an offshore environment is turbulent in nature and thus will require a turbulence flow modelling approach that can accurately capture the flow regime around the surfaces of the FOWT. Direct Numerical Simulation (DNS) provides an accurate solution for modelling external turbulent flow around a surface or body. The Reynolds Averaged Navier-Stokes Equation (RANSE) based methodology is a DNS approach that provides high fidelity simulation for external flow. Here, the DNS numerically integrates the RANS equation by determining and resolving all the spatial and temporary fluctuations/spectrum without resorting to modelling [133], [134]. Most importantly, the results from a DNS study is very useful in making sound engineering judgement and decisions because it provides very detailed information about the flow phenomena around the surface being studied.

6.1.1 Viscous Damping Numerical Calculation

The boundary conditions for viscous damping investigation are in principle the same as the boundary conditions for wave-structure interaction as illustrated in Fig. 2.18 to Fig. 2.22. However, the only key difference is that there is no wave loading considered since the numerical simulation is performed in flat wave (i.e., calm water). For this research, the total damping coefficients for the coupled heave-roll-pitch motion were investigated using a forced oscillation free decay numerical computation test. Theoretically, the total damping experienced by a floating platform consists of two elements; viscous damping and radiation damping. The strategy here will be to determine the radiation damping coefficient using a potential based solver such as ANSYS AQWA, and then theoretically calculate the total damping coefficients for heave (b_{33}), roll (b_{44}) and pitch (b_{55}) using these expressions;

$$b_{33} = 2\varsigma_{33}\sqrt{(m + m_a)\, c_{33}} \tag{6.1}$$

$$b_{44} = 2\varsigma_{44}\sqrt{(I_{44} + I_{a44})\, c_{44}} \tag{6.2}$$

$$b_{55} = 2\varsigma_{55}\sqrt{(I_{55} + I_{a55})\, c_{55}} \tag{6.3}$$

where I_{44} and I_{55} are the moments of inertia about the roll and pitch axis, respectively. Similarly, I_{a44} and I_{a55} are the added moment of inertia about the roll and pitch axis, respectively. m is the total mass of the structure while m_a is the added mass of the structure. Journee and Massie [135] in their text literature provided an analytical method for determining the non-dimensional total damping coefficient, ς_{ij}. Here, ς_{ij} is determined from the coupled heave-roll-pitch response signal in a forced oscillation free decay test which is expressed as;

$$\varsigma_{ij} = \frac{1}{2\pi} ln \left(\frac{\vartheta_o - \vartheta_1}{\vartheta_2 - \vartheta_3} \right) \tag{6.4}$$

As illustrated in Fig. 6.1, ϑ_o is the initial translational displacement for heave motion, and initial angular displacement for roll and pitch motion. ϑ_1, ϑ_2,....., ϑ_n are the zeniths of the response signals from the free decay test. Koh and Cho [136] in their recent studies investigated the heave motion of a circular cylinder with dual damping plates where the viscous damping coefficients for heave, roll, and pitch motion were obtained using these expressions;

$$b^{\psi}_{55} = 2\varsigma_{33}\sqrt{(I_{33} + I_{a33})\, c_{33}} - b^{r}_{33}\,(\omega_{0,\ 33}) \tag{6.5}$$

$$b^{\psi}_{44} = 2\varsigma_{44}\sqrt{(I_{44} + I_{a44})\, c_{44}} - b^{r}_{44}\,(\omega_{0,\ 44}) \tag{6.6}$$

$$b^{\psi}_{55} = 2\varsigma_{55}\sqrt{(I_{55} + I_{a55})\, c_{55}} - b^{r}_{55}\,(\omega_{0,\ 55}) \tag{6.7}$$

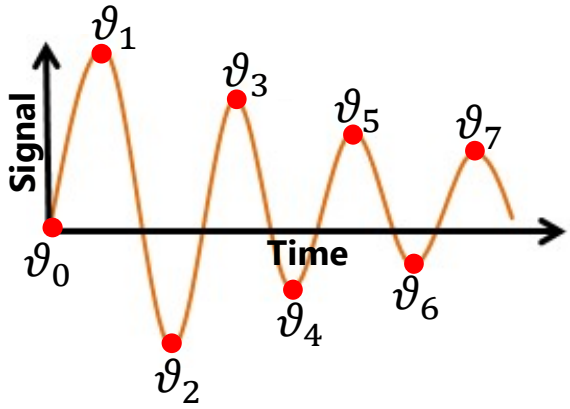

FIGURE 6.1: Free decay signals showing peaks with respect to time.

where b_{33}^{ψ}, b_{44}^{ψ} and b_{55}^{ψ} are the viscous damping coefficients for heave, roll, and pitch motion, respectively. c_{33}, c_{44}, and c_{55} are the restoring force/moment coefficients. $b_{33}^{r}\left(\omega_{0,33}\right)$, $b_{44}^{r}\left(\omega_{0,44}\right)$, and $b_{55}^{r}\left(\omega_{0,55}\right)$ are the radiation damping coefficients at the respective Undamped Natural Frequency (UNF). The radiation damping is calculated using the potential based solver in ANSYS AQWA. At the undamped natural frequency, the motion of the total mass of the structure lags the hydrodynamic forces by a phase angle of 90°. The radiation damping coefficients at the undamped natural frequency is proffered as an input in the calculation because viscous damping is frequency independent. The undamped natural frequencies are defined as $\omega_{0,33} = \sqrt{c_{33}/(m+m_a)}$, $\omega_{0,44} = \sqrt{c_{44}/(I_{44}+I_{a44})}$, and $\omega_{0,55} = \sqrt{c_{55}/(I_{55}+I_{a55})}$ for heave, roll and pitch motions, respectively.

Model Set-up, Boundary Conditions, and Pre-processing Strategies

A three-dimensional Dynamic Fluid Body Interaction (DFBI) physics continuum with overset meshing strategy was employed in performing the numerical simulation for the free decay test of TRIHF. The CAE toolkit used in this instance is STAR-CCM+ due to its computation capability, in addition to the author's familiarity with the software program. The Volume of Fluid (VOF) wave solver with Eulerian multiphase (air and water) was employed to capture the free surface of the mean sea level. The $k-\epsilon$ turbulence model with the realisable $k-\epsilon$ two-layer all $y+$ treatment was initiated to adequately capture the viscous flow conditions around the TRIHF structure. For convenience and to reduce the computational effort, only the floating platform's body was used in performing the free decay test. However, the mass, centre of mass, and moments of inertia used in performing the numerical simulation is for the complete assemblage. Fig. 6.2 shows the computational domain size and boundary conditions for the free decay test.

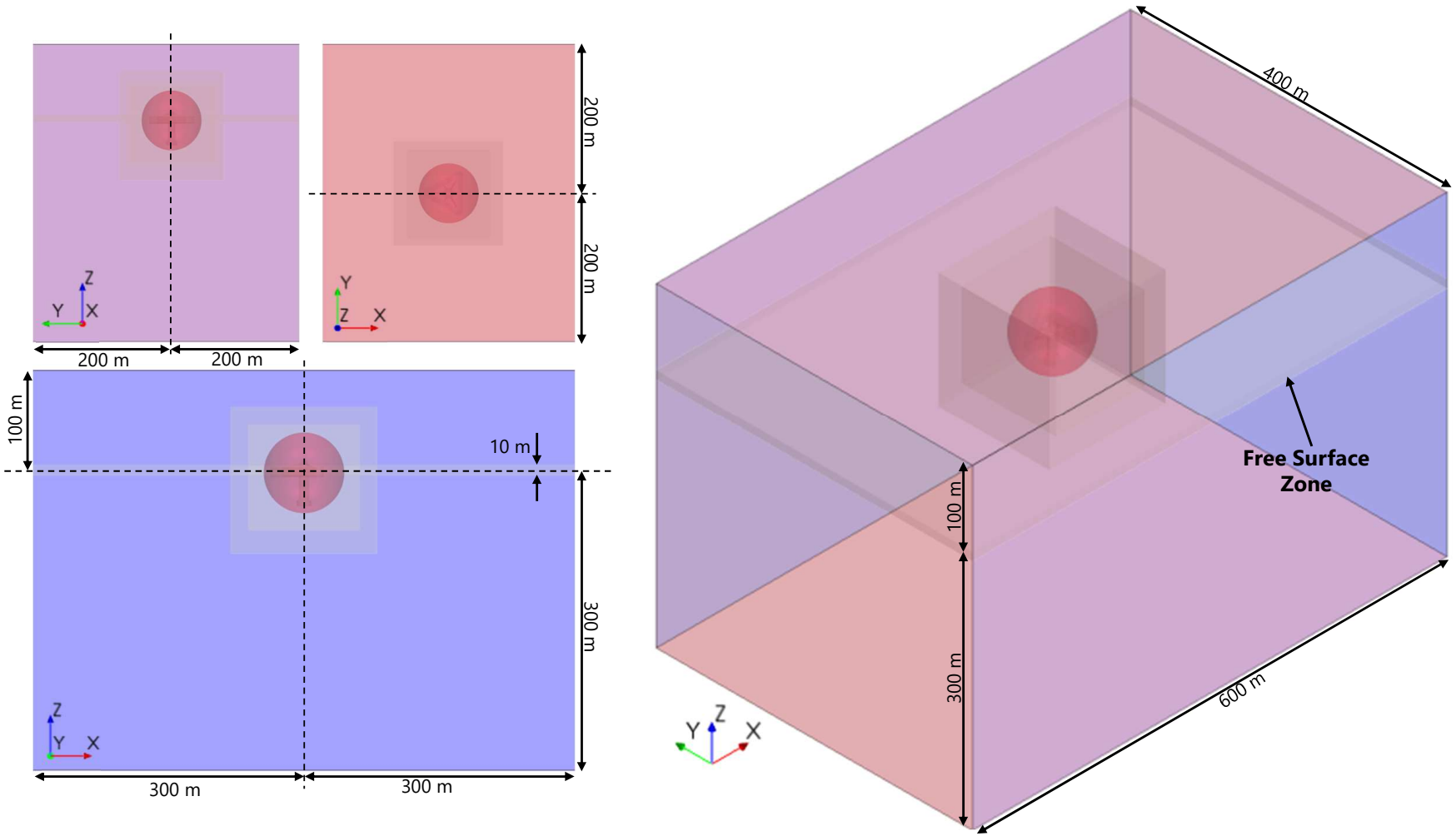

FIGURE 6.2: Computation Domain used for Free Decay Size.

As can be observed from Fig. 6.2, the size of the domain was set to 300 m in depth below the free surface zone. To avoid the development of reverse flow from the boundaries of the domain during the simulation, the floating platform was placed at the centre of the domain and the length and width of the domain were geometricized to 600 m and 400 m, respectively. Fig. 6.3 illustrates the boundary conditions for the flow domain, while Fig. 6.4 and Fig. 6.5 illustrates the section plane of the meshing scheme adopted for the simulation. The overlap mesh region acts as an interface that couples the overset mesh region containing the rigid body structure (TRIHF), and the background region which mimics the environment. An implicit-unsteady state physics continuum was initiated for the regions of interests (background and overset). Due to the presence of Eulerian multiphase fluids in different phases, the effect of gravity acting on both is modelled using the gravity model. Also, the grid around TRIHF and the water-air interface (i.e., the free surface region) was made finer to capture the relevant flow details.

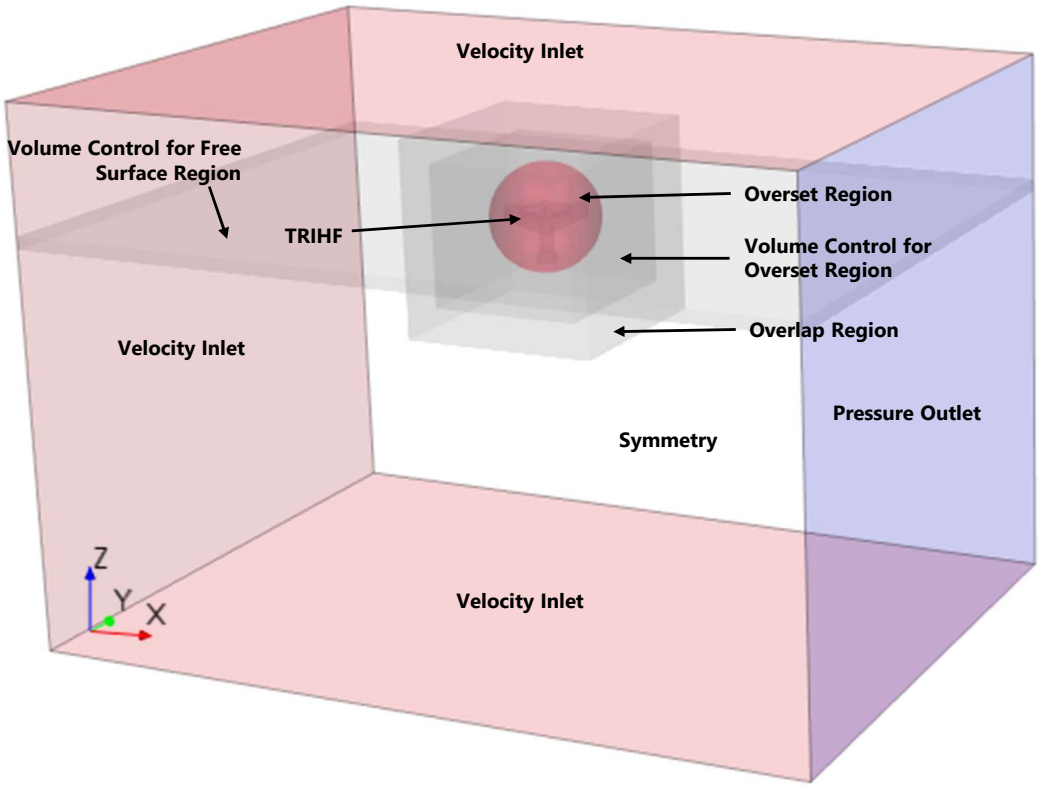

FIGURE 6.3: Boundary conditions for free decay test simulation.

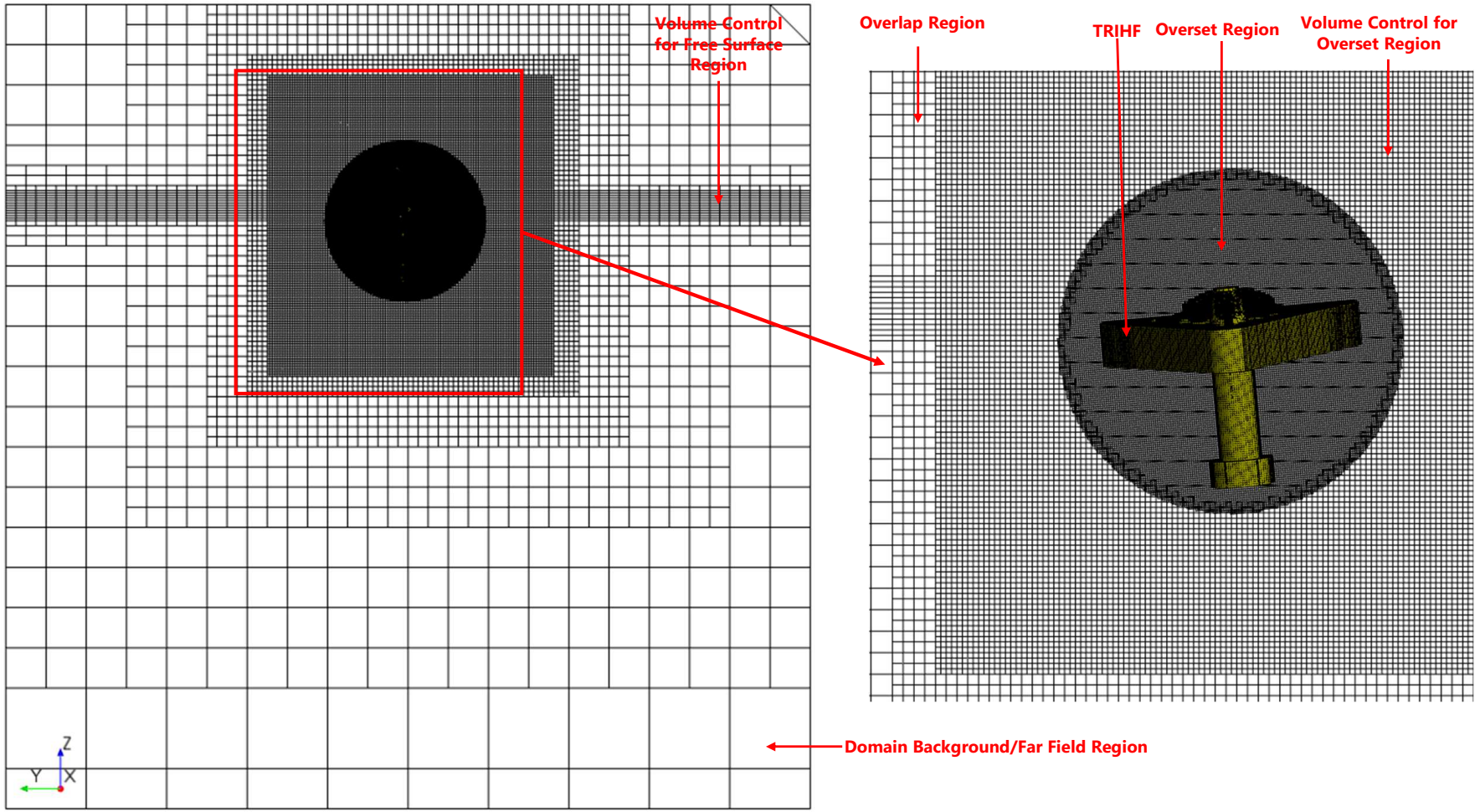

FIGURE 6.4: x-direction section plane with a zoomed view showing meshing scheme for free decay test (4.5 million cells).

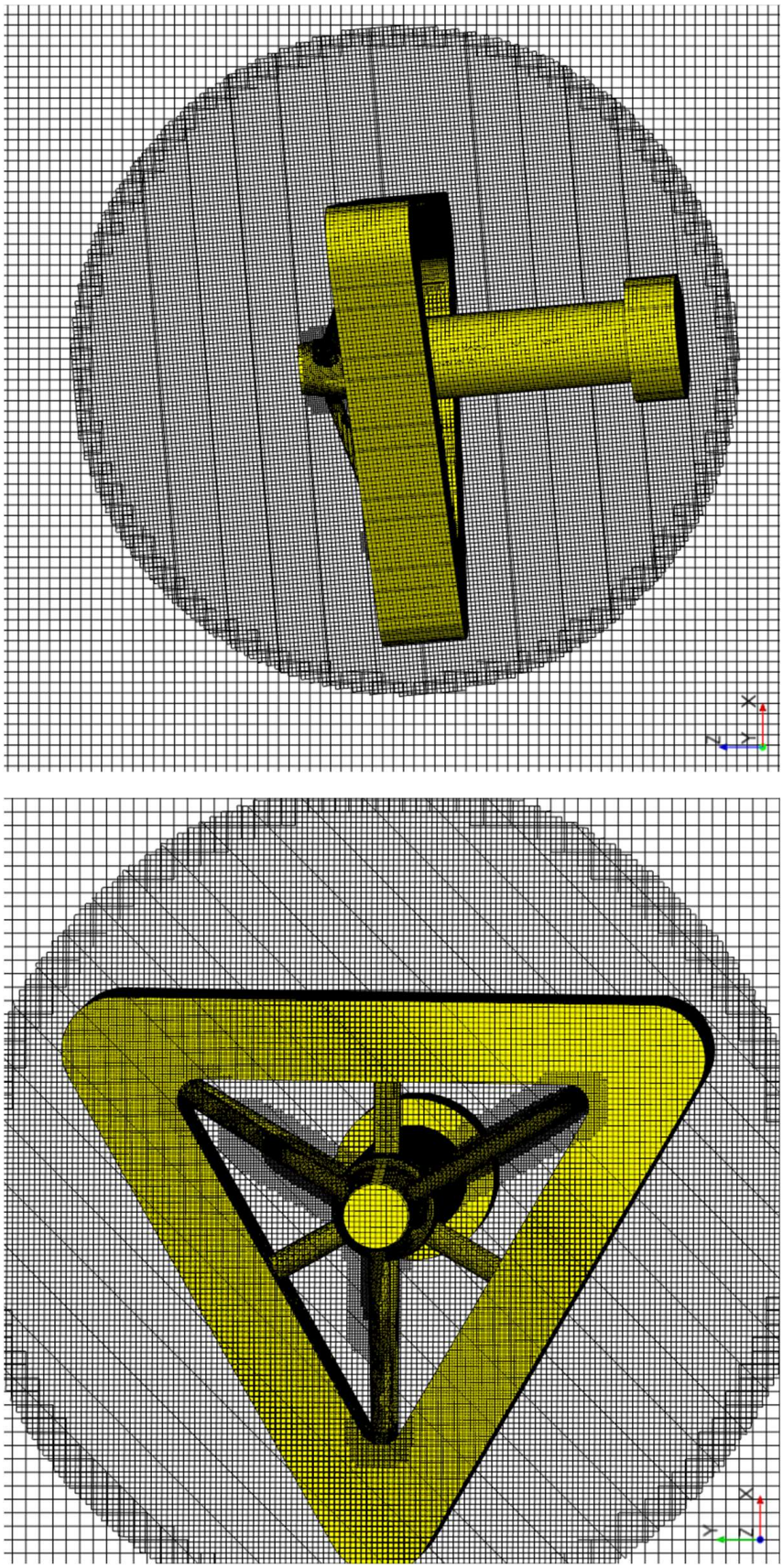

FIGURE 6.5: Section planes (left) z-direction slice plane and (right) y-direction slice plane showing meshing scheme for free decay test.

Fig. 6.6 to Fig. 6.8 below shows the scenes from cut planes on initialising the overset mesh interface and solution. After generating the mesh, TRIHF was given an initial displacement and orientations of –5 m, –5°, and –5°along the heave axis, and around the roll and pitch axis, respectively. The initial displacements for the degree of freedoms being considered has to be large enough to allow for at-least 3 peaks in the response signals. Thus, the initial displacements initiated in the CFD simulation is considered sufficient to produce at-least 3 peaks. On solving the numerical simulation, the force of gravity and buoyancy comes to play, thus restoring the platform to its initial equilibrium position. The numerical simulation was solved using a time step of 0.025 s.

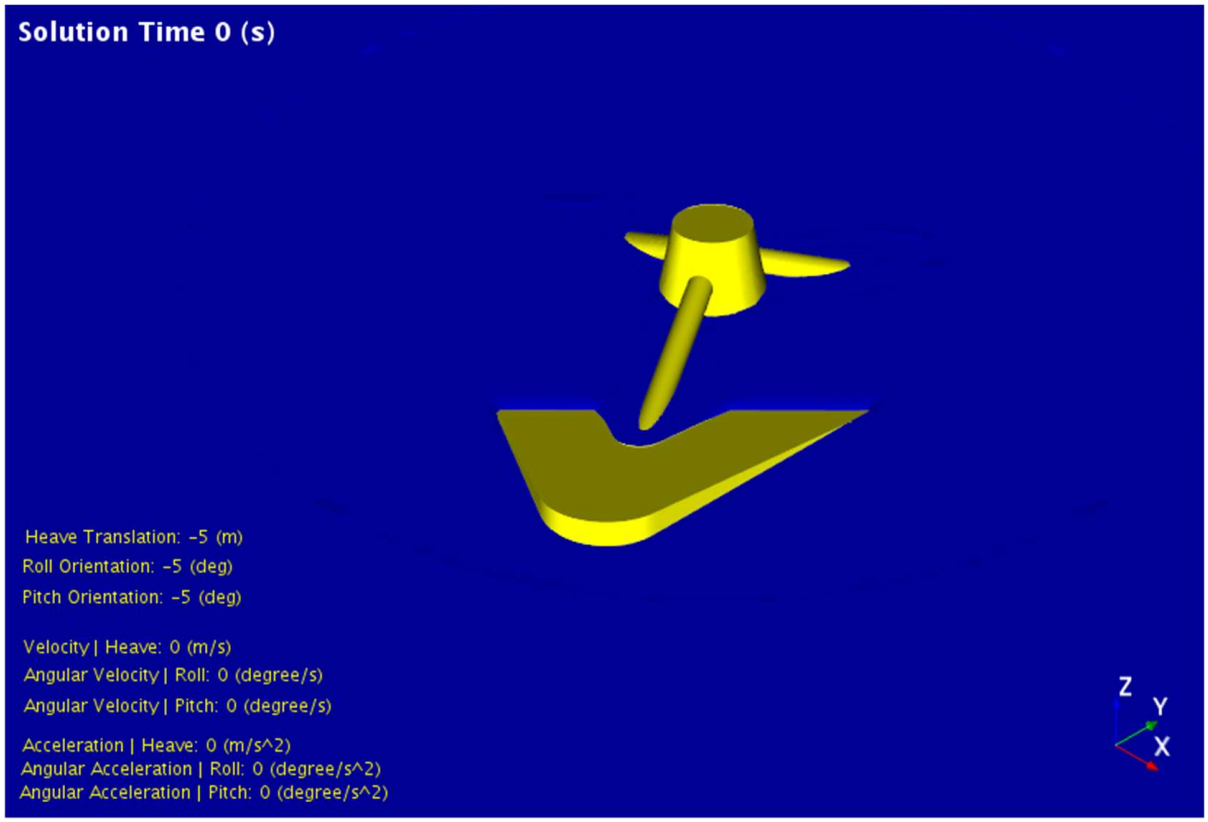

FIGURE 6.6: Initialised solution of free decay test at 0 s showing Free surface (z-direction slice plane).

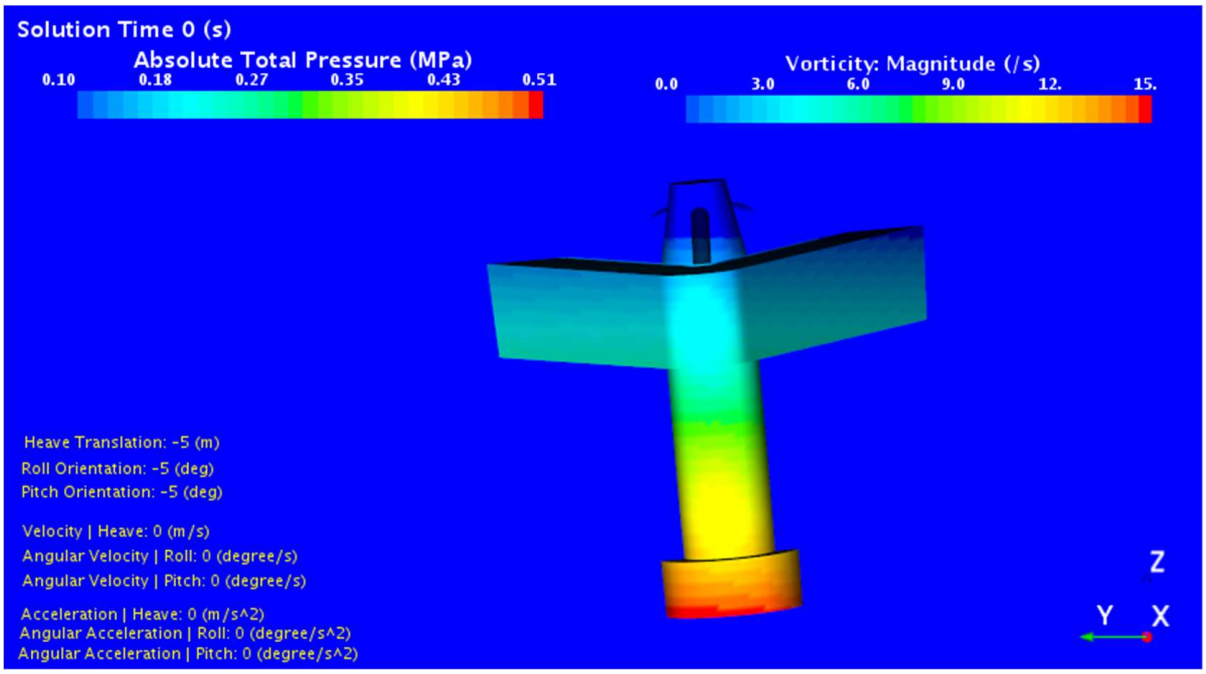

FIGURE 6.7: Initialised solution of free decay test at 0 s showing structure absolute pressure contour and flow domain vorticity (x-direction slice plane).

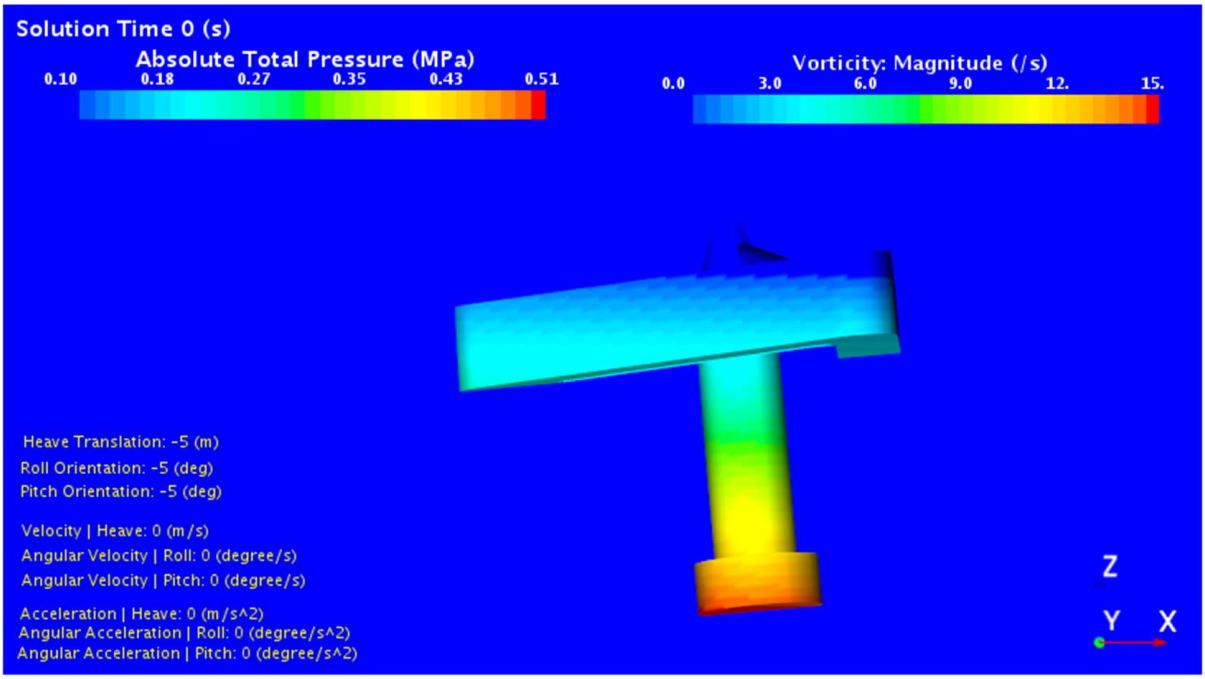

FIGURE 6.8: Initialised solution of free decay test at 0 s showing structure absolute pressure contour and flow domain vorticity (y-direction slice plane).

Non-Dimensional Total Damping Coefficient Results and Discussion

Fig. 6.9 highlights the free decay curves of TRIHF as it occurs during the simulated free decay test described in section 6.1.1. A comparison of the response signals between the 1DOF heave motion and coupled heave-roll-pitch motion free decay tests showed no significant discrepancy as shown in Fig. 6.9(top). However, to make a more conservative estimate, the peaks from the 1DOF heave motion response signal will be used in performing the viscous damping coefficient calculation. As can be seen from Fig. 6.9(bottom), the decay curves for roll and pitch are almost identical. This is an interesting observation since the TRIHF platform is symmetrical in the roll axis but non-symmetrical in the pitch axis. For heave motion, a 1DOF free decay test was done to check if roll and pitch motion have any effects on the coupled response signal for heave motion.

As can be observed from Fig. 6.9, the roll as well as the pitch response show exponentially decaying sinusoidal behaviour, as is to be expected for damped free oscillations where the amount of damping stays below the critical damping. Determining the exponential decay of the transient roll and pitch motions, respectively, using equations 6.4 to 6.7, allows for the derivation of the overall roll and pitch damping coefficients. However, more exact results could be achieved with longer measurements/simulations over roughly 10 subsequent oscillations. This way, potential errors regarding the peak/trough values as well as the oscillation frequency can be limited.

Fig. 6.10 to Fig. 6.18 contains the scenes of SWL iso-surface distribution, vorticity distribution, and absolute pressure distribution on the surface of the floating platform for the coupled heave-roll-pitch free decay test and 1DOF heave motion free decay test, respectively. As can be observed from both scenes, the Fluid-Structure Interaction (FSI) exhibits a complicated flow phenomenon in the form of ripples in the far-field and strong vortexes in the near-field of the platform. The complicated FSI is seen to create strong viscous effects, high turbulence intensity, and elevated viscous energy dissipations. A quick theoretical calculation of the anticipated maximum absolute total pressure (hydrostatic pressure[1] + atmospheric pressure[2]) for the structure is 0.46 MPa[3]. Observing the scenes showing the structure's total absolute pressure contours as presented in Fig. 6.13 to Fig. 6.18, the absolute total pressure on the surface of the platform

[1] Hydrostatic pressure $= 1025\ kg/m^3 \times 9.81\ m/s^2 \times 36\ m = 361,989\ Pa$

[2] 1 atm = 101,325 Pa

[3] Hydrostatic Pressure $(1025\ kg/m^3 \times 9.81\ m/s^2 \times 36\ m) + 1atm = 101,325\ Pa = 0.46\ MPa$

ranges from 0.076 MPa at the free surface to 0.46 MPa at the keel of the structure. Thus, it can be implied that the CFD results are very consistent with the theoretical value.

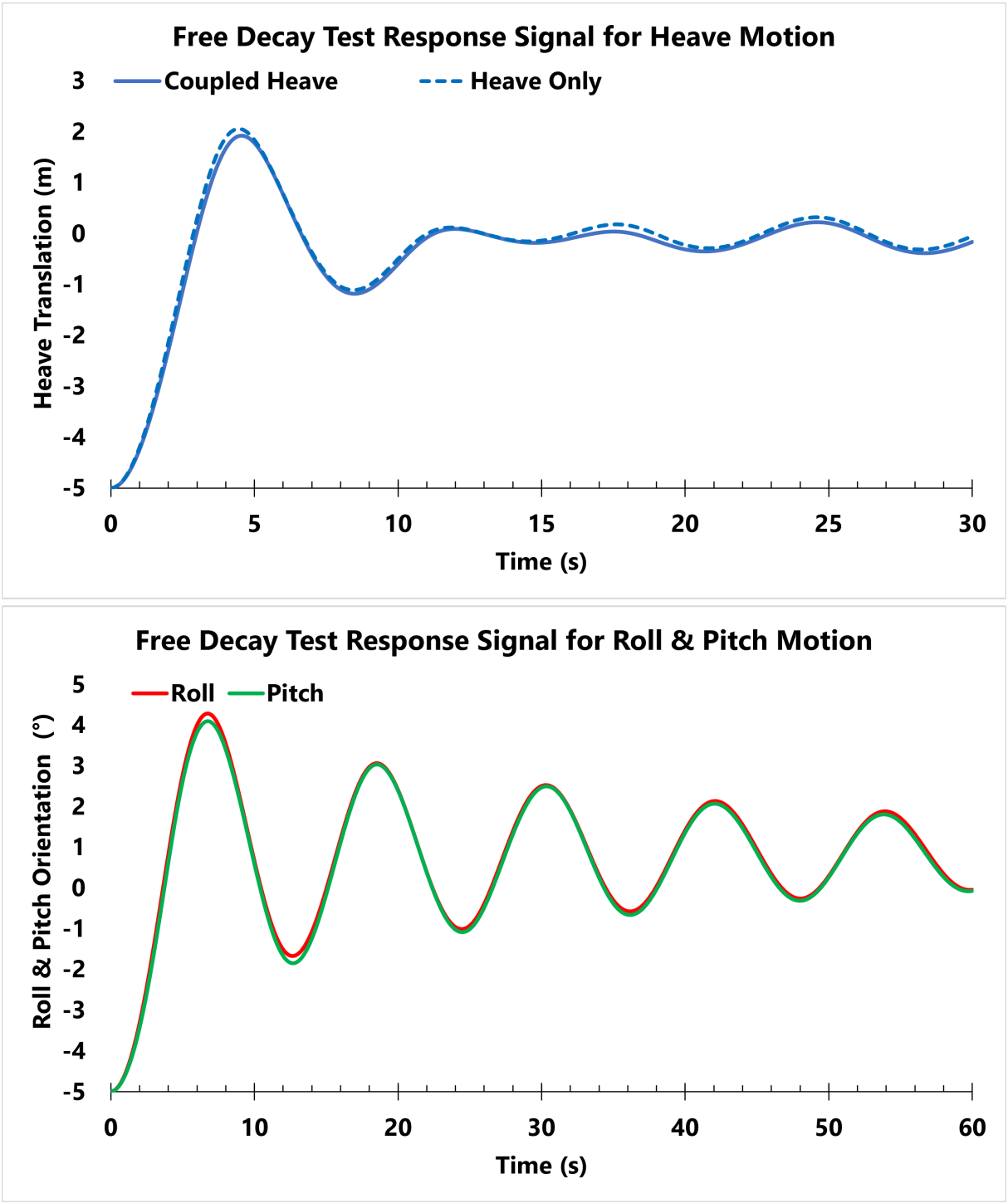

FIGURE 6.9: Free decay test result for (top) 1DOF heave motion for coupled heave-roll-pitch motion, and (bottom) roll and pitch motion.

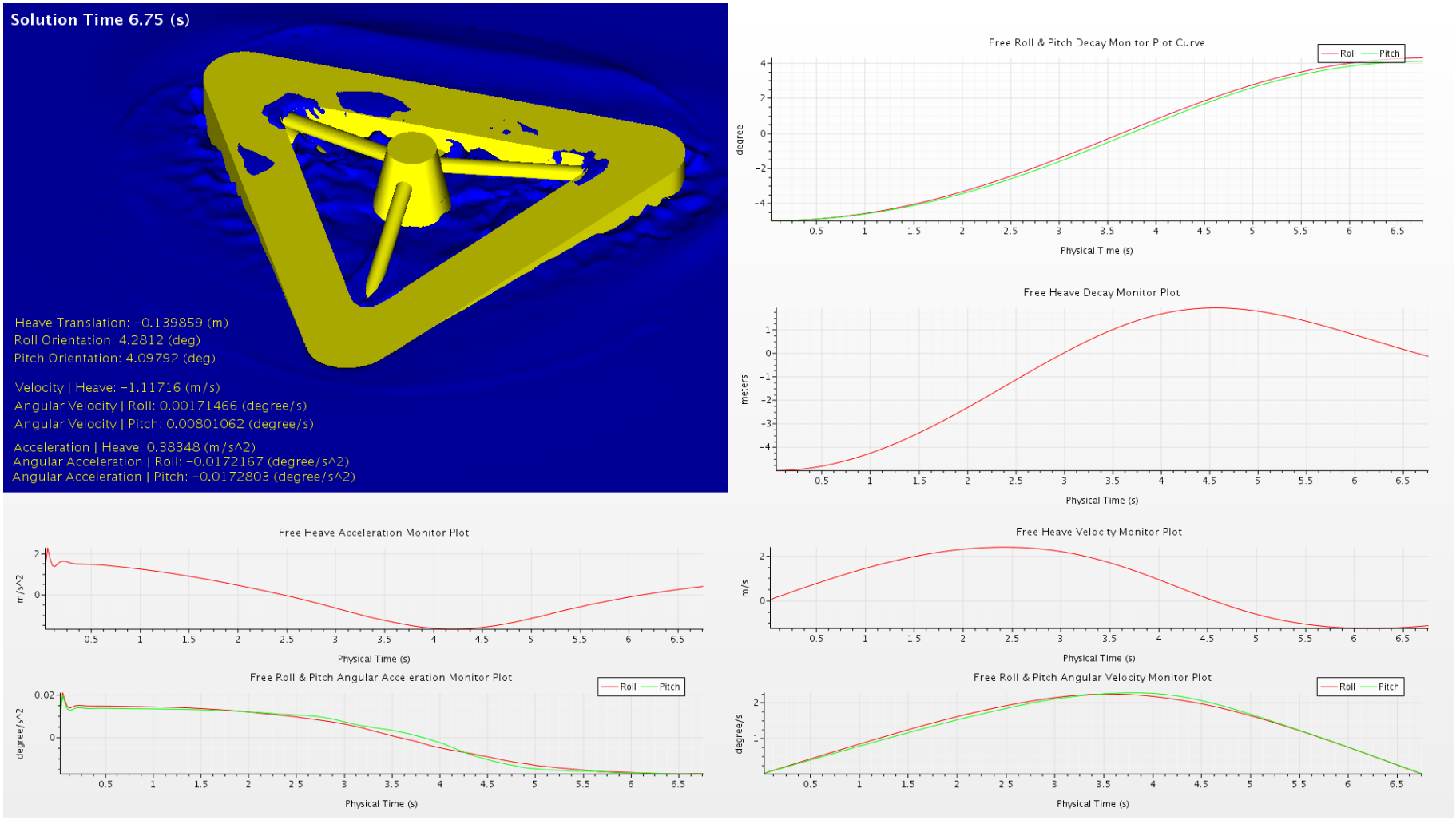

FIGURE 6.10: Scene demonstrating SWL iso-surface distribution and monitor plots for roll and pitch motion first peak at 6.75 s for the coupled heave-roll-pitch free decay test.

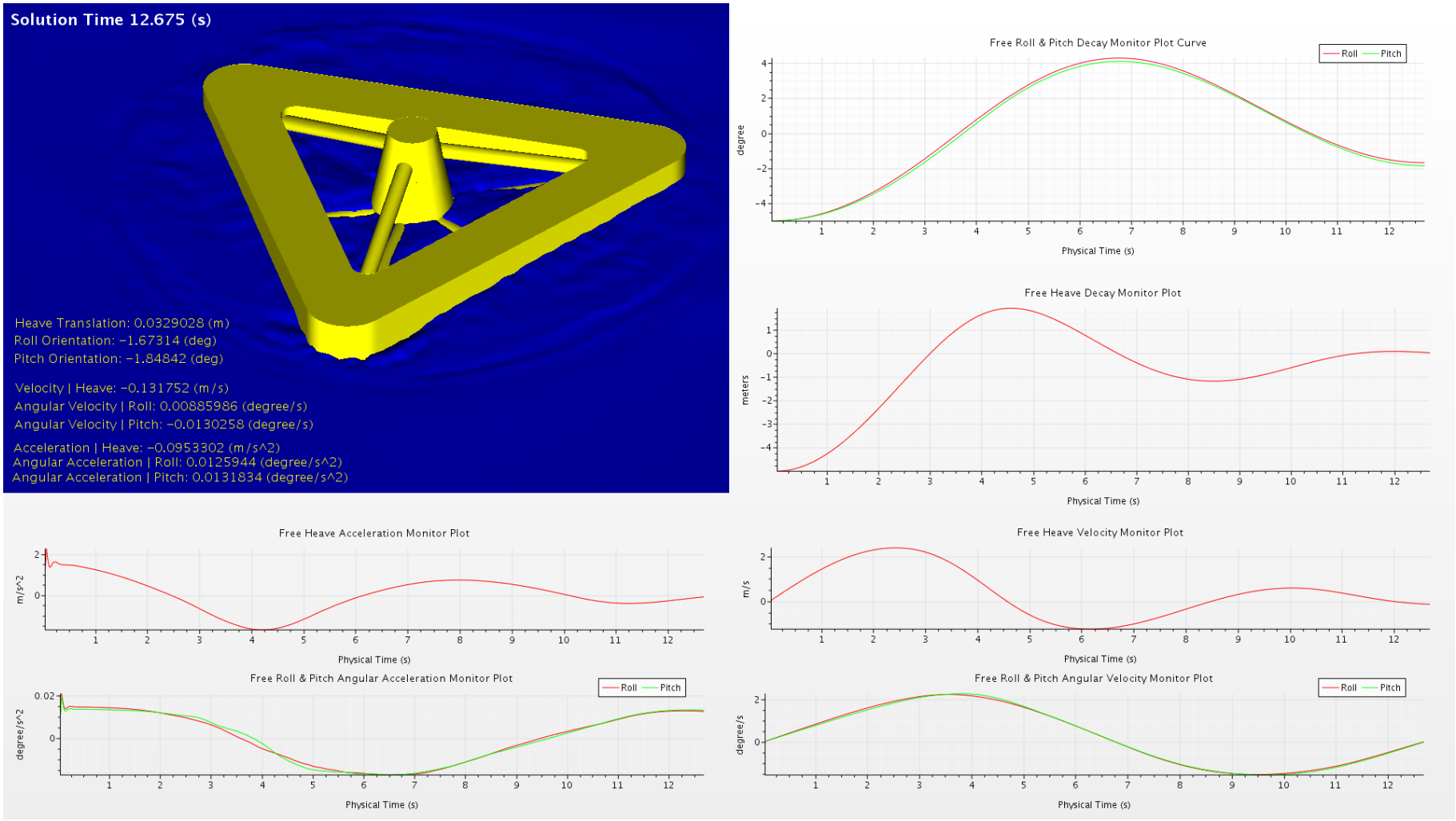

FIGURE 6.11: Scene demonstrating SWL iso-surface distribution and monitor plots for roll and pitch motion second peak at 12.68 s for the coupled heave-roll-pitch free decay test.

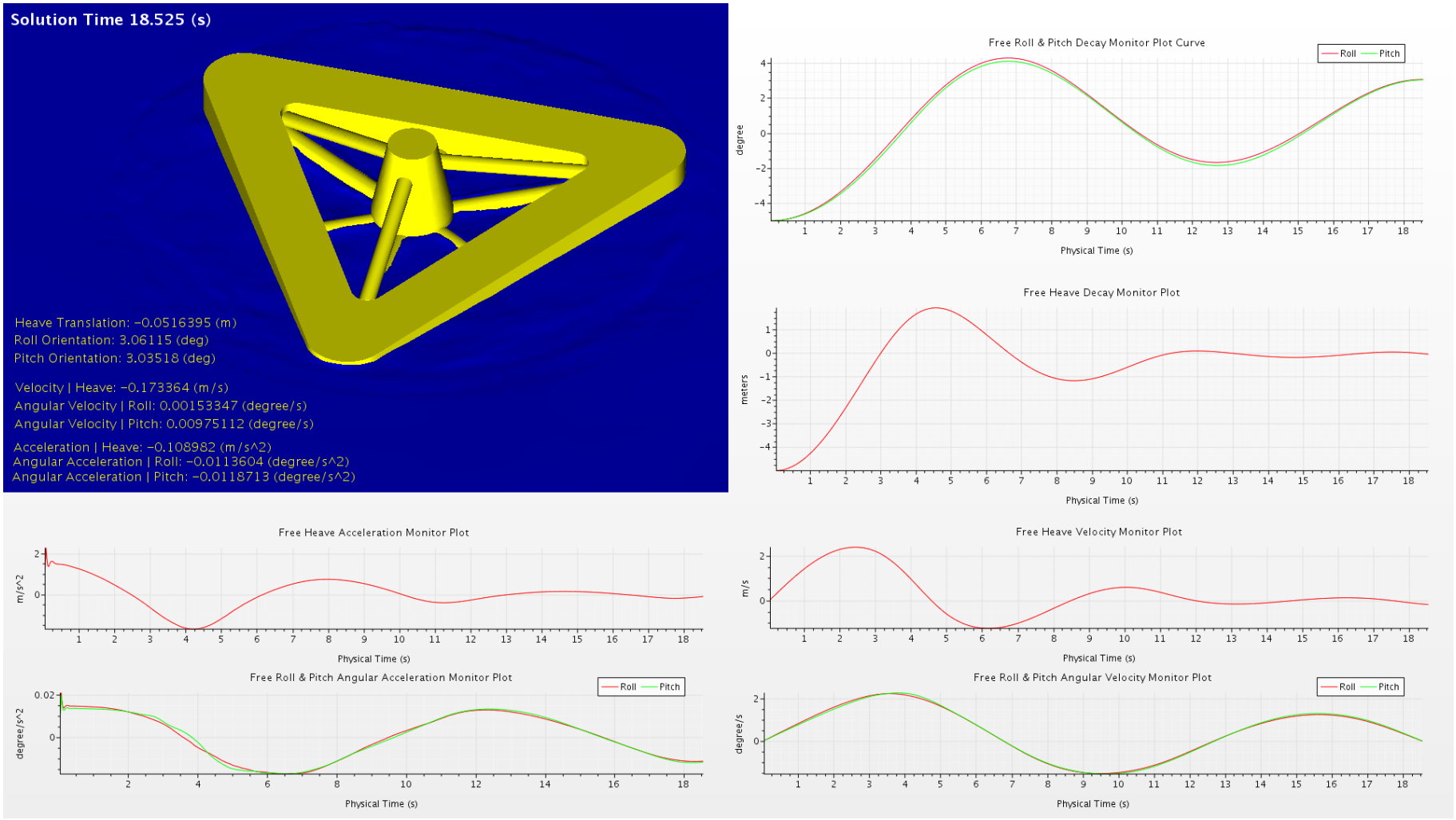

FIGURE 6.12: Scene demonstrating SWL iso-surface distribution and monitor plots for roll and pitch motion third peak at 18.53 s for the coupled heave-roll-pitch free decay test.

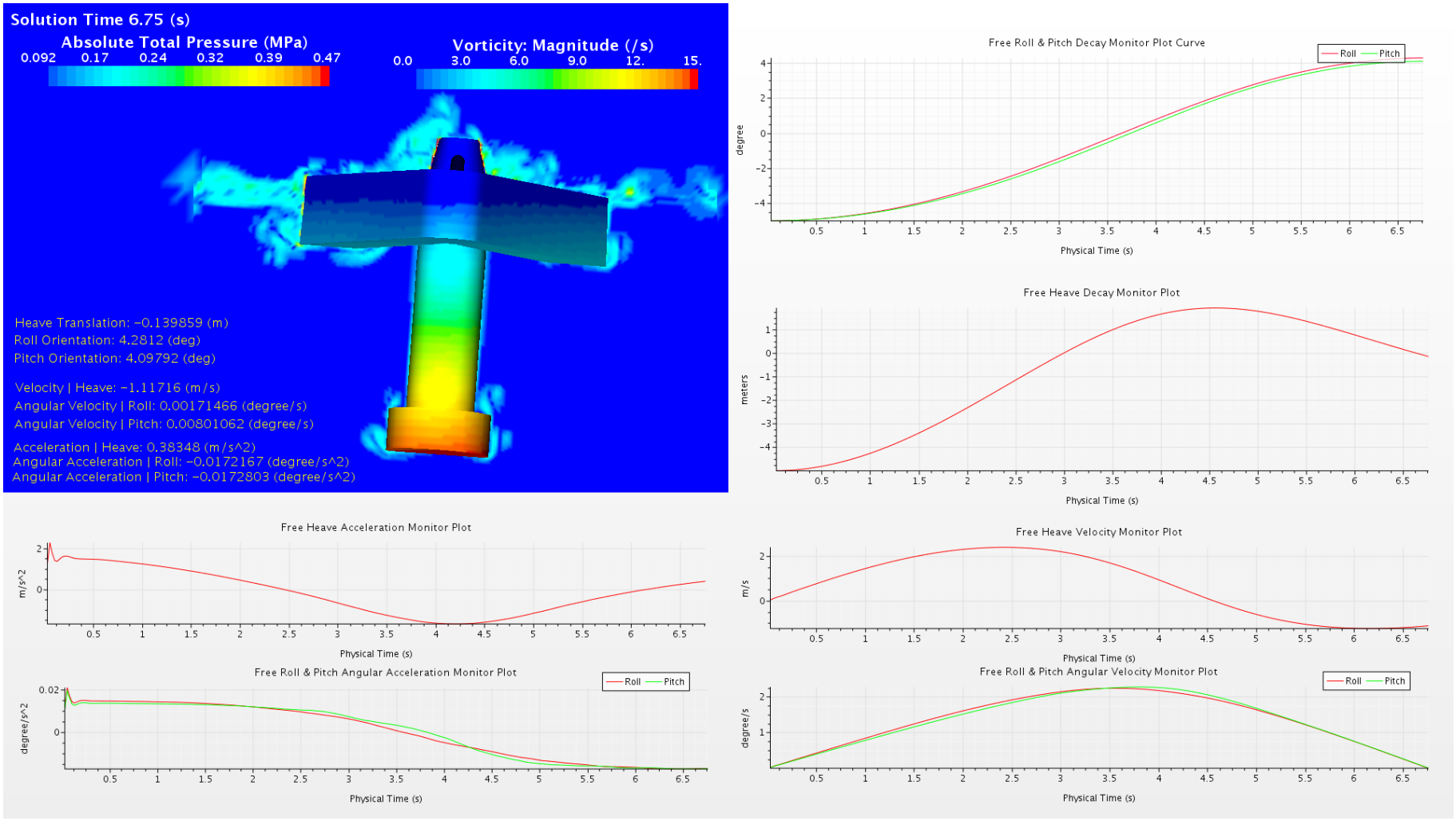

FIGURE 6.13: Scene demonstrating vorticity distribution, platform surface absolute pressure distribution, and monitor plots for roll and pitch motion first peak at 6.75 s for the coupled heave-roll-pitch free decay test (x-direction slice plane).

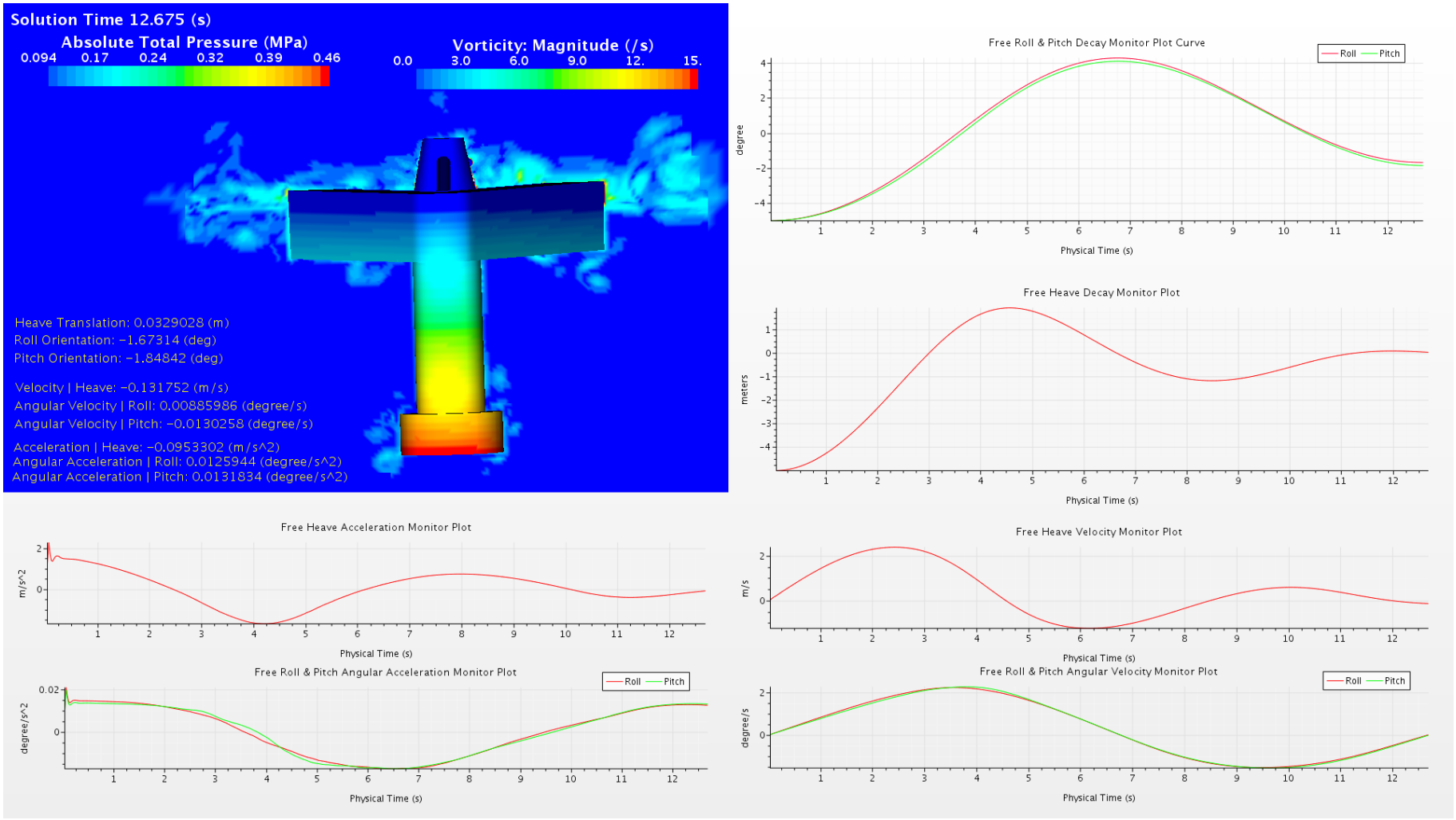

FIGURE 6.14: Scene demonstrating vorticity distribution, platform surface absolute pressure distribution, and monitor plots for roll and pitch motion second peak at 12.68 s for the coupled heave-roll-pitch free decay test (x-direction slice plane).

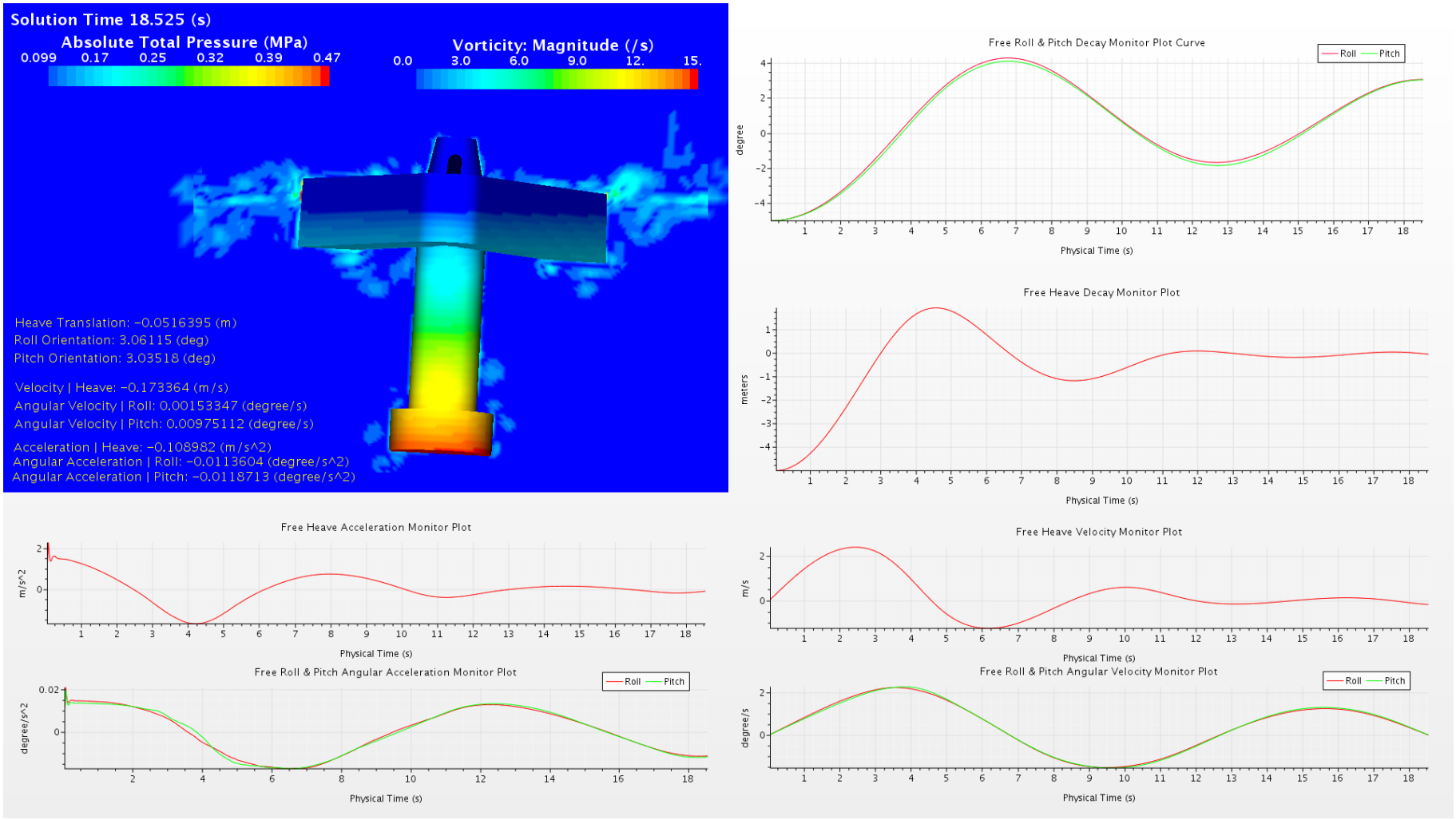

FIGURE 6.15: Scene demonstrating vorticity distribution, platform surface absolute pressure distribution, and monitor plots for roll and pitch motion third peak at 18.53 s for the coupled heave-roll-pitch free decay test (x-direction slice plane).

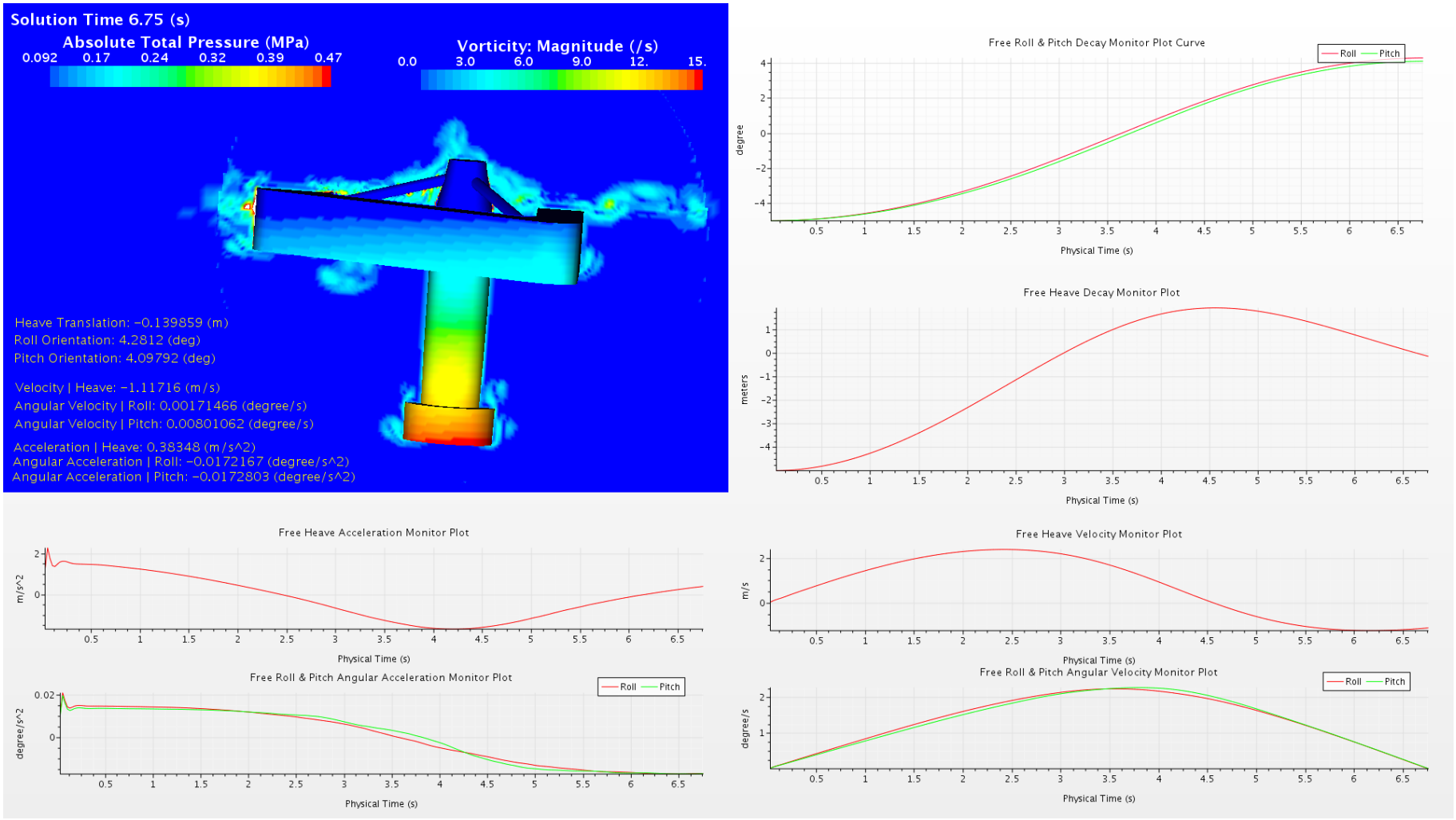

FIGURE 6.16: Scene demonstrating vorticity distribution, platform surface absolute pressure distribution, and monitor plots for roll and pitch motion first peak at 6.75 s for the coupled heave-roll-pitch free decay test (y-direction slice plane).

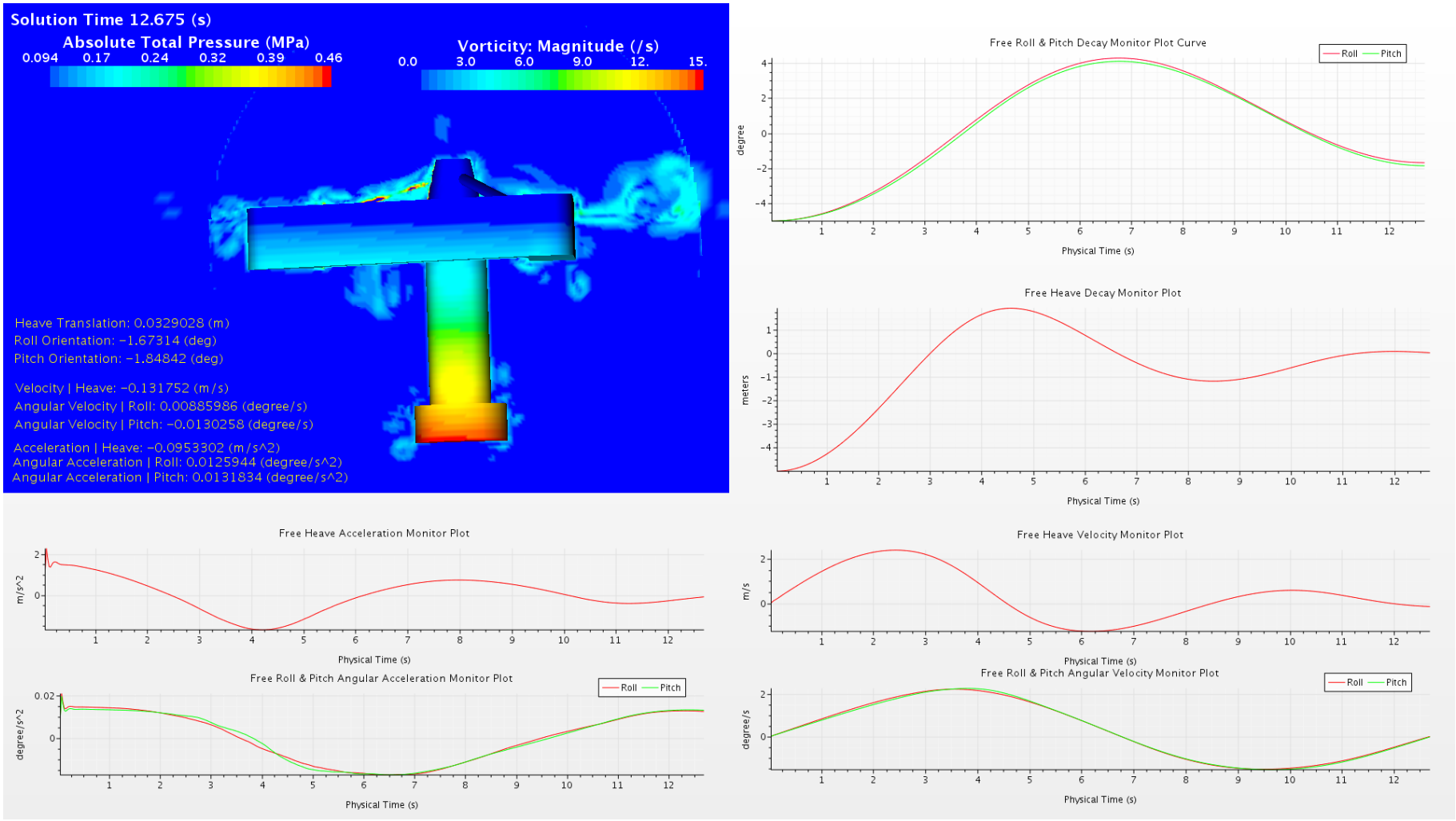

FIGURE 6.17: Scene demonstrating vorticity distribution, platform surface absolute pressure distribution, and monitor plots for roll and pitch motion second peak at 12.68 s for the coupled heave-roll-pitch free decay test (y-direction slice plane).

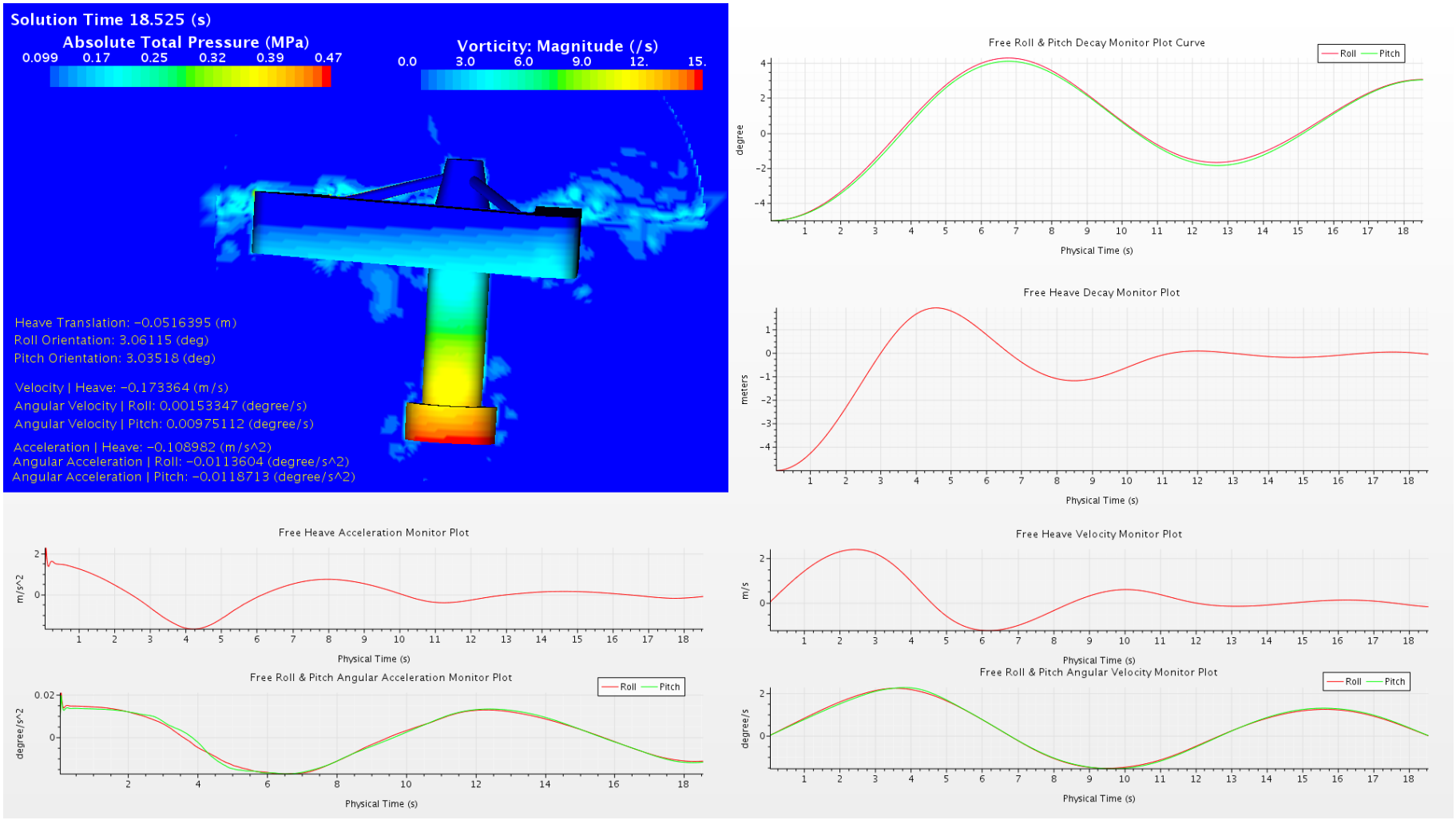

FIGURE 6.18: Scene demonstrating vorticity distribution, platform surface absolute pressure distribution, and monitor plots for roll and pitch motion third peak at 18.53 s for the coupled heave-roll-pitch free decay test (y-direction slice plane).

A critical look at the vorticity distribution presented in the scenes shown in Fig. 6.10 to Fig. 6.18 suggests that turbulence is chaotic and making some sense out of it is crucial in understanding the complex FSI exhibited by floating marine systems. Table 6.1 highlights the results from the platform's position and orientation for the first peak (ϑ_1), second peak (ϑ_2), and third peak (ϑ_3) of motion from the free decay test. By substituting these peaks of motion into equation 6.4, the non-dimensional viscous damping coefficients (ς_{ij}) for TRIHF are calculated.

TABLE 6.1: Results of non-dimensional total damping coefficients for TRIHF from free decay test.

Parameters	Heave	Roll	Pitch
ϑ_o	-5.00 m	-5.00°	-5.00°
ϑ_1	2.06 m	4.28°	4.10°
ϑ_2	-1.11 m	-1.67°	-1.85°
ϑ_3	0.12 m	3.06°	3.04°
ς_{ij}	0.2781	0.1071	0.099

In a later section of this chapter (section 6.2.2), the restoring force/moment and the added mass/moment of inertia results from a flat wave radiation/diffraction analysis will be used to compute the viscous damping coefficients for heave, roll and pitch motions using the formulation presented earlier in equations 6.5 to 6.7. Amongst others, part of the pre-solver strategies initiated for the irregular wave radiation/diffraction analysis performed for this research is the inclusion of an additional damping matrix using the pre-computed quadratic viscous damping coefficients.

6.1.2 Viscous Force Numerical Calculation

Various CFD modelling codes and methodologies are currently available for studying and predicting the external viscous flow behaviour around a structure. Some of these studies have been discussed in Section 2.2.2. One of the goals of this study is to evaluate the viscous force on the TRIHF-OWT model arising from wind and current loads. Thus, the driving parameters in addition to the level of the geometric representation of the FOWT were given careful consideration in carrying out the modelling for CFD simulation. The pre-processing strategies adopted for this CFD study are based on sound engineering judgement and detailed literature review about CFD which was done in the author's previous work [38]. For this thesis, the commercial CFD code

STAR CCM+ was used to perform a Direct Numerical Simulation (DNS) in combination with the Shear Stress Transport (SST) turbulence model. The governing RANS equations were discretized using finite element volume method.

Model Set-up, Boundary Conditions, and Pre-processing Strategies

Simulating flow through a FOWT can be regarded as an external flow situation. The sizing for the computational flow domain employed to investigate the viscous forces on the FOWT is crucial to achieving the desired goal and mitigating the potential for realising poor simulation results. Having a large flow domain may become computationally expensive whilst also having a relatively small domain may result in creating an artificial channel or constricted flow that can significantly influence the outcome of the simulation. Since the aerodynamic flow condition for an offshore environment is turbulent, having the rotating domain too close to the inlet of the domain may result in the inaccurate prediction of aerodynamic forces especially in incompressible flows. Hence, careful consideration was given in sizing the stationary (environmental) domain and positioning for the rotating (rotor) domain. The external flow domain geometry considered in this research is shown in Fig. 6.19.

As can be seen from the illustration in Fig. 6.19c, the rotor is housed in a cylindrical rotating domain that is encapsulated in another cylindrical stationary domain. The stationary domain is such that it mimics the external offshore environment by serving as an interface between the stationary domain and the rotating domain. A fluid-fluid transient rotation interface with an angular speed of 12.1 rpm at both sides of the rotating domain and stationary domain were defined to enforce kinematic continuities between the rotor and the external flow domain. Volume control for the sea's free surface zone was implemented to adequately capture the viscous effects around the floating platform. In the same vein, mesh refinement volume control regions for the FOWT near field was also executed. Fig. 6.20 describes the boundary conditions that were initiated for the CFD simulation.

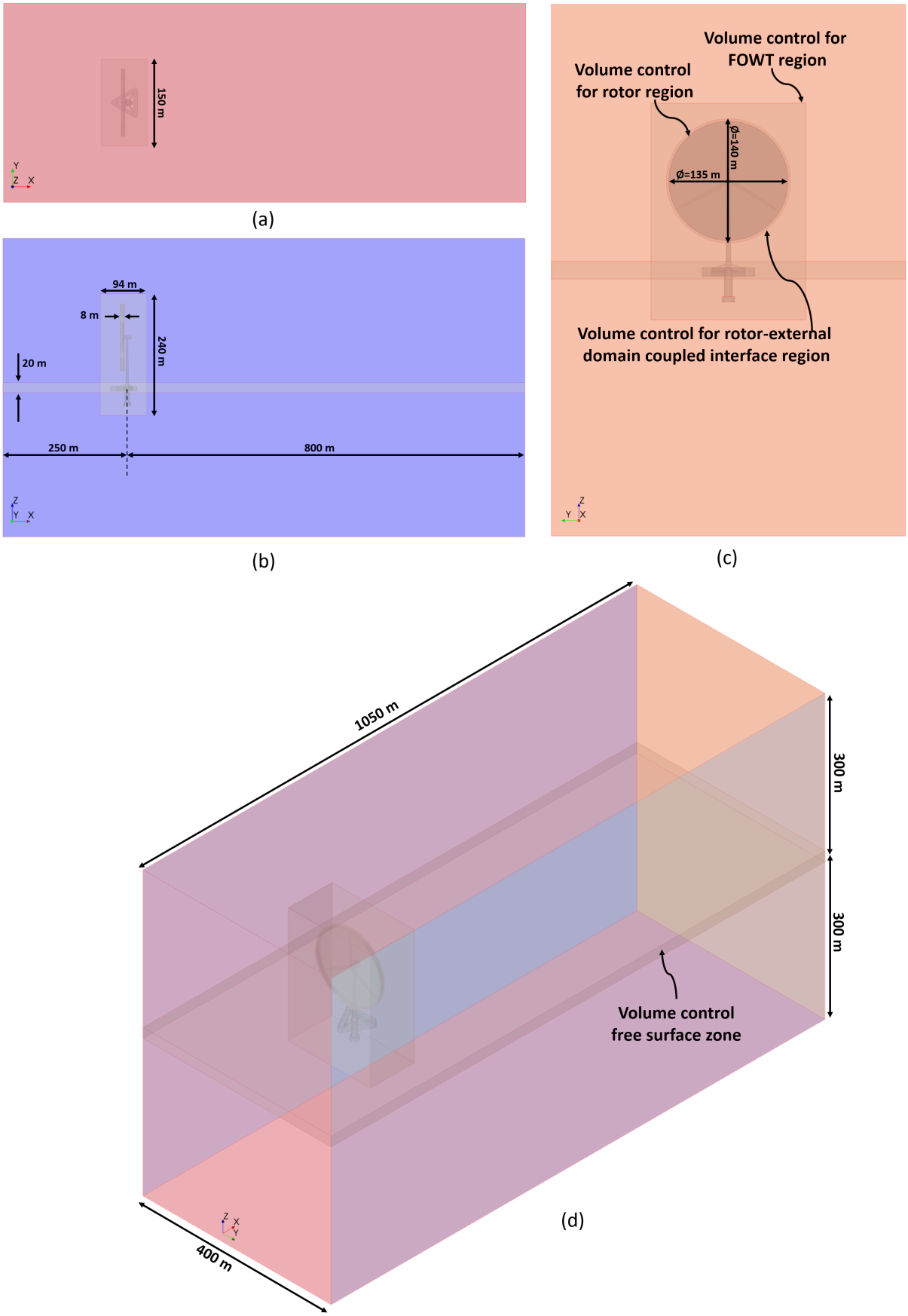

FIGURE 6.19: External flow domain used in CFD simulation showing view with respect to (a) z axis (b) y axis (c) x axis and (d) isometric view.

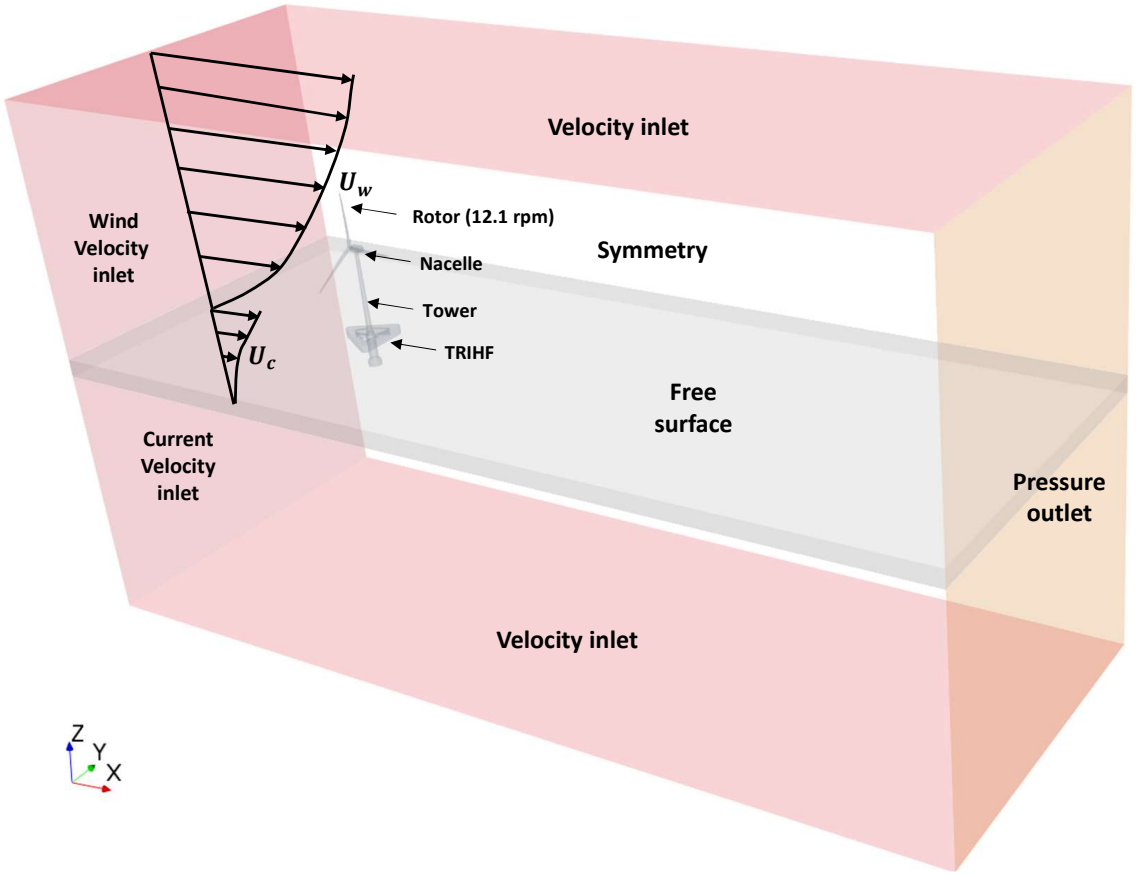

FIGURE 6.20: Flow domain boundary conditions for viscous force CFD simulation.

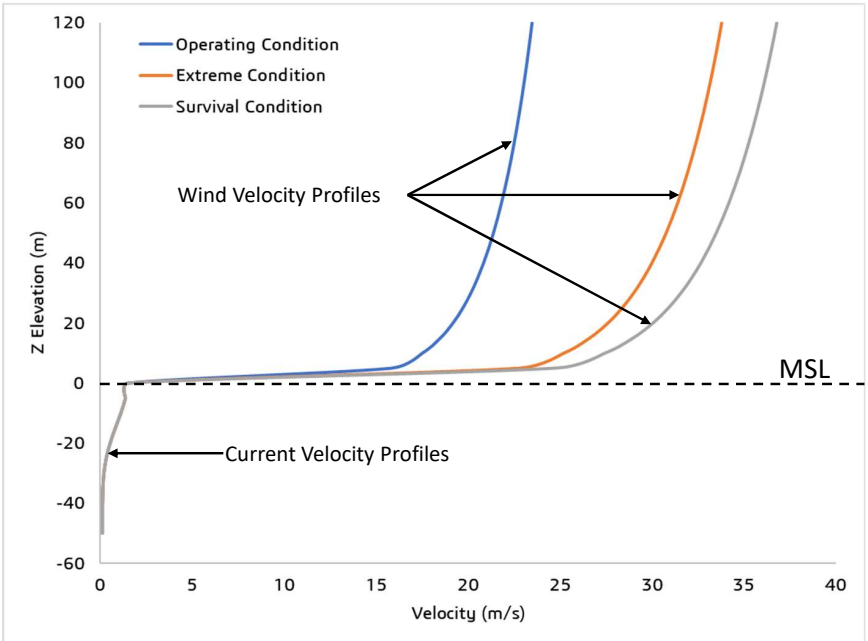

FIGURE 6.21: Wind and current velocity profile for inlet boundary condition.

The solver strategies employed for the viscous force numerical simulation are the same as the solver strategies implemented in the viscous damping numerical simulation as previously described in section 6.1.1 except for the inclusion of wind (U_w) and ocean current (U_c) velocity profile at the inlet boundary conditions as shown in Fig. 6.20. The inlet velocity profiles for wind and current are as described previously in sections 3.2.3 and 3.2.4, respectively. Fig. 6.21 shows a plot of the wind and current velocity profile as a function of elevation above and below MSL, respectively.

Meshing Strategy and Refinement Study

The mesh statistics used in performing a CFD study is key to deriving the right solution. An immense effort was invested in carrying out a mesh refinement study to facilitate and validate the appropriate mesh quality for the CFD simulation. Table 6.2 contains the setup and metrics for the three mesh refinement cases used in carrying out the mesh refinement study.

TABLE 6.2: Mesh metrics used for mesh refinement study.

Metrics	**Mesh Refinement Cases**		
	1	**2**	**3**
Default Controls			
Base size (m)	5	3.75	2.5
Target surface size = 100% of base size (m)	5	3.75	2.5
Minimum surface size = 10% of base size (m)	0.5	0.375	0.25
Surface growth rate		1.3	
Number of prism layers		20	
Prism layer total thickness = 10% of base size (m)	0.5	0.375	0.25
Maximum cell size = 1600% of base size (m)	80	60	40
Custom Controls			
Curve control = 5% of base size (m)	0.25	0.1875	0.125
Wake refinement isotropic control = 10% of base size (m)	0.5	0.375	0.25
Remesher wake refinement growth rate (m)		1.3	
Target surface size for far fields= 1600% of base size (m)	80	60	40
Target surface size for near field= 25% of Base Size (m)	1.25	0.9375	0.625
Volumetric control for FOWT region = 20% of Base Size (m)	1	0.75	0.5
Volumetric anisotropic control for free surface (X axis) = 100% of base size (m)	5	3.75	2.5
Volumetric anisotropic control for free surface (Y axis) = 100% of base size (m)	5	3.75	2.5
Volumetric anisotropic control for free surface (Z axis) = 50% of base size (m)	2.5	1.875	1.25
Total cell count	7.5×10^6	11.5×10^6	18×10^6

From fundamental knowledge and first principles of fluid dynamics, solution gradients in the near-wall region of complex geometries are envisaged to be very high. The rotor surface possesses complex aerofoil geometries with varying twist angles about its aerodynamic centre. Hence, it will not be incorrect to suggest that high solution gradients will be prominent for a rotor. A similar notion regarding high solution gradients

is also applicable to the geometry of the floating platform. With this in mind, the need for accurate numerical calculation in the near-wall regions of the FOWTs surface cannot be overemphasised. From Table 6.2 above, the far field region includes the inlet, outlet, seabed, sides, and top of the fluid domain while near field region includes the platform, tower, nacelle, and rotor surfaces.

The tactic employed to address the occurrence of high solution gradients for the CFD simulation is to pay close attention to the FOWT surface by adopting the viscous sublayer resolving approach where the distance of the first grid above the surface of the structure needs to be about a value of $y^+ = 1$. With a mesh surface growth rate not higher than 1.3, a prism layer containing about 20 layers of grids were used to ensure that the mesh will be able to adequately resolve the velocity gradients in the viscous sublayer [137], [138]. It is noteworthy that one of the limitations of the viscous sublayer resolving approach is that it significantly adds to the mesh count which can make a CFD project computationally expensive. Since the CFD simulation scheme employed to investigate the viscous dynamic loads on the FOWT's surface involves predicting the forces at the various wind and current velocities, it is often useful to be able to estimate the wall distance needed to obtain the desired y^+ value and reduce the risk of remeshing. Based on a literature search, the formula for the first cell height, Δy as a function of the boundary layer length, L, the flow Reynolds number, Re_L for a desired y^+ is given by [139];

$$\Delta_y = L \cdot y^+ \sqrt{74} \cdot Re_L^{-\frac{13}{14}} \tag{6.8}$$

By using the formulation presented in equation 6.8, Table 6.3 contains a summary of the result for the prism layer first cell height calculation that was implemented into the meshing scheme for the CFD study. In order to improve the overall quality of the existing surface and optimise the volume mesh models, the **surface remesher** meshing scheme was used to re-grid the surface of the FOWT. Also, a **trimmed mesher** scheme which provides a robust and efficient technique for producing a high-quality grid for complex mesh generation problem was utilised. The **prism layer** mesher was used to generate prismatic cell layers next to the boundary surface of the FOWT. These cells help to capture the viscous boundary layer correctly and improve the accuracy of the

flow solution. The resulting mesh distribution that was produced from the application of the three aforementioned meshing scheme is shown in Fig. 6.22 and Fig. 6.23 for mesh refinement case 3. As can be seen from Fig. 6.22a to Fig. 6.22d, a remesher wake refinement using the part-based meshing approach was implemented around the surfaces of the structure. The wake grows from the surface of the FOWT into the fluid volume of the flow domain. The implementation of a wake refinement meshing scheme facilitates a computationally less expensive CFD study by reducing the cell counts in the areas of the fluid domain that is not of interest.

TABLE 6.3: Calculation summary of first cell height for y+ function.

Parameters	Water	Air
Fluid Dynamic Viscosity (Pa.s)	8.89×10^{-4}	1.86×10^{-5}
Fluid Density, ρ (kg/m^3)	1025	1.225
Characteristics Distance, L (m)	50	50
Reynold Number @ 23.04 m/s, Re_L	1.33×10^{9}	7.61×10^{7}
Reynold Number @ 33.16 m/s, Re_L	1.91×10^{9}	1.09×10^{8}
Reynold Number @ 36.10 m/s, Re_L	2.08×10^{9}	1.19×10^{8}
Desired Y^+ Value	1	1
Prism Layer First Cell height @ 23.04 m/s, Δy (m)	1.45×10^{-6}	2.07×10^{-5}
Prism Layer First Cell height @ 33.16 m/s, Δy (m)	1.04×10^{-6}	1.47×10^{-5}
Prism Layer First Cell height @ 36.1 m/s, Δy (m)	9.57×10^{-7}	1.36×10^{-5}

Viscous Force Simulation Results and Discussion

Fig. 6.24 presents various visualisation of the initialised solution for the CFD simulation using section planes. As can be seen from these contour plots, the fluid velocity profiles as earlier presented in Fig. 6.21 were adequately modelled in the flow domain. The free surface current velocity (Fig. 6.24a) and hub height wind velocity under operating condition load case corresponds to 1.52 m/s and 23.16 m/s, respectively. The contour plots show a strong demonstration of the wind velocity increasing with elevation above the MSL and current velocity decreasing with an increase in water depth. Performing a CFD simulation where the environmental loads have been accurately modelled based on prevailing environmental conditions is crucial to avoid an overestimation of viscous forces. Also, there is a clear indication of the maximum absolute total pressure experienced at the base of the floating platform being around the magnitude of 0.46 MPa as expected. Fig. 6.25 shows the operating condition load case time history plots of forces and moments for the 3 mesh refinement cases considered in the CFD analysis.

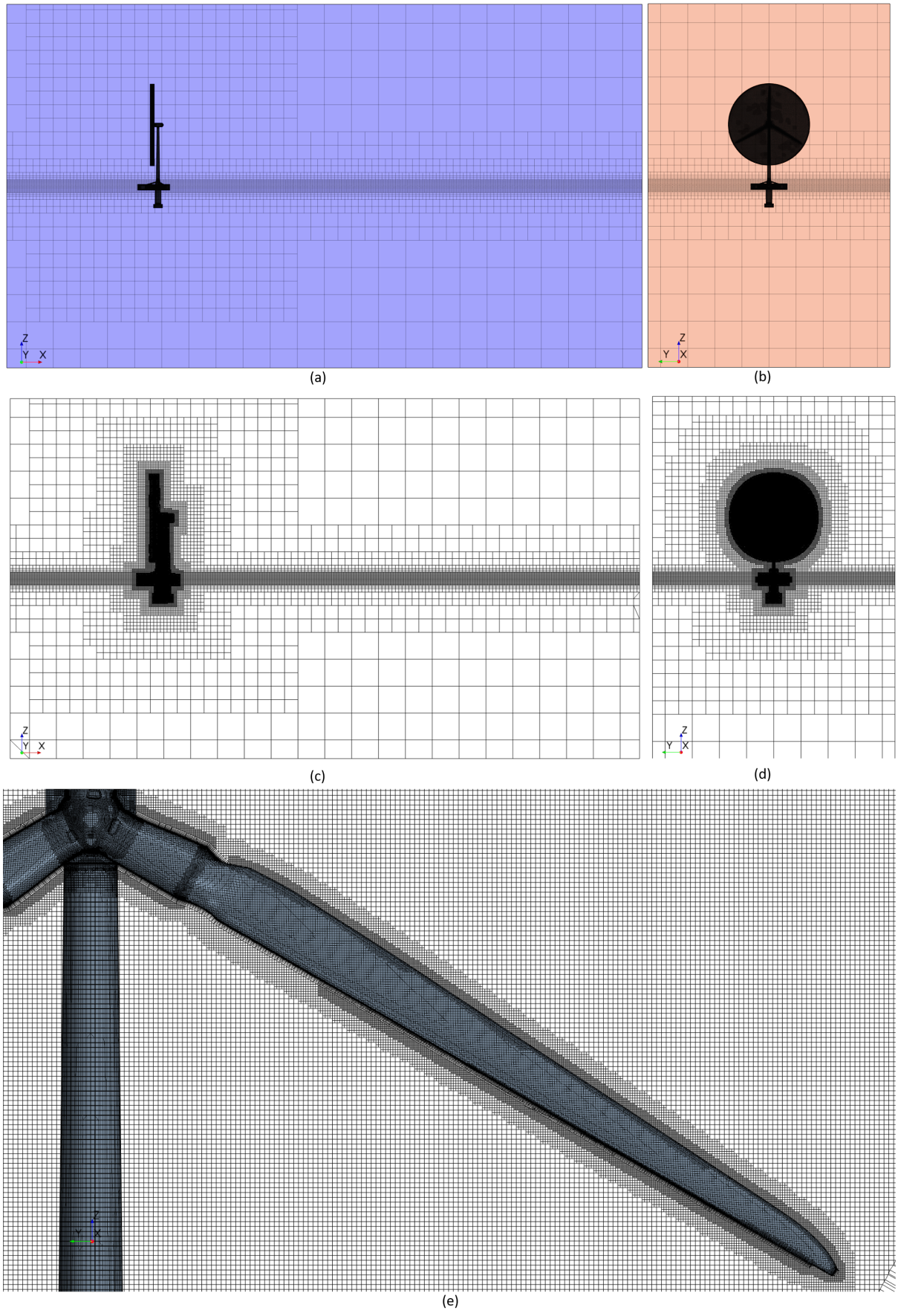

FIGURE 6.22: Flow domain mesh distribution for mesh refinement case 3; (a) far field symmetry boundary in y-axis, (b) far field inlet boundary in x-axis, (c) xz-plane, (d) yz-plane, (e) close-up view of blade and tower in yz-plane.

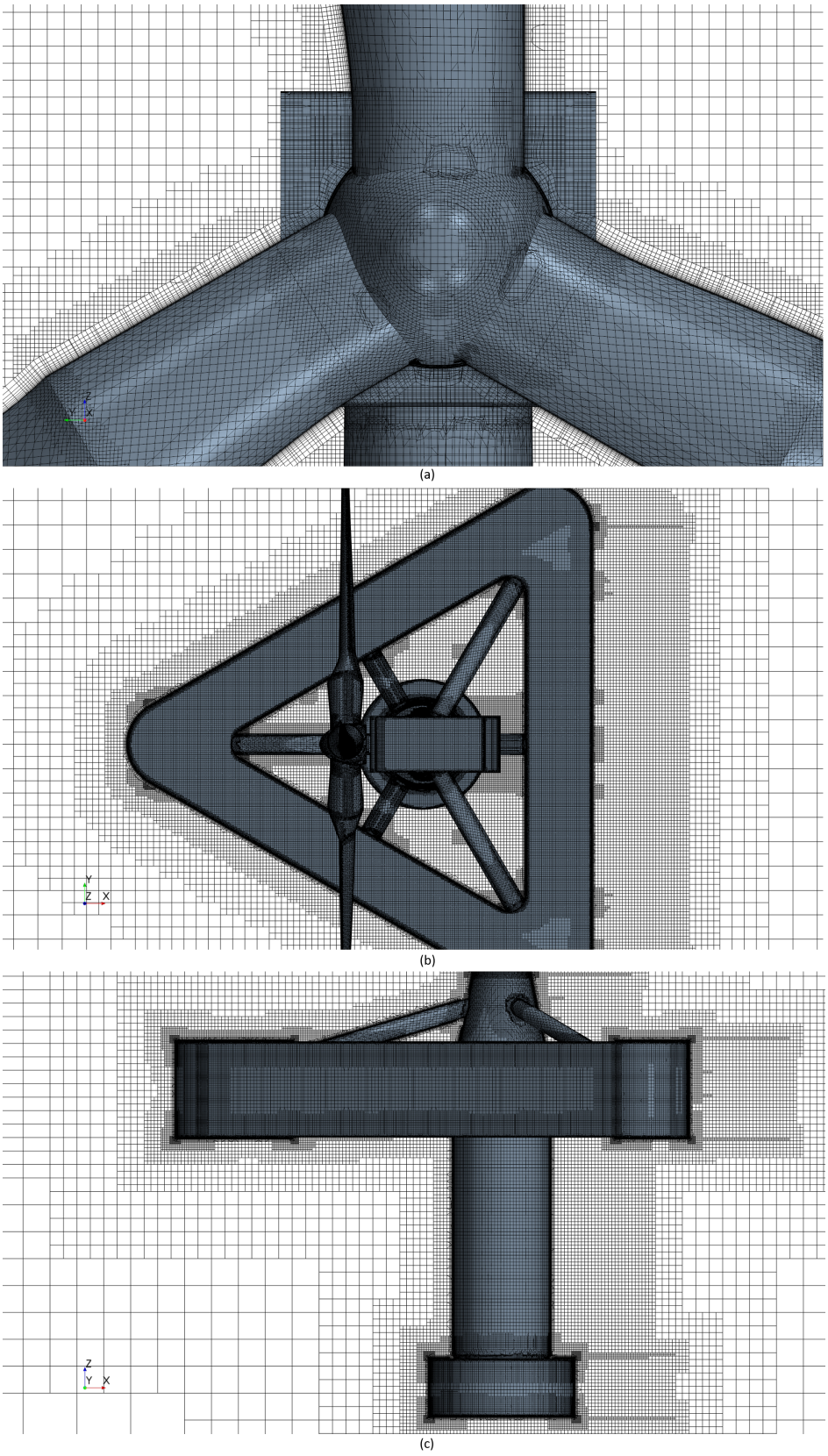

FIGURE 6.23: Flow domain mesh distribution for mesh refinement case 3; (a) close-up view of rotor, nacelle, and tower top in yz-plane, (b) close-up view around the FOWT's near field and free surface in xy-plane, (c) close-up view of platform and tower bottom in xz-plane.

As can be seen in the plots presented in Fig. 6.25a to Fig. 6.25f, the solution is not sensitive to the mesh refinement which is a clear indication of the stability and validity of the physics and pre-processing strategies implemented for the CFD simulation. Additionally, a statistical summary of the results shown in Table 6.4 further supports the consistency of the CFD study because a comparison of the time history minimum, maximum, mean, and standard deviation is seen to be very consistent across the three mesh scenarios.

The CFD simulation calculated the average rotor power to be 5 MW although the minimum and maximum values were estimated to be around the magnitude of 5.5 MW and 4.8 MW, respectively (see Table 6.4). Also, the rotor thrust coefficient was calculated to be 0.2 which is consistent with the expected value of thrust coefficient for rotors having diameters between 100 m to 120 m, and a hub height 10-minute mean wind speed of 23 m/s (as referenced in DNV-OS-J103) [48]. The platform's drag force is predominantly current-induced and was calculated to have a maximum value of 5.28 to 5.39 MN.

Another noteworthy remark is the pattern of the tower drag force curve produced from the rotor shadow effect on the tower as shown in Fig. 6.25e. Here, the rotor shadow effect on the tower relates to the shielding influence provided by the blades of the rotor when they align adjacent to the tower which causes drag force undulations on the tower that is consistent with one-third of the rotor's complete revolution. Fig. 6.26 contains a visualisation of the velocity vector flow field in the yz-plane at (0,0,0) m, and the structure absolute total pressure at different time intervals. In Fig. 6.26, the characteristics of the flow dynamics in the wake region of the FOWT is visualised using line integral convolution of the velocity vector magnitude. The line integral convolution contour plot sheds more light on the fluid dynamics flow behaviour and better describes the magnitude and direction of the fluid particles. As can be observed from the illustration, the wake in the downstream region of the rotor is composed of rotating eddies emanating from each blade. A different perspective of the flow field in the yz-plane (streamwise direction) is shown in Fig. 6.27. Here, low velocity rotating eddies are seen to form adjacent to and along the surface of the tower and nacelle.

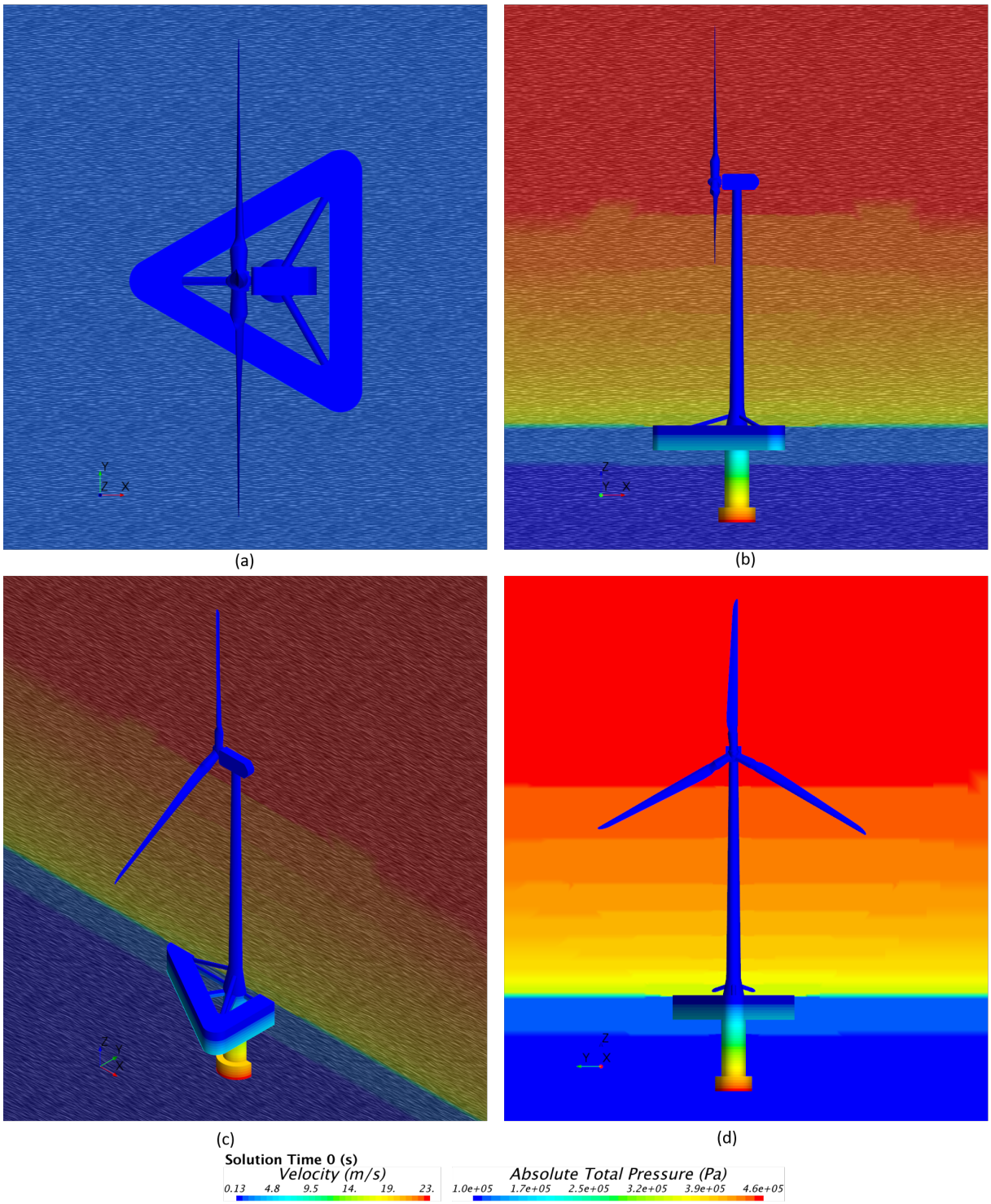

FIGURE 6.24: A visualisation of the CFD initialised solution at t = 0 s for operating condition design load case showing flow domain wind and current velocity profile direction of 0°, and structure absolute total pressure in (a) xy-plane, (b) xz-plane, (c) xz-plane isometric view, and (d) yz-plane.

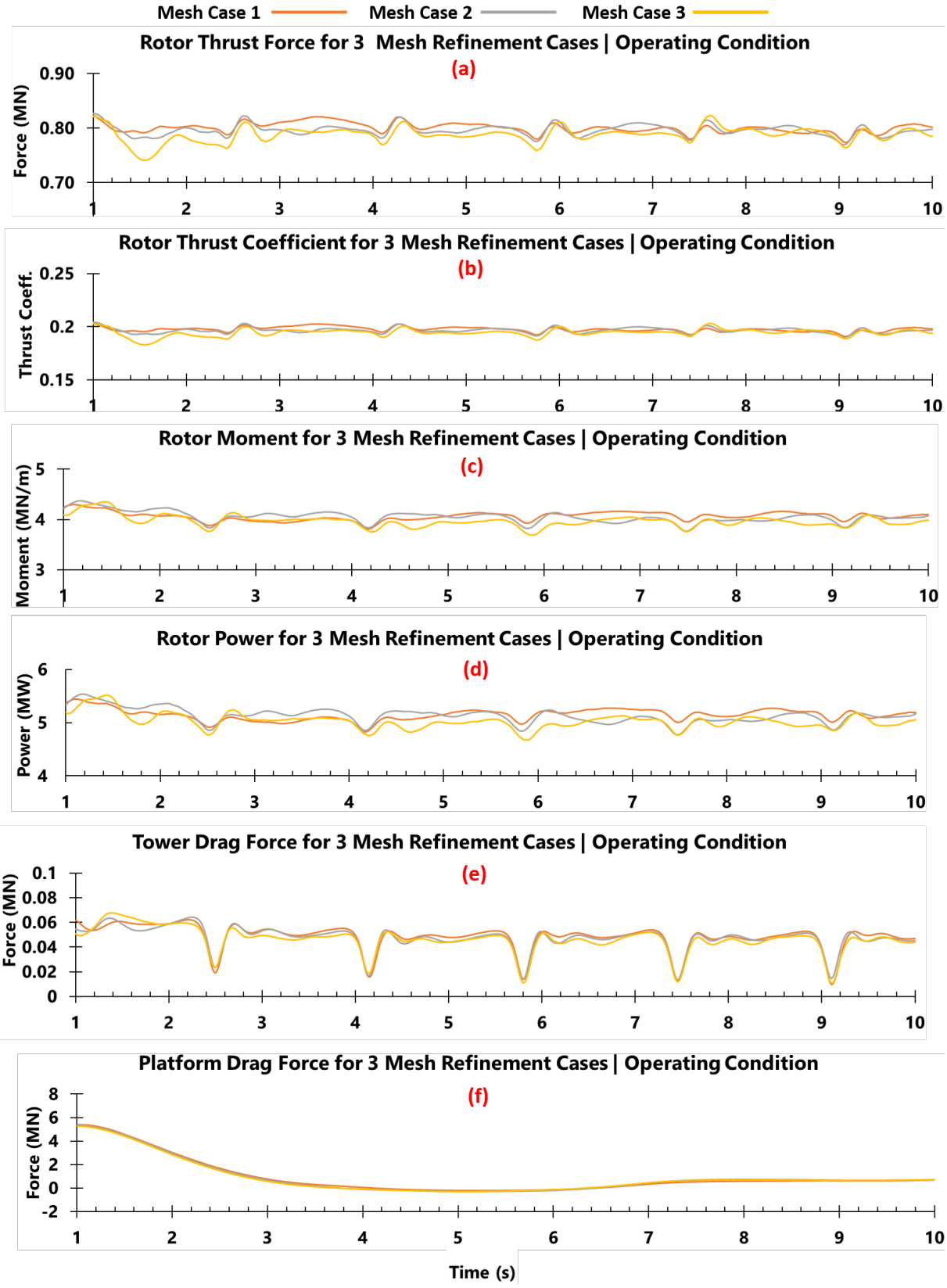

FIGURE 6.25: Plots showing time history of 3 mesh scenarios for flow direction of 0°; (a) rotor thrust force, (b) rotor thrust coefficient, (c) rotor moment, (d) rotor power, and (e) platform drag force under operating condition load case.

TABLE 6.4: Comparison of results for different mesh refinement | Operating condition load case.

Results	Mesh Refinement	Mean	Std. Dev	Maximum	Minimum
Rotor Thrust Force (N)	Case 1	8.00E+05	9.16E+03	8.23E+05	7.73E+05
	Case 2	7.96E+05	1.01E+04	8.28E+05	7.69E+05
	Case 3	7.88E+05	1.39E+04	8.23E+05	7.41E+05
Rotor Thrust Coeff.	Case 1	0.20	0.00	0.20	0.19
	Case 2	0.20	0.00	0.20	0.19
	Case 3	0.19	0.00	0.20	0.18
Rotor Moment (N.m)	Case 1	4.07E+06	8.59E+04	4.30E+06	3.81E+06
	Case 2	4.05E+06	1.11E+05	4.37E+06	3.77E+06
	Case 3	3.97E+06	1.13E+05	4.35E+06	3.69E+06
Rotor Power (Watts)	Case 1	5.15E+06	1.09E+05	5.45E+06	4.83E+06
	Case 2	5.14E+06	1.40E+05	5.54E+06	4.77E+06
	Case 3	5.03E+06	1.43E+05	5.52E+06	4.67E+06
Tower Drag Force (N)	Case 1	4.83E+04	9.92E+03	6.21E+04	9.84E+03
	Case 2	4.73E+04	9.27E+03	6.41E+04	1.31E+04
	Case 3	4.60E+04	1.00E+04	6.76E+04	1.08E+04
Platform Drag Force (N)	Case 1	9.03E+05	1.42E+06	5.39E+06	-2.13E+05
	Case 2	9.03E+05	1.41E+06	5.35E+06	-2.83E+05
	Case 3	8.63E+05	1.38E+06	5.28E+06	-3.00E+05

To better understand the characteristics of the flow field adjacent to the surface of the FOWT, velocity and pressure profiles are plotted across the domain in the stream-wise direction as shown in Fig. 6.28. Particularly of interest is Fig. 6.28a which highlights certain flow characteristics as discussed earlier in the axial momentum theory section of this thesis (section 2.1.2). As can be observed in Fig. 6.28a, the velocity of the wind is seen to evolve in the far stream region until it decays just upstream of the rotor before it flows across to the downstream region. The wind in the far wake region is seen to slowly gain speed as it flows across the domain although there is no full recovery to the initial wind speed condition of 23.16 m/s until after 350 m away from the rotor region. The stepwise rising pattern of the velocity profile can be attributed to the rotational wake reaction generated behind the rotor. The pressure plot is also seen to behave as an actuator disc which is caused by the wind flowing around the tip of the blade.

At the MSL, Fig. 6.28b provides some key information on the flow behaviour of the floating platform's near field. As can be noticed, a rapid decline in the current stream velocity is experienced in the near field region due to the obstruction of flow provided by the platform. A corresponding decline in absolute total pressure is also predicted in the near field region. A notable occurrence is a momentary spike in the current velocity just downstream of the platform.The current stream velocity is seen to peak for a moment and then decays to its initial flow velocity. The sudden peak in the

current stream velocity can be attributed to the turbulent disturbances created when the stream interacts with the complex geometry of the floating platform (see Fig. 6.32a to Fig. 6.32d).

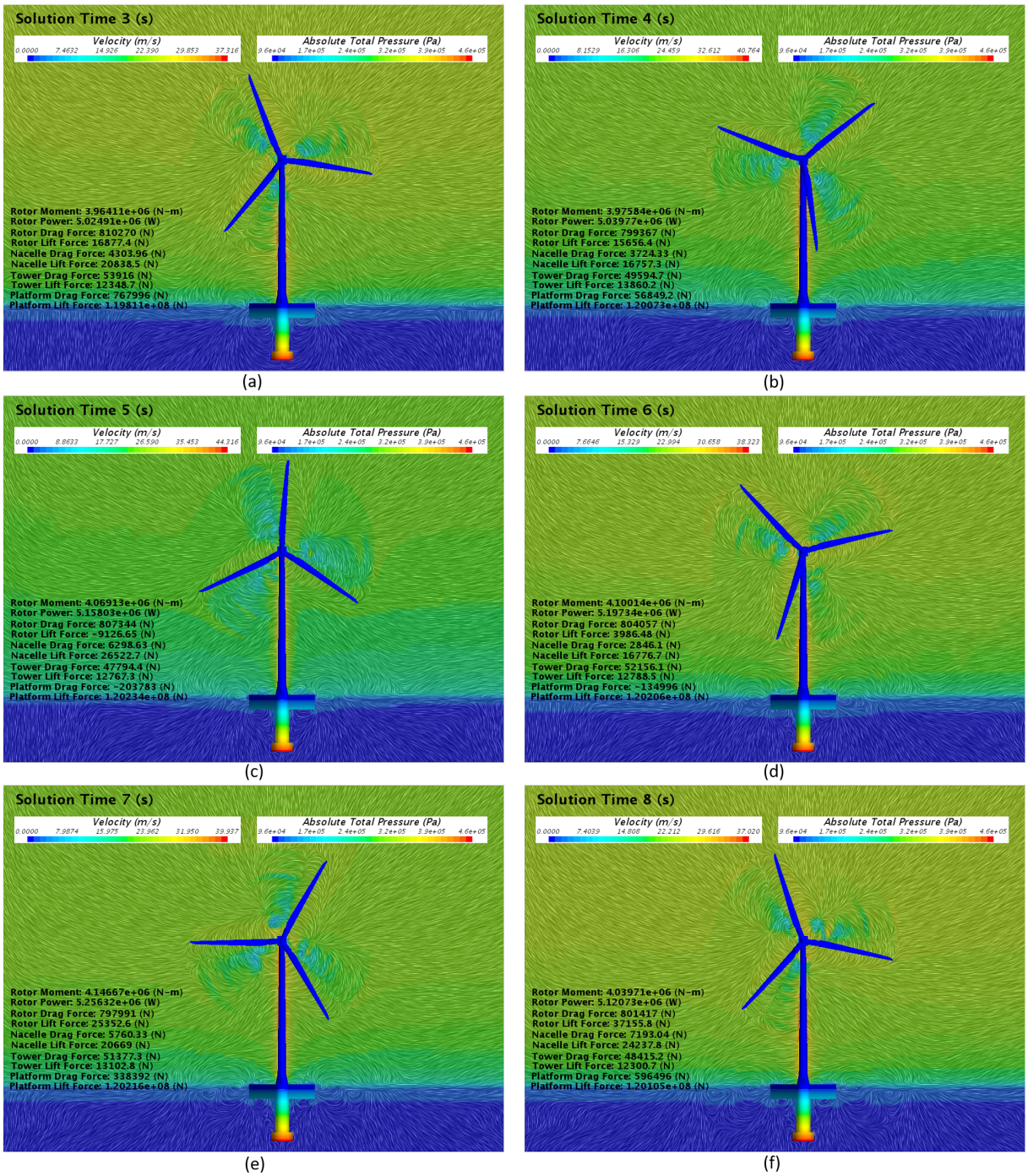

FIGURE 6.26: Visualisation showing flow domain velocity magnitude and structure absolute total pressure on the yz-plane with reference to the global coordinate (0,0,0) m, at (a) 3 s, (b) 4 s, (c) 5 s, (d) 6 s, (e) 7 s, and (f) 8 s.

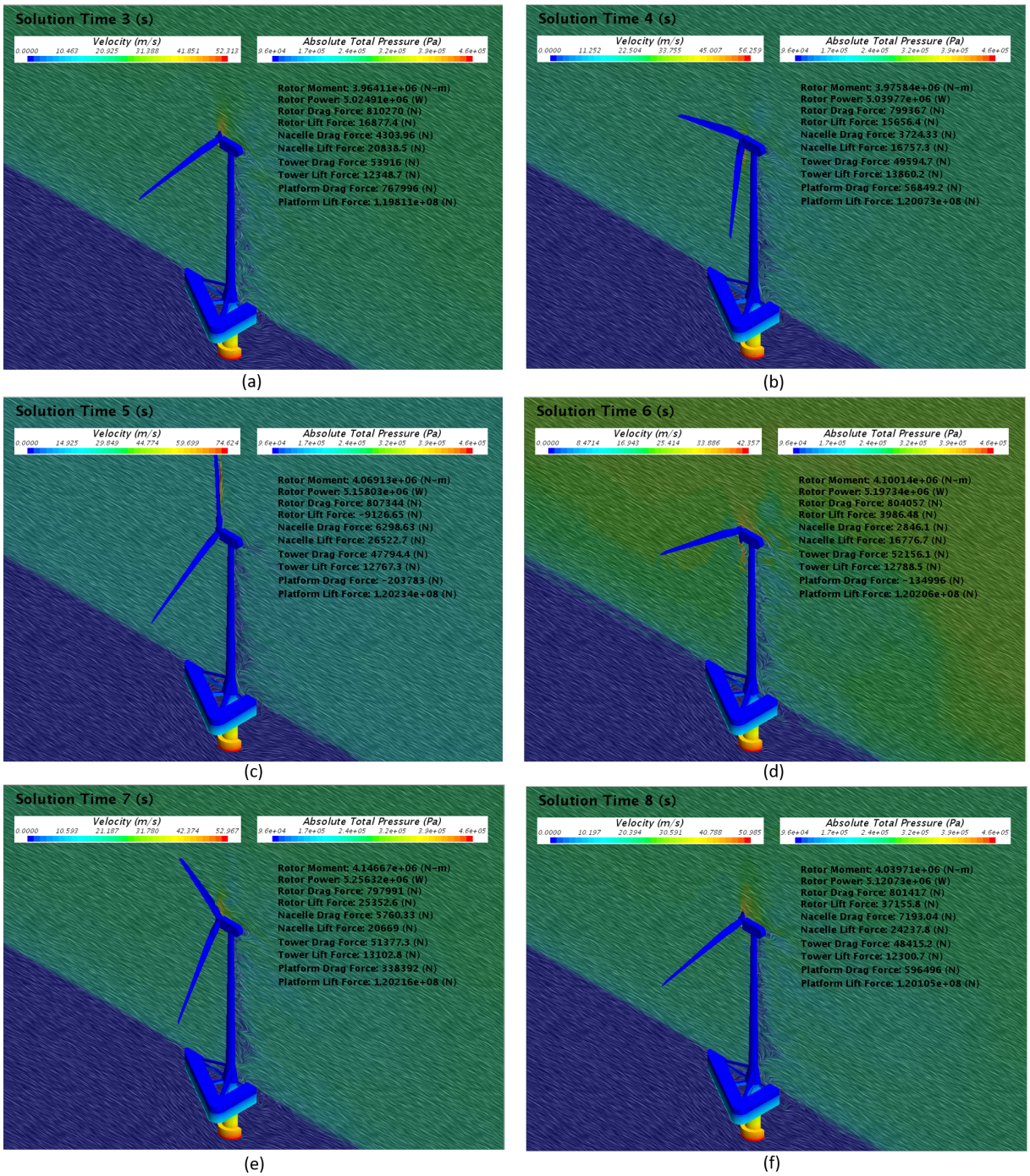

FIGURE 6.27: Visualisation showing flow domain velocity magnitude and structure absolute total pressure on the xz-plane with reference to the global coordinate (0,0,0) m, at (a) 3 s, (b) 4 s, (c) 5 s, (d) 6 s, (e) 7 s, and (f) 8 s.

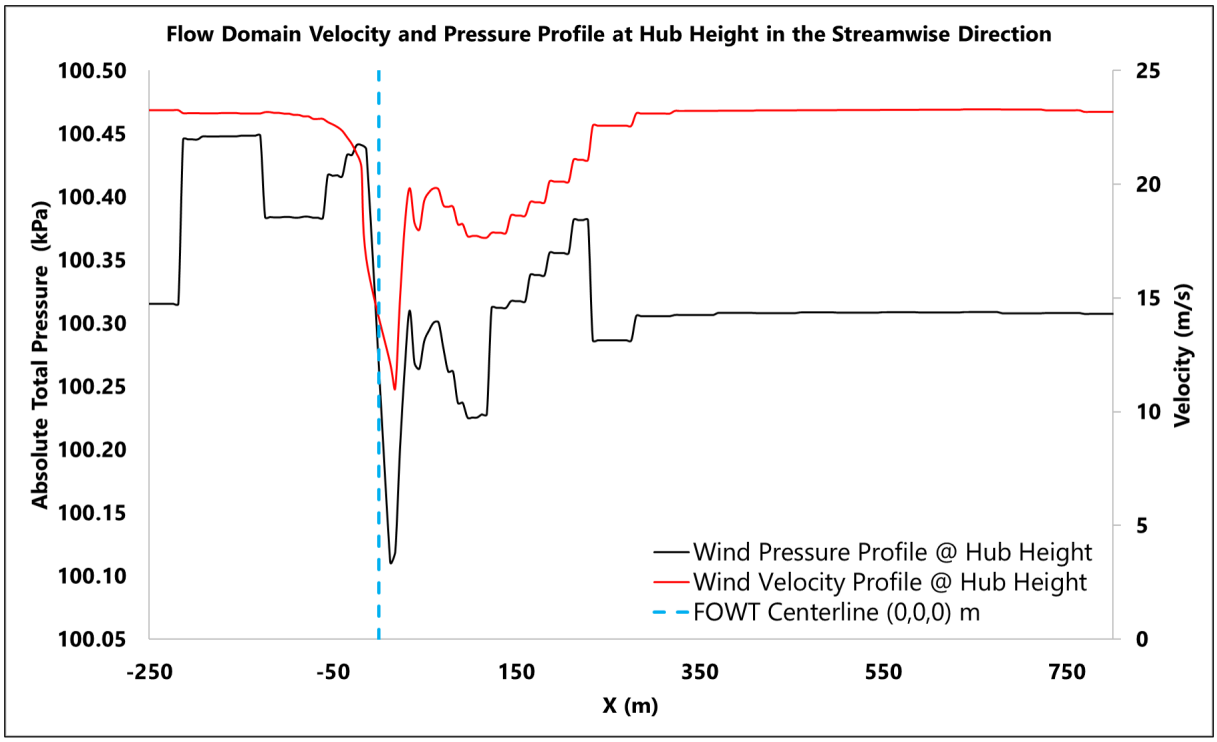

(a)

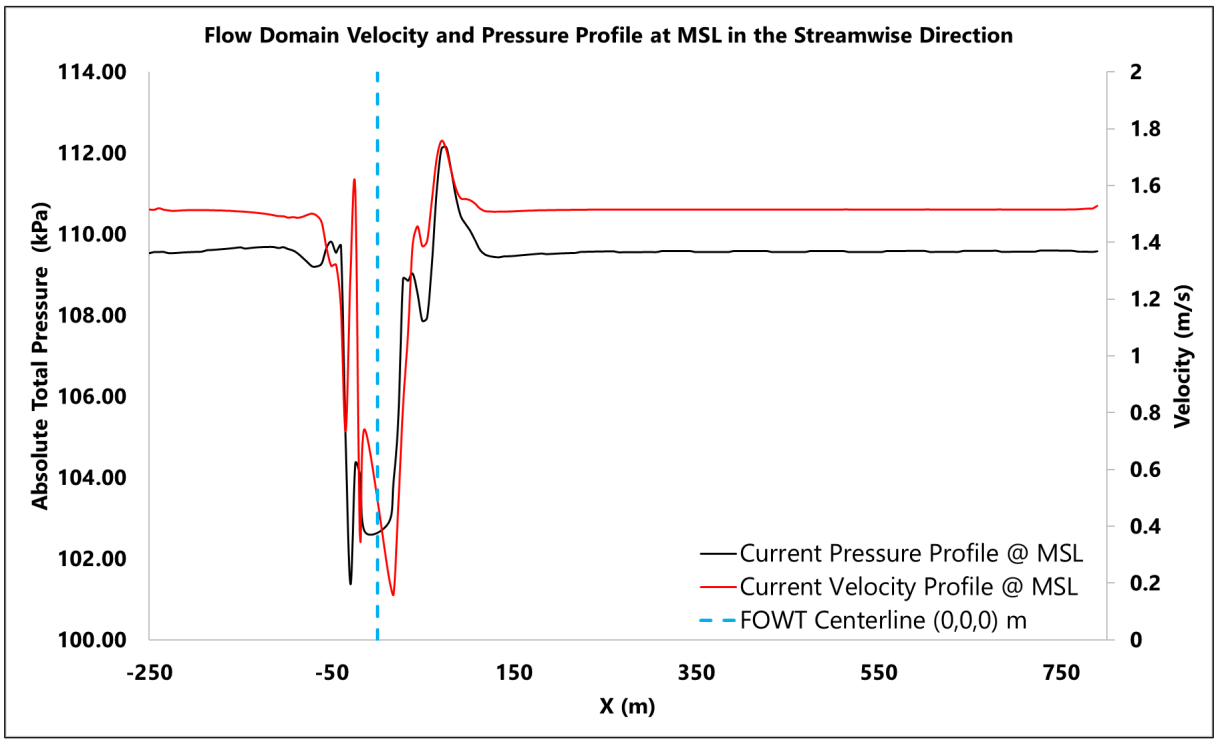

(b)

FIGURE 6.28: Plot showing the flow domain velocity and pressure profiles in the streamwise direction at the (a) hub height, and (b) MSL under operating condition load case at t = 10 s.

Another key observation is that the turbulent fluid-structure interaction creates a drag force opposite to the streamwise direction which on an occasion will become greater than the drag force in the streamwise direction. This flow behaviour produces a net negative drag force for a few seconds as can be seen on the plot in Fig. 6.25f. The magnitude of the negative drag force, in this case, ranges from -0.21 to -0.3 MN as earlier presented in Table 6.4.

Fig. 6.29 contains plots of the structure's drag force under extreme and survival load cases for three mesh refinement scenarios. Under extreme and survival load conditions the wind turbine rotor is parked (i.e., no power generation). The statistical summary of the predicted forces is presented in Table 6.5 and Table 6.6 for extreme and survival load conditions, respectively. The thrust force on the rotor under operating condition (see Table 6.4) was predicted to be higher than the drag force on the rotor under extreme/survival load conditions even though the wind velocity is higher for the later. A logical explanation to this outcome is that under the operating condition the rotor thrust force is as a result of its swept area (see Fig. 2.5) whereas under the parked condition the aerodynamic load on the rotor will be as a result of the rotor's surface normal to the upstream wind (see Fig. 6.30). From Table 6.5, Table 6.6, and the plots presented in Fig. 6.29, there is a clear indication that the floating platform encounters the highest amount of drag force. The magnitude of drag force on the platform under survival and extreme condition are a close match because the drag force on the platform is predominantly current induced. More so, the aerodynamic drag force experienced by the emerged part of the floating platform is very small when compared to the hydrodynamic drag force experienced by the submerged part of the floating platform.

The thrust force on the rotor under operating condition (see Table 6.4) was predicted to be higher than the thrust force under extreme/survival load conditions even though the wind velocity is higher for the later. A logical explanation to this outcome is that under the operating condition the rotor thrust force is as a result of its swept area (see Fig. 2.5) whereas under the parked condition the aerodynamic load on the rotor will be as a result of the rotor's surface normal to the upstream wind (Fig. 6.30). To gain an understanding of the nature and features of the boundary layer formed due to the fluid-structure interaction under extreme/survival load cases, visualisation of fluid velocity, absolute total pressure, and wall $y+$ function contour plots are presented in Fig 6.30 to Fig. 6.32. The contour plots presented in Fig. 6.30 provides a finer indication

of the flow attributes and overall magnitude of the fluid velocity at various stages of the flow in the fluid domain.

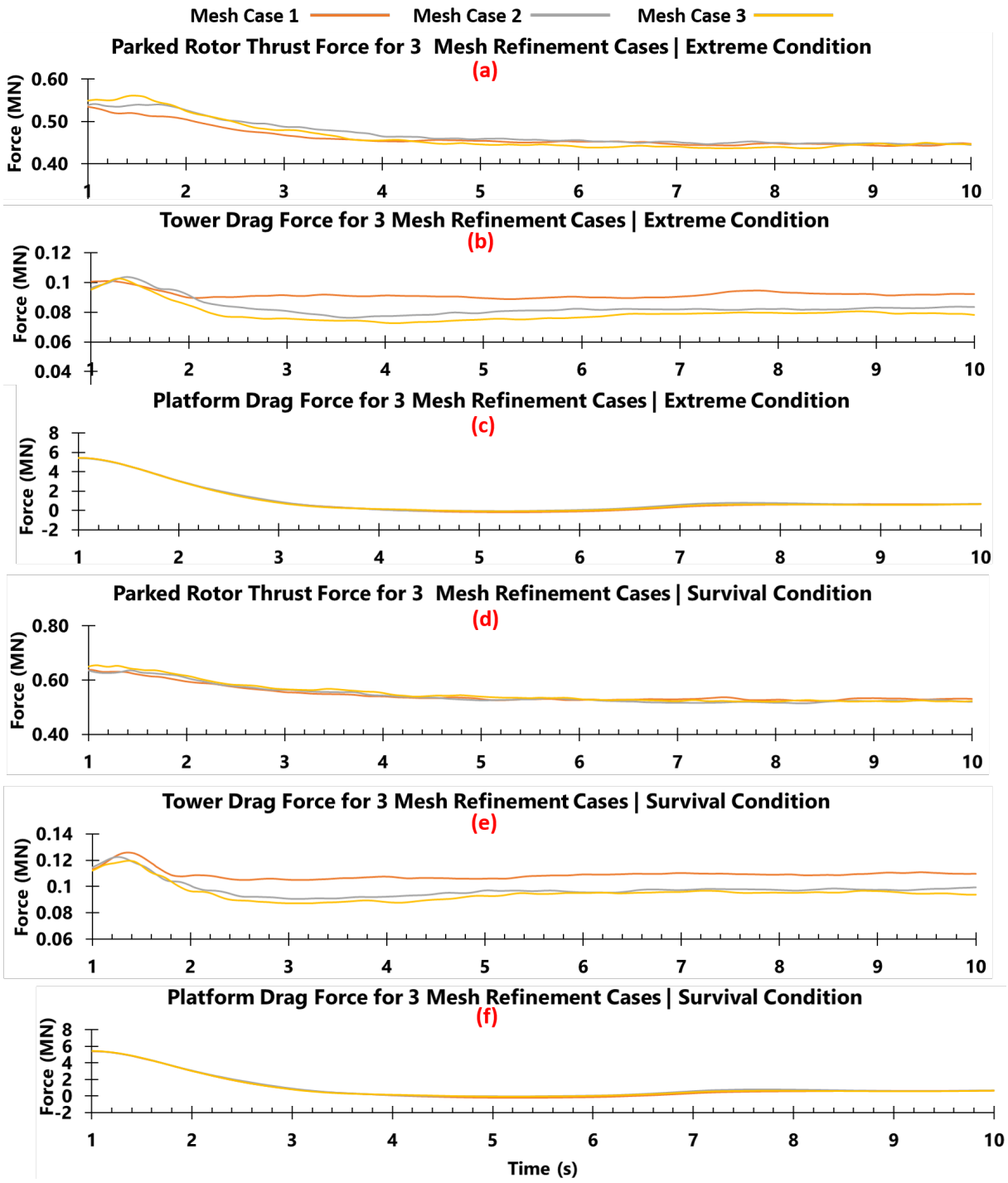

FIGURE 6.29: Plots showing time history of 3 mesh refinement cases for flow direction of 0°; (a) parked rotor thrust force under extreme condition load case, (b)parked rotor thrust force under survival condition load case, (c) tower drag force under extreme condition load case, (d) tower drag force under survival condition load case, (e) platform drag force under extreme condition load case, and (f) platform drag force under survival condition load case.

TABLE 6.5: Comparison of results for different mesh refinement | Extreme condition load case.

Results	Mesh Refinement	Mean	Std. Dev	Maximum	Minimum
Parked Rotor Drag Force (N)	Case 1	4.62E+05	2.37E+04	5.35E+05	4.42E+05
	Case 2	4.70E+05	2.98E+04	5.41E+05	4.44E+05
	Case 3	4.65E+05	3.56E+04	5.61E+05	4.37E+05
Tower Drag Force (N)	Case 1	9.20E+04	2.55E+03	1.01E+05	8.90E+04
	Case 2	8.34E+04	5.95E+03	1.04E+05	7.64E+04
	Case 3	7.93E+04	6.39E+03	1.03E+05	7.26E+04
Platform Drag Force (N)	Case 1	9.31E+05	1.42E+06	5.41E+06	-1.98E+05
	Case 2	1.00E+06	1.39E+06	5.41E+06	-6.57E+04
	Case 3	9.58E+05	1.40E+06	5.44E+06	-8.96E+04

TABLE 6.6: Comparison of results for different mesh refinement | Survival condition load case.

Results	Mesh Refinement	Mean	Std. Dev	Maximum	Minimum
Parked Rotor Thrust Force (N)	Case 1	5.48E+05	3.01E+04	6.38E+05	5.24E+05
	Case 2	5.45E+05	3.55E+04	6.37E+05	5.14E+05
	Case 3	5.51E+05	3.85E+04	6.56E+05	5.20E+05
Tower Drag Force (N)	Case 1	1.09E+05	3.88E+03	1.26E+05	1.05E+05
	Case 2	9.79E+04	6.44E+03	1.23E+05	9.07E+04
	Case 3	9.51E+04	6.92E+03	1.20E+05	8.72E+04
Platform Drag Force (N)	Case 1	9.37E+05	1.42E+06	5.41E+06	-1.89E+05
	Case 2	1.01E+06	1.39E+06	5.42E+06	-4.63E+04
	Case 3	9.60E+05	1.40E+06	5.45E+06	-7.55E+04

As can be observed around the solid boundaries of the FOWT, the no-slip condition was adhered to because the values of velocity are zero along the walls of the FOWT. Also, the absolute total pressure contour plot provides some vital information on the magnitude of surface forces per unit area on the walls of the FOWT. It is important to re-emphasise that the surface forces encountered by the FOWT are of two sources: pressure forces dues to the pressure distribution imposed by the surrounding fluid and the viscous forces due to normal and shear stress distribution. Another key observation from Fig. 6.32a to Fig. 6.32d is the symmetricity of the boundary layer on the free surface. Further away from the walls of the structure, there is an increase in the velocity of the flow field. The increase in velocity magnitude further away from the solid boundaries of the FOWT can be attributed to the diminishing effect of the no-slip boundary conditions. The wall $y+$ function as shown on the surface contour plots in Fig. 6.31 and Fig. 6.32 is seen to have a consistent value ≤ 1 across the surfaces of the FOWT which shows that the boundary layers were adequately resolved.

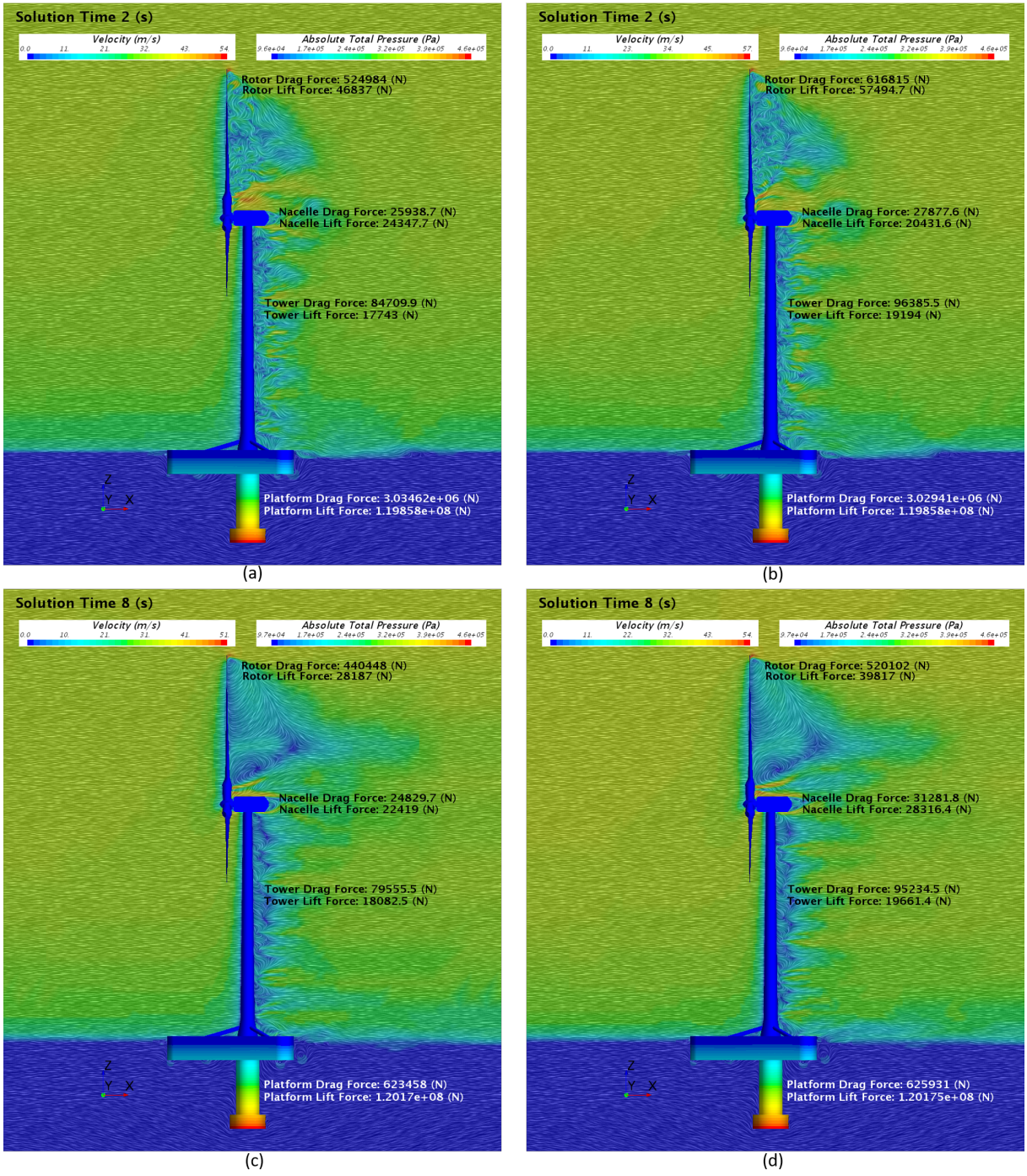

FIGURE 6.30: Visualisation showing side by side comparison of flow domain velocity magnitude and structure absolute total pressure on the xz-plane with reference to the global coordinate (0,0,0) m, at (a) 2 s under extreme condition load case (b) 2 s under survival condition load case, (c) 8 s under extreme condition load case, and (d) 8 s under survival condition load case.

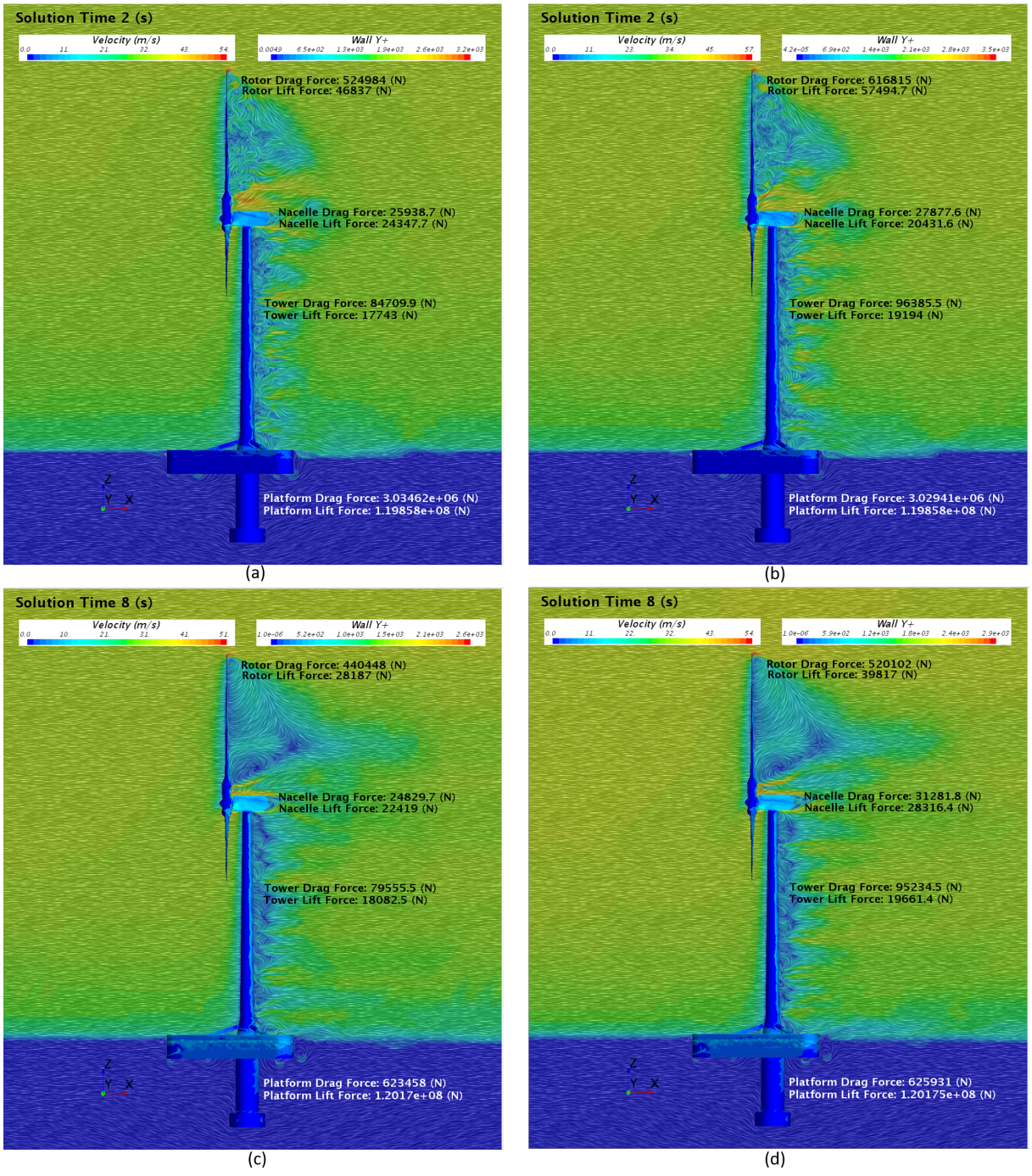

FIGURE 6.31: Visualisation showing side by side comparison of flow domain velocity magnitude and wall y+ function on the xz-plane with reference to the global coordinate (0,0,0) m, at (a) 2 s under extreme condition load case (b) 2 s under survival condition load case, (c) 8 s under extreme condition load case, and (d) 8 s under survival condition load case.

The theoretical prediction of wind and current loads on 3D floating marine structures with sufficient accuracy is challenging. Overcoming this challenge is the main drive for performing the detailed CFD study presented in this section of this thesis.

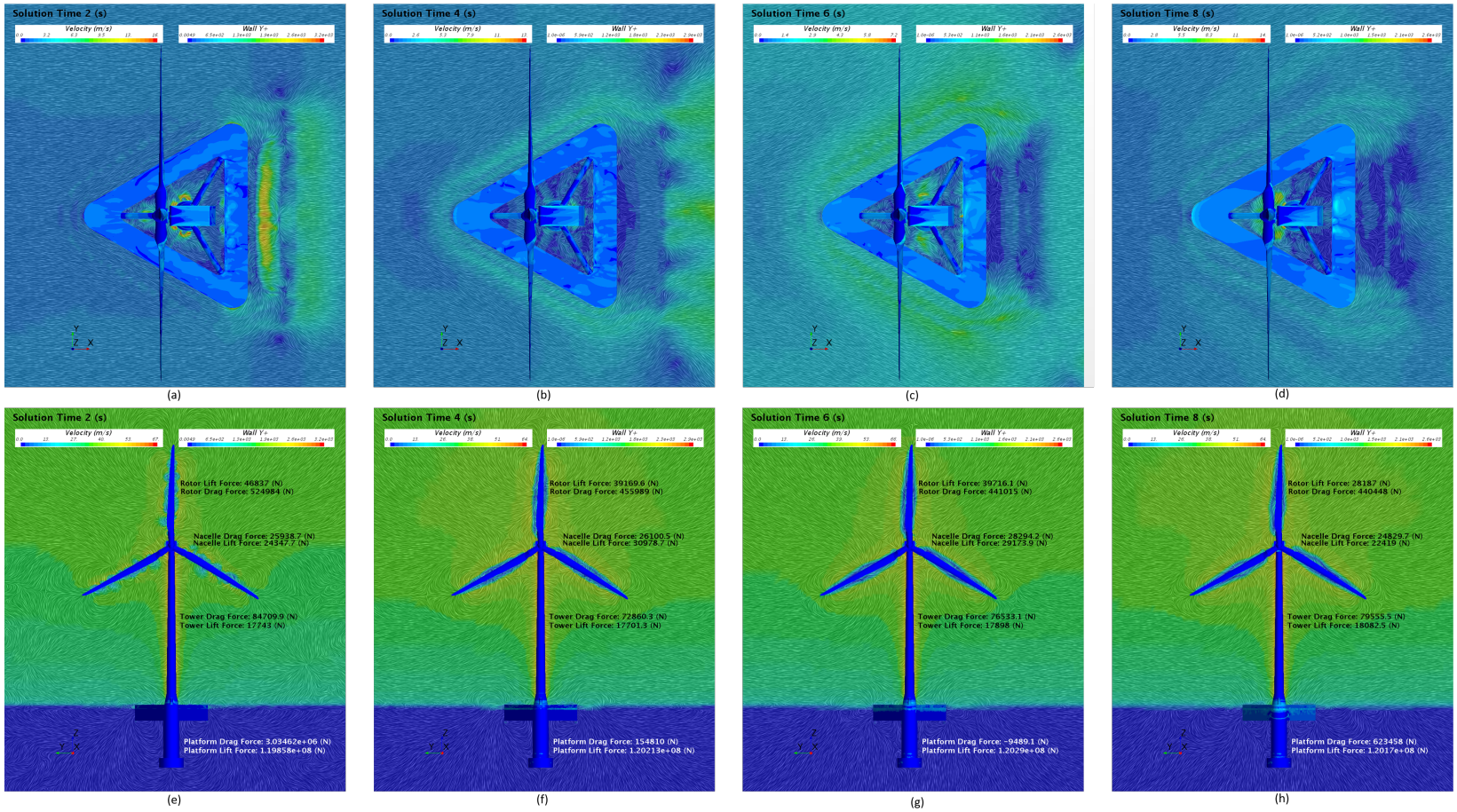

FIGURE 6.32: Visualisation showing side by side comparison of flow domain velocity magnitude and wall y+ function on the xy-plane with reference to the global coordinate (0,0,0) m, at (a) 2 s, (b) 4 s, (c) 6 s, (d) 8 s, and yz-plane with reference to the global coordinate (0,0,0) at (e) 2 s, (f) 4 s, (g) 6 s, (h) 8 s.

For floating marine structures, whose prevailing geometry and environmental flow conditions have a relatively high Reynolds number, the current or wind force ($F_{d(x,y)}$) in the streamwise direction on the structure can be approximately expressed in the form of;

$$F_{d(x,y)} = F_{\varphi(x,y)} U^2 \tag{6.9}$$

where $F_{\varphi(x,y)}$ is the current or wind force coefficient in x or y direction expressed in Ns^2/m^2. It is noteworthy that the term current or wind force coefficient is used to differentiate these coefficients from traditional drag coefficients. As expressed in equation 6.9, the force coefficients are defined as the force per unit velocity squared. In other words, the wind and current force are a function of the relative velocity between the structure and the wind/current. Table 6.7, Table 6.8, and Table 6.9 contains a summary of the simulated viscous forces and the calculated force coefficients under operating, extreme, and survival condition load case, respectively. These values are the average simulated forces on each component of the FOWT assemblage across the three mesh refinement scenarios from 1 s to 10 s. Results from 0 s to 0.975 s were excluded from the calculation of the average simulated force because of the non-linearities and under-developed flow conditions that occurs at the beginning of the simulation. The calculated values for wind and current force coefficient is defined relative to the global coordinate system in the AQWA coupled dynamics model. Here, the force coefficients are entered in the x force coefficient (translation x) field for a direction of $-180°$ to + 180°. The input is initiated such that the coefficients are applied in a moving axis system (i.e. the axes moves with the structure) as illustrated in Fig. 6.33.

TABLE 6.7: Summary of CFD simulation result and calculated viscous force coefficient for operating condition load case.

FOWT Component	Operating Condition Load Case | $U_w = 23.04\ m/s$ | $U_c = 1.52\ m/s$				
	Total Drag Force (N)	Wind Drag Force (N)	Wind Drag Force Coeff. (Ns^2/m^2)	Current Drag Force (N)	Current Drag Force Coeff. (Ns^2/m^2)
Rotor	7.95E+05	7.95E+05	1,497.63	-	-
Nacelle	4.72E+03	4.72E+03	8.89	-	-
Tower	4.72E+04	4.72E+04	88.99	-	-
Platform	8.89E+05	3.00E+05	564.85	5.90E+05	256,865.51

TABLE 6.8: Summary of CFD simulation result and calculated viscous force coefficient for extreme condition load case.

FOWT Component	Extreme Condition Load Case | $U_w = 33.16\ m/s$ | $U_c = 1.52\ m/s$				
	Total Drag Force (N)	Wind Drag Force (N)	Wind Drag Force Coeff. (Ns^2/m^2)	Current Drag Force (N)	Current Drag Force Coeff. (Ns^2/m^2)
Rotor	4.66E+05	4.66E+05	423.41	-	-
Nacelle	2.65E+04	2.65E+04	24.07	-	-
Tower	8.49E+04	8.49E+04	77.22	-	-
Platform	9.64E+05	3.74E+05	340.56	5.90E+05	256,865.51

TABLE 6.9: Summary of CFD simulation result and calculated viscous force coefficient for survival condition load case.

FOWT Component	Survival Condition Load Case | $U_w = 36.1\ m/s$ | $U_c = 1.52\ m/s$				
	Total Drag Force (N)	Wind Drag Force (N)	Wind Drag Force Coeff. (Ns^2/m^2)	Current Drag Force (N)	Current Drag Force Coeff. (Ns^2/m^2)
Rotor	5.48E+05	5.48E+05	420.65	-	-
Nacelle	2.99E+04	2.99E+04	22.98	-	-
Tower	1.01E+05	1.01E+05	77.30	-	-
Platform	9.70E+05	3.80E+05	291.74	5.90E+05	256,865.51

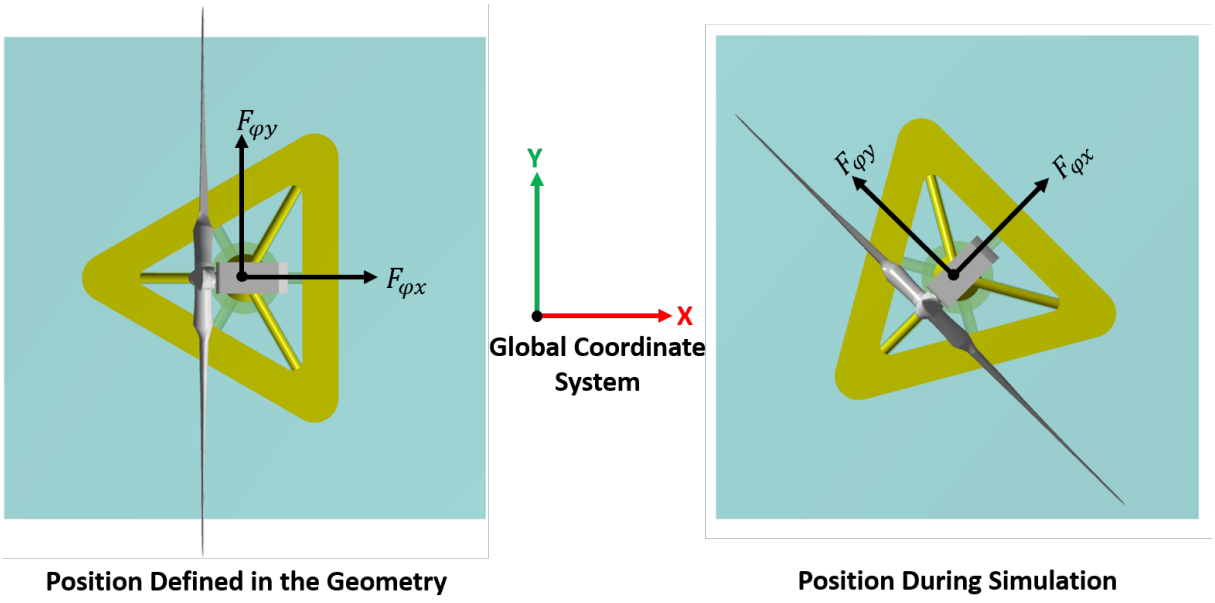

FIGURE 6.33: An illustration showing the force coefficient definition when the structure is in the position as defined in the geometry (left) and the position during simulation (right).

6.2 Coupled Dynamics Numerical Simulation

Theoretically predicting the dynamics of a FOWT is challenging. The goal of a coupled dynamics analyses is to accurately forecast the FOWT motions and the mooring system response with due consideration to WTG-floater-mooring line coupling effect. Good engineering practice requires that coupled dynamic analyses be conducted for various design conditions to encompass extreme conditions. Consequently, numerical reliability and computational proficiency is key to facilitating a practical design analysis of FOWT installations. A validation of the SHARPE numerical modeling scheme have been discussed in section 5.2. In this section, results of the engineering and mathematical analysis performed for the TRIHF-OWT concept using the SHARPE numerical modeling scheme is discussed. Precisely, this section seeks to enlighten the audience more on the focus of this research by providing a clearer understanding of the time domain and frequency domain coupled dynamics numerical simulation results. It is noteworthy that to some extent, the success of subsequent aerodynamic and hydrodynamic analyses depends on accurate modelling of the viscous damping (see section 6.1.1), viscous drag forces (see section 6.1.2) and hydrostatic loads for the floating platform. The structure weight and buoyancy force balance calculations presented in sections 4.2.1 to 4.2.3 are a starting point. Thus, radiation/diffraction analyses need to be performed with the right modelling approach using a suitable analyses tool, hence the choice for the SHARPE numerical scheme using the ANSYS AQWA code.

6.2.1 Model Set-Up and Analysis Strategy

As discussed earlier in section 5.1, the SHARPE numerical modelling scheme employs a mixed geometry model consisting of diffracting panels (Fig. 6.34) and dummy Morison elements (Fig. 6.35). Utilising a mixed geometry model of tube elements and diffracting panels enables the assessment and comparison of results for linearised drag modelling and non-linearised drag modelling in the frequency domain analysis. The mesh parameters and generated mesh information for TRIHF are contained in Table 6.10. The size of the diffracting panels is explicitly related to the maximum wave frequency that can be modelled in the diffraction analysis. For the coupled dynamics analysis, quadrilateral mesh having a maximum element size of 0.75 m were generated across the entire surface of the FOWT geometry model. However, to adequately

capture the features of the smaller elements within the hull of the platform, a finer element size of 0.375 m were created on each surface of the radial and diagonal braces.

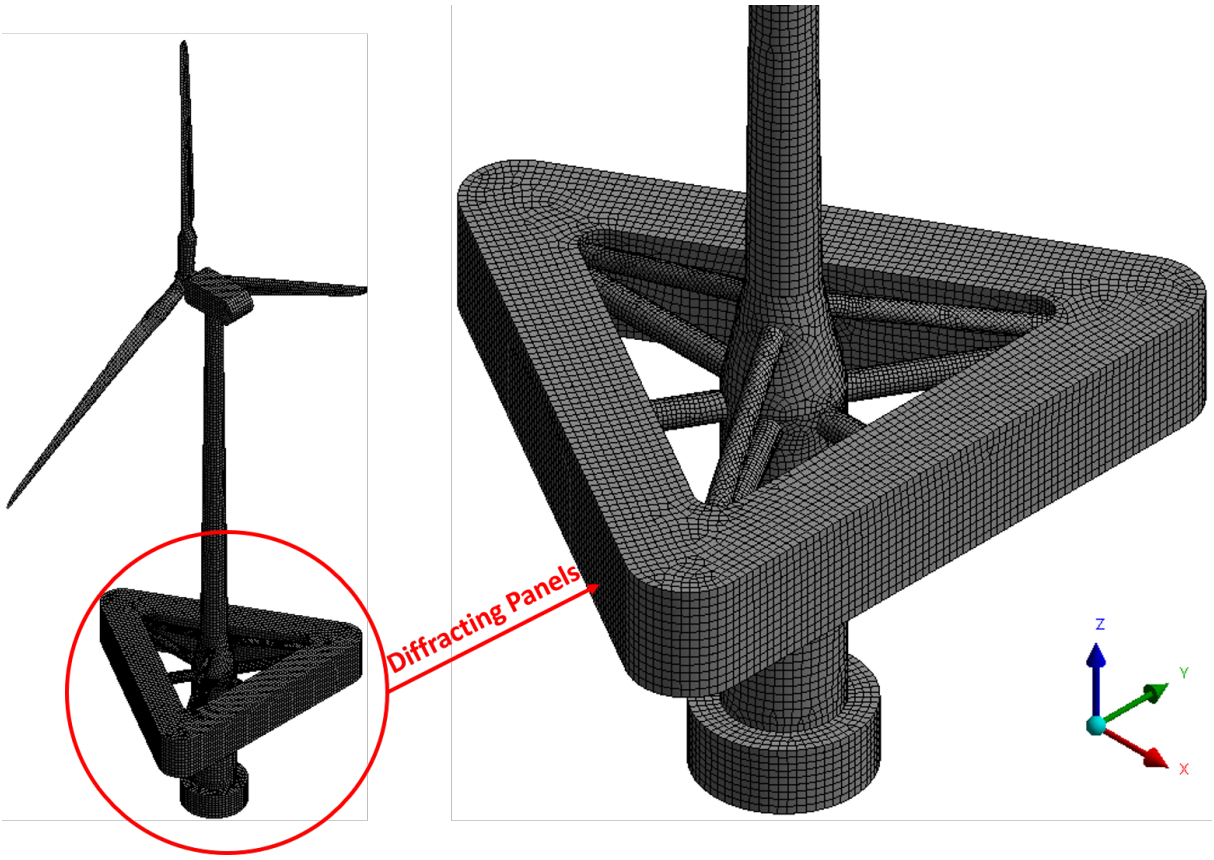

FIGURE 6.34: 3D model diffracting panels for HD and HR numerical simulation.

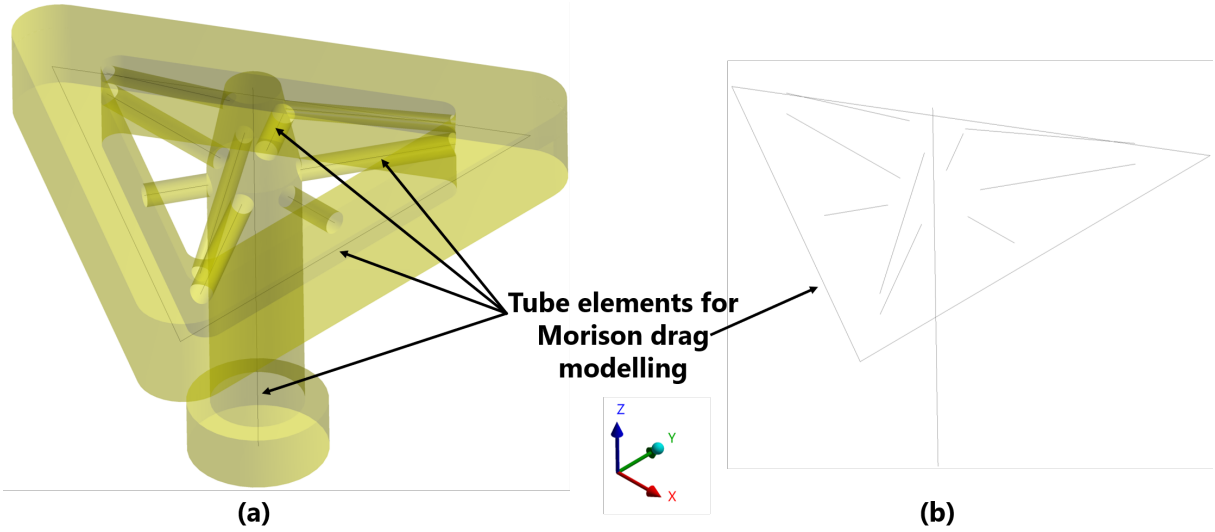

FIGURE 6.35: Illustration showing (a) tube elements defined within the diffracting geometry model (b) tube elements.

TABLE 6.10: Generated mesh information and parameters.

Parameters	Value
Total Nodes	29316
Total Elements	28760
Diffracting Nodes	13766
Diffracting Elements	13722
Line Body Nodes	1092
Line Body Elements	541
Maximum Allowed Frequency	0.529 Hz

Appendix B contains the node definitions and geometric properties of the linearising elements. Observing the values presented in the table contained in B, the tube elements have a small diameter that corresponds to the real diameter of the floating platform parts. The tubes were scaled to $1/100^{th}$ of the real diameter. This is done so that the added mass effect is not doubled up since this is computed by AQWA from the diffraction model. Consequently, to include the viscous effect, the standard drag coefficient is multiplied by 100.

The time response analysis was performed to facilitate a global performance assessment of the TRIHF platform in the time domain. The mooring cable dynamics were effectively modelled to invoke the restraining conditions on the floating platform. In addition, the convolution method used in the radiation force calculation was re-initiated. The convolution approach to the radiation force calculation in the time domain is a more rigorous computation and will enhance the capability of handling the nonlinear response of the coupled dynamics model. Furthermore, the current phase shift was accounted for and drift force with multi-directional wave interaction applied. Wave drift calculations were also made. For the floating platform's drag calculation, drift frequency velocity and wave frequency velocity were considered in the scheme.

As illustrated in Fig. 6.36a, the sea domain size ($x \times y$) set up for the analysis measures 700 m $\times$ 600 m having a water depth of 300 m. The seawater density and gravity were set to $1025 kg/m^3$ and $9.80665 m/s^2$, respectively. A total of 23 wave intermediate directions from $-180°to + 180°$ (15°step) were studied. All wave, wind and current directions are related to the local coordinate system defined in Fig. 6.36b and angle are positive in the clockwise direction.

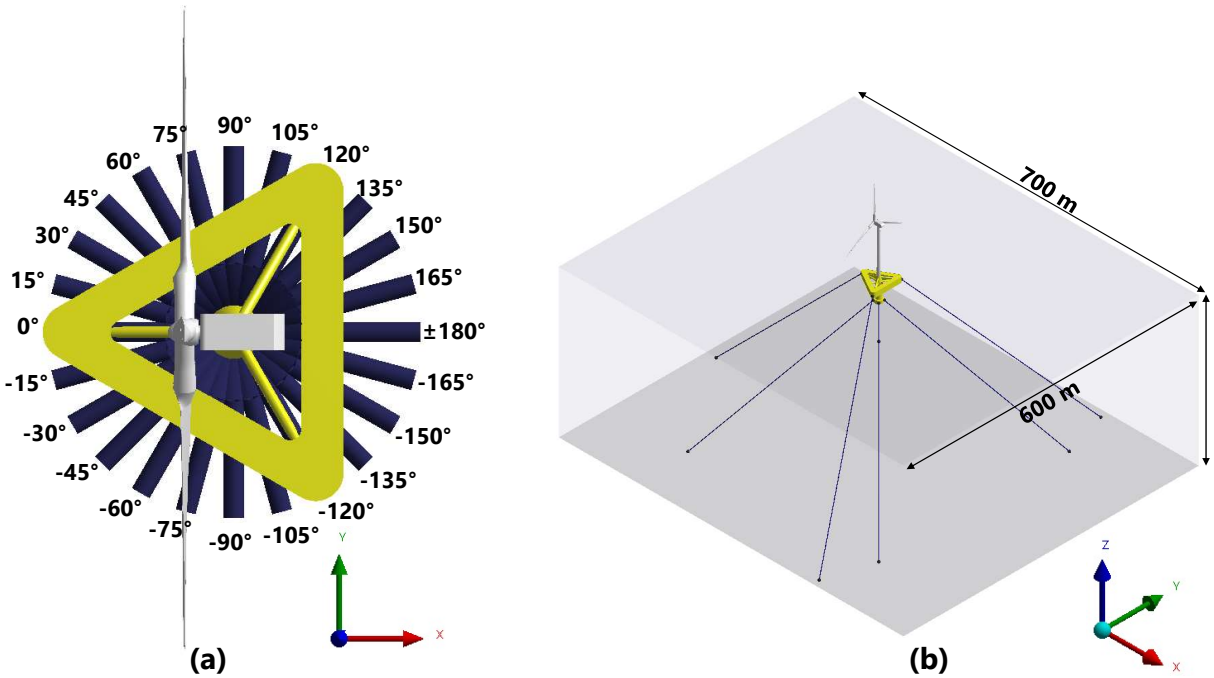

FIGURE 6.36: Illustration showing (a) direction definition for wind, wave and current, and (b) flow domain size.

6.2.2 Primal Hydrodynamic Diffraction/Radiation and Stability Analysis in Flat Wave

The goal of performing a primal flat wave hydrodynamic diffraction/radiation and stability analysis is to get a principal understanding of the floating platform's characteristics in an ideal situation where MetOcean conditions are absent. Flat wave here implies no wave loads are applied. The primal solution from flat wave analysis provides some balanced information regarding the platform's hydrostatics, added mass/moment, restoring force/moment, mooring stiffness matrix, and natural frequencies in all 6DOFs.

In addition to providing station keeping, the taut leg mooring system offers additional dynamic stability to the FOWT. Table 6.11 contains the mooring stiffness calculation output from the primal hydrodynamic diffraction/radiation analysis. The mooring stiffness is a 6×6 matrix calculated with respect to both the Fixed Reference Axes (FRA) and the FOWT Local Structure Axes (LSA). The mooring stiffness includes all the stiffness effects from all the mooring line connected to the FOWT but excludes the hydrostatic stiffness of the floating platform itself. Consequently, the mooring stiffness matrix output provided in Table 6.11 is used as an input in the diffraction/radiation

analysis step that generates displacement RAOs. This explains why the hydrodynamic analysis calculations employed for this research excludes the floating platform hydrostatic stiffness from its mooring stiffness calculation.

Table 6.12 contains a summary of the platform hydrostatics. As can be seen from the tabulated results, the Center of Gravity (CoG) position (-19.94 m) is below the Center of Buoyancy (CoB) position (-8.29 m) resulting in a CoB to CoG (GB) value of 11.64 m in both the lateral and transverse direction. Since GB $>$ 1, then the floating platform can be said to be in a stable equilibrium. Also, the metacentric height in the lateral and transverse direction being greater than zero is a further indication of the platform's hydrostatic stability.

TABLE 6.11: Mooring stiffness matrix for input into hydrodynamic diffraction/radiation analysis.

	FOWT LSA					
FRA	**X**	**Y**	**Z**	**RX**	**RY**	**RZ**
X	1780 kN/m	0 kN/m	0 kN/m	0 kN/°	0 kN/°	0 kN/°
Y	0 kN/m	1780 kN/m	0 kN/m	0 kN/°	0 kN/°	0 kN/°
Z	0 kN/m	0 kN/m	8340 kN/m	0 kN/°	0 kN/°	243 kN/°
RX	0 kN.m/m	0 kN.m/m	0 kN.m/m	3870000 kN.m/°	0 kN.m/°	0 kN.m/°
RY	0 kN.m/m	0 kN.m/m	0 kN.m/m	0 kN.m/°	3830000 kN.m/°	0 kN.m/°
RZ	0 kN.m/m	0 kN.m/m	0 kN.m/m	0 kN.m/°	0 kN.m/°	89300 kN.m/°

TABLE 6.12: Platform hydrostatic results.

Hydrostatic Results for Floating Platform						
Hydrostatic Stiffness						
Centre of Gravity (CoG) Position:	**X:**	0 m	**Y:**	0 m	**Z:**	-19.94 m
		Z		**RX**		**RY**
Heave (Z):		12640.769 kN/m		9.4678E-3 kN/°		-13.48233 kN/°
Roll (RX):		0.5424637 kN.m/m		75132.141 kN.m/°		-9.1654E-2 kN.m/°
Pitch (RY):		-772.48065 kN.m/m		-9.1654E-2 kN.m/°		75133.148 kN.m/°
Hydrostatic Displacement Properties						
Actual Volumetric Displacement:		12006.709 m³				
Centre of Buoyancy (CoB) Position:	**X:**	0 m	**Y:**	0 m	**Z:**	-8.2923403 m
Cut Water Plane Properties						
Cut Water Plane Area:		1257.5605 m²				
Principal 2nd Moments of Area:	**X:**	288398.31 m⁴	**Y:**	288399.84 m⁴		
Small Angle Stability Parameters (*with respect to Principal Axes*)						
CoB to CoG (GB):		11.648311 m				
Metacentric Heights (GMX/GMY):		35.668076 m		35.668201 m		
CoB to Metacentre (BMX/BMY):		24.019764 m		24.019892 m		
Restoring Moments (MX/MY):		75132.109 kN.m/°		75132.375 kN.m/°		

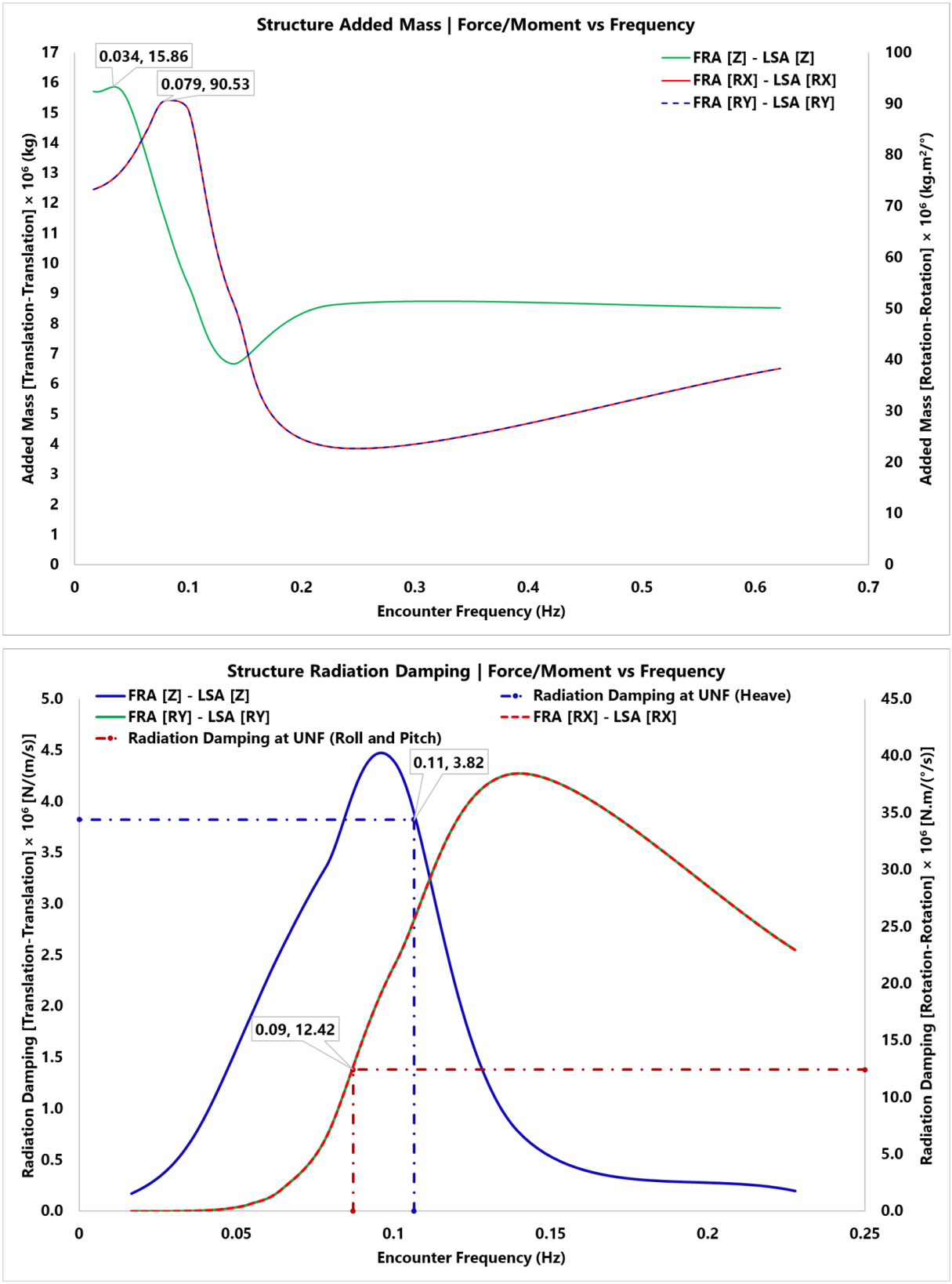

FIGURE 6.37: Plots showing structure (top) added mass and (bottom) radiation damping vs frequency.

Fig. 6.37 illustrate the plots of added mass and radiation damping magnitudes of

the platform at different frequencies. The highlighted data labels in Fig. 6.37(top) are the peak added mass and added moment of inertia with respect to the corresponding component in FRA and sub-component in LSA. Since viscous damping is frequency independent, it makes sense to utilise the radiation damping values at the Undamped Natural Frequency (UNF) of the floating platform in the viscous damping calculations. Thus, the data labels presented in Fig. 6.37(bottom) shows the radiation damping components at the UNF of the floating structure. A summary of the results for peak magnitudes of added mass and added moment of inertia, total damping coefficient, calculated UNF, radiation damping coefficient at UNF, and viscous damping coefficient is presented in Table 6.13.

Based on the outcome of the calculations performed in Table 6.13, Table 6.14 contains the resulting 6 × 6 viscous damping matrix that is used as input into the hydrodynamic diffraction/radiation analysis in an irregular wave. Table 6.15 contains the MetOcean and WTG conditions for various LCs while Table 6.16 presents details of the test matrix for the coupled dynamics simulation results that will be presented and discussed in later sections of this chapter.

TABLE 6.13: Summary of calculation and result for platform added mass, radiation damping, and viscous damping coefficient.

Parameter	FRA [Z] – LSA [Z] (Heave)	FRA [RX] – LSA [RX] (Roll)	FRA [RY] – LSA [RY] (Pitch)
Added Mass/ Moment of inertia (m_a, I_a)	15.86E+06 kg	90.53E+06 kg.m^2/°	90.53E+06 kg.m^2/°
Mass/Moment of inertia (m, I)	12.34E+06 kg	153.59E+06 kg.m^2/°	153.59E+06 kg.m^2/°
Total Mass/Moment of inertia	28.20E+06 kg	244.12E+06 kg.m^2/°	244.12E+06 kg.m^2/°
Restoring Force/Moment Coefficient (c_{ij})	12.64E+06 N/m	73.17E+06 N.m/°	73.17E+06 N.m/°
Non-dimensional total damping coefficient (ς_{ij})	0.2781	0.1071	0.0990
Total damping coefficient (b_{ij})	10.50E+06 N/(m/s)	28.64E+06 N.m/(°/s)	26.47E+06 N.m/(°/s)
Undamped Natural Frequency (UNF) ($\omega_{0,ij}$)	0.1066 Hz	0.0871 Hz	0.0871 Hz
Radiation damping @ UNF ($b^r_{ij}(\omega_{0,ij})$)	3.82E+06 N/(m/s)	12.42E+06 N.m/(°/s)	12.42E+06 N.m/(°/s)
Viscous damping coefficient (b^{ψ}_{ij})	6.68E+06 N/(m/s)	16.21+06 N.m/(°/s)	14.04E+06 N.m/(°/s)
Ratio of Viscous Damping to Total Damping	64%	57%	53%
Ratio of Viscous Damping to Radiation Damping	175%	130%	113%

TABLE 6.14: Viscous damping matrix for input into hydrodynamic diffraction/radiation analysis.

	FOWT LSA					
FRA	X	Y	Z	RX	RY	RZ
X	0.0 N/(m/s)	0.0 N/(m/s)	0.0 N/(m/s)	0.0 N/(°/s)	0.0 N/(°/s)	0.0 N/(°/s)
Y	0.0 N/(m/s)	0.0 N/(m/s)	0.0 N/(m/s)	0.0 N/(°/s)	0.0 N/(°/s)	0.0 N/(°/s)
Z	0.0 N/(m/s)	0.0 N/(m/s)	6.68E+06 N/(m/s)	0.0 N/(°/s)	0.0 N/(°/s)	0.0 N/(°/s)
RX	0.0 N.m/(m/s)	0.0 N.m/(m/s)	0.0 N.m/(m/s)	16.21E+06 N.m/(°/s)	0.0 N.m/(°/s)	0.0 N.m/(°/s)
RY	0.0 N.m/(m/s)	0.0 N.m/(m/s)	0.0 N.m/(m/s)	0.0 N.m/(°/s)	14.04E+06 N.m/(°/s)	0.0 N.m/(°/s)
RZ	0.0 N.m/(m/s)	0.0 N.m/(m/s)	0.0 N.m/(m/s)	0.0 N.m/(°/s)	0.0 N.m/(°/s)	0.0 N.m/(°/s)

TABLE 6.15: Coupled dynamics simulation LCs for Metocean and turbine conditions.

LC	Turbine Condition	Rotor Speed	Wind Velocity @ Hub Height	Wave Condition			Current Velocity
				H_s	T_p	γ	
1	Operating Condition	12.1 RPM	20.66 m/s	4.85 m	17.52 s	3.3	1.52 m/s
2	Extreme Condition	0 RPM	29.73 m/s	7.02 m	22.22 s	3.3	1.52 m/s
3	Survival Condition	0 RPM	32.37 m/s	7.65 m	23.59 s	3.3	1.52 m/s

TABLE 6.16: Coupled dynamics simulation LC test matrix.

CODE	Load Cases (LCs)	Operating Condition [LC1]	Extreme Condition [LC2]	Survival Condition [LC3]
A	Metocean	LC1A	LC2A	LC3A
B	Metocean + Mooring Stiffness	LC1B	LC2B	LC3B
C	Metocean + Viscous Damping	LC1C	LC2C	LC3C
D	Metocean + Mooring Stiffness + Viscous Damping	LC1D	LC2D	LC3D

The coupled dynamics simulations were performed for three LCs; operating condition, extreme condition, and survival condition. To explore the effects of mooring stiffness and viscous damping on the global dynamic response of the floating platform, the mooring stiffness matrix (Table 6.11) and viscous damping matrix (Table 6.14) were modelled individually and collectively in the hydrodynamic diffraction/radiation analysis for all load cases and MetOcean conditions (wind, wave, and current).

6.2.3 Hydrodynamic Diffraction/Radiation Analysis in Irregular Wave

The hydrodynamic diffraction/radiation numerical scheme employed for this thesis is based on the linear potential theory which is implemented on the assumption that the floating structure has zero or infinitesimally small forward speed. It also assumes that the fluid is inviscid and incompressible, and the fluid flow is irrotational (see Section 2.3.2).

Respond Amplitude Operators (RAOs)

A set of linear algebraic equations were solved to obtain the Response Amplitude Operators (RAOs) of the floating platform to irregular wave forces. The computed results of displacement RAOs for a wave direction of 0° with and without linearised drag modelling for LC1 are contained in Fig. 6.38 to Fig. 6.43. Each RAOs define the floating

platform response for each DOF to a specified wave direction and wave period. Essentially, the RAOs relates to the amplitude of the structure's motion to the amplitude of the wave, and a phase that relates to the timing of the structure motion relative to the wave.

Overall, initiating the mooring stiffness matrix and/or viscous damping matrix in the diffraction/radiation analysis causes the RAOs to be inconsistent with the wave forces. For instance, observing Fig. 6.40 showing plots of heave motion displacement RAOs for various scenarios of LC1, it is clear that the mooring stiffness (LC1B) and viscous damping (LC1C) reduces the displacement RAOs of the platform. However, the mooring stiffness causes a considerable reduction to the RAOs than viscous damping. Values for LC1A on the RAO plots are consistent with the wave forces and is used as a baseline in assessing the effects of viscous damping and mooring stiffness on the dynamic response of the floating platform. The stiffness matrix flattens the RAO values for roll and pitch motion while a combination of both matrices (LC1D) are seen to further reduce the RAO values.

However, looking at the plots for surge (Fig. 6.38), sway (Fig. 6.39), and yaw (Fig. 6.43) motion, the mooring stiffness matrix is seen to amplify the RAO values for these modes of motion. Although the viscous damping model indicates reduced RAO values for all the 6DOF, the mooring stiffness takes dominance in determining what the final values of the RAOs will be when modelled in combination with the viscous damping matrix. Appendix C and Appendix D contain displacement RAO results for all scenarios of LC2 and LC3, respectively. A side-by-side comparison of the displacement RAOs for LC2 and LC3 shows a very close match because the wave parameters are similar based on the data presented in Table 6.15.

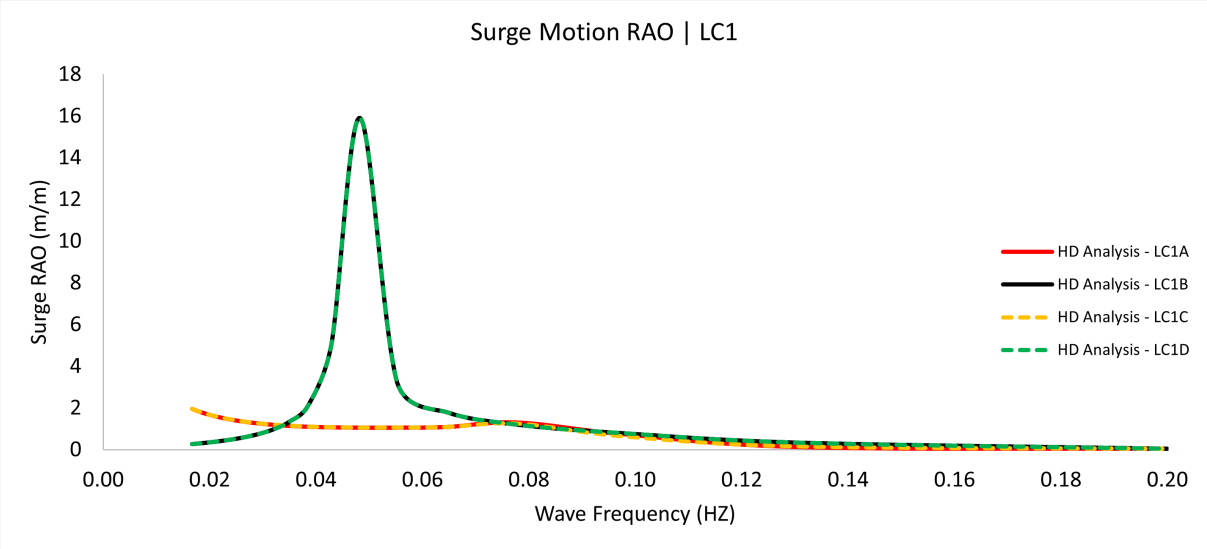

FIGURE 6.38: FOWT surge motion displacement RAOs for a wave direction of 0° for various scenarios of LC1.

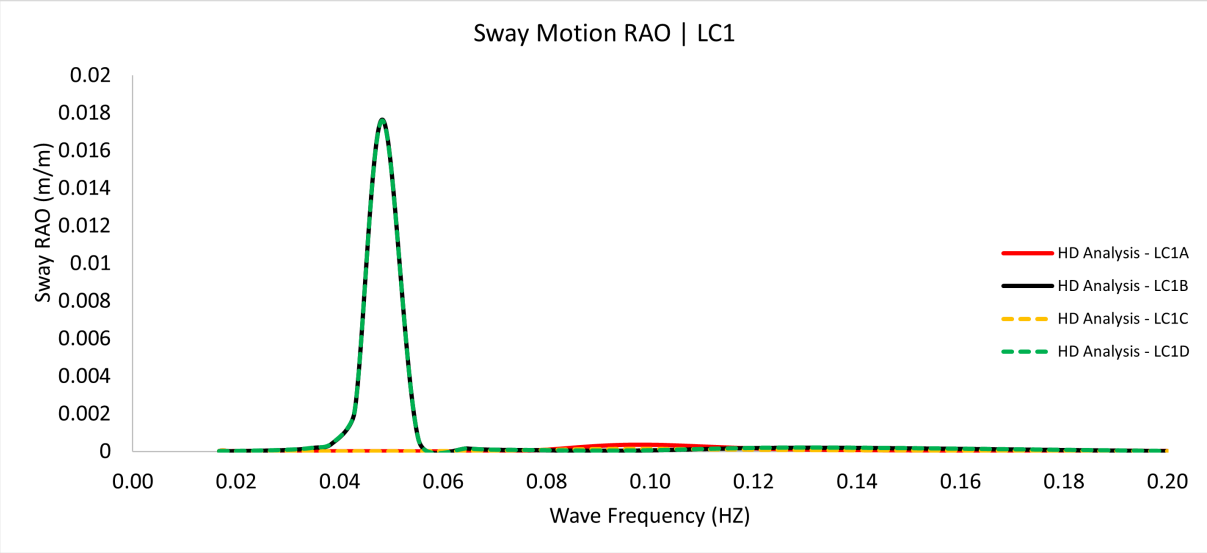

FIGURE 6.39: FOWT sway motion displacement RAOs for a wave direction of 0° for various scenarios of LC1.

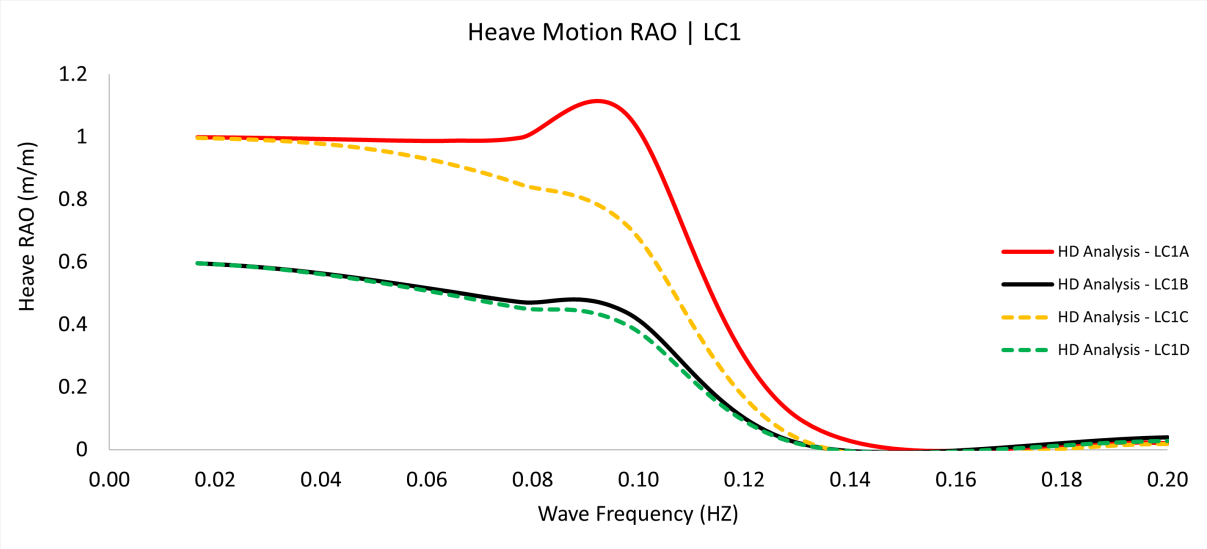

FIGURE 6.40: FOWT heave motion displacement RAOs for a wave direction of 0° for various scenarios of LC1.

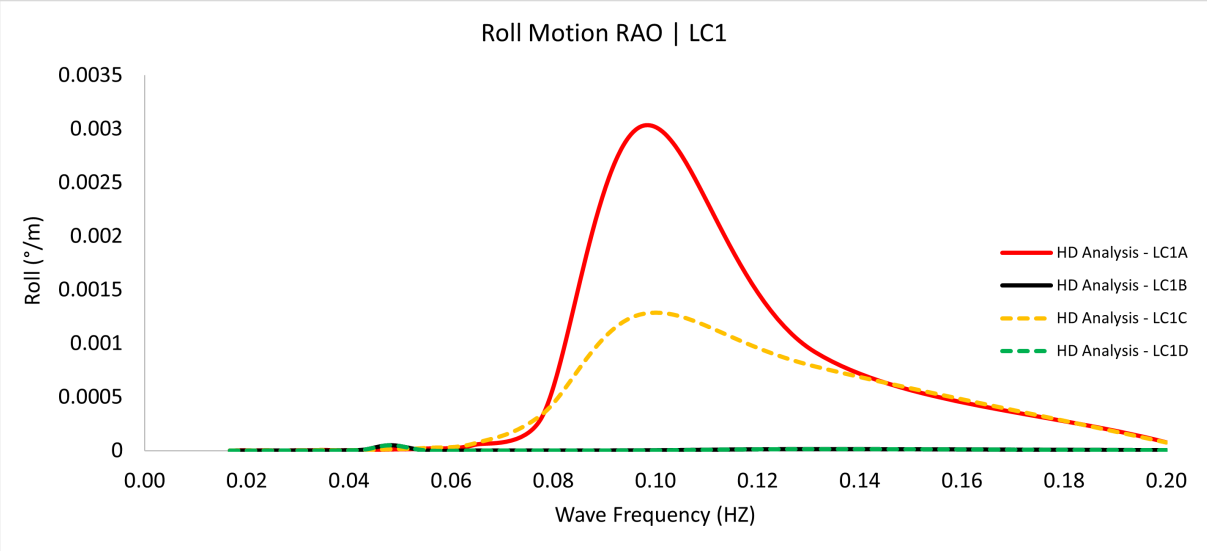

FIGURE 6.41: FOWT roll motion displacement RAOs for a wave direction of 0° for various scenarios of LC1.

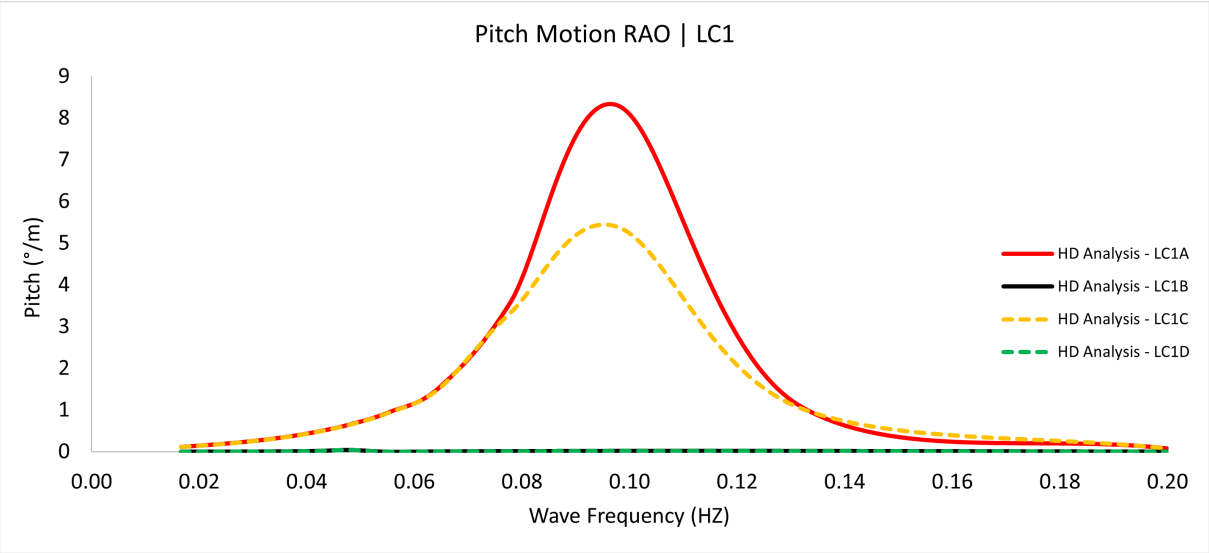

FIGURE 6.42: FOWT pitch motion displacement RAOs for a wave direction of 0° for various scenarios of LC1.

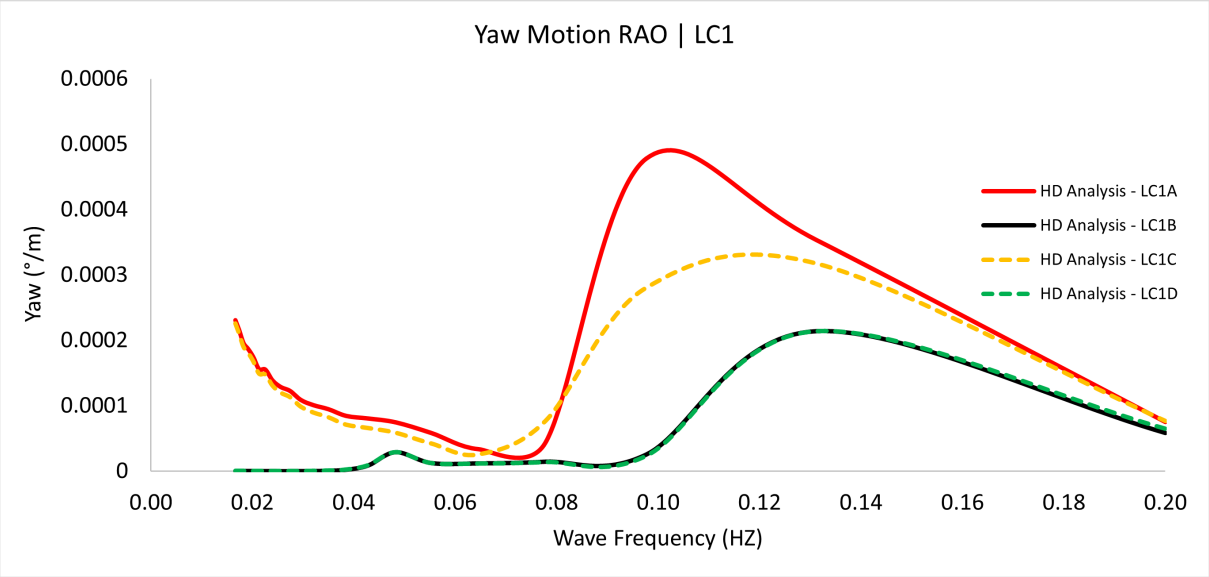

FIGURE 6.43: FOWT yaw motion displacement RAOs for a wave direction of 0° for various scenarios of LC1.

Near Field Drift Wave Forces

Low Frequency (LF) motions of a floating structure originate from low-frequency loads such as slowly varying wave drift force. The wave drift force is a second-order wave force, proportional to the square of wave amplitude. In a random sea state containing the sum of N wave components ω_i, the wave drift force oscillates at difference frequencies $\omega_i - \omega_j$ and can be expressed as;

$$q_{WA}^{(2-)}(t) = R\sum_{i}^{N} a_i H^{(2-)}(\omega_i)\, e^{i(\omega_i)t} - R\sum_{j}^{N} a_j H^{(2-)}(\omega_j)\, e^{i(\omega_j)t} \tag{6.10}$$

where a_i and a_j are the discrete wave amplitudes of the random sea state and $H^{(2-)}$ is the Quadratic Transfer Function (QTF) for the difference frequency load. The QTF depends on first order motions ${x_{WA}}^{(1)}$ and presented as a complex quantity having a second-order amplitude $\left|H^{(2+)}\right|$ and phase $a^{(2+)}$. R denotes the real part. QTF offers a convenient way to express the second-order forces in the frequency domain in terms of force spectra. The average drift force is computed by keeping only the diagonal terms in equation 6.10 so that $\omega_i = \omega_j$. Thus, the monochromatic drift force $F_d(\omega_i)$ is then defined as;

$$F_d(\omega_i) = \frac{1}{2} a_i^2 Re\left[H^{(2-)}(\omega_i, \omega_i)\right] \tag{6.11}$$

As recommended by DNV-RP-F205 [125], the investigation of the vertical mean drift force/moment is usually of interest for floating structures with small water plan area and catenary mooring. The TRIHF platform does not fall in this category because of its large waterplane area and taut leg mooring arrangement. Since TRIHF has a large waterplane area it will make sense to investigate the horizontal mean drift force/moment. For this research, the near field steady drift forces/moments are worthy of investigation to ascertain the effects of viscous damping and mooring stiffness on its magnitude. The mean drift force/moment in the vertical plane (heave, roll, and pitch) and horizontal plane (surge, sway, yaw) were computed by integrating the second-order mean wave pressure over the wetted surface of the platform using the near-field approach. The output results from AQWA code are shown on the plots in Fig. 6.44.

From the plot shown in Fig. 6.44, the near field steady drift force in global X-axis and RY-axis has peaks and undulations associated with resonance effects for all scenarios of LC1 at 0.098 Hz. In addition, there is an indication that viscous damping

effects (LC1C) triggers a considerable decline in the steady drift force/moment of the structure in the global X-axis, Y-axis, RX-axis, and RY-axis although it appears that the mooring stiffness (LC1B) has a more subduing effect on drift forces/moments in the aforementioned axis.

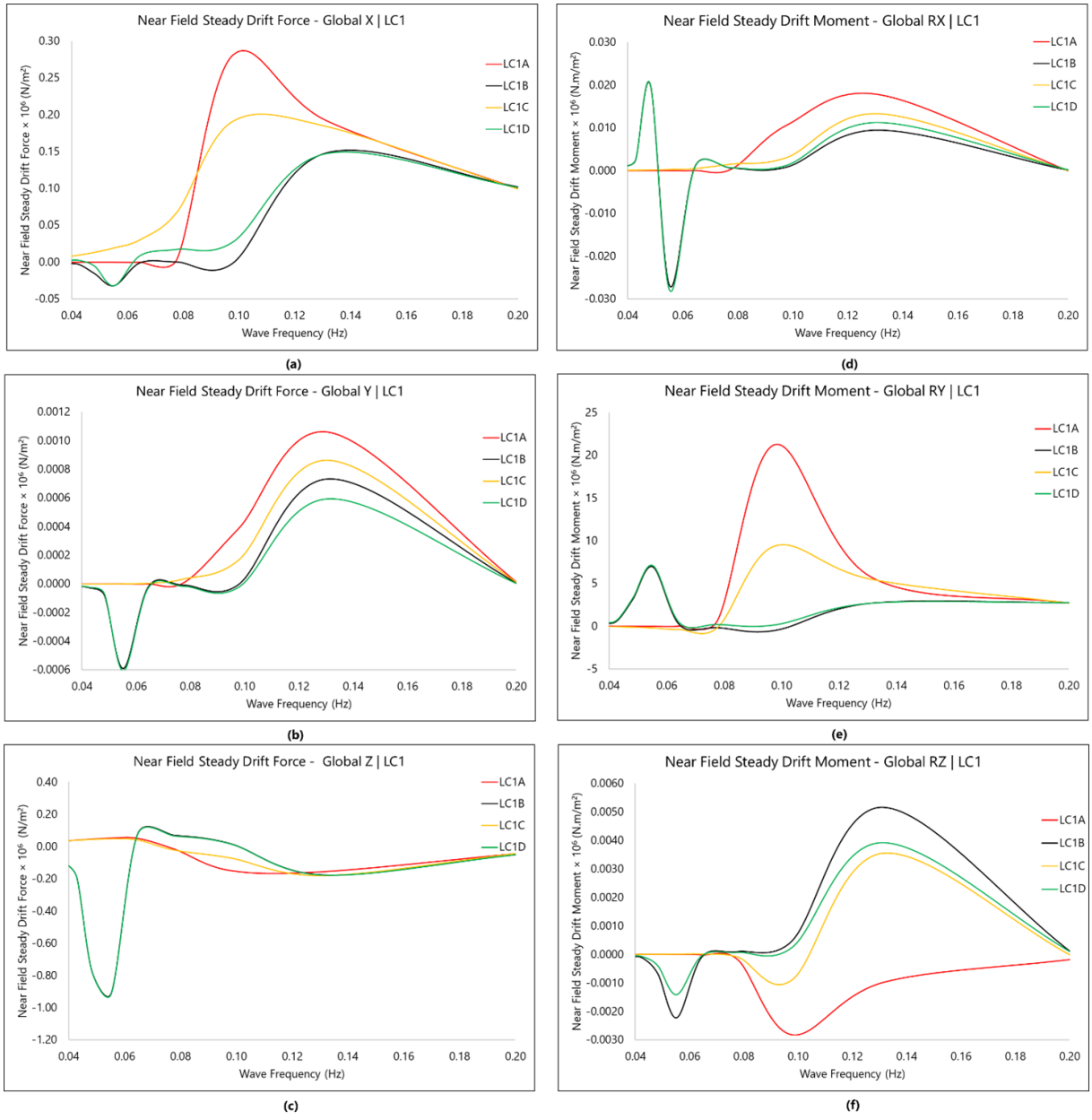

FIGURE 6.44: Near field steady drift force in global (a) X-axis, (b) Y-axis, (c) Z-axis, (d) RX-axis, (e) RY-axis, and (f) RZ-axis for a wave direction of 0° for various scenarios of LC1.

Another interesting observation in the computed drift forces/moments results is the negative drift force occurring for wave frequencies around 0.054Hz. A study conducted by Longuet-Higgins suggested that negative drift forces can be attributed partly

to the presence of higher-harmonic components of the transmitted waves and mostly to wave breaking [140]. A more recent experimental study by Hyeok-Jun and Il-Hyoung further revealed that the negative drift force can also be caused by steep waves on the submerged part of the platform [141]. In a nutshell, the negative drift force stems from the nonlinear FSIs of the waves with the submerged portions of the structure.

Structure Wave Forces, Panel Pressure and Wave Surface Elevation

Fig. 6.45 shows a plot of the structure excitation forces per unit wave amplitude as a function of the wave frequency. As can be seen from the plot, the most dominant excitation force is the Froude-Krylov (incident wave) force followed by the diffraction force. The most recessive component of the total structure excitation is the force arising from Morison drag as shown in the total excitation curve on the plot. The peak structure excitation force occurs at a wave frequency of 0.098 Hz for all components of the wave except for the linearised Morison drag which occurs at 0.2 Hz. Fig. 6.46 shows a radar chart of the structure total wave excitation force per unit wave amplitude for wave direction of -180° to +180°. From the radar chart, there is a clear indication of a higher magnitude of wave force per unit wave amplitude for wave propagation directions of 0° and 180°. Wave frequencies of 0.098 Hz, 0.131 Hz and 0.2 Hz appear to yield the highest impact of wave force. The highest magnitude of wave force per unit wave amplitude (7600 kN/m) occurs at a wave frequency and direction of 0.131 Hz and ±180°, respectively.

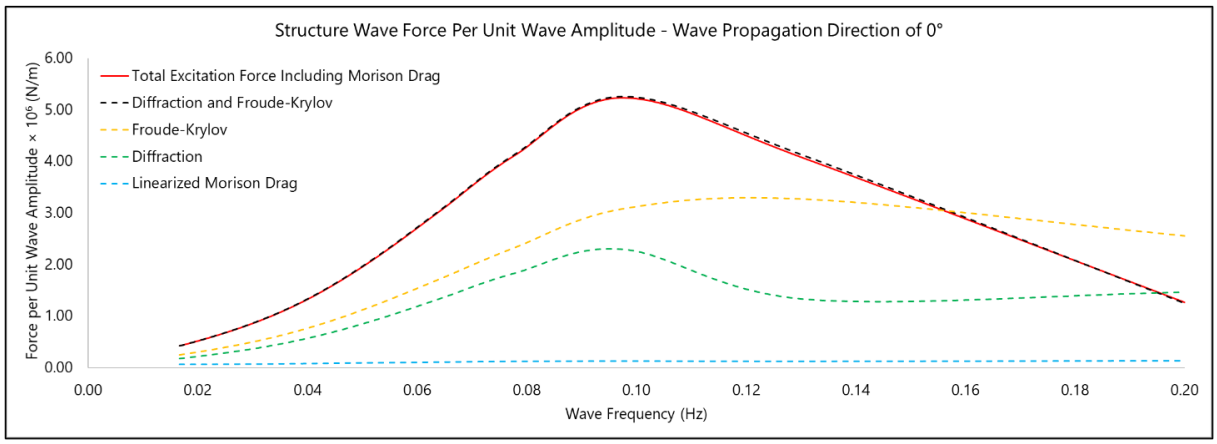

FIGURE 6.45: Plot of structure wave force per unit wave amplitude for wave direction of 0°.

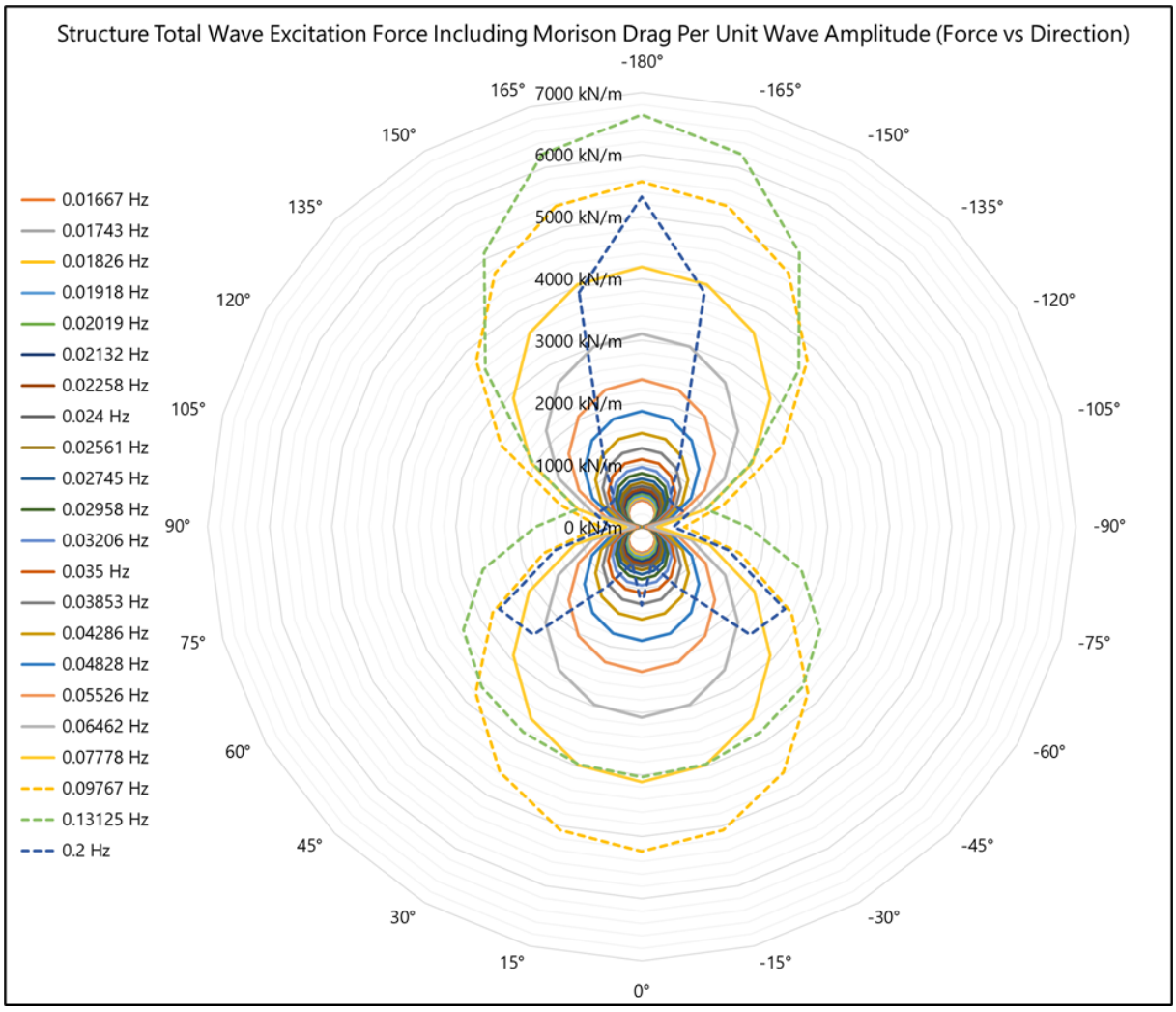

FIGURE 6.46: Radar chart of structure total wave excitation force including Morison drag per unit wave amplitude (Force vs Direction) for several wave frequencies.

Based on the coordinate and orientation definition of the hydrodynamic simulation setup provided in Fig. 6.36 and since a wave direction of ±180° is towards the stern of the floating platform, it will make more sense to focus on the wave force for a wave direction towards the bow (0°) because it is highly unlikely that the natural sea state will suddenly have a wave direction of ±180°. FOWTs are often positioned and opposed to the streamwise direction of the upstream wind. Wind-generated waves are the most important waves in the spectrum of the natural sea state. In other words, the wind and wave direction are often aligned in the real sense. From the radar chart, there is a clear indication that the highest magnitude of wave force per unit wave amplitude (6200 kN/m) occurs at a wave frequency of 0.098 Hz and wave direction of 0°. Given that the wave frequency and direction at which the maximum wave force per unit wave

amplitude occurs have been established, more emphasis will be laid on providing results for wave frequency of 0.098 Hz and wave direction of 0° going forward.

An interesting observation from the radar chart shown in Fig. 6.46 is the symmetric distribution of the wave forces per unit wave amplitude when comparing the magnitude of structure forces for wave propagation direction between 0° to -165° and 0° to 165°. In other words, the values of wave force per unit wave amplitude mirror itself on both halves of the radar chart. A logical explanation of the symmetric wave force distribution is because of the symmetricity of the platform along the x-axis. Fig. 6.47 presents the wave surface elevation contour plots of the diffraction/radiation model which shows a vivid demonstration of the platform's motion complying to the motion of the wave. The maximum panel pressure from wave components consisting of the incident wave, diffracted wave, radiation wave, hydrostatic differentials, and second-order terms is presented in Fig. 6.48. As can be seen from the colour scheme at the bottom left of the plot, the pressure pattern occurring on the surfaces of the centre column and braces in the splash zone area are seen to be higher than other parts of the platform. The maximum pressure experienced by the floating platform occurs on the bottom brace linked to the bow of the hull which is calculated to have a surface pressure of about 40.4 kN/m^2.

There is also a clear indication of other submerged members of the platform having panel pressures of magnitudes ranging from 17.5 kN/m^2 to 32.8 kN/m^2. Lower members of the platform that are far from the splash zone experience the lowest surface pressure which has a magnitude of about 6.11 kN/m^2. Fig. 6.49 demonstrates the amplitude and flow characteristics of the wave surface elevation. From the contour plot shown, there is a strong demonstration of FSI and flow separation as the wave propagates past the structure. A drop in wave surface elevation at the stern of the structure arising from wave velocity drop is observed. Also noteworthy is the increase in wave surface elevation in the moonpool of the platform.

Hydrostatic Stability Analysis in Irregular Wave

Hydrodynamic interaction between the FOWT and the hydrodynamic loads (waves) have been established in the diffraction/radiation analyses where wave forces on the floater were calculated. Moving on from there, an initial static stability analysis was performed to ascertain the floating platform's natural modes and their associated periods for compliant DOFs. The natural periods were obtained from a thorough stability analysis where drift forces and multi-directional wave interaction were considered. The results of the platform's natural period are presented in Table 6.17.

TABLE 6.17: Natural periods of floater motions for TRIHF platform for various scenarios of LC1.

Scenarios	Surge (X)	Sway (Y)	Heave (Z)	Roll (RX)	Pitch (RY)	Yaw (RZ)
LC1A	28.03 s	28.07 s	5.66 s	8.70 s	8.78 s	35.70 s
LC1B	28.07 s	28.13 s	5.67 s	8.71 s	8.77 s	38.60 s
LC1C	28.02 s	28.08 s	5.73 s	8.71 s	8.80 s	35.63 s
LC1D	28.07 s	28.12 s	5.75 s	8.72 s	8.80 s	38.59 s

The 6DOFs natural mode was observed for TRIHF by scanning a frequency range from 0.001 Hz to 10 Hz in addition to using an adaptive relative precision scanning of $\Delta f/f \geq 0.001$. Observing the computed results of natural periods in the stability analysis, it is clear that implementing the mooring stiffness matrix (LC1B) in the diffraction/radiation analysis reduces the natural periods of the platform. A similar observation is to be made for viscous damping (LC1C) although the reduction in natural period instigated by viscous damping is less significant than mooring stiffness. Results of the natural periods further demonstrate that the platform exhibits higher frequencies for motions in the vertical plane (heave, roll, and pitch) and lower frequency for motions in the horizontal plane (surge, sway, and yaw). Consequently, the platform will exhibit higher acceleration and velocity responses in the vertical plane than for the horizontal plane as will be discussed in the frequency domain analysis section (6.2.4).

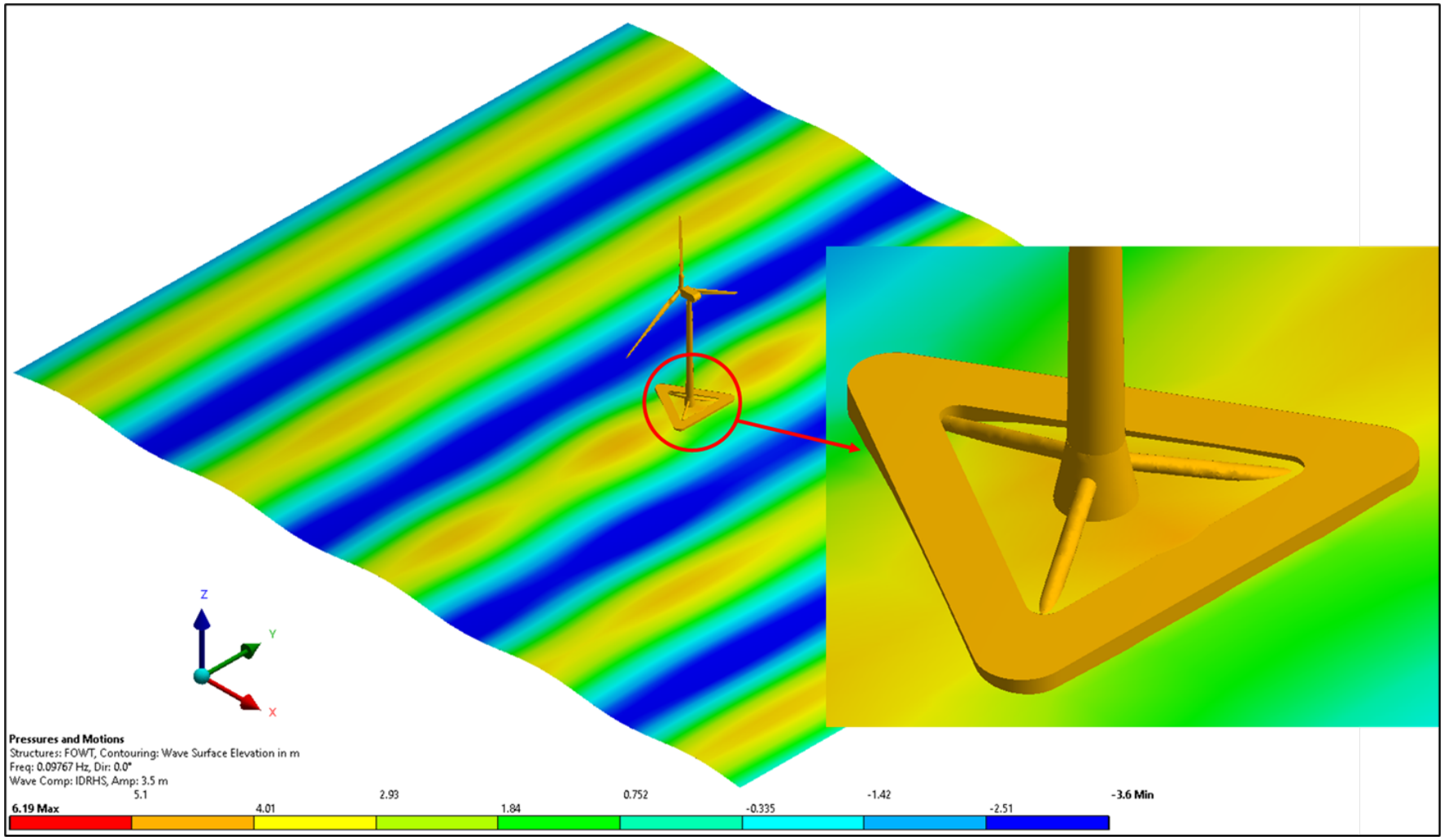

FIGURE 6.47: An aerial view (left) and close-up view (right) of wave diffraction/radiation model showing wave surface elevation for a wave amplitude, frequency, and direction of 3.5 m, 0.98 Hz, and 0°, respectively.

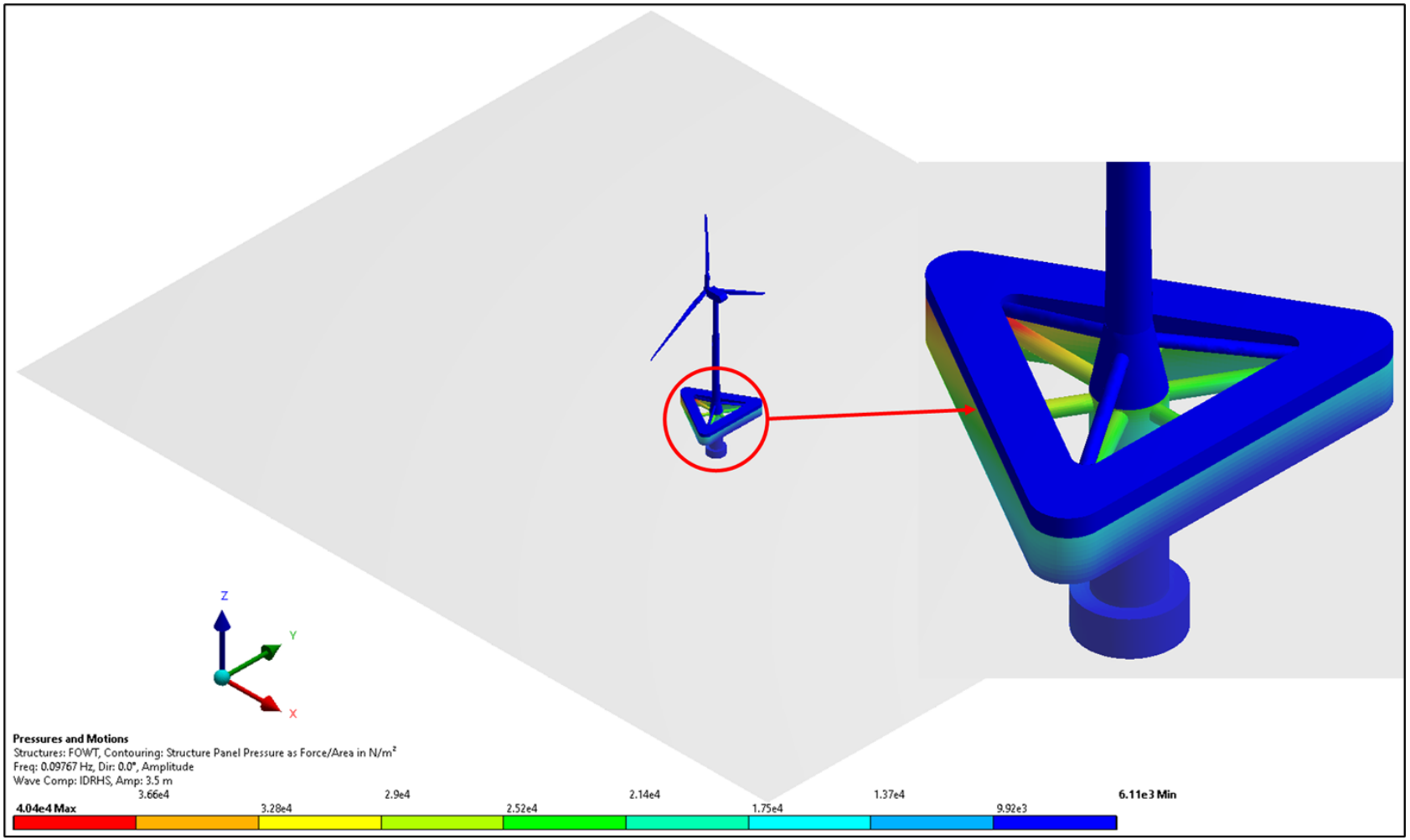

FIGURE 6.48: An aerial view (left) and close-up view (right) of wave diffraction/radiation model showing structure panel pressure amplitude for a wave amplitude, frequency, and direction of 3.5 m, 0.98 Hz, and 0°, respectively.

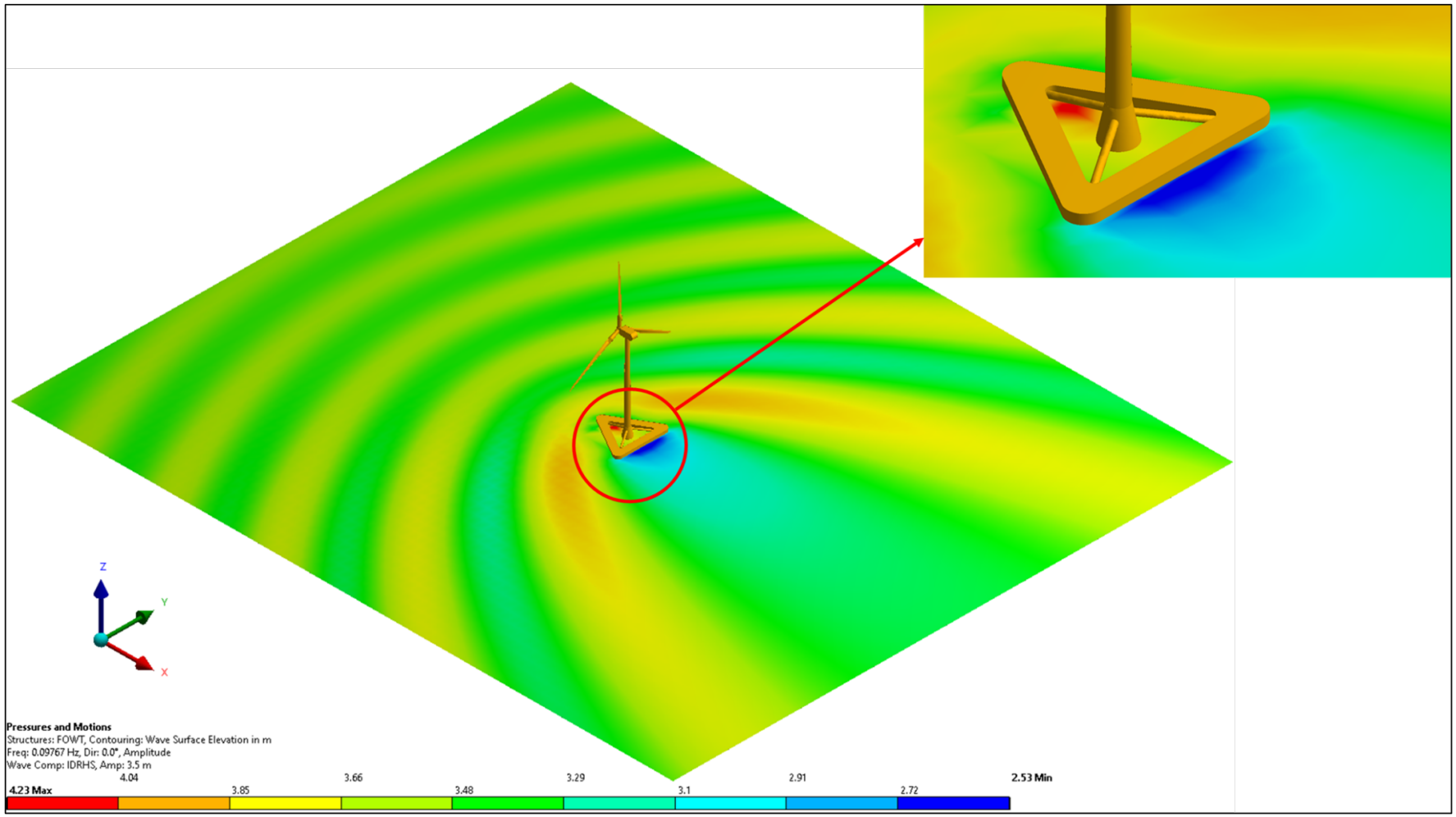

FIGURE 6.49: An aerial view (left) and close-up view (right) of wave diffraction/radiation model showing amplitudes of wave surface elevation for a wave amplitude, frequency, and direction of 3.5 m, 0.98 Hz, and 0°, respectively.

Earlier in the previous chapter (section 4.2.1), the author introduced a methodology that can be used to characterise the floater boundary conditions based on the extent of compliant or retrain for modes of motion (see Table 4.4 and Table 4.5). Fig. 6.50 contains a radar chart showing the graphical representation of the floater boundary conditions for modes of motion. This assessment is made to show how TRIHF compares with the three floating platform concepts. From the chart, it is clear that TRIHF has more attractive stability properties than other FOWT concepts due to its retrained motion in the vertical plane (heave, roll, and pitch) and neutrality (i.e. neither retrained nor compliant) for surge and sway motion. However, TRIHF is compliant for yaw motion. The goal of developing a hybrid floating platform that cuts across the three floating concepts for FOWTs is to incorporate the pros of these concepts (see Table 4.6). The outcome of the comparison between TRIHF and other floating concepts as shown in Fig.6.50 is very promising.

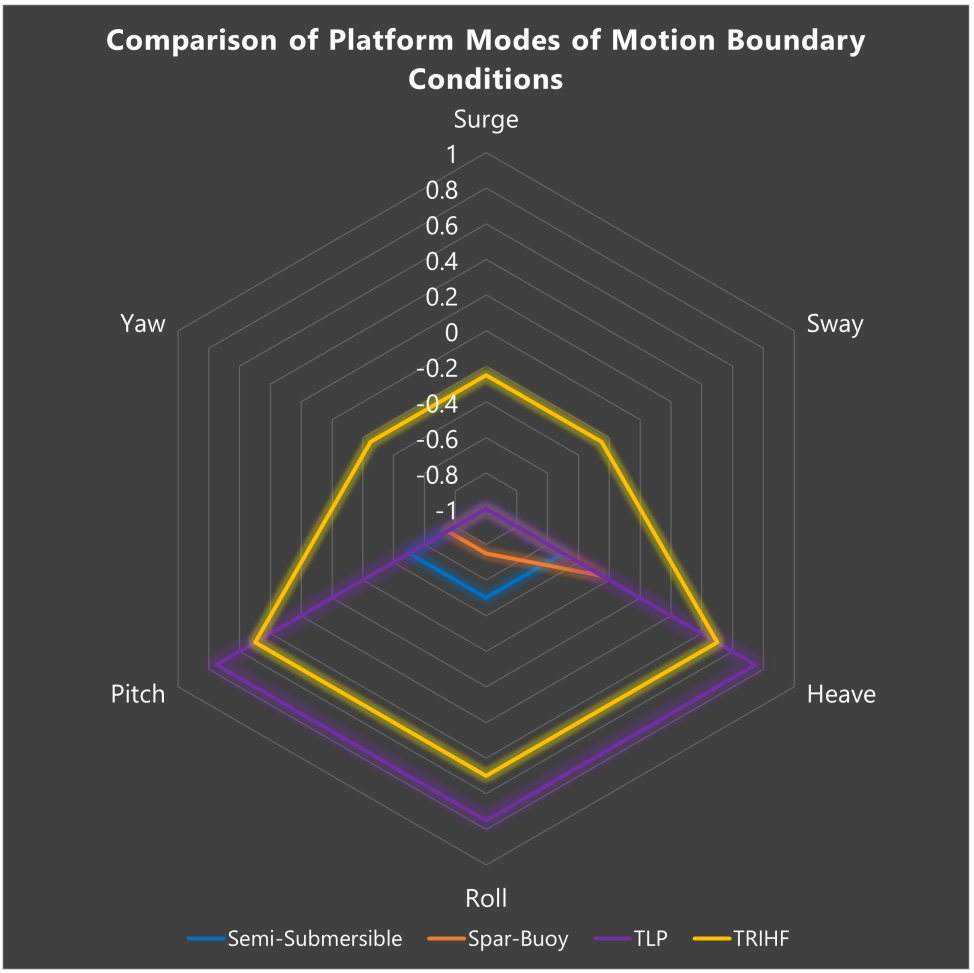

FIGURE 6.50: Modes of motion boundary condition comparison between FOWT concepts and TRIHF.

Fig. 6.51 contains a comparison of the RAO for TRIHF (LC1D) and the DeepCWind-OC5 (LC4.1) platform for all 6DOF. Here, it can be observed that the motion response per unit wave amplitude for all rotational motion is higher for the DeepCwind-OC5 when compared to the TRIHF motion. However, a slightly different scenario is observed for translational motion where the TRIHF platform is seen to have more response per unit wave amplitude than the DeepCWind-OC5 platform for surge and sway motion. Although for heave motion, the TRIHF platform appeared to have a much lower response per unit wave amplitude. The lower response per unit wave amplitude for the TRIHF platform for heave, roll, pitch, and yaw motion can be attributed to the stiffness provided by the synthetic mooring line since the mooring configuration serve to provide both stability and station keeping for the FOWT. Also, the viscous damping effect in the vertical axis of motion (heave, roll, and pitch) which has been adequately accounted for in the coupled dynamics simulation is observed to have dampened the RAOs for these motions as earlier portrayed in Fig. 6.40 to Fig. 6.42 for heave, roll and pitch motion, respectively. For the DeepCWind-OC5 platform, the catenary mooring line is configured to provide only station keeping, hence a palpable reason for its higher RAO values for heave, roll, pitch, and yaw motion.

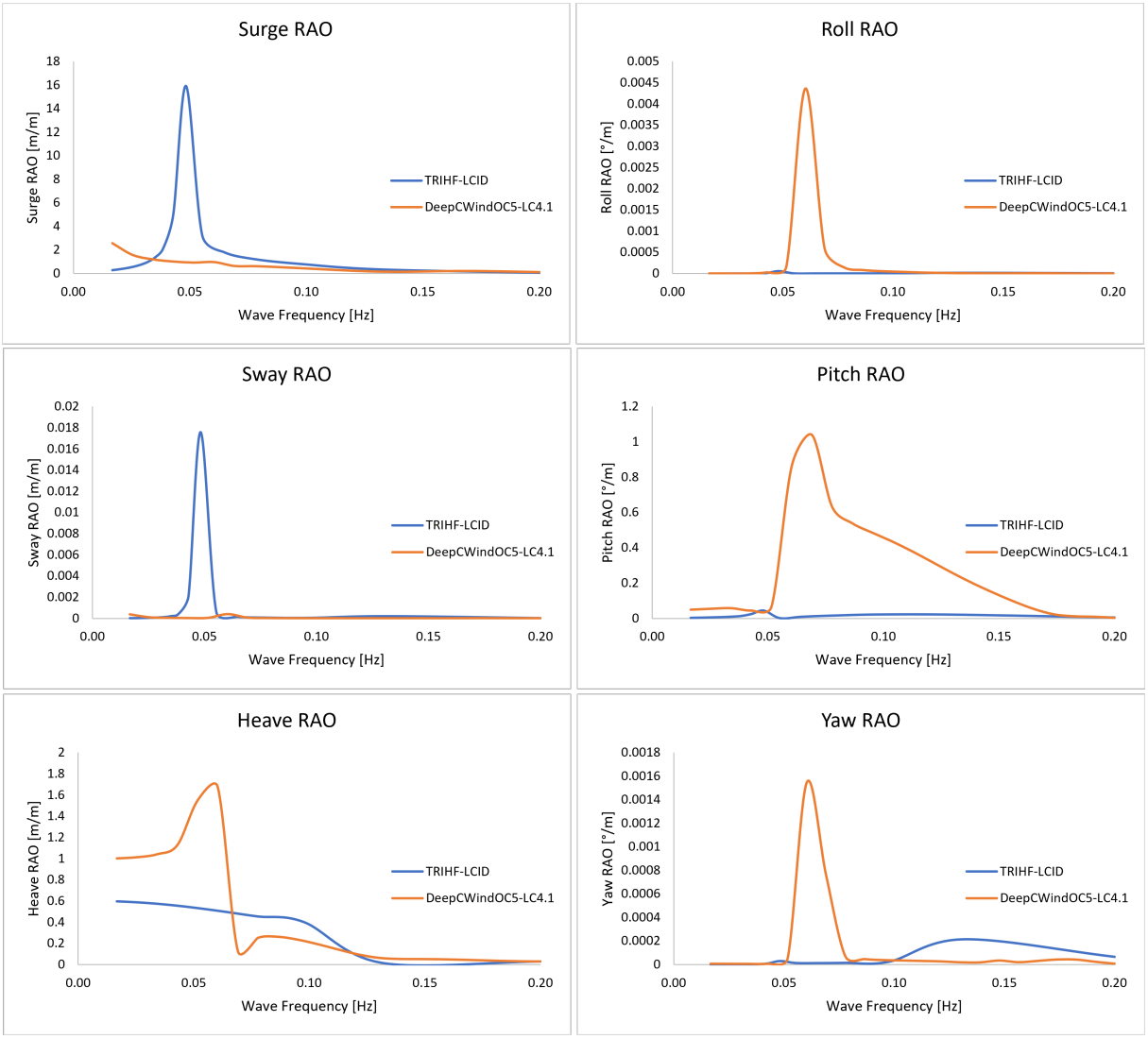

FIGURE 6.51: A comparison of RAOs between TRIHF and DeepCWind-OC5.

6.2.4 Frequency Domain (FD) Hydrodynamic Response Analysis in Irregular Wave

Determining the motions of a moored floating structure in response to environmental loads (wind, wave, and current) is a complex technique due to the presence of non-linearities (such as mooring system non-linearities) and position-dependent environmental loads. A Time-Domain (TD) analysis would be computationally prohibitive and time consuming for a systematic parametric study due to a large number of possible combinations of environmental loads. However, an FD analysis can serve as an efficient and effective tool to fulfil the requirements of evaluating the hydrodynamic response of a FOWT system for a myriad number of possible combinations of environmental load. An FD analysis is carried out using the results of the stability analysis

during which the structure's equilibrium position for all 6DOFs has been established (Table 6.18) i.e., the structure when analysed is at its equilibrium position. The mooring line stiffness and hydrostatic stiffness are re-estimated at this equilibrium position. It is noteworthy that the FD analysis does not directly include system non-linearities such as wind drag force, current drag force, drag force on Morison elements, or mooring cable dynamics. These non-linearities are first linearised and then applied to the FD motion response calculations[39].

TABLE 6.18: TRIHF equilibrium position for various scenarios of LC1.

Scenario	Surge (X)	Sway (Y)	Heave (Z)	Roll (RX)	Pitch (RY)	Yaw (RZ)
LC1A	0.61 m	0.00 m	-19.51 m	0.00°	0.50°	0.07°
LC1B	0.29 m	0.00 m	-19.44 m	0.00°	0.04°	0.00°
LC1C	0.62 m	0.00 m	-19.52 m	0.00°	0.48°	0.05°
LC1D	0.29 m	0.00 m	-19.44 m	0.00°	0.01°	0.00°

The sole aim of performing an FD motion analysis is to generate transfer functions for frequency-dependent first and second-order excitation forces. The equation of motion is solved for each of the incoming irregular wave components to examine the high or low-frequency response. Also, the FD analysis outputs the significant amplitudes of forces and responses. The force or response spectral density, $S_R(\omega)$ is numerically integrated over a finite frequency range using a 3-point Gaussian quadrature algorithm. Fig. 6.51 presents plots of wave spectra density versus platform position/orientation response spectra for various scenarios of LC1. Similar results for various scenarios of LC2 and LC3 are presented in Fig. 6.53 and Fig. 6.54, respectively.

The response spectrum provides estimates of the structure's response to nondeterministic transient dynamic motion of the random sea state. The response spectrum is a function of the platform's natural frequency and damping. Consequently, it is not a direct interpretation of the frequency content of the platform's excitation but rather the effects that the wave excitation spectra have on the floating structure. From the response spectrum results presented in Fig. 6.51, the peak response spectra for all 6DOFs are outside the frequency of the peak wave energy spectra density. Having the structure's peak response spectra outside the frequency range of the peak wave energy spectra density is crucial to avoiding any form of resonance effects between the wave motion and the FOWT. Also notable is the impact of viscous damping and mooring stiffness on the response spectra of the platform. The mooring stiffness is predicted

to knock down the response spectra for heave, roll, pitch, and yaw motion. Viscous damping has negligible effects although it is predicted to amplify the peak response spectra for roll and yaw motion. For surge, sway, heave, and pitch motion, there is a clear indication that viscous damping significantly lowers the peak response spectra. Resonance effects were predicted for heave motion response spectra for all scenarios of LC2 (see Fig. 6.53c) and LC3 (see Fig. 6.54c).

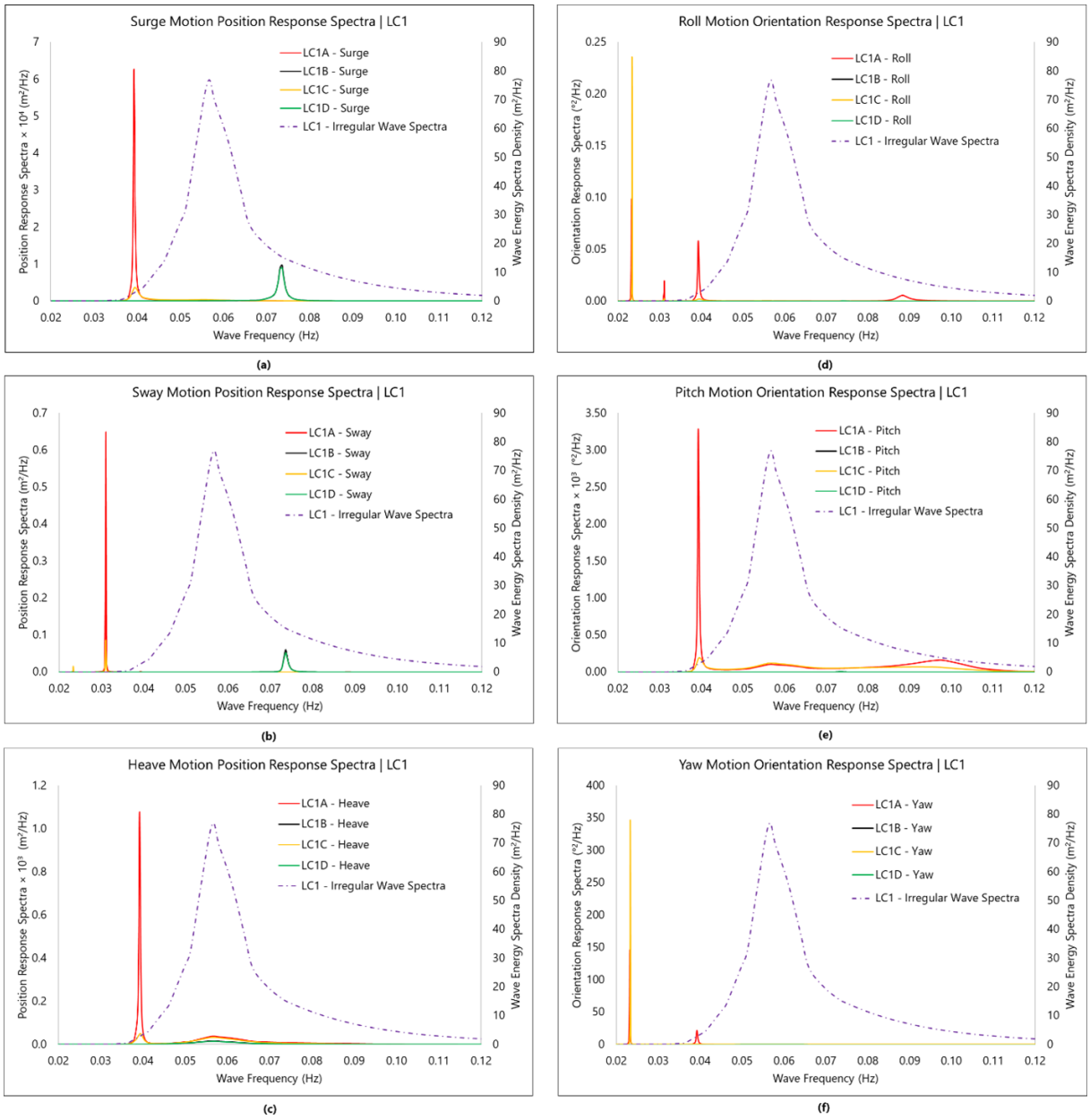

FIGURE 6.52: Plot of wave spectra density vs platform position/orientation response spectra for (a) surge, (b) sway, (c) heave, (d) roll, (e) pitch, and (f) yaw motion for various scenarios of LC1.

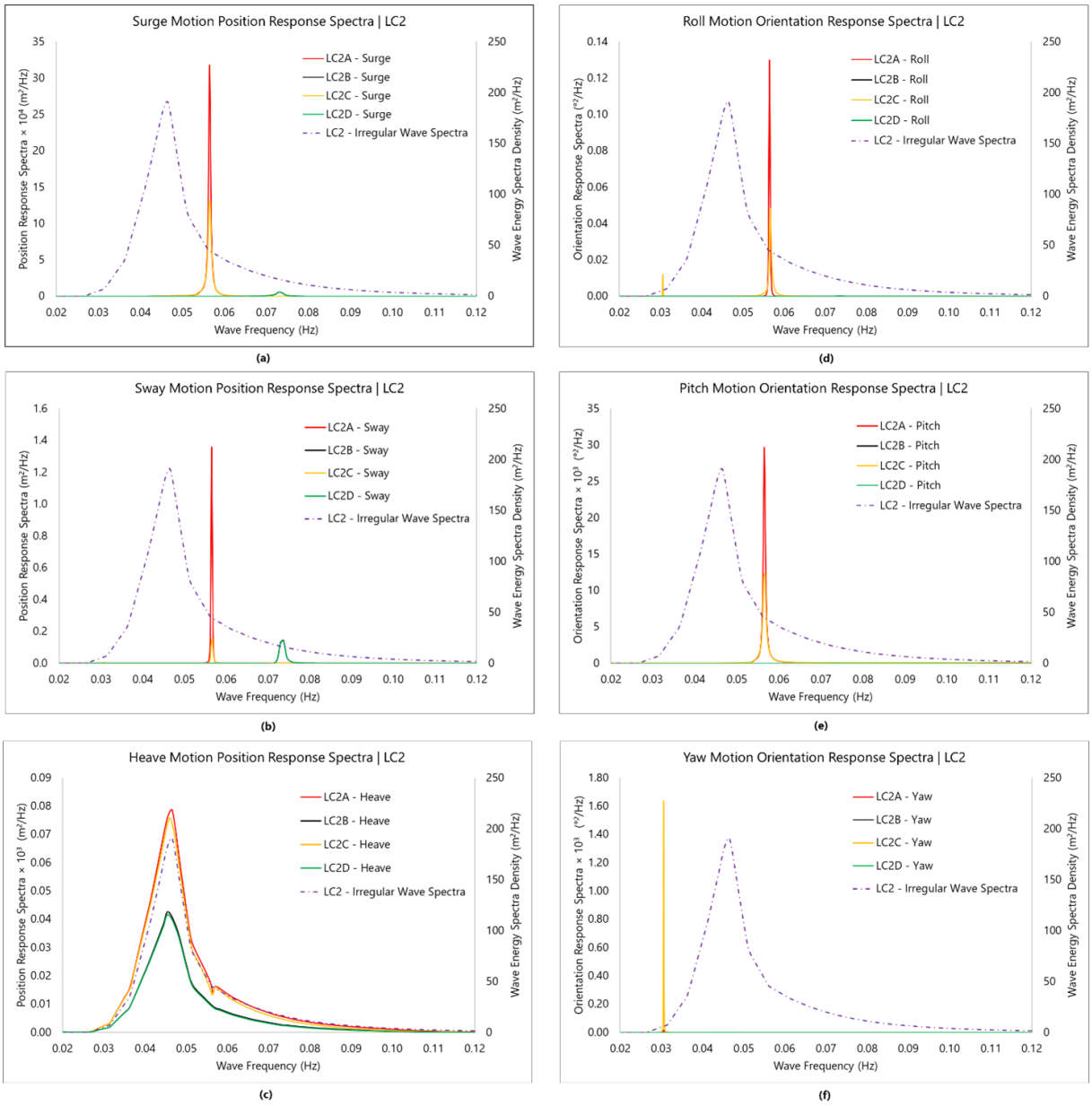

FIGURE 6.53: Plot of wave spectra density vs platform position/orientation response spectra for (a) surge, (b) sway, (c) heave, (d) roll, (e) pitch, and (f) yaw motion for various scenarios of LC2.

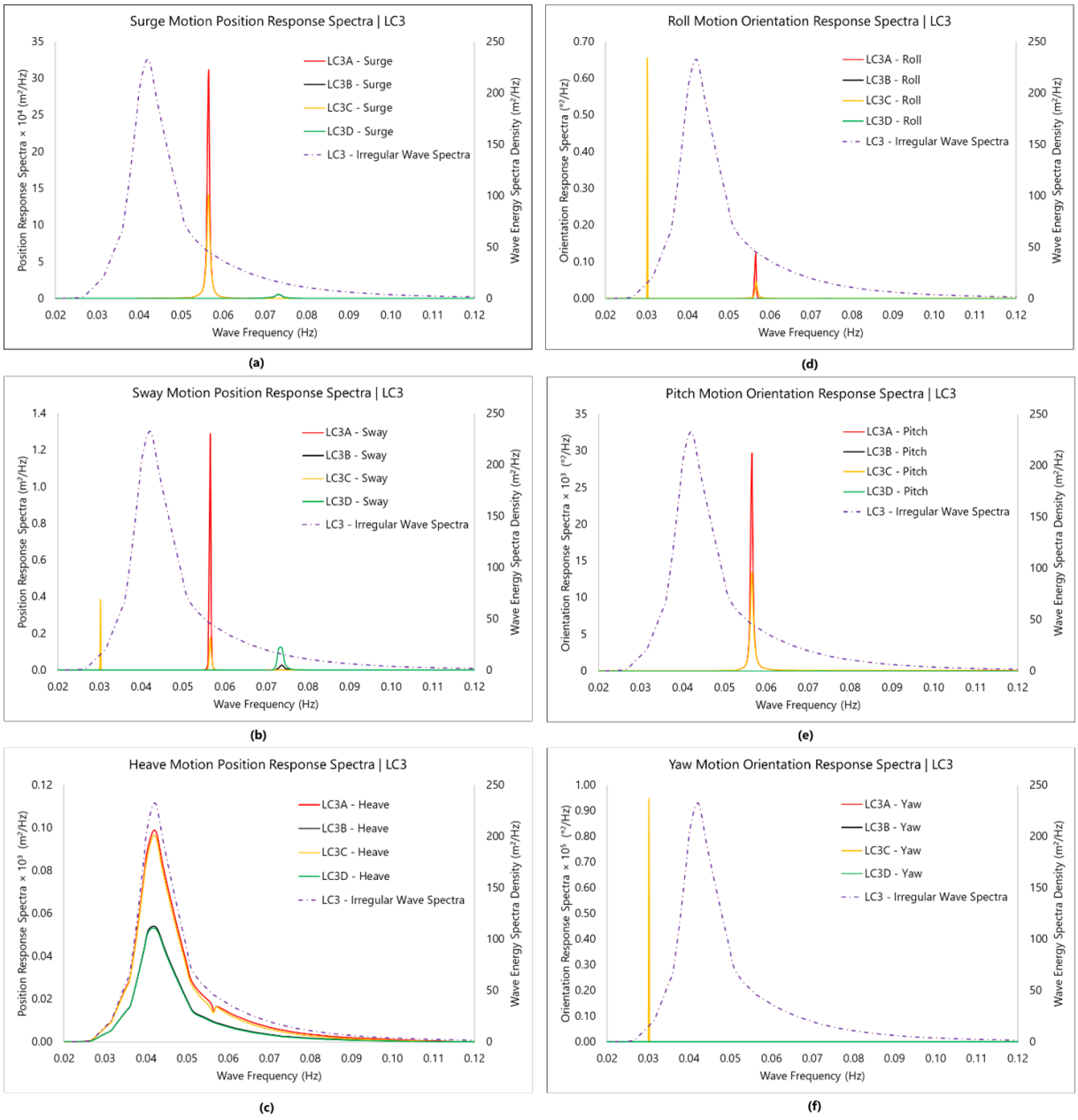

FIGURE 6.54: Plot of wave spectra density vs platform position/orientation response spectra for (a) surge, (b) sway, (c) heave, (d) roll, (e) pitch, and (f) yaw motion for various scenarios of LC3.

Calculating the response spectrum of a floating structure is done piecewise. Fig. 6.55 is a framework that illustrates the correlation between wave excitation and response in a linear system. Depending on the discrete frequencies (or period) that are given in the sea state spectrum, the response spectrum amplitude values can be calculated for each frequency for each 6DOFs. The structure response amplitudes, $\zeta_a(\omega_i)$

for each frequency can be derived from the response spectra, $S_R(\omega_i)$ using the following expression;

$$\zeta_a(\omega_i) = \sqrt{S_R(\omega_i) \cdot 2\Delta\omega} \tag{6.12}$$

where $\Delta\omega$ is the increment of the frequencies in the spectrum. Values of $S_R(\omega_i)$ for various scenarios of LC1 are already shown on the plots presented in Fig. 6.52. Fig. 6.56 contains plots showing the calculated values of $\zeta_a(\omega_i)$ for various scenarios of LC1. Results of $\zeta_a(\omega_i)$ for various scenarios of LC2 and LC3 are contained in Fig. 6.57 and Fig. 6.58, respectively.

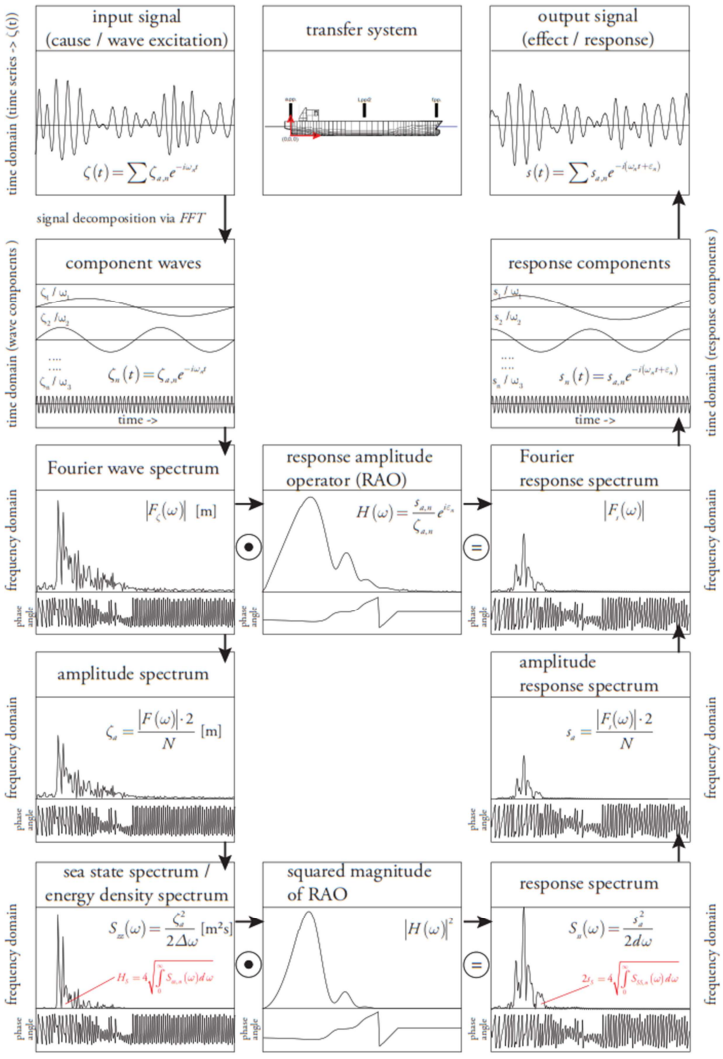

FIGURE 6.55: Floating marine structure response in random sea state. Adopted from [142].

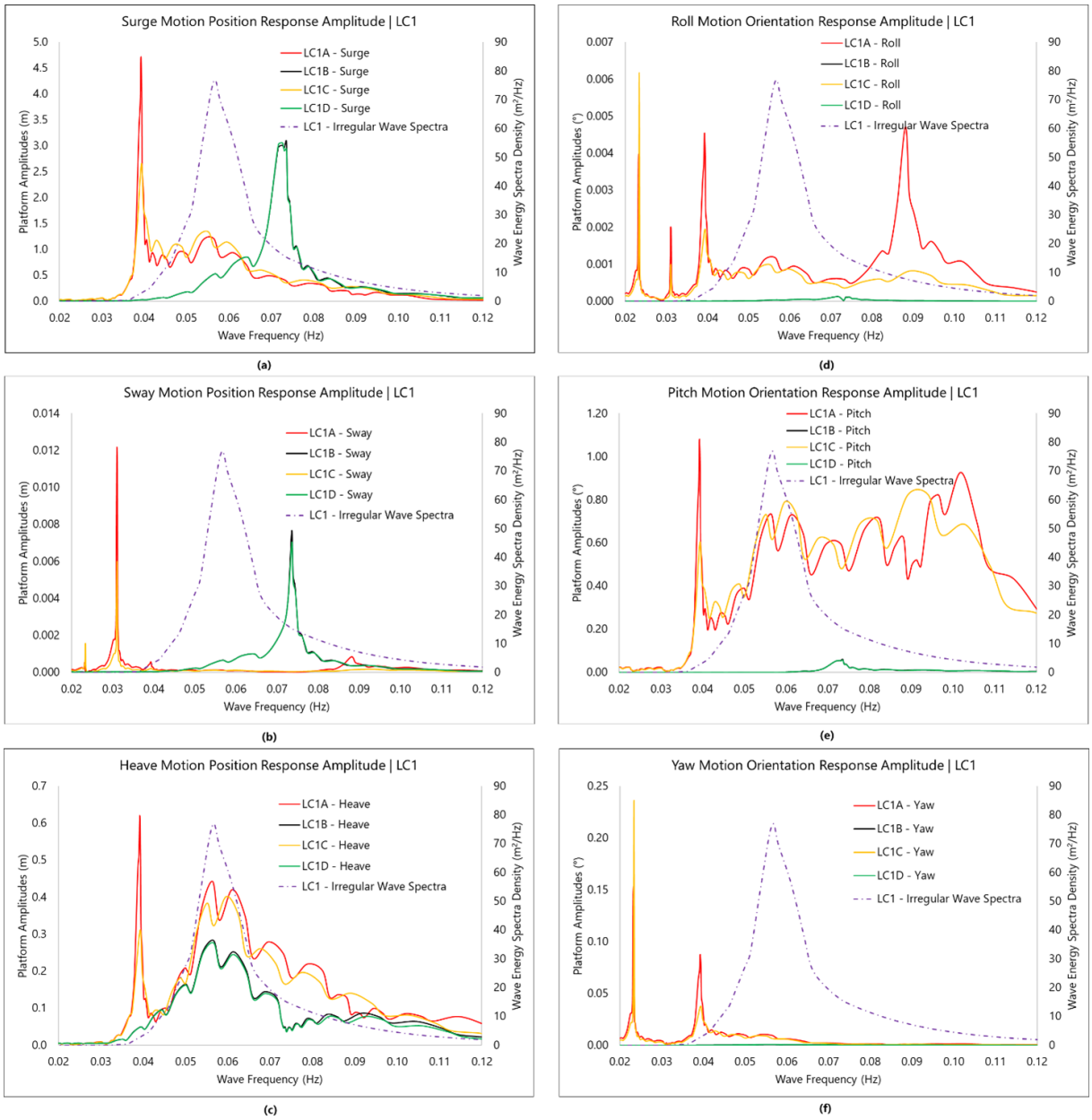

FIGURE 6.56: Plot of wave spectra density vs platform position/orientation response amplitude for (a) surge, (b) sway, (c) heave, (d) roll, (e) pitch, and (f) yaw motion for various scenarios of LC1.

The results presented in Fig. 6.56 shows a comparison of the response amplitudes for all scenarios of LC1. As have been shown in previous results for the FD analysis, there is a clear effect of mooring stiffness on the predicted values of response amplitude. For surge motion, the predicted amplitudes for LC1A and LC1B are 4.7 m and 3.1 m, respectively. Amplitudes for sway, roll, and yaw motion are anticipated to be very small. Resonance effects between the platform heave motion and wave motion were predicted for frequencies ranging between 0.04 Hz to 0.09 Hz for all scenarios of LC1.

However, the peak amplitudes for LC1A and LC1B are outside the wave frequency range containing its peak energy. In general, the predicted amplitudes for rotational motions are significantly subdued by the mooring stiffness. For translational motion, the predicted amplitudes occur at a much higher frequency due to mooring stiffness effects.

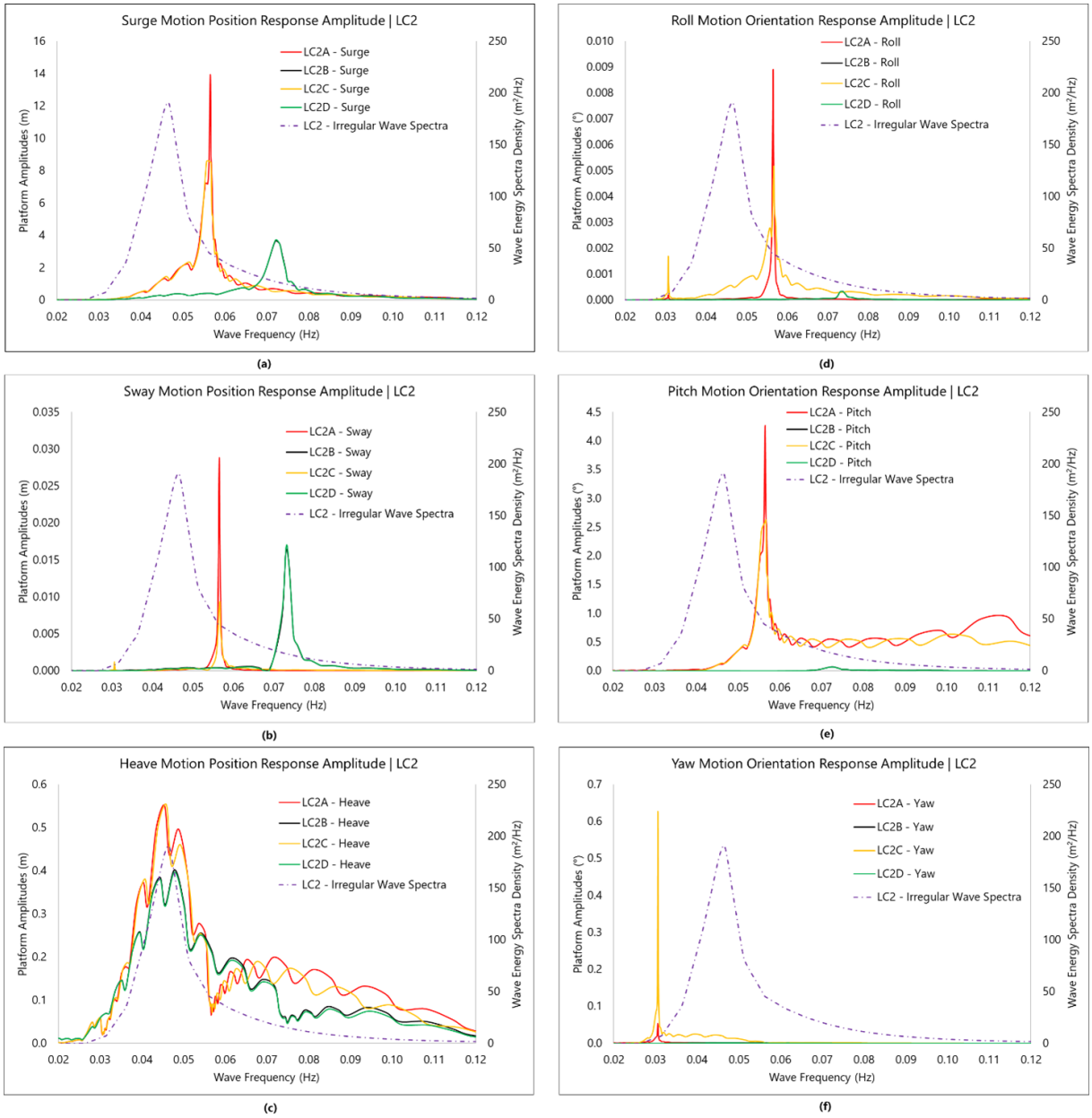

FIGURE 6.57: Plot of wave spectra density vs platform position/orientation response amplitude for (a) surge, (b) sway, (c) heave, (d) roll, (e) pitch, and (f) yaw motion for various scenarios of LC2.

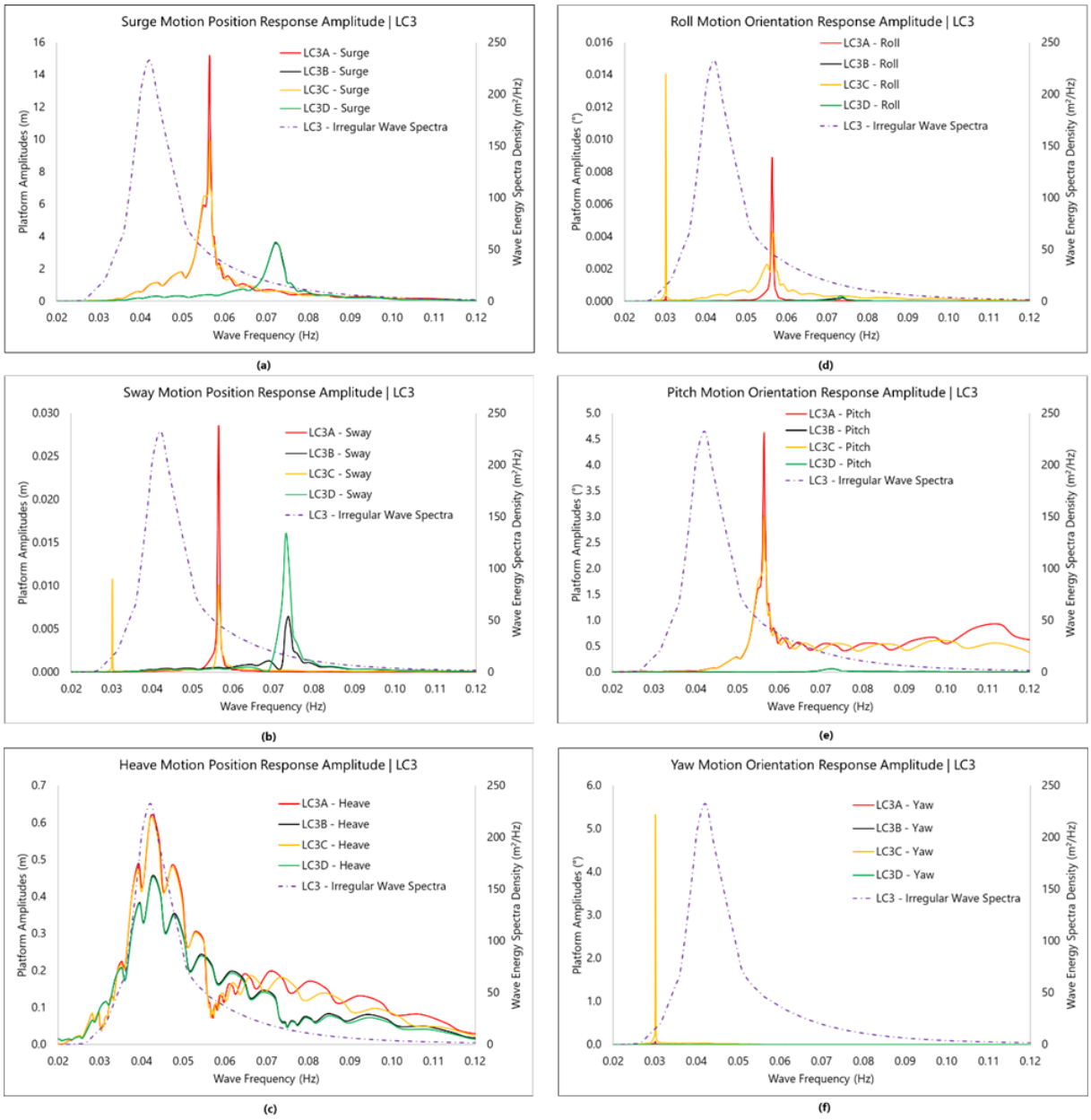

FIGURE 6.58: Plot of wave spectra density vs platform position/orientation response amplitude for (a) surge, (b) sway, (c) heave, (d) roll, (e) pitch, and (f) yaw motion for various scenarios of LC3.

Fig. 6.59 presents the force/moment spectra for various scenarios of LC1. Fig. 6.60 and Fig.6.61 contain the force/moment spectra for LC2 and LC3, respectively. The translational and rotational force spectra densities provide the evaluation of wave loads on the structure for various wave frequencies.

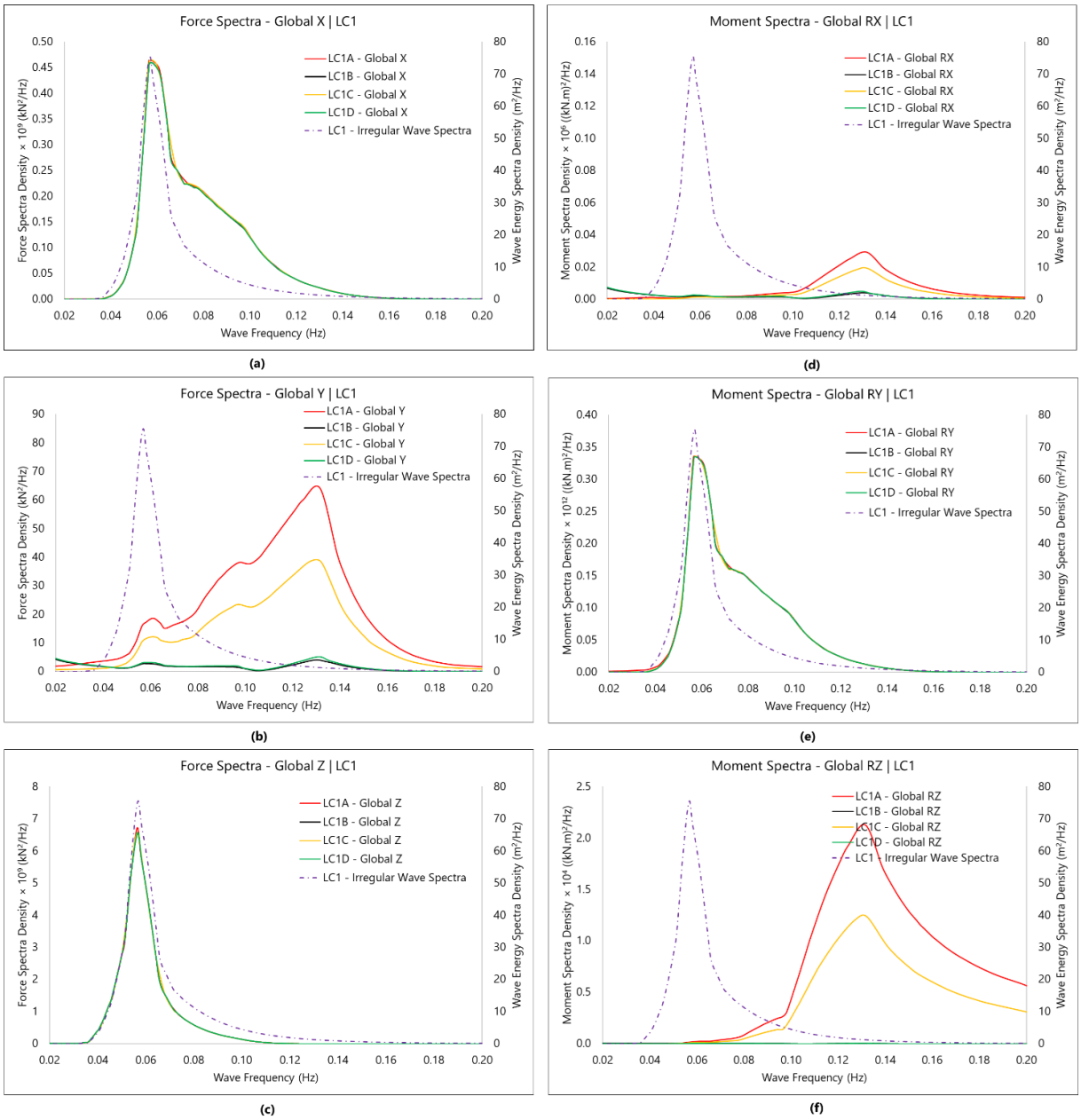

FIGURE 6.59: Plot of wave spectra density vs platform force/moment spectra for (a) X-axis, (b) Y-axis, (c) Z-axis, (d) RX-axis, (e) RY-axis, and (f) RZ-axis for various scenarios of LC1.

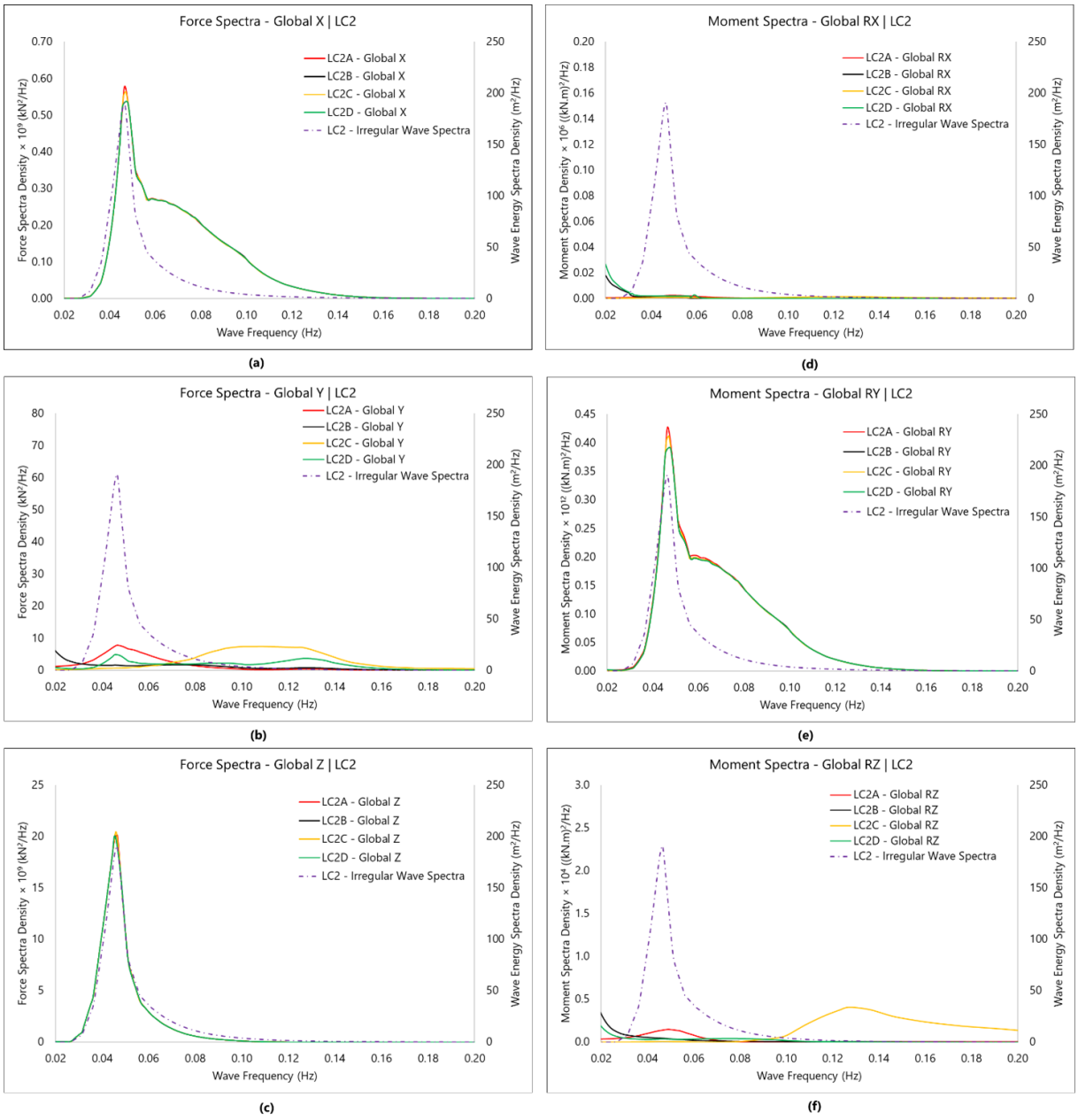

FIGURE 6.60: Plot of wave spectra density vs platform force/moment spectra for (a) X-axis, (b) Y-axis, (c) Z-axis, (d) RX-axis, (e) RY-axis, and (f) RZ-axis for various scenarios of LC2.

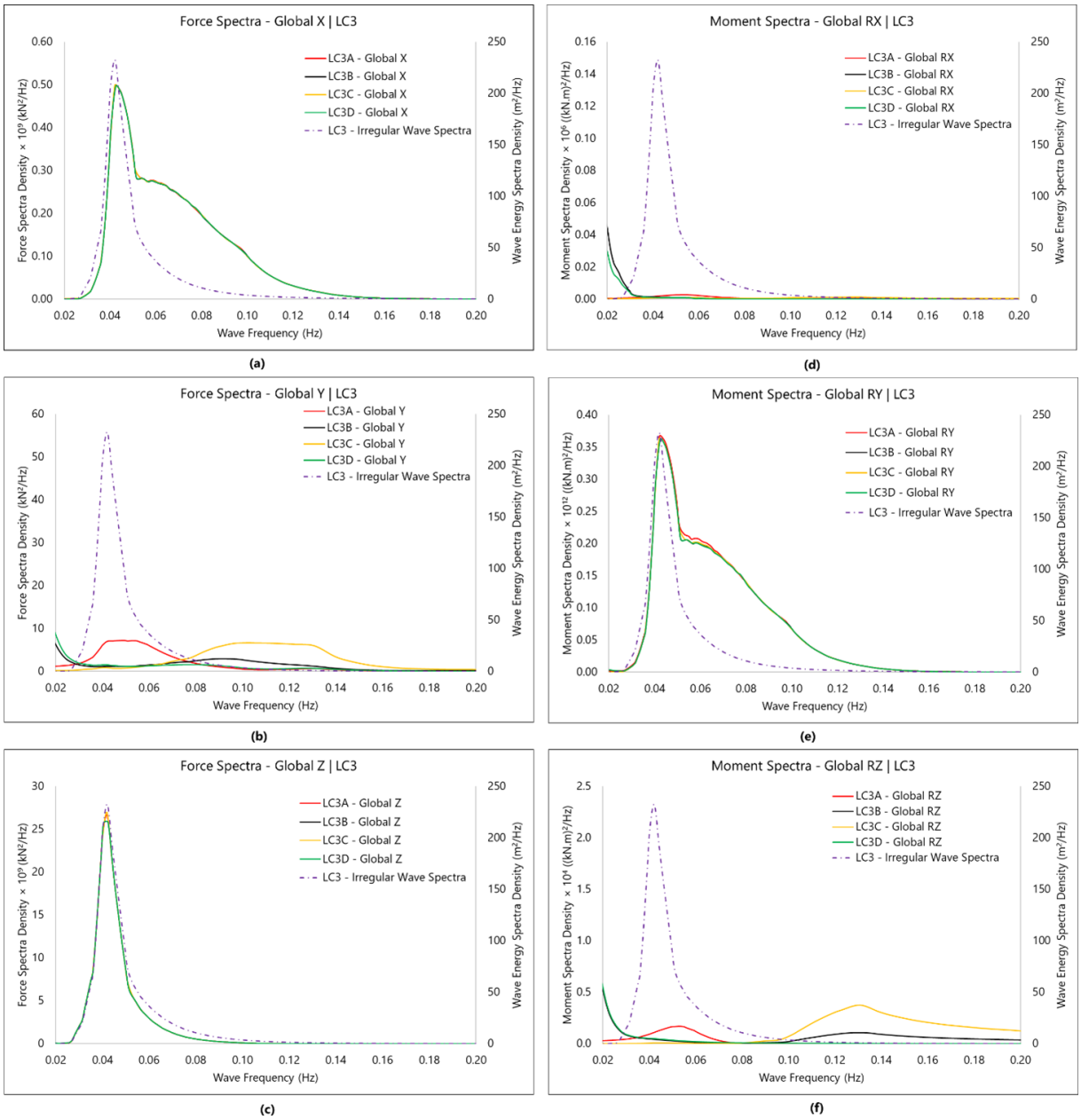

FIGURE 6.61: Plot of wave spectra density vs platform force/moment spectra for (a) X-axis, (b) Y-axis, (c) Z-axis, (d) RX-axis, (e) RY-axis, and (f) RZ-axis for various scenarios of LC3.

Resonance effects between the wave motion and structure wave force/moment spectra density were predicted to occur in the global-X, global-Z, and global-RY axis for all scenarios of LC1. A similar outcome was also produced for all scenarios of LC2 (Fig. 6.60) and LC3 (Fig. 6.61). Similar to the outcome of the calculations performed and presented in Fig. 6.56 using equation 6.12, the wave force/moment amplitudes,$F_a\ (\omega_i)$ can be predicted from the force/moment spectra, $F_S\ (\omega_i)$ for each frequency using the

following expression;

$$F_a(\omega_i) = \sqrt{F_R(\omega_i) \cdot 2\Delta\omega} \tag{6.13}$$

By implementing equation 6.13, Fig.6.12 shows plots of the wave energy spectral density vs structure force/moment amplitudes for various scenarios of LC1.

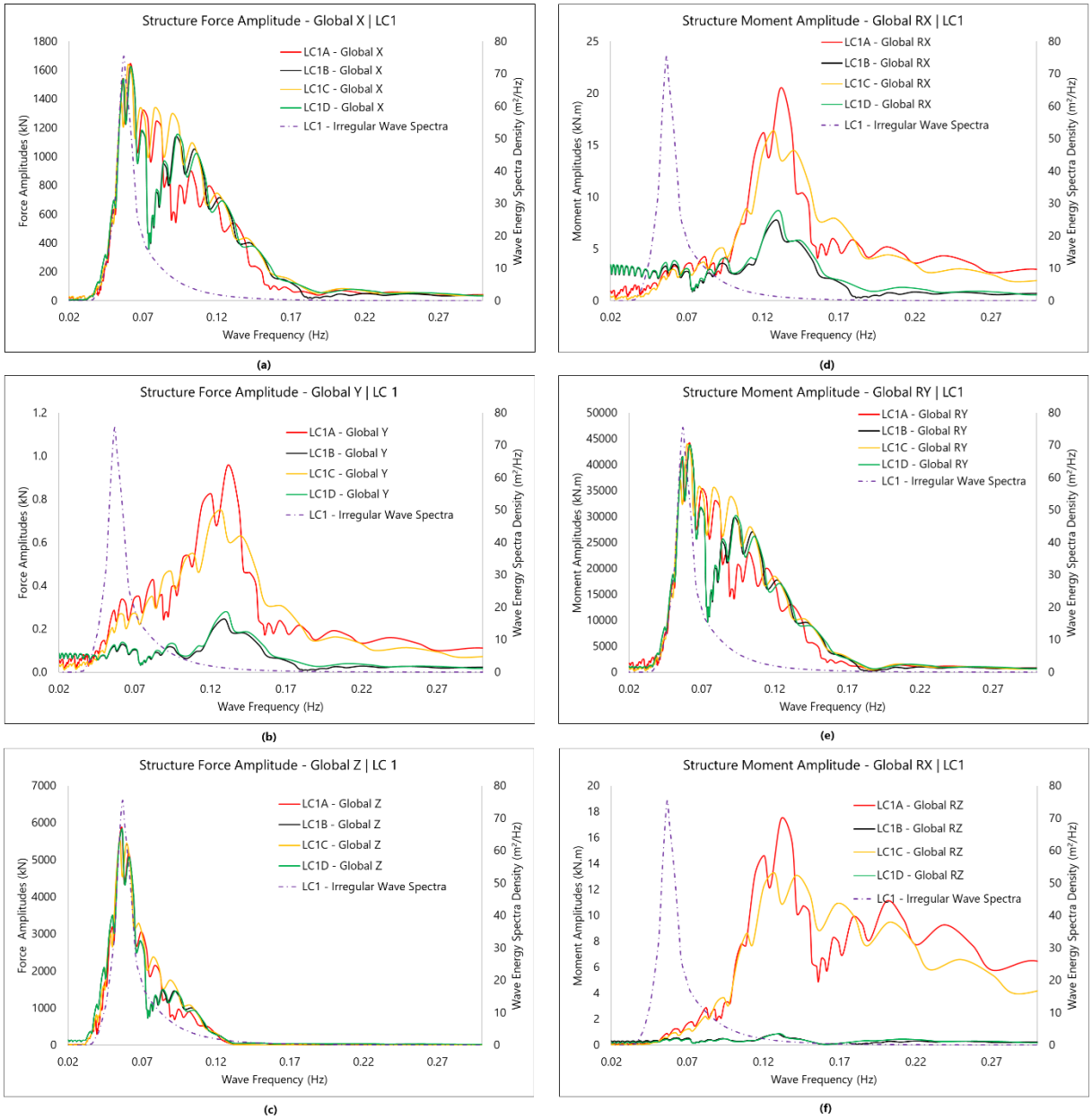

FIGURE 6.62: Plot of wave spectra density vs platform force/moment response amplitude for global (a) X-axis, (b) Y-axis, (c) Z-axis, (d) RX-axis, (e) RY-axis, and (f) RZ-axis for various scenarios of LC1.

6.2.5 Time Domain (TD) Hydrodynamic Response Analysis in Irregular Wave

For a start, a time step sensitivity analysis was completed to check the degree of sensitivity of the solution computed by the AQWA code to different time steps Fig. 6.63 contains a TD analysis of the wave surface elevation at different time steps sizes for a duration of 10800 s. As can be seen from the plot presented in Fig. 6.63(top), the solution is not sensitive to time step size. However, a time step size of 0.01 s and an output step of 1 s was specified for the simulation to adequately provide the desired number of solution points for enhanced accuracy in the TD analysis. Time history of the FOWT simulated motions under the action of wind, wave, and current forces was generated for a total number of 1080001 steps (10800 s). For each time step, the position, and velocities of the FOWT assemblage were determined using a two-stage predictor-corrector numerical integration scheme. The irregular wave response with a slow drift simulation approach was employed to simulate the real-time motion of the FOWT under the action of an irregular wave.

The Rayleigh probability distribution can be used to provide a good estimate of the maximum wave height expected in a wave record. According to DNV-OS-J101 [92], in deep waters the 50-year wave height will take on a value greater than $H_{max} = 1.86H_s$. According to [143], the maximum wave height in a wave record may be found from;

$$H_{max} = 0.707\sqrt{lnJ} \cdot H_s \tag{6.14}$$

where J and H_{max} are the number of waves and maximum wave height in a random sea, respectively. The rationale behind the extracted value of H_{max} from the simulation data is presented in Fig. 6.63(bottom). The value of J was determined by counting the number of peaks in the wave surface elevation time series using an advance formulae technique in Microsoft excel. A summary of the calculated values of J, the expected H_{max} using the Rayleigh distribution, and the calculated H_{max} from the simulation are presented in Table 6.19. As can be observed from the results presented in Table 6.19, the H_{max} value from the TD simulation reaches 94% of the expected value calculated from the Rayleigh distribution. However, a comparison of the H_{max} value from the TD simulation to the 2% probability of exceedance wave height [143] as shown in Fig. 6.64 reveals a higher value than the expected. The reason for the difference in H_{max} value from the expected Rayleigh distribution value and the 2% probability of exceedance

value is unknown and will require further investigation. Nonetheless, as a Rule-of-Thumb, the maximum wave height in a random sea state is usually about two times the significant wave height [143]. The H_{max} from the TD simulation is 1.75 times the significant wave height.

TABLE 6.19: Calculated Wave Parameters for Time Domain Simulation.

Wave Parameters	**Values**
Number of Waves (J)	1107
Significant Wave Height (H_s)	7.02 m
Expected $H_{\max}$ from Rayleigh Distribution (using equation 6.14)	13.14 m
Ratio of expected H_{max} to H_s	1.87
Highest Wave Crest from Simulation Result	6.86 m
Time of Occurrence for Highest Wave Crest	7235 s
Neighbouring Trough to Highest Wave Crest	-5.45 m
Time of Occurrence for Neighbouring Trough to Highest Wave Crest	7226 s
H_{max} from Simulation	12.31 m

Structure Position Responses

Wave Frequency (WF) structure motions for TRIHF were calculated by a combination of diffraction theory and Morison's equation while the strip theory for slender structures was applied to the mooring cables. The JONSWAP spectrum was used to induce the sea states while the Ochi and Shin wind spectrum was used to model wind loads on the assemblage of the FOWT above the MSL. Also, a current velocity-depth profile was implemented into the hydrodynamic model. For the analysis of Low Frequency (LF) motion response, environmental actions due to the wind, waves, and currents were all considered. All modes of motion were analysed and the results of the floating platform's actual response, LF response, and WF response for all scenarios of LC1 are presented in Fig. 6.65, Fig. 6.66, and Fig. 6.67, respectively. A time series of the RAO based motion response (see Fig. 6.68) which ignores the effects of mooring connections and only considers RAO from the applied wave was done to evaluate the performance of the structure to wave only loads.

From the time series plots of the platform motion presented above, there is a clear indication of how viscous damping (LC1C), mooring stiffness (LC1B), and a combination of both (LCID) affects the motion of the platform. There is minimal effect of viscous damping and mooring stiffness on heave and surge motion actual response although a significant condensing effect is predicted for other DOFs.

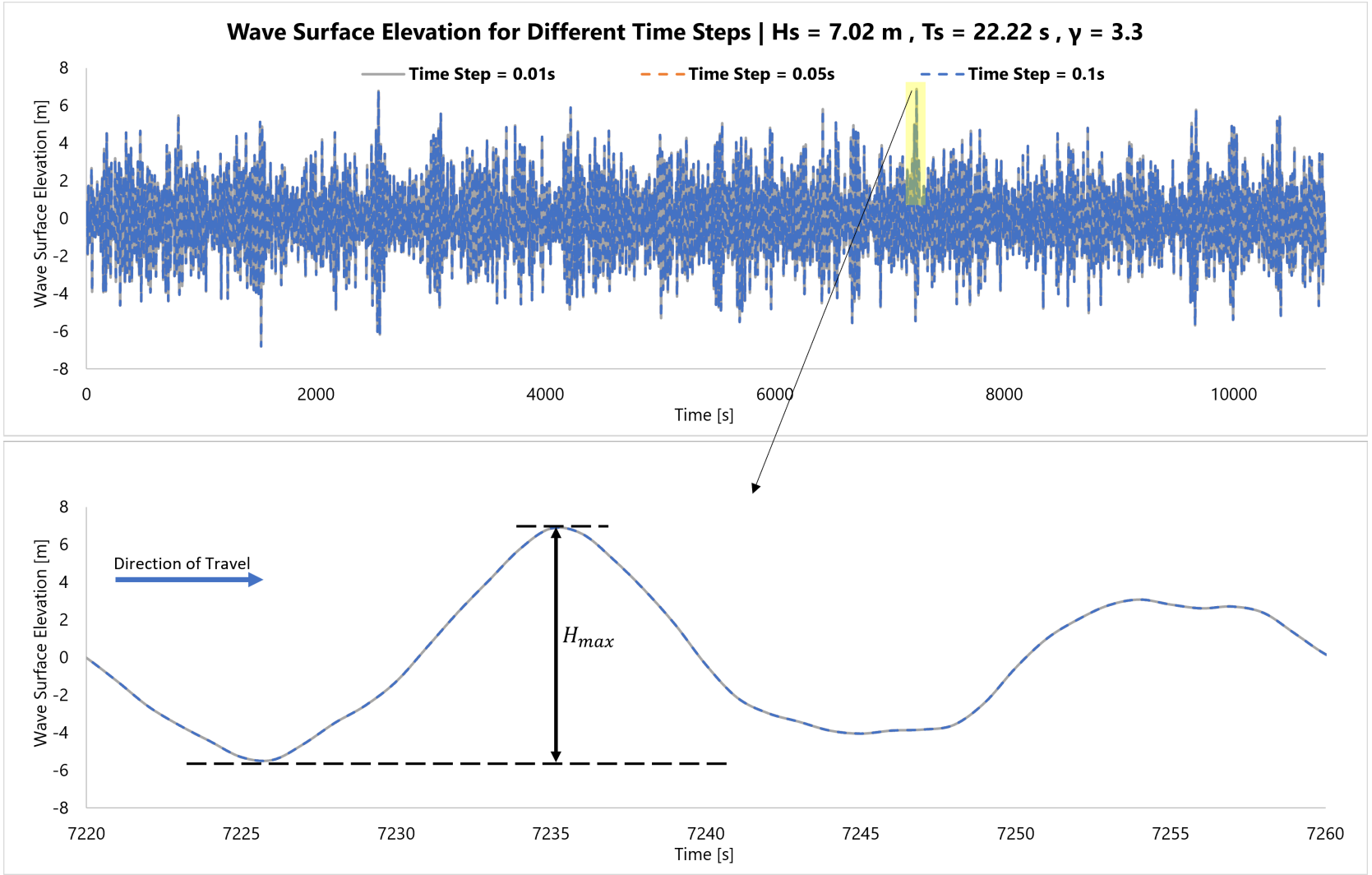

FIGURE 6.63: Time series of wave surface elevation for (a) different values of time steps (b) zoomed in plot showing maximum wave height.

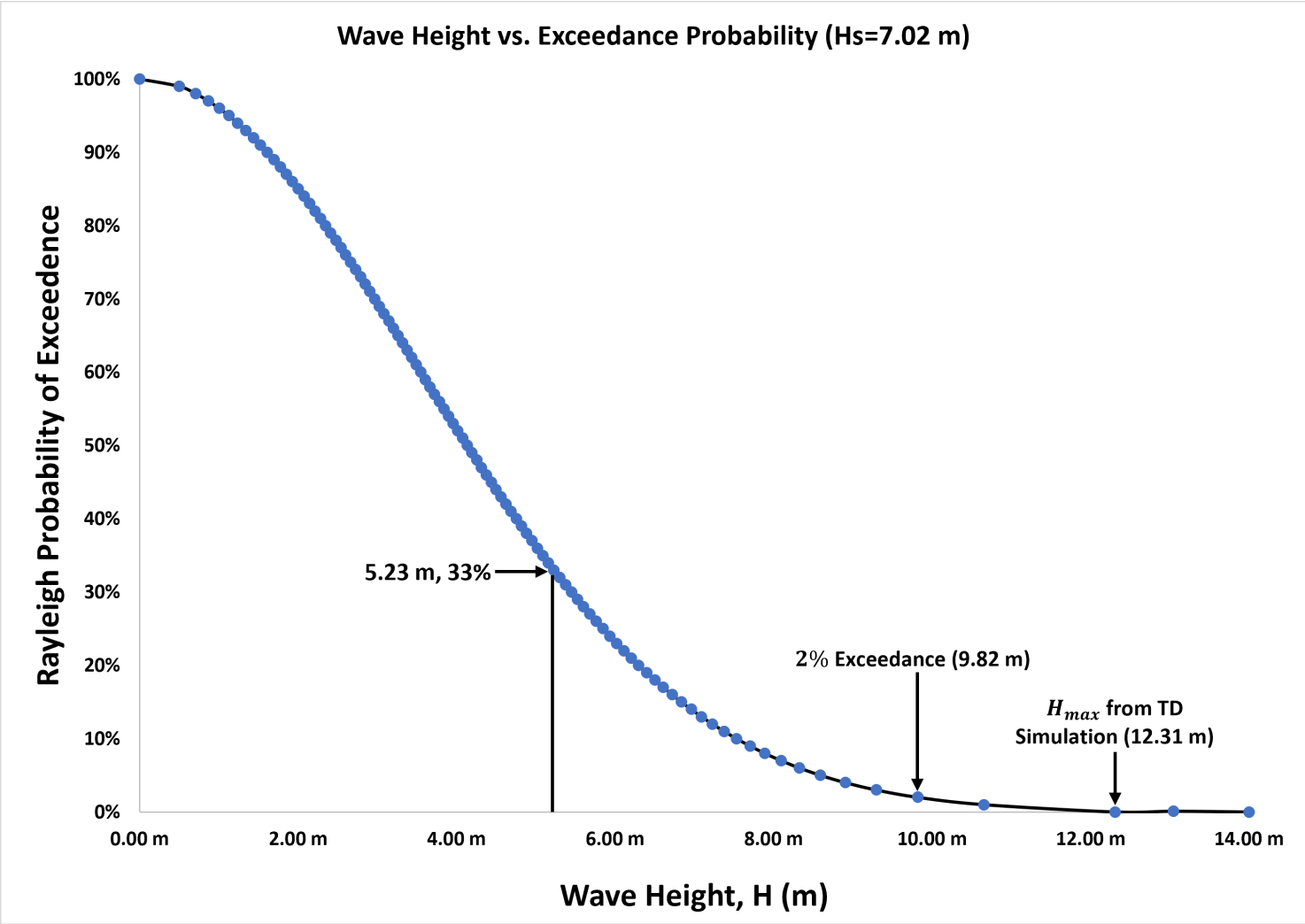

FIGURE 6.64: Plot of Rayleigh Probability of Exceedance vs. Wave Height according to [143].

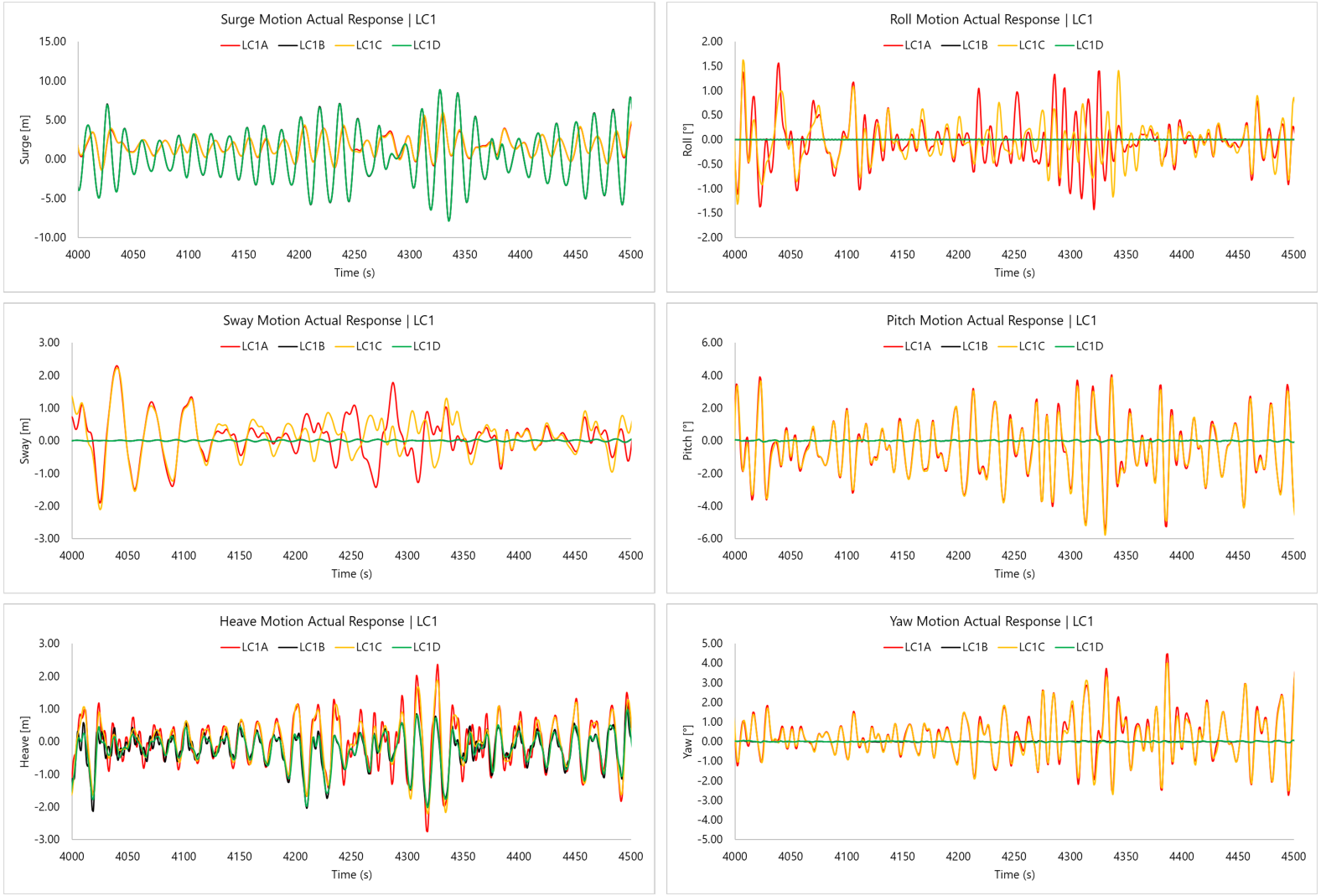

FIGURE 6.65: Plots showing time series of structure actual position response for all 6DOF for an irregular wave direction of 0° for various scenarios of LC1.

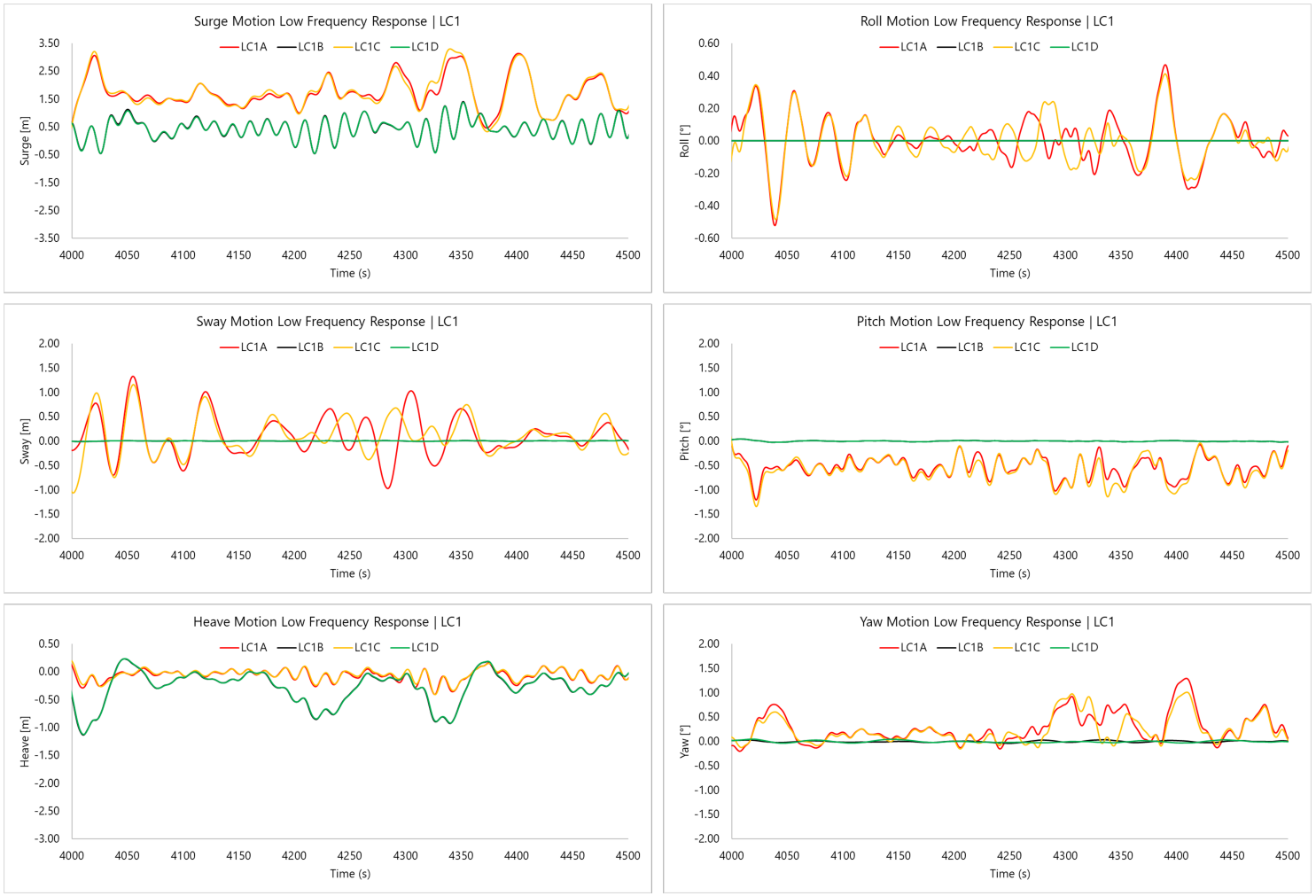

FIGURE 6.66: Plots showing time series of structure low-frequency response for all 6DOFs for an irregular wave direction of 0° for various scenarios of LC1.

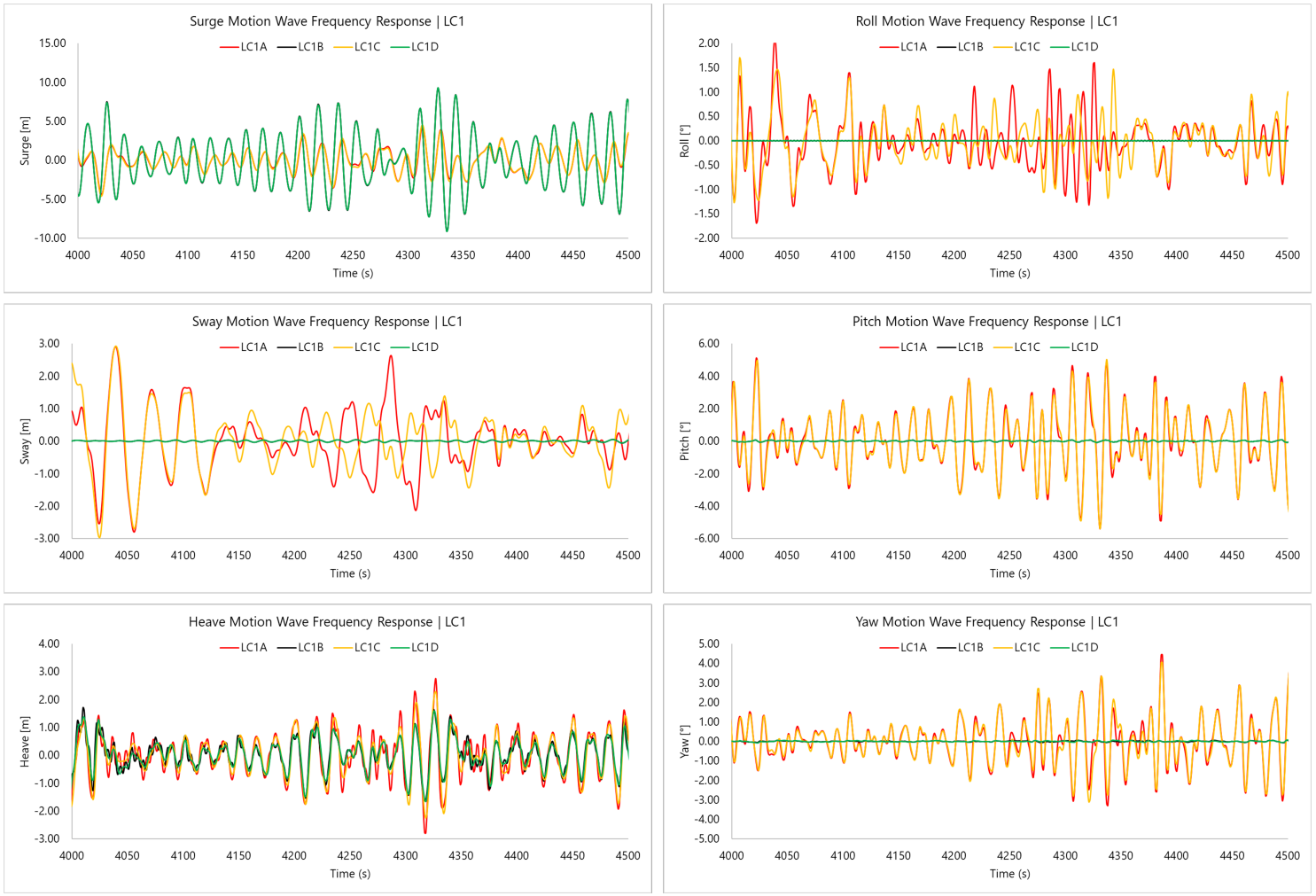

FIGURE 6.67: Plots showing time series of structure wave frequency response for all 6DOFs for an irregular wave direction of 0° for various scenarios of LC1.

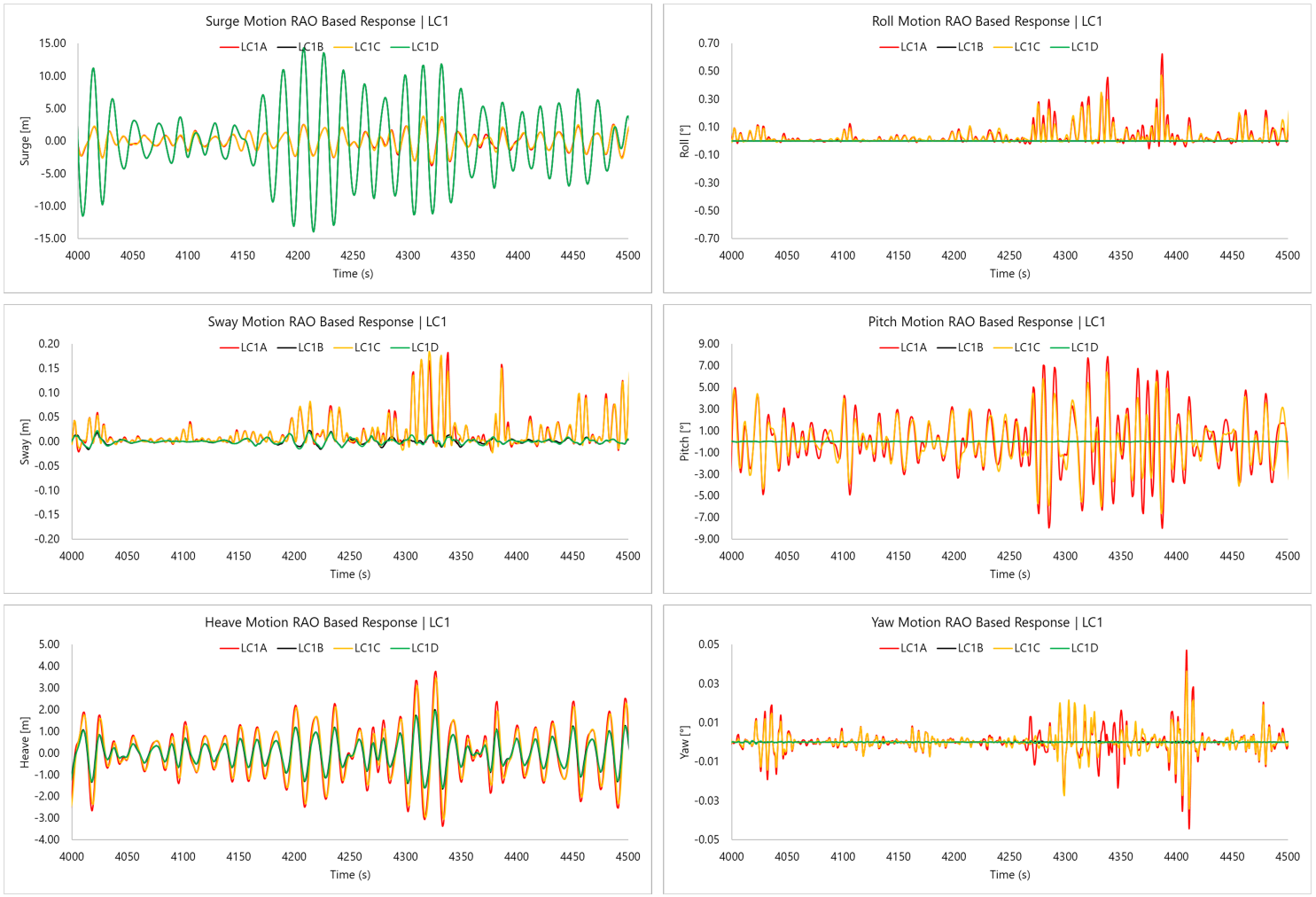

FIGURE 6.68: Plots showing time series of structure RAO based response for 6DOFs for an irregular wave direction of 0° for various scenarios of LC1.

There is also an understandable observation that the structure's motion is dominated by WF response. The LF response is predicted to have more effect on surge motion than other DOFs. For all scenarios of LC1, the predicted maximum response for surge, sway and heave motion are 11.92 m, 4.83 m, and 2.39 m, respectively. For rotational motion, the anticipated maximum for roll motion is 10.20°, while pitch and yaw motion are expected to have maximum values of 8.81° and 28.51° respectively. It is noteworthy that the maximums for motions in the vertical plane occurred for LC1A because the influence of the mooring stiffness and viscous damping are not considered for this LC. However, looking at a more wholistic modelling approach (LC1D) that accounts for both the mooring stiffness and viscous damping, the maximum values for heave, roll, and pitch motion were predicted to be 1.09 m, 0.01°, and 0.13°, respectively. Consequently, not accounting for viscous damping and mooring stiffness will overestimate the motion response in the vertical plane of motion. On the contrary, not accounting for the mooring stiffness under-predicts the structure's response for surge motion as can be observed for LC1A where the predicted maximum value for surge was 7.44 m when compared to 11.92 m as predicted for LC1B. More statistical details on the structure motion for all scenarios of LC2 and LC3 are provided in Table 6.20 to Table 6.25.

Structure Velocity and Acceleration Responses

The FOWT was modelled as a rigid structure that is free to move in the presence of environmental loads. Independent flow field models were obtained by the linear superposition of two independent flow fields; a far-field due to wave motion and relatively unaffected by the FOWT motion and a near field resulting from the FOWT motion. Computed results of time series for actual responses for structure velocity/angular velocity, and acceleration/angular acceleration are presented in Fig. 6.69 and Fig. 6.70, respectively. Results from the computed time series plot show that the platform tends to have higher motion responses for surge and pitch motion for both velocity and acceleration. Viscous damping is predicted to condense the velocity and acceleration for roll motion. For all scenarios of LC1, the anticipated maximum motion velocity in X, Y and Z direction is 4.81 m/s, 0.77 m/s, and 1.88 m/s, respectively. More details on the time history statistics for the structure's velocity and acceleration for LC1, LC2 and LC3 are presented in Table 6.20 to Table 6.25.

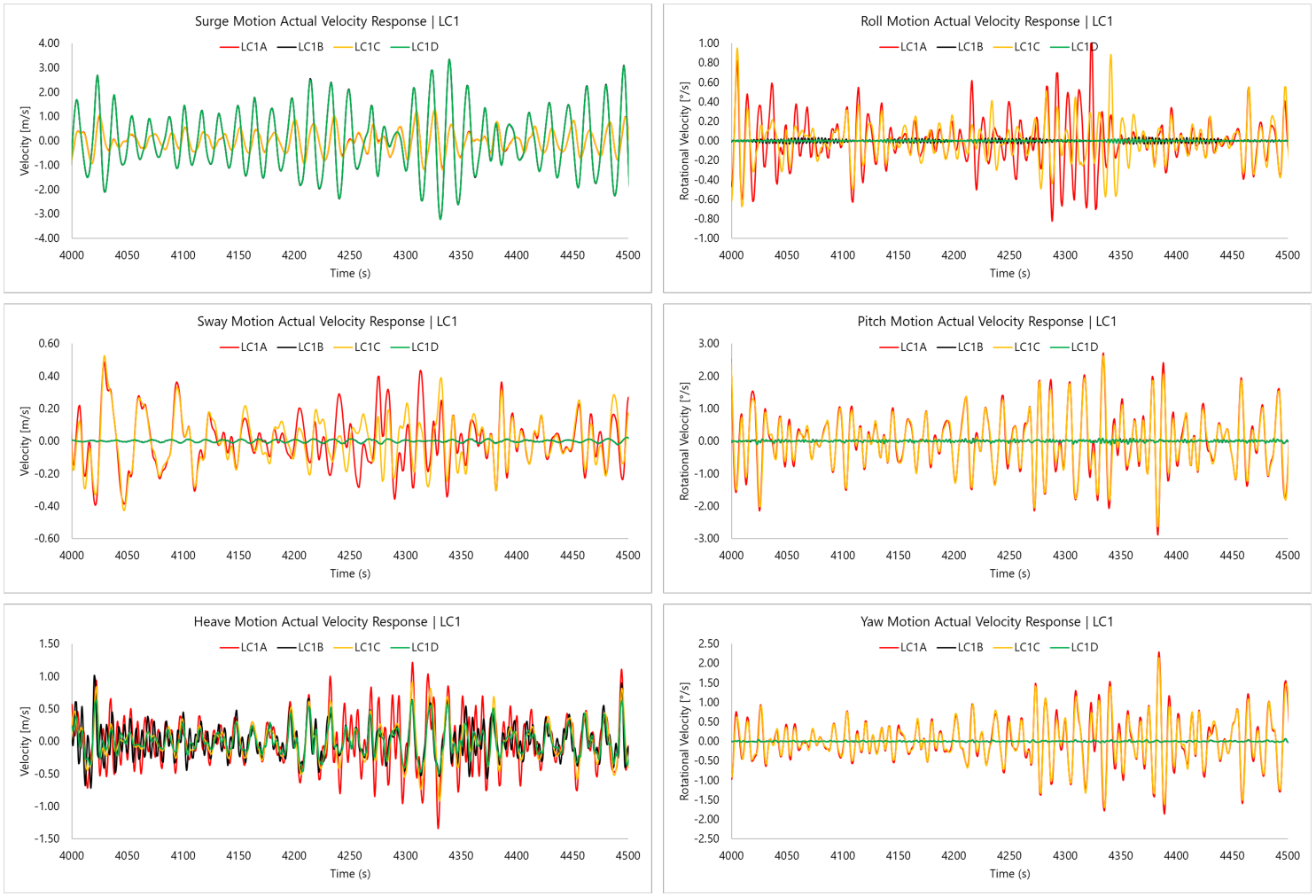

FIGURE 6.69: Plots showing time series of structure actual velocity response for all 6DOF for an irregular wave direction of 0° for various scenarios of LC1.



FIGURE 6.70: Plots showing time series of structure actual acceleration response for all 6DOF for an irregular wave direction of 0° for various scenarios of LC1.

Structure and Mooring Fairlead Forces

The computation of hydrodynamic wave forces on an offshore floating platform is one of the primary tasks in the design of the structure and also one of the most complex tasks since it involves the complex interaction between the waves and the structure in addition to the coupled effect of the mooring cable. Mean wind forces and current forces were calculated using drag force formulation and force coefficients that are dependent on the angular orientation of the floating platform relative to the incoming fluid flow direction. The wind and current force coefficients were implemented into the AQWA program to facilitate the adequate representation of viscous drag forces on the structure rigid body due to wind and current flow. Mean wave forces contained components of both viscous effects and potential effects based on results of a prior first-order analysis which provides mean drift force coefficients for each mode of motion as a function of wave frequency, current speed, and angular orientation of the structure.

An accurate prediction of the structure forces on a floating platform is crucial in performing fatigue design and structural analysis. This is required to ensure that the desired structural integrity is achieved and more importantly to ensure that the floating platform can stand the test of time when subjected to extreme environmental loading. Time series of rotor thrust, rotor thrust coefficient, hydrodynamic force, wind force, and mooring cable fairlead tension are presented in Fig. 6.71. The peak rotor thrust force and thrust coefficient were predicted to be 1.23×10^6 N and 0.29, respectively for LC1. For current drag force, the anticipated maximum is 6.88×10^6 N. The expected maximum wind force on the tower for LC1 is 1.25×10^5 N.

The time series plot shown in Fig. 6.71a indicates an interesting trend for the tension experienced by the fairlead tension of cable 1. A logical explanation for the higher fairlead tension experienced by cable 1 from the other two cables can be attributed to the upstream wave interaction with cable 1. Also noteworthy is the fairlead tension experienced by cable 4. Here, cable 4 is seen to experience tensions in the magnitude similar to that suffered by cable 1 which can be attributed to the support it provide for the counterweight at the bottom of TRIHF.

Fig. 6.71b presents a time series of the hydrodynamic forces experienced by TRIHF. As can be observed from this plot, the radiation force and diffraction force appear to be the dominant hydrodynamic force. Forces due to Morison drag and current appear to be in the same magnitude. The motion analysis time history statistics of various

structure parameters for all scenarios of LC1, LC2, and LC3 are presented in Table 6.20 to Table 6.25. The kurtosis for the time series values of each parameter has been calculated to identify outliers that may occur due to nonlinearities in the TD analysis. Values of kurtosis < 3 indicates a small number of outliers while values > 3 indicate large number outliers.

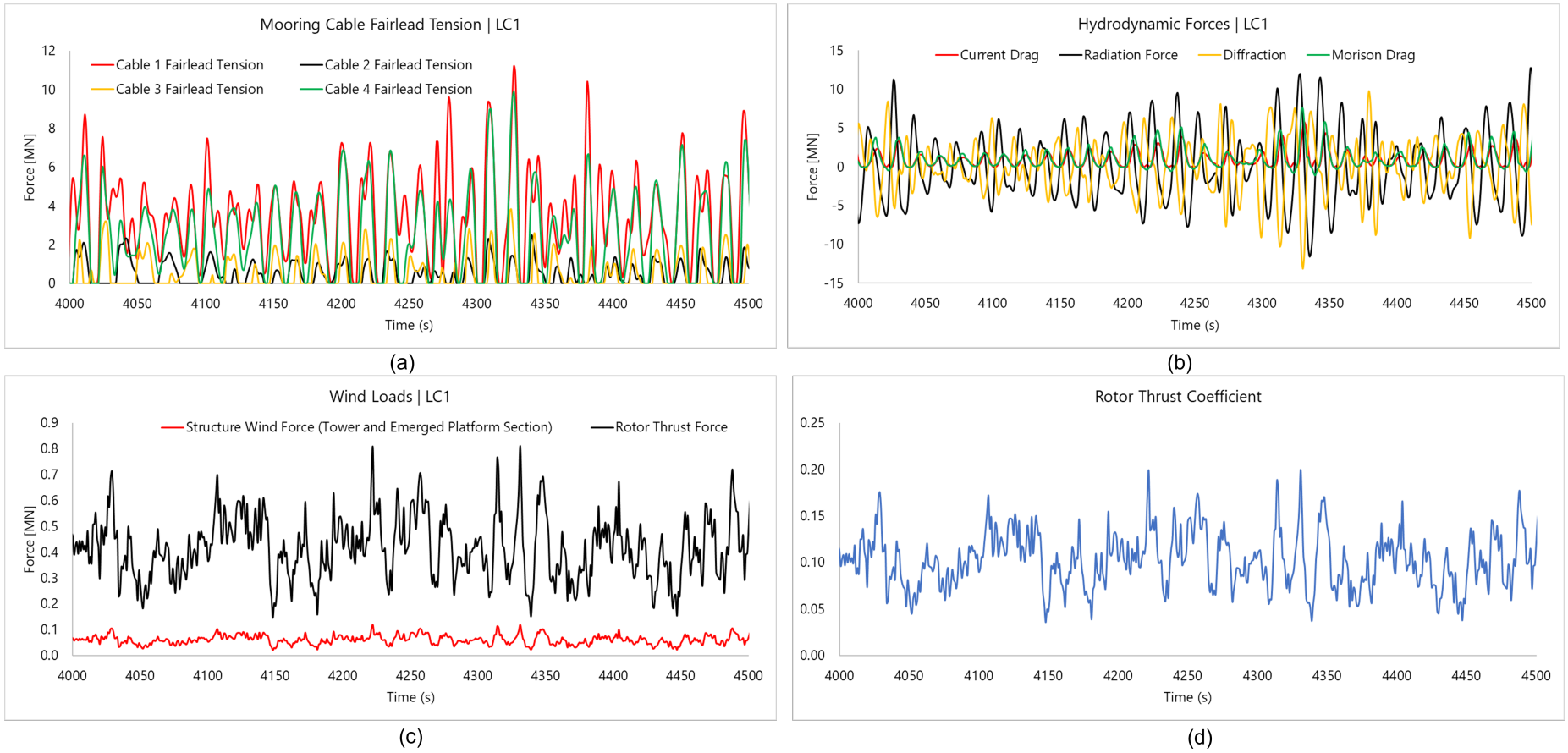

FIGURE 6.71: Plots showing time series of (a) mooring cable fairlead tension, (b) hydrodynamic forces, (c) wind loads, and (d) rotor thrust coefficient for an irregular wave direction of 0°, wind direction of 0°, and current direction of 0°.

TABLE 6.20: Motion Analysis Time History Statistics for LC1A and LC1B.

Parameters	LC1A					LC1B				
	Avg.	Max	Min	Std.Dev	Kurt	Avg.	Max	Min	Std.Dev	Kurt
WAVE SURFACE ELEVATION [m]	0.024	1.96	-1.52	0.48	0.24	0.021	1.655	-1.256	0.416	0.061
WAVE VELOCITY [m/s]	-5.239	15.45	-22.57	3.27	1.63	-5.483	5.787	-15.404	2.830	-0.183
WAVE ACCELERATION [m/s^2]	0.003	16.05	-15.22	1.96	4.77	0.001	4.515	-3.511	1.112	-0.211
STRUCTURE SURGE POSITION [m]	1.840	7.44	-2.64	1.22	0.45	0.458	11.917	-9.619	2.882	-0.192
STRUCTURE SWAY POSITION [m]	0.213	4.83	-3.98	1.00	1.56	0.001	0.095	-0.076	0.015	3.336
STRUCTURE HEAVE POSITION [m]	-0.094	2.39	-3.65	0.77	0.34	-0.248	1.303	-3.065	0.510	1.729
STRUCTURE ROLL POSITION [°]	0.012	10.20	-9.01	1.16	6.68	0.000	0.037	-0.042	0.010	1.587
STRUCTURE PITCH POSITION [°]	-0.533	8.81	-8.20	1.92	0.61	-0.001	0.175	-0.268	0.033	2.108
STRUCTURE YAW POSITION [°]	0.112	28.51	-28.28	2.50	31.31	-0.003	0.147	-0.204	0.027	4.922
STRUCTURE SURGE VELOCITY [m/s]	0.000	1.93	-1.72	0.44	0.20	0.000	4.816	-3.659	1.132	-0.178
STRUCTURE SWAY VELOCITY [m/s]	0.001	0.77	-0.80	0.20	0.74	0.000	0.032	-0.035	0.006	1.869
STRUCTURE HEAVE VELOCITY [m/s]	0.000	1.88	-1.56	0.44	0.50	0.000	1.220	-0.832	0.250	0.727
STRUCTURE ROLL VELOCITY [°/s]	-0.010	4.11	-9.69	0.72	20.20	0.000	0.167	-0.185	0.041	1.587
STRUCTURE PITCH VELOCITY [°/s]	0.005	7.34	-7.04	1.04	2.57	0.000	0.851	-0.951	0.051	103.151
STRUCTURE YAW VELOCITY [°/s]	-0.001	20.88	-19.12	1.36	58.45	0.000	0.135	-0.081	0.015	4.811
STRUCTURE SURGE ACCELERATION [m/s^2]	-0.002	0.82	-1.31	0.19	1.35	0.000	1.626	-1.985	0.467	-0.107
STRUCTURE SWAY ACCELERATION [m/s^2]	0.000	0.31	-0.45	0.06	1.76	0.000	0.049	-0.043	0.012	1.292
STRUCTURE HEAVE ACCELERATION [m/s^2]	0.000	1.32	-1.43	0.36	0.29	0.000	0.854	-0.833	0.199	0.523
STRUCTURE ROLL ACCELERATION [°/s^2]	0.001	2.75	-3.54	0.55	2.90	0.000	0.754	-0.686	0.176	1.593
STRUCTURE PITCH ACCELERATION [°/s^2]	-0.002	7.04	-5.62	0.65	6.49	-0.001	4.724	-2.764	0.210	140.663
STRUCTURE YAW ACCELERATION [°/s^2]	0.004	15.11	-14.85	1.77	9.51	0.001	0.427	-0.399	0.071	3.520
STRUCTURE SURGE RAO BASED POSITION [m]	0.001	4.86	-4.82	1.21	-0.13	0.010	22.589	-22.019	5.830	0.610
STRUCTURE SWAY RAO BASED POSITION [m]	-0.004	0.64	-0.65	0.06	27.65	0.000	0.048	-0.035	0.007	4.298
STRUCTURE HEAVE RAO BASED POSITION [m]	-0.001	4.27	-4.70	1.14	0.01	-0.001	2.169	-2.500	0.586	-0.007
STRUCTURE ROLL RAO BASED POSITION [°]	0.000	2.09	-1.32	0.15	48.57	0.000	0.000	0.000	0.000	2.556
STRUCTURE PITCH RAO BASED POSITION [°]	0.000	9.63	-10.85	2.82	0.11	0.000	0.062	-0.065	0.018	0.215
STRUCTURE YAW RAO BASED POSITION [°]	0.000	0.20	-0.25	0.01	77.65	0.000	0.001	-0.001	0.000	5.567
STRUCTURE SURGE RAO BASED VELOCITY [m/s]	0.000	1.87	-1.89	0.51	-0.16	-0.002	7.279	-8.030	1.997	0.458
STRUCTURE SWAY RAO BASED VELOCITY [m/s]	0.001	0.16	-0.47	0.02	81.44	0.000	0.012	-0.013	0.002	4.055
STRUCTURE HEAVE RAO BASED VELOCITY [m/s]	0.000	1.99	-1.91	0.50	0.07	-0.001	1.013	-0.901	0.249	0.044
STRUCTURE ROLL RAO BASED VELOCITY [°/s]	0.002	1.04	-1.59	0.08	79.22	0.000	0.000	0.000	0.000	9.244

TABLE 6.20: Motion Analysis Time History Statistics for LC1A and LC1B (contd).

Parameters	LC1A					LC1B				
	Avg.	Max	Min	Std.Dev	Kurt	Avg.	Max	Min	Std.Dev	Kurt
STRUCTURE PITCH RAO BASED VELOCITY [°/s]	0.000	6.44	-6.21	1.76	0.09	0.000	0.031	-0.032	0.009	0.067
STRUCTURE YAW RAO BASED VELOCITY [°/s]	0.000	0.32	-0.21	0.01	88.05	0.000	0.001	-0.001	0.000	5.266
STRUCTURE SURGE RAO BASED ACCELERATION [m/s^2]	0.000	0.78	-0.86	0.23	-0.10	-0.001	2.686	-2.513	0.708	0.336
STRUCTURE SWAY RAO BASED ACCELERATION [m/s^2]	0.000	0.12	-0.16	0.01	34.62	0.000	0.004	-0.005	0.001	4.677
STRUCTURE HEAVE RAO BASED ACCELERATION [m/s^2]	0.000	0.88	-1.02	0.25	0.15	0.000	0.438	-0.491	0.119	0.125
STRUCTURE ROLL RAO BASED ACCELERATION [°/s^2]	-0.002	0.46	-0.96	0.06	56.06	0.000	0.000	0.000	0.000	5.125
STRUCTURE PITCH RAO BASED ACCELERATION [°/s^2]	0.000	3.99	-3.97	1.18	0.06	0.000	0.021	-0.021	0.006	-0.034
STRUCTURE YAW RAO BASED ACCELERATION [°/s^2]	0.000	0.37	-0.31	0.02	67.36	0.000	0.002	-0.002	0.000	4.043
STRUCTURE SURGE WAVE FREQ POSITION [m]	0.001	5.61	-4.96	1.41	0.54	0.001	12.169	-11.202	3.126	-0.178
STRUCTURE SWAY WAVE FREQ POSITION [m]	0.004	5.54	-6.11	1.52	1.29	0.000	0.097	-0.090	0.017	3.178
STRUCTURE HEAVE WAVE FREQ POSITION [m]	-0.001	2.91	-3.65	0.82	0.27	0.000	2.001	-2.817	0.539	0.805
STRUCTURE ROLL WAVE FREQ POSITION [°]	-0.050	5.71	-17.74	1.39	25.00	0.000	0.037	-0.042	0.010	1.587
STRUCTURE PITCH WAVE FREQ POSITION [°]	0.009	8.09	-12.19	2.04	0.73	0.000	0.401	-0.219	0.037	10.121
STRUCTURE YAW WAVE FREQ POSITION [°]	-0.027	25.21	-35.66	2.72	30.19	0.000	0.166	-0.225	0.030	4.571
STRUCTURE SURGE WAVE FREQ VELOCITY [m/s]	0.000	2.04	-1.90	0.49	0.18	0.000	5.176	-3.983	1.221	-0.178
STRUCTURE SWAY WAVE FREQ VELOCITY [m/s]	0.001	1.00	-1.12	0.28	0.99	0.000	0.034	-0.038	0.007	2.027
STRUCTURE HEAVE WAVE FREQ VELOCITY [m/s]	0.000	1.97	-1.63	0.46	0.52	0.000	1.374	-0.889	0.262	0.800
STRUCTURE ROLL WAVE FREQ VELOCITY [°/s]	-0.003	5.25	-9.00	0.74	14.22	0.000	0.167	-0.185	0.042	1.587
STRUCTURE PITCH WAVE FREQ VELOCITY [°/s]	0.001	7.68	-7.07	1.09	2.40	0.000	0.846	-0.954	0.051	104.427
STRUCTURE YAW WAVE FREQ VELOCITY [°/s]	0.004	21.79	-19.48	1.42	56.27	0.000	0.143	-0.081	0.015	4.993
STRUCTURE SURGE WAVE FREQ ACCELERATION [m/s^2]	0.003	0.86	-0.81	0.21	0.27	0.000	1.739	-2.124	0.501	-0.118
STRUCTURE SWAY WAVE FREQ ACCELERATION [m/s^2]	0.000	0.65	-0.82	0.09	5.30	0.000	0.049	-0.043	0.012	1.268
STRUCTURE HEAVE WAVE FREQ ACCELERATION [m/s^2]	-0.001	2.81	-2.52	0.39	1.89	0.000	0.870	-0.855	0.203	0.523
STRUCTURE ROLL WAVE FREQ ACCELERATION [°/s^2]	-0.001	11.75	-12.05	0.88	43.36	0.000	0.770	-0.683	0.178	1.453
STRUCTURE PITCH WAVE FREQ ACCELERATION [°/s^2]	0.003	17.13	-13.83	1.15	44.21	-0.002	4.193	-2.768	0.199	113.824
STRUCTURE YAW WAVE FREQ ACCELERATION [°/s^2]	-0.006	38.01	-49.87	3.19	52.20	-0.001	0.546	-0.458	0.082	3.513
STRUCTURE SURGE LOW FREQ POSITION [m]	1.839	4.13	-0.05	0.52	1.25	0.458	1.590	-0.673	0.307	0.632
STRUCTURE SWAY LOW FREQ POSITION [m]	0.209	3.50	-2.64	0.76	1.76	0.001	0.017	-0.011	0.004	1.642
STRUCTURE HEAVE LOW FREQ POSITION [m]	-0.093	0.16	-0.87	0.11	3.60	-0.248	0.306	-1.539	0.242	3.381
STRUCTURE ROLL LOW FREQ POSITION [°]	0.059	11.72	-1.67	0.62	134.42	0.000	0.000	0.000	0.000	0.970

TABLE 6.20: Motion Analysis Time History Statistics for LC1A and LC1B (contd).

Parameters	LC1A					LC1B				
	Avg.	Max	Min	Std.Dev	Kurt	Avg.	Max	Min	Std.Dev	Kurt
STRUCTURE PITCH LOW FREQ POSITION [°]	-0.553	5.56	-2.18	0.32	62.59	-0.001	0.147	-0.268	0.017	87.705
STRUCTURE YAW LOW FREQ POSITION [°]	0.142	7.70	-4.92	0.90	23.29	-0.003	0.038	-0.052	0.013	0.655
STRUCTURE SURGE LOW FREQ VELOCITY [m/s]	0.000	0.23	-0.26	0.07	0.82	0.000	0.329	-0.361	0.094	-0.082
STRUCTURE SWAY LOW FREQ VELOCITY [m/s]	0.000	0.41	-0.43	0.10	1.58	0.000	0.003	-0.003	0.001	2.751
STRUCTURE HEAVE LOW FREQ VELOCITY [m/s]	0.000	0.08	-0.13	0.02	0.63	0.000	0.096	-0.153	0.023	3.007
STRUCTURE ROLL LOW FREQ VELOCITY [°/s]	-0.007	0.21	-1.41	0.09	81.80	0.000	0.000	0.000	0.000	0.889
STRUCTURE PITCH LOW FREQ VELOCITY [°/s]	0.004	0.23	-0.34	0.06	0.86	0.000	0.023	-0.012	0.002	50.266
STRUCTURE YAW LOW FREQ VELOCITY [°/s]	-0.005	0.86	-0.94	0.11	22.89	0.000	0.006	-0.008	0.001	1.194
STRUCTURE SURGE LOW FREQ ACCELERATION [m/s^2]	0.000	0.06	-0.06	0.02	0.49	0.000	0.139	-0.125	0.035	-0.177
STRUCTURE SWAY LOW FREQ ACCELERATION [m/s^2]	0.000	0.06	-0.06	0.02	1.20	0.000	0.001	-0.001	0.000	3.203
STRUCTURE HEAVE LOW FREQ ACCELERATION [m/s^2]	0.000	0.04	-0.04	0.01	0.25	0.000	0.027	-0.028	0.006	0.653
STRUCTURE ROLL LOW FREQ ACCELERATION [°/s^2]	0.000	0.07	-0.16	0.01	11.78	0.000	0.000	0.000	0.000	1.587
STRUCTURE PITCH LOW FREQ ACCELERATION [°/s^2]	0.000	0.10	-0.13	0.02	0.66	0.000	0.004	-0.003	0.000	7.516
STRUCTURE YAW LOW FREQ ACCELERATION [°/s^2]	0.000	0.30	-0.39	0.03	28.98	0.000	0.002	-0.002	0.000	4.566
MORISON DRAG FORCE - X [N]	7.63E+05	6.93E+06	-1.21E+06	4.09E+05	2.66E+01	1.01E+06	8.37E+06	-2.41E+06	1.14E+06	2.84E+00
MORISON DRAG FORCE - Y [N]	1.17E+04	4.95E+06	-2.99E+06	2.09E+05	1.61E+02	1.74E+02	3.08E+04	-3.48E+04	5.69E+03	2.33E+00
MORISON DRAG FORCE - Z [N]	-7.65E+03	3.05E+06	-3.24E+06	3.05E+05	8.73E+00	-3.97E+04	9.09E+05	-2.50E+06	2.58E+05	6.26E+00
MORISON DRAG MOMENT - X [N.m]	-1.64E+05	1.20E+08	-1.28E+08	6.31E+06	1.52E+02	-2.54E+03	1.51E+06	-1.17E+06	2.04E+05	3.93E+00
MORISON DRAG MOMENT - Y [N.m]	1.19E+07	1.71E+08	-6.69E+07	9.70E+06	2.89E+01	1.49E+07	1.15E+08	-2.62E+07	1.60E+07	2.89E+00
MORISON DRAG MOMENT - Z [N.m]	3.11E+05	2.41E+08	-1.53E+08	9.95E+06	2.11E+02	-1.77E+03	4.29E+05	-4.52E+05	6.70E+04	5.30E+00
WAVE INERTIA FORCE - X [N]	1.78E+00	5.53E+02	-5.21E+02	1.35E+02	2.69E-01	3.03E+00	5.76E+02	-4.91E+02	1.34E+02	1.07E-01
WAVE INERTIA FORCE - Y [N]	4.57E-02	4.06E+01	-5.53E+01	4.39E+00	2.37E+01	-2.31E-03	3.82E-01	-9.45E-01	5.56E-02	3.21E+01
WAVE INERTIA FORCE - Z [N]	-1.10E+01	5.05E+02	-8.04E+02	1.53E+02	2.60E-01	-8.61E+00	4.49E+02	-7.02E+02	1.54E+02	6.34E-02
WAVE INERTIA MOMENT - X [N.m]	-4.33E+00	3.02E+03	-2.06E+03	3.12E+02	1.57E+01	1.90E-01	2.41E+02	-1.15E+02	6.58E+00	6.57E+02
WAVE INERTIA MOMENT - Y [N.m]	9.13E+01	6.13E+03	-6.59E+03	1.84E+03	3.53E-03	2.30E+01	5.99E+03	-6.00E+03	1.84E+03	-1.79E-01
WAVE INERTIA MOMENT - Z [N.m]	-7.76E+00	1.42E+03	-1.87E+03	1.78E+02	1.71E+01	-3.61E-02	4.61E+01	-1.37E+02	2.72E+00	1.23E+03
FROUDE KRYLOV FORCE - X [N]	3.05E+00	8.50E+02	-8.02E+02	2.06E+02	2.59E-01	4.41E+00	8.49E+02	-7.68E+02	2.04E+02	1.23E-01
FROUDE KRYLOV FORCE - Y [N]	1.73E-05	3.73E-02	-2.54E-02	2.25E-03	7.47E+01	6.85E-09	1.90E-04	-1.53E-04	7.47E-06	2.51E+02
FROUDE KRYLOV FORCE - Z [N]	-1.40E+01	6.60E+02	-1.02E+03	1.99E+02	2.29E-01	-1.20E+01	5.68E+02	-9.04E+02	2.00E+02	9.16E-02
FROUDE KRYLOV MOMENT - X [N.m]	-2.40E+00	3.04E+03	-2.15E+03	2.89E+02	1.94E+01	9.87E-02	1.15E+02	-8.54E+01	4.06E+00	3.27E+02
FROUDE KRYLOV MOMENT - Y [N.m]	1.22E+02	9.11E+03	-9.99E+03	2.46E+03	2.03E-01	4.77E+01	9.27E+03	-7.67E+03	2.46E+03	-5.27E-02

TABLE 6.20: Motion Analysis Time History Statistics for LC1A and LC1B (contd).

Parameters	LC1A					LC1B				
	Avg.	Max	Min	Std.Dev	Kurt	Avg.	Max	Min	Std.Dev	Kurt
FROUDE KRYLOV MOMENT - Z [N.m]	-1.08E+01	1.71E+03	-2.18E+03	2.15E+02	2.04E+01	-3.24E-02	2.55E+01	-4.69E+01	2.02E+00	7.33E+01
DIFFRACTION FORCE - X [N]	-1.49E+03	1.51E+07	-1.47E+07	3.73E+06	1.08E-01	-6.88E+03	1.50E+07	-1.46E+07	3.73E+06	1.08E-01
DIFFRACTION FORCE - Y [N]	1.20E+04	2.48E+06	-1.41E+06	1.71E+05	3.26E+01	2.09E+02	2.90E+04	-2.54E+04	2.60E+03	1.91E+01
DIFFRACTION FORCE - Z [N]	-1.30E+04	3.79E+07	-4.39E+07	1.01E+07	-2.06E-02	-1.02E+04	3.77E+07	-4.39E+07	1.01E+07	-2.08E-02
DIFFRACTION MOMENT - X [N.m]	-3.20E+05	3.66E+07	-6.76E+07	4.50E+06	3.43E+01	-5.83E+03	6.41E+05	-7.72E+05	6.83E+04	1.87E+01
DIFFRACTION MOMENT - Y [N.m]	-3.68E+04	3.94E+08	-3.84E+08	9.87E+07	9.68E-02	-1.80E+05	3.91E+08	-3.81E+08	9.89E+07	9.64E-02
DIFFRACTION MOMENT - Z [N.m]	1.58E+03	8.53E+06	-9.23E+06	5.13E+05	8.70E+01	5.41E+00	5.71E+04	-4.93E+04	7.25E+03	6.14E+00
RADIATION FORCE - X [N]	2.12E+04	8.28E+06	-7.92E+06	1.77E+06	6.58E-01	2.38E+03	1.90E+07	-1.39E+07	4.36E+06	-6.27E-02
RADIATION FORCE - Y [N]	1.04E+04	6.41E+06	-6.97E+06	1.26E+06	2.66E+00	-3.87E+02	3.78E+05	-3.59E+05	9.04E+04	1.20E+00
RADIATION FORCE - Z [N]	-2.61E+03	1.13E+07	-1.15E+07	2.91E+06	2.53E-01	3.29E+02	6.09E+06	-7.82E+06	1.76E+06	4.15E-01
RADIATION MOMENT - X [N.m]	-2.96E+05	2.35E+08	-2.19E+08	4.39E+07	2.51E+00	1.59E+04	2.74E+07	-2.99E+07	6.98E+06	1.56E+00
RADIATION MOMENT - Y [N.m]	3.68E+05	3.19E+08	-3.21E+08	4.50E+07	2.98E+00	6.69E+04	3.13E+08	-2.09E+08	6.99E+07	-2.91E-02
RADIATION MOMENT - Z [N.m]	-7.62E+04	4.10E+08	-4.12E+08	4.69E+07	1.07E+01	-1.77E+04	6.65E+06	-6.05E+06	1.12E+06	3.17E+00
TOTAL FORCE - X [N]	-2.53E+04	8.93E+06	-1.43E+07	2.09E+06	1.35E+00	-2.00E+03	1.77E+07	-2.16E+07	5.09E+06	-1.07E-01
TOTAL FORCE - Y [N]	9.96E+02	3.42E+06	-4.90E+06	6.65E+05	1.76E+00	1.02E+02	5.32E+05	-4.68E+05	1.26E+05	1.29E+00
TOTAL FORCE - Z [N]	3.76E+03	1.43E+07	-1.56E+07	3.97E+06	2.93E-01	-6.28E+02	9.30E+06	-9.07E+06	2.17E+06	5.23E-01
TOTAL MOMENT - X [N.m]	1.30E+05	4.67E+08	-5.72E+08	8.33E+07	3.79E+00	-4.76E+04	1.16E+08	-1.05E+08	2.69E+07	1.59E+00
TOTAL MOMENT - Y [N.m]	-1.40E+06	8.50E+08	-8.54E+08	1.00E+08	5.25E+00	-1.59E+05	7.24E+08	-4.24E+08	3.22E+07	1.41E+02
TOTAL MOMENT - Z [N.m]	9.99E+04	2.36E+08	-2.62E+08	2.36E+07	1.72E+01	1.49E+04	5.43E+06	-5.13E+06	8.94E+05	4.14E+00
STRUCTURE CURRENT DRAG FORCE - X [N]	6.49E+05	2.71E+06	1.57E+03	3.42E+05	5.90E-01	9.18E+05	6.88E+06	8.01E-02	9.36E+05	2.44E+00
STRUCTURE WIND FORCE - X [N]	6.10E+04	1.24E+05	1.71E+04	1.59E+04	-3.79E-02	6.12E+04	1.25E+05	8.59E+03	1.75E+04	4.61E-02
ROTOR THRUST FORCE [N]	4.21E+05	1.23E+06	6.72E+01	1.42E+05	8.51E-01	4.15E+05	8.44E+05	5.89E+04	1.18E+05	4.35E-02
MOORING CABLE 1 TENSION [N]	3.77E+06	1.69E+07	0.00E+00	2.57E+06	8.97E-01	3.09E+06	2.15E+07	0.00E+00	3.73E+06	7.31E-01
MOORING CABLE 2 TENSION [N]	7.60E+05	1.93E+07	0.00E+00	1.21E+06	3.99E+01	8.88E+05	5.44E+06	0.00E+00	1.12E+06	4.79E-01
MOORING CABLE 3 TENSION [N]	7.08E+05	1.43E+07	0.00E+00	1.15E+06	1.40E+01	8.92E+05	5.50E+06	0.00E+00	1.13E+06	4.88E-01
MOORING CABLE 4 TENSION [N]	2.56E+06	1.20E+07	0.00E+00	2.30E+06	-5.73E-02	1.49E+06	7.14E+06	0.00E+00	1.32E+06	-3.63E-01

TABLE 6.21: Motion Analysis Time History Statistics for LC1C and LC1D.

Parameters	LC1C					LC1D				
	Avg.	Max	Min	Std.Dev	Kurt	Avg.	Max	Min	Std.Dev	Kurt
WAVE SURFACE ELEVATION [m]	0.021	1.594	-1.155	0.371	0.046	0.021	1.586	-1.025	0.384	0.047
WAVE VELOCITY [m/s]	-5.377	4.811	-15.485	2.878	0.139	-5.488	5.740	-15.424	2.813	-0.181
WAVE ACCELERATION [m/s^2]	0.002	6.067	-6.320	1.609	0.258	0.001	4.569	-3.496	1.104	-0.205
STRUCTURE SURGE POSITION [m]	1.813	7.790	-2.356	1.272	0.605	0.453	11.880	-9.640	2.865	-0.190
STRUCTURE SWAY POSITION [m]	0.183	4.356	-3.967	0.971	1.800	0.001	0.097	-0.078	0.016	3.270
STRUCTURE HEAVE POSITION [m]	-0.067	2.112	-3.528	0.644	0.444	-0.245	1.092	-3.160	0.487	1.997
STRUCTURE ROLL POSITION [°]	0.009	3.903	-3.540	0.753	2.186	0.000	0.014	-0.019	0.004	1.701
STRUCTURE PITCH POSITION [°]	-0.598	5.436	-7.756	1.771	0.151	-0.001	0.134	-0.271	0.032	1.624
STRUCTURE YAW POSITION [°]	0.056	24.583	-25.880	2.446	30.493	-0.002	0.143	-0.203	0.027	4.902
STRUCTURE SURGE VELOCITY [m/s]	0.000	1.968	-1.774	0.455	0.206	0.000	4.791	-3.637	1.126	-0.179
STRUCTURE SWAY VELOCITY [m/s]	0.000	0.730	-0.804	0.190	1.281	0.000	0.032	-0.035	0.006	3.101
STRUCTURE HEAVE VELOCITY [m/s]	0.000	1.624	-1.000	0.273	1.230	0.000	1.026	-0.722	0.204	0.778
STRUCTURE ROLL VELOCITY [°/s]	0.001	1.733	-2.083	0.404	2.130	0.000	0.074	-0.068	0.017	1.725
STRUCTURE PITCH VELOCITY [°/s]	0.006	3.209	-3.559	0.896	0.218	0.000	0.807	-0.929	0.041	147.883
STRUCTURE YAW VELOCITY [°/s]	-0.002	9.369	-11.831	0.984	27.538	0.000	0.133	-0.079	0.014	6.080
STRUCTURE SURGE ACCELERATION [m/s^2]	-0.001	0.806	-0.735	0.189	0.383	0.000	1.628	-2.013	0.465	-0.098
STRUCTURE SWAY ACCELERATION [m/s^2]	0.000	0.256	-0.199	0.049	1.610	0.000	0.022	-0.018	0.005	0.617
STRUCTURE HEAVE ACCELERATION [m/s^2]	0.000	1.012	-1.045	0.145	4.870	0.000	0.471	-0.627	0.118	1.132
STRUCTURE ROLL ACCELERATION [°/s^2]	0.001	2.335	-2.708	0.447	4.023	0.000	0.326	-0.267	0.071	1.632
STRUCTURE PITCH ACCELERATION [°/s^2]	-0.003	4.994	-4.331	0.595	6.759	-0.001	4.766	-2.457	0.166	244.786
STRUCTURE YAW ACCELERATION [°/s^2]	-0.002	8.197	-8.799	1.509	3.734	0.001	0.368	-0.380	0.061	3.828
STRUCTURE SURGE RAO BASED POSITION [m]	0.001	4.598	-4.983	1.209	-0.090	0.009	22.589	-22.020	5.830	0.610
STRUCTURE SWAY RAO BASED POSITION [m]	-0.003	0.739	-0.620	0.062	35.714	0.000	0.056	-0.035	0.007	5.314
STRUCTURE HEAVE RAO BASED POSITION [m]	-0.001	3.958	-4.436	1.043	-0.018	0.000	2.147	-2.433	0.573	-0.014
STRUCTURE ROLL RAO BASED POSITION [°]	-0.002	1.524	-1.054	0.121	37.029	0.000	0.000	0.000	0.000	3.107
STRUCTURE PITCH RAO BASED POSITION [°]	0.000	8.087	-8.754	2.313	0.088	0.000	0.062	-0.065	0.018	0.215
STRUCTURE YAW RAO BASED POSITION [°]	0.000	0.262	-0.212	0.013	96.208	0.000	0.001	-0.001	0.000	11.412
STRUCTURE SURGE RAO BASED VELOCITY [m/s]	0.000	1.839	-1.893	0.510	-0.104	-0.002	7.279	-8.031	1.997	0.458
STRUCTURE SWAY RAO BASED VELOCITY [m/s]	0.001	0.192	-0.364	0.025	50.791	0.000	0.010	-0.013	0.002	3.892
STRUCTURE HEAVE RAO BASED VELOCITY [m/s]	0.000	1.788	-1.558	0.440	0.024	-0.001	0.987	-0.879	0.241	0.032
STRUCTURE ROLL RAO BASED VELOCITY [°/s]	0.000	0.574	-0.999	0.061	56.472	0.000	0.000	0.000	0.000	9.323

TABLE 6.21: Motion Analysis Time History Statistics for LC1C and LC1D (contd).

Parameters	LC1C					LC1D				
	Avg.	Max	Min	Std.Dev	Kurt	Avg.	Max	Min	Std.Dev	Kurt
STRUCTURE PITCH RAO BASED VELOCITY [°/s]	0.000	4.977	-5.112	1.353	0.124	0.000	0.031	-0.032	0.009	0.067
STRUCTURE YAW RAO BASED VELOCITY [°/s]	0.000	0.329	-0.219	0.015	128.116	0.000	0.002	-0.002	0.000	9.960
STRUCTURE SURGE RAO BASED ACCELERATION [m/s^2]	0.000	0.837	-0.863	0.236	-0.053	-0.001	2.686	-2.513	0.708	0.336
STRUCTURE SWAY RAO BASED ACCELERATION [m/s^2]	0.000	0.120	-0.125	0.011	30.782	0.000	0.004	-0.006	0.001	5.671
STRUCTURE HEAVE RAO BASED ACCELERATION [m/s^2]	0.000	0.748	-0.828	0.206	0.098	0.000	0.422	-0.447	0.113	0.108
STRUCTURE ROLL RAO BASED ACCELERATION [°/s^2]	0.000	0.501	-0.613	0.043	49.947	0.000	0.000	0.000	0.000	5.715
STRUCTURE PITCH RAO BASED ACCELERATION [°/s^2]	0.000	3.285	-2.956	0.869	0.104	0.000	0.021	-0.021	0.006	-0.034
STRUCTURE YAW RAO BASED ACCELERATION [°/s^2]	0.000	0.418	-0.439	0.023	113.684	0.000	0.002	-0.002	0.000	6.838
STRUCTURE SURGE WAVE FREQ POSITION [m]	-0.001	5.894	-5.256	1.484	0.688	0.000	12.166	-11.193	3.107	-0.175
STRUCTURE SWAY WAVE FREQ POSITION [m]	0.004	6.685	-7.038	1.468	2.089	0.000	0.099	-0.093	0.017	3.094
STRUCTURE HEAVE WAVE FREQ POSITION [m]	0.000	2.698	-3.548	0.697	0.380	0.000	1.819	-2.949	0.517	0.871
STRUCTURE ROLL WAVE FREQ POSITION [°]	0.005	4.775	-4.553	0.880	2.459	0.000	0.014	-0.019	0.004	1.694
STRUCTURE PITCH WAVE FREQ POSITION [°]	0.020	7.372	-7.426	1.896	0.122	0.000	0.394	-0.192	0.037	9.107
STRUCTURE YAW WAVE FREQ POSITION [°]	-0.019	28.621	-37.055	2.849	37.841	0.000	0.177	-0.226	0.030	5.135
STRUCTURE SURGE WAVE FREQ VELOCITY [m/s]	-0.001	2.034	-2.020	0.500	0.182	0.000	5.152	-3.961	1.215	-0.180
STRUCTURE SWAY WAVE FREQ VELOCITY [m/s]	0.000	1.176	-1.109	0.269	1.675	0.000	0.034	-0.039	0.007	3.121
STRUCTURE HEAVE WAVE FREQ VELOCITY [m/s]	0.000	1.751	-1.062	0.292	1.216	0.000	1.174	-0.784	0.217	0.895
STRUCTURE ROLL WAVE FREQ VELOCITY [°/s]	0.000	1.956	-1.938	0.422	2.113	0.000	0.074	-0.068	0.017	1.725
STRUCTURE PITCH WAVE FREQ VELOCITY [°/s]	0.001	3.394	-3.693	0.938	0.209	0.000	0.802	-0.933	0.041	146.759
STRUCTURE YAW WAVE FREQ VELOCITY [°/s]	-0.002	9.338	-13.105	1.062	29.482	0.000	0.140	-0.079	0.014	6.169
STRUCTURE SURGE WAVE FREQ ACCELERATION [m/s^2]	0.001	0.870	-0.794	0.209	0.229	0.000	1.741	-2.152	0.499	-0.109
STRUCTURE SWAY WAVE FREQ ACCELERATION [m/s^2]	0.000	0.392	-0.410	0.076	2.049	0.000	0.022	-0.019	0.005	0.518
STRUCTURE HEAVE WAVE FREQ ACCELERATION [m/s^2]	0.000	1.033	-1.022	0.172	2.919	0.000	0.484	-0.653	0.123	1.127
STRUCTURE ROLL WAVE FREQ ACCELERATION [°/s^2]	-0.001	3.458	-3.744	0.527	6.542	0.000	0.333	-0.262	0.074	1.266
STRUCTURE PITCH WAVE FREQ ACCELERATION [°/s^2]	0.001	5.797	-7.051	0.786	9.274	-0.001	3.844	-2.461	0.152	166.039
STRUCTURE YAW WAVE FREQ ACCELERATION [°/s^2]	0.004	13.793	-13.448	2.074	8.495	-0.001	0.559	-0.357	0.073	3.833
STRUCTURE SURGE LOW FREQ POSITION [m]	1.814	4.748	-0.062	0.584	1.649	0.452	1.561	-0.658	0.303	0.640
STRUCTURE SWAY LOW FREQ POSITION [m]	0.179	3.537	-3.198	0.706	3.074	0.001	0.016	-0.012	0.004	1.401
STRUCTURE HEAVE LOW FREQ POSITION [m]	-0.067	0.204	-0.656	0.098	2.081	-0.245	0.313	-1.523	0.241	3.344
STRUCTURE ROLL LOW FREQ POSITION [°]	0.004	1.548	-1.464	0.258	5.031	0.000	0.000	-0.001	0.000	1.192

TABLE 6.21: Motion Analysis Time History Statistics for LC1C and LC1D (contd).

Parameters	LC1C					LC1D				
	Avg.	Max	Min	Std.Dev	Kurt	Avg.	Max	Min	Std.Dev	Kurt
STRUCTURE PITCH LOW FREQ POSITION [°]	-0.619	0.471	-2.746	0.288	4.251	-0.001	0.148	-0.271	0.017	87.691
STRUCTURE YAW LOW FREQ POSITION [°]	0.078	11.238	-8.230	0.918	44.141	-0.002	0.053	-0.060	0.015	1.578
STRUCTURE SURGE LOW FREQ VELOCITY [m/s]	0.000	0.252	-0.296	0.072	1.029	0.000	0.329	-0.361	0.094	-0.078
STRUCTURE SWAY LOW FREQ VELOCITY [m/s]	0.000	0.480	-0.517	0.099	2.832	0.000	0.003	-0.003	0.001	2.592
STRUCTURE HEAVE LOW FREQ VELOCITY [m/s]	0.000	0.066	-0.127	0.021	0.776	0.000	0.097	-0.149	0.022	3.009
STRUCTURE ROLL LOW FREQ VELOCITY [°/s]	0.001	0.198	-0.223	0.041	3.800	0.000	0.000	0.000	0.000	0.909
STRUCTURE PITCH LOW FREQ VELOCITY [°/s]	0.004	0.231	-0.204	0.055	0.233	0.000	0.023	-0.012	0.002	50.849
STRUCTURE YAW LOW FREQ VELOCITY [°/s]	-0.001	1.464	-1.496	0.126	49.020	0.000	0.009	-0.007	0.001	2.778
STRUCTURE SURGE LOW FREQ ACCELERATION [m/s^2]	0.000	0.068	-0.062	0.017	0.631	0.000	0.139	-0.125	0.035	-0.175
STRUCTURE SWAY LOW FREQ ACCELERATION [m/s^2]	0.000	0.072	-0.072	0.016	1.993	0.000	0.001	-0.001	0.000	3.120
STRUCTURE HEAVE LOW FREQ ACCELERATION [m/s^2]	0.000	0.034	-0.039	0.008	0.341	0.000	0.025	-0.030	0.006	0.674
STRUCTURE ROLL LOW FREQ ACCELERATION [°/s^2]	0.000	0.051	-0.046	0.010	1.999	0.000	0.000	0.000	0.000	1.701
STRUCTURE PITCH LOW FREQ ACCELERATION [°/s^2]	0.000	0.082	-0.084	0.021	0.118	0.000	0.004	-0.002	0.000	6.633
STRUCTURE YAW LOW FREQ ACCELERATION [°/s^2]	0.000	0.317	-0.438	0.032	40.557	0.000	0.002	-0.002	0.000	5.000
MORISON DRAG FORCE - X [N]	7.36E+05	4.20E+06	1.19E+04	3.47E+05	4.95E+00	1.00E+06	8.36E+06	-2.40E+06	1.13E+06	2.90E+00
MORISON DRAG FORCE - Y [N]	5.52E+03	8.67E+05	-9.49E+05	1.10E+05	5.83E+00	2.00E+02	3.08E+04	-2.27E+04	4.17E+03	4.59E+00
MORISON DRAG FORCE - Z [N]	-2.17E+04	5.13E+05	-1.18E+06	1.60E+05	3.22E+00	-4.21E+04	6.10E+05	-2.05E+06	2.36E+05	6.48E+00
MORISON DRAG MOMENT - X [N.m]	-1.04E+05	2.28E+07	-1.82E+07	2.25E+06	8.15E+00	-3.34E+03	4.31E+05	-5.40E+05	9.48E+04	2.39E+00
MORISON DRAG MOMENT - Y [N.m]	1.15E+07	6.79E+07	-6.68E+06	7.76E+06	2.05E+00	1.48E+07	1.16E+08	-2.56E+07	1.59E+07	3.06E+00
MORISON DRAG MOMENT - Z [N.m]	1.49E+05	1.13E+08	-6.71E+07	5.24E+06	1.05E+02	-1.64E+03	4.21E+05	-4.71E+05	5.99E+04	7.34E+00
WAVE INERTIA FORCE - X [N]	2.18E+00	5.43E+02	-5.44E+02	1.36E+02	2.62E-01	3.17E+00	5.69E+02	-4.92E+02	1.34E+02	9.91E-02
WAVE INERTIA FORCE - Y [N]	1.48E-02	4.88E+01	-6.50E+01	4.30E+00	3.67E+01	-2.24E-03	3.63E-01	-9.35E-01	5.34E-02	3.61E+01
WAVE INERTIA FORCE - Z [N]	-1.11E+01	4.43E+02	-8.02E+02	1.51E+02	2.12E-01	-8.94E+00	4.46E+02	-6.94E+02	1.54E+02	6.64E-02
WAVE INERTIA MOMENT - X [N.m]	4.65E+00	2.93E+03	-1.89E+03	2.82E+02	1.77E+01	1.19E-01	9.11E+01	-4.86E+01	3.38E+00	1.51E+02
WAVE INERTIA MOMENT - Y [N.m]	1.17E+02	5.76E+03	-6.84E+03	1.86E+03	-5.12E-02	2.07E+01	5.77E+03	-5.90E+03	1.84E+03	-1.82E-01
WAVE INERTIA MOMENT - Z [N.m]	-7.50E+00	1.49E+03	-1.86E+03	1.69E+02	2.18E+01	-1.08E-02	2.39E+01	-2.25E+01	1.79E+00	2.46E+01
FROUDE KRYLOV FORCE - X [N]	3.42E+00	8.29E+02	-8.08E+02	2.06E+02	2.41E-01	4.60E+00	8.40E+02	-7.70E+02	2.04E+02	1.19E-01
FROUDE KRYLOV FORCE - Y [N]	-1.42E-05	3.40E-02	-4.08E-02	1.92E-03	1.53E+02	-4.10E-08	6.54E-05	-7.96E-05	3.56E-06	1.18E+02
FROUDE KRYLOV FORCE - Z [N]	-1.42E+01	5.63E+02	-1.02E+03	1.97E+02	1.77E-01	-1.23E+01	5.67E+02	-9.11E+02	2.00E+02	9.08E-02
FROUDE KRYLOV MOMENT - X [N.m]	5.72E+00	2.97E+03	-1.96E+03	2.57E+02	2.21E+01	6.67E-02	1.35E+02	-5.02E+01	3.22E+00	7.31E+02
FROUDE KRYLOV MOMENT - Y [N.m]	1.48E+02	8.87E+03	-1.03E+04	2.47E+03	1.65E-01	4.69E+01	9.28E+03	-7.82E+03	2.46E+03	-6.58E-02

TABLE 6.21: Motion Analysis Time History Statistics for LC1C and LC1D (contd).

Parameters	LC1C					LC1D				
	Avg.	Max	Min	Std.Dev	Kurt	Avg.	Max	Min	Std.Dev	Kurt
FROUDE KRYLOV MOMENT - Z [N.m]	-1.05E+01	1.77E+03	-2.24E+03	1.97E+02	2.76E+01	-7.40E-03	3.84E+01	-2.25E+01	1.86E+00	5.16E+01
DIFFRACTION FORCE - X [N]	-1.11E+03	1.51E+07	-1.47E+07	3.73E+06	1.08E-01	-6.87E+03	1.50E+07	-1.46E+07	3.73E+06	1.08E-01
DIFFRACTION FORCE - Y [N]	9.09E+03	2.10E+06	-1.64E+06	1.68E+05	3.26E+01	1.93E+02	2.88E+04	-2.56E+04	2.59E+03	1.93E+01
DIFFRACTION FORCE - Z [N]	-1.33E+04	3.80E+07	-4.39E+07	1.01E+07	-1.99E-02	-1.01E+04	3.77E+07	-4.39E+07	1.01E+07	-2.09E-02
DIFFRACTION MOMENT - X [N.m]	-2.39E+05	4.29E+07	-5.75E+07	4.39E+06	3.36E+01	-5.42E+03	6.45E+05	-7.66E+05	6.78E+04	1.91E+01
DIFFRACTION MOMENT - Y [N.m]	-2.58E+04	3.95E+08	-3.85E+08	9.87E+07	9.69E-02	-1.80E+05	3.91E+08	-3.81E+08	9.89E+07	9.64E-02
DIFFRACTION MOMENT - Z [N.m]	9.49E+02	9.58E+06	-1.50E+07	5.53E+05	1.74E+02	4.05E+00	6.54E+04	-8.62E+04	8.73E+03	1.22E+01
RADIATION FORCE - X [N]	7.70E+03	8.48E+06	-8.27E+06	1.80E+06	8.29E-01	2.24E+03	1.90E+07	-1.39E+07	4.34E+06	-5.71E-02
RADIATION FORCE - Y [N]	5.00E+03	5.16E+06	-6.42E+06	1.04E+06	3.44E+00	-3.91E+02	1.65E+05	-1.63E+05	4.22E+04	4.71E-01
RADIATION FORCE - Z [N]	2.13E+03	1.37E+07	-9.38E+06	1.52E+06	5.69E+00	-3.73E+02	4.66E+06	-4.97E+06	1.14E+06	6.51E-01
RADIATION MOMENT - X [N.m]	-1.54E+05	2.17E+08	-1.80E+08	3.57E+07	3.78E+00	1.57E+04	1.05E+07	-1.28E+07	2.87E+06	1.47E+00
RADIATION MOMENT - Y [N.m]	1.85E+05	2.94E+08	-3.38E+08	4.28E+07	5.43E+00	6.55E+04	3.12E+08	-2.09E+08	6.94E+07	-1.74E-02
RADIATION MOMENT - Z [N.m]	3.50E+04	2.19E+08	-2.09E+08	3.88E+07	3.80E+00	-1.68E+04	6.71E+06	-5.23E+06	9.93E+05	3.58E+00
TOTAL FORCE - X [N]	-6.77E+03	8.78E+06	-8.00E+06	2.06E+06	3.83E-01	-1.82E+03	1.77E+07	-2.19E+07	5.07E+06	-9.80E-02
TOTAL FORCE - Y [N]	1.80E+02	2.79E+06	-2.16E+06	5.33E+05	1.61E+00	1.44E+02	2.41E+05	-1.95E+05	5.68E+04	6.17E-01
TOTAL FORCE - Z [N]	-1.84E+02	1.10E+07	-1.14E+07	1.58E+06	4.87E+00	3.14E+02	5.13E+06	-6.83E+06	1.28E+06	1.13E+00
TOTAL MOMENT - X [N.m]	2.35E+05	3.26E+08	-3.90E+08	6.49E+07	3.58E+00	-4.76E+04	5.01E+07	-4.07E+07	1.09E+07	1.64E+00
TOTAL MOMENT - Y [N.m]	-5.84E+05	7.86E+08	-6.69E+08	9.12E+07	7.13E+00	-1.63E+05	7.31E+08	-3.77E+08	2.54E+07	2.45E+02
TOTAL MOMENT - Z [N.m]	1.23E+05	1.07E+08	-1.15E+08	1.89E+07	3.95E+00	1.45E+04	4.70E+06	-4.83E+06	7.78E+05	3.87E+00
STRUCTURE CURRENT DRAG FORCE - X [N]	6.52E+05	2.82E+06	1.39E+03	3.53E+05	7.18E-01	9.15E+05	6.82E+06	5.36E+00	9.32E+05	2.46E+00
STRUCTURE WIND FORCE - X [N]	6.10E+04	1.24E+05	1.73E+04	1.59E+04	-3.23E-02	6.12E+04	1.25E+05	8.61E+03	1.75E+04	4.62E-02
ROTOR THRUST FORCE [N]	4.17E+05	9.93E+05	6.35E+04	1.32E+05	2.68E-01	4.15E+05	8.43E+05	5.96E+04	1.18E+05	4.44E-02
MOORING CABLE 1 TENSION [N]	3.66E+06	1.46E+07	0.00E+00	2.35E+06	1.03E-01	3.66E+06	1.46E+07	0.00E+00	2.35E+06	1.03E-01
MOORING CABLE 2 TENSION [N]	6.18E+05	7.13E+06	0.00E+00	8.34E+05	7.01E+00	6.18E+05	7.13E+06	0.00E+00	8.34E+05	7.01E+00
MOORING CABLE 3 TENSION [N]	5.86E+05	7.79E+06	0.00E+00	8.99E+05	5.94E+00	5.86E+05	7.79E+06	0.00E+00	8.99E+05	5.94E+00
MOORING CABLE 4 TENSION [N]	2.48E+06	1.07E+07	0.00E+00	2.06E+06	-2.51E-01	2.48E+06	1.07E+07	0.00E+00	2.06E+06	-2.51E-01

TABLE 6.22: Motion Analysis Time History Statistics for LC2A and LC2B.

Parameters	LC2A					LC2B				
	Avg.	Max	Min	Std.Dev	Kurt	Avg.	Max	Min	Std.Dev	Kurt
WAVE SURFACE ELEVATION [m]	-0.001	6.864	-6.804	1.824	-0.002	-0.001	6.864	-6.804	1.824	-0.002
WAVE VELOCITY [m/s]	0.020	3.000	-2.194	0.664	0.152	0.020	3.000	-2.194	0.664	0.152
WAVE ACCELERATION [m/s^2]	0.000	1.445	-1.276	0.380	-0.076	0.000	1.445	-1.276	0.380	-0.076
STRUCTURE SURGE POSITION [m]	1.864	12.384	-7.519	2.478	0.298	0.023	12.712	-13.133	3.923	-0.152
STRUCTURE SWAY POSITION [m]	0.013	9.167	-8.947	1.657	5.859	0.012	0.511	-0.228	0.039	19.672
STRUCTURE HEAVE POSITION [m]	-0.096	4.369	-6.557	1.281	0.642	-0.574	2.157	-10.325	1.487	3.734
STRUCTURE ROLL POSITION [°]	0.000	5.593	-3.915	0.665	8.414	0.000	0.014	-0.006	0.001	34.814
STRUCTURE PITCH POSITION [°]	-0.900	9.804	-11.496	2.636	0.185	0.021	0.337	-0.126	0.049	2.313
STRUCTURE YAW POSITION [°]	-0.001	2.917	-2.811	0.365	10.697	-0.106	0.456	-2.675	0.212	17.553
STRUCTURE SURGE VELOCITY [m/s]	0.000	3.584	-2.432	0.748	0.247	0.001	4.783	-3.808	1.345	-0.254
STRUCTURE SWAY VELOCITY [m/s]	0.000	1.434	-1.656	0.281	6.471	0.000	0.093	-0.121	0.011	13.426
STRUCTURE HEAVE VELOCITY [m/s]	0.000	3.309	-2.341	0.591	0.719	0.000	2.505	-2.213	0.430	1.133
STRUCTURE ROLL VELOCITY [°/s]	0.000	2.298	-2.034	0.285	6.218	0.000	0.016	-0.015	0.002	5.688
STRUCTURE PITCH VELOCITY [°/s]	0.000	4.309	-5.639	1.348	0.263	0.000	0.161	-0.248	0.033	1.283
STRUCTURE YAW VELOCITY [°/s]	0.000	0.848	-0.863	0.101	13.021	0.000	0.496	-0.187	0.038	18.655
STRUCTURE SURGE ACCELERATION [m/s^2]	0.000	1.052	-1.199	0.264	0.308	0.000	1.755	-1.935	0.499	0.065
STRUCTURE SWAY ACCELERATION [m/s^2]	0.000	0.381	-0.407	0.056	6.447	0.000	0.044	-0.034	0.004	14.352
STRUCTURE HEAVE ACCELERATION [m/s^2]	0.000	1.821	-2.554	0.454	0.242	0.000	1.630	-1.587	0.365	0.714
STRUCTURE ROLL ACCELERATION [°/s^2]	0.000	1.140	-1.254	0.183	5.396	0.000	0.068	-0.065	0.009	5.609
STRUCTURE PITCH ACCELERATION [°/s^2]	0.000	2.755	-3.721	0.841	0.448	0.000	1.053	-0.920	0.130	1.431
STRUCTURE YAW ACCELERATION [°/s^2]	0.000	0.439	-0.379	0.044	16.207	0.000	0.262	-0.122	0.015	37.272
STRUCTURE SURGE RAO BASED POSITION [m]	0.002	7.206	-7.135	1.926	-0.006	0.034	43.981	-43.912	14.236	-0.333
STRUCTURE SWAY RAO BASED POSITION [m]	0.000	0.234	-0.226	0.019	33.808	0.009	1.205	-1.256	0.093	32.763
STRUCTURE HEAVE RAO BASED POSITION [m]	-0.003	6.952	-6.406	1.791	-0.010	0.000	3.732	-3.441	0.972	-0.011
STRUCTURE ROLL RAO BASED POSITION [°]	0.000	0.247	-0.389	0.025	30.091	0.000	0.003	-0.003	0.000	33.701
STRUCTURE PITCH RAO BASED POSITION [°]	-0.002	9.768	-10.307	2.806	-0.089	0.000	0.123	-0.130	0.040	-0.225
STRUCTURE YAW RAO BASED POSITION [°]	0.000	0.052	-0.048	0.003	25.958	0.000	0.037	-0.036	0.002	31.297
STRUCTURE SURGE RAO BASED VELOCITY [m/s]	-0.001	2.460	-2.344	0.659	-0.011	0.001	14.166	-14.113	4.570	-0.332
STRUCTURE SWAY RAO BASED VELOCITY [m/s]	0.000	0.074	-0.074	0.006	28.314	-0.004	0.306	-0.404	0.030	31.955
STRUCTURE HEAVE RAO BASED VELOCITY [m/s]	0.000	2.421	-2.038	0.633	0.004	-0.001	1.275	-1.083	0.331	-0.010
STRUCTURE ROLL RAO BASED VELOCITY [°/s]	0.000	0.138	-0.195	0.015	23.726	0.000	0.001	-0.001	0.000	32.766
STRUCTURE PITCH RAO BASED VELOCITY [°/s]	0.000	6.363	-6.231	1.688	-0.157	0.000	0.046	-0.049	0.014	-0.210
STRUCTURE YAW RAO BASED VELOCITY [°/s]	0.000	0.045	-0.034	0.004	18.462	0.000	0.046	-0.034	0.003	25.302
STRUCTURE SURGE RAO BASED ACCELERATION [m/s^2]	0.000	0.880	-0.875	0.258	-0.031	-0.004	4.781	-4.577	1.483	-0.315
STRUCTURE SWAY RAO BASED ACCELERATION [m/s^2]	0.000	0.038	-0.027	0.002	36.561	-0.001	0.142	-0.126	0.010	35.417

TABLE 6.22: Motion Analysis Time History Statistics for LC2A and LC2B (contd).

Parameters	LC2A					LC2B				
	Avg.	Max	Min	Std.Dev	Kurt	Avg.	Max	Min	Std.Dev	Kurt
STRUCTURE HEAVE RAO BASED ACCELERATION [m/s^2]	0.000	0.932	-0.926	0.268	0.005	0.000	0.479	-0.461	0.132	0.013
STRUCTURE ROLL RAO BASED ACCELERATION [°/s^2]	0.000	0.120	-0.104	0.010	23.159	0.000	0.001	-0.001	0.000	34.358
STRUCTURE PITCH RAO BASED ACCELERATION [°/s^2]	0.000	3.969	-4.173	1.117	-0.194	0.000	0.025	-0.025	0.007	-0.117
STRUCTURE YAW RAO BASED ACCELERATION [°/s^2]	0.000	0.047	-0.051	0.005	13.709	0.000	0.054	-0.053	0.005	19.213
STRUCTURE SURGE WAVE FREQ POSITION [m]	-0.001	12.110	-11.012	2.755	0.366	-0.002	15.544	-12.262	4.201	-0.081
STRUCTURE SWAY WAVE FREQ POSITION [m]	-0.001	12.348	-12.454	2.240	6.061	0.000	0.258	-0.536	0.040	19.929
STRUCTURE HEAVE WAVE FREQ POSITION [m]	0.000	5.045	-6.689	1.371	0.516	0.000	6.951	-6.933	1.373	1.618
STRUCTURE ROLL WAVE FREQ POSITION [°]	0.000	6.757	-4.733	0.787	7.915	0.000	0.015	-0.020	0.002	19.313
STRUCTURE PITCH WAVE FREQ POSITION [°]	0.001	11.426	-10.880	2.768	0.167	0.000	0.208	-0.238	0.046	1.120
STRUCTURE YAW WAVE FREQ POSITION [°]	-0.001	3.401	-3.777	0.497	9.212	0.000	1.872	-1.607	0.280	6.940
STRUCTURE SURGE WAVE FREQ VELOCITY [m/s]	0.000	3.879	-2.597	0.812	0.290	0.001	5.029	-4.097	1.431	-0.245
STRUCTURE SWAY WAVE FREQ VELOCITY [m/s]	0.000	2.020	-2.170	0.371	6.722	0.000	0.102	-0.129	0.011	13.617
STRUCTURE HEAVE WAVE FREQ VELOCITY [m/s]	0.000	3.433	-2.390	0.612	0.755	0.000	2.602	-2.227	0.451	1.119
STRUCTURE ROLL WAVE FREQ VELOCITY [°/s]	0.000	2.307	-2.218	0.298	6.411	0.000	0.017	-0.014	0.002	5.725
STRUCTURE PITCH WAVE FREQ VELOCITY [°/s]	0.000	4.357	-5.858	1.386	0.268	0.000	0.163	-0.248	0.034	1.270
STRUCTURE YAW WAVE FREQ VELOCITY [°/s]	0.000	0.920	-1.011	0.114	12.786	0.000	0.611	-0.241	0.046	19.765
STRUCTURE SURGE WAVE FREQ ACCELERATION [m/s^2]	0.000	1.125	-1.281	0.280	0.317	0.000	1.837	-2.035	0.526	0.057
STRUCTURE SWAY WAVE FREQ ACCELERATION [m/s^2]	0.000	0.450	-0.465	0.069	5.838	0.000	0.048	-0.036	0.004	14.699
STRUCTURE HEAVE WAVE FREQ ACCELERATION [m/s^2]	0.000	1.866	-2.580	0.459	0.248	0.000	1.662	-1.602	0.368	0.728
STRUCTURE ROLL WAVE FREQ ACCELERATION [°/s^2]	0.000	1.142	-1.299	0.186	5.442	0.000	0.068	-0.065	0.009	5.607
STRUCTURE PITCH WAVE FREQ ACCELERATION [°/s^2]	0.000	2.819	-3.773	0.857	0.447	0.000	0.690	-0.930	0.130	1.083
STRUCTURE YAW WAVE FREQ ACCELERATION [°/s^2]	0.000	0.450	-0.390	0.046	15.927	0.000	0.270	-0.131	0.016	34.259
STRUCTURE SURGE LOW FREQ POSITION [m]	1.865	5.024	-0.464	0.670	1.312	0.025	1.744	-3.130	0.623	1.328
STRUCTURE SWAY LOW FREQ POSITION [m]	0.014	4.532	-4.618	0.706	8.030	0.012	0.309	-0.111	0.029	20.814
STRUCTURE HEAVE LOW FREQ POSITION [m]	-0.179	0.260	-1.048	0.175	1.065	-0.630	3.019	-8.520	1.438	2.589
STRUCTURE ROLL LOW FREQ POSITION [°]	0.000	0.893	-1.119	0.165	7.605	0.000	0.016	-0.012	0.002	20.896
STRUCTURE PITCH LOW FREQ POSITION [°]	-0.901	-0.327	-1.904	0.210	0.428	0.021	0.278	-0.104	0.047	2.589
STRUCTURE YAW LOW FREQ POSITION [°]	0.001	1.339	-1.324	0.243	4.973	-0.107	0.988	-2.057	0.249	9.087
STRUCTURE SURGE LOW FREQ VELOCITY [m/s]	0.000	0.288	-0.352	0.082	0.662	0.000	0.326	-0.335	0.097	0.198
STRUCTURE SWAY LOW FREQ VELOCITY [m/s]	0.000	0.514	-0.624	0.099	6.864	0.000	0.010	-0.017	0.002	13.727
STRUCTURE HEAVE LOW FREQ VELOCITY [m/s]	0.000	0.095	-0.147	0.031	0.497	0.000	0.399	-0.323	0.079	1.790
STRUCTURE ROLL LOW FREQ VELOCITY [°/s]	0.000	0.188	-0.164	0.027	7.528	0.000	0.001	-0.001	0.000	21.428
STRUCTURE PITCH LOW FREQ VELOCITY [°/s]	0.000	0.219	-0.187	0.052	0.050	0.000	0.011	-0.014	0.003	1.771
STRUCTURE YAW LOW FREQ VELOCITY [°/s]	0.000	0.156	-0.173	0.024	6.053	0.000	0.136	-0.115	0.018	7.372
STRUCTURE SURGE LOW FREQ ACCELERATION [m/s^2]	0.000	0.087	-0.075	0.019	0.363	0.000	0.110	-0.085	0.030	-0.071

TABLE 6.22: Motion Analysis Time History Statistics for LC2A and LC2B (contd).

Parameters	LC2A					LC2B				
	Avg.	Max	Min	Std.Dev	Kurt	Avg.	Max	Min	Std.Dev	Kurt
STRUCTURE SWAY LOW FREQ ACCELERATION [m/s^2]	0.000	0.084	-0.082	0.016	5.968	0.000	0.002	-0.004	0.000	19.330
STRUCTURE HEAVE LOW FREQ ACCELERATION [m/s^2]	0.000	0.035	-0.046	0.010	0.398	0.000	0.050	-0.045	0.009	1.328
STRUCTURE ROLL LOW FREQ ACCELERATION [°/s^2]	0.000	0.046	-0.033	0.006	6.788	0.000	0.000	0.000	0.000	18.542
STRUCTURE PITCH LOW FREQ ACCELERATION [°/s^2]	0.000	0.078	-0.078	0.020	0.152	0.000	0.001	-0.002	0.000	0.911
STRUCTURE YAW LOW FREQ ACCELERATION [°/s^2]	0.000	0.024	-0.024	0.003	9.194	0.000	0.014	-0.009	0.002	7.301
MORISON DRAG FORCE - X [N]	7.81E+05	3.44E+06	-1.42E+05	4.53E+05	1.29E+00	1.26E+06	1.26E+07	-4.19E+06	1.80E+06	3.28E+00
MORISON DRAG FORCE - Y [N]	1.12E+03	1.22E+06	-1.01E+06	1.65E+05	1.14E+01	5.09E+02	2.33E+05	-1.20E+05	1.10E+04	7.56E+01
MORISON DRAG FORCE - Z [N]	-2.02E+04	3.02E+06	-2.21E+06	3.70E+05	3.52E+00	-4.20E+04	2.25E+06	-3.51E+06	4.08E+05	7.58E+00
MORISON DRAG MOMENT - X [N.m]	-2.55E+04	1.50E+07	-1.90E+07	2.24E+06	1.12E+01	-5.11E+03	1.69E+06	-2.79E+06	1.44E+05	6.32E+01
MORISON DRAG MOMENT - Y [N.m]	1.21E+07	7.53E+07	-1.77E+07	1.03E+07	1.61E+00	1.87E+07	1.93E+08	-4.71E+07	2.49E+07	3.93E+00
MORISON DRAG MOMENT - Z [N.m]	3.80E+03	6.99E+06	-7.91E+06	6.35E+05	2.15E+01	-5.12E+04	1.06E+06	-6.57E+06	3.08E+05	7.01E+01
WAVE INERTIA FORCE - X [N]	3.39E+00	5.09E+02	-5.63E+02	1.43E+02	1.74E-01	3.67E+00	5.28E+02	-4.53E+02	1.42E+02	-4.70E-02
WAVE INERTIA FORCE - Y [N]	3.31E-04	2.64E+01	-2.79E+01	1.72E+00	3.91E+01	-1.23E-02	3.09E+00	-3.85E+00	3.07E-01	2.45E+01
WAVE INERTIA FORCE - Z [N]	-1.52E+01	5.30E+02	-6.83E+02	1.64E+02	2.64E-01	-6.51E+00	5.78E+02	-5.76E+02	1.65E+02	-8.48E-02
WAVE INERTIA MOMENT - X [N.m]	-2.49E+00	1.88E+03	-1.98E+03	1.50E+02	5.19E+01	2.43E-01	1.38E+02	-1.19E+02	1.18E+01	2.23E+01
WAVE INERTIA MOMENT - Y [N.m]	1.07E+02	8.33E+03	-6.99E+03	1.54E+03	2.90E-01	3.51E+01	5.28E+03	-5.69E+03	1.48E+03	-1.79E-01
WAVE INERTIA MOMENT - Z [N.m]	-2.53E+00	1.21E+03	-2.22E+03	9.98E+01	1.15E+02	7.14E-02	6.61E+01	-7.78E+01	6.95E+00	1.97E+01
FROUDE KRYLOV FORCE - X [N]	5.20E+00	7.99E+02	-7.96E+02	2.23E+02	1.28E-01	5.40E+00	7.92E+02	-6.93E+02	2.21E+02	-7.02E-02
FROUDE KRYLOV FORCE - Y [N]	-6.13E-06	2.49E-02	-1.98E-02	1.12E-03	1.06E+02	2.01E-08	5.25E-05	-5.17E-05	5.57E-06	1.98E+01
FROUDE KRYLOV FORCE - Z [N]	-1.92E+01	6.97E+02	-8.56E+02	2.14E+02	1.94E-01	-9.99E+00	7.50E+02	-8.15E+02	2.18E+02	5.13E-03
FROUDE KRYLOV MOMENT - X [N.m]	-2.39E+00	1.82E+03	-1.98E+03	1.56E+02	5.31E+01	2.35E-02	7.66E+01	-6.93E+01	6.95E+00	2.02E+01
FROUDE KRYLOV MOMENT - Y [N.m]	1.42E+02	9.90E+03	-1.11E+04	2.53E+03	2.48E-01	6.65E+01	9.27E+03	-8.53E+03	2.51E+03	-1.61E-02
FROUDE KRYLOV MOMENT - Z [N.m]	-3.66E+00	1.92E+03	-2.68E+03	1.35E+02	1.10E+02	7.51E-02	6.62E+01	-7.76E+01	6.97E+00	1.97E+01
DIFFRACTION FORCE - X [N]	-2.75E+03	1.58E+07	-1.35E+07	4.24E+06	8.29E-03	-7.63E+03	1.58E+07	-1.32E+07	4.24E+06	6.98E-03
DIFFRACTION FORCE - Y [N]	-4.03E+02	3.90E+05	-5.53E+05	3.85E+04	3.40E+01	-3.12E+03	4.40E+05	-3.76E+05	2.75E+04	4.08E+01
DIFFRACTION FORCE - Z [N]	-3.03E+04	6.91E+07	-6.41E+07	1.79E+07	-8.58E-03	4.18E+03	6.89E+07	-6.42E+07	1.79E+07	-8.30E-03
DIFFRACTION MOMENT - X [N.m]	1.10E+04	1.47E+07	-1.06E+07	1.03E+06	3.47E+01	8.18E+04	1.00E+07	-1.11E+07	7.26E+05	4.00E+01
DIFFRACTION MOMENT - Y [N.m]	-6.70E+04	4.18E+08	-3.57E+08	1.13E+08	9.32E-03	-2.03E+05	4.18E+08	-3.61E+08	1.13E+08	8.23E-03
DIFFRACTION MOMENT - Z [N.m]	3.74E+01	1.54E+06	-1.63E+06	1.29E+05	1.89E+01	-6.14E+01	1.84E+06	-2.56E+06	1.46E+05	3.16E+01
RADIATION FORCE - X [N]	-2.11E+02	7.09E+06	-9.60E+06	2.19E+06	3.46E-01	5.88E+02	1.82E+07	-1.47E+07	4.57E+06	7.63E-02
RADIATION FORCE - Y [N]	3.04E+01	3.52E+06	-4.02E+06	5.28E+05	6.37E+00	-2.09E+02	3.49E+05	-3.69E+05	3.44E+04	1.38E+01
RADIATION FORCE - Z [N]	-2.35E+02	1.94E+07	-1.71E+07	3.75E+06	3.49E-01	-4.16E+02	1.51E+07	-1.46E+07	3.17E+06	7.09E-01
RADIATION MOMENT - X [N.m]	-1.94E+03	1.05E+08	-9.73E+07	1.38E+07	5.25E+00	4.32E+03	6.16E+06	-5.91E+06	6.52E+05	1.04E+01
RADIATION MOMENT - Y [N.m]	-1.14E+04	2.07E+08	-2.06E+08	5.65E+07	9.40E-02	1.19E+04	2.89E+08	-2.39E+08	7.22E+07	1.23E-01
RADIATION MOMENT - Z [N.m]	3.16E+02	9.11E+06	-1.09E+07	1.09E+06	1.68E+01	2.54E+02	4.43E+06	-6.64E+06	3.63E+05	4.05E+01
TOTAL FORCE - X [N]	-3.94E+02	1.15E+07	-1.31E+07	2.88E+06	3.08E-01	-4.92E+02	1.91E+07	-2.11E+07	5.44E+06	6.50E-02

TABLE 6.22: Motion Analysis Time History Statistics for LC2A and LC2B (contd).

Parameters	LC2A					LC2B				
	Avg.	Max	Min	Std.Dev	Kurt	Avg.	Max	Min	Std.Dev	Kurt
TOTAL FORCE - Y [N]	9.35E+01	4.16E+06	-4.43E+06	6.05E+05	6.45E+00	-2.32E+01	4.84E+05	-3.74E+05	4.21E+04	1.44E+01
TOTAL FORCE - Z [N]	4.30E+02	1.98E+07	-2.78E+07	4.94E+06	2.42E-01	5.34E+02	1.78E+07	-1.73E+07	3.97E+06	7.14E-01
TOTAL MOMENT - X [N.m]	-1.01E+03	1.76E+08	-1.94E+08	2.79E+07	5.42E+00	4.57E+03	1.03E+07	-9.91E+06	1.43E+06	5.60E+00
TOTAL MOMENT - Y [N.m]	3.60E+04	4.22E+08	-5.70E+08	1.29E+08	4.48E-01	-9.10E+03	1.61E+08	-1.41E+08	1.99E+07	1.43E+00
TOTAL MOMENT - Z [N.m]	2.24E+01	9.82E+06	-1.50E+07	1.17E+06	1.85E+01	-1.51E+00	3.41E+06	-1.60E+06	1.94E+05	3.73E+01
STRUCTURE CURRENT DRAG FORCE - X [N]	7.54E+05	4.00E+06	2.68E-01	5.80E+05	1.35E+00	1.05E+06	7.28E+06	4.34E-01	1.13E+06	2.24E+00
STRUCTURE WIND FORCE - X [N]	1.20E+05	2.76E+05	2.67E+04	3.44E+04	1.20E-01	1.20E+05	2.71E+05	2.34E+04	3.60E+04	8.36E-03
MOORING CABLE 1 TENSION [N]	3.78E+06	1.88E+07	0.00E+00	3.33E+06	3.92E-02	2.88E+06	2.03E+07	0.00E+00	4.01E+06	1.04E+00
MOORING CABLE 2 TENSION [N]	1.18E+06	1.18E+07	0.00E+00	1.50E+06	2.41E+00	6.78E+05	7.39E+06	0.00E+00	1.13E+06	2.66E+00
MOORING CABLE 3 TENSION [N]	1.18E+06	9.14E+06	0.00E+00	1.51E+06	1.87E+00	6.77E+05	7.38E+06	0.00E+00	1.13E+06	2.72E+00
MOORING CABLE 4 TENSION [N]	3.29E+06	2.08E+07	0.00E+00	3.43E+06	4.06E-01	9.02E+05	8.34E+06	0.00E+00	1.37E+06	2.34E+00

TABLE 6.23: Motion Analysis Time History Statistics for LC2C and LC2D.

Parameters	LC2C					LC2D				
	Avg.	Max	Min	Std.Dev	Kurt	Avg.	Max	Min	Std.Dev	Kurt
WAVE SURFACE ELEVATION [m]	-0.001	6.864	-6.804	1.824	-0.002	-0.001	6.864	-6.804	1.824	-0.002
WAVE VELOCITY [m/s]	0.020	3.000	-2.194	0.664	0.152	0.020	3.000	-2.194	0.664	0.152
WAVE ACCELERATION [m/s^2]	0.000	1.445	-1.276	0.380	-0.076	0.000	1.445	-1.276	0.380	-0.076
STRUCTURE SURGE POSITION [m]	1.736	12.116	-7.571	2.483	0.261	0.020	13.062	-13.289	3.930	-0.128
STRUCTURE SWAY POSITION [m]	-0.001	6.836	-6.955	0.715	26.372	0.014	0.591	-0.257	0.045	19.216
STRUCTURE HEAVE POSITION [m]	-0.009	3.742	-5.123	1.158	0.513	-0.561	2.153	-9.674	1.465	3.713
STRUCTURE ROLL POSITION [°]	0.000	3.138	-3.471	0.290	27.805	0.000	0.016	-0.008	0.001	41.847
STRUCTURE PITCH POSITION [°]	-0.946	7.537	-11.060	2.442	0.179	0.021	0.336	-0.130	0.049	2.378
STRUCTURE YAW POSITION [°]	-0.001	2.480	-3.146	0.216	41.012	-0.129	0.504	-3.148	0.256	16.353
STRUCTURE SURGE VELOCITY [m/s]	0.000	3.278	-2.344	0.747	0.154	0.001	4.772	-3.820	1.347	-0.247
STRUCTURE SWAY VELOCITY [m/s]	0.000	1.304	-1.178	0.123	27.588	0.000	0.107	-0.140	0.012	13.035
STRUCTURE HEAVE VELOCITY [m/s]	0.000	2.138	-1.171	0.401	1.155	0.000	1.719	-1.676	0.349	1.130
STRUCTURE ROLL VELOCITY [°/s]	0.000	1.078	-1.198	0.117	20.553	0.000	0.012	-0.010	0.001	7.166
STRUCTURE PITCH VELOCITY [°/s]	0.000	3.599	-4.994	1.168	0.404	0.000	0.128	-0.239	0.025	2.431
STRUCTURE YAW VELOCITY [°/s]	0.000	1.011	-0.615	0.053	71.444	0.000	0.583	-0.223	0.046	17.175
STRUCTURE SURGE ACCELERATION [m/s^2]	0.000	1.002	-1.147	0.259	0.348	0.000	1.720	-2.023	0.499	0.105
STRUCTURE SWAY ACCELERATION [m/s^2]	0.000	0.266	-0.213	0.024	22.740	0.000	0.047	-0.039	0.005	13.412
STRUCTURE HEAVE ACCELERATION [m/s^2]	0.000	0.905	-1.019	0.179	1.739	0.000	1.022	-1.076	0.231	0.593
STRUCTURE ROLL ACCELERATION [°/s^2]	0.000	0.663	-0.706	0.072	17.982	0.000	0.049	-0.049	0.007	7.078
STRUCTURE PITCH ACCELERATION [°/s^2]	0.000	2.428	-3.297	0.695	0.564	0.000	1.048	-0.853	0.087	4.006
STRUCTURE YAW ACCELERATION [°/s^2]	0.000	0.343	-0.300	0.021	64.923	0.000	0.289	-0.154	0.018	32.640
STRUCTURE SURGE RAO BASED POSITION [m]	0.002	6.928	-7.377	1.927	-0.003	0.034	43.957	-43.905	14.236	-0.333
STRUCTURE SWAY RAO BASED POSITION [m]	0.000	0.225	-0.155	0.011	112.174	0.011	1.439	-1.455	0.112	30.861
STRUCTURE HEAVE RAO BASED POSITION [m]	-0.002	6.681	-5.972	1.710	-0.013	0.000	3.686	-3.373	0.960	-0.011
STRUCTURE ROLL RAO BASED POSITION [°]	0.000	0.268	-0.208	0.013	82.268	0.000	0.004	-0.004	0.000	31.891
STRUCTURE PITCH RAO BASED POSITION [°]	-0.002	8.005	-8.726	2.363	-0.014	0.000	0.123	-0.130	0.040	-0.225
STRUCTURE YAW RAO BASED POSITION [°]	0.000	0.040	-0.025	0.002	45.134	0.000	0.043	-0.042	0.003	30.118
STRUCTURE SURGE RAO BASED VELOCITY [m/s]	-0.001	2.489	-2.382	0.663	0.006	0.001	14.158	-14.115	4.570	-0.332
STRUCTURE SWAY RAO BASED VELOCITY [m/s]	0.000	0.055	-0.047	0.003	63.888	-0.005	0.355	-0.466	0.036	30.177
STRUCTURE HEAVE RAO BASED VELOCITY [m/s]	-0.001	2.216	-1.857	0.582	-0.007	-0.001	1.270	-1.054	0.324	-0.012
STRUCTURE ROLL RAO BASED VELOCITY [°/s]	0.000	0.092	-0.091	0.007	40.661	0.000	0.001	-0.001	0.000	31.572
STRUCTURE PITCH RAO BASED VELOCITY [°/s]	0.000	4.851	-4.364	1.317	-0.086	0.000	0.046	-0.049	0.014	-0.210
STRUCTURE YAW RAO BASED VELOCITY [°/s]	0.000	0.040	-0.028	0.002	47.562	0.000	0.054	-0.041	0.004	24.405
STRUCTURE SURGE RAO BASED ACCELERATION [m/s^2]	0.000	0.941	-0.900	0.262	0.012	-0.004	4.778	-4.577	1.483	-0.315
STRUCTURE SWAY RAO BASED ACCELERATION [m/s^2]	0.000	0.027	-0.027	0.001	95.404	-0.001	0.165	-0.151	0.012	33.256

TABLE 6.23: Motion Analysis Time History Statistics for LC2C and LC2D (contd).

Parameters	LC2C					LC2D				
	Avg.	Max	Min	Std.Dev	Kurt	Avg.	Max	Min	Std.Dev	Kurt
STRUCTURE HEAVE RAO BASED ACCELERATION [m/s^2]	0.000	0.816	-0.801	0.230	0.016	0.000	0.451	-0.437	0.127	0.010
STRUCTURE ROLL RAO BASED ACCELERATION [°/s^2]	0.000	0.058	-0.061	0.004	46.284	0.000	0.001	-0.001	0.000	31.833
STRUCTURE PITCH RAO BASED ACCELERATION [°/s^2]	0.000	3.009	-3.123	0.827	-0.131	0.000	0.025	-0.025	0.007	-0.117
STRUCTURE YAW RAO BASED ACCELERATION [°/s^2]	0.000	0.040	-0.049	0.003	44.148	0.000	0.064	-0.063	0.006	18.534
STRUCTURE SURGE WAVE FREQ POSITION [m]	-0.001	11.883	-11.599	2.802	0.362	-0.002	15.885	-12.423	4.208	-0.054
STRUCTURE SWAY WAVE FREQ POSITION [m]	-0.001	8.961	-8.555	0.957	25.693	0.000	0.303	-0.612	0.047	18.945
STRUCTURE HEAVE WAVE FREQ POSITION [m]	0.000	4.456	-5.344	1.250	0.389	0.000	6.743	-6.486	1.348	1.576
STRUCTURE ROLL WAVE FREQ POSITION [°]	0.000	3.494	-4.021	0.344	26.676	0.000	0.016	-0.020	0.002	19.194
STRUCTURE PITCH WAVE FREQ POSITION [°]	0.000	9.168	-10.224	2.580	0.117	0.000	0.214	-0.231	0.046	1.167
STRUCTURE YAW WAVE FREQ POSITION [°]	-0.002	4.020	-2.957	0.300	33.758	0.000	2.173	-1.937	0.339	6.677
STRUCTURE SURGE WAVE FREQ VELOCITY [m/s]	-0.001	3.495	-2.658	0.812	0.204	0.001	5.079	-4.101	1.432	-0.236
STRUCTURE SWAY WAVE FREQ VELOCITY [m/s]	0.000	1.639	-1.573	0.160	28.449	0.000	0.122	-0.150	0.013	13.286
STRUCTURE HEAVE WAVE FREQ VELOCITY [m/s]	0.000	2.252	-1.227	0.427	1.127	0.000	1.831	-1.686	0.374	1.161
STRUCTURE ROLL WAVE FREQ VELOCITY [°/s]	0.000	1.156	-1.297	0.124	21.134	0.000	0.012	-0.010	0.001	7.124
STRUCTURE PITCH WAVE FREQ VELOCITY [°/s]	0.000	3.657	-5.105	1.206	0.400	0.000	0.130	-0.239	0.026	2.388
STRUCTURE YAW WAVE FREQ VELOCITY [°/s]	0.000	1.167	-0.703	0.062	66.809	0.000	0.721	-0.292	0.056	18.283
STRUCTURE SURGE WAVE FREQ ACCELERATION [m/s^2]	0.000	1.053	-1.222	0.276	0.355	0.000	1.803	-2.135	0.526	0.097
STRUCTURE SWAY WAVE FREQ ACCELERATION [m/s^2]	0.000	0.314	-0.254	0.030	22.196	0.000	0.051	-0.041	0.005	13.754
STRUCTURE HEAVE WAVE FREQ ACCELERATION [m/s^2]	0.000	0.937	-1.039	0.186	1.656	0.000	1.044	-1.087	0.235	0.632
STRUCTURE ROLL WAVE FREQ ACCELERATION [°/s^2]	0.000	0.673	-0.729	0.073	18.182	0.000	0.049	-0.049	0.007	7.090
STRUCTURE PITCH WAVE FREQ ACCELERATION [°/s^2]	0.000	2.486	-3.353	0.709	0.559	0.000	0.600	-0.863	0.087	2.246
STRUCTURE YAW WAVE FREQ ACCELERATION [°/s^2]	0.000	0.358	-0.329	0.022	63.467	0.000	0.299	-0.164	0.019	30.038
STRUCTURE SURGE LOW FREQ POSITION [m]	1.737	4.176	-0.438	0.667	0.445	0.022	1.739	-3.172	0.626	1.391
STRUCTURE SWAY LOW FREQ POSITION [m]	0.000	2.565	-3.104	0.312	23.607	0.014	0.357	-0.126	0.034	20.118
STRUCTURE HEAVE LOW FREQ POSITION [m]	-0.135	0.298	-0.906	0.168	1.130	-0.627	3.019	-8.522	1.440	2.588
STRUCTURE ROLL LOW FREQ POSITION [°]	0.000	0.651	-0.721	0.069	27.912	0.000	0.019	-0.014	0.002	19.740
STRUCTURE PITCH LOW FREQ POSITION [°]	-0.946	-0.243	-2.113	0.248	0.470	0.021	0.278	-0.104	0.047	2.567
STRUCTURE YAW LOW FREQ POSITION [°]	0.001	0.904	-1.539	0.144	21.217	-0.129	1.163	-2.412	0.301	8.557
STRUCTURE SURGE LOW FREQ VELOCITY [m/s]	0.000	0.319	-0.357	0.087	0.660	0.000	0.334	-0.338	0.097	0.227
STRUCTURE SWAY LOW FREQ VELOCITY [m/s]	0.000	0.396	-0.394	0.042	25.376	0.000	0.013	-0.019	0.002	13.211
STRUCTURE HEAVE LOW FREQ VELOCITY [m/s]	0.000	0.090	-0.135	0.030	0.523	0.000	0.394	-0.324	0.079	1.789
STRUCTURE ROLL LOW FREQ VELOCITY [°/s]	0.000	0.112	-0.128	0.012	29.214	0.000	0.001	-0.001	0.000	20.309
STRUCTURE PITCH LOW FREQ VELOCITY [°/s]	0.000	0.191	-0.172	0.052	-0.034	0.000	0.011	-0.014	0.003	1.766
STRUCTURE YAW LOW FREQ VELOCITY [°/s]	0.000	0.140	-0.161	0.015	23.048	0.000	0.160	-0.137	0.022	7.077
STRUCTURE SURGE LOW FREQ ACCELERATION [m/s^2]	0.000	0.083	-0.079	0.020	0.357	0.000	0.113	-0.086	0.030	-0.044

TABLE 6.23: Motion Analysis Time History Statistics for LC2C and LC2D (contd).

Parameters	LC2C					LC2D				
	Avg.	Max	Min	Std.Dev	Kurt	Avg.	Max	Min	Std.Dev	Kurt
STRUCTURE SWAY LOW FREQ ACCELERATION [m/s^2]	0.000	0.061	-0.060	0.007	25.638	0.000	0.002	-0.004	0.000	18.597
STRUCTURE HEAVE LOW FREQ ACCELERATION [m/s^2]	0.000	0.032	-0.037	0.009	0.318	0.000	0.046	-0.040	0.009	1.273
STRUCTURE ROLL LOW FREQ ACCELERATION [°/s^2]	0.000	0.023	-0.027	0.002	23.496	0.000	0.000	0.000	0.000	19.097
STRUCTURE PITCH LOW FREQ ACCELERATION [°/s^2]	0.000	0.061	-0.074	0.018	0.109	0.000	0.001	-0.002	0.000	0.950
STRUCTURE YAW LOW FREQ ACCELERATION [°/s^2]	0.000	0.030	-0.020	0.002	36.752	0.000	0.016	-0.011	0.002	6.918
MORISON DRAG FORCE - X [N]	7.43E+05	3.30E+06	-7.48E+04	4.29E+05	1.18E+00	1.26E+06	1.26E+07	-4.23E+06	1.80E+06	3.39E+00
MORISON DRAG FORCE - Y [N]	-2.09E+02	6.64E+05	-9.22E+05	6.76E+04	4.22E+01	7.15E+02	2.74E+05	-1.36E+05	1.30E+04	7.43E+01
MORISON DRAG FORCE - Z [N]	-3.01E+04	6.12E+05	-1.29E+06	1.84E+05	2.39E+00	-4.97E+04	1.60E+06	-3.23E+06	3.52E+05	8.67E+00
MORISON DRAG MOMENT - X [N.m]	2.46E+03	1.01E+07	-9.67E+06	8.59E+05	3.19E+01	-7.64E+03	1.68E+06	-3.32E+06	1.68E+05	6.22E+01
MORISON DRAG MOMENT - Y [N.m]	1.14E+07	6.71E+07	-9.67E+06	9.10E+06	1.50E+00	1.87E+07	1.92E+08	-4.89E+07	2.49E+07	4.07E+00
MORISON DRAG MOMENT - Z [N.m]	-4.07E+03	4.31E+06	-7.29E+06	3.16E+05	9.05E+01	-6.42E+04	1.18E+06	-7.84E+06	3.77E+05	6.51E+01
WAVE INERTIA FORCE - X [N]	5.09E+00	5.10E+02	-5.92E+02	1.42E+02	2.11E-01	3.75E+00	5.28E+02	-4.53E+02	1.42E+02	-5.46E-02
WAVE INERTIA FORCE - Y [N]	4.92E-03	2.58E+01	-2.11E+01	9.57E-01	1.57E+02	-1.53E-02	3.83E+00	-4.51E+00	3.72E-01	2.41E+01
WAVE INERTIA FORCE - Z [N]	-1.71E+01	4.99E+02	-6.62E+02	1.60E+02	2.49E-01	-6.70E+00	5.83E+02	-5.79E+02	1.65E+02	-8.15E-02
WAVE INERTIA MOMENT - X [N.m]	2.22E+00	1.89E+03	-1.92E+03	7.68E+01	2.08E+02	2.82E-01	1.74E+02	-1.47E+02	1.43E+01	2.22E+01
WAVE INERTIA MOMENT - Y [N.m]	1.66E+02	5.25E+03	-7.36E+03	1.55E+03	2.29E-01	3.68E+01	5.26E+03	-5.62E+03	1.48E+03	-1.79E-01
WAVE INERTIA MOMENT - Z [N.m]	5.05E-01	1.11E+03	-9.81E+02	4.79E+01	1.87E+02	3.85E-02	7.71E+01	-9.20E+01	8.42E+00	1.96E+01
FROUDE KRYLOV FORCE - X [N]	7.61E+00	7.98E+02	-8.32E+02	2.22E+02	1.52E-01	5.47E+00	7.90E+02	-6.91E+02	2.21E+02	-7.68E-02
FROUDE KRYLOV FORCE - Y [N]	1.80E-06	1.47E-02	-2.06E-02	7.37E-04	2.71E+02	-4.40E-08	5.33E-05	-5.87E-05	5.45E-06	1.95E+01
FROUDE KRYLOV FORCE - Z [N]	-2.12E+01	6.60E+02	-8.48E+02	2.10E+02	1.50E-01	-1.02E+01	7.54E+02	-8.15E+02	2.18E+02	5.42E-03
FROUDE KRYLOV MOMENT - X [N.m]	2.45E+00	1.87E+03	-2.02E+03	8.10E+01	2.00E+02	1.32E-02	9.68E+01	-8.21E+01	8.44E+00	2.02E+01
FROUDE KRYLOV MOMENT - Y [N.m]	2.15E+02	9.27E+03	-1.18E+04	2.52E+03	2.76E-01	6.80E+01	9.27E+03	-8.54E+03	2.51E+03	-1.58E-02
FROUDE KRYLOV MOMENT - Z [N.m]	5.35E-01	1.79E+03	-1.52E+03	6.79E+01	2.37E+02	4.47E-02	7.73E+01	-9.18E+01	8.44E+00	1.96E+01
DIFFRACTION FORCE - X [N]	-2.83E+03	1.58E+07	-1.35E+07	4.24E+06	8.49E-03	-7.67E+03	1.58E+07	-1.32E+07	4.24E+06	6.81E-03
DIFFRACTION FORCE - Y [N]	-3.50E+02	4.80E+05	-5.31E+05	2.36E+04	1.17E+02	-3.70E+03	5.13E+05	-4.52E+05	3.30E+04	3.84E+01
DIFFRACTION FORCE - Z [N]	-3.03E+04	6.91E+07	-6.42E+07	1.79E+07	-8.41E-03	4.07E+03	6.89E+07	-6.42E+07	1.79E+07	-8.31E-03
DIFFRACTION MOMENT - X [N.m]	9.26E+03	1.40E+07	-1.26E+07	6.28E+05	1.17E+02	9.68E+04	1.21E+07	-1.29E+07	8.71E+05	3.77E+01
DIFFRACTION MOMENT - Y [N.m]	-6.91E+04	4.18E+08	-3.58E+08	1.13E+08	9.52E-03	-2.04E+05	4.18E+08	-3.61E+08	1.13E+08	8.08E-03
DIFFRACTION MOMENT - Z [N.m]	-8.62E+00	1.14E+06	-1.45E+06	7.42E+04	4.30E+01	-7.25E+01	2.26E+06	-3.00E+06	1.76E+05	3.01E+01
RADIATION FORCE - X [N]	-4.62E+02	6.54E+06	-8.60E+06	2.04E+06	4.23E-01	4.73E+02	1.89E+07	-1.44E+07	4.57E+06	1.06E-01
RADIATION FORCE - Y [N]	6.54E+01	2.22E+06	-2.20E+06	2.21E+05	2.08E+01	-3.18E+02	4.02E+05	-4.24E+05	4.02E+04	1.33E+01
RADIATION FORCE - Z [N]	-2.36E+02	7.82E+06	-1.04E+07	2.02E+06	1.07E+00	-3.72E+02	8.41E+06	-1.00E+07	2.16E+06	6.83E-01
RADIATION MOMENT - X [N.m]	-1.99E+03	6.10E+07	-5.66E+07	5.41E+06	1.80E+01	7.42E+03	6.86E+06	-6.84E+06	6.83E+05	1.13E+01
RADIATION MOMENT - Y [N.m]	-1.63E+04	1.74E+08	-1.63E+08	4.52E+07	2.02E-01	8.09E+03	2.97E+08	-2.28E+08	7.21E+07	1.43E-01
RADIATION MOMENT - Z [N.m]	4.45E+02	7.29E+06	-8.00E+06	5.08E+05	6.54E+01	2.79E+02	5.24E+06	-7.38E+06	4.45E+05	3.52E+01
TOTAL FORCE - X [N]	9.51E+01	1.09E+07	-1.25E+07	2.83E+06	3.48E-01	-3.78E+02	1.87E+07	-2.20E+07	5.44E+06	1.05E-01

TABLE 6.23: Motion Analysis Time History Statistics for LC2C and LC2D (contd).

Parameters	LC2C					LC2D				
	Avg.	Max	Min	Std.Dev	Kurt	Avg.	Max	Min	Std.Dev	Kurt
TOTAL FORCE - Y [N]	1.30E+01	2.90E+06	-2.32E+06	2.65E+05	2.27E+01	1.90E+00	5.13E+05	-4.28E+05	4.94E+04	1.34E+01
TOTAL FORCE - Z [N]	4.71E+02	9.86E+06	-1.11E+07	1.95E+06	1.74E+00	5.15E+02	1.11E+07	-1.17E+07	2.52E+06	5.93E-01
TOTAL MOMENT - X [N.m]	-4.19E+03	1.02E+08	-1.04E+08	1.10E+07	1.78E+01	1.60E+02	7.49E+06	-7.57E+06	1.03E+06	7.06E+00
TOTAL MOMENT - Y [N.m]	4.10E+04	3.72E+08	-5.05E+08	1.07E+08	5.64E-01	3.12E+03	1.61E+08	-1.31E+08	1.34E+07	4.01E+00
TOTAL MOMENT - Z [N.m]	-3.72E+02	6.30E+06	-6.63E+06	4.70E+05	4.23E+01	-1.38E+01	3.76E+06	-2.01E+06	2.37E+05	3.26E+01
STRUCTURE CURRENT DRAG FORCE - X [N]	7.37E+05	3.83E+06	1.52E-01	5.79E+05	1.11E+00	1.05E+06	7.31E+06	2.13E-01	1.14E+06	2.29E+00
STRUCTURE WIND FORCE - X [N]	1.20E+05	2.76E+05	2.67E+04	3.44E+04	1.21E-01	1.20E+05	2.70E+05	2.34E+04	3.60E+04	8.68E-03
MOORING CABLE 1 TENSION [N]	3.58E+06	1.65E+07	0.00E+00	3.15E+06	-1.47E-01	2.87E+06	2.06E+07	0.00E+00	4.01E+06	1.17E+00
MOORING CABLE 2 TENSION [N]	9.42E+05	6.33E+06	0.00E+00	1.12E+06	1.03E+00	6.67E+05	7.37E+06	0.00E+00	1.09E+06	2.38E+00
MOORING CABLE 3 TENSION [N]	9.43E+05	7.53E+06	0.00E+00	1.13E+06	1.31E+00	6.67E+05	7.35E+06	0.00E+00	1.10E+06	2.46E+00
MOORING CABLE 4 TENSION [N]	3.23E+06	1.76E+07	0.00E+00	3.20E+06	4.84E-02	8.72E+05	8.58E+06	0.00E+00	1.32E+06	2.16E+00

TABLE 6.24: Motion Analysis Time History Statistics for LC3A and LC3B.

Parameters	LC3A					LC3B				
	Avg.	Max	Min	Std.Dev	Kurt	Avg.	Max	Min	Std.Dev	Kurt
WAVE SURFACE ELEVATION [m]	0.000	6.415	-7.125	1.822	0.041	0.000	6.415	-7.125	1.822	0.041
WAVE VELOCITY [m/s]	0.019	2.953	-2.067	0.644	0.145	0.019	2.953	-2.067	0.644	0.145
WAVE ACCELERATION [m/s^2]	0.000	1.396	-1.365	0.361	-0.134	0.000	1.396	-1.365	0.361	-0.134
STRUCTURE SURGE POSITION [m]	1.655	11.460	-8.225	2.668	0.086	0.013	13.564	-16.204	3.613	0.286
STRUCTURE SWAY POSITION [m]	0.001	3.877	-4.638	0.583	13.769	0.019	1.335	-0.857	0.089	40.601
STRUCTURE HEAVE POSITION [m]	-0.068	4.622	-7.056	1.283	0.949	-0.675	2.641	-16.699	1.802	8.187
STRUCTURE ROLL POSITION [°]	0.000	2.547	-2.721	0.278	18.880	0.001	0.058	-0.018	0.003	112.320
STRUCTURE PITCH POSITION [°]	-0.903	8.314	-10.839	2.597	0.068	0.025	0.478	-0.187	0.059	5.316
STRUCTURE YAW POSITION [°]	-0.001	2.891	-3.956	0.236	62.755	-0.153	1.615	-5.484	0.384	39.529
STRUCTURE SURGE VELOCITY [m/s]	0.000	3.202	-2.548	0.765	0.117	0.001	4.863	-3.578	1.231	-0.059
STRUCTURE SWAY VELOCITY [m/s]	0.000	0.750	-0.893	0.100	16.297	0.000	0.300	-0.312	0.024	43.833
STRUCTURE HEAVE VELOCITY [m/s]	0.000	2.736	-2.060	0.581	0.563	0.000	2.777	-2.575	0.540	0.659
STRUCTURE ROLL VELOCITY [°/s]	0.000	1.281	-1.184	0.137	15.092	0.000	0.033	-0.037	0.004	13.580
STRUCTURE PITCH VELOCITY [°/s]	0.000	4.107	-5.602	1.325	0.254	0.000	0.246	-0.335	0.034	2.952
STRUCTURE YAW VELOCITY [°/s]	0.000	1.284	-0.760	0.059	112.038	0.000	1.100	-0.354	0.055	74.378
STRUCTURE SURGE ACCELERATION [m/s^2]	0.000	1.100	-1.104	0.258	0.176	0.000	1.410	-2.094	0.463	0.127
STRUCTURE SWAY ACCELERATION [m/s^2]	0.000	0.182	-0.167	0.022	13.989	0.000	0.131	-0.107	0.008	46.173
STRUCTURE HEAVE ACCELERATION [m/s^2]	0.000	1.436	-2.020	0.447	0.177	0.000	2.243	-1.955	0.532	-0.053
STRUCTURE ROLL ACCELERATION [°/s^2]	0.000	0.892	-0.729	0.093	14.544	0.000	0.174	-0.165	0.017	14.934
STRUCTURE PITCH ACCELERATION [°/s^2]	0.000	2.812	-3.746	0.835	0.458	0.000	1.442	-1.236	0.133	4.741
STRUCTURE YAW ACCELERATION [°/s^2]	0.000	0.655	-0.605	0.024	139.059	0.000	0.763	-0.322	0.023	170.815
STRUCTURE SURGE RAO BASED POSITION [m]	0.002	6.988	-7.784	1.944	0.055	0.020	44.567	-44.532	11.392	0.170
STRUCTURE SWAY RAO BASED POSITION [m]	0.001	0.331	-0.082	0.012	193.663	0.003	1.652	-2.844	0.141	91.582
STRUCTURE HEAVE RAO BASED POSITION [m]	-0.002	6.326	-7.169	1.791	0.041	0.001	3.450	-3.906	0.979	0.046
STRUCTURE ROLL RAO BASED POSITION [°]	0.000	0.419	-0.271	0.017	156.851	0.000	0.011	-0.006	0.000	144.382
STRUCTURE PITCH RAO BASED POSITION [°]	-0.001	11.504	-9.513	2.726	-0.114	0.000	0.149	-0.130	0.035	0.131
STRUCTURE YAW RAO BASED POSITION [°]	0.000	0.032	-0.036	0.002	44.652	0.000	0.105	-0.081	0.005	71.280
STRUCTURE SURGE RAO BASED VELOCITY [m/s]	-0.001	2.483	-2.599	0.641	0.052	0.001	13.937	-14.098	3.615	0.144
STRUCTURE SWAY RAO BASED VELOCITY [m/s]	0.000	0.078	-0.059	0.003	115.461	-0.002	0.828	-0.908	0.046	102.581
STRUCTURE HEAVE RAO BASED VELOCITY [m/s]	0.000	2.267	-2.305	0.613	0.020	0.000	1.208	-1.221	0.321	0.037
STRUCTURE ROLL RAO BASED VELOCITY [°/s]	0.000	0.178	-0.247	0.010	133.973	0.000	0.004	-0.003	0.000	194.955
STRUCTURE PITCH RAO BASED VELOCITY [°/s]	0.000	6.479	-6.280	1.644	-0.205	0.000	0.051	-0.046	0.012	0.117
STRUCTURE YAW RAO BASED VELOCITY [°/s]	0.000	0.031	-0.040	0.002	42.037	0.000	0.126	-0.093	0.006	61.415
STRUCTURE SURGE RAO BASED ACCELERATION [m/s^2]	0.000	1.024	-0.945	0.248	-0.015	-0.002	4.692	-4.448	1.168	0.112
STRUCTURE SWAY RAO BASED ACCELERATION [m/s^2]	0.000	0.013	-0.041	0.001	185.612	0.000	0.324	-0.173	0.015	104.574

TABLE 6.24: Motion Analysis Time History Statistics for LC3A and LC3B (contd).

Parameters	LC3A					LC3B				
	Avg.	Max	Min	Std.Dev	Kurt	Avg.	Max	Min	Std.Dev	Kurt
STRUCTURE HEAVE RAO BASED ACCELERATION [m/s^2]	0.000	0.869	-0.997	0.257	-0.084	0.000	0.447	-0.496	0.126	-0.055
STRUCTURE ROLL RAO BASED ACCELERATION [°/s^2]	0.000	0.119	-0.170	0.007	137.175	0.000	0.002	-0.002	0.000	136.292
STRUCTURE PITCH RAO BASED ACCELERATION [°/s^2]	0.000	3.421	-3.991	1.088	-0.246	0.000	0.021	-0.023	0.006	-0.102
STRUCTURE YAW RAO BASED ACCELERATION [°/s^2]	0.000	0.042	-0.038	0.003	37.804	0.000	0.140	-0.155	0.009	50.912
STRUCTURE SURGE WAVE FREQ POSITION [m]	0.001	11.576	-10.594	2.978	0.102	0.000	16.526	-15.039	3.847	0.328
STRUCTURE SWAY WAVE FREQ POSITION [m]	0.000	4.999	-6.398	0.784	13.826	0.000	1.204	-1.332	0.093	46.945
STRUCTURE HEAVE WAVE FREQ POSITION [m]	0.000	5.351	-7.172	1.374	0.790	0.001	9.594	-10.613	1.628	2.675
STRUCTURE ROLL WAVE FREQ POSITION [°]	0.000	2.787	-3.188	0.313	18.769	0.000	0.040	-0.049	0.004	31.502
STRUCTURE PITCH WAVE FREQ POSITION [°]	0.000	9.583	-10.212	2.724	0.048	0.000	0.227	-0.277	0.054	1.361
STRUCTURE YAW WAVE FREQ POSITION [°]	0.000	4.367	-3.529	0.296	41.922	0.000	6.889	-4.124	0.547	32.408
STRUCTURE SURGE WAVE FREQ VELOCITY [m/s]	0.000	3.427	-2.640	0.830	0.126	0.001	5.218	-3.815	1.301	-0.033
STRUCTURE SWAY WAVE FREQ VELOCITY [m/s]	0.000	0.944	-1.094	0.127	16.115	0.000	0.352	-0.320	0.025	43.777
STRUCTURE HEAVE WAVE FREQ VELOCITY [m/s]	0.000	2.868	-2.125	0.600	0.593	0.000	3.214	-3.053	0.560	0.848
STRUCTURE ROLL WAVE FREQ VELOCITY [°/s]	0.000	1.344	-1.184	0.141	15.416	0.000	0.035	-0.036	0.004	13.606
STRUCTURE PITCH WAVE FREQ VELOCITY [°/s]	0.000	4.218	-5.746	1.359	0.256	0.000	0.248	-0.335	0.034	2.894
STRUCTURE YAW WAVE FREQ VELOCITY [°/s]	0.000	1.418	-0.824	0.066	104.149	0.000	1.305	-0.760	0.071	56.243
STRUCTURE SURGE WAVE FREQ ACCELERATION [m/s^2]	0.000	1.163	-1.163	0.274	0.178	0.000	1.460	-2.200	0.484	0.129
STRUCTURE SWAY WAVE FREQ ACCELERATION [m/s^2]	0.000	0.209	-0.186	0.026	13.592	0.000	0.139	-0.111	0.009	45.822
STRUCTURE HEAVE WAVE FREQ ACCELERATION [m/s^2]	0.000	1.480	-2.040	0.452	0.180	0.000	2.275	-1.991	0.535	-0.042
STRUCTURE ROLL WAVE FREQ ACCELERATION [°/s^2]	0.000	0.900	-0.729	0.095	14.594	0.000	0.173	-0.167	0.017	14.897
STRUCTURE PITCH WAVE FREQ ACCELERATION [°/s^2]	0.000	2.874	-3.784	0.849	0.459	0.000	1.221	-1.250	0.133	3.611
STRUCTURE YAW WAVE FREQ ACCELERATION [°/s^2]	0.000	0.670	-0.633	0.025	136.243	0.000	0.763	-0.360	0.024	147.997
STRUCTURE SURGE LOW FREQ POSITION [m]	1.654	3.587	-0.724	0.597	0.482	0.013	2.016	-4.132	0.712	2.254
STRUCTURE SWAY LOW FREQ POSITION [m]	0.001	1.967	-2.987	0.269	23.591	0.019	0.717	-0.384	0.070	29.348
STRUCTURE HEAVE LOW FREQ POSITION [m]	-0.164	0.305	-0.982	0.171	1.152	-0.756	2.933	-13.187	1.840	6.311
STRUCTURE ROLL LOW FREQ POSITION [°]	0.001	0.488	-0.351	0.053	15.170	0.000	0.039	-0.033	0.004	29.221
STRUCTURE PITCH LOW FREQ POSITION [°]	-0.902	-0.295	-1.896	0.199	0.558	0.025	0.449	-0.118	0.062	6.182
STRUCTURE YAW LOW FREQ POSITION [°]	-0.002	1.187	-1.429	0.151	17.558	-0.153	3.438	-5.557	0.514	25.267
STRUCTURE SURGE LOW FREQ VELOCITY [m/s]	0.000	0.284	-0.323	0.081	0.356	0.000	0.360	-0.408	0.084	0.806
STRUCTURE SWAY LOW FREQ VELOCITY [m/s]	0.000	0.241	-0.303	0.033	16.655	0.000	0.044	-0.052	0.004	34.337
STRUCTURE HEAVE LOW FREQ VELOCITY [m/s]	0.000	0.096	-0.136	0.029	0.591	0.000	0.485	-0.441	0.094	2.511
STRUCTURE ROLL LOW FREQ VELOCITY [°/s]	0.000	0.075	-0.066	0.008	17.427	0.000	0.002	-0.003	0.000	32.088
STRUCTURE PITCH LOW FREQ VELOCITY [°/s]	0.000	0.167	-0.163	0.047	-0.002	0.000	0.014	-0.016	0.003	2.485
STRUCTURE YAW LOW FREQ VELOCITY [°/s]	0.000	0.130	-0.140	0.013	20.872	0.000	0.409	-0.236	0.036	27.880
STRUCTURE SURGE LOW FREQ ACCELERATION [m/s^2]	0.000	0.074	-0.063	0.019	0.104	0.000	0.106	-0.091	0.024	0.338

TABLE 6.24: Motion Analysis Time History Statistics for LC3A and LC3B (contd).

Parameters	LC3A					LC3B				
	Avg.	Max	Min	Std.Dev	Kurt	Avg.	Max	Min	Std.Dev	Kurt
STRUCTURE SWAY LOW FREQ ACCELERATION [m/s^2]	0.000	0.031	-0.038	0.005	13.618	0.000	0.008	-0.008	0.001	47.002
STRUCTURE HEAVE LOW FREQ ACCELERATION [m/s^2]	0.000	0.033	-0.044	0.009	0.674	0.000	0.054	-0.062	0.010	2.256
STRUCTURE ROLL LOW FREQ ACCELERATION [°/s^2]	0.000	0.017	-0.019	0.002	16.444	0.000	0.000	0.000	0.000	30.969
STRUCTURE PITCH LOW FREQ ACCELERATION [°/s^2]	0.000	0.061	-0.064	0.017	0.037	0.000	0.001	-0.002	0.000	1.242
STRUCTURE YAW LOW FREQ ACCELERATION [°/s^2]	0.000	0.029	-0.019	0.002	44.966	0.000	0.042	-0.028	0.003	32.241
MORISON DRAG FORCE - X [N]	7.76E+05	3.85E+06	-2.65E+04	4.74E+05	2.08E+00	1.18E+06	1.28E+07	-4.56E+06	1.61E+06	4.09E+00
MORISON DRAG FORCE - Y [N]	3.13E+02	6.08E+05	-5.49E+05	5.26E+04	2.13E+01	9.17E+02	6.03E+05	-2.73E+05	2.32E+04	1.64E+02
MORISON DRAG FORCE - Z [N]	-1.90E+04	2.19E+06	-2.25E+06	3.51E+05	2.96E+00	-2.80E+04	3.86E+06	-4.63E+06	4.93E+05	7.25E+00
MORISON DRAG MOMENT - X [N.m]	-5.87E+03	8.88E+06	-9.87E+06	8.70E+05	2.29E+01	-9.21E+03	5.41E+06	-7.13E+06	3.13E+05	1.23E+02
MORISON DRAG MOMENT - Y [N.m]	1.19E+07	7.34E+07	-1.69E+07	1.02E+07	1.89E+00	1.76E+07	1.85E+08	-5.24E+07	2.26E+07	4.94E+00
MORISON DRAG MOMENT - Z [N.m]	-9.10E+02	5.89E+06	-7.00E+06	3.21E+05	8.40E+01	-5.48E+04	4.18E+06	-1.27E+07	4.57E+05	1.86E+02
WAVE INERTIA FORCE - X [N]	3.00E+00	5.62E+02	-5.75E+02	1.37E+02	1.27E-01	2.92E+00	5.31E+02	-5.08E+02	1.36E+02	-4.70E-02
WAVE INERTIA FORCE - Y [N]	6.70E-03	2.29E+01	-1.20E+01	7.89E-01	1.69E+02	-1.17E-02	5.36E+00	-5.96E+00	4.20E-01	3.31E+01
WAVE INERTIA FORCE - Z [N]	-1.35E+01	4.97E+02	-7.58E+02	1.59E+02	2.21E-01	-8.70E+00	4.95E+02	-6.06E+02	1.58E+02	-7.67E-02
WAVE INERTIA MOMENT - X [N.m]	-1.12E-01	1.61E+03	-1.37E+03	6.97E+01	1.63E+02	1.85E-01	1.58E+02	-2.46E+02	1.65E+01	2.80E+01
WAVE INERTIA MOMENT - Y [N.m]	9.13E+01	7.43E+03	-6.86E+03	1.54E+03	2.29E-01	3.41E+01	5.13E+03	-6.36E+03	1.44E+03	-1.23E-01
WAVE INERTIA MOMENT - Z [N.m]	3.41E-01	1.15E+03	-9.73E+02	4.44E+01	2.41E+02	9.64E-02	1.26E+02	-1.35E+02	1.00E+01	2.34E+01
FROUDE KRYLOV FORCE - X [N]	4.74E+00	9.02E+02	-8.14E+02	2.14E+02	9.83E-02	4.26E+00	7.98E+02	-7.80E+02	2.12E+02	-9.00E-02
FROUDE KRYLOV FORCE - Y [N]	-6.51E-06	1.08E-02	-2.33E-02	6.11E-04	3.24E+02	5.41E-08	4.68E-05	-3.89E-05	4.93E-06	1.89E+01
FROUDE KRYLOV FORCE - Z [N]	-1.72E+01	6.40E+02	-9.60E+02	2.06E+02	1.76E-01	-1.20E+01	6.50E+02	-8.53E+02	2.08E+02	1.77E-02
FROUDE KRYLOV MOMENT - X [N.m]	-6.79E-02	1.55E+03	-1.38E+03	7.13E+01	1.76E+02	-1.82E-02	9.04E+01	-1.65E+02	1.01E+01	2.72E+01
FROUDE KRYLOV MOMENT - Y [N.m]	1.26E+02	9.69E+03	-1.06E+04	2.51E+03	1.31E-01	5.85E+01	9.55E+03	-9.13E+03	2.47E+03	-3.73E-02
FROUDE KRYLOV MOMENT - Z [N.m]	5.19E-01	1.43E+03	-1.22E+03	5.89E+01	2.33E+02	1.01E-01	1.26E+02	-1.35E+02	1.01E+01	2.33E+01
DIFFRACTION FORCE - X [N]	-2.20E+03	1.58E+07	-1.53E+07	4.06E+06	1.09E-02	-5.35E+03	1.57E+07	-1.52E+07	4.06E+06	7.46E-03
DIFFRACTION FORCE - Y [N]	-1.01E+03	2.89E+05	-5.69E+05	2.43E+04	1.38E+02	-3.34E+03	9.77E+05	-1.65E+06	5.37E+04	2.32E+02
DIFFRACTION FORCE - Z [N]	-1.83E+04	6.46E+07	-7.23E+07	1.82E+07	5.15E-02	1.37E+04	6.43E+07	-7.22E+07	1.82E+07	5.07E-02
DIFFRACTION MOMENT - X [N.m]	2.70E+04	1.49E+07	-7.40E+06	6.47E+05	1.38E+02	8.77E+04	4.36E+07	-2.55E+07	1.42E+06	2.35E+02
DIFFRACTION MOMENT - Y [N.m]	-5.50E+04	4.23E+08	-4.03E+08	1.08E+08	6.55E-03	-1.43E+05	4.28E+08	-3.99E+08	1.08E+08	3.00E-03
DIFFRACTION MOMENT - Z [N.m]	-8.14E+00	1.14E+06	-1.10E+06	7.72E+04	3.80E+01	-7.33E+01	6.09E+06	-5.76E+06	2.89E+05	7.35E+01
RADIATION FORCE - X [N]	3.88E+02	8.16E+06	-9.48E+06	2.20E+06	2.11E-01	9.87E+02	1.89E+07	-1.17E+07	4.25E+06	1.09E-01
RADIATION FORCE - Y [N]	-1.00E+01	2.06E+06	-2.31E+06	2.42E+05	1.58E+01	-2.76E+02	8.61E+05	-1.05E+06	7.38E+04	4.17E+01
RADIATION FORCE - Z [N]	7.95E+02	1.60E+07	-1.41E+07	3.67E+06	2.40E-01	3.18E+02	1.91E+07	-1.85E+07	4.55E+06	-7.72E-03
RADIATION MOMENT - X [N.m]	3.41E+02	5.83E+07	-6.89E+07	6.93E+06	1.36E+01	6.33E+03	2.13E+07	-1.80E+07	1.33E+06	3.47E+01
RADIATION MOMENT - Y [N.m]	1.12E+03	2.38E+08	-2.21E+08	5.71E+07	-2.62E-02	1.65E+04	2.92E+08	-2.02E+08	6.74E+07	1.40E-01
RADIATION MOMENT - Z [N.m]	-3.36E+02	1.27E+07	-1.48E+07	5.76E+05	1.13E+02	2.35E+02	6.52E+06	-1.57E+07	5.33E+05	1.40E+02
TOTAL FORCE - X [N]	-8.26E+02	1.20E+07	-1.20E+07	2.81E+06	1.76E-01	-1.16E+03	1.54E+07	-2.28E+07	5.04E+06	1.27E-01

TABLE 6.24: Motion Analysis Time History Statistics for LC3A and LC3B (contd).

Parameters	LC3A					LC3B				
	Avg.	Max	Min	Std.Dev	Kurt	Avg.	Max	Min	Std.Dev	Kurt
TOTAL FORCE - Y [N]	7.49E+00	1.98E+06	-1.82E+06	2.39E+05	1.40E+01	2.44E+00	1.43E+06	-1.16E+06	9.09E+04	4.62E+01
TOTAL FORCE - Z [N]	-1.01E+03	1.56E+07	-2.20E+07	4.87E+06	1.77E-01	4.03E+00	2.44E+07	-2.13E+07	5.79E+06	-5.26E-02
TOTAL MOMENT - X [N.m]	-8.26E+03	1.36E+08	-1.11E+08	1.43E+07	1.45E+01	9.89E+02	2.67E+07	-2.53E+07	2.61E+06	1.49E+01
TOTAL MOMENT - Y [N.m]	1.71E+04	4.31E+08	-5.74E+08	1.28E+08	4.58E-01	-8.43E+03	2.21E+08	-1.89E+08	2.03E+07	4.74E+00
TOTAL MOMENT - Z [N.m]	1.01E+02	6.24E+06	-1.18E+07	5.37E+05	6.53E+01	-2.29E+01	9.92E+06	-4.25E+06	2.93E+05	1.71E+02
STRUCTURE CURRENT DRAG FORCE - X [N]	7.42E+05	4.24E+06	9.81E-02	5.94E+05	1.78E+00	9.79E+05	6.65E+06	6.09E-01	1.03E+06	2.61E+00
STRUCTURE WIND FORCE - X [N]	1.40E+05	3.33E+05	2.76E+04	4.09E+04	8.75E-02	1.40E+05	3.24E+05	2.84E+04	4.24E+04	1.03E-02
MOORING CABLE 1 TENSION [N]	3.67E+06	1.89E+07	0.00E+00	3.39E+06	-1.70E-02	2.59E+06	1.96E+07	0.00E+00	3.65E+06	1.34E+00
MOORING CABLE 2 TENSION [N]	1.06E+06	7.50E+06	0.00E+00	1.34E+06	1.01E+00	6.83E+05	9.12E+06	0.00E+00	1.16E+06	3.42E+00
MOORING CABLE 3 TENSION [N]	1.06E+06	7.79E+06	0.00E+00	1.33E+06	1.08E+00	6.85E+05	9.12E+06	0.00E+00	1.17E+06	3.48E+00
MOORING CABLE 4 TENSION [N]	3.33E+06	2.13E+07	0.00E+00	3.41E+06	3.18E-01	1.08E+06	1.04E+07	0.00E+00	1.66E+06	2.62E+00

TABLE 6.25: Motion Analysis Time History Statistics for LC3C and LC3D.

Parameters	LC3C					LC3D				
	Avg.	Max	Min	Std.Dev	Kurt	Avg.	Max	Min	Std.Dev	Kurt
WAVE SURFACE ELEVATION [m]	0.000	6.415	-7.125	1.822	0.041	0.000	6.415	-7.125	1.822	0.041
WAVE VELOCITY [m/s]	0.019	2.953	-2.067	0.644	0.145	0.019	2.953	-2.067	0.644	0.145
WAVE ACCELERATION [m/s^2]	0.000	1.396	-1.365	0.361	-0.134	0.000	1.396	-1.365	0.361	-0.134
STRUCTURE SURGE POSITION [m]	1.619	11.241	-7.468	2.671	0.077	0.003	13.575	-16.328	3.620	0.304
STRUCTURE SWAY POSITION [m]	0.001	3.301	-3.481	0.264	78.611	0.023	1.667	-1.126	0.109	42.897
STRUCTURE HEAVE POSITION [m]	-0.024	3.505	-5.994	1.168	0.762	-0.670	2.494	-16.435	1.770	8.630
STRUCTURE ROLL POSITION [°]	0.001	2.193	-1.888	0.114	116.210	0.001	0.073	-0.021	0.003	132.837
STRUCTURE PITCH POSITION [°]	-0.951	7.251	-10.342	2.395	0.037	0.025	0.476	-0.178	0.059	5.422
STRUCTURE YAW POSITION [°]	0.001	3.841	-2.826	0.144	275.954	-0.187	2.047	-6.933	0.475	41.632
STRUCTURE SURGE VELOCITY [m/s]	0.000	3.124	-2.428	0.762	0.035	0.001	4.853	-3.579	1.232	-0.063
STRUCTURE SWAY VELOCITY [m/s]	0.000	0.650	-0.680	0.044	96.995	0.000	0.398	-0.392	0.029	47.918
STRUCTURE HEAVE VELOCITY [m/s]	0.000	2.086	-1.317	0.392	1.201	0.000	2.015	-2.403	0.392	1.683
STRUCTURE ROLL VELOCITY [°/s]	0.000	0.740	-0.876	0.049	94.493	0.000	0.035	-0.037	0.003	26.483
STRUCTURE PITCH VELOCITY [°/s]	0.000	3.527	-4.983	1.135	0.332	0.000	0.192	-0.323	0.025	5.713
STRUCTURE YAW VELOCITY [°/s]	0.000	0.575	-1.278	0.037	467.516	0.000	1.343	-0.445	0.068	75.158
STRUCTURE SURGE ACCELERATION [m/s^2]	0.000	1.078	-1.076	0.253	0.212	0.000	1.410	-2.128	0.463	0.147
STRUCTURE SWAY ACCELERATION [m/s^2]	0.000	0.135	-0.136	0.009	85.402	0.000	0.158	-0.134	0.010	49.151
STRUCTURE HEAVE ACCELERATION [m/s^2]	0.000	0.830	-0.898	0.175	1.702	0.000	1.443	-1.300	0.294	0.603
STRUCTURE ROLL ACCELERATION [°/s^2]	0.000	0.488	-0.569	0.030	95.272	0.000	0.156	-0.146	0.013	25.453
STRUCTURE PITCH ACCELERATION [°/s^2]	0.000	2.366	-2.996	0.681	0.531	0.000	1.440	-1.150	0.083	17.316
STRUCTURE YAW ACCELERATION [°/s^2]	0.000	0.466	-0.537	0.014	579.503	0.000	0.904	-0.378	0.027	153.963
STRUCTURE SURGE RAO BASED POSITION [m]	0.002	7.107	-7.723	1.945	0.062	0.021	44.569	-44.529	11.391	0.170
STRUCTURE SWAY RAO BASED POSITION [m]	0.000	0.057	-0.337	0.009	624.914	0.003	2.179	-3.577	0.176	92.847
STRUCTURE HEAVE RAO BASED POSITION [m]	-0.001	6.148	-6.875	1.716	0.050	0.001	3.418	-3.842	0.968	0.048
STRUCTURE ROLL RAO BASED POSITION [°]	0.000	0.131	-0.395	0.009	795.886	0.000	0.013	-0.007	0.001	143.487
STRUCTURE PITCH RAO BASED POSITION [°]	-0.001	8.221	-8.365	2.290	-0.063	0.000	0.149	-0.130	0.035	0.130
STRUCTURE YAW RAO BASED POSITION [°]	0.000	0.016	-0.025	0.001	211.276	0.000	0.133	-0.101	0.006	73.525
STRUCTURE SURGE RAO BASED VELOCITY [m/s]	-0.001	2.452	-2.580	0.644	0.047	0.001	13.936	-14.099	3.615	0.143
STRUCTURE SWAY RAO BASED VELOCITY [m/s]	0.000	0.064	-0.075	0.002	421.490	-0.003	1.059	-1.124	0.057	103.267
STRUCTURE HEAVE RAO BASED VELOCITY [m/s]	-0.001	2.131	-2.107	0.563	0.041	0.000	1.166	-1.200	0.315	0.040
STRUCTURE ROLL RAO BASED VELOCITY [°/s]	0.000	0.125	-0.142	0.004	424.652	0.000	0.005	-0.004	0.000	188.935
STRUCTURE PITCH RAO BASED VELOCITY [°/s]	0.000	4.526	-4.060	1.281	-0.171	0.000	0.050	-0.046	0.012	0.117
STRUCTURE YAW RAO BASED VELOCITY [°/s]	0.000	0.024	-0.029	0.001	243.786	0.000	0.159	-0.119	0.008	62.832
STRUCTURE SURGE RAO BASED ACCELERATION [m/s^2]	0.000	1.022	-0.959	0.252	-0.001	-0.002	4.692	-4.448	1.168	0.111
STRUCTURE SWAY RAO BASED ACCELERATION [m/s^2]	0.000	0.041	-0.011	0.001	708.663	0.000	0.406	-0.228	0.018	106.466

TABLE 6.25: Motion Analysis Time History Statistics for LC3C and LC3D (contd).

Parameters	LC3C					LC3D				
	Avg.	Max	Min	Std.Dev	Kurt	Avg.	Max	Min	Std.Dev	Kurt
STRUCTURE HEAVE RAO BASED ACCELERATION [m/s^2]	0.000	0.760	-0.849	0.220	-0.042	0.000	0.425	-0.479	0.122	-0.040
STRUCTURE ROLL RAO BASED ACCELERATION [°/s^2]	0.000	0.102	-0.058	0.003	467.796	0.000	0.002	-0.003	0.000	136.783
STRUCTURE PITCH RAO BASED ACCELERATION [°/s^2]	0.000	2.572	-2.724	0.805	-0.232	0.000	0.021	-0.023	0.006	-0.102
STRUCTURE YAW RAO BASED ACCELERATION [°/s^2]	0.000	0.037	-0.039	0.001	256.038	0.000	0.175	-0.196	0.011	51.750
STRUCTURE SURGE WAVE FREQ POSITION [m]	0.001	10.956	-10.749	2.994	0.106	0.000	16.549	-15.101	3.855	0.345
STRUCTURE SWAY WAVE FREQ POSITION [m]	0.000	4.011	-4.420	0.356	69.069	0.000	1.446	-1.662	0.115	48.107
STRUCTURE HEAVE WAVE FREQ POSITION [m]	0.000	4.185	-6.245	1.260	0.595	0.001	9.428	-10.114	1.592	2.800
STRUCTURE ROLL WAVE FREQ POSITION [°]	0.000	2.439	-2.127	0.131	114.397	0.000	0.045	-0.059	0.005	32.430
STRUCTURE PITCH WAVE FREQ POSITION [°]	0.000	8.365	-9.607	2.527	-0.011	0.000	0.227	-0.269	0.053	1.392
STRUCTURE YAW WAVE FREQ POSITION [°]	0.000	3.660	-4.228	0.181	218.565	0.000	8.561	-5.079	0.681	32.843
STRUCTURE SURGE WAVE FREQ VELOCITY [m/s]	0.000	3.315	-2.591	0.827	0.045	0.001	5.212	-3.813	1.302	-0.036
STRUCTURE SWAY WAVE FREQ VELOCITY [m/s]	0.000	0.765	-0.836	0.057	88.437	0.000	0.464	-0.405	0.031	48.125
STRUCTURE HEAVE WAVE FREQ VELOCITY [m/s]	0.000	2.213	-1.378	0.416	1.182	0.000	2.273	-2.411	0.417	1.858
STRUCTURE ROLL WAVE FREQ VELOCITY [°/s]	0.000	0.764	-0.934	0.051	97.199	0.000	0.035	-0.034	0.003	26.351
STRUCTURE PITCH WAVE FREQ VELOCITY [°/s]	0.000	3.625	-5.110	1.169	0.329	0.000	0.193	-0.324	0.025	5.465
STRUCTURE YAW WAVE FREQ VELOCITY [°/s]	0.000	0.632	-1.423	0.041	467.317	0.000	1.585	-0.949	0.088	58.129
STRUCTURE SURGE WAVE FREQ ACCELERATION [m/s^2]	0.000	1.129	-1.136	0.269	0.206	0.000	1.403	-2.234	0.484	0.150
STRUCTURE SWAY WAVE FREQ ACCELERATION [m/s^2]	0.000	0.159	-0.153	0.011	82.830	0.000	0.168	-0.139	0.011	48.819
STRUCTURE HEAVE WAVE FREQ ACCELERATION [m/s^2]	0.000	0.869	-0.916	0.181	1.651	0.000	1.431	-1.342	0.298	0.648
STRUCTURE ROLL WAVE FREQ ACCELERATION [°/s^2]	0.000	0.499	-0.583	0.031	95.869	0.000	0.156	-0.145	0.013	25.474
STRUCTURE PITCH WAVE FREQ ACCELERATION [°/s^2]	0.000	2.423	-3.037	0.694	0.527	0.000	0.947	-1.165	0.082	9.750
STRUCTURE YAW WAVE FREQ ACCELERATION [°/s^2]	0.000	0.490	-0.555	0.014	560.536	0.000	0.905	-0.425	0.029	133.712
STRUCTURE SURGE LOW FREQ POSITION [m]	1.618	3.982	-0.977	0.651	0.477	0.003	2.016	-4.231	0.722	2.393
STRUCTURE SWAY LOW FREQ POSITION [m]	0.001	2.170	-1.062	0.124	119.286	0.023	0.859	-0.449	0.086	29.046
STRUCTURE HEAVE LOW FREQ POSITION [m]	-0.136	0.302	-0.932	0.167	1.314	-0.751	2.966	-13.179	1.844	6.283
STRUCTURE ROLL LOW FREQ POSITION [°]	0.000	0.363	-0.320	0.024	90.174	0.001	0.047	-0.041	0.005	29.260
STRUCTURE PITCH LOW FREQ POSITION [°]	-0.951	-0.299	-2.152	0.232	1.135	0.025	0.449	-0.117	0.062	6.131
STRUCTURE YAW LOW FREQ POSITION [°]	0.001	1.377	-1.095	0.078	132.371	-0.188	4.306	-6.948	0.640	25.566
STRUCTURE SURGE LOW FREQ VELOCITY [m/s]	0.000	0.344	-0.334	0.084	0.437	0.000	0.366	-0.413	0.085	0.823
STRUCTURE SWAY LOW FREQ VELOCITY [m/s]	0.000	0.196	-0.203	0.015	77.589	0.000	0.054	-0.066	0.005	34.600
STRUCTURE HEAVE LOW FREQ VELOCITY [m/s]	0.000	0.091	-0.135	0.028	0.682	0.000	0.479	-0.438	0.094	2.493
STRUCTURE ROLL LOW FREQ VELOCITY [°/s]	0.000	0.061	-0.055	0.004	103.312	0.000	0.003	-0.003	0.000	32.403
STRUCTURE PITCH LOW FREQ VELOCITY [°/s]	0.000	0.168	-0.165	0.047	-0.029	0.000	0.014	-0.016	0.003	2.480
STRUCTURE YAW LOW FREQ VELOCITY [°/s]	0.000	0.151	-0.092	0.007	131.523	0.000	0.510	-0.294	0.045	27.975
STRUCTURE SURGE LOW FREQ ACCELERATION [m/s^2]	0.000	0.069	-0.069	0.019	0.099	0.000	0.106	-0.091	0.024	0.354

TABLE 6.25: Motion Analysis Time History Statistics for LC3C and LC3D (contd).

Parameters	LC3C					LC3D				
	Avg.	Max	Min	Std.Dev	Kurt	Avg.	Max	Min	Std.Dev	Kurt
STRUCTURE SWAY LOW FREQ ACCELERATION [m/s^2]	0.000	0.024	-0.027	0.002	68.457	0.000	0.010	-0.010	0.001	47.859
STRUCTURE HEAVE LOW FREQ ACCELERATION [m/s^2]	0.000	0.027	-0.038	0.008	0.506	0.000	0.054	-0.059	0.010	2.363
STRUCTURE ROLL LOW FREQ ACCELERATION [°/s^2]	0.000	0.014	-0.012	0.001	98.221	0.000	0.000	0.000	0.000	31.971
STRUCTURE PITCH LOW FREQ ACCELERATION [°/s^2]	0.000	0.051	-0.060	0.016	-0.023	0.000	0.001	-0.002	0.000	1.275
STRUCTURE YAW LOW FREQ ACCELERATION [°/s^2]	0.000	0.020	-0.028	0.001	237.756	0.000	0.053	-0.035	0.004	32.921
MORISON DRAG FORCE - X [N]	7.45E+05	3.55E+06	-4.55E+04	4.56E+05	1.98E+00	1.17E+06	1.29E+07	-4.60E+06	1.61E+06	4.18E+00
MORISON DRAG FORCE - Y [N]	1.34E+02	3.93E+05	-3.29E+05	2.23E+04	1.14E+02	1.18E+03	7.52E+05	-3.34E+05	2.87E+04	1.75E+02
MORISON DRAG FORCE - Z [N]	-2.94E+04	6.88E+05	-1.32E+06	1.76E+05	3.30E+00	-3.96E+04	2.50E+06	-4.70E+06	3.60E+05	1.29E+01
MORISON DRAG MOMENT - X [N.m]	-6.14E+01	6.06E+06	-5.88E+06	3.07E+05	1.13E+02	-1.18E+04	6.78E+06	-9.20E+06	3.83E+05	1.42E+02
MORISON DRAG MOMENT - Y [N.m]	1.14E+07	6.89E+07	-1.18E+07	9.09E+06	1.82E+00	1.74E+07	1.87E+08	-5.62E+07	2.26E+07	5.10E+00
MORISON DRAG MOMENT - Z [N.m]	5.33E+02	5.25E+06	-3.30E+06	1.75E+05	3.02E+02	-6.87E+04	5.37E+06	-1.63E+07	5.66E+05	1.93E+02
WAVE INERTIA FORCE - X [N]	4.53E+00	5.58E+02	-5.73E+02	1.37E+02	1.39E-01	3.15E+00	5.28E+02	-5.08E+02	1.37E+02	-5.99E-02
WAVE INERTIA FORCE - Y [N]	3.43E-04	2.80E+01	-3.73E+01	5.98E-01	1.96E+03	-1.55E-02	6.72E+00	-7.41E+00	5.17E-01	3.31E+01
WAVE INERTIA FORCE - Z [N]	-1.55E+01	4.73E+02	-7.63E+02	1.55E+02	2.14E-01	-8.28E+00	4.89E+02	-6.08E+02	1.58E+02	-8.86E-02
WAVE INERTIA MOMENT - X [N.m]	-2.25E-01	1.11E+03	-1.76E+03	4.38E+01	6.52E+02	2.54E-01	1.98E+02	-3.07E+02	2.02E+01	2.73E+01
WAVE INERTIA MOMENT - Y [N.m]	1.46E+02	5.71E+03	-6.73E+03	1.53E+03	9.93E-02	3.30E+01	5.22E+03	-6.27E+03	1.45E+03	-1.42E-01
WAVE INERTIA MOMENT - Z [N.m]	-6.85E-03	1.14E+03	-1.02E+03	3.11E+01	7.33E+02	3.28E-02	1.47E+02	-1.83E+02	1.23E+01	2.41E+01
FROUDE KRYLOV FORCE - X [N]	6.84E+00	8.95E+02	-8.16E+02	2.14E+02	1.00E-01	4.57E+00	7.91E+02	-7.81E+02	2.12E+02	-1.01E-01
FROUDE KRYLOV FORCE - Y [N]	1.65E-06	1.27E-02	-1.13E-02	3.34E-04	5.97E+02	-6.14E-08	5.06E-05	-4.04E-05	4.89E-06	1.71E+01
FROUDE KRYLOV FORCE - Z [N]	-1.92E+01	6.27E+02	-9.66E+02	2.02E+02	1.33E-01	-1.16E+01	6.46E+02	-8.54E+02	2.08E+02	6.00E-03
FROUDE KRYLOV MOMENT - X [N.m]	-2.12E-01	1.13E+03	-1.92E+03	4.77E+01	6.55E+02	-2.20E-02	1.11E+02	-2.04E+02	1.23E+01	2.60E+01
FROUDE KRYLOV MOMENT - Y [N.m]	1.91E+02	9.67E+03	-1.04E+04	2.51E+03	1.16E-01	5.89E+01	9.62E+03	-9.10E+03	2.48E+03	-4.84E-02
FROUDE KRYLOV MOMENT - Z [N.m]	-5.87E-04	2.07E+03	-2.20E+03	4.66E+01	1.13E+03	4.32E-02	1.48E+02	-1.82E+02	1.23E+01	2.41E+01
DIFFRACTION FORCE - X [N]	-2.30E+03	1.58E+07	-1.53E+07	4.07E+06	1.09E-02	-5.37E+03	1.57E+07	-1.52E+07	4.06E+06	6.95E-03
DIFFRACTION FORCE - Y [N]	5.71E+02	5.61E+05	-1.55E+05	1.63E+04	5.06E+02	-3.94E+03	1.23E+06	-2.05E+06	6.66E+04	2.32E+02
DIFFRACTION FORCE - Z [N]	-1.82E+04	6.45E+07	-7.22E+07	1.82E+07	5.15E-02	1.37E+04	6.43E+07	-7.22E+07	1.82E+07	5.06E-02
DIFFRACTION MOMENT - X [N.m]	-1.53E+04	4.00E+06	-1.48E+07	4.37E+05	5.08E+02	1.03E+05	5.41E+07	-3.21E+07	1.76E+06	2.36E+02
DIFFRACTION MOMENT - Y [N.m]	-5.78E+04	4.24E+08	-4.03E+08	1.08E+08	6.52E-03	-1.44E+05	4.28E+08	-3.99E+08	1.08E+08	2.49E-03
DIFFRACTION MOMENT - Z [N.m]	9.33E+00	8.45E+05	-1.10E+06	3.74E+04	2.35E+02	-8.64E+01	7.69E+06	-7.26E+06	3.60E+05	7.58E+01
RADIATION FORCE - X [N]	2.86E+02	6.89E+06	-8.84E+06	2.04E+06	3.34E-01	4.84E+02	1.89E+07	-1.16E+07	4.25E+06	1.18E-01
RADIATION FORCE - Y [N]	-3.25E+00	1.55E+06	-1.54E+06	8.44E+04	1.20E+02	-3.92E+02	1.11E+06	-1.25E+06	9.11E+04	4.72E+01
RADIATION FORCE - Z [N]	2.51E+02	7.57E+06	-9.67E+06	1.95E+06	1.13E+00	3.22E+02	1.19E+07	-1.50E+07	2.67E+06	8.68E-01
RADIATION MOMENT - X [N.m]	9.27E+01	3.68E+07	-3.73E+07	2.19E+06	9.81E+01	9.77E+03	2.30E+07	-1.93E+07	1.50E+06	4.53E+01
RADIATION MOMENT - Y [N.m]	-8.04E+01	1.86E+08	-1.87E+08	4.53E+07	5.98E-02	-5.21E+02	2.84E+08	-1.84E+08	6.73E+07	1.36E-01
RADIATION MOMENT - Z [N.m]	1.87E+02	1.22E+07	-9.73E+06	3.24E+05	5.30E+02	1.83E+02	6.96E+06	-1.80E+07	6.51E+05	1.25E+02
TOTAL FORCE - X [N]	-7.12E+02	1.17E+07	-1.17E+07	2.76E+06	2.12E-01	-7.58E+02	1.54E+07	-2.32E+07	5.04E+06	1.47E-01

TABLE 6.25: Motion Analysis Time History Statistics for LC3C and LC3D (contd).

Parameters	LC3C					LC3D				
	Avg.	Max	Min	Std.Dev	Kurt	Avg.	Max	Min	Std.Dev	Kurt
TOTAL FORCE - Y [N]	-3.44E+00	1.47E+06	-1.48E+06	1.00E+05	8.54E+01	2.13E+01	1.72E+06	-1.46E+06	1.12E+05	4.92E+01
TOTAL FORCE - Z [N]	-1.20E+02	9.04E+06	-9.79E+06	1.91E+06	1.70E+00	-5.62E+01	1.57E+07	-1.42E+07	3.21E+06	6.03E-01
TOTAL MOMENT - X [N.m]	4.47E+03	7.43E+07	-8.72E+07	4.64E+06	9.39E+01	-4.16E+03	2.39E+07	-2.23E+07	1.92E+06	2.55E+01
TOTAL MOMENT - Y [N.m]	1.21E+04	3.63E+08	-4.59E+08	1.04E+08	5.31E-01	4.26E+04	2.21E+08	-1.76E+08	1.27E+07	1.73E+01
TOTAL MOMENT - Z [N.m]	-4.34E+01	7.91E+06	-6.14E+06	2.47E+05	2.96E+02	1.82E+01	1.18E+07	-4.98E+06	3.55E+05	1.54E+02
STRUCTURE CURRENT DRAG FORCE - X [N]	7.39E+05	4.00E+06	5.38E-01	5.91E+05	1.45E+00	9.79E+05	6.65E+06	2.37E+00	1.03E+06	2.62E+00
STRUCTURE WIND FORCE - X [N]	1.40E+05	3.32E+05	2.78E+04	4.09E+04	8.41E-02	1.40E+05	3.24E+05	2.84E+04	4.24E+04	1.17E-02
MOORING CABLE 1 TENSION [N]	3.58E+06	1.77E+07	0.00E+00	3.24E+06	-1.31E-01	2.57E+06	2.00E+07	0.00E+00	3.64E+06	1.43E+00
MOORING CABLE 2 TENSION [N]	9.25E+05	6.00E+06	0.00E+00	1.10E+06	7.25E-01	6.61E+05	9.12E+06	0.00E+00	1.11E+06	3.09E+00
MOORING CABLE 3 TENSION [N]	9.23E+05	5.65E+06	0.00E+00	1.10E+06	7.19E-01	6.65E+05	9.11E+06	0.00E+00	1.12E+06	3.14E+00
MOORING CABLE 4 TENSION [N]	3.25E+06	1.71E+07	0.00E+00	3.21E+06	7.34E-02	1.01E+06	9.88E+06	0.00E+00	1.53E+06	2.63E+00

Chapter 7

Conclusion and Outlook

Based on the motivation for carrying out this research as earlier stated in Section 1.3 and research goals in Section 1.4 of this thesis, an environmental scoping assessment of the potential project development areas for offshore wind energy in New Zealand was sufficiently presented. A hybrid floating platform concept identified as the TRIgon Hybrid Floater (TRIHF) that cuts across the design principles of the three main floating platform concepts (TLP, semi-submersible, spar buoy) for offshore wind turbines was introduced. The coupled dynamics global performance investigation of the hybrid floating platform concept was successfully carried out where all environmental conditions of wind, wave, and current were adequately accounted for and thus representative of a realistic scenario. A new coupled dynamics simulation strategy (SHARPE) was introduced and executed using the AQWA program. In this new approach, a separate multi-physics unsteady state volume of fluid CFD simulation was utilised to provide force coefficient results for viscous drag modelling and viscous damping coefficient results for viscous damping modelling in AQWA. The coupled dynamics numerical simulation was performed in both frequency domain and time domain.

The effects of viscous damping on the motion response and hydrodynamic loads of the structure were adequately analysed. Based on the results from the simulation, it is concluded that the TRIHF platform concept meets design requirements regarding global motion, acceleration, and structure dynamic loads under operating, extreme, and survival environmental loading. However, further studies still need to be done to assess snap loads on the mooring cable and also check for redundancies in the mooring configuration. Since the mooring line provides dynamic stability to the FOWT assemblage, it will be interesting to investigate the dynamic response of the structure whenever one or several mooring lines break. Also, further structural assessment and detailed design study still needs to be performed to determine the structural responses

of TRIHF due to pressure and inertia loading using a mechanical Finite Element Analyses (FEA) model. Cost implication and further optimisation studies surrounding the constructability of TRIHF need to be investigated to ensure the concept is feasible to implement. More importantly, a scaled model experiment still needs to be conducted to verify the global dynamic loads and motions for the TRIHF platform by using the results obtained in this thesis as a benchmark. Furthermore, future studies will be the further validation of the SHARPE numerical modelling scheme using experimental test data from other FOWT pilot projects that are cropping up around the globe.

Appendix A

Matlab Code used for Pre-processing Metocean Hindcast Data

A.1 Current MetOcean Data

```
>> ncdisp('Non-Tidal Sea Level and Non Tidal Current\Non-Tidal Sea Level and Current.nc')
Source:
        C:Non-Tidal Sea Level and Non Tidal Current\Non-Tidal Sea Level and Current.nc
Format:
        64bit
Global Attributes:
        institution             = 'MSL'
        source                  = 'UDS'
        title                   = 'UDS data request'
        history                 = 'Mon Mar  5 16:49:26 2018: ncrcat -O /home/fmonetti/UDS_data/FWTS_ROMS/Monthly
                                  2018-03-05 00:29:34 UTC : UDS Query: datum=msl&xy=174.7223,-35.8584,176.6424,↙
-37.2085&slfmt=bln&fmt=nc&var=uo,vo,uso,vso,ssh&type=hc&bnd=174.722300,176.642400,-37.208500,-35.858400↙
&sort=quality,-res&spinup=0&stepback=1&dset=roms_nz_3D,roms_nz_surf&dim=2.0,2.0&time=19790101.↙
000000,19790131.230000'
        NCO                     = '"4.5.4"'
        nco_openmp_thread_number = 1
Dimensions:
        dum1 = 1
        site = 2
        lev  = 28
        time = 109769 (UNLIMITED)
Variables:
    dum1
        Size:       1x1
        Dimensions: dum1
        Datatype:   int32
    lat
        Size:       2x1
        Dimensions: site
        Datatype:   single
    lev
        Size:       28x1
        Dimensions: lev
        Datatype:   int32
    lon
        Size:       2x1
        Dimensions: site
        Datatype:   single
    site
        Size:       2x1
        Dimensions: site
        Datatype:   int32
    ssh
        Size:       1x2x109769
        Dimensions: dum1,site,time
        Datatype:   single
        Attributes:
                missing_value = 9.969209968386869e+36
                long_name     = 'Sea surface height'
                units         = 'm'
                vpair         = 'None'
    time
        Size:       109769x1
        Dimensions: time
        Datatype:   double
        Attributes:
                units = 'days since 0001-01-01 00:00:00'
    uo
        Size:       1x2x28x109769
```

```
        Dimensions: dum1,site,lev,time
        Datatype:   single
        Attributes:
                missing_value = 9.969209968386869e+36
                long_name     = 'Eastwards current'
                units         = 'm/s'
                vpair         = 'None'
    uso
        Size:       1x2x109769
        Dimensions: dum1,site,time
        Datatype:   single
        Attributes:
                missing_value = 9.969209968386869e+36
                long_name     = 'Eastwards surface current'
                units         = 'm/s'
                vpair         = 'None'
    vo
        Size:       1x2x28x109769
        Dimensions: dum1,site,lev,time
        Datatype:   single
        Attributes:
                missing_value = 9.969209968386869e+36
                long_name     = 'Northwards current'
                units         = 'm/s'
                vpair         = 'None'
    vso
        Size:       1x2x109769
        Dimensions: dum1,site,time
        Datatype:   single
        Attributes:
                missing_value = 9.969209968386869e+36
                long_name     = 'Northwards surface current'
                units         = 'm/s'
                vpair         = 'None'
A=ncread('Non-Tidal Sea Level and Non Tidal Current\Non-Tidal Sea Level and Current.nc','ssh');
B=ncread('Non-Tidal Sea Level and Non Tidal Current\Non-Tidal Sea Level and Current.nc','uo');
C=ncread('Non-Tidal Sea Level and Non Tidal Current\Non-Tidal Sea Level and Current.nc','uso');
D=ncread('Non-Tidal Sea Level and Non Tidal Current\Non-Tidal Sea Level and Current.nc','vo');
E=ncread('Non-Tidal Sea Level and Non Tidal Current\Non-Tidal Sea Level and Current.nc','vso');
F=squeeze(A);
G=squeeze(B);
H=squeeze(C);
I=squeeze(D);
J=squeeze(E);
A1=transpose(F);
B1=transpose(H);
C1=transpose(J);
Sea_Surface_Height='Non-Tidal Sea Level and Non Tidal Current\Sea Surface Height.xlsx';
Eastwards_Surface_Current='Non-Tidal Sea Level and Non Tidal Current\Eastwards Surface Current.xlsx';
Northwards_Surface_Current='Non-Tidal Sea Level and Non Tidal Current\Northwards Surface Current.xlsx';
xlswrite(Sea_Surface_Height,A1);
xlswrite(Eastwards_Surface_Current,B1);
xlswrite(Northwards_Surface_Current,C1);
```

A.2 Wind MetOcean Data

```
>> ncdisp('10-min wind data at 10-m Above Sea Level\Wind.nc')
Source:
        C:10-min wind data at 10-m Above Sea Level\Wind.nc
Format:
        64bit
Global Attributes:
        institution             = 'MSL'
        source                  = 'UDS'
        title                   = 'UDS data request'
        history                 = 'Mon Mar  5 13:29:27 2018: ncrcat -O /home/fmonetti/UDS_data/FWTS_WRF/Monthly
                                  2018-03-05 00:07:09 UTC : UDS Query: datum=msl&xy=174.7223,-35.8584,176.6424,↙
-37.2085&slfmt=bln&fmt=nc&var=ugrd10m,vgrd10m&type=hc&bnd=174.722300,176.642400,-37.208500,↙
-35.858400&sort=quality,-res&spinup=0&stepback=1&dset=nzra1_nz&dim=2.0,2.0&time=19790101.↙
000000,19790131.230000'
        NCO                     = '"4.5.4"'
        nco_openmp_thread_number = 1
Dimensions:
        dum1 = 1
        site = 2
        time = 324336 (UNLIMITED)
Variables:
    dum1
        Size:       1x1
        Dimensions: dum1
        Datatype:   int32
    lat
        Size:       2x1
        Dimensions: site
        Datatype:   single
    lon
        Size:       2x1
        Dimensions: site
        Datatype:   single
    site
        Size:       2x1
        Dimensions: site
        Datatype:   int32
    time
        Size:       324336x1
        Dimensions: time
        Datatype:   double
        Attributes:
                units = 'days since 0001-01-01 00:00:00'
    ugrd10m
        Size:       1x2x324336
        Dimensions: dum1,site,time
        Datatype:   single
        Attributes:
                missing_value = 9.969209968386869e+36
                long_name     = '10 m u wind [m/s]'
                units         = 'm/s'
                vpair         = 'None'
    vgrd10m
        Size:       1x2x324336
        Dimensions: dum1,site,time
        Datatype:   single
        Attributes:
                missing_value = 9.969209968386869e+36
                long_name     = '10 m v wind [m/s]'
```

```
57                  units       = 'm/s'
58                  vpair       = 'None'
59 A=ncread('10-min wind data at 10-m Above Sea Level\Wind.nc','ugrd10m');
60 B=ncread('10-min wind data at 10-m Above Sea Level\Wind.nc','vgrd10m');
61 M=squeeze(A);
62 N=squeeze(B);
63 X=transpose(M);
64 Y=transpose(N);
65 Eastward_Wind='10-min wind data at 10-m Above Sea Level\Eastward_Wind.xlsx';
66 Northward_Wind='10-min wind data at 10-m Above Sea Level\Northward_Wind.xlsx';
67 xlswrite(Eastward_Wind,X);
68 xlswrite(Northward_Wind,Y);
```

A.3 Wave MetOcean Data

```
>> ncdisp('Wave Data\Wave.nc')
Source:
        C:Wave Data\Wave.nc
Format:
        64bit
Global Attributes:
        institution          = 'MSL'
        source               = 'UDS'
        title                = 'UDS data request'
        history              = 'Tue Mar  6 11:19:30 2018: ncrcat -O /home/fmonetti/UDS_data/FWTS_SWAN/Monthly
                               2018-03-05 21:01:53 UTC : UDS Query: eval=dum=hs**2-hs_sw8**2,hs_sea8=dum**0.↙
5&datum=msl&xy=174.7223,-35.8584,176.6424,-37.2085&slfmt=bln&fmt=nc&var=dpm,dpm_sea8,dpm_sw8,hs,↙
hs_sea8,hs_sw8,tp,tp_sea8,tp_sw8&type=hc&bnd=174.722300,176.642400,-37.208500,-35.858400&sort=quality,-↙
res&spinup=0&stepback=1&dset=swan_nzra_nz-nzn&dim=2.0,2.0&time=19790101.000000,19790131.230000'
        NCO                  = '"4.5.4"'
        nco_openmp_thread_number = 1
Dimensions:
        time = 108555 (UNLIMITED)
        site = 2
        dum1 = 1
Variables:
    dpm
        Size:       1x2x108555
        Dimensions: dum1,site,time
        Datatype:   single
        Attributes:
                missing_value = 9.969209968386869e+36
                long_name     = 'Peak wave direction'
                units         = 'deg'
                vpair         = 'None'
    dpm_sea8
        Size:       1x2x108555
        Dimensions: dum1,site,time
        Datatype:   single
        Attributes:
                missing_value = 9.969209968386869e+36
                long_name     = 'Sea peak wave direction [8s]'
                units         = 'deg'
                vpair         = 'None'
    dpm_sw8
        Size:       1x2x108555
        Dimensions: dum1,site,time
        Datatype:   single
        Attributes:
                missing_value = 9.969209968386869e+36
                long_name     = 'Swell peak wave direction [8s]'
                units         = 'deg'
                vpair         = 'None'
    dum
        Size:       1x2x108555
        Dimensions: dum1,site,time
        Datatype:   single
        Attributes:
                units         = 'm'
                long_name     = 'Significant wave height'
                vpair         = 'None'
                missing_value = 9.969209968386869e+36
    dum1
        Size:       1x1
```

```
        Dimensions: dum1
        Datatype:   int32
hs
        Size:       1x2x108555
        Dimensions: dum1,site,time
        Datatype:   single
        Attributes:
                missing_value = 9.969209968386869e+36
                long_name     = 'Significant wave height'
                units         = 'm'
                vpair         = 'None'
hs_sea8
        Size:       1x2x108555
        Dimensions: dum1,site,time
        Datatype:   single
        Attributes:
                units         = 'm'
                long_name     = 'Significant wave height'
                vpair         = 'None'
                missing_value = 9.969209968386869e+36
hs_sw8
        Size:       1x2x108555
        Dimensions: dum1,site,time
        Datatype:   single
        Attributes:
                missing_value = 9.969209968386869e+36
                long_name     = 'Swell significant wave height'
                units         = 'm'
                vpair         = 'None'
lat
        Size:       2x1
        Dimensions: site
        Datatype:   single
lon
        Size:       2x1
        Dimensions: site
        Datatype:   single
site
        Size:       2x1
        Dimensions: site
        Datatype:   int32
time
        Size:       108555x1
        Dimensions: time
        Datatype:   double
        Attributes:
                units = 'days since 0001-01-01 00:00:00'
tp
        Size:       1x2x108555
        Dimensions: dum1,site,time
        Datatype:   single
        Attributes:
                missing_value = 9.969209968386869e+36
                long_name     = 'Peak wave period'
                units         = 's'
                vpair         = 'None'
tp_sea8
        Size:       1x2x108555
        Dimensions: dum1,site,time
```

```
        Datatype:   single
        Attributes:
                missing_value = 9.969209968386869e+36
                long_name     = 'Sea peak period'
                units         = 's'
                vpair         = 'None'
    tp_sw8
        Size:       1x2x108555
        Dimensions: dum1,site,time
        Datatype:   single
        Attributes:
                missing_value = 9.969209968386869e+36
                long_name     = 'Swell peak period'
                units         = 's'
                vpair         = 'None'
A=ncread('Wave Data\Wave.nc','hs');
B=ncread('Wave Data\Wave.nc','hs_sea8');
C=ncread('Wave.nc','hs_sw8');
D=ncread('Wave.nc','tp');
E=ncread('Wave.nc','tp_sea8');
F=ncread('Wave.nc','tp_sw8');
G=ncread('Wave Data\Wave.nc','dpm');
H=ncread('Wave Data\Wave.nc','dpm_sea8');
I=ncread('Wave Data\Wave.nc','dpm_sw8');
R=squeeze(A);
S=squeeze(B);
T=squeeze(C);
U=squeeze(D);
V=squeeze(E);
W=squeeze(F);
X=squeeze(G);
Y=squeeze(H);
Z=squeeze(I);
R1=transpose(R);
S1=transpose(S);
T1=transpose(T);
U1=transpose(U);
V1=transpose(V);
W1=transpose(W);
X1=transpose(X);
Y1=transpose(Y);
Z1=transpose(Z);
Total_Significant_Wave_Height='Wave Data\Total Significant Wave Height.xlsx';
Total_Significant_Wave_Height_of_Swell_Component='Wave Data\Total Significant Wave Height of Swell Component.xlsx';
Total_Significant_Wave_Height_of_Sea_Component='Wave Data\Total Significant Wave Height of Sea Component.xlsx';
Total_Peak_Period='Wave Data\Total Peak Period.xlsx';
Total_Peak_Period_of_Swell_Component='Wave Data\Total Peak Period of Swell Component.xlsx';
Total_Peak_Period_of_Sea_Component='Wave Data\Total Peak Period of Sea Component.xlsx';
Mean_Direction_at_Peak_Frequency='Wave Data\Mean Direction at Peak Frequency.xlsx';
Mean_Direction_at_Peak_Frequency_of_Swell_Component='Wave Data\Mean Direction at Peak Frequency of Swell Component.xlsx';
Mean_Direction_at_Peak_Frequency_of_Sea_Component='Wave Data\Mean Direction at Peak Frequency of Sea Component.xlsx';
xlswrite(Total_Significant_Wave_Height,R1);
xlswrite(Total_Significant_Wave_Height_of_Swell_Component,S1);
xlswrite(Total_Significant_Wave_Height_of_Sea_Component,T1);
xlswrite(Total_Peak_Period,U1);
```

```
xlswrite(Total_Peak_Period_of_Swell_Component,V1);
xlswrite(Total_Peak_Period_of_Sea_Component,W1);
xlswrite(Mean_Direction_at_Peak_Frequency,X1);
xlswrite(Mean_Direction_at_Peak_Frequency_of_Swell_Component,Y1);
xlswrite(Mean_Direction_at_Peak_Frequency_of_Sea_Component,Z1);
```

Appendix B

Linearising Element Nodes Definition

TABLE B.1: Linearising Element Nodes Definition

Linearisation Elements	Spatial Location (m)			Actual Diameter (m)	Actual Thickness (m)	Scaled Diameter (m)	Scaled Thickness (m)	Radius (m)	
	X	Y	Z					Outer	Inner
Center Column Point 1	0	0	-36	10.30	0.02	0.103	0.0002	0.0515	0.0513
Center Column Point 2	0	0	10						
Bottom Brace 1 - Point 1	-21.87	0	-1.5	2.50	0.02	0.025	0.0002	0.0125	0.0123
Bottom Brace 1 - Point 2	-5	0	-1.5						
Bottom Brace 2 - Point 1	10.93	18.94	-1.5	2.50	0.02	0.025	0.0002	0.0125	0.0123
Bottom Brace 2 - Point 2	2.5	4.33	-1.5						
Bottom Brace 3 - Point 1	10.93	-18.94	-1.5	2.50	0.02	0.025	0.0002	0.0125	0.0123
Bottom Brace 3 - Point 2	2.5	-4.33	-1.5						
Short Bottom Brace 1 - Point 1	-5.97	10.33	-1.5	2.50	0.02	0.025	0.0002	0.0125	0.0123
Short Bottom Brace 1 - Point 2	-2.5	4.33	-1.5						
Short Bottom Brace 2 - Point 1	11.93	0	-1.5	2.50	0.02	0.025	0.0002	0.0125	0.0123
Short Bottom Brace 2 - Point 2	5	0	-1.5						
Short Bottom Brace 3 - Point 1	-5.97	-10.33	-1.5	2.50	0.02	0.025	0.0002	0.0125	0.0123
Short Bottom Brace 3 - Point 2	-2.5	-4.33	-1.5						
Top Brace 1 - Point 1	-21.87	0	1.15	2.00	0.015	0.02	0.00015	0.01	0.00985
Top Brace 1 - Point 2	-3.5	0	6.61						
Top Brace 2 - Point 1	10.93	18.94	1.15	2.00	0.015	0.02	0.00015	0.01	0.00985
Top Brace 2 - Point 2	1.75	3.03	6.61						
Top Brace 3 - Point 1	10.93	-18.94	1.15	2.00	0.015	0.02	0.00015	0.01	0.00985
Top Brace 3 - Point 2	1.75	-3.03	6.61						
Main Hull Point 1	-30	0	-2	7.5	0.02	0.075	0.0002	0.0375	0.0373
Main Hull Point 2	15	25.98	-2						
Main Hull Point 3	15	-25.98	-2						

Appendix C

RAO Displacement Results for LC2

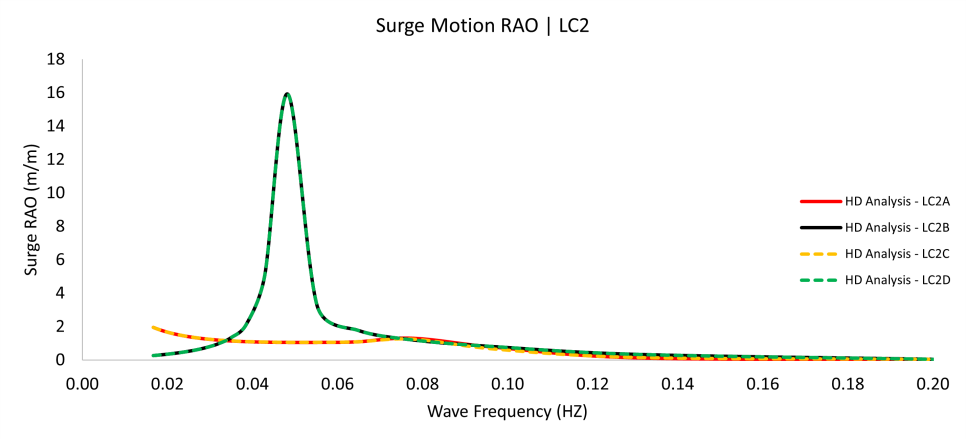

FIGURE C.1: FOWT surge motion displacement RAOs for a wave direction of 0 ° for various scenarios of LC2

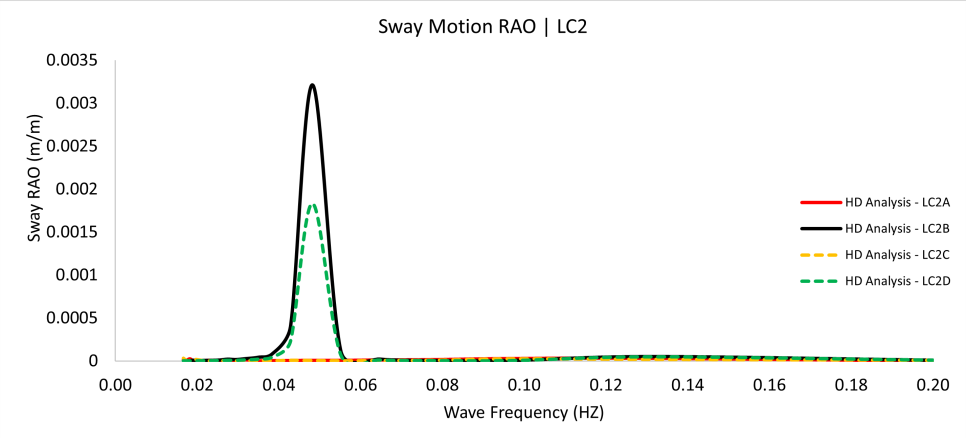

FIGURE C.2: FOWT sway motion displacement RAOs for a wave direction of 0° for various scenarios of LC2

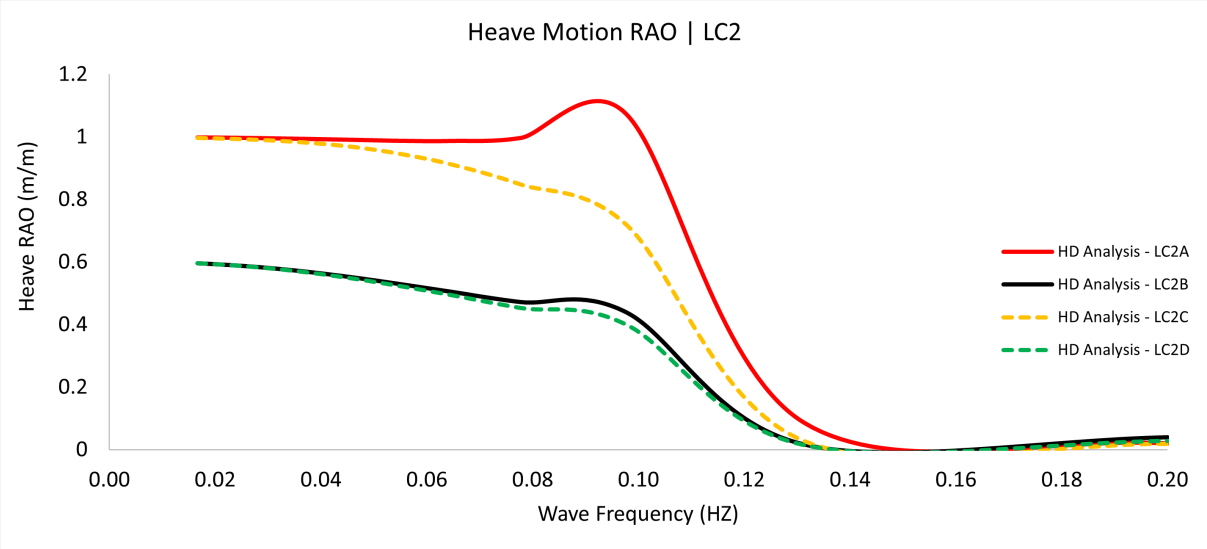

FIGURE C.3: FOWT heave motion displacement RAOs for a wave direction of 0° for various scenarios of LC2

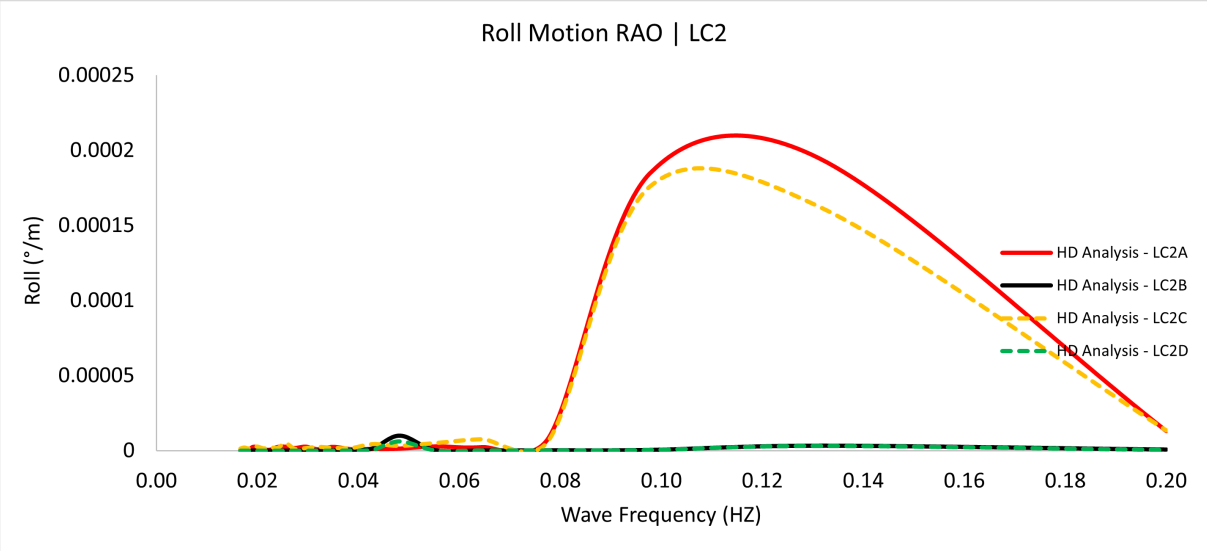

FIGURE C.4: FOWT roll motion displacement RAOs for a wave direction of 0° for various scenarios of LC2

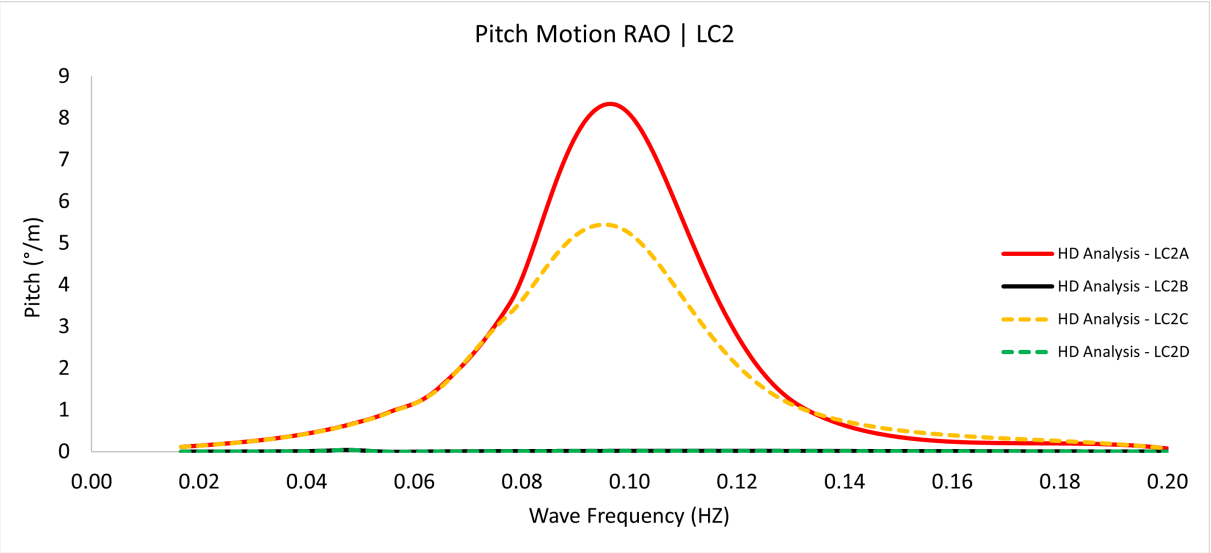

FIGURE C.5: FOWT pitch motion displacement RAOs for a wave direction of 0° for various scenarios of LC2

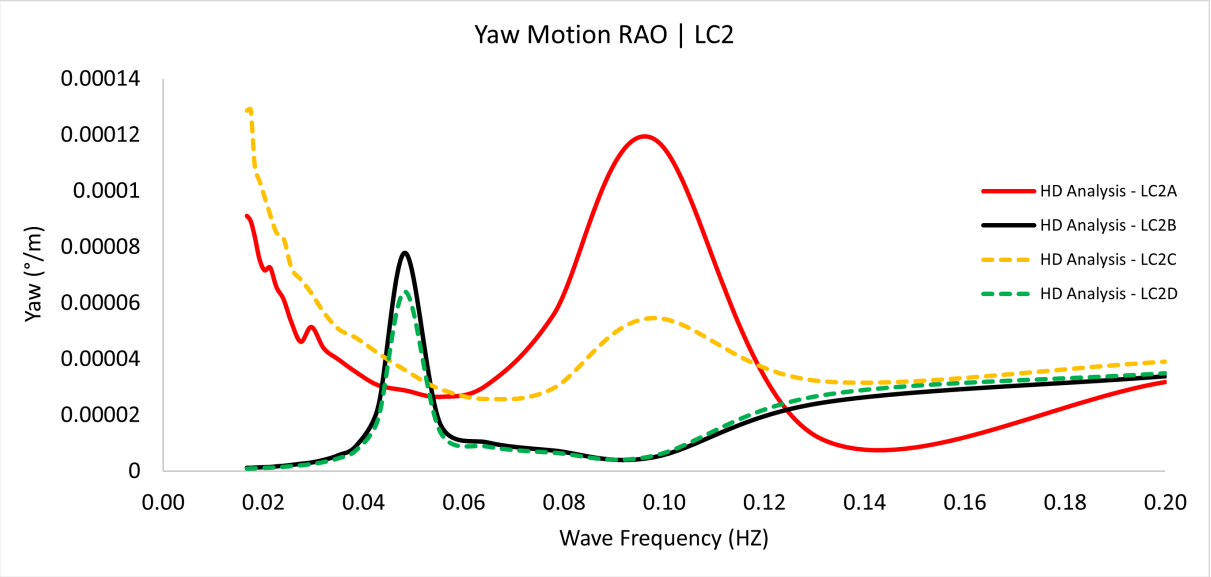

FIGURE C.6: FOWT yaw motion displacement RAOs for a wave direction of 0° for various scenarios of LC2

Appendix D

RAO Displacement Results for LC3

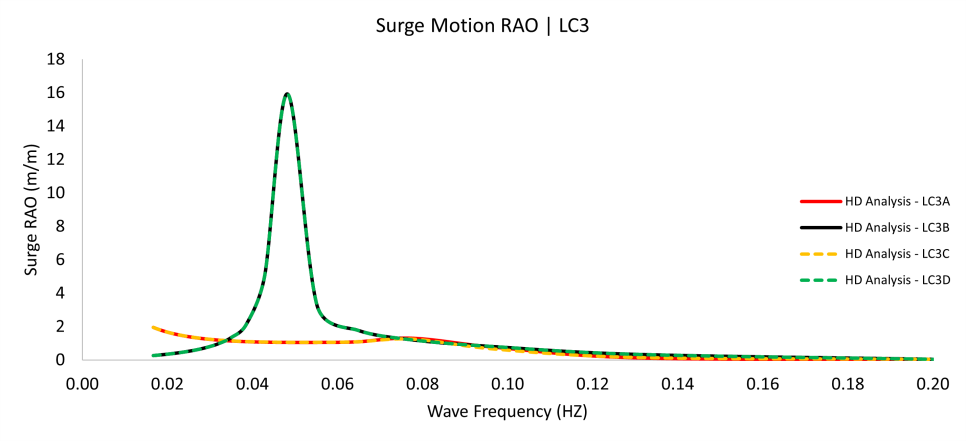

FIGURE D.1: FOWT surge motion displacement RAOs for a wave direction of 0° for various scenarios of LC3

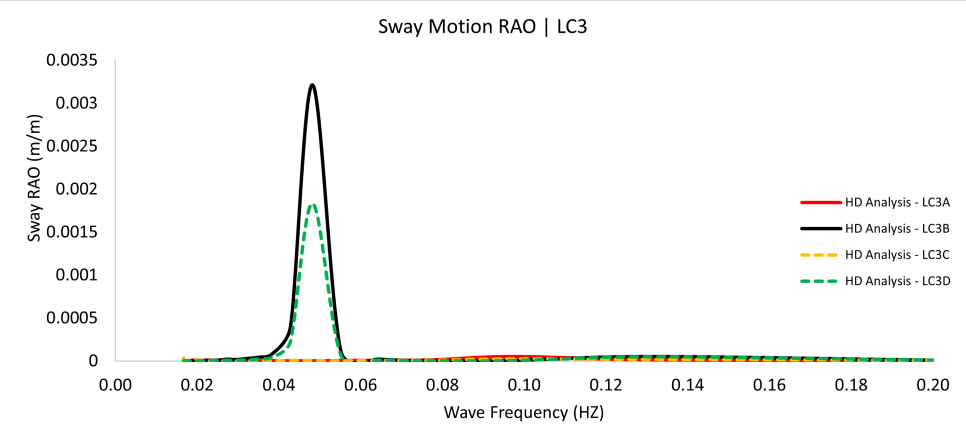

FIGURE D.2: FOWT sway motion displacement RAOs for a wave direction of 0° for various scenarios of LC3

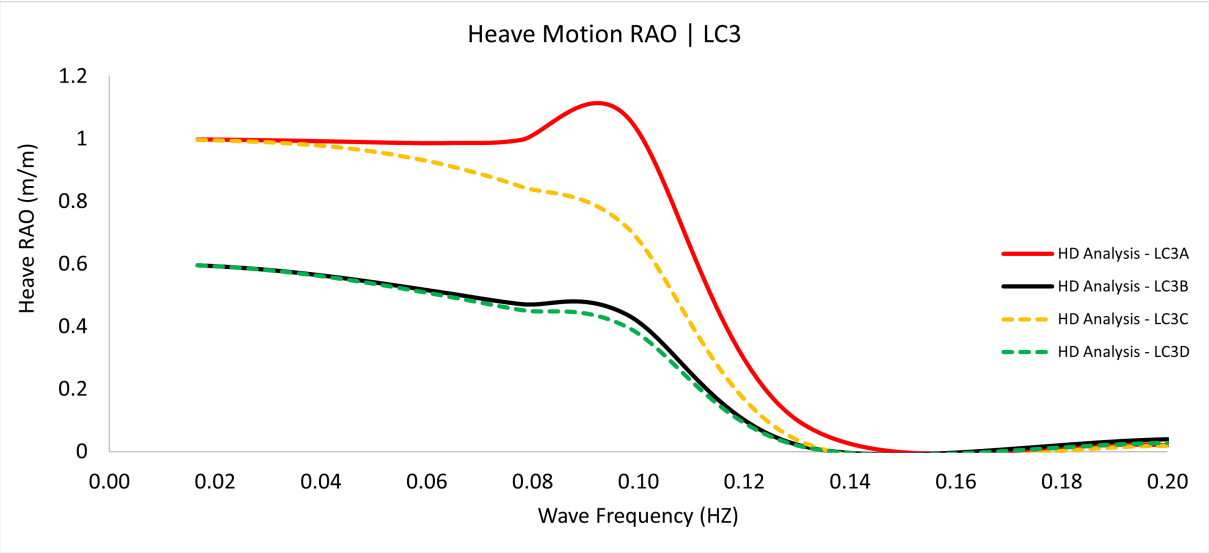

FIGURE D.3: FOWT heave motion displacement RAOs for a wave direction of 0° for various scenarios of LC3

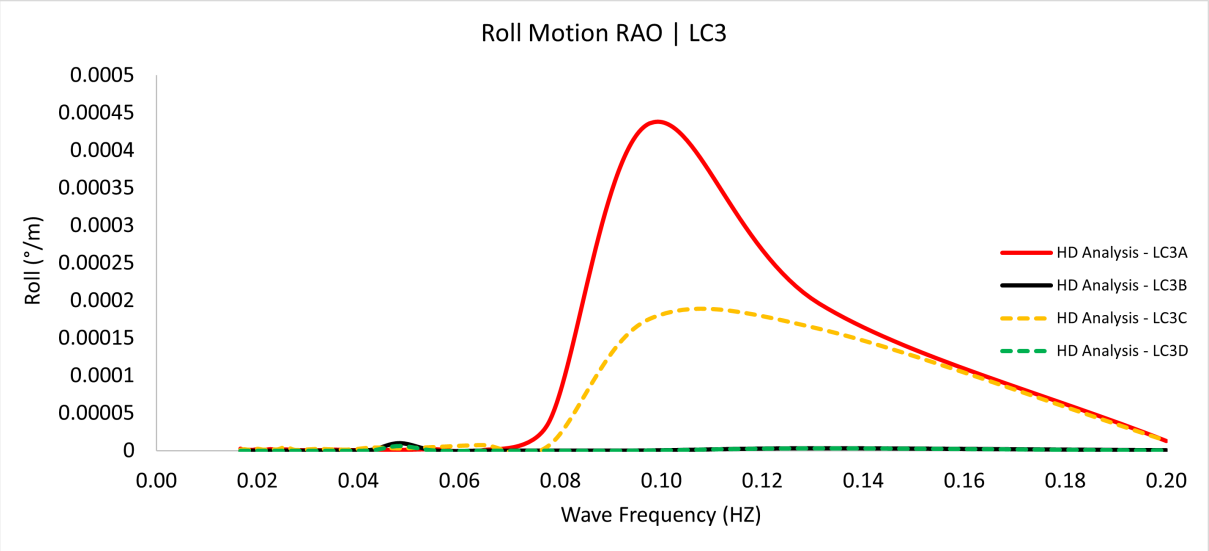

FIGURE D.4: FOWT roll motion displacement RAOs for a wave direction of 0° for various scenarios of LC3

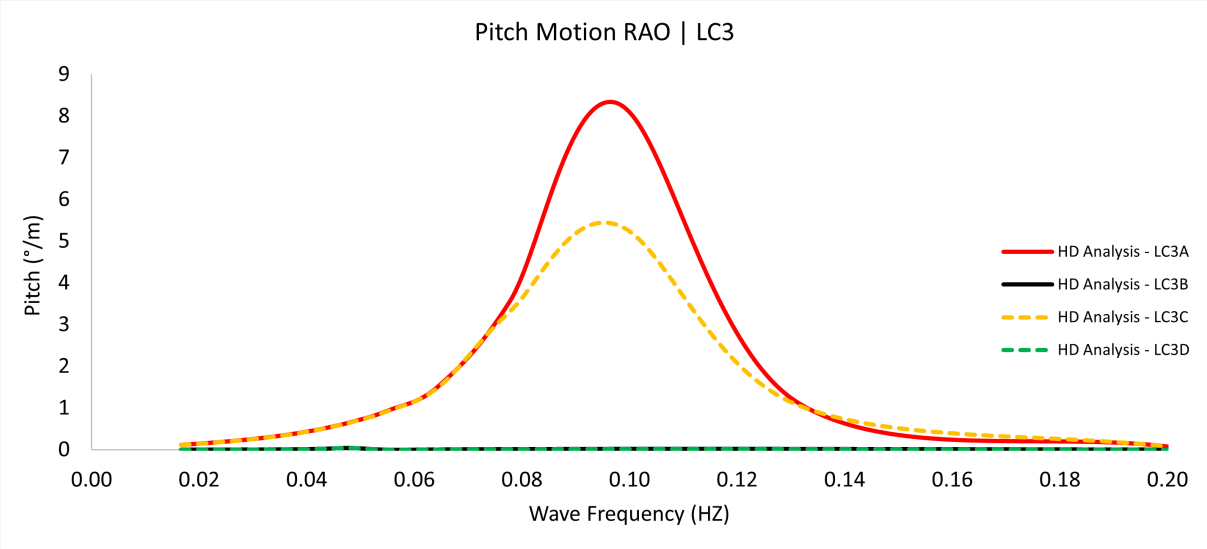

FIGURE D.5: FOWT pitch motion displacement RAOs for a wave direction of 0° for various scenarios of LC3

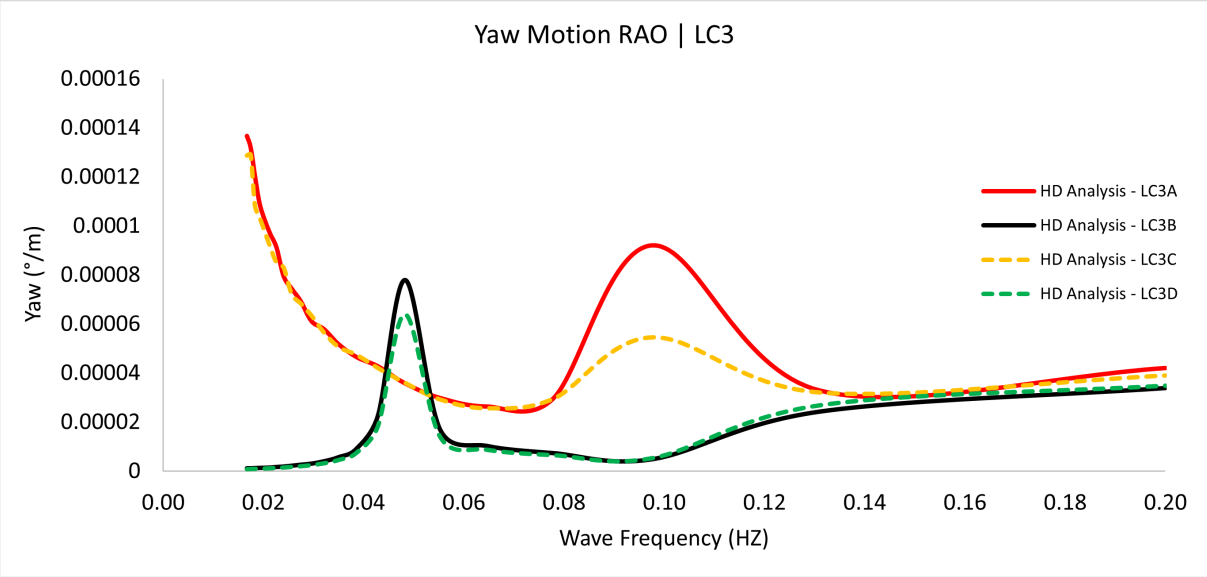

FIGURE D.6: FOWT yaw motion displacement RAOs for a wave direction of 0° for various scenarios of LC3

Bibliography

[1] R. Lizet, F. Daniel, and B. Guy, "The european offshore wind industry - key trends and statistics 2019," European Wind Energy Association (EWEA), Report, 2019.

[2] Global Wind Energy Council (GWEC), "Global wind statistics 2019," Global Wind Energy Council (GWEC), Report, 2019.

[3] Transparency Research Market, "Offshore wind energy market - global industry analysis, size, share, growth, trends, and forecast 2014 - 2022," Transparency Market Research, Report, 2015.

[4] Xodus Group Limited, *Hywind Scotland Pilot Park Project - EIA Scoping Report*. Edinburgh: Xodus Group Limited, 2013.

[5] Principal, *Wind Float*. Principal Power, 2015. [Online]. Available: http://www.principlepowerinc.com/en/windfloat.

[6] U. Tomoaki, S. Iku, and S. Takashi, "Floating offshore wind turbines in goto islands, nagasaki, japan," in *Large Floating Structures: Technological Advances*, C. Wang and B. Wang, Eds., Springer, pp. 129–156. DOI: https://doi.org/10.1007/978-981-13-8743-2_20.

[7] Fukushima Offshore Wind Consortium, *Fukushima Floating Offshore Wind Farm Demonstration Project*. Fukushima Offshore Wind Consortium, 2013. [Online]. Available: http://www.fukushima-forward.jp/project01/english/index.html.

[8] W. Steel, *France Gears up for Floating Wind*. Renewable World Energy, 2016. [Online]. Available: http://www.renewableenergyworld.com/articles/2016/11/france-gears-up-for-floating-wind.html.

[9] H. Stiesdal, "A new floater for offshore wind: 1 year and still on the right path," Stiesdal Offshore Technology A/S, Report, 2016.

[10] C. Pepe, "Tetraspar: Industralised floating foundation," Stiesdal Offshore Technology A/S, Report, 2017.

[11] W. David, "Gicon floating foundation construction underway," Wind Power Offshore, Report, 2014.

[12] SAITEC, *SAITEC Unveils New Floating Wind Platform*. 2017. [Online]. Available: http://www.saitec-offshore.com/2017/06/02/saitec-unveils-new-floating-wind-platform.

[13] H. Liz, *U.S. Conditions Drive Innovation in Offshore Wind Foundations*. Washington: Department of Energy, 2017.

[14] European Wind Energy Association (EWEA), *Wind Energy Basics: How a Wind Turbine Works*. Brussels: European Wind Energy Association, 2015.

[15] K. Madjid and M. Constantine, "Dynamic analysis of a braceless semisubmersible offshore wind turbine in operational conditions," *12th Deep Sea Offshore Wind R&D Conference, EERA DeepWind'2015*, vol. 80, pp. 21–29, 2015.

[16] J. D. Alexander, A. C. Brent, and G. P. Eric, "Development and validation of a tightly coupled cfd/6-dof solver for simulating floating offshore wind turbine platforms," *Ocean Engineering*, vol. 110, pp. 98–105, 2015.

[17] C. Antoni, G. Xin, S. Lian, and S. Fotis, "Fluid–structure interaction simulation of floating structures interacting with complex, large-scale ocean waves and atmospheric turbulence with application to floating offshore wind turbines," *Journal of Computational Physics*, vol. 355, pp. 144–175, 2018.

[18] G. Barakos, R. Steijl, K. Badcock, and A. Brocklehurst, "Development of cfd capability for full helicopter engineering analysis," in *31st European Rotorcraft Forum.*.

[19] P. Blanca and M. Aaron, "An investigation into the limitations of the panel method and the gap effects for a fixed and a floating structure subject to waves," in *Proceedings of the ASME 2016 35th International Conference on Ocean, Offshore and Arctic Engineering*.

[20] S. Boo, D. Kim, and S. Allen-Sheely, "Dynamic performance analysis of a new semi type floating offshore wind turbine platform," in *22nd Offshore Symposium*.

[21] M. R. Gomez-Gesteira, B. Crespo, A. Dalrymple, R. Narayanaswamy, M. Dominguez, and J. Sphysics, "Development of a free-surface fluid solver - part 1: Theory and formulations.," *Computers & Geosciences*, vol. 48, pp. 289–299, 2012.

[22] Y. Han, C. Le, H. Ding, Z. Cheng, and P. Zhang, "Stability and dynamic response analysis of a submerged tension leg," *Ocean Engineering*, vol. 129, pp. 68–82, 2017.

[23] A. Henderson and M. Patel, "On the modelling of floating offshore wind turbine," *Wind Energy*, pp. 53–86, 2003.

[24] F. Huijs, R. de-Bruijn, and F. Savenije, "Concept design verification of a semi-submersible floating wind turbine using coupled simulations," in *EERA DeepWind'2014, 11th Deep Sea Offshore Wind R&D Conference*.

[25] J. Jonkman, "The new modularisation framework for fast wind turbine cae tool," in *51st AIAA Aerospace Sciences Meeting*.

[26] J. Jonkman and D. Matha, *Dynamics of Offshore Floating Wind Turbine - Analysis of 3 Concepts*. Wind Energy, 2010.

[27] J. Jonkman, S. Butterfield, W. Musial, and G. Scott, *Definition of a 5-MW Reference Wind Turbine for Offshore System Development*. Colorado: National Renewable Energy Laboratory, 2009.

[28] J. Jonkman, *Dynamics Modeling and Loads Analysis of an Offshore Floating Wind Turbine, Doctoral Dissertation, University of Colorado at Boulder*. Boulder, Colorado: University of Colorado at Boulder, 2007.

[29] A. J. Coulling, A. J. Goupee, A. N. Robertson, J. M. Jonkman, and H. J. Dagher, "Validation of a fast semi-submersible floating wind turbine numerical model with deepcwind test data," *Journal of Renewable and Sustainable Energy*, vol. 5, no. 2, 2013, ISSN: 1941-7012. DOI: 10.1063/1.4796197.

[30] A. N. Robertson, F. Wendt, J. M. Jonkman, *et al.*, "OC5 project phase II: Validation of global loads of the deepcwind floating semisubmersible wind turbine," *Energy Procedia*, vol. 137, pp. 38–57, 2017, ISSN: 18766102. DOI: 10.1016/j.egypro.2017.10.333. [Online]. Available: http://www.sciencedirect.com/science/article/pii/S1876610217352931.

[31] The National Aeronautics and Space Administration (NASA), *Eastman N. 'Jake' Jacobs*. The National Aeronautics and Space Administration (NASA), 2017. [Online]. Available: https://www.nasa.gov/langley/hall-of-honor/eastman-n-jacobs.

[32] NASA, *NACA Airfoils*. The National Aeronautics and Space Administration (NASA), 2017. [Online]. Available: https://www.nasa.gov/image-feature/langley/100/naca-airfoils.

[33] The National Aeronautics and Space Administration (NASA), *Incorrect Theory 1*. National Aeronautics and Space Administration (NASA), 2000. [Online]. Available: https://www.grc.nasa.gov/www/k-12/airplane/wrong1.html.

[34] M. Hansen, "General introduction to wind turbines," in *Aerodynamics of Wind Turbines*. Routledge: Routledge, 2015, p. 3.

[35] H. Yi and S. R. Singiresu, "Robust design of horizontal axis wind turbines using taguchi method," *Journal of Mechanical Design*, vol. 133, 2011.

[36] S. Mathew, *Wind Energy: Fundamentals, Resource Analysis and Economics*. New York: Springer, 2006.

[37] T. Burton, D. Sharpe, N. Jenkins, and E. Bossanyi, *Wind Energy Handbook*. John Wiley & Sons, 2001, p. 64, ISBN: 9780471489979.

[38] C. Chima, "Computational Fluid Dynamics (CFD) Investigation of Hydrodynamic Loading on Subsea Gratings," Thesis, 2015. DOI: http://dx.doi.org/10.13140/RG.2.1.4367.6407.

[39] ANSYS Inc, *Aqwa Theory Manual*. Canonsburg: ANSYS Inc, 2015.

[40] N. Barltrop, *Floating Structures: A Guide for Design and analysis*. CMPT and OPL, 1998.

[41] C. Srinivasan, *Dynamic Analysis and Design of Offshore Structures*. New Delhi: Springer, 2015.

[42] A. Davenport, "The spectrum of horizontal gustiness near the ground in high winds," *Journal Roy, Meteorol Society*, vol. 87, pp. 194–211, 1961.

[43] R. Harris, "The nature of wind, the modern design of wind-sensitive structures," *Const. Ind. Res & Inf. Assn.*, pp. 29–55, 1971.

[44] J. Kaimal, "Spectral characteristics of surface layer turbulence," *Roy. Meteorol Society*, vol. 98, pp. 563–589, 1972.

[45] American Petroleum Institute (API), *Planning, Designing and Constructing Fixed Offshore Platforms - Working Stress Design, API RP2A-WSD*, 21st Edition. Washington: American Petroleum Institute (API), 2014.

[46] M. Ochi and Y. Shin, "Wind turbulent spectral for design consideration of offshore structures," in *Offshore Technology Conference (OTC)*.

[47] Det Norske Veritas (DNV), *2.3.4: Wind Spectra* (Recommended Practice (DNV-RP-C205): Enviromental Conditions and Environmental Loads). Oslo: Det Norske Veritas (DNV), 2010, p. 20.

[48] Det Norske Veritas (DNV), *Design of Floating Wind Turbine Structures (DNV-OS-J103)*. Oslo: DET Norske Veritas AS, 2013.

[49] Det Norske Veritas (DNV), *Stability and Watertight Integrity (DNV-OS-C301)*. DET Norske Veritas AS, 2011.

[50] Z. Ye, A. v. Zuijlen, and G. v. Bussel, "The mexico rotor aerodynamic loads prediction: Zigzag tape effects and laminar-turbulent transition modeling in cfd," *Journal of Wind Engineering & Industrial Aerodynamics*, vol. 168, pp. 152–163, 2010.

[51] J. Zhiyu, K. Madjid, and M. Torgeir, "Dynamic response analysis of wind turbines under blade pitch system fault, grid loss, and shutdown events," *Wind Energy*, vol. 17, pp. 1385–1409, 2013.

[52] E. S. Politis, P. K. Chaviaropoulos, V. A. Riziotis, S. G. Voutsinas, and I. Romero-Sanz, *Stability analysis of parked wind turbine blades*. Greece, 2009.

[53] R. Shirzadeh, W. Weijtjens, P. Guillaume, and C. Devriendt, "The dynamics of an offshore wind turbine in parked conditions: A comparison between simulations and measurements," *Wind Energy*, vol. 18, pp. 1685–1702, 2015.

[54] E. Mahmoud, B. Mogens, G. Zhen, and M. Torgeir, "Response analysis and comparison of a spar-type floating offshore wind turbine and an onshore wind turbine under blade pitch controller faults," *Wind Energy*, vol. 19, pp. 35–50, 2016.

[55] S. Emil, S. Asgeir, and E. Lene, "Wind model for simulation of thrust variations on a wind turbine," in *13th Deep Sea Offshore Wind R&D Conference, EERA DeepWind*.

[56] M. Borg and M. Collu, "Frequency-domain characteristics of aerodynamic loads of offshore floating vertical axis wind turbines," *Applied Energy*, vol. 155, pp. 629–636, 2015.

[57] Q. Li, K. Yasunari, M. Takao, M. Junsuke, and I. Kohei, "Fundamental study on aerodynamic force of floating offshore wind turbine with cyclic pitch mechanism.," *Energy*, vol. 99, pp. 20–31, 2016.

[58] S. M. Salman, R. Adil, K. Trond, and T. Mandar, "Quasi-static & dynamic numerical modelling of full scale nrel 5 mw wind turbine," in *14th Deep Sea Offshore Wind R&D Conference, EERA DeepWind'2017*.

[59] W. Binrong, T. Xinliang, D. Xingjian, P. Zhike, and Z. Wenming, "Influences of surge motion on the power and thrust characteristics of an offshore floating wind turbine," *Energy*, no. 141, pp. 2054–2068, 2017.

[60] S. Xin, C. Jinge, H. Ping, Z. Xiaocheng, and D. Zhaohui, "Study of the unsteady aerodynamics of floating wind turbines," *Energy*, vol. 143, pp. 793–809, 2018.

[61] B. Dose, H. Rahimi, J. Peinke, B. Stoevesandt, and I. Herraez, "Fluid-structure coupled computations of the nrel 5mw wind turbine by means of cfd," *Renewable Energy*, 2018.

[62] C. Srinivasan and S. K. Bhattacharyya, *Analysis and Design of Offshore Structures with illustrated examples*. Human Resource Development Center for Offshore and Plant Engineering (HOPE Center): Changwon National University Press, Republic of Korea, 2012.

[63] B. L. Méhauté, *An introduction to hydrodynamics and water waves*. Springer, 1976.

[64] J. Wheeler, "Method for calculating forces," *Journal of Petroleum*, vol. 22, no. 3, pp. 359–367, 1970.

[65] S. Chakrabarti, *Offshore structure modeling*. Singapore: World Scientific, 1994.

[66] G. Rodenbusch and G. Forristall, "An empirical model for random directional wave kinematics near the free surface," in *Proceedings of the 18th Offshore Technology Conference*.

[67] P. Marshall and R. Inglis, "Wave kinematics and force coefficients," in *ASCE Structures*.

[68] N. Barltrop, *Floating Structures: A guide for design and analysis*. CMPT and OPL, 1998, vol. 1.

[69] X. Chen, "The set-down in the second-order stokes'waves," in *Seventh International Conference on Hydrodynamics*.

[70] American Petroleum Institute (API), *Recommended practice for planning, designing and constructing fixed offshore platforms*. Washinton DC: American Petroleum Institute (API), 1989.

[71] S. Wanan, *Fluid Dynamics: Boundary Element Method (BEM) - Wave Structure Interaction Fundamentals*. 2019.

[72] K. James, *Mathematical Physics with Partial Differential Equations*. Elsevier, 2018.

[73] V. J. Katz, "The history of stokes's theorem," *Mathematics Magazine*, vol. 52, no. 3, pp. 146–156, 1979.

[74] M. Anderson, "Who gave you the epsilon?: And other tales of mathematical history," *Mathematical Association of America*, pp. 78–79, 2009.

[75] A. Mariam, M.-C. Sergio-Camilo, H. Ahmad, and B. Seddik, *A comparative study on a pumping wave energy conversion system*. IEEE, 2012.

[76] Det Norske Veritas(DNV), *Loads and Sites Conditions for Wind Turbines (DNVGL-ST-0437)*. Oslo: DET Norske Veritas AS, 2016.

[77] E. Marino, C. Lugni, and C. Borri, "A novel numerical strategy for the simulation of irregular nonlinear waves and their effects on the dynamic response of offshore wind turbines," *Computer Methods in Applied Mechanics and Engineering*, no. 255, pp. 275–288, 2013.

[78] Y. Ma, Z. Hu, and L. Xiao, "Wind-wave induced dynamic response analysis for motions and mooring loads of a spar-type offshore floating wind turbine.," *Journal of Hydrodynamics*, vol. 26, no. 6, pp. 865–874, 2015.

[79] A. Ullah, N. Muhammad, and D. Choi, "Effect of hydrostatic nonlinearity on the large amplitude response of a spar type floating wind turbine.," *Ocean Engineering*, vol. 172, no. 172, pp. 803–816, 2019.

[80] K. Ye and J. Ji, "Current, wave, wind and interaction induced dynamic response of a 5mw spar-type offshore direct-drive wind turbine.," *Engineering Structure*, vol. 178, pp. 395–409, 2019.

[81] C. Zhenju, L. Shewen, and L. Yu, "Influence of second order wave excitation loads on coupled response of an offshore floating wind turbine," *International Journal of Naval Architecture and Ocean Engineering*, vol. 12, pp. 367–375, 2020.

[82] P.-J. Antonio, B. Michael, and B. Henrik, "An efficient frequency-domain model for quick load analysis of floating offshore wind turbines," *Wind Energy Science*, vol. 3, pp. 693–712, 2018.

[83] D. P. Thanh, H. Shin, B. Kim, and K. Jung, *Motion of OC4 5MW Semi-Submersible Offshore Wind Turbine in Irregular Waves*. 2013. DOI: 10.1115/OMAE2013-10463.

[84] H. Matthew and G. Andrew, "Validation of a lumped-mass mooring line model with deepcwind," *Ocean Engineering*, vol. 104, pp. 590–603, 2015.

[85] P. Blanca, "Engineering approach for quay-side ring subject to waves," in *SNAME World Maritime Technology Conference.*.

[86] V. Leble and G. Barakos, "A coupled floating offshore wind turbine analysis with high-fidelity methods," in *13th Deep Sea Offshore Wind R&D Conference, EERA DeepWind'2016*, Elsevier, pp. 523–530.

[87] M. Gomez-Gesteira, B. Rogers, A. Crespo, R. Dalrymple, M. Narayanaswamy, and J. Dominguez, "Development of a free-surface fluid solver - part 1: Theory and formulations.," *Computers & Geosciences*, vol. 48, pp. 289–299, 2012.

[88] M. Woodgate, G. Barakos, N. Scrase, and T. Neville, "Simulation of helicopter ditching using smoothed particle hydrodynamics," in *39th European Rotorcraft Forum*.

[89] M. K. Al-Solihat and M. Nahon, "Flexible multibody dynamic modeling of a floating wind turbine," *International Journal of Mechanical Sciences*, pp. 518–529, 2018.

[90] Y. Bae and M. Kim, "Ocean engineering," *Rotor-floater-tether coupled dynamics including second-order sum–frequency wave loads for a mono-column-TLP-type Foating Offshore Wind Turbine*, vol. 61, pp. 109–122, 2013.

[91] Y. Bae and M. Kim, "Ocean engineering," *Coupled Dynamic Analysis of Multiple Wind Turbines*, vol. 92, pp. 175–187, 2014.

[92] Det Norske Veritas (DNV), *Design of Offshore Wind Turbine Structures (DNV-OS-J101)*. Oslo: DET Norske Veritas AS, 2014.

[93] National Institute of Water and Atmospheric (NIWA), *New Zealand Bathymetric Undersea Feature Names with Contours*. Auckland: National Institute of Water and Atmospheric (NIWA), 2008.

[94] P. Anni, d. A. Adrian, and H. Scott, *Fixed vs Floating Foundations*. 2020. [Online]. Available: https://www.xodusgroup.com/wp-content/uploads/2020/06/Fixed-vs-Floating-Wind.pdf.

[95] Transpower-Limited, *Transpower Transmission Network: North Island*. Auckland: Transpower, 2014.

[96] Northport-Limited, *Northport offers deep-water access to the world | Northport*. 2018. [Online]. Available: http://www.northport.co.nz/.

[97] MarineTraffic, *Ship Tracking Intelligence Service*. marinetraffic.com, 2020. [Online]. Available: www.marinetraffic.com.

[98] Ministry for Primary Industries, *New Zealand Amateur Fishing - Amateur and Charter Fishing Vessels*. Auckland: Ministry for Primary Industries, 2015.

[99] Civil Aviation Authority (CAA) of New Zealand, *Part 77 - Objects and Activities Affecting Navigable Airspace*. Auckalnd: Civil Aviation Authority (CAA) of New Zealand, 2014.

[100] Airshare, *New Zealand Airspace Maps for Drone Pilots*. Airways New Zealand, 2020. [Online]. Available: https://www.airshare.co.nz/maps.

[101] Ufocus, *New Zealand Scheduled Flight Paths Map*. 2020. [Online]. Available: http://www.ufocusnz.org.nz/content/New-Zealand-Scheduled-Flight-Paths-Map/74.aspx.

[102] Department of Conservation (Te Papa Atawhai), *Marine Reserves Maps in New Zealand*. Auckland: Department of Conservation (Te Papa Atawhai), 2018.

[103] National Institute of Water and Atmospheric (NIWA), *New Zealand Regional Bathymetry (2016)*. Auckland: National Institute of Water and Atmospheric (NIWA) Research, 2016.

[104] National Institute of Water and Atmospheric (NIWA), *New map reveals New Zealand's seafloor in stunning detail*. Auckland: National Institute of Water and Atmospheric (NIWA), 2012.

[105] A. Rowden, *Sea floor - Life on the deep sea floor*. Te Ara - the Encyclopedia of New Zealand, 2006. [Online]. Available: http://www.TeAra.govt.nz/en/map/8953/chatham-rise.

[106] S. MetOcean, *MetoceanView*. MetOcean Solutions. [Online]. Available: https://metoceanview.com/.

[107] V. Chow, "Frequency analysis of hydrological data with special application to rainfall intensities," in University of Illinois, 1953, ch. 12, pp. 18–20.

[108] M. Venkatesh, *Frequency Analysis - Reading: Applied Hydrology Chapter 12*. 2006, pp. 1–28.

[109] V. Chow, "A general formula for hydrologic frequency analysis," *Transactions American Geophysical Union*, vol. 32, no. 2, pp. 231–237, 1951.

[110] S. Jean-Baptiste, "Uncertainty in peakedness factor estimation by jonswap spectral fitting from measurements," in *ASME 2013 32nd International Conference on Ocean, Offshore and Arctic Engineering*, vol. 5.

[111] W. Musial, S. Butterfield, and A. Boone, "Feasibility of floating platform systems for wind turbines.," in *23rd ASME Wind Energy Symposium*.

[112] D. J. Malcolm and A. C. Hansen, *WindPACT Turbine Rotor Design Study*. National Renewable Energy Laboratory, 2002.

[113] H. Kooijman, C. Lindenburg, D. Winkelaar, and E. van der Hooft, "Aero-elastic modelling of the dowec 6 mw pre-design in phatas (dowec-f1w2-hjk-01-046/9)," 2003.

[114] N. Timmer, *NREL 5MW Blade Aerofoil*. Delft: Faculty of Aerospace Engineering, Delft University of Technology, 2011.

[115] Wind and wet, *Airfoil Tools*. [Online]. Available: http://airfoiltools.com.

[116] R. James and C. Ross, *Floating Offshore Wind: Market and Technology Review*. 2015.

[117] E. Mast, R. Rawlinson, and C. Sixtensson, *Market study floating wind in the Netherlands: Potential of Floating offshore wind*. 2015.

[118] A. Bossler, "Floating Offshore Wind Foundations: Industry Projects in the USA, Europe and Japan," Maine International Consulting, Inc., Report, 2011.

[119] F. Rob, "Rising to the engineering challenge of floating offshore wind," Feritech, Report, 2021. [Online]. Available: https://www.feritech.com/rising-to-the-engineering-challenge-of-floating-offshore-wind/.

[120] G. Stewart and M. Muskulus, "A review and comparison of floating offshore wind turbine model experiments," *Energy Procedia*, vol. 94, pp. 227–231, 2016. DOI: 10.1016/j.egypro.2016.09.228.

[121] C. M. Wang, T. Utsunomiya, S. C. Wee, and Y. S. Choo, "Research on floating wind turbines: A literature survey," *The IES Journal Part A: Civil & Structural Engineering*, vol. 3, no. 4, pp. 267–277, 2010, ISSN: 1937-3260. DOI: 10.1080/19373260.2010.517395. [Online]. Available: https://doi.org/10.1080/19373260.2010.517395.

[122] K. P. Thiagarajan and H. J. Dagher, "A review of floating platform concepts for offshore wind energy generation," *Journal of Offshore Mechanics and Arctic Engineering*, vol. 136, no. 2, 2014, ISSN: 0892-7219. DOI: 10.1115/1.4026607. [Online]. Available: https://doi.org/10.1115/1.4026607.

[123] S. Butterfield, W. Musial, J. Jonkman, and P. Sclavounos, "Engineering challenges for floating offshore wind turbines," Research Org.: National Renewable Energy Lab. (NREL), Golden, CO (United States), 2007. [Online]. Available: https://www.osti.gov/biblio/917212%20https://www.osti.gov/servlets/purl/917212.

[124] L. Carol, *NREL Market Report Finds U.S. Offshore Wind Industry Poised for Multigigawatt Surge*. National Renewable Energy Laboratory (US Department of Energy), 2017. [Online]. Available: https://www.nrel.gov/news/program/2017/nrel-market-report-finds-us-offshore-wind-industry-poised-multigigawatt-surge.html.

[125] Det Norske Veritas(DNV), *Global Performance Analysis of Deepwater Floating Structures (DNV-RP-F205)*. Hovik: Det Norske Veritas (DNV), 2004.

[126] P. Daniel, *Ballast for offshore wind turbines*. Sweden, 2020. [Online]. Available: https://www.lkabminerals.com/en/industry-uses/offshore-energy/offshore-wind-structures/.

[127] American Galvanizers Association, *Weight Increase*. 2020. [Online]. Available: https://galvanizeit.org/design-and-fabrication/design-considerations/weight-increase.

[128] F. L. James, "Table 12-1 in the procedure handbook of arc welding helps determine weld metal needs based on joint geometry.," in *The Procedure Handbook of Arc Welding*. 2003.

[129] Lankhorst, *Ropes for Deepwater Mooring*. 2020. [Online]. Available: www.lankhorstropes.com.

[130] DeepRope, *Deepwater Mooring Lines*. 2007. [Online]. Available: www.vryhof.com.

[131] M. Al-Solihat and M. Nahon, *Mooring and hydrostatic restoring of offshore floating wind turbine platforms*, Generic, 2014. DOI: 10.1109/OCEANS.2014.7003269.

[132] C. Clement, S. Kosleck, and T. Lie, "Investigation of viscous damping effect on the coupled dynamic response of a hybrid floating platform concept for offshore wind turbines," *Ocean Engineering*, vol. 225, p. 108 836, 2021, ISSN: 0029-8018. DOI: https://doi.org/10.1016/j.oceaneng.2021.108836. [Online]. Available: https://www.sciencedirect.com/science/article/pii/S0029801821002717.

[133] J. John D. Anderson, *Computational Fluid Dynamics: The Basics with Applications*. New York: McGraw-Hill, Inc., 1995.

[134] V. R. Vivek, "Chapter 3 - turbulent flow processes: Modeling approaches," in *Computational Flow Modeling for Chemical Reactor Engineering*. California: Academic Press, 2002, pp. 64–70.

[135] J. Journée and W. Massie, *Offshore Hydromechanics*, 1st ed. Delft University of Technology, 2001, pp. 303–310.

[136] H.-J. Koh and I.-H. Cho, "Heave motion response of a circular cylinder with the dual damping plates," *Ocean Engineering*, vol. 125, pp. 95–102, 2016, ISSN: 00298018. DOI: 10.1016/j.oceaneng.2016.07.037.

[137] ANSYS Inc, *Introduction to ANSYS CFX - Lecture 7: Turbulence Modeling*. Pennsylvania: ANSYS Inc., 2015.

[138] U. Piomelli, "Large-eddy simulation: Achievements and challenges," *Progress in Aerospace Sciences*, vol. 35, pp. 335–362, 1999.

[139] ANSYS Inc, *ANSYS CFX-Solver Modeling Guide*. Canonsburg: ANSYS Inc., 2013.

[140] M. Longuet-Higgins, "The mean forces exerted by waves on floating or submerged bodies with applications to sand bars and power machines," *Proceedings of the Royal Society*, no. 352, pp. 463–480, 1977.

[141] K. Hyeok-Jun and I.-H. Cho, "Computation of the inviscid drift force caused by nonlinear waves on a submerged circular cylinder," *Inter J Nav Archit Oc Engng*, vol. 3, pp. 201–207, 2011.

[142] K. Sascha, "Prediction of wave–structure interaction by advanced wave field forecast," Thesis, 2013.

[143] Electronic Book Section. [Online]. Available: https://www.usna.edu/NAOE/_files/documents/Courses/EN330/Rayleigh-Probability-Distribution-Applied-to-Random-Wave-Heights.pdf.